IMPERIAL COLLEGE OF SCIENCE, TECHNOLOGY AND MEDICINE

University of London

THE REFLECTION COEFFICIENT FROM INTERFACE LAYERS IN NDT OF ADHESIVE JOINTS

by

Tomasz Piotr Pialucha

A thesis submitted to the University of London for
the degree of Doctor of Philosophy

Department of Mechanical Engineering
Imperial College of Science, Technology and Medicine

January 1992

BIBL
LONDON
UNIV

Abstract

The structural integrity of adhesive joints is known to be dependent on the properties of the adhesive (cohesive properties) and the properties of the adherend/adhesive interface (adhesive properties). Despite a substantial research effort worldwide there is no currently available nondestructive technique to test for interfacial defects in adhesive joints. However, ultrasonic methods have been identified as the most promising techniques for these purposes. It is therefore desirable to asses their suitability.

This thesis presents an evaluation of the ultrasonic reflection coefficient method and, in particular, the oblique incidence method, for the nondestructive characterisation of adherend/adhesive interfaces in bonded joints. The technique uses two ultrasonic transducers inclined at an angle, operating in a pitch-catch mode, with respect to the tested joint.

A theoretical model is developed which is capable of accurate predictions of reflection and transmission coefficients from isotropic multilayered, viscoelastic plates, excited at normal and oblique incidences by ultrasonic transducers of finite sizes. Experiments are performed on simple model systems for the theory validation. The measured reflection coefficient amplitudes are found to be within 5 % of the predicted values.

Theoretical and experimental work is carried out to find the optimal arrangement of the probes, frequency range and type of reflection in order to achieve maximum sensitivity to changes in the adherend/adhesive interfaces. It is found that the oblique incidence techniques can offer a substantial increase in sensitivity to interfacial properties over the current standard inspection techniques, but the results obtained indicate that the improvement is unlikely to be sufficient for the technique to be used as a new reliable nondestructive procedure.

Acknowledgements

Contents

CHAPTER 1

Background

CHAPTER 2

The reflection coefficient from the interface between two
semi-infinite viscoelastic media

CHAPTER 3

The reflection coefficient from a multilayered
viscoelastic plate

CHAPTER 4

Theoretical predictions of the reflection coefficient
from thin layers

CHAPTER 5

Validation of the theory.
Accuracy of the reflection coefficient measurements

CHAPTER 6

Monitoring of interfacial conditions at a glass/epoxy interface using the reflection coefficient technique

CHAPTER 7

Sensitivity of the reflection coefficient method for the determination of the interfacial properties in adhesive joints

CHAPTER 8

Conclusions and suggestions for further work

Appendix A   Amplitude spectrum method for the measurement of phase velocity.

Appendix B   Phase velocity and attenuation of the shear wave in viscous fluids.

Appendix C   Frequency-thickness product invariance of the wave equation.

List of tables

List of figures

Nomenclature

$\mathscr{B}$	Stress-displacement transfer matrix for a boundary
c	Phase velocity
d	Thickness of a layer
E	Elastic constant
f	Frequency
i	Imaginary part, also an index
j	Index
k	Index, also a magnitude of a wavenumber vector
$\bar{k}$	Wavenumber
L	Thickness of a layer
$\mathscr{K}$	Stiffness matrix of a boundary
$\mathscr{L}$	Stress-displacement transfer matrix for a layer
$\mathscr{M}$	Stress-displacement field matrix for a single layer
$\bar{N}$	Vector characterising the direction of wave propagation
$\mathscr{P}$	Stress-displacement transfer matrix for a plate
R	Reflection coefficient
R_{LL}	Longitudinal-longitudinal reflection coefficient
R_{LS}	Longitudinal-shear reflection coefficient
R_{SL}	Shear-longitudinal reflection coefficient
R_{SS}	Shear-shear reflection coefficient
R_p	Complex amplitude of a reflected longitudinal wave
T_s	Complex amplitude of a reflected shear wave
T	Transmission coefficient
T_p	Complex amplitude of a transmitted longitudinal wave
T_s	Complex amplitude of a transmitted shear wave
$\bar{u}$	Displacement field
$\bar{x}$	Position of a given point with respect to the origin of a coordinate system

z	Acoustic impedance
α	Complex number characterising the velocity and attenuation of a longitudinal wave
β	Complex number characterising the velocity and attenuation of a shear wave
δ_{ij}	Kronecker delta
ε	Strain
θ	Angle of incidence, also an angle between two vectors
λ	Lamé's constant
μ	Lamé's constant
ρ	Density
σ	Stress component
$\bar{\sigma}$	Stress vector
ϕ	Wave potential
φ	Phase angle
$\bar{\psi}$	Wave potential
ω	Angular frequency

CHAPTER 1

Background

1.1 Introduction

In order to maintain their top positions in world markets, highly developed industrial nations constantly increase the quality and cost effectiveness of their products. It is therefore of crucial importance for these countries to be innovative in design, manufacturing and service support of their products. Nondestructive testing is the field of science and engineering which provides the industry with the necessary tools to determine the quality of products during both manufacturing and service. Nondestructive testing, therefore, plays an ever increasing role in maintaining the leading edge over the competitors in areas where the reliability of products are of prime importance, especially in the nuclear, defence and aerospace industries.

Nondestructive testing (NDT) techniques are those which can define the quality of the product without causing damage to it. It is therefore natural that nondestructive testing enjoys increasing demand in industry and a substantial research effort is put towards development and improvement of NDT methods.

In section 1.2 different types of defects found in adhesive joints are described and classified into three basic categories: disbonds and porosity, poor cohesion and poor adhesion.

In section 1.3 the various NDT techniques used for the detection of disbonds and porosity are reviewed and the current advances in testing for cohesive properties in adhesive joints are presented.

In section 1.4 the problem of testing for poor adhesion using ultrasonic waves, which is the subject of this thesis, is given more detailed attention. In this section various theoretical models of an interface between two solids are presented. Two different testing strategies for poor adhesion, the modal approach and the reflection coefficient approach, are introduced and discussed in more detail.

In section 1.5 the main objectives of this thesis are formulated and the main anticipated

difficulties are listed. In section 1.6 the outline of the thesis is presented and the contents and a purpose of each chapter are briefly described.

1.2 Defects in adhesive joints

The types of defects found in adhesive joints have been classified by many authors (Kinloch 1983, Adams and Wake 1984, Guyott *et al.* 1986). The description given here follows that of Cawley (1992).

There are three different classes of defects which occur in adhesive joints; these are:
1. complete disbonds, voids or porosity in the adhesive layer;
2. poor cohesion (ie a weak adhesive layer);
3. poor adhesion (ie a weak interface between the adhesive layer and one or both adherends);

and an ultimate goal for NDT techniques is to detect all three. Each of these factors affecting joint strength is discussed in more detail below.

Porosity is caused by volatiles and entrained air in the adhesive. It is therefore present to some extend in most bondlines. Voids in the adhesive are similar to porosity except that the individual defect volume can be much greater. They are caused by air or gases becoming trapped by the pattern of laying the adhesive.

Disbonds are essentially large, flat voids which can be caused by the presence of grease or other contaminants on an adherend. In this case, the defects surfaces are generally in close proximity or touching which can make them very difficult to detect. Disbonds may also occur as a result of impact or environmental degradation after manufacture.

It should be emphasised that the significance of a particular defect depends critically on its position within a joint. For example, Wang *et al.* (1971) showed that a large disbonded area in the central region of a lap joint had little effect on the joint strength. However, a smaller defect towards the end of the overlap would have a serious effect because of the much greater stress in this region.

A weak adhesive layer, giving poor cohesive properties, can result from either incomplete mixing, incorrect formulation or inadequate cure of the adhesive. Incomplete mixing is chiefly a problem with two part adhesives, and their incorrect formulation can result from, for example, the dispenser of one of the parts being partially blocked. In general, film adhesives avoid these problems so with these adhesive systems, miscuring is the most likely cause of poor cohesive

properties.

If the adherend surface is contaminated by oil deposits or loose oxide layers prior to bonding, or if a two part adhesive is left too long after mixing and forms a 'skin', the interface between the adhesive and the adherend may be weak, leading to poor adhesion. A disbond may be regarded as an extreme case of poor adhesion.

The adhesive/adherend interface is very important in determining the resistance of a joint to environmental attack, particularly when one or both adherends are aluminium. Before bonding, the adherend surfaces are not only cleaned carefully, but they may be treated to grow favourable oxide or other layers which reduce their succeptibility to environmental attack (Kinloch 1983). Some manufacturers apply a primer to the freshly prepared surfaces while others insist that the joints are made within fixed time.

1.3   Testing for disbonds, porosity and poor cohesion

The field of the NDT of adhesive joints has been reviewed by several authors in the last five years (Stone 1986, Thompson and Thompson 1988, Guyott *et al.* 1986, Light and Kwun 1989). The description given here follows that of Cawley (1992).

1.3.1 Disbonds, voids and porosity

Conventional Ultrasonics

Time domain ultrasonics is one of the most widely used methods of nondestructive examination. It can be used readily to detect voids and disbonds and has the potential for detecting very small, distributed defects such as porosity. The test may be carried out either with a single transducer in pulse-echo mode, or with two transducers in through transmission mode.

As the pulse of ultrasound passes through the joint, part of its energy is reflected at each boundary. The amplitude of reflection at a boundary is dependent on the acoustic impedance of the materials on either side of it, and on the angle of incidence of the ultrasound. The acoustic impedance of a material, z, is given by,

$$z = \rho c, \tag{1.1}$$

where ρ is the density and c is the phase velocity of sound in the material. In most tests used in

industry, the transducer is normal to the structure and the reflection coefficient, R_{12}, from a boundary between two media of impedance z_1 and z_2 when the ultrasound is incident in material 1 is given by (Brekhovskikh 1980),

$$R_{12} = \frac{z_2 - z_1}{z_1 + z_2} \qquad (1.2)$$

Hence, if there is a large difference in the acoustic impedance of the materials, the reflected signal is large. Since air has a very low acoustic impedance relative to solids and liquids, it is difficult to propagate ultrasonic energy from the transducer, through air, into the structure to be tested. The transducer is therefore coupled to the structure via a medium which has an acoustic impedance closer to that of the structure. The structure and the transducer are frequently immersed in a water bath; the ultrasound then propagates across the water filled gap (typically 25 - 100 mm, depending on the transducer) into the testpiece. An alternative is to use a water jet transducer in which the ultrasound propagates along a moving column of water (jet). Small scale inspections, particularly in the field, are commonly done with hand-held contact transducers, coupling being provided by a thin layer of gel between the transducer and the structure. Some work at low ultrasonic frequencies has also been carried out using roller probes in which the ultrasonic transducer is held inside a wheel, the sound being propagated into the specimen via soft rubber tyre. However, this method is not satisfactory for the detailed characterisation of defects (Stone and Clarke 1987). Serious problems can arise if the couplant or some of other liquid such as water or fuel is allowed to penetrate a disbond. The presence of the liquid reduces the reflection coefficient and the defect becomes more difficult to detect.

Since a defect such as disbond or void containing air or any other low density substance has a very low acoustic impedance relative to the adhesive or adherend, a strong reflection will be obtained. The amplitude of the signal transmitted through the bondline will therefore be reduced.

The magnitude of the reflected echoes can be displayed with respect to time and be used to indicate the presence of defects. A display of this type is commonly called an A-scan. B and C scans are also commonly used to display the test results. In the B scan presentation, the vertical axis is time, the presence of echoes being indicated by intensity variations. The horizontal axis gives position information, so an image of cross section of the component is built up. If the amplitude of a particular echo is monitored at each point on the surface of the work, a C-scan can be produced. Measurements at each point are taken using a scanning mechanism which produces a plan of the defects positions but gives no information about their depth.

If immersion testing is used, the amplitude of the echo received from a reflector plate placed

below the bottom adherend is often monitored and used to produce a C-scan map. A delamination whose plan dimensions exceed those of the ultrasonic beam will almost completely remove this echo, while the presence of porosity will cause attenuation of the signal due to scattering of the ultrasound by small gas bubbles. Examples of A, B and C scans can be found in Guyott *et al.* (1986).

Ultrasonic bondtesters

A number of bondtesters operating in the frequency range between 100 kHz and 1 MHz are widely marketed. The Bondascope manufactured by NDT Instruments measures the magnitude and phase of the ultrasonic impedance of a bonded structure, and displays the result as a 'flying dot' on an oscilloscope screen Guyott *et al.* (1986). Changes in the magnitude and phase of the impedance can be related to the existence and depth of disbonds or delaminations, though small voids and porosity cannot be detected. The Fokker Bond Tester Mk II uses spectroscopic approach: it monitors frequency and amplitude changes in the first two modes of through-thickness vibration of a system comprising a transducer coupled to the structure. Changes in resonance frequency reveal the existence and depth of disbonds and delaminations. The instrument can detect disbonds satisfactorily with any adhesive system, but it is not sensitive to changes in the cohesive properties of modern, high-strength adhesives.

Sonic vibration

While ultrasonic methods are capable of detecting disbonds, voids and porosity, since the probe has to be scanned over each point at which the structure must be inspected, they suffer from the disadvantage of being slow, and the need to apply couplant is also a major drawback in many circumstances.

Sonic vibration methods offer one means of avoiding the need to apply a coupling fluid. The coin-tap test in which region of the structure to be tested is tapped with a coin, the operator listening to the sound, is probably the best known of these techniques. It is found that defective areas sound duller than good areas (Cawley and Adams 1988, Adams and Cawley 1989). It has been shown that the difference between good and defective structures can be detected simply by tapping the structure using a small hammer with a force transducer incorporated in its head, and monitoring the force input to the structure during the tap. This has led to the development of an instrument which carries out the test automatically and gives an objective measure of integrity of the structure.

The mechanical impedance method (Cawley 1987) can also be used for the detection of

delaminations in composite materials and disbonds in adhesive joints. The point impedance at the site of a disbond or delamination is lower than in good areas of structure so impedance measurements can be used to detect the defects. The impedance change produced by a given size of defect reduces as the depth of the defect increases, so the sensitivity of the test is highest for defects close to the surface. This is also true of the coin-tap test.

The major application area of these techniques is in the field, where the use of coupling fluids is particularly inconvenient, and where it is frequently only necessary to detect quite large defects. They are also useful for the inspection of thin-skinned honeycomb structures in which the skins are porous, which means that coupling fluids cannot be used. Further details of these and other sonic vibration techniques can be found in Cawley (1990).

Thermography

Passive thermography is one method which shows considerable promise for the quick inspection of large areas of structure. It involves the measurement of the surface temperature of the structure after the application of a heating transient, usually with an infra-red camera, and anomalies in the temperature distribution reveal the presence of defects. The performance of the method is strongly dependent on the heat source used, a flash gun generally being the most suitable.

It has been shown that the feasibility of the method is greatly enhanced by the use of a video recorder to store the rapidly changing temperature pattern after the structure surface is heated and that this makes it possible to detect defects in conducting materials whose effect on the temperature distribution is very short-lived. The method can be employed with the heat source and camera on the same side of the structure (pulse-echo) and on opposite sides (through-transmission). The through-transmission method can detect deeper defects than the pulse-echo technique, but for defects close to the surface, pulse-echo is superior. Further details of the method can be found in Reynolds (1984) and Reynolds (1988).

Other methods

X radiography is not widely applied to the NDT of adhesive joints. This is partly because defects such as disbonds tend to be normal to the X-ray beam, whereas defects are easiest to detect if they are parallel to the beam. Also, if the adherends are metallic, the detection of anomalies in the adhesive is extremely difficult since the absorbtion in the adherend is high, and any lack of adhesive makes a negligible difference to the overall absorption.

Unlike X-rays, neutrons are more strongly absorbed by adhesive than by metals, so neutron radiography could be used to detect disbonds in joints with metal adherends. Neutron radiography should also be very sensitive to the presence of moisture in the joint, and so could possibly be used to monitor the progress of environmental degradation. However, as Bar-Cohen (1986) points out, neutron sources are inconvenient for use in large scale NDT.

Like thermorgaphy, optical holography and shearography offer the possibility of inspecting large areas of structure quickly for the presence of disbonds. They detect anomalies in the displacement or, in the case of shearography, strain patterns on the structure when it is stressed by vibration, static loading or thermal transients. If the optical system used has a large field of view, it is possible to inspect an extensive area in one test, so the method can be used for the quick inspection of large structures. However, the equipment costs are high and, unless a pulse system is used, the structure must generally be mounted on a table which is isolated from extraneous vibration. Recent work on holography is reported by Lokberg and Malmo (1988), and further discussion of shearography can be found in Hung (1989).

1.3.2 Cohesive strength

If the adherend surface preparation has been carried out correctly, the strength of a joint is generally controlled by the cohesive properties of the adhesive layer. Therefore, although problems with cohesive properties are less common than those associated with the adhesive/adherend interface, it would be desirable to be able to measure the cohesive properties of the adhesive nondestructively. Also, if ultrasonic reflection coefficient measurements are used to monitor the adhesive/adherend interface, the measured reflection amplitudes will depend on the acoustic properties of the adhesive, so it is important that these are known.

Some progress is being made on the development of tests for cohesive properties and one commercially available instrument, the Fokker Bond Tester Mk II does claim to be able to detect poor cohesion (Schliekelmann 1975). The device measures the frequencies of the first two modes of the transducer coupled to the joint. However, recent work (Guyott et al. 1987) has shown that it is not sensitive to variations in the cohesive properties of modern high strength adhesives, though it can still be used to detect disbonds.

Research has continued and subsequent work has used ultrasonic spectroscopy to measure the frequencies of the through-thickness modes of the joint itself, in order to monitor the quality of cohesion. A detailed analysis conducted by Guyott and Cawley (1988), and Cawley and Hodson (1988) suggested that it is possible to calculate values of adhesive modulus and thickness from measurements of the resonant frequencies. However, recent work conducted by

Dewen (1992), showed that this approach is insufficiently robust for industrial applications.

Another idea which has been recently investigated by Dewen (1992) is to use the time-of-flight in the adhesive layer and the reflection coefficient at the adherend/adhesive interface to infer the elastic modulus and thickness of the bond line. Dewen (1992) showed that this technique is more robust than ultrasonic spectroscopy and that the longitudinal wave velocity in the adhesive can be determined with a maximum error of 6% and the bondline thickness to within micrometer accuracy.

Since the cohesive strength of the adhesive is a function of the degree of cross linking of the polymer during cure, and this mechanism also controls the modulus, there is a good correlation between adhesive modulus and cohesive strength. The cohesive strength of a joint is also weaker function of the thickness of the adhesive layer. It seems therefore that monitoring the adhesive modulus and thickness would provide a valuable means of checking the cohesive strength of a joint.

Another possible technique for monitoring the cohesive properties of a joint is the measurement of the dielectric relaxation characteristics of the adhesive. Organic molecules containing molecular dipoles are capable of exhibiting a frequency and temperature dependent dielectric permittivity. As the cure of an adhesive proceeds, the degree to which dipoles can reorient themselves will firstly be influenced by the increase in viscosity which accompanies the chain extension process, then by the suppression of bulk motion by the process of gelation, and finally by an increase in the glass transition temperature.

Matiss and Shtrauss (1988) have shown that relaxation spectrum measurements at very low frequencies between 1 mHz and 1 Hz are very effective for monitoring the degree of cure of an epoxy resin, and they have worked on a measurement system which only requires access to one side of a joint. Work on this subject is also being done by a group headed by Pethrick (Jeffrey et al. 1988) who have shown that dielectric measurements are very sensitive to the moisture content of the adhesive. This suggests that the technique may provide a means of monitoring the progress of environmental attack which, although its chief effect is to reduce the strength of the adhesive/ adherend interface, also leads to hydration of the adhesive layer.

1.4 Testing for poor adhesion

Currently, there is no satisfactory nondestructive technique to test for adhesion strength in bonded joints. In order to secure sufficient quality of adhesion strength in bonded structures,

manufacturers implement costly and cumbersome process control procedures, frequently involving destructive testing of samples taken from production lines. Despite substantial research effort and many theories being proposed, the adhesion between two surfaces is not well understood (Adams and Wake 1984, Stone 1986, Kinloch 1987, Light and Kwun 1989). Therefore NDT can at best be used to attempt to determine whether a tested interface has the same features as a reference one, which is assumed to be satisfactory.

Two basic approaches have been investigated for the ultrasonic determination of the interfacial properties in adhesive joints, namely modal solutions and reflection coefficient techniques. Both approaches have been attempted to make predictions of response of the joint assuming a certain model of the adhesive/adherend interface. Different interfacial models which have been used are described below.

1.4.1 Theoretical models of the adherend/adhesive interface

For theoretical purposes, the notion of an interface layer with its own acoustic properties and thickness is usually introduced. This means that the ultrasonic response from the adherend/interface layer/adhesive system rather than the simple adherend/adhesive system is analysed. The thickness of the interface layer is typically of the order of 1 μm and depends on the surface characteristics like roughness, the presence of contaminants and the type of oxide on the surface of the adherend. However, the wavelength of the ultrasonic waves used currently in nondestructive testing are at least one hundred times larger than the thickness of the interface layer. Tattersall (1973) assumed that the thickness of such an interface layer is therefore negligible and its elastic properties can be modelled as a spring. Later on a number of researchers studying different thin layer or interfacial problems arrived at essentially the same spring model as Tattersall did in 1973, and were able to relate the stiffness of the interface to different features of the measured system. Nowadays, the spring model is the most commonly used approximation of a thin layer. Different cases leading to the spring model are listed below.

- A thin solid layer can sometimes be modelled using spring model. The normal and transverse stiffness of the layer can be related to the thickness of the layer and its elastic constants. A more detailed discussion of this is given in chapter 4 of this thesis.

- A thin liquid layer can be modelled in a similar manner as the thin solid layer. In the transverse direction the behaviour of such a layer can be modelled by 'transverse slip' or 'viscous slip' depending on the layer's thickness, the viscosity of the liquid and the frequency of excitation (Kühn and Lutsch 1961, Schoenberg 1980, Rokhlin and Marom 1986), while the stiffness in the normal direction can be calculated in the same manner as in

the case of a solid layer.

- When two surfaces are in intimate contact with each other and there is no viscous coupling between them then a dry contact takes place. Transmission of forces across the interface is achieved by the large number of small contacts distributed randomly in the plane of the interface. The stiffness of the interface can be related to the statistical descriptions of the surfaces and the mechanical properties of the materials in contact (Haines 1980). Haines' spring model has been used by a number of researchers investigating the reflection coefficient from contacting surfaces (Arakawa 1983, Krolikowski et al. 1989, Nagy 1990).

- When the adhesive/adherend interface is not perfect and an array of small debonded areas, which cannot be resolved individually by an ultrasonic transducer, is formed then a partial bond takes place. This bond has some, although somewhat reduced, strength. Certain statistical properties of the partial bond like the size and density of the debonded areas can be related to the interface stiffness (Angel and Achenbach 1985, Achenbach and Kitahara 1986, Sotiropoulos and Achenbach 1988, Nagy 1990)

- A kissing bond can occur as a result of plastic contact between the surfaces. In such a case the interface has no strength apart from some "sticking" effect at the surfaces (Nagy 1990). This can take place in diffusion bonded joints where the materials are pressed together at elevated temperatures. In adhesively bonded joints this may possibly occur if, for example, the adhesive is bonded to a very thin layer of a mould release agent deposited on the surface of the adherend. If the mechanical properties of the contacting materials and a statistical description of the mating surfaces (like mean separation) are known then the stiffness of the interface can be calculated using Haines' (1980) approach.

Another, more complicated model of the interface, is to consider it as a finite thickness intermediate isotropic layer with its own density, longitudinal and shear velocity and thickness (Alers 1976, Nagy and Adler 1989 (b), Dale and Rose 1990). Recently Wang and Rokhlin (1990) measured properties of thick layer of PAA oxide and employed an anisotropic layer model to correlate the experiments with theory.

1.4.2   Different testing strategies

From the conceptual point of view, the adhesive bond is usually considered as a five layered plate, the adherend/interface/adhesive/ interface/adherend system, where each of the layers has its own acoustic properties. A successful testing technique should be capable of monitoring certain changes in the elastic properties of either or both interfacial layers in a joint. Two different testing approaches have been proposed in the literature. The first one is the modal

approach using Leaky Lamb Waves (LLW), guided waves (trapped modes) in the adhesive layer, or interface waves to determine the boundary conditions across the adhesive and adherend. The second approach is to monitor the reflectivity of ultrasonic bulk waves from adherend/adhesive interface, and is known as the reflection coefficient technique.

Modal approach

Leaky Lamb Waves (LLW) are waves propagating along a plate (see fig. 1.1(a)). If the plate is an adhesive joint then the velocity and the wavelength of Leaky Lamb Waves depend on the mechanical properties of the adhesive and adherends and the boundary conditions between them. For theoretical purposes the adhesive joint is usually modelled as a three layered plate, an adherend/adhesive/adherend system with 'imperfect' boundary conditions introduced between one or both adherend/adhesive interfaces. In experimental investigations the Leaky Lamb Waves are usually excited and received by ultrasonic transducers operating in a pitch-catch mode underwater whose angles of incidence with respect to a tested plate can be accurately adjusted. Theoretical predictions of the frequencies and the velocities at which the Leaky Lamb Waves can propagate in a given adhesive joint are often displayed in the form of dispersion curves and compared with experiments. In experimental investigations the Leaky Lamb Waves are usually excited and received by ultrasonic transducers operating with immersion coupling in a pitch-catch mode, whose angles of incidence with respect to a tested plate can be accurately adjusted. Several researchers have tried to use the LLW technique for nondestructive evaluation of adhesive joints and particularly to monitor their interfacial properties but their findings are preliminary.

One of the recent publications from the group in the University of Paris headed by Quentin and de Billy (Leomy et al. 1989) used LLW technique on samples of adhesively bonded duraluminium plates to brass substrates and brass plates to duraluminium substrates. Comparison between the measurements and theoretically generated dispersion curves revealed that most of the experimental plots were not predicted by the elastic theory used, and it was concluded that attenuation should be included in the model. In another investigation (Guy 1992) steel-to-steel adhesive joints with different surface preparations, including oil contamination, were considered. Theoretical model predictions and experimental investigations led the researchers to conclude that the LLW technique is only very weakly sensitive to different interfacial conditions between steel and epoxy.

Rokhlin (Rokhlin et al. 1990) used the LLW technique to monitor the degree of cure of two very thin epoxy films in a five-layer system consisting of aluminium/epoxy/plastic/epoxy/ aluminium. During the curing process, the boundary conditions between the aluminium

adherends and the plastic layer changed from 'weak' to 'good'. Comparison between theoretical predictions and the measurements was essentially qualitative and some results were left unexplained. However, the work demonstrated good sensitivity of the LLW technique to adhesion type imperfections.

Guided waves (trapped modes) are the type of waves which propagate along the adhesive layer, and unlike the Leaky Lamb Waves, do not extend over the entire thickness of an adhesive joint (see fig. 1.1(b)). The adhesive layer acts here as a waveguide and the energy is concentrated almost entirely in the bondline (Alers and Thompson 1976). True guided modes are not coupled to any of the bulk waves in the surrounding media; they are therefore less suitable for NDT applications since they are difficult to excite and receive through the adherend. One possibility is to use Rayleigh waves propagating along the surface of the adherend plates, which are mode-converted into guided interface waves when going through the joint (see fig. 1.2). A few preliminary studies, both theoretical and experimental, have been conducted on this subject showing that the guided waves are much more sensitive to both adhesive and cohesive type defects than Lamb modes (Nagy and Adler 1989 (b), Nagy *et al.* 1990, Nagy and Adler 1991).

Nagy and Adler (1989 (a)) used a Leaky Guided Wave technique to monitor changes in the interfacial properties in adhesive joints caused by the presence of a thin layer of mould release agent applied to the adherend prior to bonding. One of the main conclusions of the paper is that the presence of the mould release affects the amplitudes of the Lamb modes rather than the frequencies at which they propagate.

Interface waves propagate along the adhesive/adherend interface (see fig. 1.1(c)). The mechanical energy of these waves is almost entirely concentrated in the vicinity of the adhesive/adherend interface and the properties of the interface waves are dependent on the mechanical properties in the interfacial region. This makes them potentially well suited for monitoring the interfacial conditions between the adherend and adhesive. Despite its apparent attractions, there is only a handful of reports on the application of interface waves to the adhesion problem (Rokhlin *et al.* 1981, Rokhlin 1982, Pilarski 1985, Nagy and Adler 1989 (b)). Application of the technique to the surface contact characterisation between two solids has been reported by Murty and Kumar (1991). In all the reported investigations known to the author, the interface waves were ~~exited~~ *excited* using the mode-conversion technique from the Rayleigh wave to the interface wave, described above in the context of guided waves applications.

Reflection coefficient approach

In the reflection coefficient method the reflectivity of bulk waves, (longitudinal or shear), at the

adherend/adhesive interface is measured. Measurements can be conducted at normal and oblique incidence with respect to the monitored interface as well as at different frequencies of excitation. The results of the measurements are then related to the mechanical properties of the interfacial layer.

Tattersall (1973) assumed a simple one-dimensional spring model for the interface between two solids and used this to study the reflection coefficients at normal incidence between an aluminium block and low density polyethylene cast on the aluminium face. Using the spring model of the interface, Tattersall derived an expression for the reflection coefficient,

$$R_{12} = \frac{z_1 - z_2 + i\omega(z_1 z_2/k)}{z_1 + z_2 + i\omega(z_1 z_2/k)},$$

(1.3)

where z_1 and z_2 are the acoustic impedances of medium 1 and medium 2, defined by eqn 1.1, and k is the stiffness of the interface. The model proposed by Tattersall therefore predicts that the reflection coefficient from an imperfect interface will be frequency dependent. Equation 1.3 can be considered as an extension of the standard textbook expression of the reflection coefficient from a flat interface between two materials without a spring in between (see eqn 1.2), which is frequency independent. Tattersall concluded that using the spring model it is possible to account for presence of gaseous contamination at the interface. Because of its simplicity the spring model has been used in a number of applications where the concept of 'thin layer' or 'thin imperfection' could be applied (see section 1.4 of this thesis for more details).

Alers (1976) considered three different models of interfaces, an isotropic layer of finite thickness, a diffuse layer and the spring model, and performed normal incidence reflectivity measurements from bonded interfaces using Plexiglas (Lucite) adherends. Two different types of bonds were investigated in his work. The first of them was an 'adhesive' type of bond which was created by applying solvent on the surfaces of the adherends before pushing the adherends together. The second set of joints, a 'thermal' type, were created by pushing the Plexiglas adherends together at elevated temperature. The normal incidence longitudinal reflection coefficient was measured and then destructive tests were carried out in order to find some relationship between the reflection coefficient and strength for both 'thermal' and 'adhesive' types of the interfaces. Alers was not able to correlate the ultrasonic reflectivity from the interfaces with their strength and concluded that better understanding of wave interaction with imperfect boundaries is required. He also suggested that some alternative technique is needed to achieve the required sensitivity to interfacial integrity.

Rokhlin and Marom (1986) proposed a novel technique, based on an idea in the paper by Kühn and Lutsch (1961), to monitor the degree of cure in adhesives. They measured the longitudinal wave oblique incidence reflection coefficient from thin adhesive films between two steel plates and between steel and Plexiglas plates. They showed that during the curing cycle, thin adhesive layers undergo changes from 'slip' to 'rigid' conditions. The experimentally determined reflection coefficient curves showed very good agreement with theoretical predictions and the researchers concluded that the oblique incidence method can be used to monitor changes from the 'slip' to 'rigid' conditions across thin layers and can be used for cure-monitoring of thin adhesive layers.

Pilarski and Rose (1988) progressed the ultrasonic oblique incidence approach, proposed by Rokhlin and Marom (1986), and used it as an alternative to the normal incidence technique in the evaluation of aluminium-to-aluminium adhesive joints. The experimental evidence gathered thus far suggested that the normal incidence was not sensitive enough to be used successfully (Thompson and Thompson 1988). The normal incidence method relies on changes in the interface stiffness solely in the direction normal to the interface. However, if the interfacial imperfections affected the transverse stiffness of the boundary then the oblique incidence method would have much higher sensitivity then the normal incidence tests. A two dimensional model of the interface was proposed, with normal and tangential stiffnesses. A full set of reflection coefficients (longitudinal-longitudinal, longitudinal-shear, shear-longitudinal and shear-shear (see fig. 1.3)) from the aluminium/epoxy interface was theoretically calculated assuming 'rigid' and 'slip' boundary conditions between the adhesive and the adherend. Tests on adhesive bonds with two different surface preparations were conducted which indicated good sensitivity of the oblique incidence method in practice. Pilarski and Rose concluded that the oblique incidence method opens up a new direction in the search for a robust NDT technique testing for interfacial strength. Theoretical and experimental studies on the oblique incidence technique were presented by Pilarski and Rose in several papers (Pilarski 1985, Pilarski et al. 1987, Pilarski et al. 1990, Rose et al. 1990 (a), (b)); however they are all of a preliminary nature. Theoretical investigations were mostly based on the 'rigid' and 'slip' boundary interface model which represent two extreme cases of 'good' and 'weak' adhesive joint and are very seldom, if at all, found in reality. The experimental investigations conducted by Pilarski and Rose so far have not been systematic enough to provide a firm basis for the acceptance of the oblique incidence reflection coefficient as a better technique for the determination of interfacial properties in adhesive joints.

1.4.3 Conclusions

Despite substantial efforts made for over twenty years, the problem of testing for poor adhesion

has not been solved. It has not been definitely determined whether or not an ultrasonic technique can be used for the determination of interfacial weakness in adhesive bonds. The most promising techniques are the guided wave (trapped mode), the interface wave and the oblique incidence refection coefficient techniques. However, the studies conducted and published on these three techniques are of a preliminary nature and further research is needed to fully asses their applicability. This thesis considers the reflection coefficient method.

1.5 Problem summary

In summary, the problem is to determine the mechanical boundary conditions between the layers of an adhesive joint, by sending longitudinal waves from a liquid into the joint and receiving back the resulting reflections (see fig. 1.3). It is assumed that the adhesive joint consists of two flat layers of metal joined by a flat layer of epoxy resin.

The main anticipated difficulties are as follows:

a. The thickness of the aluminium/epoxy interface layer is usually of the order of 1 μm. This makes it impossible to determine the mechanical properties of the layer by the conventional ultrasonic techniques which are used for material evaluation because the wavelength of the waves is much longer than the interface layer thickness.

b. In order to increase the impact toughness of adhesive joints, the adhesive is usually modified (for example with rubber) so that it exhibits viscoelastic properties. This means that the reflection coefficient from the interface can be affected by the viscoelastic behaviour of the adhesive. This behaviour is, in general, frequency dependent.

c. The transducers used to excite the plates and to receive the reflected field are of finite size. This raises questions about the applicability of the infinite plane wave theory to realistic cases.

1.6 Outline of the thesis

The aim of the research reported here was to conduct further detailed studies of all stages of the reflection coefficient technique. This research includes the theoretical modelling of the adhesive and adherend layers and the interfaces between them, sensitivity studies to determine the most

useful practical testing arrangements, the construction and application of an appropriate measurement rig, and experimental investigations to quantitatively validate the theoretical models used.

In chapter 2 the concept of a viscoelastic medium is introduced by assuming that any viscoelastic material can be fully described by its density and another four independent variables, two of them being Lamé's constants and the remaining two characterising the damping properties of the material. A wave equation of motion is derived on the basis of this assumption, and it is shown that harmonic plane waves satisfy the equation. The reflection and transmission coefficients are defined in terms of these harmonic plane waves.

Having established the equation for infinite plane waves the theory is progressed to the realistic field generated by finite sized transducers. This is achieved by decomposing the field into harmonic infinite plane waves whose reflection coefficients are readily found. Subsequently this process is also used to determine the field received by a finite sized transducer by the synthesis of the harmonic infinite plane wave solutions.

In chapter 3 the theory of plane wave reflection and transmission from multilayered viscoelastic plates is given. This theory makes it possible to calculate reflection coefficients of any multilayered viscoelastic plate with any boundary conditions between the layers. The only limitation is that the boundary conditions have to be linear.

In chapter 4 a theoretical study of ultrasonic reflectivity from thin solid and liquid layers is presented and a thin layer approximation is derived. Parametric studies of reflection coefficients at normal and oblique incidences are conducted and compared with the spring model and the thin layer approximation.

In chapter 5 the oblique incidence reflection coefficient testing rig constructed for the purposes of this thesis is presented. Ultrasonic reflectivity measurements from single-layered and multi-layered systems are compared with theoretical predictions to validate the theory derived in chapters 2 and 3. The measurement error of the oblique incidence method is estimated and the applicability of the plane wave theory and the finite transducer theory is discussed.

In chapter 6 the monitoring of interfacial conditions in a glass/epoxy joint at the normal and oblique angles of incidences using longitudinal and shear waves is performed. The computer model, derived and validated in this thesis, was used to find the best testing strategy for the interfacial weakness determination. Oblique incidence tests were then conducted at these selected angles.

In chapter 7 an attempt to monitor interfacial conditions of the aluminium/epoxy joints is presented. Using the theoretical models and experimental tools developed in previous chapters the applicability of the oblique incidence method to the adhesion problem in real aluminium-to-aluminium joints is discussed.

Chapter 8 presents main conclusions of the thesis and contains recommendations and suggestions for future work.
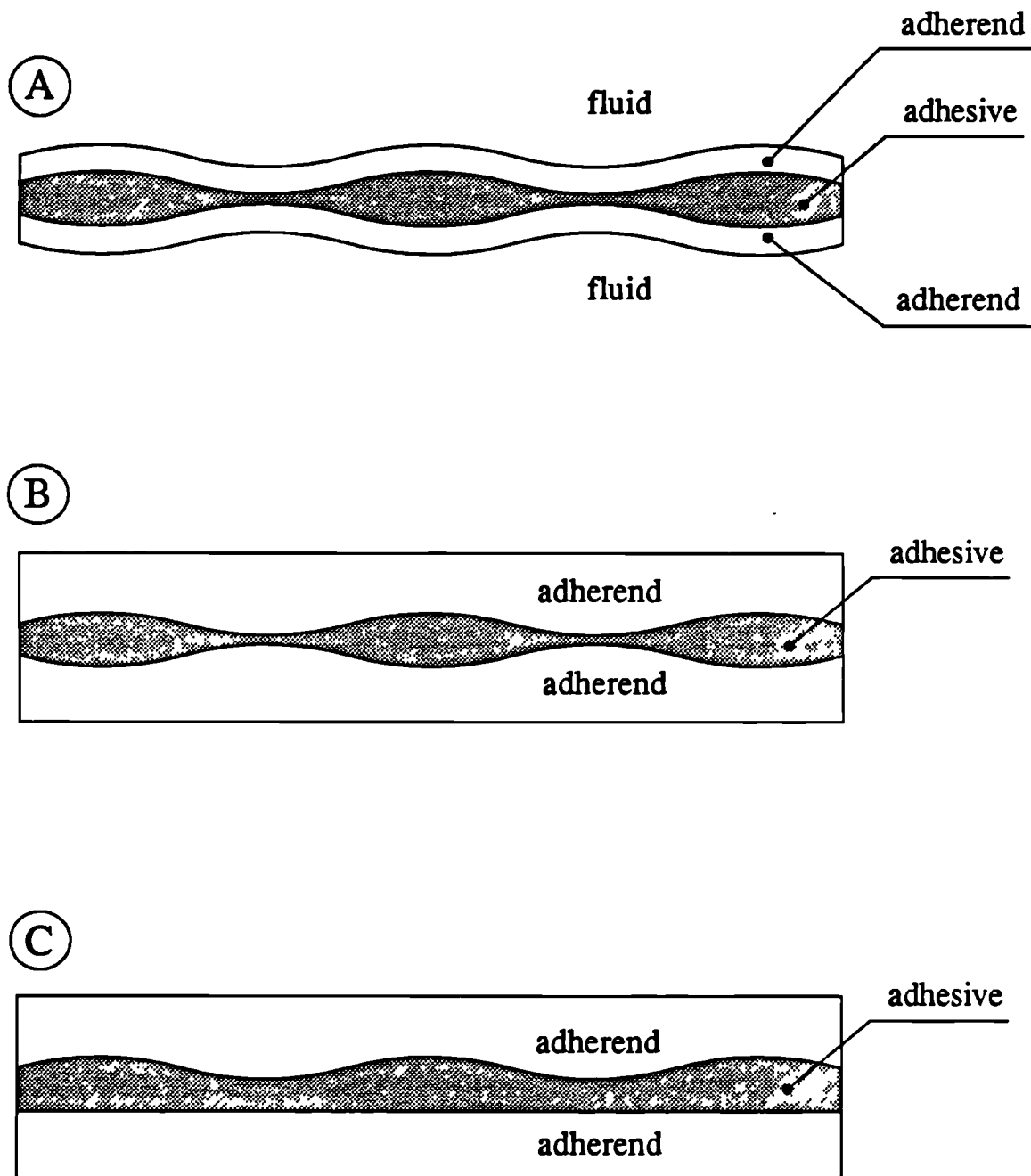
Fig 1.1   Different plate waves used for the adhesion testing

    (A)   Leaky Lamb Waves (LLW)

    (B)   Guided waves (trapped modes)

    (C)   Interface waves

Rayleigh
wave

Mode-converted
guided wave

Rayleigh
wave
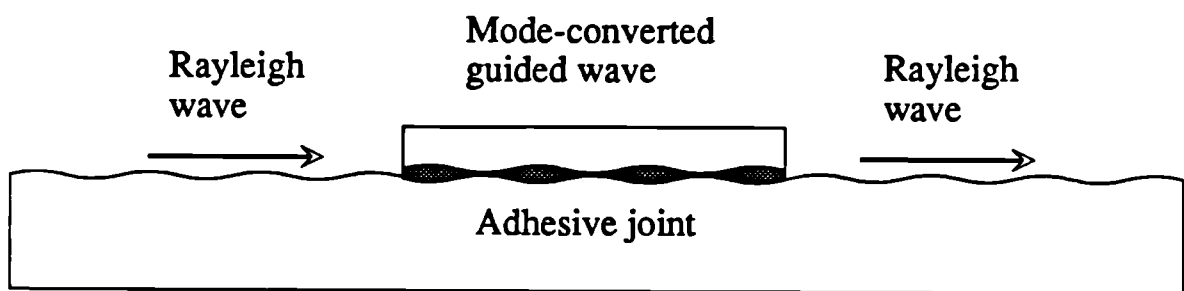
Adhesive joint

Fig 1.2   Generation of guided waves in an adhesive joint using
the mode-conversion phenomenon.
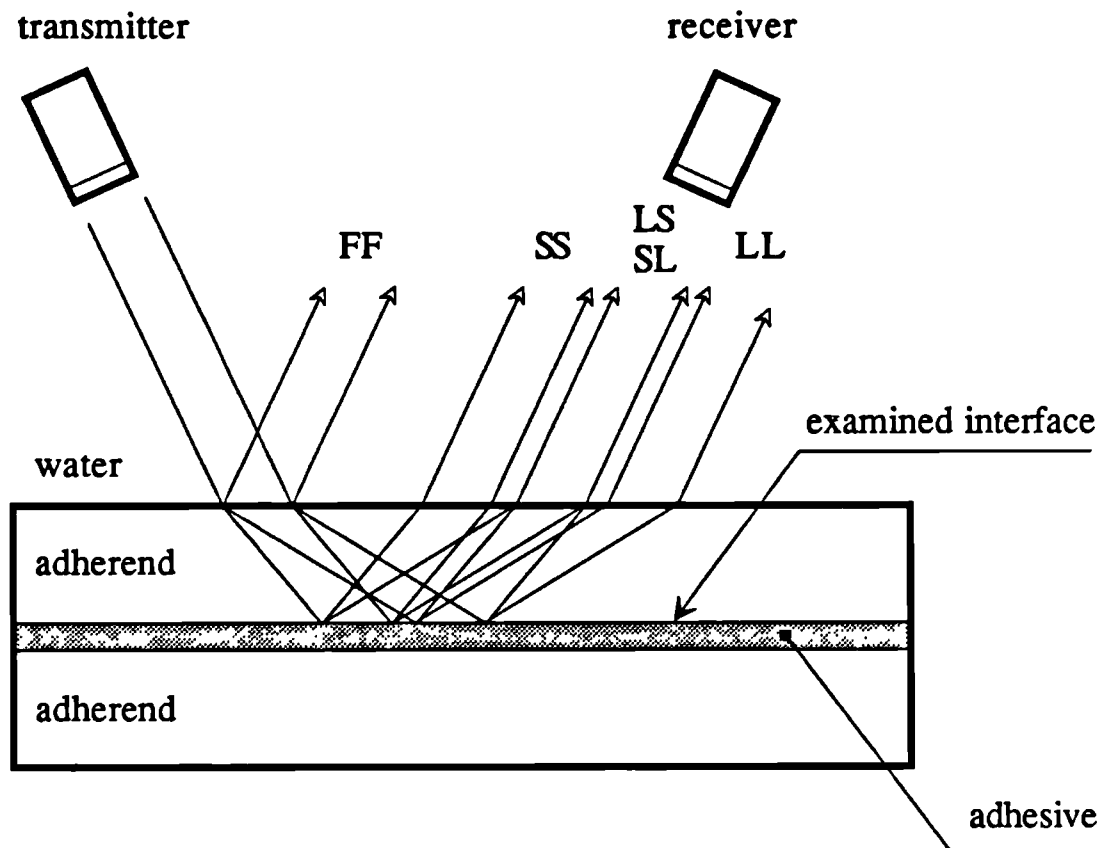
Fig 1.3 Oblique incidence reflection coefficient method.
FF front face reflection
LL longitudinal-longitudinal reflection
LS longitudinal-shear reflection
SL shear-longitudinal relection
SS shear-shear reflection

CHAPTER 2

The reflection coefficient from the interface between two semi-infinite viscoelastic media

2.1 Introduction

Chapter 2 is concerned with the reflection and transmission of acoustic waves at a single interface between two semi-infinite viscoelastic media. The chapter is divided into four sections, the first presenting the harmonic plane wave concept, the second applying the plane wave theory to solve a single interface reflection coefficient problem, the third one giving a solution method for the reflection and transmission fields generated by transducers of finite dimensions. The final section summarises the main points made in the chapter.

In section 2.2 the concept of harmonic longitudinal and shear plane waves is presented as a solution of a wave equation in an unbounded viscoelastic medium. The solution follows a standard procedure for a wave equation. Firstly the definition of strain and stress is given. Then the governing equation for viscoelastic media, relating the stress field to the strain field, is obtained under the assumption that any viscoelastic medium can be comprehensively characterised by its density and another four independent constants, two of them being Lamé's constants and the remaining two characterising the damping properties of the medium. In order to relate the stress field to the displacement field, the equation of motion for an infinitesimally small volume of the medium is given. Combining the equation of motion with the governing equation and the definition of strain the wave equation in terms of the displacement field is derived.

To solve the equation the Helmholtz representation of the displacement field is then applied which conveniently decouples the wave equation into two independent wave equations, the solutions of which yield two harmonic plane waves: a longitudinal plane wave and a shear plane wave in terms of the wave potential fields. The wave potential fields are related to the displacement field by the Helmholtz representation and therefore the wave equation solutions can be obtained in terms of the displacement field.

Having done the necessary calculations it is found that the longitudinal plane wave field consists solely of the harmonic displacement in the direction of propagation of the wave, and

the shear wave causes the particles to move solely in the direction perpendicular to the direction of propagation of the wave. This statement applies only to propagating (homogeneous) longitudinal and shear waves which is the case when an infinite medium is considered. Sometimes it is important to calculate the stress at a given point in the medium. The constitutive equation, relating the stress field to the strain field, makes it possible to calculate the stress tensor components due to the longitudinal and shear plane waves.

Section 2.3 deals with the generation of the reflected and transmitted harmonic plane waves at a plane boundary between two viscoelastic materials. At the beginning of section the Snell's law equation for viscoelastic media is given, which shows that the angular frequency of the waves and their wavenumber components parallel to the interface must be preserved (ie they are invariant in transmission and reflection from a plane interface). It is shown in this section that these two invariants reduce the maximum number of the reflected and transmitted waves to four: two reflected waves and two transmitted waves. Therefore the stress-displacement field due to the four harmonic waves is calculated as a superposition of the stress-displacement fields due to each of the four plane harmonic waves. This equation, relating the stress-displacement field to the four harmonic wave amplitudes, describes a general form of the reflected or transmitted field between any pair of viscoelastic media separated by a plane boundary. If the relationship between the stress-displacement field on one side of the boundary and the stress-displacement field on the other side of the boundary is known (eg in the form of a stiffness matrix), then it is possible to calculate the amplitudes of the reflected or transmitted harmonic plane waves, that is to calculate the reflection and transmission coefficients of the system. The last subsection of section 2.3 deals with the boundary stiffness matrix and completes the derivations of the equations relating the stress-displacement field across the plane interface.

In section 2.4 the problem of the reflection and transmission of the field at a single interface generated by a finite transducer in an inviscid fluid is presented. It is possible to obtain an exact solution of the field generated by a finite transducer using Huyghens principle ie by summation of spherical waves from the face of the transducer. However, this will lead to cumbersome equations when deriving the reflected and transmitted field at plane interfaces. It is therefore more convenient to form the radiated field as a superposition of harmonic plane waves as it is possible to obtain solutions for the reflection and transmission coefficients from plane boundaries in a relatively straightforward manner.

Section 2.5 is the conclusion section and repeats the most important findings of this chapter in a concise form.

2.2 Plane wave in an infinite viscoelastic medium

2.2.1 Plane wave as a solution of the wave equation

In a viscoelastic medium the stress-strain equations can be written as (see for example Love 1944, Becker and Richardson 1970),

$$\sigma_{ij} = \lambda \delta_{ij} \varepsilon_{kk} + 2\mu \varepsilon_{ij} + \frac{\lambda'}{\omega} \delta_{ij} \frac{\partial}{\partial t} \varepsilon_{kk} + \frac{2\mu'}{\omega} \frac{\partial}{\partial t} \varepsilon_{ij}, \tag{2.1}$$

where σ_{ij} is stress, ε_{ij} is strain, λ and μ are the Lamé's constants, λ' and μ' characterise attenuation of the medium, ω is the frequency, and δ_{ij} is the Kronecker delta i,j=1,...,3. The equation of motion is,

$$\frac{\partial}{\partial x_j} \sigma_{ij} = \rho \frac{\partial^2}{\partial t^2} u_i, \tag{2.2}$$

where ρ is the density of the medium and x_j, j=1,...,3 is the Cartesian coordinate system and u_i, i=1,...,3 are the components of the displacement from the position of equilibrium. Strain is defined in terms of displacement as,

$$\varepsilon_{ij} = \frac{1}{2} (\frac{\partial}{\partial x_j} u_i + \frac{\partial}{\partial x_i} u_j). \tag{2.3}$$

Substituting (2.2) and (2.3) into (2.1) we can obtain the equation of motion in terms of the displacement $\bar{u}$.

$$\mu \nabla^2 \bar{u} + (\lambda + \mu) \nabla (\nabla \cdot \bar{u}) + \frac{\mu'}{\omega} \nabla^2 \frac{\partial}{\partial t} \bar{u} + \frac{\lambda' + \mu'}{\omega} \nabla (\nabla \cdot \frac{\partial}{\partial t} \bar{u}) = \rho \frac{\partial^2}{\partial t^2} \bar{u} \tag{2.4}$$

Using the Helmholtz representation (see for example Malvern 1969) we can express an arbitrary continuous differentiable field as a superposition of an irrotational (potential) field $\bar{L}$ and a rotational (solenoidal) field $\bar{S}$. This can be expressed as, $\bar{u} = \bar{L} + \bar{S}$, where $\bar{L} = \nabla \phi$ and $\bar{S} = \nabla \times \bar{\psi}$. The scalar function ϕ and the vector function $\bar{\psi}$ are called the wave potentials. Equation (2.4) then becomes a set of two uncoupled equations for ϕ and $\bar{\psi}$,

$$[(\lambda + 2\mu) + \frac{\lambda' + 2\mu'}{\omega} \frac{\partial}{\partial t}] \nabla^2 \phi = \rho \frac{\partial^2}{\partial t^2} \phi, \tag{2.5}$$

$$[\mu + \frac{\mu'}{\omega} \frac{\partial}{\partial t}] \nabla^2 \bar{\psi} = \rho \frac{\partial^2}{\partial t^2} \bar{\psi}. \tag{2.6}$$

Let us assume solutions,

$$\phi(\overline{x},t) = \phi(\omega) \, e^{i\omega(\overline{N}\bullet\overline{x}/\alpha \, - \, t)} \, , \tag{2.7}$$

and,

$$\overline{\psi}(\overline{x},t) = \overline{\psi}(\omega) \, e^{i\omega(\overline{N}\bullet\overline{x}/\beta \, - \, t)} \, , \tag{2.8}$$

where $\overline{N}$ is a complex vector, $\bullet$ is the dot product symbol, and α and β are complex. The operators for these solutions are,

$$\frac{\partial}{\partial t} = -i\omega; \quad \frac{\partial^2}{\partial t^2} = -\omega^2; \tag{2.9}$$

$$\frac{\partial}{\partial x_i} = \frac{i\omega}{c} \, N_i; \quad \frac{\partial^2}{\partial x_i^2} = -(\frac{\omega}{c})^2 N_i^2; \quad \text{where} \quad c = \alpha \text{ or } c = \beta, \tag{2.10}$$

$$\nabla^2 = (\frac{\partial^2}{\partial x_1^2} + \frac{\partial^2}{\partial x_2^2} + \frac{\partial^2}{\partial x_3^2}) = -(\frac{\omega}{c})^2 \, \overline{N} \bullet \overline{N}; \quad \text{where} \quad c = \alpha \text{ or } c = \beta. \tag{2.11}$$

Assuming these solutions equations (2.5) and (2.6) become,

$$[\, (\lambda + 2\mu) + \frac{\lambda' + 2\mu'}{\omega} (-i\omega)] \, [-(\frac{\omega}{\alpha})^2] \, \overline{N} \bullet \overline{N} \, \phi = -\rho\omega^2\phi \, , \tag{2.12}$$

$$[\, \mu + \frac{\mu'}{\omega} (-i\omega)] \, [-(\frac{\omega}{\beta})^2] \, \overline{N} \bullet \overline{N} \, \overline{\psi} = -\rho\omega^2\overline{\psi} \, . \tag{2.13}$$

These equations can be simplified to,

$$[\, (\lambda + 2\mu) - i(\lambda' + 2\mu')] \, \overline{N} \bullet \overline{N} = \rho\alpha^2 \, , \tag{2.14}$$

$$[\, \mu - i\mu'] \, \overline{N} \bullet \overline{N} = \rho\beta^2 \, . \tag{2.15}$$

Equations (2.14) and (2.15) are equivalent to equation (2.4) with the displacement field split into the rotational $\overline{S}$ and irrotational $\overline{L}$ displacements and assuming that the motion is harmonic. To simplify the two equations we can normalise the complex vector $\overline{N}$ defining it as being of unit amplitude,

$$\overline{N} \bullet \overline{N} = 1 \, . \tag{2.16}$$

Equations (2.14) and (2.15) become,

$$\alpha^2 = \frac{(\lambda+2\mu) - i(\lambda'+2\mu')}{\rho},$$ (2.17)

$$\beta^2 = \frac{\mu - i\mu'}{\rho}.$$ (2.18)

Thus equations (2.7) and (2.8) are solutions of equations (2.5) and (2.6) provided that equations (2.16), (2.17) and (2.18) are satisfied.

The equations for a totally elastic solid can be obtained by setting $\lambda'=0$ and $\mu'=0$, ie by removing the viscous terms from eqn (2.1). The equations for a viscous fluid can be obtained by removing the shear stiffness (setting $\mu=0$), and multiplying λ' and μ' by ω. In this case eqn (2.1) becomes the Navier-Stokes equation. The inviscid (Newtonian) fluid model is obtained by setting $\mu=0$, $\lambda'=0$ and $\mu'=0$.

2.2.2 Displacement field for longitudinal and shear plane waves

Let us, for convenience, choose a Cartesian coordinate system so that $N_3=0$. The wave potentials, given by equations (2.7) and (2.8), can be therefore expressed in terms of x_1 and x_2 coordinates only, reducing the case to the two-dimensional plane strain problem, $\frac{\partial}{\partial x_3} = 0$.

Displacement field due to a wave potential ϕ of unit amplitude

The displacement field due to the wave potential ϕ is,

$$\bar{L} = \nabla\phi = \{ \frac{\partial}{\partial x_1}, \frac{\partial}{\partial x_2}, 0 \} \phi.$$ (2.19)

Substituting eqn (2.7) into (2.19) we have,

$$L_1 = \frac{\partial\phi}{\partial x_1} = i\omega\frac{N_1}{\alpha} \phi(\omega),$$ (2.20)

$$L_2 = \frac{\partial\phi}{\partial x_2} = i\omega\frac{N_2}{\alpha} \phi(\omega),$$ (2.21)

$$L_3 = 0.$$ (2.22)

Therefore we have,

$$\bar{L} = \left\{ \begin{matrix} u_1 \\ u_2 \end{matrix} \right\} = \left\{ \begin{matrix} N_1 \\ N_2 \end{matrix} \right\} \frac{i\omega}{\alpha} \, e^{i\omega(N_1 x_1/\alpha \, + \, N_2 x_2/\alpha \, - \, t)}. \tag{2.23}$$

Equation (2.23) describes the displacement field due to a wave potential ϕ of unit, real amplitude.

Displacement field due to a wave potential $\bar{\psi}$ of unit amplitude

The rotational wave potential can be expressed as,

$$\bar{\psi} = \bar{I}_3 \, \psi(\omega) \, e^{i\omega(N_1 x_1/\beta \, + \, N_2 x_2/\beta \, - \, t)}. \tag{2.24}$$

where $\bar{I}_3$ denotes the unit vector along the x_3 coordinate. The displacement field is,

$$\bar{S} = \nabla \times \bar{\psi} = \begin{vmatrix} \bar{I}_1 & \bar{I}_2 & \bar{I}_3 \\ \frac{\partial}{\partial x_1} & \frac{\partial}{\partial x_2} & \frac{\partial}{\partial x_3} \\ 0 & 0 & \psi \end{vmatrix} = \bar{I}_1 \frac{\partial \psi}{\partial x_2} - \bar{I}_2 \frac{\partial \psi}{\partial x_1}. \tag{2.25}$$

Substituting eqn (2.24) into (2.25) we have,

$$S_1 = \frac{\partial \psi}{\partial x_2} = i\omega \frac{N_2}{\beta} \, \psi(\bar{x}, t), \tag{2.26}$$

$$S_2 = \frac{\partial \psi}{\partial x_1} = -i\omega \frac{N_1}{\beta} \, \psi(\bar{x}, t), \tag{2.27}$$

$$S_3 = 0. \tag{2.28}$$

Therefore we have,

$$\bar{S} = \left\{ \begin{matrix} u_1 \\ u_2 \end{matrix} \right\} = \left\{ \begin{matrix} N_2 \\ -N_1 \end{matrix} \right\} \frac{i\omega}{\beta} \, e^{i\omega(N_1 x_1/\beta \, + \, N_2 x_2/\beta \, - \, t)}. \tag{2.29}$$

Equation (2.29) describes the displacement field due to a wave potential $\bar{\psi}$ of unit, real

amplitude.

Definition of longitudinal and shear waves in terms of the displacement field

From now on we will assume that the longitudinal and shear harmonic plane waves are given in terms of the displacement field as,

$$\bar{L} = \begin{Bmatrix} u_1 \\ u_2 \end{Bmatrix} = \begin{Bmatrix} N_1 \\ N_2 \end{Bmatrix} e^{i\omega(N_1 x_1/\alpha + N_2 x_2/\alpha - t)}, \qquad (2.30)$$

$$\bar{S} = \begin{Bmatrix} u_1 \\ u_2 \end{Bmatrix} = \begin{Bmatrix} N_2 \\ -N_1 \end{Bmatrix} e^{i\omega(N_1 x_1/\beta + N_2 x_2/\beta - t)}. \qquad (2.31)$$

Comparing eqn (2.30) and (2.31) with (2.23) and (2.29) it can be seen that the terms $\dfrac{i\omega}{\alpha}$ and $\dfrac{i\omega}{\beta}$ have been dropped out. This has been done purely for convenience. Formally, we could assume appropriate wave potentials (for example, assuming $\phi_{new}(\bar{x},t) = \dfrac{\alpha}{i\omega} \phi(\bar{x},t)$ to arrive at the displacement fields given by equations (2.30) and (2.31).

Attenuation and phase velocity of a plane wave

Let us take a longitudinal wave. Its displacement field can be expressed as,

$$\bar{u}(\bar{x},t) = \bar{N} e^{i\omega(\bar{N}\cdot\bar{x}/\alpha - t)}. \qquad (2.32)$$

Sometimes it is convenient to describe plane waves in a form,

$$\bar{u}(\bar{x},t) = \bar{N} e^{i(\bar{k}\cdot\bar{x} - \omega t)}, \qquad (2.33)$$

where,

$$\bar{k} = \omega\bar{N}/\alpha , \qquad (2.34)$$

is known as a wavenumber and describes the spatial properties of a harmonic plane wave of angular frequency ω; $\bar{k}$ is a complex vector which can be expressed as a sum of its real and imaginary parts,

$$\bar{k} = \bar{k}_{re} + i\bar{k}_{im}. \qquad (2.35)$$

Now, eqn (2.32) becomes,

$$\overline{u}(\overline{x},t) = \overline{N} \, e^{i(\overline{k}_{re}\bullet\overline{x} \, - \, \omega t)} \, e^{-\overline{k}_{im}\bullet\overline{x}} \,. \tag{2.36}$$

The phase of the wave is defined by the term,

$$\phi(\overline{x},t) = \overline{k}_{re}\bullet\overline{x} - \omega t \,, \tag{2.37}$$

and its amplitude by the term $e^{-\overline{k}_{im}\bullet\overline{x}}$. A wavefront of the wave is defined as a surface in space at which the displacement field assumes the same phase at a given instant, $t=t_0$. From eqn (2.37) we have, $\phi_0 = \overline{k}_{re}\bullet\overline{x} - \omega t_0$, which gives,

$$|\overline{k}_{re}| \, |\overline{x}| \cos(\theta) = \phi_0 + \omega t_0 = const\,. \tag{2.38}$$

The angle θ is the angle between vectors $\overline{k}_{re}$ and $\overline{x}$, as shown in fig. 2.1.

From eqn (2.38) it can be seen that the wavefront of the plane wave is a plane perpendicular to the real part of the wavenumber. Equation (2.37) shows that the planes of constant phase change their spatial position with time. We can therefore lock on to a given wavefront and follow it in time. The velocity at which we would have to move in space in order to follow this wavefront is defined as the phase velocity. By eqn (2.38) the position of a given wavefront is,

$$\overline{k}_{re}\bullet\overline{x} = \phi_0 + \omega t \,, \tag{2.39}$$

which, after differentiation with respect to time gives,

$$\overline{k}_{re}\bullet\overline{c} = |\overline{k}_{re}| \, |\overline{c}| \cos(\theta) = \omega, \tag{2.40}$$

where the phase velocity vector $\overline{c} = \frac{\partial}{\partial t}\overline{x}$, and θ is the angle between $\overline{c}$ and $\overline{k}_{re}$. If the phase velocity is defined as a vector perpendicular to the surface of constant phase, then the phase velocity can be obtained without ambiguity as a vector parallel to $\overline{k}_{re}$, and eqn (2.40) becomes, $|\overline{k}_{re}| \, |\overline{c}| = \omega$, which, using eqn (2.34), gives the expression for the magnitude of the phase velocity as,

$$|\overline{c}| = \frac{\omega}{|\overline{k}_{re}|}\,. \tag{2.41}$$

The spatial variation of the field amplitude is defined by the term $e^{-\overline{k}_{im}\bullet\overline{x}}$ of eqn (2.36). Therefore the planes of constant amplitude are perpendicular to $\overline{k}_{im}$ and the gradient of the amplitude is parallel to $\overline{k}_{im}$.

If a plane wave propagates in a perfectly elastic medium then either the wave amplitude is the same everywhere in the medium, or the amplitude of the wave is exponentially decaying, planes of constant phases and planes of constant amplitudes of the wave being perpendicular to each other. In other words, either $\bar{k}_{im}$ vanishes or vectors $\bar{k}_{im}$ and $\bar{k}_{re}$ are mutually perpendicular. To show this, consider the square of the wavenumber. From eqn (2.35) we have,

$$k^2 = \bar{k}^2 = (\bar{k}_{re} + i\bar{k}_{im})^2 = k_{re}^2 - k_{im}^2 + 2i\,\bar{k}_{re}\bullet\bar{k}_{im} \ .$$

(2.42)

Equation (2.34) gives,

$$k^2 = (\frac{\omega}{\alpha})^2, \quad \text{(because } \bar{N}\bullet\bar{N} \equiv 1, \text{ eqn (2.16))}.$$

(2.43)

If the medium is elastic then, from eqn (2.17), α is real and, consequently, k^2 takes on a real positive value. As the imaginary part of k^2 is zero then, from eqn (2.42), the dot product of the vectors $\bar{k}_{re}$ and $\bar{k}_{im}$ is zero. This means that either $\bar{k}_{im}=\{0\}$ or $\bar{k}_{re}$ and $\bar{k}_{im}$ are perpendicular to each other.

It may be readily shown that shear wave attenuation and phase velocity follow the same form.

2.2.3 Stress field due to longitudinal and shear waves in plane strain

Having defined the longitudinal and shear wave displacement fields by eqn (2.30) and (2.31), it is now possible to calculate the stress fields. Stresses have been defined in terms of strains in eqn (2.1) as,

$$\sigma_{ij} = \lambda\delta_{ij}\varepsilon_{kk} + 2\mu\varepsilon_{ij} + \frac{\lambda'}{\omega}\delta_{ij}\frac{\partial}{\partial t}\varepsilon_{kk} + \frac{2\mu'}{\omega}\frac{\partial}{\partial t}\varepsilon_{ij},$$

(2.44)

For a harmonic process $\frac{\partial}{\partial t} = -i\omega$, so,

$$\sigma_{ij} = \delta_{ij}(\lambda - i\lambda')\,\varepsilon_{kk} + 2(\mu - i\mu')\,\varepsilon_{ij}.$$

(2.45)

Assuming plane strain in the x_1, x_2 plane, the stress field vector acting on a plane perpendicular to x_2 axis is two-dimensional. Noting that $\varepsilon_{kk} = \varepsilon_{11} + \varepsilon_{22}$, we can evaluate the components of the stress vector acting on a plane perpendicular to x_2 axis, using eqn (2.45),

$$\sigma_{21} = 2(\mu - i\mu')\,\varepsilon_{12},$$

(2.46)

$$\sigma_{22} = (\lambda - i\lambda')(\varepsilon_{11} + \varepsilon_{22}) + 2(\mu - i\mu')\varepsilon_{22}. \tag{2.47}$$

Now, using eqn (2.17) and (2.18) we can express the stresses as,

$$\sigma_{21} = 2\rho\beta^2\varepsilon_{12}, \tag{2.48}$$

$$\sigma_{22} = \rho\alpha^2(\varepsilon_{11} + \varepsilon_{22}) - 2\rho\beta^2\varepsilon_{11}. \tag{2.49}$$

Using the definition of strain in eqn (2.3) we have,

$$\sigma_{21} = \rho\beta^2\left(\frac{\partial}{\partial x_2}u_1 + \frac{\partial}{\partial x_1}u_2\right), \tag{2.50}$$

$$\sigma_{22} = \rho\left[\alpha^2\left(\frac{\partial}{\partial x_1}u_1 + \frac{\partial}{\partial x_2}u_2\right) - 2\beta^2\frac{\partial}{\partial x_1}u_1\right]. \tag{2.51}$$

Substituting eqn (2.30) and (2.31) into (2.50) and (2.51) we have, for longitudinal plane waves:

$$\sigma_{21} = 2i\omega\rho N_1 N_2\beta^2/\alpha\ e^{i\omega(\bar{N}\bullet\bar{x}/\alpha\ -\ t)}, \tag{2.52}$$

$$\sigma_{22} = (i\omega\rho\alpha - 2i\omega\rho N_1^2\beta^2/\alpha)\ e^{i\omega(\bar{N}\bullet\bar{x}/\alpha\ -\ t)}, \tag{2.53}$$

and for shear plane waves:

$$\sigma_{21} = i\omega\rho(N_2^2 - N_1^2)\beta\ e^{i\omega(\bar{N}\bullet\bar{x}/\alpha\ -\ t)}, \tag{2.54}$$

$$\sigma_{22} = -2i\omega\rho N_1 N_2\beta\ e^{i\omega(\bar{N}\bullet\bar{x}/\alpha\ -\ t)}. \tag{2.55}$$

2.3 Plane waves as reflected and transmitted fields at a plane interface

2.3.1 Snell's law

Derivations presented in this subsection are, in its approach, similar to any good textbook approach (see, for example, Brekhovskikh 1980, or Graff 1975).

Let us consider a system consisting of two semi-infinite media with their common boundary at $x_2 = 0$, and a harmonic plane wave incident on the boundary. The incident wave generates n-1 refracted and reflected waves of arbitrary frequencies and directions of propagations. Therefore there are n different plane waves in the whole system, with index numbers m = 1,...,n. The incident harmonic plane wave can be expressed by,

$$\bar{u} = \bar{N}_{[1]} A_1 e^{i\omega_1(\bar{N}_{[1]} \bullet \bar{x}/\alpha_1 - t)},$$
(2.56)

where the subscript $_{[1]}$ denotes the index number of the wave. Let us assume that at the boundary the incident wave generates j reflected and n-j-1 refracted waves. The reflected waves have index number m = 2,...,j and the refracted waves have index number m = j+1,...,n. The reflected and refracted waves can be expressed as,

$$\bar{u} = \bar{N}_{[m]} A_m e^{i\omega_m(\bar{N}_{[m]} \bullet \bar{x}/\alpha_m - t)}; \quad A_m \neq 0, \quad m = 2,...,n.$$
(2.57)

In section 2.2.3 it has been shown that if a given plane wave can be expressed as in eqn (2.56) and (2.57), then the stress field component σ_{21}, or σ_{22}, can be expressed in a form,

$$B_m e^{i\omega_m(\bar{N}_{[m]} \bullet \bar{x}/\alpha_m - t)}; \quad B_m \neq 0, \quad m = 1,...,n,$$
(2.58)

where B_m are complex constants. The displacement components u_1 and u_2 for each plane wave are also expressed in a form given by eqn (2.58). Let us assume that one of the displacement components u_1 or u_2, or one of the stress components σ_{21}, or σ_{22}, is continuous across the interface $x_2 = 0$. It is therefore valid to equate the value of this component on both sides of the interface. Using eqn (2.58) the continuity across the boundary can be expressed in a form,

$$B_1 e^{i\omega_1(s_1 x_1 - t)} - B_2 e^{i\omega_2(s_2 x_2 - t)} -...- B_j e^{i\omega_j(s_j x_j - t)}$$
$$+ B_{j+1} e^{i\omega_{j+1}(s_{j+1} x_{j+1} - t)} + ... + B_n e^{i\omega_n(s_n x_n - t)} = 0,$$
(2.59)

where,

$$s_m = \frac{N_{[m]1}}{\alpha_m}; \quad m = 1,...,n,$$
(2.60)

and $N_{[m]1}$ is the $\bar{N}_{[m]}$ component along the x_1 coordinate. Setting $x_1 = 0$, eqn (2.59) becomes,

$$B_1 e^{i\omega_1 t} - B_2 e^{i\omega_2 t} -...- B_j e^{i\omega_j t} + B_{j+1} e^{i\omega_{j+1} t} + ... + B_n e^{i\omega_n t} = 0,$$
(2.61)

which, by the Fourier theorem, leads to the equation,

$$\omega_m = \omega_1; \quad m = 2,...,n, \tag{2.62}$$

because it is impossible to obtain a harmonic process of a given frequency ω_1 by superposition of harmonic processes of frequencies different than ω_1. Similarly, setting $t = 0$ in eqn (2.59), and using eqn (2.62) we have,

$$B_1 \, e^{is_1 x_1} - B_2 \, e^{is_2 x_1} -...- B_j \, e^{is_j x_1} + B_{j+1} \, e^{is_{j+1} x_1} + ...+ B_n \, e^{is_n x_1} = 0, \tag{2.63}$$

which gives,

$$s_m = s_1; \quad m = 2,...,n. \tag{2.64}$$

Using eqn (2.60), eqn (2.64) can be re-written as,

$$\frac{N_{[m]1}}{\alpha_m} = \frac{N_{[1]1}}{\alpha_1}; \quad m = 2,...,n. \tag{2.65}$$

Using eqn (2.34) and (2.62) it can be seen that eqn (2.65) can be expressed in terms of wavenumbers as,

$$k_{[m]1} = k_{[1]1}; \quad m = 2,...,n. \tag{2.66}$$

Equation (2.66) shows that the wavenumber components parallel to the interface are all equal to each other.

If the incident wave propagates in a non-attenuating medium then, by eqn (2.17) and (2.34), the wavenumber $\bar{k}_{[1]}$ becomes real. Equation (2.66) then shows that in this case, all the wavenumber components parallel to the interface become real and attenuation can take place only in the direction perpendicular to the interface plane.

If the media on both sides of the interface are non-attenuating, then by eqn (2.17), α_m become real and equal to the longitudinal phase velocities and, by eqn (2.18), β_m become real and equal to the shear phase velocities. Then eqn (2.66) becomes the Snell's law equation (see for example Brekhovskikh, 1980).

Equations (2.64), (2.65) and (2.66) are equivalent to each other and are analogous to the Snell's law when the system is totally elastic. These equations,together with eqn (2.62), state that the angular frequency $\omega = \omega_m$, $m = 1,...,n$ and the complex value of $s = s_m$, $m = 1,...,n$

is preserved on both sides of the interface and is therefore spatially invariant everywhere in the system. Let us then call s the Snell constant.

Some simplifications derived from the Snell's law

As eqn (2.62) and (2.65) are preserved across plane interfaces between viscoelastic media, it is sometimes convenient to describe plane waves in terms of the Snell constant s, defined by eqn (2.60). Let us assume that a given longitudinal plane wave can be expressed as,

$$\bar{u} = \begin{Bmatrix} N_1 \\ N_2 \end{Bmatrix} e^{i\omega(\bar{N}\bullet\bar{x}/\alpha - t)}, \tag{2.67}$$

and a shear plane wave can be expressed as,

$$\bar{u} = \begin{Bmatrix} N_2 \\ -N_1 \end{Bmatrix} e^{i\omega(\bar{N}\bullet\bar{x}/\beta - t)}. \tag{2.68}$$

By Snell's law, $N_1/\beta = N_1/\alpha = s = $ const, which is spatially invariant. Making use of the definition, $\bar{N}\bullet\bar{N} \equiv 1$, stated in eqn (2.16) it can be seen that $N_2 = (1-N_1^2)^{1/2}$, which gives two different solution pairs,

$$N_1 = cs, \quad N_2 = (1 - c^2 s^2)^{1/2}, \quad \text{and}$$

$$N_1 = cs, \quad N_2 = -(1 - c^2 s^2)^{1/2}, \quad \text{where } c = \alpha \text{ or } c = \beta. \tag{2.69}$$

Equation (2.69) shows that for each of the values of c there can be only two different pairs $\{N_1,N_2\}$. When N_2 is positive then the first solution pair, $\{N_1,N_2\}$, corresponds to a wave propagating in the upward direction and the second solution pair, $\{N_1,-N_2\}$, corresponds to a wave propagating downwards. Therefore there are only four different plane waves satisfying eqn (2.62) and (2.65) simultaneously: two for c=α and two for c=β. Substituting eqn (2.69) into (2.67) and (2.68), we obtain the following expressions for the longitudinal and shear waves propagating 'upwards',

$$\bar{u} = \begin{Bmatrix} \alpha s \\ (1-\alpha^2 s^2)^{1/2} \end{Bmatrix} e^{i\omega(1-\alpha^2 s^2)^{1/2}\alpha^{-1} x_2} \, e^{i\omega(sx_1-t)}, \tag{2.70}$$

$$\bar{u} = \begin{Bmatrix} (1-\beta^2 s^2)^{1/2} \\ -\beta s \end{Bmatrix} e^{i\omega(1-\beta^2 s^2)^{1/2}\beta^{-1} x_2} \, e^{i\omega(sx_1-t)}. \tag{2.71}$$

Substituting eqn (2.70) into equations (2.52) and (2.53), we can express the components of the stress acting on a plane perpendicular to x_2 axis due to harmonic longitudinal plane waves as,

$$\sigma_{21} = 2i\omega\rho s\beta^2(1-\alpha^2 s^2)^{1/2} \, e^{i\omega(1-\alpha^2 s^2)^{1/2}\alpha^{-1}x_2} \, e^{i\omega(sx_1-t)}, \tag{2.72}$$

$$\sigma_{22} = i\omega\rho\alpha(1-2\beta^2 s^2) \, e^{i\omega(1-\alpha^2 s^2)^{1/2}\alpha^{-1}x_2} \, e^{i\omega(sx_1-t)}. \tag{2.73}$$

Substituting eqn (2.71) into equations (2.54) and (2.55), we can express the components of the stress acting on a plane perpendicular to x_2 axis due to harmonic shear plane waves as,

$$\sigma_{21} = i\omega\rho\beta(1-2\beta^2 s^2) \, e^{i\omega(1-\beta^2 s^2)^{1/2}\beta^{-1}x_2} \, e^{i\omega(sx_1-t)}, \tag{2.74}$$

$$\sigma_{22} = -2i\omega\rho s\beta^2(1-\beta^2 s^2)^{1/2} \, e^{i\omega(1-\beta^2 s^2)^{1/2}\beta^{-1}x_2} \, e^{i\omega(sx_1-t)}. \tag{2.75}$$

2.3.2 Displacement and stress field in a layer

In section 2.3.1 it has been shown that if it is assumed that the refracted and reflected waves are plane waves then they have to have the same frequencies, eqn (2.62), and also satisfy Snell's Law stated in eqn (2.65). In that section it was also shown that there are only four different plane waves satisfying eqn (2.62) and (2.65) simultaneously in a given infinite viscoelastic medium: two longitudinal plane waves and two shear plane waves. Let us, therefore, denote the amplitudes of the four waves as,

T_p - the amplitude of the longitudinal wave 'up',

R_p - the amplitude of the longitudinal wave 'down',

T_s - the amplitude of the shear wave 'up',

R_s - the amplitude of the shear wave 'down',

(see fig. 2.2), and derive an equation for the displacement and the stress field in the layer in terms of T_p, R_p, T_s, and R_s. In other words we want to find the transformation matrix $\mathcal{M}$, so that,

$$\mathcal{M} \begin{Bmatrix} R_p \\ R_s \\ T_p \\ T_s \end{Bmatrix} = \begin{Bmatrix} \sigma_{22} \\ \sigma_{21} \\ u_1 \\ u_2 \end{Bmatrix}. \tag{2.76}$$

Let us denote,

$$A = (1-\alpha^2 s^2)^{1/2}, \quad B = (1-\beta^2 s^2)^{1/2}, \quad C = 1-2\beta^2 s^2.$$

$$g_p = e^{i\omega A\alpha^{-1}x_2}, \quad g_s = e^{i\omega B\beta^{-1}x_2}, \tag{2.77}$$

Then the displacement and the stress fields for each component wave can be expressed as follows. Using eqn (2.67), (2.52) and (2.53) we have for the longitudinal wave 'up',

$$\bar{u} = \begin{Bmatrix} u_1 \\ u_2 \end{Bmatrix} = T_p \begin{Bmatrix} \alpha s \\ A \end{Bmatrix} g_p\, e^{i\omega(sx_1-t)}, \tag{2.78}$$

$$\sigma_{12} = T_p\, 2i\omega\rho s\beta^2 A\, g_p\, e^{i\omega(sx_1-t)}, \tag{2.79}$$

$$\sigma_{22} = T_p\, i\omega\rho\alpha C\, g_p\, e^{i\omega(sx_1-t)}. \tag{2.80}$$

Using eqn (2.67), (2.52) and (2.53) we have for the longitudinal wave 'down',

$$\bar{u} = \begin{Bmatrix} u_1 \\ u_2 \end{Bmatrix} = R_p \begin{Bmatrix} \alpha s \\ -A \end{Bmatrix} g_p^{-1}\, e^{i\omega(sx_1-t)}, \tag{2.81}$$

$$\sigma_{12} = -R_p\, 2i\omega\rho s\beta^2 A\, g_p^{-1}\, e^{i\omega(sx_1-t)}, \tag{2.82}$$

$$\sigma_{22} = R_p\, i\omega\rho\alpha C\, g_p^{-1}\, e^{i\omega(sx_1-t)}. \tag{2.83}$$

Using eqn (2.68), (2.54) and (2.55) we have for the shear wave 'up',

$$\bar{u} = \begin{Bmatrix} u_1 \\ u_2 \end{Bmatrix} = T_s \begin{Bmatrix} B \\ -\beta s \end{Bmatrix} g_s\, e^{i\omega(sx_1-t)}, \tag{2.84}$$

$$\sigma_{12} = T_s\, i\omega\rho\beta C\, g_s\, e^{i\omega(sx_1-t)}, \tag{2.85}$$

$$\sigma_{22} = -T_s \, 2i\omega\rho s\beta^2 B \, g_s \, e^{i\omega(sx_1-t)}.$$

(2.86)

Using eqn (2.68), (2.54) and (2.55) we have for the shear wave 'down',

$$\bar{u} = \begin{Bmatrix} u_1 \\ u_2 \end{Bmatrix} = R_s \begin{Bmatrix} -B \\ -\beta s \end{Bmatrix} g_s^{-1} \, e^{i\omega(sx_1-t)},$$

(2.87)

$$\sigma_{12} = R_s \, i\omega\rho\beta C \, g_s^{-1} \, e^{i\omega(sx_1-t)},$$

(2.88)

$$\sigma_{22} = R_s \, 2i\omega\rho s\beta^2 B \, g_s^{-1} \, e^{i\omega(sx_1-t)}.$$

(2.89)

Combining equations (2.77)-(2.89) we can describe the displacement-stress field in matrix notation as,

$$\begin{bmatrix} i\omega\rho\alpha C g_p^{-1} & 2i\omega\rho s\beta^2 B g_s^{-1} & i\omega\rho\alpha C g_p & -2i\omega\rho s\beta^2 B g_s \\ -2i\omega\rho s\beta^2 A g_p^{-1} & i\omega\rho\beta C g_s^{-1} & 2i\omega\rho s\beta^2 A g_p & i\omega\rho\beta C g_s \\ \alpha s g_p^{-1} & -B g_s^{-1} & \alpha s g_p & B g_s \\ -A g_p^{-1} & -\beta s g_s^{-1} & A g_p & -\beta s g_s \end{bmatrix} \begin{Bmatrix} R_p \\ R_s \\ T_p \\ T_s \end{Bmatrix} = \begin{Bmatrix} \sigma_{22} \\ \sigma_{21} \\ u_1 \\ u_2 \end{Bmatrix},$$

(2.90)

where the common term, $e^{i\omega(sx_1-t)}$, has been omitted here for clarity. The formulation given by eqn (2.90) is similar in concept to that of Thomson (1950) and Haskell (1953), where the matrix formulation was applied to elastic media. Propagation and reflection of ultrasonic waves in viscoelastic media were considered in a number of recent publications (see for example Becker and Richardson 1970, Fiorito et al. 1985, Deschamps 1990).

Reflection coefficient for a plane wave at a single interface between two viscoelastic media

Consider the interface between medium 1 and medium 2, both of which are viscoelastic. The interface lies in the x_1,x_3 plane, and satisfies the equation $x_2 = 0$. A longitudinal plane wave of unit amplitude is incident on the interface from medium 1, the direction of propagation being in the x_1,x_2 plane. The angle of incidence of the plane wave to the normal to the interface is

denoted by θ. Let us assume that the displacement and stress field is continuous across the boundary $x_2 = 0$ and the reflected and refracted field can be expressed as a sum of plane waves. From section 2.3.1 it follows that all the plane waves must have the same frequency and must satisfy Snell's Law. In other words, equations (2.62) and (2.65) are preserved on both sides of the interface. Consequently, the analysis given in section 2.3.2 shows that on each side of the boundary there may be at most four different plane waves satisfying eqn (2.62) and (2.65) simultaneously and, therefore, eqn (2.90) describing the displacement and stress field is valid on both sides of the boundary if appropriate values of mechanical constants are inserted into eqn (2.77).

Let us therefore denote the amplitudes of the plane waves in medium 1 as, R_{p1}, R_{s1}, T_{p1}, T_{s1} and in medium 2 as, R_{p2}, R_{s2}, T_{p2}, T_{s2}, (see fig. 2.3). Using eqn (2.90) the displacement and stress field in medium 1 can be expressed as,

$$
\begin{bmatrix}
i\omega\rho_1\alpha_1 C_1 g_{p1}^{-1} & 1i\omega\rho_1 s\beta_1^{-1} B g_{s1}^{-1} & i\omega\rho_1\alpha_1 C_1 g_{p1} & -1i\omega\rho_1 s\beta_1^1 B_1 g_{s1} \\
-1i\omega\rho_1 s\beta_1^1 A_1 g_{p1}^{-1} & i\omega\rho_1\beta_1 C_1 g_{s1}^{-1} & 1i\omega\rho_1 s\beta_1^1 A_1 g_{p1} & i\omega\rho_1\beta_1 C_1 g_{s1} \\
\alpha_1 s g_{p1}^{-1} & -B_1 g_{s1}^{-1} & \alpha_1 s g_{p1} & B_1 g_{s1} \\
-A_1 g_{p1}^{-1} & -\beta_1 s g_{s1}^{-1} & A_1 g_{p1} & -\beta_1 s g_{s1}
\end{bmatrix}
\begin{Bmatrix}
R_{p1} \\ R_{s1} \\ T_{p1} \\ T_{s1}
\end{Bmatrix}
=
\begin{Bmatrix}
\sigma_{22[1]} \\ \sigma_{12[1]} \\ u_{1[1]} \\ u_{2[1]}
\end{Bmatrix},
\qquad (2.91)
$$

or,

$$
\mathcal{M}_1 \left\{ \begin{Bmatrix} R_1 \\ T_1 \end{Bmatrix} \right\} = \left\{ \begin{Bmatrix} \sigma_1 \\ u_1 \end{Bmatrix} \right\}.
\qquad (2.92)
$$

Similarly, the displacement and stress field in medium 2 can be expressed as,

$$
\begin{bmatrix}
i\omega\rho_2\alpha_2 C_2 g_{p2}^{-1} & 2i\omega\rho_2 s\beta_2^{-2} B g_{s2}^{-1} & i\omega\rho_2\alpha_2 C_2 g_{p2} & -2i\omega\rho_2 s\beta_2^2 B_2 g_{s2} \\
-2i\omega\rho_2 s\beta_2^2 A_2 g_{p2}^{-1} & i\omega\rho_2\beta_2 C_2 g_{s2}^{-1} & 2i\omega\rho_2 s\beta_2^2 A_2 g_{p2} & i\omega\rho_2\beta_2 C_2 g_{s2} \\
\alpha_2 s g_{p2}^{-1} & -B_2 g_{s2}^{-1} & \alpha_2 s g_{p2} & B_2 g_{s2} \\
-A_2 g_{p2}^{-1} & -\beta_2 s g_{s2}^{-1} & A_2 g_{p2} & -\beta_2 s g_{s2}
\end{bmatrix}
\begin{Bmatrix}
R_{p2} \\ R_{s2} \\ T_{p2} \\ T_{s2}
\end{Bmatrix}
=
\begin{Bmatrix}
\sigma_{22[2]} \\ \sigma_{12[2]} \\ u_{1[2]} \\ u_{2[2]}
\end{Bmatrix},
\qquad (2.93)
$$

or,

$$
\mathcal{M}_2 \left\{ \begin{Bmatrix} R_2 \\ T_2 \end{Bmatrix} \right\} = \left\{ \begin{Bmatrix} \sigma_2 \\ u_2 \end{Bmatrix} \right\}.
\qquad (2.94)
$$

Using eqn (2.92) and (2.94), the requirement of stress and displacement continuity across the boundary can be expressed as,

$$
\mathcal{M}_1 \left\{ \begin{Bmatrix} R_1 \\ T_1 \end{Bmatrix} \right\} = \mathcal{M}_2 \left\{ \begin{Bmatrix} R_2 \\ T_2 \end{Bmatrix} \right\}.
$$

(2.95)

Consider now a single longitudinal plane wave of unit amplitude incident on the interface from medium 1. We also assume that there are no other waves incident on the boundary. $\{T_1\}$ is the vector of the longitudinal and shear wave amplitudes incident on the boundary from medium 1 and is therefore known. Since there are no waves incident on the boundary from medium 2, $\{R_2\}$ is null. Thus $T_{p1}=1$, and $T_{s1}= R_{p2}= R_{s2}=0$, giving,

$$
\{T_1\} = \begin{Bmatrix} 1 \\ 0 \end{Bmatrix}, \text{ and } \{R_2\} = \begin{Bmatrix} 0 \\ 0 \end{Bmatrix}.
$$

(2.96)

The remaining four complex values of R_{p1}, R_{s1}, T_{p2}, T_{s2}, which are the amplitudes of reflected and transmitted waves across the interface, are to be calculated. Equation (2.95) can be re-written as,

$$
[\mathcal{M}_{R1} \quad \mathcal{M}_{T1}] \left\{ \begin{Bmatrix} R_1 \\ T_1 \end{Bmatrix} \right\} = [\mathcal{M}_{R2} \quad \mathcal{M}_{T2}] \left\{ \begin{Bmatrix} R_2 \\ T_2 \end{Bmatrix} \right\},
$$

(2.97)

where $\mathcal{M}_{R1}$, $\mathcal{M}_{T1}$, and $\mathcal{M}_{R2}$, $\mathcal{M}_{T2}$ are of dimensions 2x4 and are submatrices of $\mathcal{M}_1$ and $\mathcal{M}_2$, respectively. Equation (2.97) may be re-written to give,

$$
[\mathcal{M}_{R1} \quad \text{-}\mathcal{M}_{T2}] \left\{ \begin{Bmatrix} R_1 \\ T_2 \end{Bmatrix} \right\} = [\mathcal{M}_{R2} \quad \text{-}\mathcal{M}_{T1}] \left\{ \begin{Bmatrix} R_2 \\ T_1 \end{Bmatrix} \right\}.
$$

(2.98)

The right-hand side of the eqn (2.98) is known, therefore eqn (2.98) is a system of four linear equation with four complex unknowns. The solution of eqn (2.98) yields two reflection coefficients: longitudinal R_{p1} and shear R_{s1}, and two transmission coefficients, longitudinal T_{p2} and shear T_{s2}, as functions of Snell's constant, s, which in turn can be related to the angle of incidence of the longitudinal wave from medium 1, by eqn (2.60).

2.3.3 Boundary stiffness matrix

In section 2.3.2 the derivations of reflected and transmitted harmonic plane waves were carried out assuming that the displacement and stress fields are continuous across the boundary. This corresponds to the case of a perfect bond between two media, where the displacements are transmitted across the boundary unchanged. However, when the rigidity of the interface is assumed to be finite, then the particle displacement on each side of a boundary may not be

identical. In such cases it is necessary to take the stiffness of the interface into consideration when calculating reflected and transmitted waves at the boundary. There are a number of circumstances in which an interface between two solids can be approximated to a massless spring (see for example Tattersall 1973, Nagy 1990, Arakawa 1983, Pilarski and Rose 1988). More detailed discussion of this can be found in subsection 1.4.1 of this thesis.

In general, the boundary stiffness matrix is defined by six independent constants. However, when the mechanical properties of the interfaces are the same regardless of the sense of an axis perpendicular to the interface, and the mechanical properties are isotropic in the plane parallel to the interface, the number of constants fully defining the boundary can be reduced to two: the normal stiffness and the tangential stiffness. This can be shown as follows.

Consider an interface which allows for discontinuities of the displacement field. The difference of the displacement across the boundary can be expressed as the discontinuity vector $\Delta \overline{u}$ (see fig. 2.4).

Across the boundary the stress field is continuous, that is, the stresses on both sides of the boundary are equal. Moreover, let us assume that there is a linear relationship between the stress vector and the discontinuity vector at the boundary. This can be expressed in matrix notation as,

$$\begin{Bmatrix} \sigma_{21} \\ \sigma_{22} \\ \sigma_{23} \end{Bmatrix} = \begin{bmatrix} k_{11} & k_{12} & k_{13} \\ k_{21} & k_{22} & k_{23} \\ k_{31} & k_{32} & k_{33} \end{bmatrix} \begin{Bmatrix} \Delta u_1 \\ \Delta u_2 \\ \Delta u_3 \end{Bmatrix} ,$$
(2.99)

or, more concisely,

$$\overline{\sigma} = \mathcal{K} \, \Delta \overline{u} ,$$
(2.100)

where Δu_i, $i = 1,....,3$ is the difference in the displacement between two media across the boundary in the ith direction. The complex stiffness matrix, $\mathcal{K}$, represents the mechanical properties of the boundary. From the Betti theorem of reciprocity (see for example Timoshenko and Goodier 1970), matrix $\mathcal{K}$ is symmetric ie $k_{ij} = k_{ji}$, $i,j = 1,....,3$, and therefore, it can be defined by six independent constants.

If we assume that the stiffness of the boundary is invariant in a given linear coordinate transform $\mathcal{T}$, like rotation or inversion then, using eqn (2.100), this statement can be expressed

as,

$$\mathcal{F}(\mathcal{K}\,\Delta\bar{u}) = \mathcal{K}\,(\mathcal{F}\,\Delta\bar{u}), \tag{2.101}$$

which means that the same value of stress vector is obtained before and after the coordinate transformation. Dropping out the brackets and assuming that $\Delta\bar{u}\neq\{0\}$, we have,

$$\mathcal{F}\,\mathcal{K} = \mathcal{K}\,\mathcal{F}\,. \tag{2.102}$$

Invariance in inversion of the x_2 axis

If it is assumed that the mechanical properties of the boundary are the same regardless of the sense of the x_2 axis, then the stiffness matrix $\mathcal{K}$ must be invariant in inversion of the x_2 axis. Now the coordinate transformation matrix is,

$$\mathcal{F} = \begin{bmatrix} 1 & 0 & 0 \\ 0 & -1 & 0 \\ 0 & 0 & 1 \end{bmatrix}. \tag{2.103}$$

Substituting eqn (2.103) into eqn (2.102) and using the symmetry of $\mathcal{K}$, we have, $k_{12} = k_{21} = k_{23} = k_{32} = 0$, and $\mathcal{K}$ becomes,

$$\mathcal{K} = \begin{bmatrix} k_{11} & 0 & k_{13} \\ 0 & k_{22} & 0 \\ k_{31} & 0 & k_{33} \end{bmatrix}. \tag{2.104}$$

Invariance in rotation about the x_2 axis

If the mechanical properties of the boundary are isotropic in the x_1,x_3 plane, then the stiffness matrix remains the same in rotation about the x_2 axis. Here the transformation matrix is,

$$\mathcal{F} = \begin{bmatrix} \cos\theta & 0 & -\sin\theta \\ 0 & 1 & 0 \\ \sin\theta & 0 & \cos\theta \end{bmatrix}, \tag{2.105}$$

where θ denotes an angle of rotation around the x_2 axis. Substituting eqn (2.105) into eqn (2.102) and using the symmetry of $\mathcal{K}$, we have, $k_{13} = k_{31} = 0$, and $k_{11} = k_{33}$. If we denote $k_{11} = k_{33} = k_T$ and $k_{22} = k_N$, then the matrix $\mathcal{K}$ becomes,

$$\mathcal{K} = \begin{bmatrix} k_T & 0 & 0 \\ 0 & k_N & 0 \\ 0 & 0 & k_T \end{bmatrix},$$

(2.106)

where, the (in general) complex values of k_T and k_N are the tangential and normal stiffnesses respectively.

Sometimes it is convenient to describe the mechanical properties of the boundary by its stress-displacement transfer matrix, relating the stress-displacement field on one side of the boundary to that on the other. This can be expressed as,

$$\mathcal{B} \left\{ \begin{array}{c} \overline{\sigma} \\ \overline{u} \end{array} \right\}_{[1]} = \left\{ \begin{array}{c} \overline{\sigma} \\ \overline{u} \end{array} \right\}_{[2]},$$

(2.107)

where $\mathcal{B}$ is the stress-displacement boundary transfer matrix, and the index numbers [1] and [2] refer to the stress and displacement fields at the boundary in medium 1 and medium 2, respectively. From the assumptions stated at the beginning of this section, the stress field is equal on both sides of the boundary,

$$\overline{\sigma}_{[2]} = \overline{\sigma}_{[1]}.$$

(2.108)

Using eqn (2.100) the displacement field at the boundary in medium 2 can be expressed in terms of the stress-displacement field at the boundary in medium 1 as,

$$\overline{u}_{[2]} = \overline{u}_{[1]} + \mathcal{K}^{-1} \overline{\sigma}_{[1]}.$$

(2.109)

In some cases, for example when calculating the stress-displacement field of a plane wave whose direction of propagation is parallel to the (x_1, x_2) plane, it is sufficient to consider equations (2.108) and (2.109) in their two dimensional form. In that case $\mathcal{K}$ becomes a 2×2 matrix and its inverse becomes,

$$\mathcal{K}^{-1} = \begin{bmatrix} 0 & 1/k_T \\ 1/k_N & 0 \end{bmatrix}.$$

(2.110)

Equations (2.108) and (2.109) can be then expressed in matrix notation as,

$$
\begin{bmatrix} 1 & 0 & 0 & 0 \\ 0 & 1 & 0 & 0 \\ 0 & 1/k_N & 1 & 0 \\ 1/k_T & 0 & 0 & 1 \end{bmatrix} \begin{Bmatrix} \sigma_{22} \\ \sigma_{21} \\ u_1 \\ u_2 \end{Bmatrix}_{[1]} = \begin{Bmatrix} \sigma_{22} \\ \sigma_{21} \\ u_1 \\ u_2 \end{Bmatrix}_{[2]} , \qquad (2.111)
$$

where the 4×4 matrix is the boundary transfer matrix $\mathscr{B}$ for the plane strain case in the (x_1, x_2) plane. Expression of the form of eqn (2.111) has been given by a number of authors (see for example Schoenberg 1980, Pilarski et al. 1990).

There are three limiting cases of the boundary stiffness matrix (see for example Pilarski and Rose 1988):

Total debonding takes place when $k_T = 0$ and $k_N = 0$, which means that the stresses on both sides of the boundary vanish and the displacements on both sides of the boundary can be arbitrary. In other words, the two media have free surfaces and there is no transmission of stresses across the boundary.

The ideal connection, or 'welded' boundary condition takes place when $k_T \rightarrow \infty$ and $k_N \rightarrow \infty$. In this case the stress and displacement fields are continuous across the boundary.

The 'smooth' boundary condition occurs when $k_T = 0$ and $k_N \rightarrow \infty$. This boundary condition allows for free tangential displacements across the boundary with zero tangential stresses and continuous normal stresses and displacements. In other words the two media are in intimate contact, sliding on each other in a frictionless manner.

Further analysis of the spring model and comparisons of its performance against more accurate theories is given in section 4.5 of this thesis.

2.4   Finite transducer

In section 2.3 the problem of the propagation of plane waves and their interaction with plane boundaries has been discussed in detail and the theory for the calculation of ultrasonic reflection coefficients from single boundaries has been given. These derivations assumed that the incident field is a plane harmonic wave extending infinitely along the interface. However, because the transducers used to generate ultrasound are of finite dimensions, they cannot produce single infinite plane waves. It is therefore desirable to address the applicabilty of the infinite plane

wave theory to real cases.

In this section it is shown that the ultrasonic fields generated by transducers of finite dimensions can be decomposed into infinite plane wave components using Fourier transformation. In other words, the acoustic fields generated by ultrasonic probes can be represented as the sum of infinite harmonic plane waves propagating in different directions. The theory presented here can, in general, be used in either two or three dimensions. The derivation shown here considers the two dimensional plane strain case.

2.4.1 Transducer generating a single infinite plane wave

Let us assume an infinite inviscid liquid half space from the surface of an infinite transducer at $x_2=0$ and continuing towards positive values of x_2 (see fig. 2.5). The infinite transducer generates a harmonic longitudinal plane wave in the liquid given by the equation,

$$\bar{u} = A \begin{Bmatrix} N_1 \\ N_2 \end{Bmatrix} e^{i\omega(\bar{N}\bullet\bar{x}/\alpha - t)} . \tag{2.112}$$

Let us determine the displacement boundary conditions which support the generation of the wave described by eqn (2.112). Setting $x_2=0$ in eqn (2.112), we have,

$$\bar{u} = A \begin{Bmatrix} N_1 \\ N_2 \end{Bmatrix} e^{i\omega(N_1 x_1/\alpha - t)} . \tag{2.113}$$

From eqn (2.113) it can be seen that the movement of the liquid at the surface of the transducer consists of displacement components both normal (u_2) and parallel (u_1) to the surface of the transducer as shown in fig. 2.5. If the face of the transducer moves in this manner then the single plane wave described by eqn (2.112) will be generated. For our purposes it is convenient to ignore the component of movement parallel to the face of the transducer, and it can be shown that this has a negligible effect in liquids as follows. Consider the motion of the face of the transducer consisting entirely of movement parallel to the face of the transducer,

$$\bar{u} = A \begin{Bmatrix} -N_1 \\ 0 \end{Bmatrix} e^{i\omega(N_1 x_1/\alpha - t)} . \tag{2.114}$$

For a solid moving in a perfect, inviscid, liquid no wave will be generated as there is no coupling mechanism on the boundary. In practice, when the viscosity of the liquid is taken into account, some shear wave field will be generated, but because of the viscosity, this field is bound to attenuate in an extremely short distance.

Now if the two different motions of the transducer, described by equations (2.113) and (2.114), are added together,

$$\bar{u} = A \begin{Bmatrix} N_1 \\ N_2 \end{Bmatrix} e^{i\omega(N_1 x_1/\alpha - t)} + A \begin{Bmatrix} -N_1 \\ 0 \end{Bmatrix} e^{i\omega(N_1 x_1/\alpha - t)},$$ (2.115)

then, the field generated by the transducer will be the superposition of the fields generated by each of the motions separately. As the second term in eqn (1.115) has no effect on the wave generation in an inviscid liquid, then the motion of the transducer given by,

$$\bar{u} = A \begin{Bmatrix} 0 \\ N_2 \end{Bmatrix} e^{i\omega(N_1 x_1/\alpha - t)},$$ (2.116)

must generate the same field as the motion described by eqn (2.113).

2.4.2 Field generated by a finite transducer in liquid

As can be seen from eqn (2.116), the generation of a plane wave can only be achieved by a transducer extending infinitely in the x_1 direction, whose normal displacement at its face is governed by the equation,

$$u_2 = AN_2 \, e^{i\omega(N_1 x_1/\alpha - t)}.$$ (2.117)

In reality, however, the transducer is of finite size, the displacement at its face being an arbitrary continuous function. It is therefore necessary to consider the case of the finite transducer and to derive the expression for the displacement field generated in a liquid. Let us assume that at the boundary $x_2 = 0$ the normal displacement is given in a form, $u_2 = f(x_1) \, e^{-i\omega t}$ as shown schematically in fig. 2.6.

Function $f(x_1)$ is continuous and vanishes outside the surface of the transducer, and therefore satisfies the Dirichlet condition and is absolutely integrable. By the Fourier theorem it is valid to describe $f(x_1)$ in a Fourier integral form as (Bracewell 1965),

$$f(x_1) = \frac{1}{2\pi} \int_{-\infty}^{+\infty} \left\{ \int_{-\infty}^{+\infty} f(x_1) \, e^{-ik_1 x_1} dx_1 \right\} e^{ik_1 x_1} \, dk_1,$$ (2.118)

which states that the normal displacement at the boundary can be formed by superposition of spatial harmonic components,

$$u_2(x_1) = B(k_1) e^{ik_1 x_1} e^{-i\omega t} ,$$

(2.119)

the amplitudes of which are given by the Fourier integral,

$$B(k_1) = \frac{1}{2\pi} \int_{-\infty}^{+\infty} f(x_1) e^{-ik_1 x_1} dx_1 .$$

(2.120)

Equations (2.119) and (2.117) describe the same harmonic motion of the front face of the transducer if $k_1 = \omega N_1/\alpha$, and $B(k_1) = AN_2$. Therefore, setting

$$N_1 = \frac{\alpha k_1}{\omega}, \quad N_2 = (1-N_1^2)^{1/2}, \quad A(k_1) = \frac{B(k_1)}{N_2} ,$$

(2.121)

each of the harmonic components, given by eqn (2.119), generates a plane wave, described by eqn (2.112), in the liquid. Using the principle of superposition it is now valid to sum all the plane waves generated by spatial harmonic components of the displacement field $f(x_1) e^{-i\omega t}$ to form the field generated by the finite transducer,

$$\bar{u} = \int_{-\infty}^{+\infty} A \begin{Bmatrix} N_1 \\ N_2 \end{Bmatrix} e^{i\omega(\bar{N} \cdot \bar{x}/\alpha - t)} dk_1 ,$$

(2.122)

where $\bar{N}$ and A are functions of k_1, given by eqn (2.121).

According to the assumptions, $f(x_1)$ vanishes outside the range $<x_{1a}, x_{1b}>$, and therefore the infinite Fourier integral in eqn (2.120) can be replaced by a finite Fourier integral,

$$B(k_1) = \frac{1}{2\pi} \int_{x_{1a}}^{x_{1b}} f(x_1) e^{-ik_1 x_1} dx_1 .$$

(2.123)

If it is assumed that the function $f(x_1)$ fully "fills" the range $<x_{1a}, x_{1b}>$ then it is possible to show (see for example Randall 1987) that the function B assumes significant values only between $-k_{1d}$ and k_{1d}, where k_{1d} is a real positive value approximately equal to $(x_{1b}-x_{1a})^{-1}$,

$$B(k_1) = \begin{cases} \text{significant} & -k_{1d} \le k_1 \le k_{1d}, \text{ where } k_{1d} \approx (x_{1b}-x_{1a})^{-1} \\ \approx 0 \text{ elsewhere} \end{cases} .$$

(2.124)

In other words, the k_1 domain bandwidth of the function $f(x_1)$ is approximately equal to the reciprocal of the spatial width of the transducer. Therefore the wider the transducer the narrower the k_1 bandwidth of the generated field. The wavenumber of a given plane wave can

be described using eqn (2.34) as,

$$\bar{k} = \frac{\omega}{\alpha} \bar{N} ,$$ (2.125)

Since in an inviscid fluid the loss terms are zero, α is real by eqn (2.17), and the phase velocity, $c = \alpha$, by eqn (2.41). The wavenumber component parallel to the face of the transducer can be evaluated as,

$$k_1 = |\bar{k}| \sin\theta = \frac{\omega}{c} \sin\theta,$$ (2.126)

where θ is the angle between the direction of propagation of the plane wave and the normal to the face of the transducer. Equation (2.126) can be rewritten as,

$$\theta = \sin^{-1}(k_1 \frac{c}{\omega}),$$ (2.127)

which allows us to state that if the generated field has a narrow k_1 bandwidth (wide transducer) then it consists of the plane waves whose directions of propagation are close to the perpendicular to the face of the transducer. If the k_1 bandwidth of the field is wide (narrow transducer) then it consists of plane waves of wider spread of directions of propagation. The angular spread of the field is also dependent on the frequency, ω, of the harmonic process. Equation (2.127) shows that the angular spread of the field decreases with frequency.

As the k_1 bandwidth of the generated field is finite then the infinite inverse Fourier integral in eqn (2.122) can be replaced by a finite one without a significant loss in accuracy,

$$\bar{u} \approx \int_{-k_{1d}}^{k_{1d}} A \begin{Bmatrix} N_1 \\ N_2 \end{Bmatrix} e^{i\omega(\bar{N}\cdot\bar{x}/\alpha - t)} dk_1 ,$$ (2.128)

It can be seen from eqn (2.123) and (2.128) that the spatial decomposition (forward Fourier transform) and synthesis (inverse Fourier transform) can be performed on a finite range of the x_1 space and k_1 space. Therefore the Fast Fourier Transform algorithm can be employed for numerical evaluations of equations (2.122) and (2.123) without significant deterioration of computation accuracy.

Displacement field generated by a finite transducer

To show how to use equations (2.122) and (2.123) let us calculate the ultrasonic field generated by a 10 mm wide transducer in water. Since the two dimensional plane strain theory is to be

applied here, the transducer is assumed to be placed perpendicular to x_1, x_2 plane (see fig. 2.6) so that it extends infinitely in the direction normal to the x_1, x_2 plane. The transducer is of finite dimensions in the $x1$ direction and $x_{1b} - x_{1a} = 10$ mm. If the normal displacement at the face of the transducer is known then, in accordance with eqn (2.122), it is possible to obtain the expression for the displacement field in the fluid as a superposition of longitudinal plane waves. The displacement field at $x_2=0$ is therefore given by,

$$\bar{u}(x_1,0) = \int_{-\infty}^{+\infty} A \begin{Bmatrix} N_1 \\ N_2 \end{Bmatrix} e^{i\omega(N_1 x_1/\alpha - t)} \, dk_1 \, . \tag{2.129}$$

At a distance l_2 in the direction normal to the surface of the transducer the displacement field is,

$$\bar{u}(x_1,l_2) = \int_{-\infty}^{+\infty} A \begin{Bmatrix} N_1 \\ N_2 \end{Bmatrix} e^{i\omega[(N_1 x_1 + N_2 l_2)/\alpha - t]} \, dk_1, \tag{2.130}$$

which shows that the phase of each of the plane wave components shifts in proportion to the product, $N_2 l_2$, and the amplitude remains the same. Therefore, in order to compute the displacement field at the distance l_2 from the face of the transducer, it is valid to decompose the normal displacement at the face of the transducer into sinusoidal components, shift the phase of each component by $\omega N_2 l_2/\alpha$ and synthesise the field back by adding all the components together.

The method was used to calculate ultrasonic field distributions in front of 10 mm wide transducers in water outputing energy at different frequencies and with different displacement shapes at their faces. Figures 2.7 and 2.8 show the computed displacement component normal to the face of the transmitter. The field is generated in water by transmitters with Gaussian and tapered normal displacement patterns at their faces. The Gaussian profile is defined by the function $f(x) = \exp(-x^2)$. The tapered profile is a modified rectangular window function, increasing over 10 % of its width from zero to unity in a half sine manner, then maintaining the unity value over the next 80 % of its width, and then finally decreasing from unity to zero over 10 % of its width again in a half-sine shape manner (see fig. 2.9).

In figures 2.7 and 2.8, 10 mm wide transducers are placed at the origin of the Cartesian coordinate system and generate fields in the positive direction of the vertical axis, which is shown in the middle of each plot. This way each of the four figures show the vertical component of the displacement field in a square extending from 100 mm to the left of the transducer to 100 mm to the right of the transducer in the horizontal direction and from zero to 200 mm in the vertical direction. In fig. 2.7 both transducers operate at the frequency of 2 MHz, and in fig. 2.8 the probes operate at the frequency of 10 MHz.

Comparing figures 2.7 (a) with 2.8 (a), and 2.7 (b) with 2.8 (b), it can be seen that the spread of the generated field is frequency dependent and is smaller for higher frequencies. Indeed, the area isonified by the transducer operating at the frequency of 10 MHz (fig 2.8 (a)), is contained in much closer proximity to the transducer's axis of symmetry than in the case of the same transducer operating at a frequency of 2 MHz, shown in fig. 2.7 (a).

Transducers with tapered displacement patterns generate fields with very strong middle lobe and much weaker side lobes (see figures 2.7 (b) and 2.8 (b)), sometimes referred to as the edge waves (see for example Guyott and Cawley, 1988). The edge wave phenomenon is not seen for the Gaussian type transducers (see figures 2.7(a), and 2.8(a))

Comparison of the plane wave decomposition approach with the Huyghens principle method

Probably the most popular way to solve the radiation problem of the finite transducer is to employ Huyghens principle by integrating the Green's function over the transducer's area (see for example Morse and Ingard 1968). For the comparison between the Huyghens principle approach and the Fourier decomposition and synthesis method, the normal displacement field 200 mm away from the 10 mm wide transducer was computed. Figure 2.10 shows the results of the calculations. The vertical axis represents the amplitude of the displacement in the direction perpendicular to the face of the transducer, while the horizontal axis represents the distance away from the transducer's axis of symmetry. Figures 2.9 (a) and 2.9 (b) look identical, indicating perfect agreement between the Huyghens principle approach and the Fourier decomposition method.

2.4.3 Reflected field generated by a finite transducer in liquid

So far in this section we have been concerned with the generation of a field by a finite transducer. Let us now study the reflection of a finite beam from a plane interface. Consider therefore a finite transducer in an inviscid fluid and a boundary at $x_2=0$ as shown in fig. 2.11.

The axis of the transducer is inclined at an angle θ with respect to the normal to the interface and placed so that its face is at a distance d_1 from the origin of the x_1, x_2 coordinate system. The total field generated by the transducer will now be composed of the incident and the reflected field. The incident field can be found by the Fourier decomposition and synthesis of the plane wave components as was shown in the previous sections. If the reflection coefficient

of each of the plane wave components is known then the reflected field can be evaluated by the summation of the reflected plane waves as they are the response to the incident plane waves. The Fourier decomposition of the incident field is performed in x_1', x_2' coordinates (the transmitter coordinates) and the synthesis of the reflected field in the x_1'', x_2'' coordinate system (the receiver coordinates).

If the reflection coefficient is independent of the angle of incidence and is equal unity then the reflected field at the face of the receiver can be evaluated using eqn (2.130),

$$\bar{u}(x_1'',0) = \int_{-\infty}^{+\infty} A \begin{Bmatrix} N_1' \\ N_2' \end{Bmatrix} e^{i\omega[(N_1''x_1''+N_2''l_2'')/\alpha - t]} dk_1, \tag{2.131}$$

where (see fig. 2.12) $N_2'' = -N_2'$, $N_1'' = N_1'$ and $l_2'' = -(d_1+d_2)$. Note that the distance l_2' along x_2'' coordinate has to be taken with the negative sign because the reflected waves propagate in the direction opposite to the x_2'' axis.

Now let us assume that the reflection coefficient of a plane wave of wavenumber k_1, given in the x_1, x_2 coordinate system, is $R(k_1)$. Decomposing the wavenumber vector into the x_1', x_2' coordinate system (see fig. 2.13), the x_1 component of the wavenumber is,

$$k_1 = -k_1'\cos\theta + k_2'\sin\theta; \quad (k_2' = (k'^2-k_1'^2)^{1/2}, \quad Re(k_2')\geq 0). \tag{2.132}$$

The Fourier synthesis of the reflected field can now be calculated as,

$$\bar{u}(x_1'',0) = \int_{-\infty}^{+\infty} A \, R(-k_1'\cos\theta+k_2'\sin\theta) \begin{Bmatrix} N_1' \\ N_2' \end{Bmatrix} e^{i\omega[(N_1''x_1''+N_2''l_2'')/\alpha - t]} dk_1. \tag{2.133}$$

If the function describing the displacement field at the face of the transmitter fully "fills" the width of the transducer then, by eqn (2.124), the k_1' bandwidth of the generated field is $2k_{1d}'$. The integral in eqn (2.133) can then be approximated by a finite integral without a significant loss in accuracy,

$$\bar{u}(x_1'',0) \approx \int_{-k_{1d}'}^{k_{1d}'} A \, R(-k_1'\cos\theta+k_2'\sin\theta) \begin{Bmatrix} N_1' \\ N_2' \end{Bmatrix} e^{i\omega[(N_1''x_1''+N_2''l_2'')/\alpha - t]} dk_1. \tag{2.134}$$

Equation (2.134) describes, in the receiver coordinate system, the displacement field reflected from a boundary whose reflection coefficient is a complex function $R(k_1)$, where k_1 is the horizontal wavenumber component of an incident plane wave at the boundary (see fig. 2.13). Equations similar in form to eqn (2.134), were derived by other researchers studying the reflection of bounded beams from plane interfaces (see for example Ngoc and Mayer 1979,

1980 as well as Nayfeh and Chimenti 1984).

This equation can now be used to obtain the displacement field distribution at the face of the receiver (see fig. 2.14). By integration of the normal component of the displacement field over the face of the receiver, the overall effect of the reflected field on the receiving transducer can be calculated. If we assume that the electric potential generated by the receiver is proportional to the average displacement field at the receiver's face then the voltage generated by the receiver is proportional to the area integral of the reflected field over the receiver's face.

2.5 Conclusions

It has been assumed that viscoelastic materials can be characterised by two complex Lamé's constants and the density. Under this assumption it has been shown that longitudinal and shear plane waves satisfy the equation of motion of viscoelastic materials and the wavenumbers of the plane waves are, in general, complex vectors. Plane waves propagate in the direction of the real part of the wavenumber and attenuate in the direction of the imaginary part of the wavenumber.

It has been shown that at an interface between two media the reflected and transmitted plane waves retain their frequencies and wavenumber components parallel to the interface. Using this finding it has been proved that a single plane wave can, in general, excite only four different plane waves in a viscoelastic layer. Therefore any response of a viscoelastic layer to a single plane wave excitation can be described using a combination of at most four different plane waves propagating within the layer. This greatly simplifies calculations when the reflection or transmission coefficients of multilayered systems are required.

It has been shown that the acoustic field generated by a finite-sized transducer can be decomposed into plane waves and the response of a given system to such an excitation can be calculated as the sum of the responses to each of the plane wave components. The decomposition of the field can be achieved using Fourier transformation and the sum (integral) of the plane wave components can be obtained using inverse Fourier transformation.

The theory presented in this chapter can be used to calculate the distribution of the field generated by a finite sized transducer (radiation problem), the interaction of the field with plane interfaces (reflection problem) and, subsequently, to find the distribution of the acoustic field at the face of the receiver. The theory presented in this chapter can therefore be used to quantitatively predict results obtained in laboratory tests where finite sized transducers are always used.
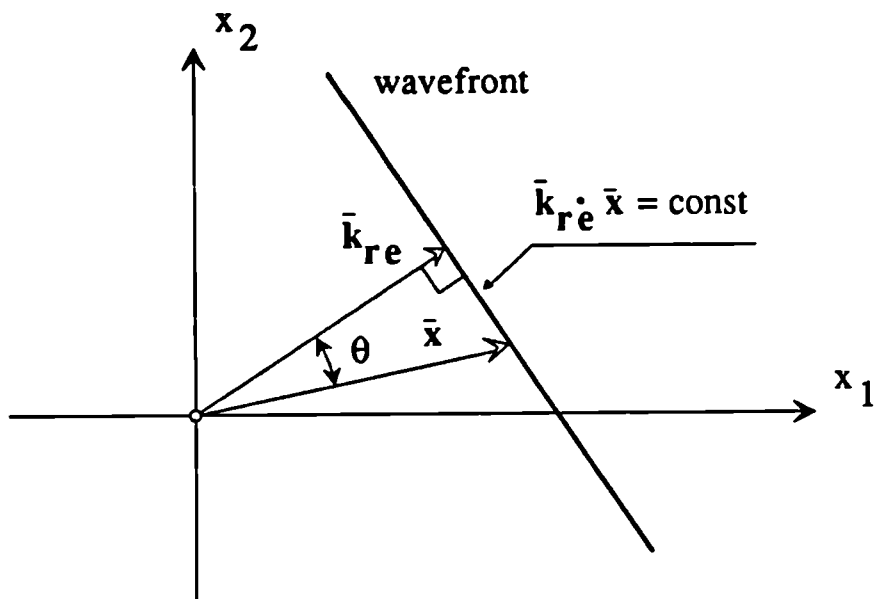
Fig. 2.1 Wavefront of a plane wave.
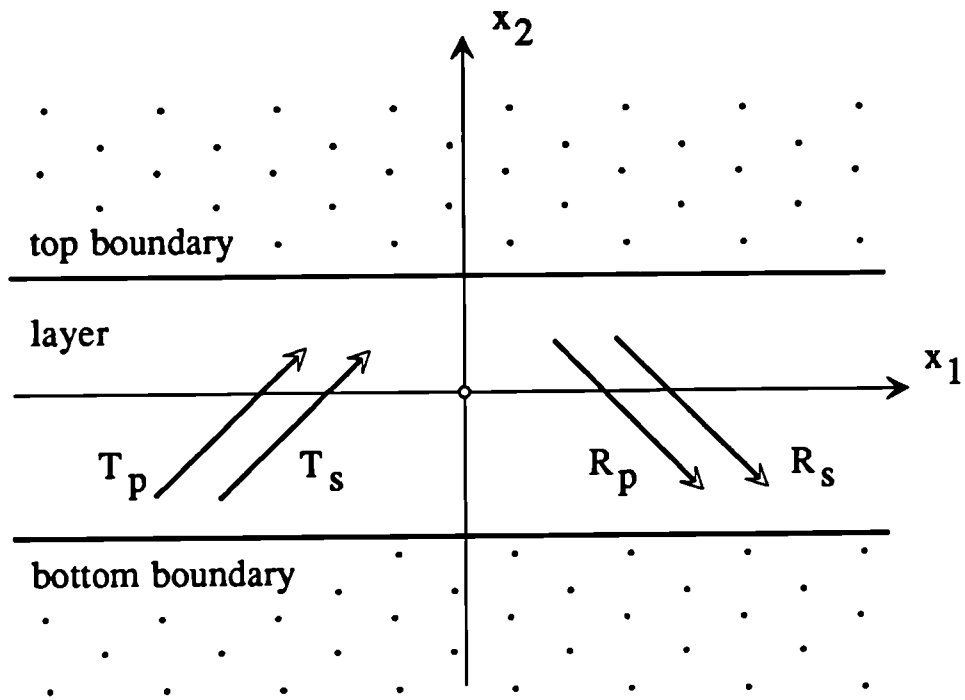
Fig. 2.2 Four waves of amplitudes Tp, Rp, Ts, and Rs in a layer.

waves incident
from medium 2

waves generated at interface
and propagating in medium 2

R_{p2}

R_{s2}

T_{p2}

T_{s2}

medium 2

interface

x_2

x_1

T_{p1}

T_{s1}

R_{p1}

R_{s1}

medium 1

waves incident
from medium 1

waves generated at interface
and propagating in medium 1
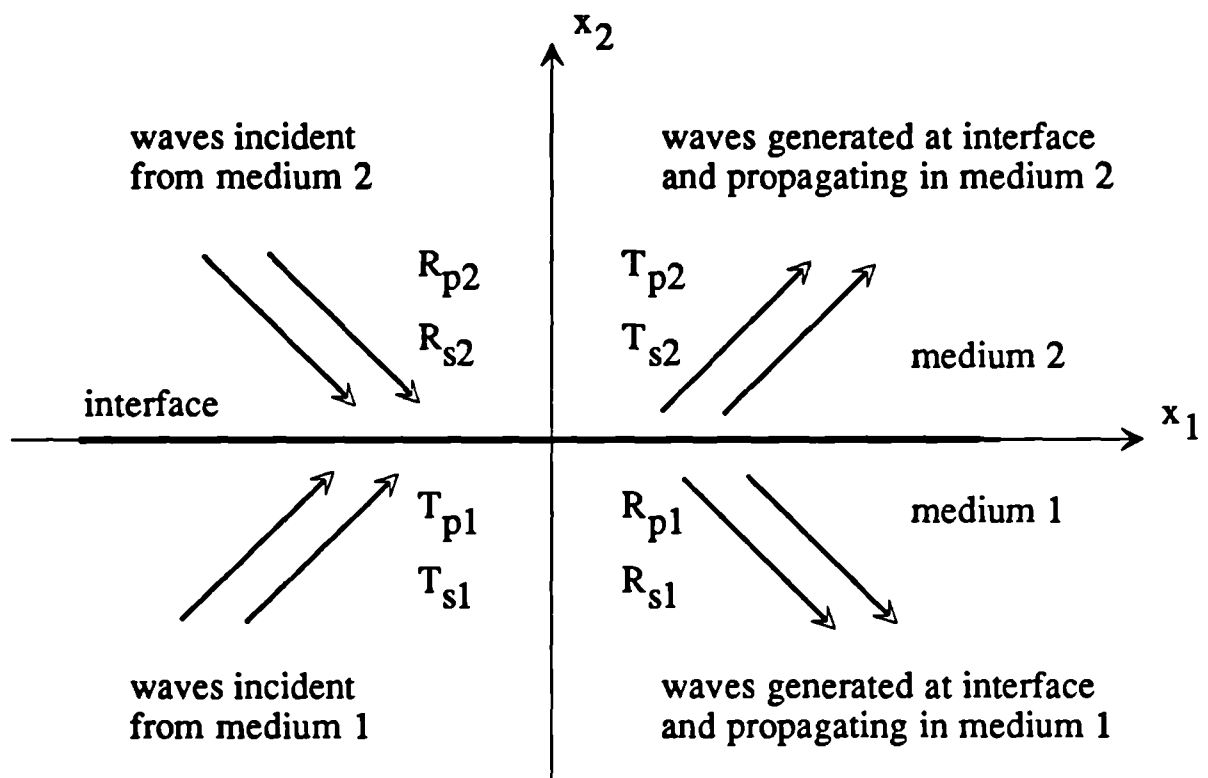
Fig. 2.3 Schematic diagram of waves at a single interface.
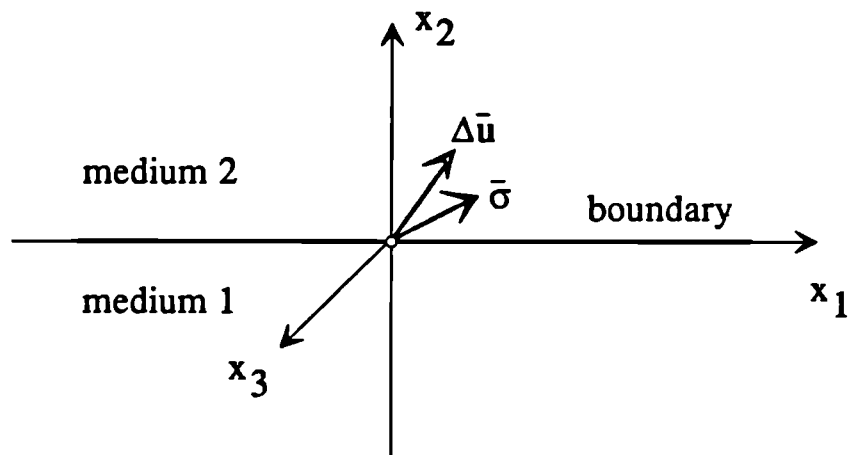
Fig. 2.4 The stress and the discontinuity vector at the boundary.
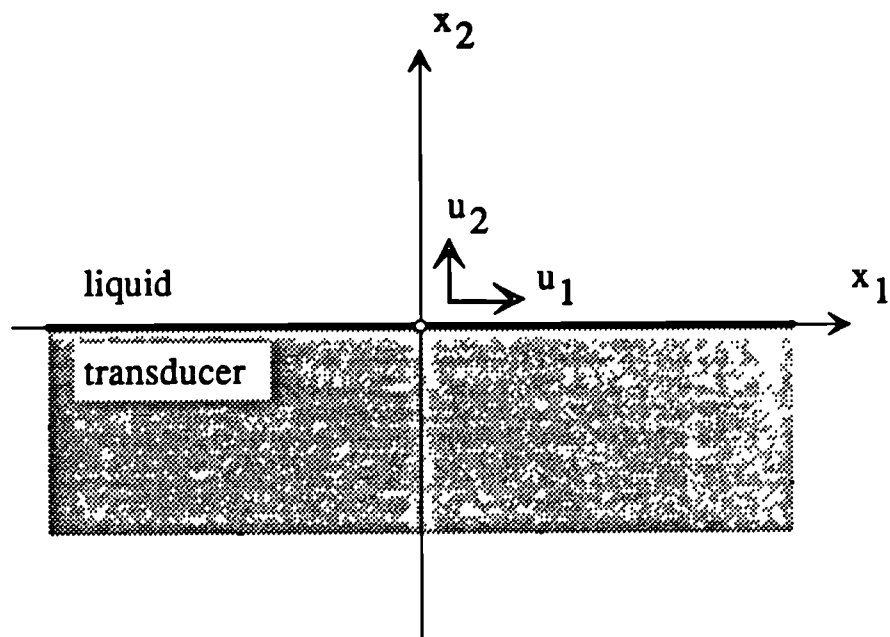
Fig. 2.5 Infinite transducer in liquid. Arrangement of the coordinate system.
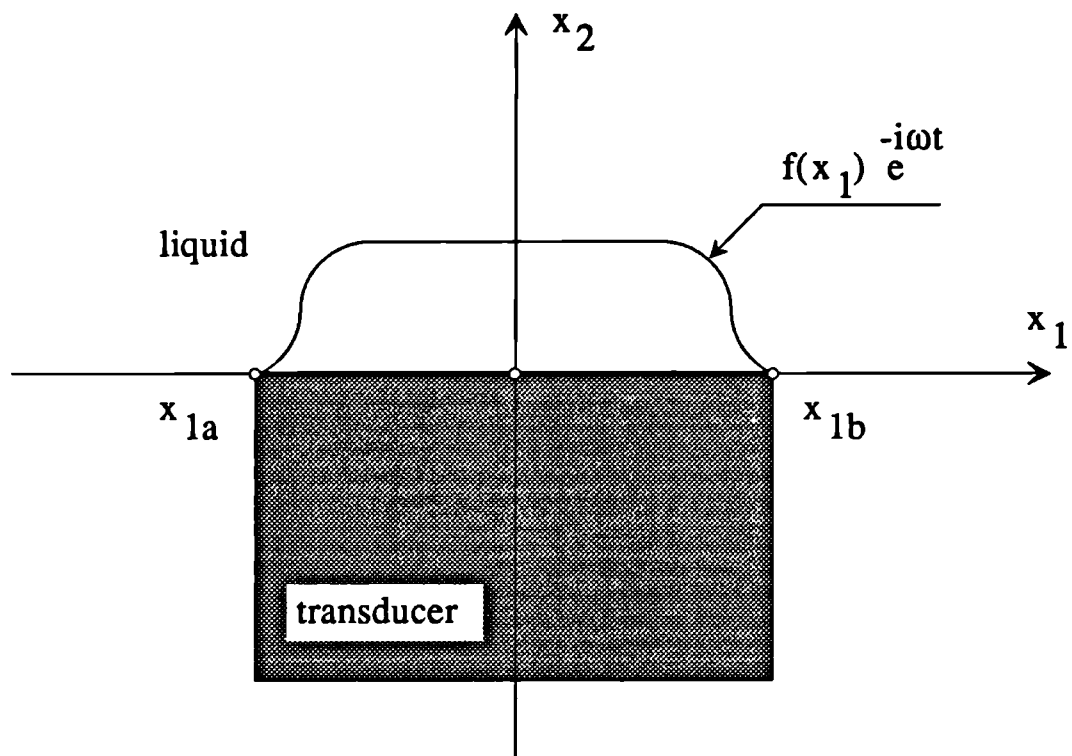
Fig. 2.6 Finite transducer in liquid. Arrrangement
of the coordinate system.
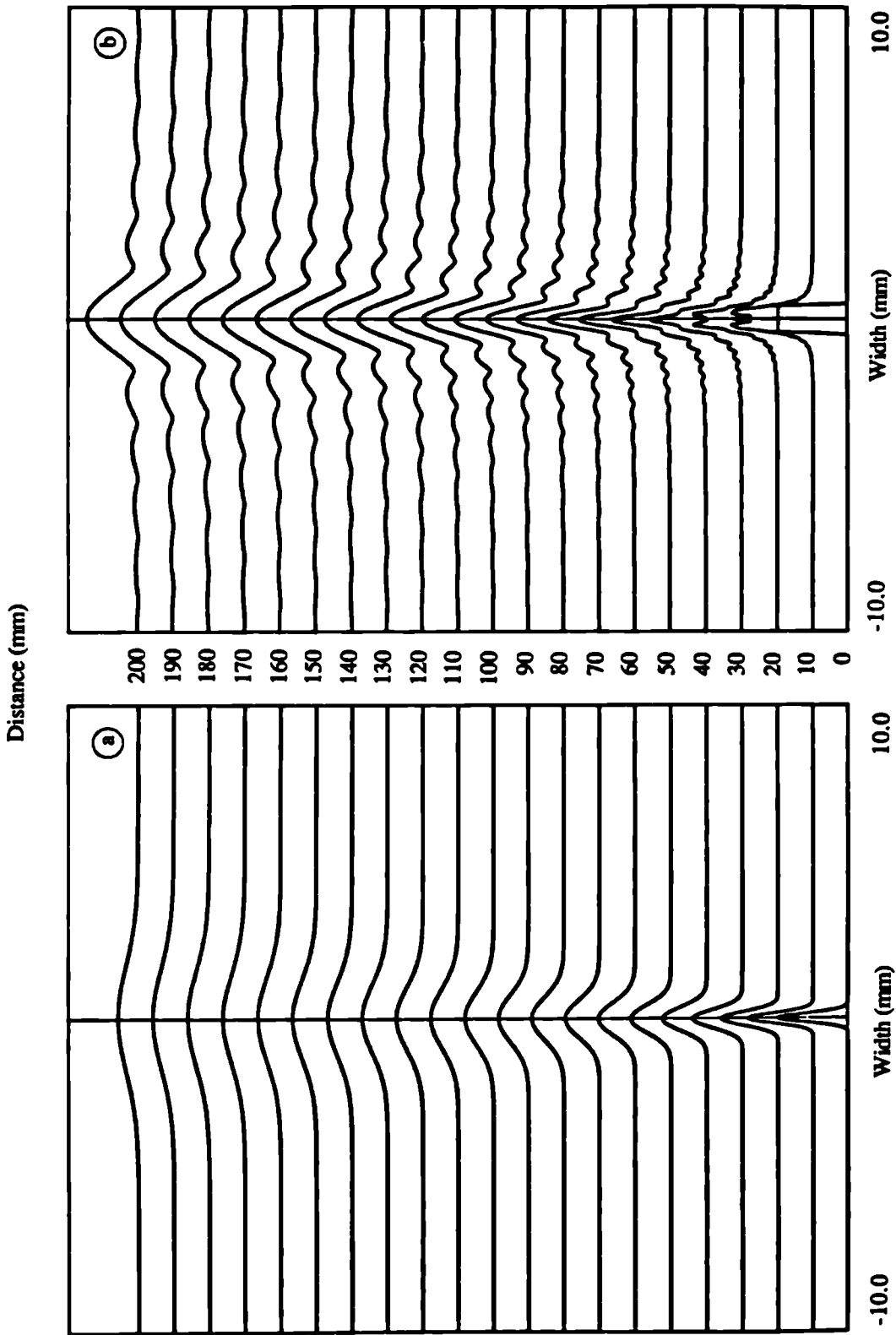
Fig. 2.7   Comparison between fields generated in water by 10 mm wide transducers with different face displacement patterns. Frequency 2 MHz. (a) Gaussian dipsplacement pattern, (b) Tapered displacement pattern.
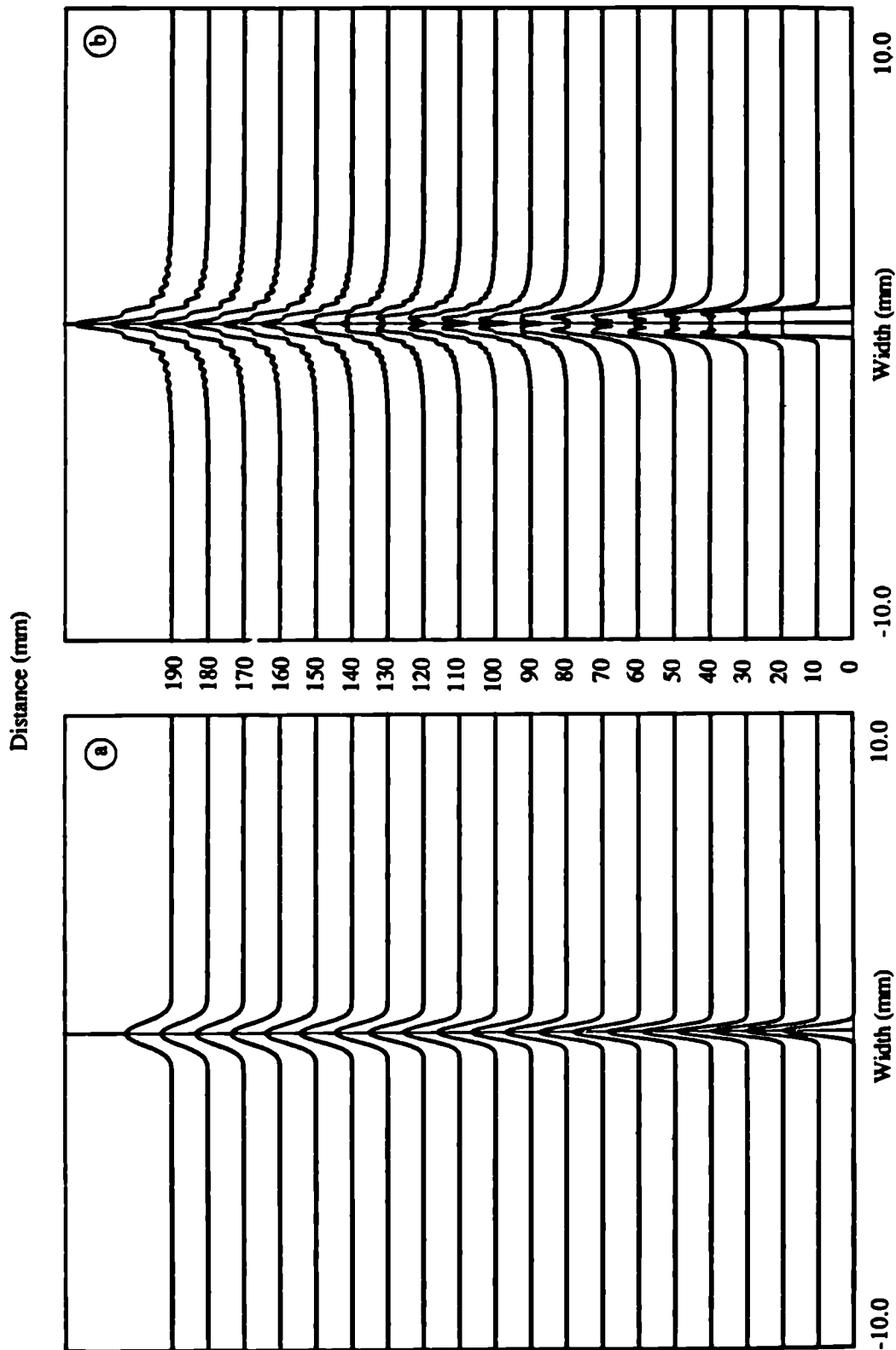
Fig. 2.8   Comparison between fields generated in water by 10 mm wide transducers with different face displacement patterns. Frequency 10 MHz. (a) Gaussian dipsplacement pattern, (b) Tapered displacement pattern.
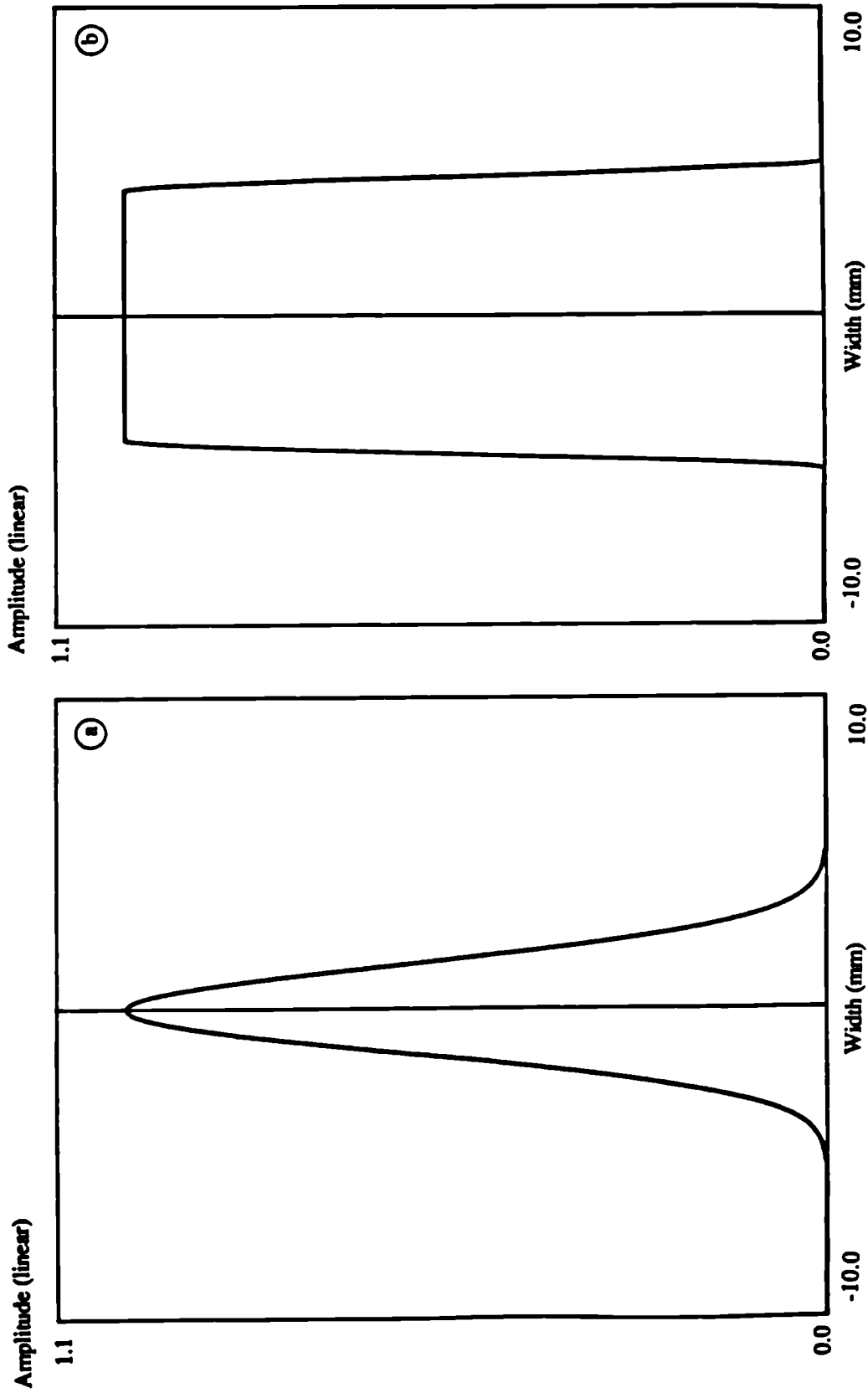
Fig. 2.9   Displacement patterns across the face of a 10 mm wide transducer
(a) Gaussian displacement pattern, (b) Tapered displacement pattern,
distance 200 mm in water.
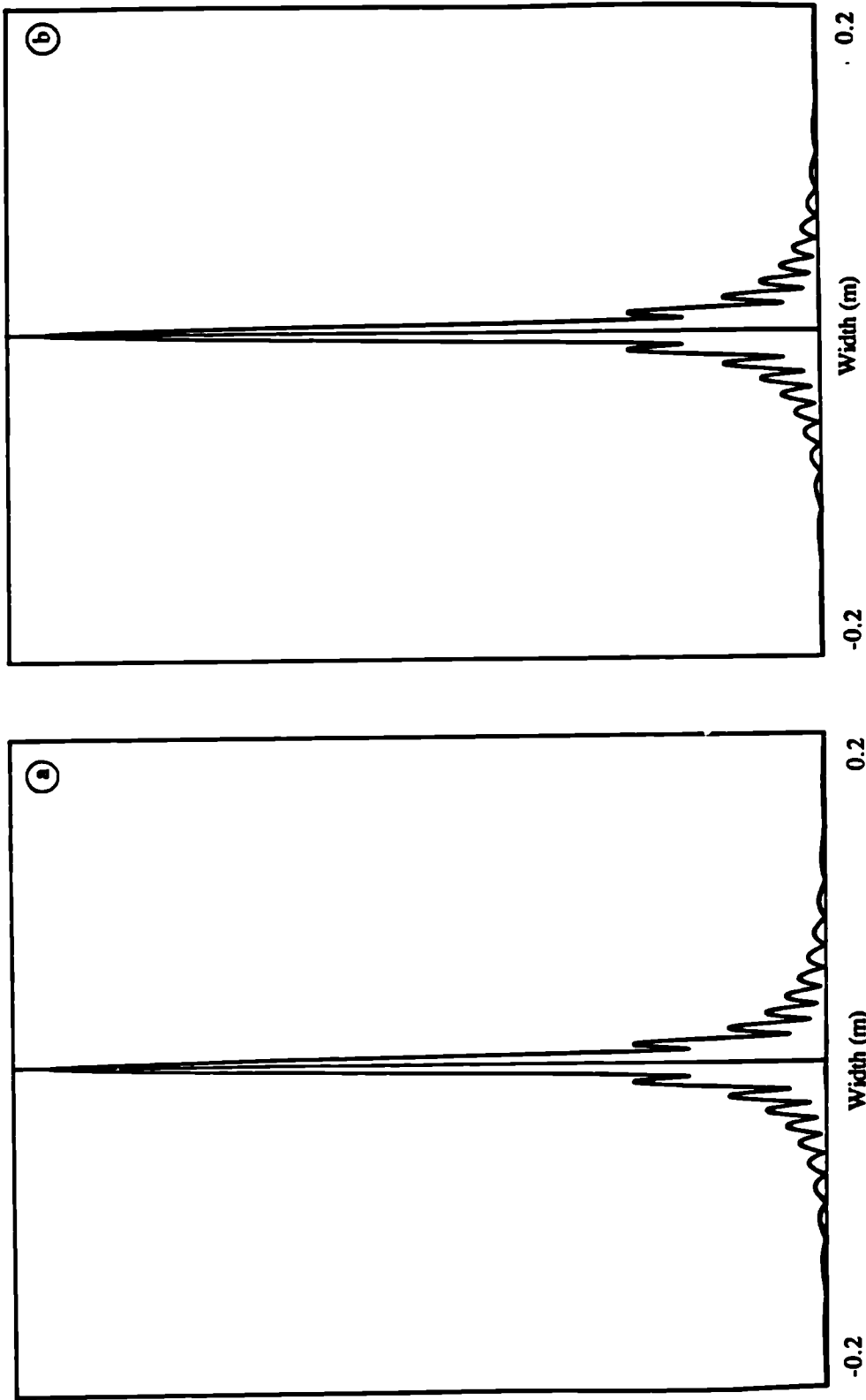
Fig. 2.10   Comparison between the Fourier decompostion method, (a), and the Huyghens principle approach, (b). Transducer width 10 mm, frequency 2 MHz, tapered displacement pattern, distance 200 mm in water.
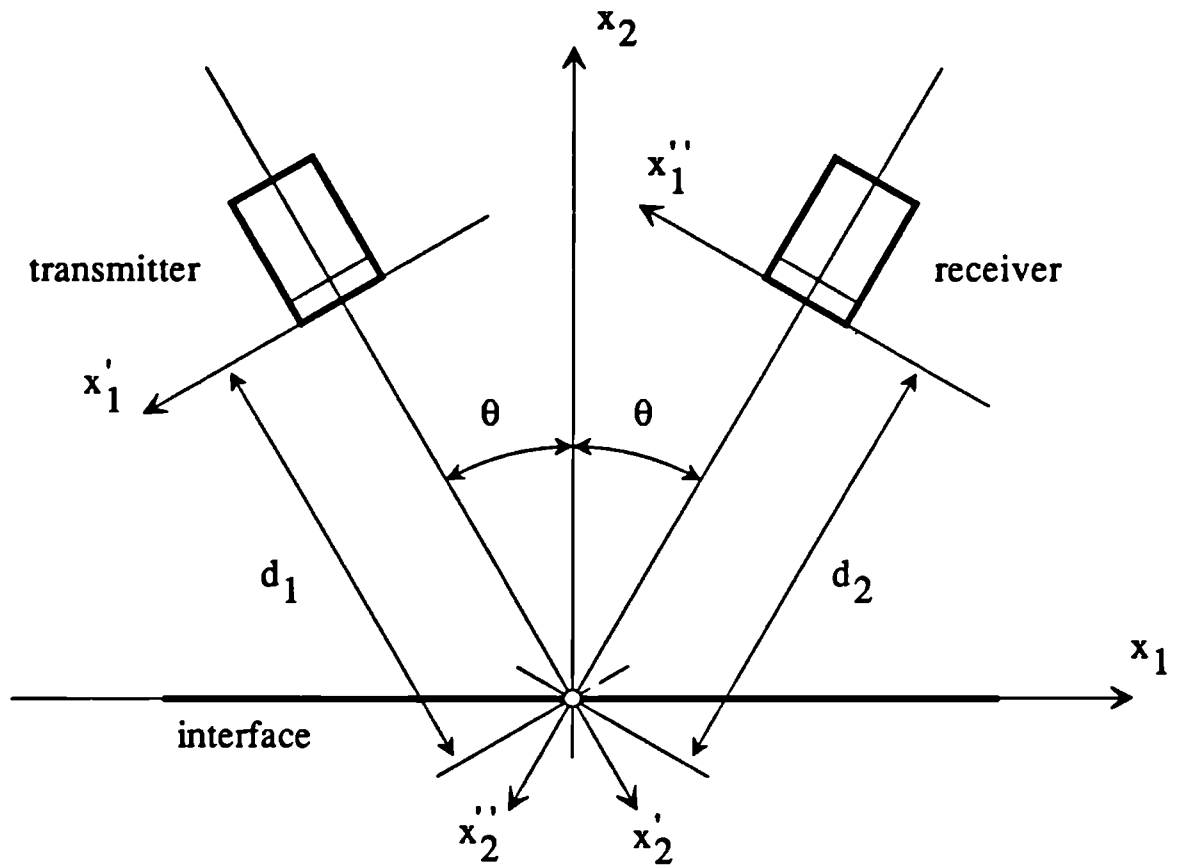
Fig. 2.11   Arrangements of the probes and their coordinate
systems with respect to the interface.
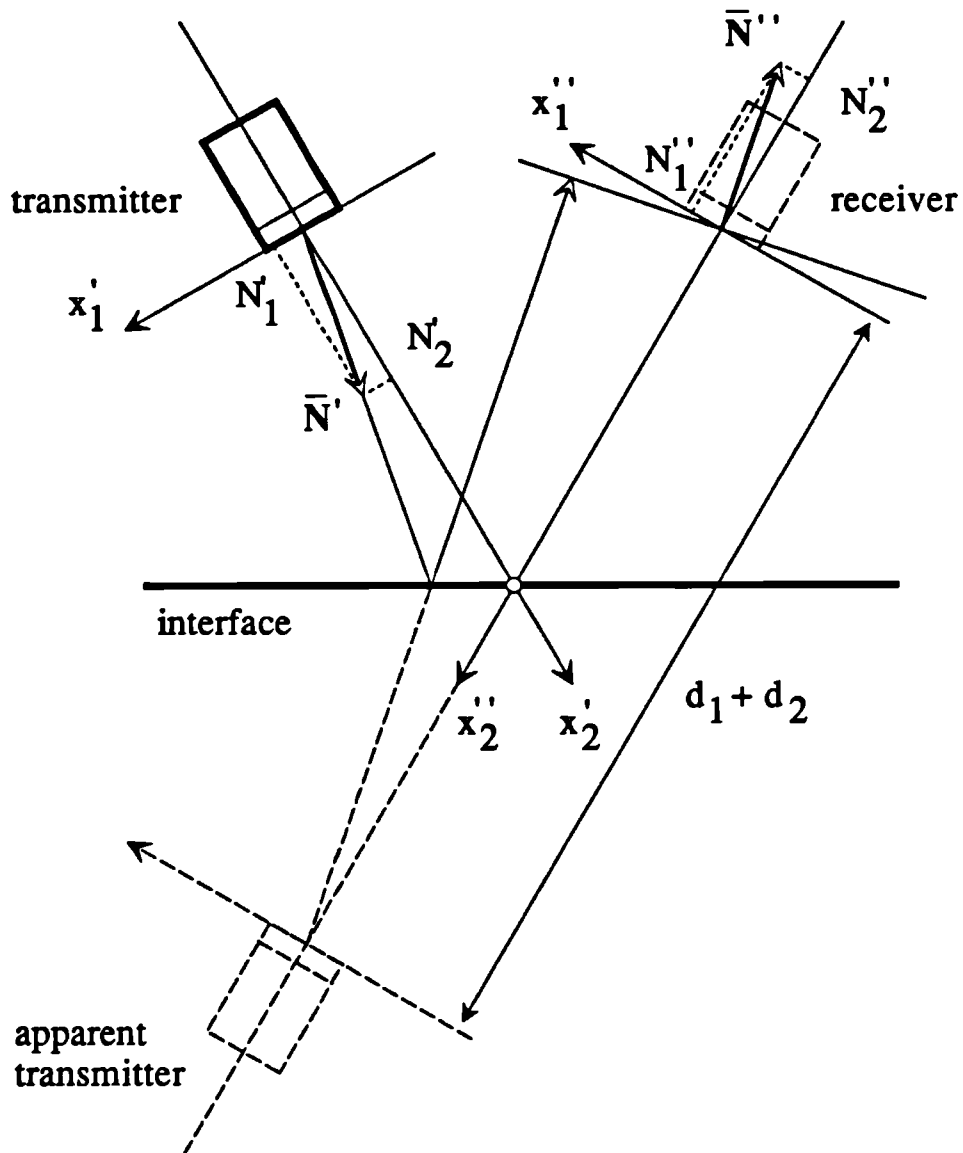
Fig. 2.12 Reflected wave in the receiver's coordinate system.
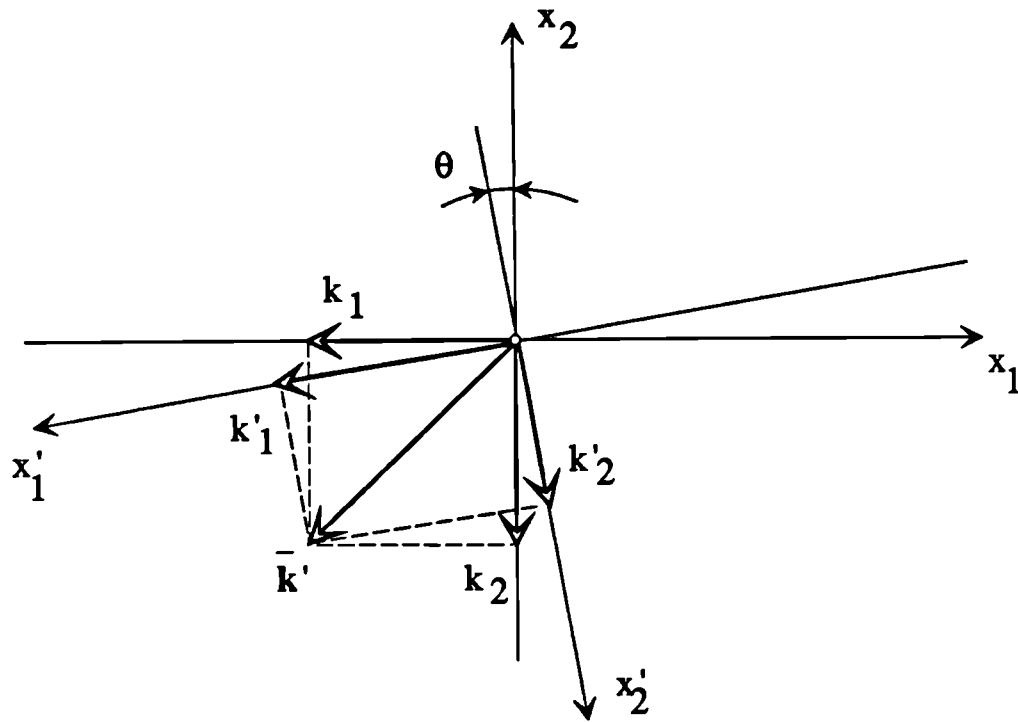
Fig. 2.13   The wavenumber vector in the transmitter
and interface coordinate systems.
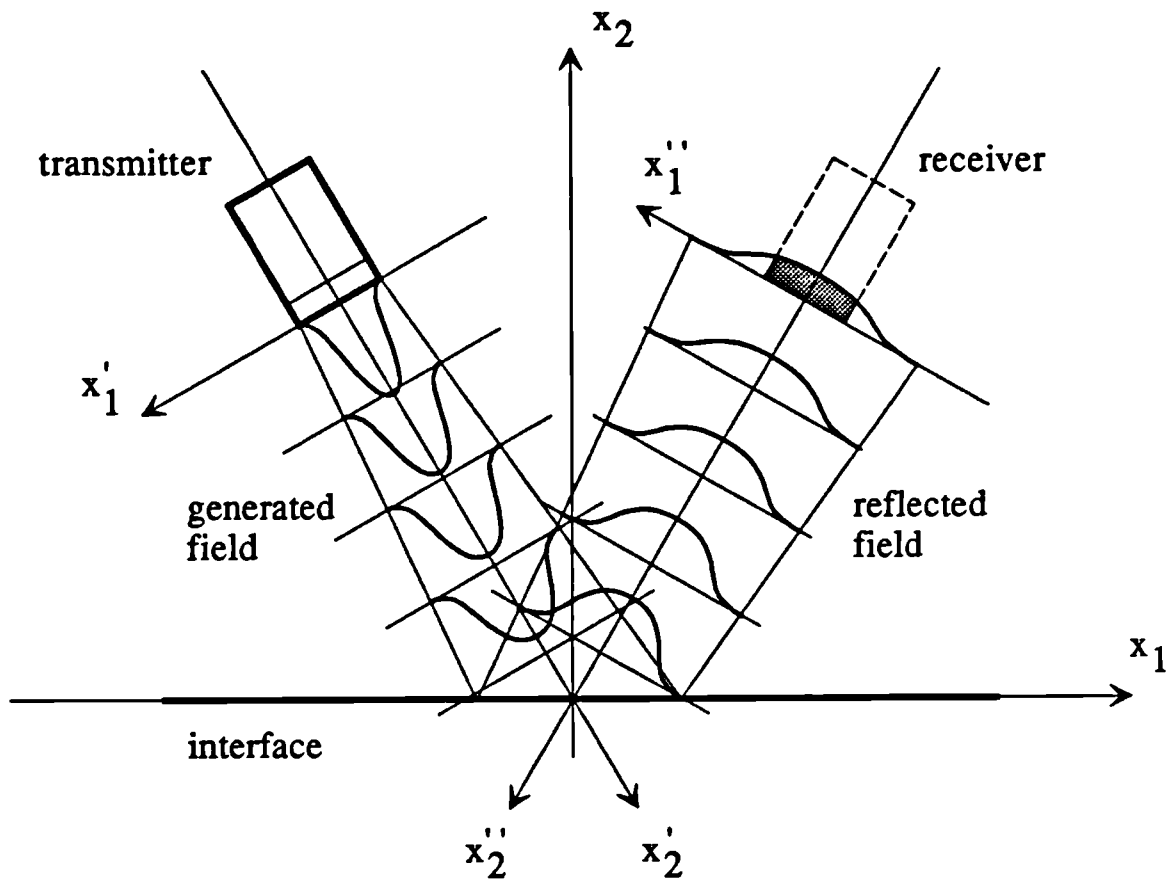
Fig. 2.14 Calculation of the effect the reflected field has on the receiving transducer. The shaded area marks the part of the reflected field taken for the evaluation of the response of the receiver.

CHAPTER 3

The reflection coefficient from a multilayered viscoelastic plate

3.1 Introduction

Chapter 3 is concerned with the reflection and transmission of acoustic waves from multilayered viscoelastic plates. The chapter is divided into four sections, the first applying the time domain approach to find the plate response to a pulse excitation, the second giving a solution method for the problem of reflection and transmission from the plate in the frequency domain, the third describing a procedure for the calculation of the fields reflected from and transmitted by the plate when excited by a finite transducer, and the last containing the main conclusions of the chapter.

In section 3.2 the response of a plate to a pulse excitation is derived by studying the pulse propagation and reflection from the boundaries of the plate. If it is assumed that the plate is non-dispersive, then the pulses do not change their shape during the propagation across the plate and on reflection from the boundaries. The time domain response from the plate will then consist of a series of equally delayed pulses, decaying with time. Such a response can be theoretically derived and the frequency response of the plate can then be obtained by calculation of the Fourier integral over the time domain response. This approach formed a basis of a new method for determination of phase velocities in viscoelastic materials which has been developed and compared with an existing technique presented by Sachse and Pao (1978).

In section 3.3 the frequency response of a multilayered viscoelastic plate is calculated directly in the frequency domain without prior derivation of its time domain response. This makes it possible to study the behaviour of viscoelastic and dispersive multilayered plates in a relatively straightforward manner. The time domain response from these plates can then be obtained by calculation of the inverse Fourier transform integral over the frequency domain response.

Section 3.4 develops the theory presented in section 3.3 for the case of finite transducer excitation. The acoustic field generated by a finite transducer can be decomposed into its

harmonic plane wave components. For each of the plane wave components the reflected and transmitted harmonic plane waves can be calculated. The overall acoustic field for the system can then be calculated by summation of the reflected and transmitted harmonic plane waves.

In section 3.5 the main conclusions of the chapter are presented in a concise form.

3.2 The reflection coefficient from a viscoelastic plate at normal incidence: the time domain approach

In chapter 2 we were concerned with the reflection coefficient from a single interface between two semi-infinite media. Now let us consider a plate of finite thickness being excited by an infinite plane wave. To simplify the case let us assume that the wave hits the plate boundary at normal incidence and for convenient comparison with experiment let us assume that the plate is subjected to a pulse excitation. Then it is possible to show that for a perfectly elastic plate, the shape of the pulse does not change on reflection and transmission at the plate faces. Therefore as a result of multiple reflections the received signal consists of a family of pulses of exactly the same shape but magnitudes decreasing with time. In order to obtain the reflection coefficient as a function of frequency, a Fourier integral is calculated. This makes it possible to determine the resonant frequencies of the plate and to relate them to the phase velocity of the bulk longitudinal wave within the plate. This relationship can be used to find the value of the phase velocity of the bulk wave within the plate experimentally.

This approach was developed earlier in the project and has since been used for the experimental evaluation of phase velocities of bulk waves in adhesive joints. However, it has not been used as a main tool for the theoretical analysis in the subsequent work and so a paper which was written on it is presented in Appendix A.

3.3 The reflection coefficient of an infinite beam from a multilayered, viscoelastic plate: the frequency domain approach

In section 3.2 and Appendix A the derivation of the reflection coefficient from a plate at normal incidence was carried out in the time domain. The plate response to a plane wave pulse of infinite spatial extent was analysed using simple geometric relations and the assumption that the pulse shape is left unchanged on reflection and transmission at the plate boundaries which is the case when nondispersive materials are considered. However, the frequency domain approach, which was introduced in chapter 2, is more powerful and is capable of solving more

complicated problems such as reflection, transmission and propagation of ultrasonic waves through dispersive media. In this method, first the steady state response to an infinite harmonic plane wave is calculated. Then, in order to obtain the response to pulse excitation, a harmonic synthesis of the reflected field is carried out. Also a finite transducer problem can be transformed to a harmonic plane wave reflection coefficient problem as has been shown in chapter 2. Therefore it is useful to continue the frequency domain, infinite plane wave approach started in chapter 2 to implement a full, multilayered viscoelastic model with different boundary conditions between the layers. More extensive presentation of the Fourier decomposition method and its applications to acoustics and ultrasonics can be found in good textbooks such as Morse and Ingard (1968), Brekhovskikh (1980), or Fahy (1985). A very good general introduction to the subject of frequency analysis is presented in Randall (1987).

In the first part of this section a solution procedure based on transfer matrices is presented. This approach follows in principle that of Thomson (1950) and Haskell (1953). Some examples of the reflection coefficient predictions using this technique are given and compared with the time domain approach presented in Appendix A.

In the second part of this section the problem of instability of the Thomson-Haskell algorithm is discussed in some detail. An alternative solution procedure, the global matrix algorithm, is developed. The global matrix technique is similar in approach to that introduced by Knopoff (1964) but offers a significant improvement in numerical stability over both the Thomson-Haskell and the Knopoff methods.

3.3.1 Wave coupling algorithm; transfer matrices approach

The transfer matrices approach was introduced by Thomson (1950) and corrected by Haskell (1953). It has subsequently been used widely in seismic applications as well as in ultrasonics. The method was limited to elastic media. Propagation and reflection of ultrasonic waves in viscoelastic media were considered in a number of recent publications (see for example Becker and Richardson 1970, Fiorito et al. 1985, Deschamps 1990).

Let us consider an n-1 layered plate in a Cartesian coordinate system so that the plate boundaries are normal to the x_2 axis. The media are numbered consecutively from 1 to n+1 so that the semi-infinite spaces are numbered 1 and n+1 respectively (see fig. 3.1). The x_2 coordinates at which the layer interfaces are placed are denoted by y_i, where i=1,....,n is the number of the interface.

Relationship between the stress-displacement vectors at the top and bottom boundaries of a single layer

Let us take the kth layer (see fig. 3.2). As has been shown in section 2.3.1, there are at most four different plane waves in the layer, two waves propagating in the positive x_2 direction (transmitted waves), the amplitudes of which are stored in vector $\{T_k\}$, and two propagating in the negative x_2 direction (reflected waves), the amplitudes of which are stored in vector $\{R_k\}$.

Using eqn (2.90) it is possible to relate the displacement and stress field to the amplitude vectors in a form,

$$\begin{bmatrix} i\omega\rho\alpha C g_p^{-1} & 2i\omega\rho\beta^2 B g_s^{-1} & i\omega\rho\alpha C g_p & -2i\omega\rho\beta^2 B g_s \\ -2i\omega\rho\beta^2 A g_p^{-1} & i\omega\rho\beta C g_s^{-1} & 2i\omega\rho\beta^2 A g_p & i\omega\rho\beta C g_s \\ \alpha s g_p^{-1} & -B g_s^{-1} & \alpha s g_p & B g_s \\ -A g_p^{-1} & -\beta s g_s^{-1} & A g_p & -\beta s g_s \end{bmatrix} \begin{Bmatrix} R_p \\ R_s \\ T_p \\ T_s \end{Bmatrix} = \begin{Bmatrix} \sigma_{22} \\ \sigma_{21} \\ u_1 \\ u_2 \end{Bmatrix}, \tag{3.1}$$

where (see eqn 2.77),

$$A = (1-\alpha^2 s^2)^{1/2}, \quad B = (1-\beta^2 s^2)^{1/2}, \quad C = 1-2\beta^2 s^2,$$

$$g_p = e^{i\omega A \alpha^{-1} x_2}, \quad g_s = e^{i\omega B \beta^{-1} x_2}. \tag{3.2}$$

Equation (3.1) can be expressed in matrix from as,

$$\{V_k(x_2)\} = \mathcal{M}_k(x_2) \left\{ \begin{Bmatrix} R_k \\ T_k \end{Bmatrix} \right\}, \quad \text{where } \{V_k(x_2)\} = \begin{Bmatrix} \overline{\sigma}(x_2) \\ \overline{u}(x_2) \end{Bmatrix}. \tag{3.3}$$

Vector $\{V_k(x_2)\}$ is the stress-displacement vector in the kth layer and matrix $\mathcal{M}_k(x_2)$ is, in general, 4×4 complex. In order to obtain a transfer matrix, relating the stress-displacement field at one boundary to the stress-displacement field at the other boundary, eqn (3.1) can be used. Figure 3.2 shows the position of the coordinate system used for the evaluation of the stress and displacement field in the kth layer. The origin of the system has been moved to the bottom of the layer to simplify derivations. In this 'local' system of coordinates the vertical coordinate takes on zero value at the bottom of the kth and at the top of the layer equals d_k, which is the layer thickness. Let us denote the local coordinate system as (x_1', x_2').

Setting $x_2' = 0$ in eqn (3.1), the stress-displacement field at the bottom boundary of the kth layer

can be expressed as,

$$\{V_k(0)\} = \mathcal{M}_k(0) \left\{ \begin{array}{c} \{R_k\} \\ \{T_k\} \end{array} \right\} ,$$

(3.4)

and, for the top boundary, setting $x_2' = d_k$ in eqn (3.1), we have,

$$\{V_k(d_k)\} = \mathcal{M}_k(d_k) \left\{ \begin{array}{c} \{R_k\} \\ \{T_k\} \end{array} \right\} .$$

(3.5)

From eqn (3.4) we have,

$$\left\{ \begin{array}{c} \{R_k\} \\ \{T_k\} \end{array} \right\} = \mathcal{M}_k^{-1}(0) \{V_k(0)\} .$$

(3.6)

Substituting eqn (3.5) into eqn (3.6), we have,

$$\{V_k(d_k)\} = \mathcal{L}_k \{V_k(0)\}$$

(3.7)

where,

$$\mathcal{L}_k = \mathcal{M}_k(d_k) \; \mathcal{M}_k^{-1}(0).$$

(3.8)

$\mathcal{L}_k$ is the transfer matrix for the kth layer and relates the stress-displacement field on the bottom boundary of the layer to the the stress-displacement field on the top boundary of the layer.

Relationship between the stress-displacement vectors across a single boundary between two layers

In certain cases it is useful to account for interfacial imperfections across the layers (see sections 1.4.1 and 2.3.3 of this thesis). In such cases the interface can be given its own transfer matrix, relating the stress-displacement field on one side of the boundary to the other side of the boundary (see fig. 3.3). This relationship can be expressed in the form of eqn (2.107) as,

$$\{V(y_k^+)\} = \mathcal{B}_k \{V(y_k^-)\},$$

(3.9)

where $\{V(y_k^-)\}$ and $\{V(y_k^+)\}$ are the stress-displacement field at the bottom and the top of the kth interface. The boundary transfer matrix $\mathcal{B}_k$ is given by eqn (2.111).

Relationship between the stress-displacement vectors at the top and bottom boundaries of an entire multilayered plate

Having developed the transfer matrices for the layers and the boundaries, it is now possible to relate the stress-displacement field on one side of the whole plate (ie at $x_2 = y_1^-$) to the the other side of the plate (ie at $x_2 = y_n^+$). Using eqn (3.31), (3.34) and (3.36) we have,

$$\{V(y_1^-)\} = \mathcal{M}_1(0) \left\{ \begin{array}{c} \{R_1\} \\ \{T_1\} \end{array} \right\},$$

$$\{V(y_1^+)\} = \mathcal{B}_1 \{V_1(y_1^-)\},$$

$$\{V(y_2^-)\} = \mathcal{L}_2 \{V_2(y_1^+)\},$$

$$\{V(y_2^+)\} = \mathcal{B}_2 \{V_2(y_2^-)\},$$

$$\{V(y_3^-)\} = \mathcal{L}_3 \{V_3(y_2^+)\},$$

$$\ldots$$

$$\{V(y_n^-)\} = \mathcal{L}_n \{V_n(y_{n-1}^+)\},$$

$$\{V(y_n^+)\} = \mathcal{B}_n \{V_n(y_n^-)\},$$

$$\{V(y_n^+)\} = \mathcal{M}_{n+1}(0) \left\{ \begin{array}{c} \{R_{n+1}\} \\ \{T_{n+1}\} \end{array} \right\}. \tag{3.10}$$

Back substituting the stress-displacement vectors $\{V(y_k^+)\}$ and $\{V(y_k^-)\}$, k=1,...,n+1 in eqn (3.10) we have,

$$\mathcal{M}_{n+1}(y_n^+) \left\{ \begin{array}{c} \{R_{n+1}\} \\ \{T_{n+1}\} \end{array} \right\} = \mathcal{P} \, \mathcal{M}_1(y_1^-) \left\{ \begin{array}{c} \{R_1\} \\ \{T_1\} \end{array} \right\}, \tag{3.11}$$

where $\mathcal{P}$ is the stress-displacement transfer matrix for the entire plate,

$$\mathcal{P} = \mathcal{B}_n \, \mathcal{L}_n \, \cdots \, \mathcal{B}_2 \, \mathcal{L}_2 \, \mathcal{B}_1. \tag{3.12}$$

Equation (3.11) relates the harmonic plane wave amplitudes on one side of the plate to the harmonic plane wave amplitudes on the other side of the plate and constitutes four linear complex equations. The equation is similar in form to eqn (2.95) and yields the reflected and transmitted plane wave amplitudes $\{R_1\}$, $\{T_{n+1}\}$, if appropriate values of incident wave amplitudes $\{T_1\}$, $\{R_{n+1}\}$, are inserted. For example, in order to calculate the reflection and transmission coefficients due to a longitudinal wave incident from medium 1, it is necessary to set $\{T_1\} = \left\{ \begin{array}{c} 1 \\ 0 \end{array} \right\}$, and $\{R_{n+1}\} = \left\{ \begin{array}{c} 0 \\ 0 \end{array} \right\}$ in eqn (3.11). The solution can then be carried out in a similar way to the single interface problem, as shown in equations (2.97) and (2.98). Equation

(3.10) is a generalisation of eqn (2.95) derived for a single interface problem, and can be reduced to eqn (2.95) by setting the transfer matrix $\mathscr{P}$ to unity.

Reflection coefficient from an aluminium plate in water

Figure 3.4 shows the reflection coefficient from a 3.2 mm thick aluminium plate in water as a function of frequency computed using the frequency domain approach. The excitation was assumed to be an infinite harmonic longitudinal wave at normal incidence. The phase velocities of the longitudinal wave in aluminium and in water are shown in table 3.1.

material	density ρ (kg/m^3)	longitudinal velocity c_L (m/s)	shear velocity c_S (m/s)
aluminium	2820	6348	3120
water	1170	1490	10

Table 3.1 Acoustic properties of aluminium and water used in the reflection coefficient calculations.

As can be seen from fig. 3.4 the frequency domain normal incidence reflection coefficient from an aluminium plate in water is a periodic function with equally spaced minima, the first one being at zero frequency. This is in perfect agreement with the derivations presented in Appendix A (see figures 4 and 8 of Appendix A). It can also be shown (see section 4.2 for details) that at its minima the reflection coefficient from a perfectly elastic aluminium layer in water assumes zero value. In fig. 3.4 the curve does not touch zero line because the minima of the reflection coefficient lie in between the points used for the evaluation of the function.

In order to model the spectrum received by a typical 10 MHz transducer in the pulse-echo mode, it is necessary to multiply the reflection coefficient from fig. 3.4 by a frequency response function of the transducer. Figure 3.5 shows the reflection coefficient from fig. 3.4 after it has been 'filtered' by a typical 10 MHz transducer. The inverse Fourier transform of the filtered reflection coefficient yields the time domain response of the reflected field received by the transducer (see fig. 3.6). Comparing this theoretically calculated response of the plate with the measurements (see fig. 1 of Appendix A), good agreement between them can be seen.

Figure 3.7 shows the predicted transmission coefficient of a 3.2 mm thick aluminium plate at normal incidence and fig. 3.8 shows the transmission coefficient filtered by the the same frequency response function of the receiving transducer as was used in fig. 3.5. Figure 3.9 shows the time domain response of the transmitted field obtained by inverse Fourier

transformation of the reflection coefficient spectrum shown in fig. 3.8.

The next four figures, from 3.10 to 3.13, show the reflection and transmission coefficients for the same 3.2 mm thick aluminium plate submerged in water and excited by an infinite plane wave at an incidence angle of 0.5 degrees. Figure 3.10 shows the frequency response of the aluminium plate computed using the infinite harmonic wave coupling approach. Shear mode excitation is clearly visible here. The small 'glitches' visible in the figure are the through-thickness shear modes of the plate. Figure 3.11 shows the time domain reflection response obtained from the inverse Fourier transform of the reflection coefficient windowed by the frequency response function of a typical 10 MHz transducer. The small humps between the main longitudinal reflections are the mode converted shear waves within the plate. Figure 3.12 shows the frequency domain transmission response of the plate excited at an angle of incidence of 0.5 degrees, and again, the small glitches visible in the figure are through-thickness shear resonances of the plate. Figure 3.13 shows the time domain response received by a typical 10 MHz probe in through-transmission mode.

Reflection coefficient from an epoxy resin plate in water

It has been shown above that the normal incidence response from an aluminium plate in water can be obtained using either the frequency domain approach, or the time domain analysis, described in section 3.2 and Appendix A. In both cases it was assumed that the aluminium plate is perfectly elastic (non-attenuating), for which the time domain response consisted of a family of equally spaced reflectionsdiffering only in their magnitude and maintaining their shape throughout the whole time of observation (see fig. 3.6 and fig. 1 of Appendix A). However, if the mechanical properties of the system are frequency dependent then the time domain approach is no longer applicable. Indeed, since the reflected and transmitted pulses change their shape as they propagate and interact with boundaries the derivation presented in Appendix A become approximate or entirely inapplicable.

The frequency domain approach, however, can cope with these cases accurately and conveniently by solving equations directly in the frequency domain and, if necessary, the inverse Fourier transform may be used to obtain the time domain solutions. To illustrate the idea, a material similar to epoxy resin was chosen, setting the longitudinal phase velocity frequency dependent and increasing linearly from 2610 m/s at low frequencies to 2810 m/s at 20 MHz, as shown in fig. 3.14. Attenuation of the bulk longitudinal wave was set to 0.01 nepers, which means that the longitudinal wave is attenuated by factor of $e^{-0.01}$ per wavelength. The dispersion of this system was studied by considering the longitudinal wave pulse shown in fig. 3.15(a) to be exited in this material. Figure 3.15(b) shows the longitudinal signal which

would be received 10 mm away from the point of excitation. It is clear that the pulse shape has been significantly changed.

To show the application of the frequency domain approach to a more complicated case, a 3.15 mm thick epoxy resin plate with frequency dependent material properties was chosen. The model consisted of the plate loaded by a water half-space on one side and an air half-space on the other side. The dispersion characteristics of the bulk longitudinal wave, which is the frequency variation of its phase velocity and the attenuation, were chosen so that comparisons with the experiments presented in Appendix A could be made. The velocity was set to vary linearly from 2610 m/s at very low frequencies to 2690 m/s at 20 MHz. The attenuation was set to 0.1 nepers, which means that the wave is decreased by a factor of $e^{-0.1}$ per wavelength. Figure 3.16 shows the amplitude spectrum of the reflected field at normal incidence, windowed by a frequency response function of a typical 10 MHz transducer. The spectrum is in a very close agreement with the measurements shown in fig. 11 of Appendix A. Figure 3.17 shows the predicted time domain response from the epoxy plate at normal incidence. Changes in the pulse shape are clearly visible here. Figure 3.17 is in a good agreement with the measured time domain response discussed in Appendix A and shown there in fig. 10.

3.3.2   Numerical instability of transfer matrices formulation. Global matrix algorithm

Numerical instability of the wave coupling algorithm

The transfer matrices approach for the solution of the reflection coefficient problem of multilayered systems seems to be very powerful and neat. However, there are some cases where the wave coupling algorithm fails to work properly. The method relies on the assumption that it is always possible to relate the stress-displacement vector on one side of a layer to the stress-displacement vector on the other side of the layer. During the derivation of the technique this is done in two stages. Firstly the stress-displacement field on both sides of the layer is related to the amplitudes of four waves within the layer (eqn (3.2) and (3.3)). Then the plane wave amplitudes, which are the parameters of the two equations, can be eliminated to yield the transfer matrix directly linking the stress-displacement conditions on both sides of the layer (eqn (3.5)), and the relationship is one-to-one. This means that if the stress-displacement vector on one side of the layer is known then there is only one stress-displacement vector on the other side corresponding to that vector. In principle, in any physical system this is always the case. However, when calculations of the stress-displacement field are made on a computer with finite precision then in some cases the round-off errors may lead to numerical instability. Let us study this in more detail.

We learned from the previous chapters that there are at most four plane waves in a layer: two longitudinal and two shear (see fig. 3.18). For convenience, the waves propagating from the botom to the top of the layer will be called transmitted waves, and those propagating from the top to the bottom will be called reflected waves. Let us now consider the case when the longitudinal type of wave is inhomogeneous in the layer. This means that there are two inhomogeneous waves in the system: the transmitted longitudinal wave and the reflected longitudinal wave. These waves are evanescent in the direction perpendicular to the interfaces of the layer, and the variation of their amplitudes in that direction is given by eqn (3.2),

$$g_p = e^{i\omega(1-\alpha^2 s^2)^{1/2} \alpha^{-1} x_2}.$$

(3.13)

The requirement for generation of inhomogeneous waves is that $\alpha^2 s^2 > 1$, that is,

$$(1-\alpha^2 s^2)^{1/2} = i\zeta, \quad \text{where } \zeta \text{ is real.}$$

(3.14)

In such a case eqn (3.13) becomes,

$$g_p = e^{-\omega\zeta \alpha^{-1} x_2},$$

(3.15)

which describes an exponential decay along the x_2 axis which is frequency dependent.

In order to illustate the situation with some examples let us calculate the rate of decay of longitudinal waves in an aluminium plate being excited at 20 degrees from water at different frequencies. We assume a velocity in water $c_L = 1490$ m/s, and a longitudinal velocity in aluminium $c_{Al} = 6400$ m/s. Since the longitudinal critical angle for for aluminium in water is about 13 degrees, the longitudinal wave is evanescent (inhomogeneous) here. Table 3.2 shows the magnitude of the longitudinal wave 5 mm away from the interface for frequencies of 1 MHz, 2 MHz, 5 MHz, and 10 MHz assuming that its value is unity at the boundary.

Frequency (MHz)	Amplitude 5 mm away from interface
1.0	5.08 E-3
2.0	25.83 E-6
5.0	3.39 E-12
10.0	11.51 E-21

Table 3.2. Example of decay of inhomogeneous wave 5 mm away from interface.

As can be seen from the table, the inhomogeneous waves decay very abruptly at higher

frequencies. Therefore, for any finite precision of calculations there will be a frequency above which the amplitude of the wave will decay to a magnitude which can not be distinguished from zero a short distance away from the interface, as shown schematically in fig. 3.19. This in turn means that such an inhomogeneous wave will strongly contribute to the stress-displacement field on one side of the layer while it will effectively not be present on the the other side at all. A significant change in the wave amplitude would therefore make a substantial difference in the stress-displacement field on one side of the layer while making no difference on the other side. This violates the one-to-one relationship between the stress-displacement vectors at the two boundaries of the layer. From the numerical point of view, the transfer matrix $\mathcal{L}$ will rapidly become ill conditioned making calculations erroneous or impossible, for any finite precision of calculations. Figure 3.20 shows the reflection coefficient from a 5 mm thick aluminium plate in water computed at an excitation frequency of 6 MHz, using the 64 bit floating point precision of calculations. From the graph it can be seen that calculations become unstable for angles above 20 degrees.

Global matrix algorithm

A number of researchers have proposed solutions to the instabilty problem of the Thomson-Haskell technique, mainly for seismological applications (see for example Dunkin 1965, Abo-Zena 1979). In the approach presented below, the reflection coefficient of multilayered systems is calculated without using transfer matrices at all. In order to do so we will avoid the elimination of wave amplitudes in our derivations. The method derived here is similar to that proposed by Knopoff (1964). However, an important development is introduced. Knopoff retained the spatial origin for all wave components in each layer as the top of the layer. This gave him an improvement in stability over the transfer matrices method but the numerical instability could still occur at high frequency-thickness products. The method proposed here removes the instability entirely by placing the origin of all waves at their entry to the layer. To the author's knowledge this is the first time that this has been proposed.

Let us, once again, consider a multilayered system shown schematically in fig. 3.1 and the kth layer shown in fig. 3.21. In the derivations which will follow here the stress-displacement field is expressed in terms of the amplitudes of four waves present in the layer. Let us assume that the waves propagating in the upward direction in the layer will be expressed in terms of (x_1', x_2') coordinates, while the waves propagating 'down' will be expressed in the (x_1'', x_2'') coordinate system.

Making use of eqn (3.1) the stress-displacement field at the top boundary of the kth layer can be expressed as,

$$
\begin{bmatrix}
i\omega\rho\alpha C & 2i\omega\rho s\beta^2 B & i\omega\rho\alpha C g_p & -2i\omega\rho s\beta^2 B g_s \\
-2i\omega\rho s\beta^2 A & i\omega\rho\beta C & 2i\omega\rho s\beta^2 A g_p & i\omega\rho\beta C g_s \\
\alpha s & -B & \alpha s g_p & B g_s \\
-A & -\beta s & A g_p & -\beta s g_s
\end{bmatrix}
\begin{Bmatrix} R_p \\ R_s \\ T_p \\ T_s \end{Bmatrix}
=
\begin{Bmatrix} \sigma_{22} \\ \sigma_{21} \\ u_1 \\ u_2 \end{Bmatrix}_{top}
, \qquad (3.16)
$$

and at the bottom of the layer,

$$
\begin{bmatrix}
i\omega\rho\alpha C g_p & 2i\omega\rho s\beta^2 B g_s & i\omega\rho\alpha C & -2i\omega\rho s\beta^2 B \\
-2i\omega\rho s\beta^2 A g_p & i\omega\rho\beta C g_s & 2i\omega\rho s\beta^2 A & i\omega\rho\beta C \\
\alpha s g_p & -B g_s & \alpha s & B \\
-A g_p & -\beta s g_s & A & -\beta s
\end{bmatrix}
\begin{Bmatrix} R_p \\ R_s \\ T_p \\ T_s \end{Bmatrix}
=
\begin{Bmatrix} \sigma_{22} \\ \sigma_{21} \\ u_1 \\ u_2 \end{Bmatrix}_{bottom}
, \qquad (3.17)
$$

where,

$$
A = (1-\alpha^2 s^2)^{1/2}, \quad B = (1-\beta^2 s^2)^{1/2}, \quad C = 1-2\beta^2 s^2,
$$

$$
g_p = e^{i\omega A\alpha^{-1} d_k}, \quad g_s = e^{i\omega B\beta^{-1} d_k}. \qquad (3.18)
$$

d_k is the thickness of the kth layer (see fig. 3.21) and can can be expressed in terms of global coordinates as,

$$
d_k = y_k - y_{k-1}. \qquad (3.19)
$$

Using Knopoff's technique, the stress-displacement field at the bottom boundary of the layer is given by eqn (3.17), while the stress-displacement field at the top boundary of the layer is calculated as,

$$
\begin{bmatrix}
i\omega\rho\alpha C g_p^{-1} & 2i\omega\rho s\beta^2 B g_s^{-1} & i\omega\rho\alpha C g_p & -2i\omega\rho s\beta^2 B g_s \\
-2i\omega\rho s\beta^2 A g_p^{-1} & i\omega\rho\beta C g_s^{-1} & 2i\omega\rho s\beta^2 A g_p & i\omega\rho\beta C g_s \\
\alpha s g_p^{-1} & -B g_s^{-1} & \alpha s g_p & B g_s \\
-A g_p^{-1} & -\beta s g_s^{-1} & A g_p & -\beta s g_s
\end{bmatrix}
\begin{Bmatrix} R_p \\ R_s \\ T_p \\ T_s \end{Bmatrix}
=
\begin{Bmatrix} \sigma_{22} \\ \sigma_{21} \\ u_1 \\ u_2 \end{Bmatrix}_{top}
. \qquad (3.20)
$$

Let us assume that one of the types of waves is inhomogeneous in the layer, for example the longitudinal waves (see figures 3.18 and 3.19). As has been shown above (see table 3.2), the

amplitudes of inhomogeneous waves decay very abruptly across the plate, expecially for high frequencies of excitation, as given by eqn (3.15). Therefore, the amplitude of g_p calculated over the entire thickness of the layer, given by eqn (3.18), becomes very small. The amplitude of the inverse of g_p therefore becomes very large. This can lead to numerical instability when calculating g_p^{-1} terms in eqn (3.20). This is not the case when eqn (3.16) is used instead.

The stress-displacement field at a boundary between k^{th} and $k+1^{th}$ layers (top of the kth layer), given by eqn 3.16, can be expressed in a more concise form as,

$$\{V(y_k)\} = \mathcal{M}_{k_{top}} \left\{ \begin{matrix} \{R_k\} \\ \{T_k\} \end{matrix} \right\}, \text{ where } \{V(y_k)\} = \left\{ \begin{matrix} \bar{\sigma}(y_k) \\ \bar{u}(y_k) \end{matrix} \right\}. \tag{3.21}$$

The same stress-displacement vector can be expressed in terms of plane waves in the $k+1^{th}$ layer as,

$$\{V(y_k)\} = \mathcal{M}_{k+1_{bot}} \left\{ \begin{matrix} \{R_{k+1}\} \\ \{T_{k+1}\} \end{matrix} \right\}. \tag{3.22}$$

If the stress-displacement field is continuous across the boundary then combining eqn (3.21) and (3.22) we have,

$$\mathcal{M}_{k_{top}} \left\{ \begin{matrix} \{R_k\} \\ \{T_k\} \end{matrix} \right\} - \mathcal{M}_{k+1_{bot}} \left\{ \begin{matrix} \{R_{k+1}\} \\ \{T_{k+1}\} \end{matrix} \right\} = \{0\}. \tag{3.23}$$

Here the independent variables are the amplitudes of the plane waves in the neighbouring layers.

Sometimes it is useful to incorporate a spring boundary condition between two layers to account for some imperfections at the boundary between them (see sections 1.4.1 and 2.3.3 of this thesis for more details). If there is a spring boundary condition between the kth and $k+1^{th}$ layer (see fig. 3.3) then the stress-diplacement field is not continuous across the boundary and equations (3.16) and (3.17) become,

$$\{V(y_k^-)\} = \mathcal{M}_{k_{top}} \left\{ \begin{matrix} \{R_k\} \\ \{T_k\} \end{matrix} \right\}, \tag{3.24}$$

and,

$$\{V(y_k^+)\} = \mathcal{M}_{k+1_{bot}} \left\{ \begin{matrix} \{R_{k+1}\} \\ \{T_{k+1}\} \end{matrix} \right\}, \tag{3.25}$$

where $\{V(y_k^-)\}$ and $\{V(y_k^+)\}$ are the stress-displacement vectors on the bottom and top of the interface respectively. In order to link the two vectors the spring model has to be introduced.

This can be done by utilising the boundary stiffness matrix introduced in section 2.3.3 and used in section 3.3.1 (see eqn (3.9)),

$$\{V(y_k^+)\} = \mathcal{B}_k \{V(y_k^-)\} .$$ (3.26)

Combining equations (3.24), (3.25) and (3.26) we can express the discontinuity across boundaries in the form of two equations as follows,

$$\mathcal{M}_{k_{top}} \left\{ \begin{matrix} \{R_k\} \\ \{T_k\} \end{matrix} \right\} - \{V(y_k^-)\} = \{0\} ,$$ (3.27)

and,

$$\mathcal{B}_k \{V(y_k^-)\} - \mathcal{M}_{k+1_{bot}} \left\{ \begin{matrix} \{R_{k+1}\} \\ \{T_{k+1}\} \end{matrix} \right\} = \{0\} .$$ (3.28)

Now, using equations (3.23), (3.27) and (3.28), and setting the index $k=1,...,n$, we are in position to write the system of equations for the entire multilayered plate.

$$\mathcal{M}_{1_{top}} \left\{ \begin{matrix} \{R_1\} \\ \{T_1\} \end{matrix} \right\} - \{V(y_1^-)\} = \{0\} ,$$

$$\mathcal{B}_1 \{V(y_1^-)\} - \mathcal{M}_{2_{bot}} \left\{ \begin{matrix} \{R_2\} \\ \{T_2\} \end{matrix} \right\} = \{0\} ,$$

$$\mathcal{M}_{2_{top}} \left\{ \begin{matrix} \{R_2\} \\ \{T_2\} \end{matrix} \right\} - \{V(y_2^-)\} = \{0\} ,$$

$$\mathcal{B}_2 \{V(y_2^-)\} - \mathcal{M}_{3_{bot}} \left\{ \begin{matrix} \{R_3\} \\ \{T_3\} \end{matrix} \right\} = \{0\} ,$$

$$...$$

$$\mathcal{M}_{n_{top}} \left\{ \begin{matrix} \{R_n\} \\ \{T_n\} \end{matrix} \right\} - \{V(y_n^-)\} = \{0\} ,$$

$$\mathcal{B}_n \{V(y_n^-)\} - \mathcal{M}_{n+1_{bot}} \left\{ \begin{matrix} \{R_{n+1}\} \\ \{T_{n+1}\} \end{matrix} \right\} = \{0\} .$$ (3.29)

The first equation of the system of equations (3.29) can be re-written as,

$$\mathcal{M}_{R1} \{R_1\} - \{V(y_1^-)\} = - \mathcal{M}_{T1} \{T_1\} ,$$ (3.30)

where $\mathcal{M}_{R1}$ and $\mathcal{M}_{T1}$ are 4×2 sub-matrices of $\mathcal{M}_{1_{top}}$. Similarly, the last equation of the system of equations (3.29) can be expressed as,

$$\mathcal{B}_n \{V(y_n^-)\} - \mathcal{M}_{Tn+1} \{T_{n+1}\} = \mathcal{M}_{Rn+1} \{R_{n+1}\} ,$$ (3.31)

where $\mathcal{M}_{Rn+1}$ and $\mathcal{M}_{Tn+1}$ are 4×2 sub-matrices of $\mathcal{M}_{n+1\,bot}$. Now, using eqn (3.30) and (3.31), the system of equations (3.29) can be expressed in matrix notation as given by eqn (3.32) below.

$\mathcal{M}_{R1}$	$-[I]$	0	0	0	0	0	0	0
0	$\mathcal{B}_1$	$-\mathcal{M}_2$	0	0	0	0	0	0
0	0	$\mathcal{M}_2$	$-[I]$	0	0	0	0	0
0	0	0	$\mathcal{B}_2$	$-\mathcal{M}_3$	0	0	0	0
				$\cdots$				
0	0	0	0	0	0	$\mathcal{M}_n$	$-[I]$	0
0	0	0	0	0	0	0	$\mathcal{B}_n$	$-\mathcal{M}_{Tn+1}$

$\{R_1\}$
$\{V_{(y1^-)}\}$
$\left\{\begin{matrix}\{R_2\}\\\{T_2\}\end{matrix}\right\}$
$\left\{\begin{matrix}\{R_3\}\\\{T_3\}\end{matrix}\right\}$
$\cdots$
$\{V_{(y_n^-)}\}$
$\{T_{n+1}\}$

$=$

$-\mathcal{M}_{T1}\{T_1\}$
0
0
$\cdots$
0
0
$\mathcal{M}_{Rn+1}\{R_{n+1}\}$

(3.32)

This is a system of 8n linear complex equations with 8n unknowns and yields the reflected and transmitted plane wave amplitudes $\{R_1\}$, $\{T_{n+1}\}$ and also all the plane wave amplitudes in the intermediate layers of the plate $\{R_k\}$, $\{T_k\}$, k=2,...,n if appropriate values of incident wave amplitudes $\{T_1\}$, $\{R_{n+1}\}$, are inserted. To calculate the reflection and transmission coefficients due to a longitudinal wave incident from medium 1, it is necessary to set $\{T_1\} = \left\{\begin{matrix}1\\0\end{matrix}\right\}$, and $\{R_{n+1}\} = \left\{\begin{matrix}0\\0\end{matrix}\right\}$ on the right-hand side of equation (3.32). To calculate the reflection and transmission coefficients due to a shear wave incident from medium 1, it is necessary to set $\{T_1\} = \left\{\begin{matrix}0\\1\end{matrix}\right\}$, and $\{R_{n+1}\} = \left\{\begin{matrix}0\\0\end{matrix}\right\}$ on the right-hand side of equation (3.32).

Figure 3.20(b) shows the reflection coefficient from a 5 mm thick aluminium plate in water at 6 MHz using the global matrix algorithm. This graph corresponds exactly to the case of fig. 3.20(a) where the wave coupling approach was used. It can be seen from fig. 3.20(a) that the global matrix procedure provides a stable solution to the problem.

3.4 The reflection coefficient of the finite beam from the multilayered, viscoelastic plate

In section 2.4.3 the reflection of the finite beam from a single interface between two semi-infinite half-spaces was discussed in detail. It was shown that the incident beam from the finite-sized transducer can be decomposed into a series of plane waves, all of them having the same frequency but each of them propagating in different directions (see fig. 3.21). This plane wave decomposition can be achieved using eqn (2.120) using the forward Fourier transformation.

After the decomposition of the incident field into plane waves, evaluation of the reflected field is relatively straightforward. Indeed, the magnitude and phase of each of the reflected plane waves can be calculated using the global matrix reflection coefficient algorithm described in detail in section 3.3.2 and expressed in eqn (3.32). Since the incident field can be formed as the sum (or an integral) of the incident plane wave components, then the reflected field is the sum (or an integral) of the reflected plane waves. The summation of the plane waves can be performed using the inverse Fourier transformation.

As one can see, the solution procedure for both a single interface and a multilayered plate follows exactly the same steps, namely decomposition into plane wave components (forward Fourier transformation), evaluation of the amplitudes and phases of each reflected plane wave component (reflection coefficient), and finally the summation (synthesis) of the reflected plane waves (inverse Fourier transformation). The only difference between the single and the multilayered case is in the evaluation of the plane wave reflection coefficient. In chapter 2, where a single interface problem was considered, the plane wave reflection coefficient, $R(k_1)$, was evaluated using eqn (2.98), and the summation of all plane wave components performed using eqn (2.134). When a multilayered viscoelastic plate considered, eqn (3.32) rather than (2.98) have to be employed to calculate the plane wave reflection coefficient $R(k_1)$. The summation of the reflected plane waves is then conducted using eqn (2.134), as in the case of the single interface problem.

The Fourier decomposition and synthesis method used in this section and in section 2.4.3 can be implemented in either two or three dimensional space. All the derivations presented here have been conducted in two dimensions, the (x_1, x_2) space, assuming plane strain. This, for example, means that the transmitter (see for example fig. 3.22) has finite dimensions in the (x_1, x_2) plane while it extends infinitely in the direction perpendicular to the (x_1, x_2) plane.

For the purposes of this thesis a computer program was written, capable of solving the problem of the finite beam reflection from multilayered viscoelastic plates in two dimensions. The solution procedure follows closely the theory presented in this chapter.

3.5   Conclusions

It has been shown in this chapter that, in order to predict the response of an elastic nondispersive plate to the normal incidence pulse excitation, two different approaches can be taken. The first one is to obtain the time domain response of the plate by calculating the time delays and amplitudes of echoes coming from the plate. The response of the plate in the frequency domain can then be obtained by performing the Fourier transformation of the time domain signal. This technique was developed in the early stages of this project and is presented in Appendix A. The second approach is to consider the behaviour of the plate under a harmonic plane wave excitation and therefore to calculate spectrum of the plate response of the system directly in the frequency domain. The time domain signal can then be obtained by performing the inverse Fourier transformation of the calculated spectrum.

The frequency domain solution procedure based on the Thomson-Haskell method has been developed and compared with the time domain approach by studying the normal incidence response from an aluminium plate in water. Comparison between the two methods showed, as expected, exact agreement.

It has been shown in this chapter that the time domain approach is only applicable in cases when the material properties are independent of the frequency of excitation (nondispersive materials). The frequency domain approach, however, is able to cope with dispersive and attenuating materials and therefore is more general and more suitable for the purposes of this thesis.

It has been shown that when the frequency of excitation is high and there are inhomogeneous waves present in a thick plate then the Thomson-Haskell technique becomes numerically unstable and produces erroneous results. An alternative approach, the global matrix technique, has been employed to solve the reflection coefficient problem.

Finally, the problem of the finite transducer excitation has been addressed in this chapter. The solution procedure, introduced in chapter 2, has been extended here for the case of multilayered viscoelastic plates. The theory presented in this chapter, involving spatial Fourier decomposition, the global matrix reflection coefficient technique and the inverse Fourier transformation, has been used to develop a computer program to form a theoretical basis for comparisons with the experimental investigations presented further in this thesis.
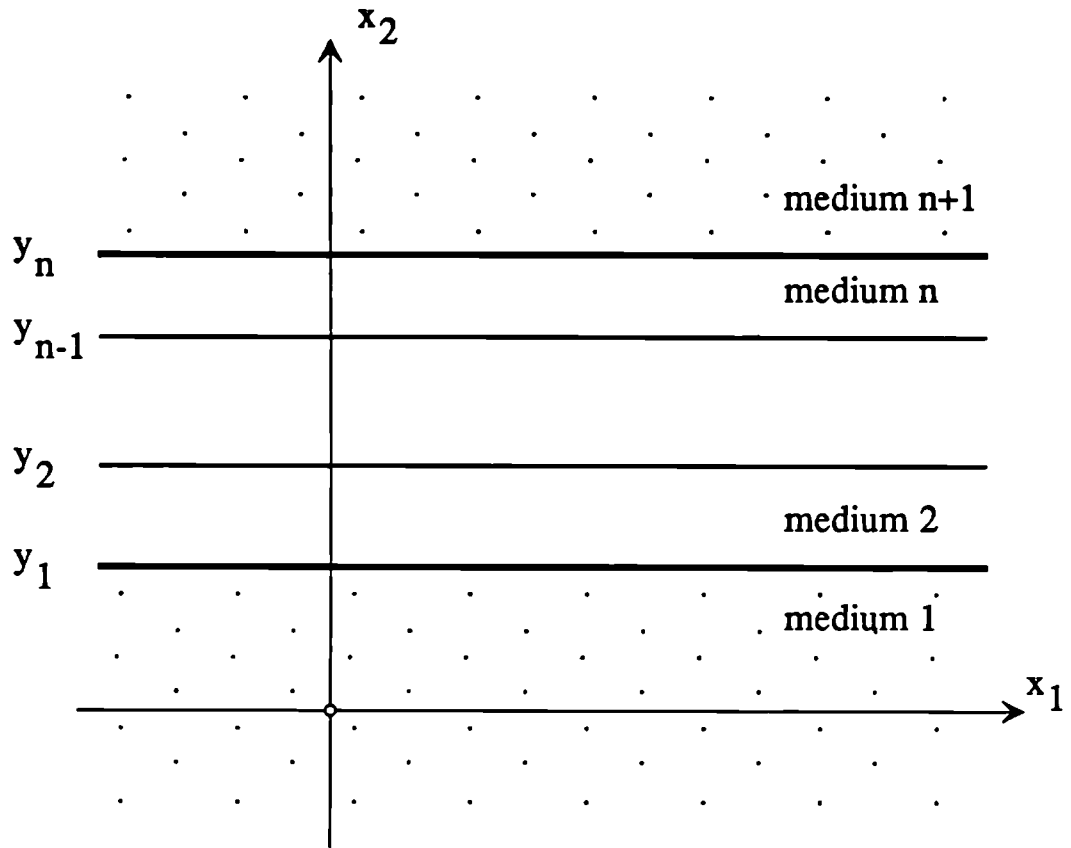
Fig. 3.1 Coordinate system for the multilayered plate.
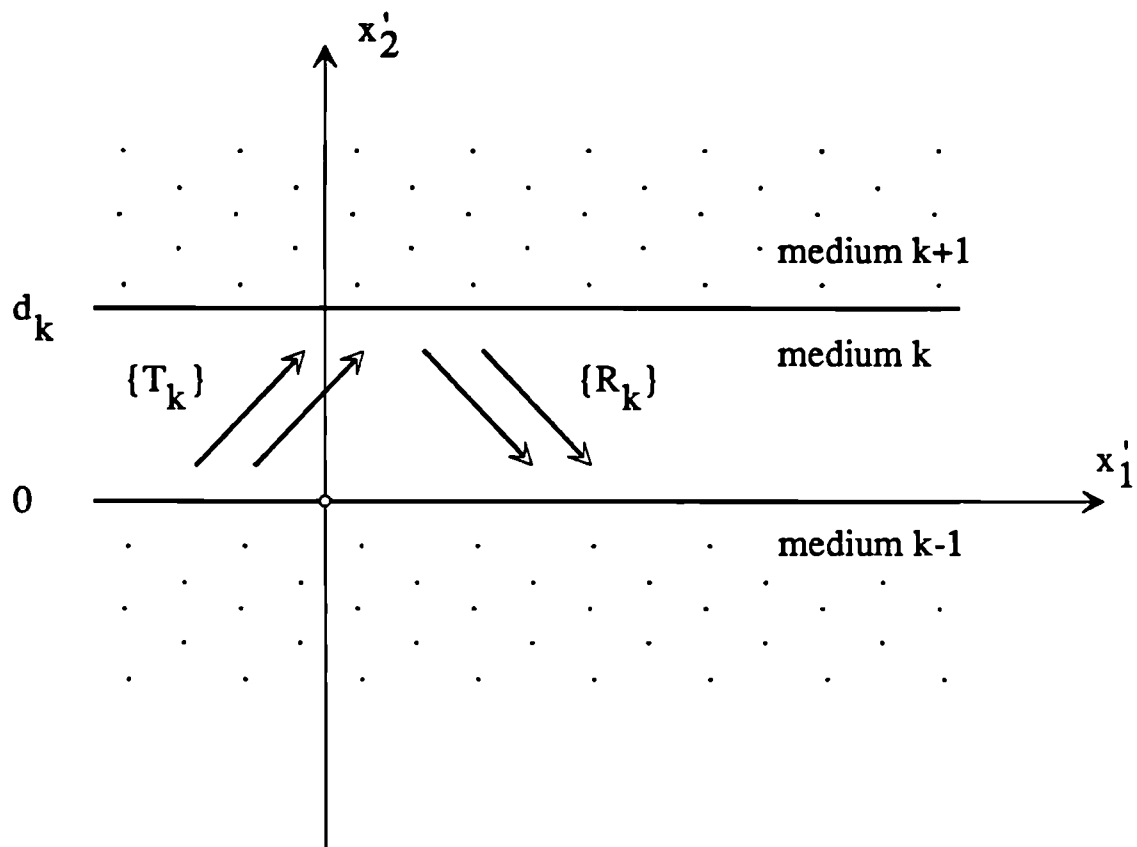
Fig. 3.2 Plane waves in the kth layer.
To simplify deriavtions, a local coordinate system has
been introduced with the origin at the bottom of the layer.
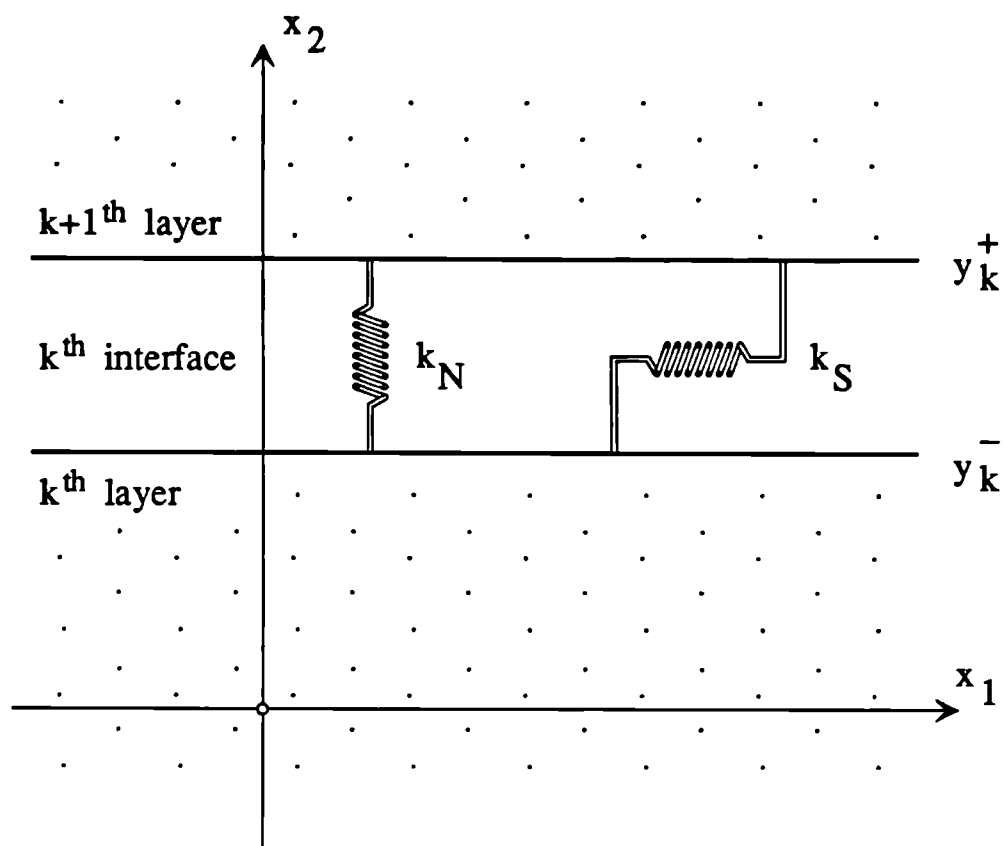
Fig. 3.3   Spring boundary conditions between two layers.
Normal and transverse stress at the boundary is
proportional to the displacement discontinuity
across the interface.
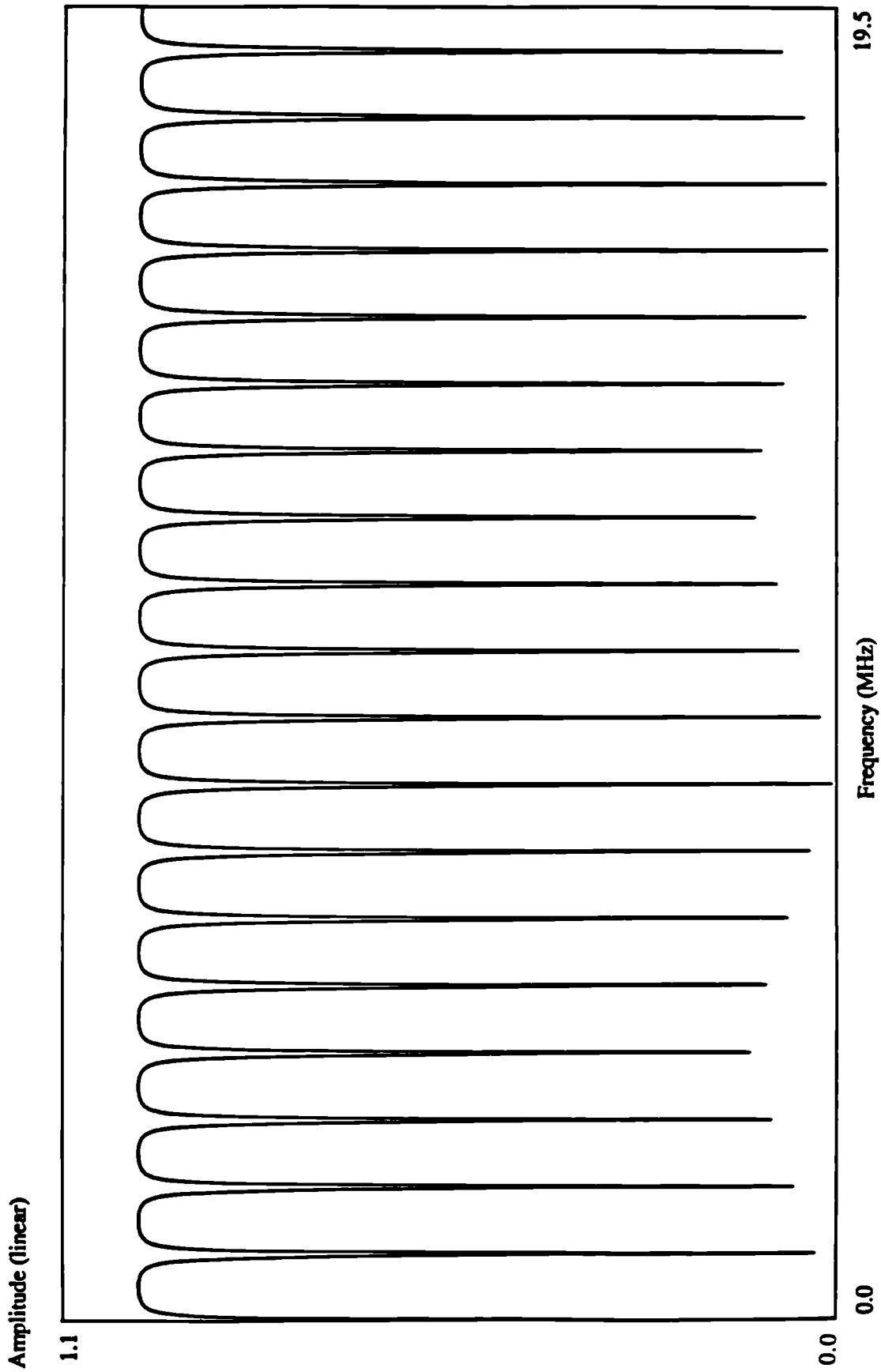
Fig. 3.4 Normal incidence. Frequency domain variation of the reflection coefficient from 3.2 mm thick aluminium plate in water.
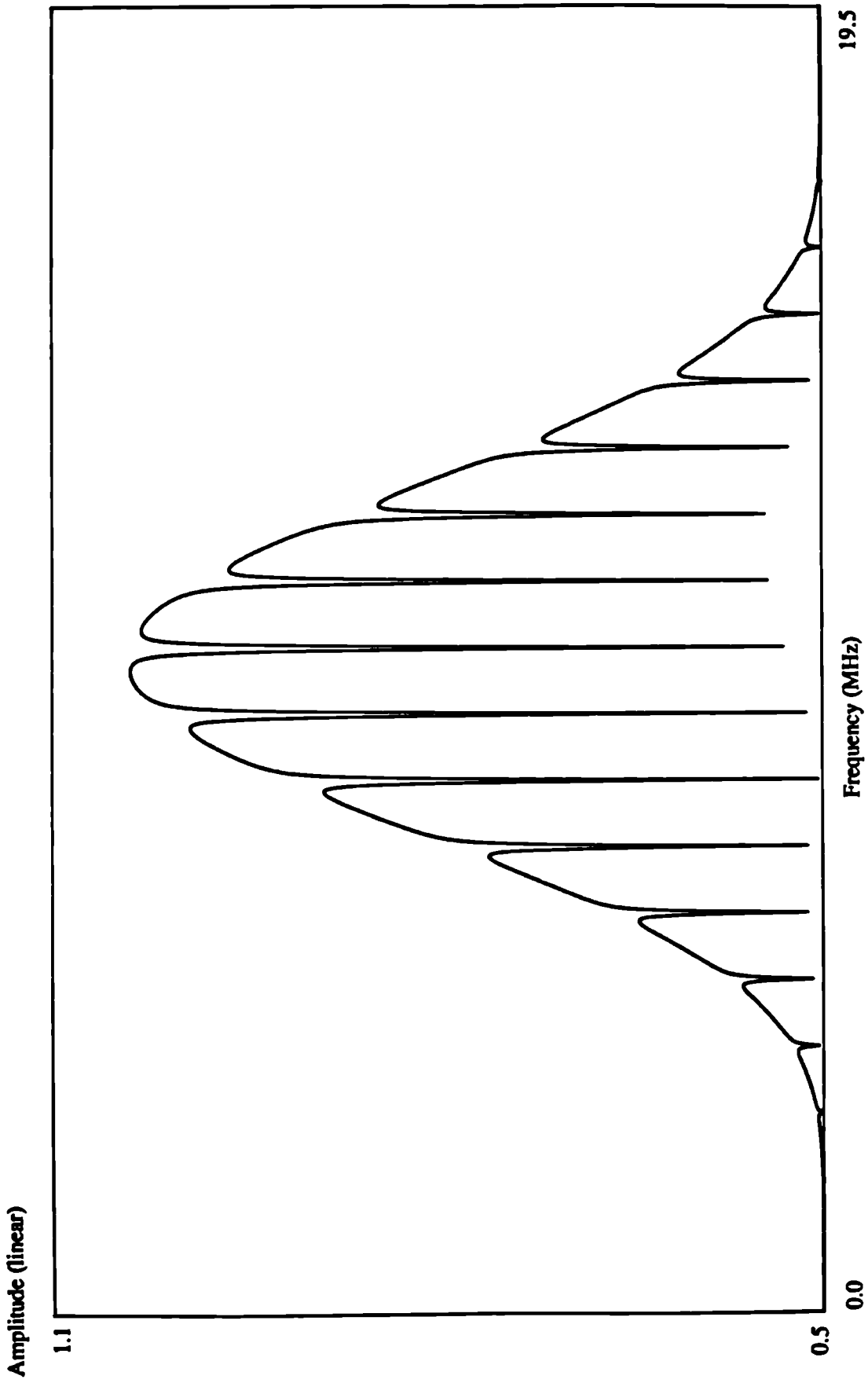
Fig. 3.5   Normal incidence. Frequency domain variation of the reflection coefficient from 3.2 mm thick aluminium plate in water windowed by a frequency response of a typical 10 MHz transducer.
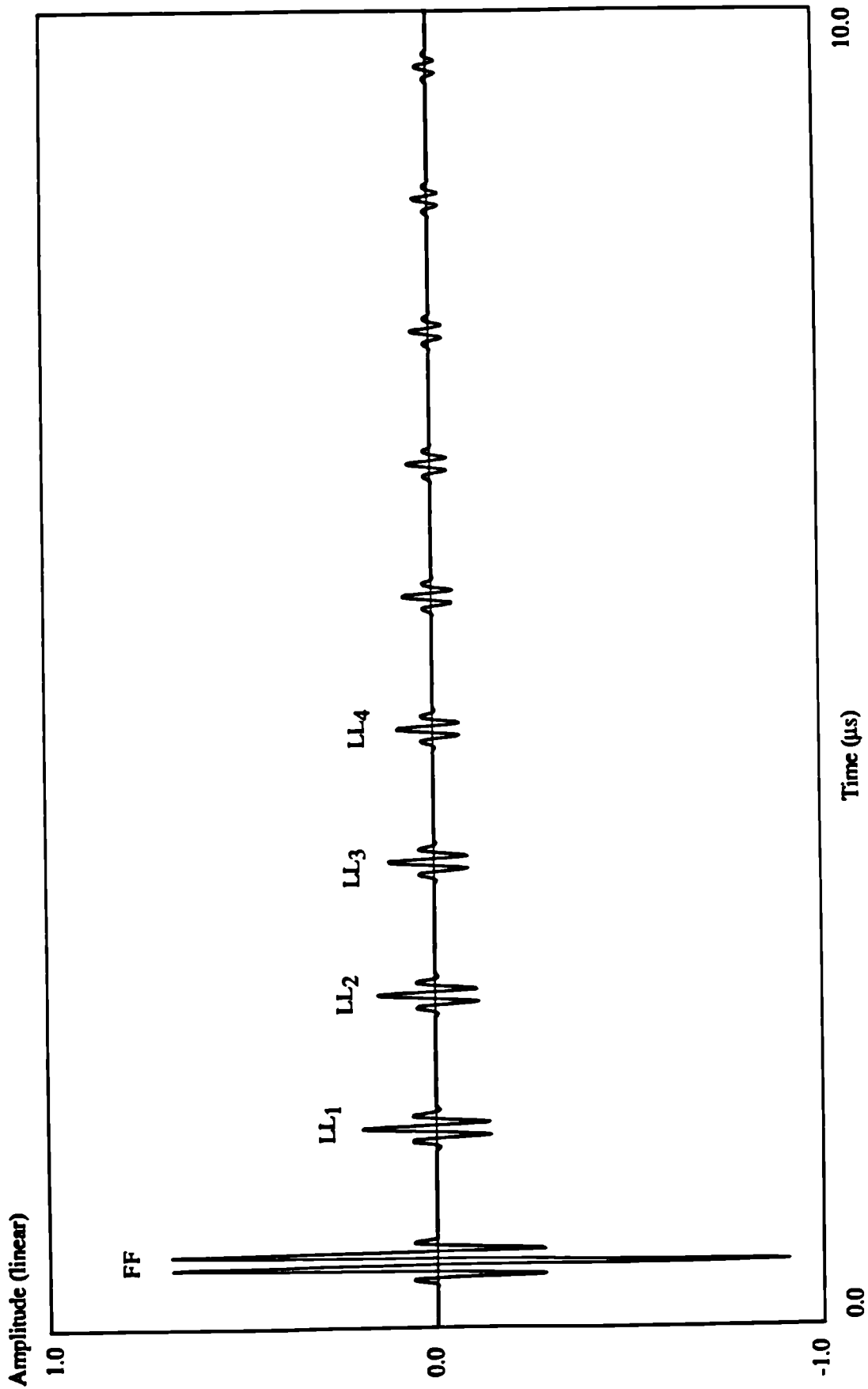
Fig. 3.6   Normal incidence. Reflected longitudinal wave from 3.2 mm thick aluminium plate in water.

Amplitude (linear)

1.1
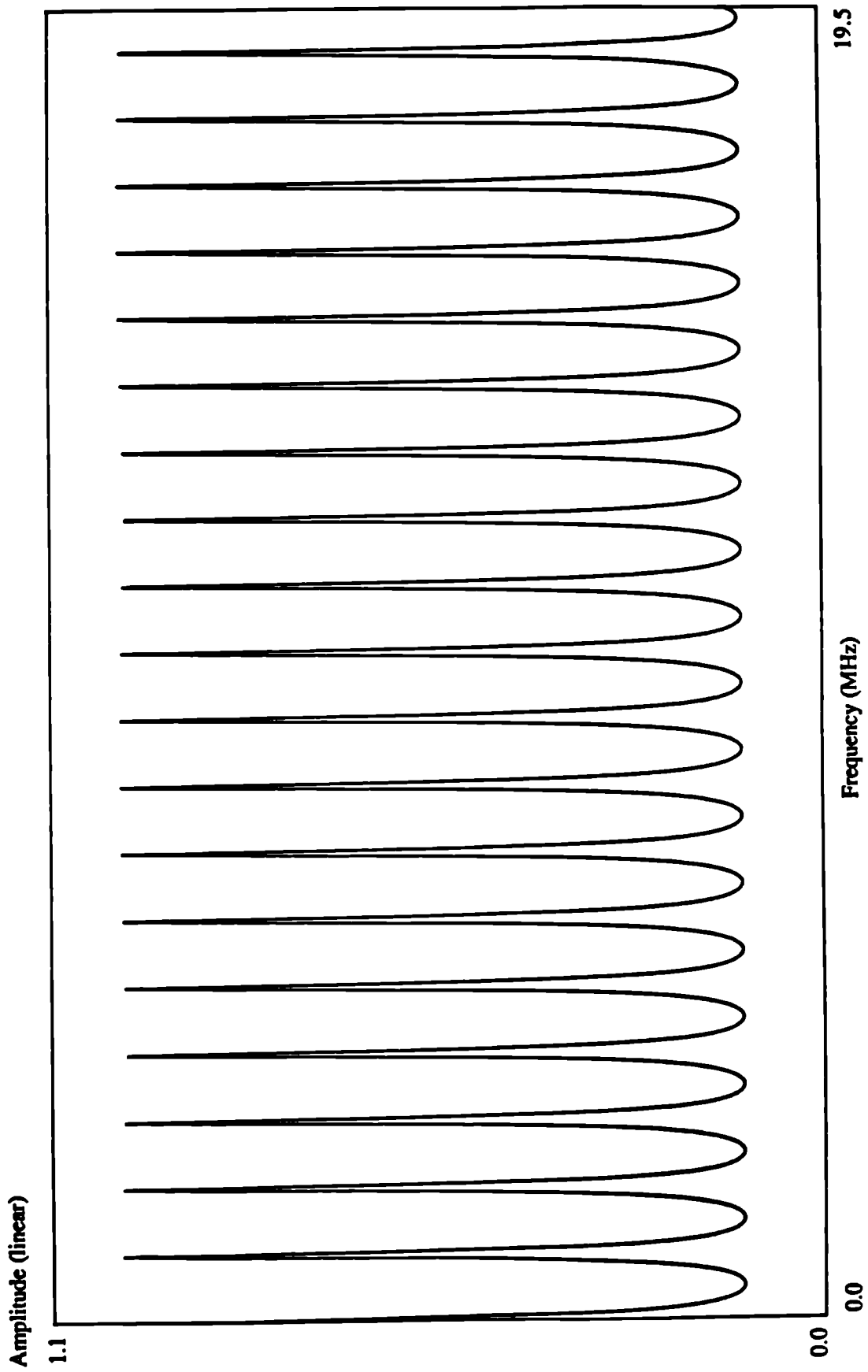
Fig. 3.7   Normal incidence. Frequency domain variation of the Trasmission coefficient from 3.2 mm thick aluminium plate in water.

Frequency (MHz)

0.0

19.5

0.0
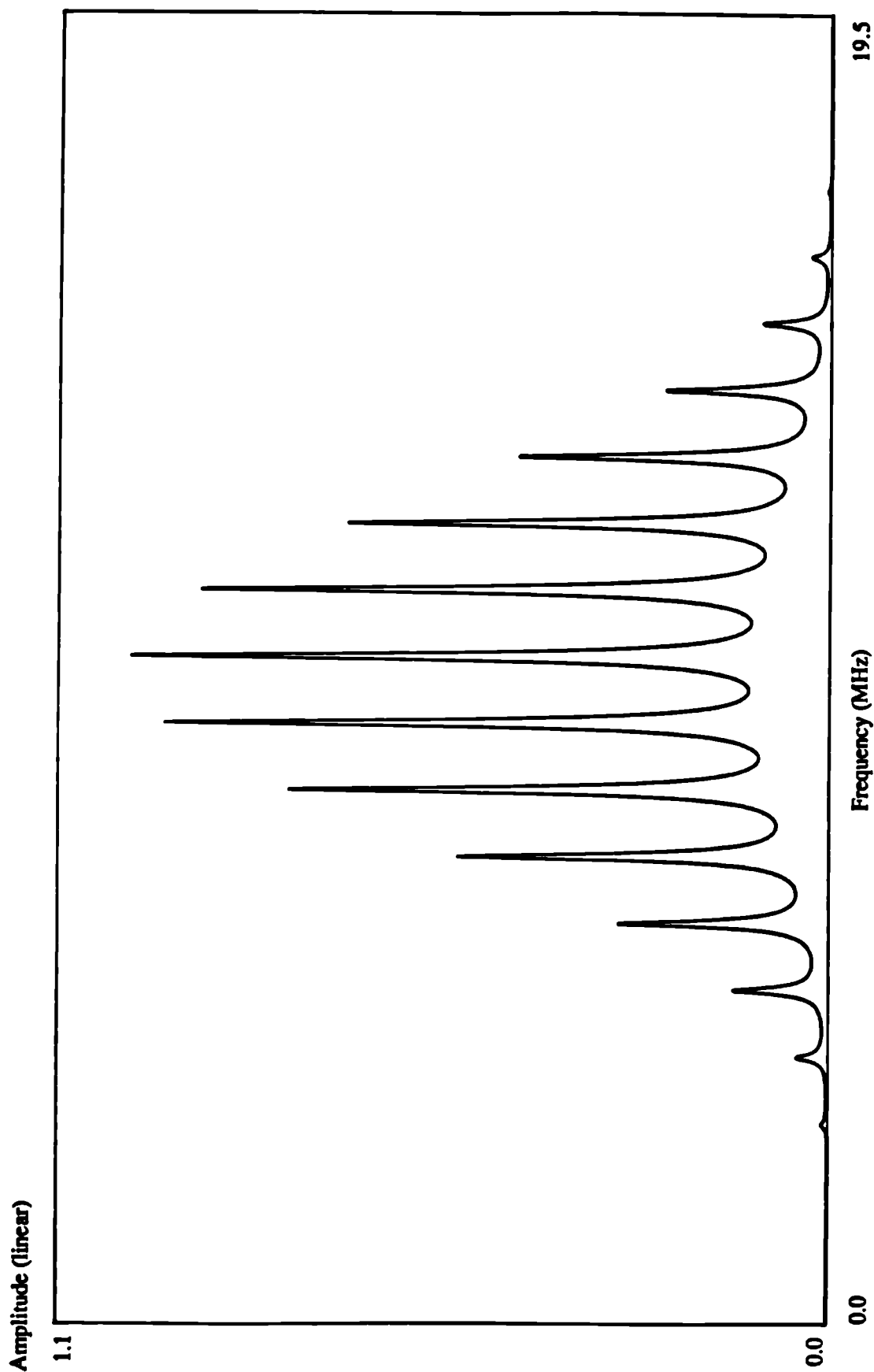
Fig. 3.8 Normal incidence. Frequency domain variation of the transmission coefficient from 3.2 mm thick aluminium plate in water windowed by a frequency response of a typical 10 MHz transducer.
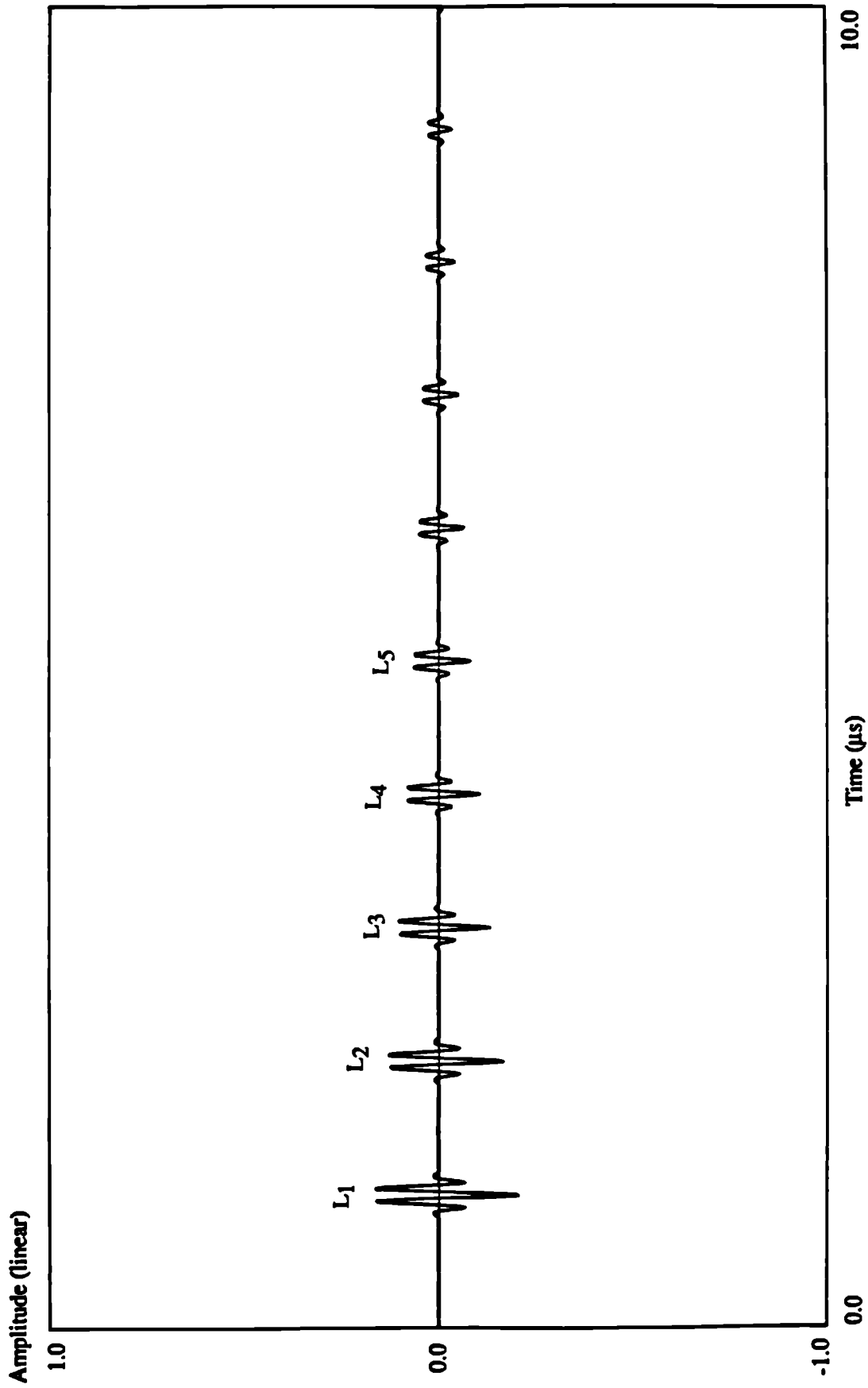
Fig. 3.9   Normal incidence. Transmitted longitudinal wave from 3.2 mm thick aluminium plate in water.
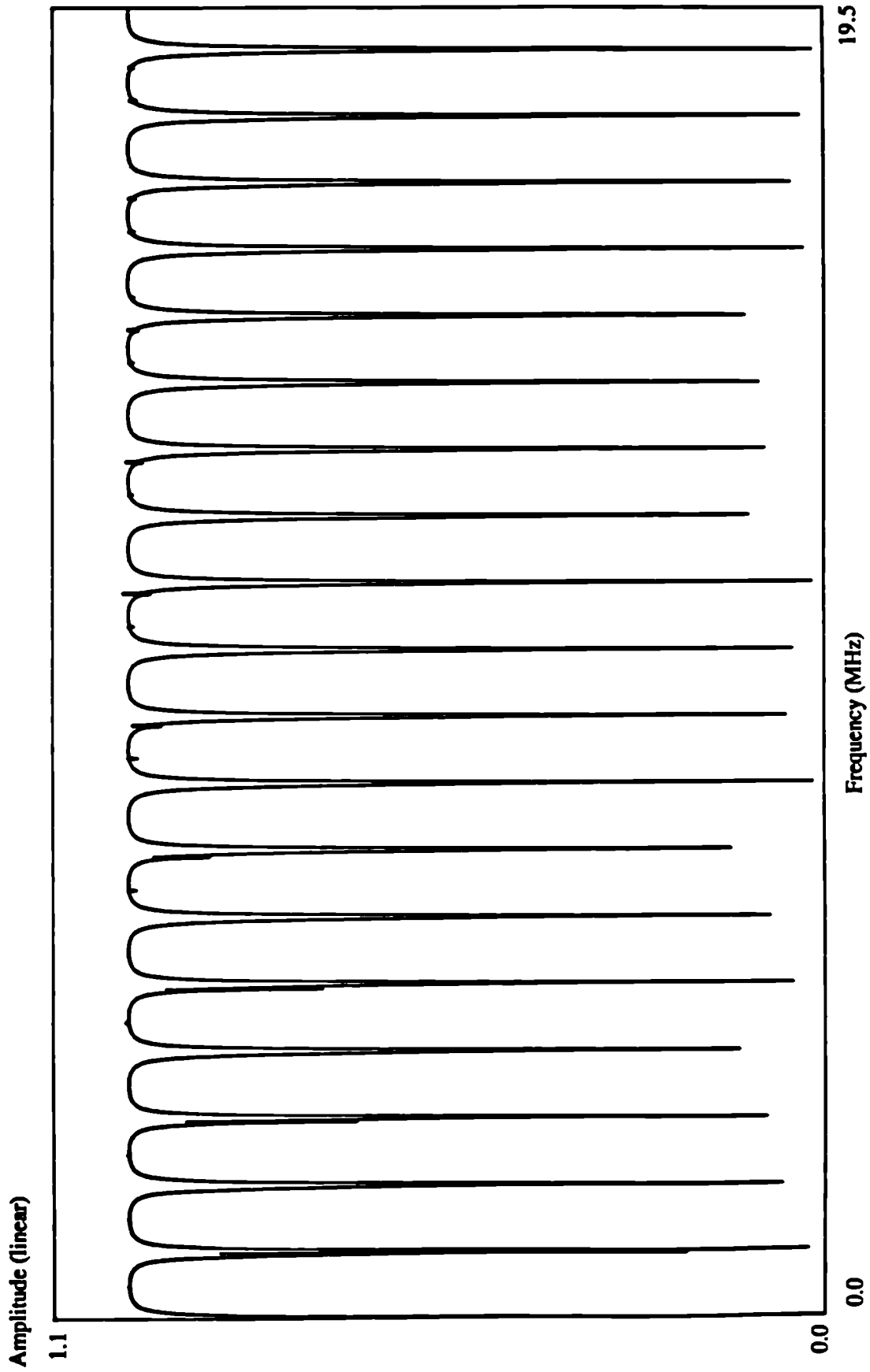
Fig. 3.10 Incidence 0.5 degree. Frequency domain variation of the reflection coeffficient from 3.2 mm thick aluminium plate in water. Visible glitches are the shear modes.
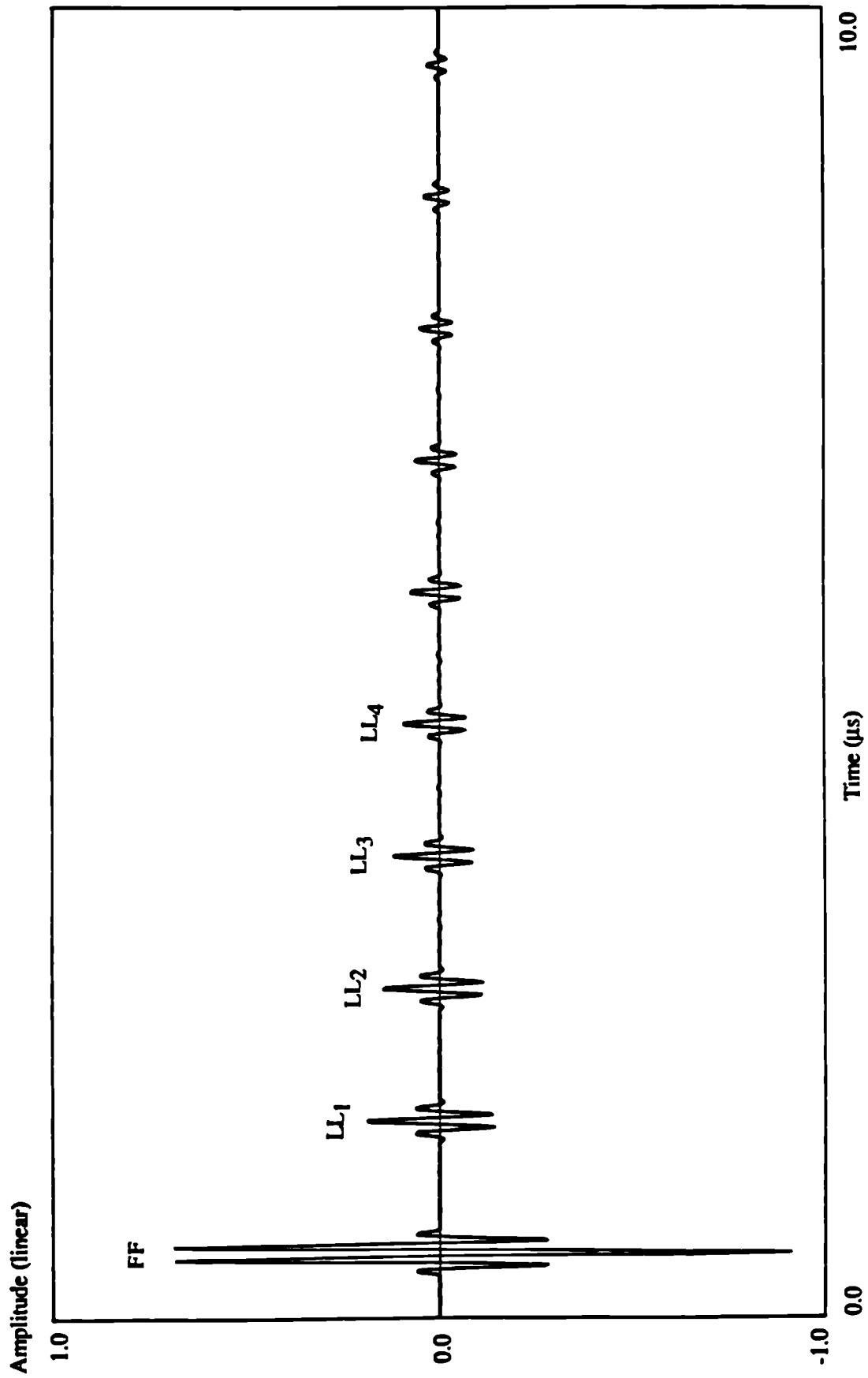
Figure 3.11   Incidence 0.5 degrees. Reflected longitudinal wave from 3.2 mm thick
aluminium plate in water.

Amplitude (linear)

1.1

Frequency (MHz)

0.0   19.5

0.0
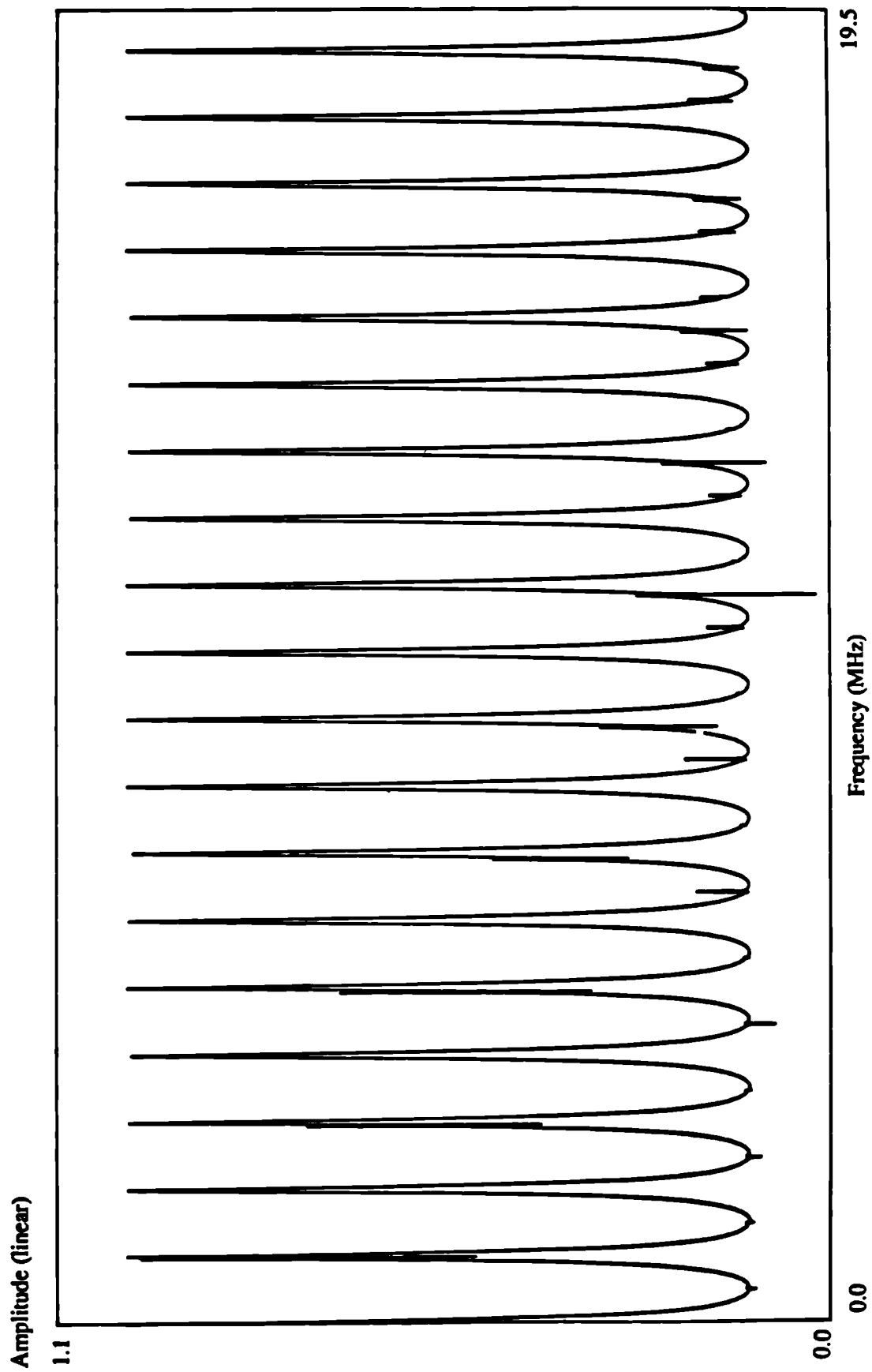
Fig. 3.12 Incidence 0.5 degree. Frequency domain variation of the transmission coeffficient from 3.2 mm thick aluminium plate in water. Visible glitches are the shear modes.
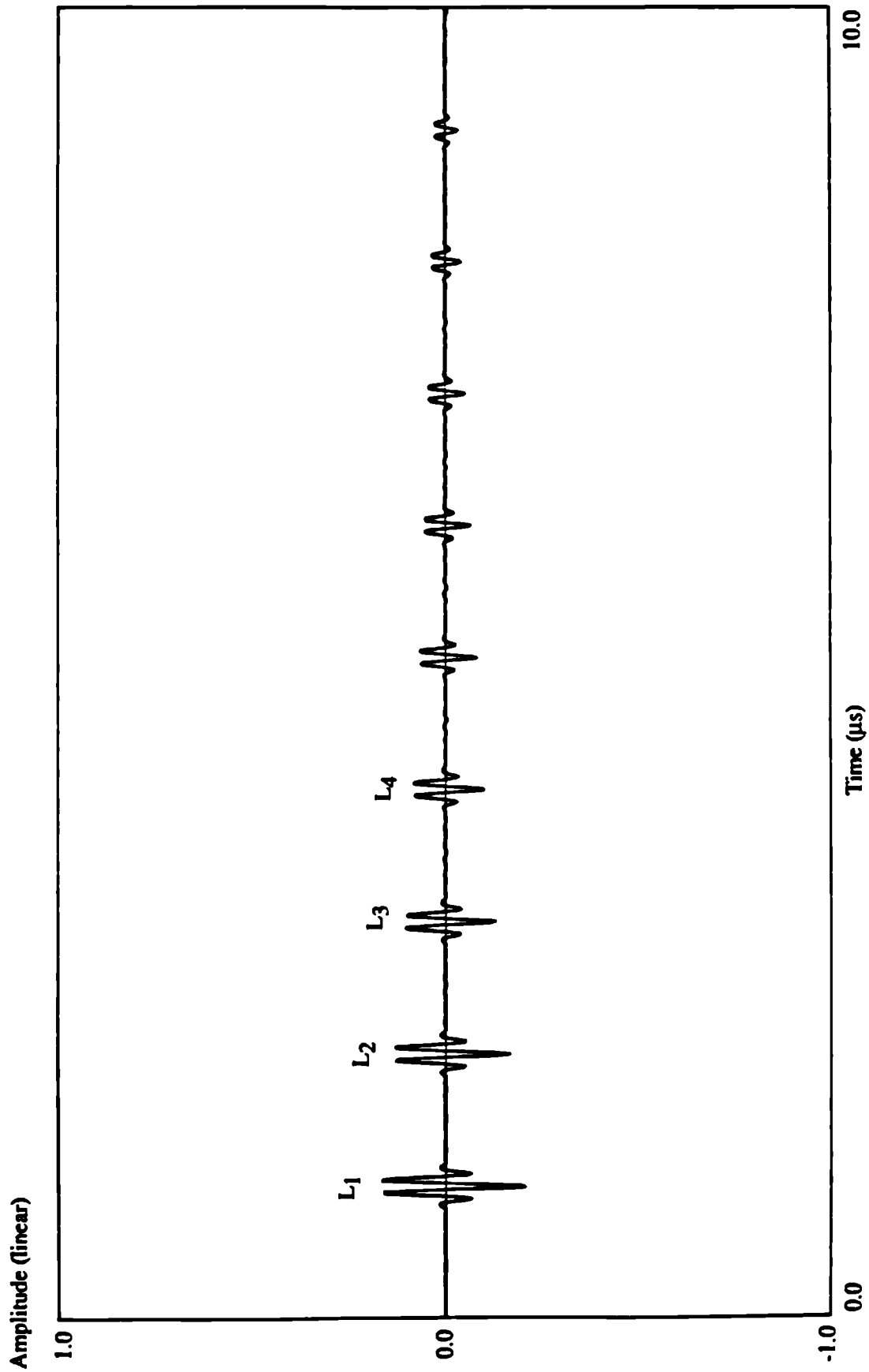
Figure 3.13   Incidence 0.5 degrees. Transmitted longitudinal wave from 3.2 mm thick aluminium plate in water.
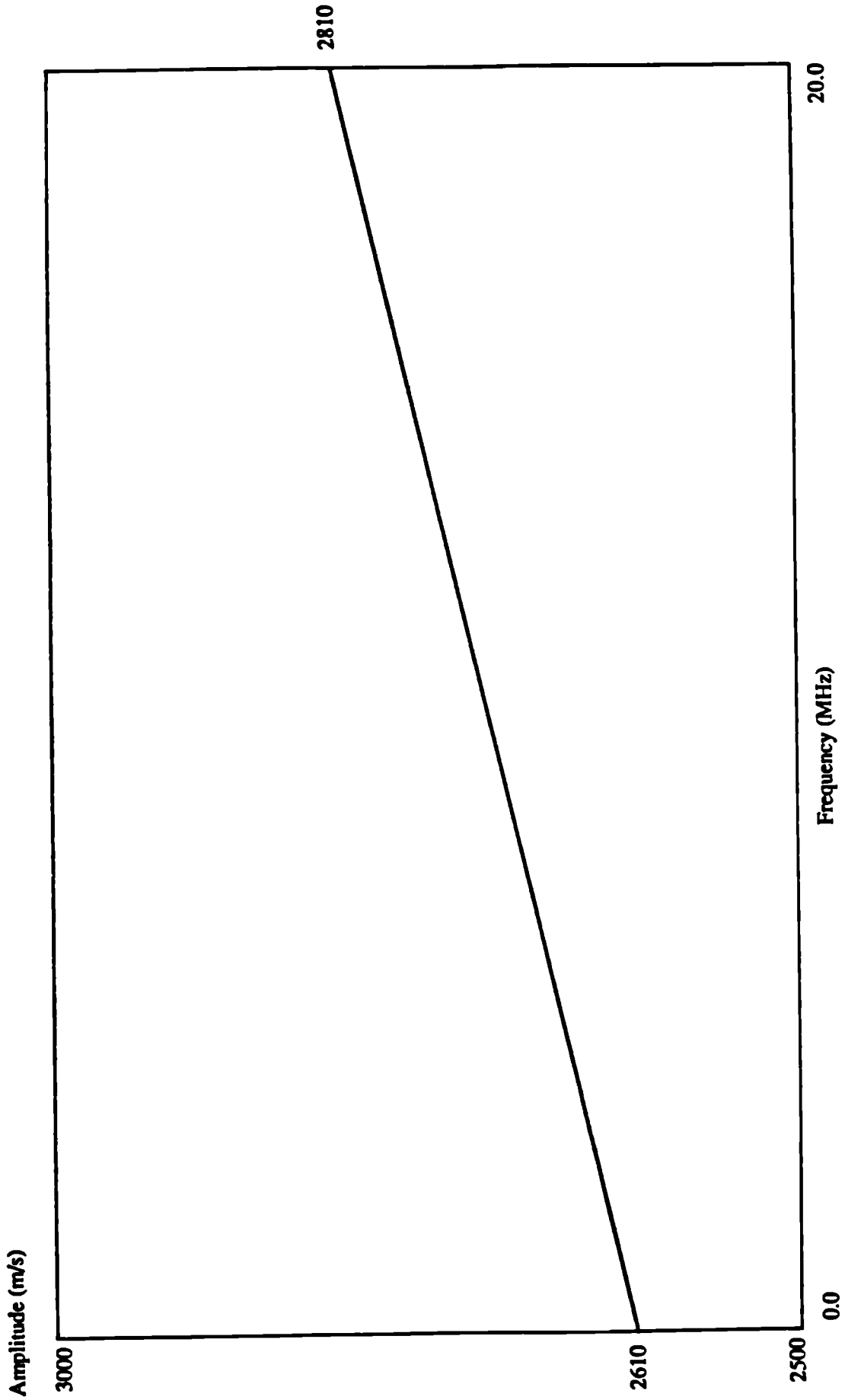
Fig. 3.14   Variation of the longitudinal phase velocity with frequency. Velocity increases
linearly from 2610 m/s at very low freqencies to 2810 m/s at 20 MHz.
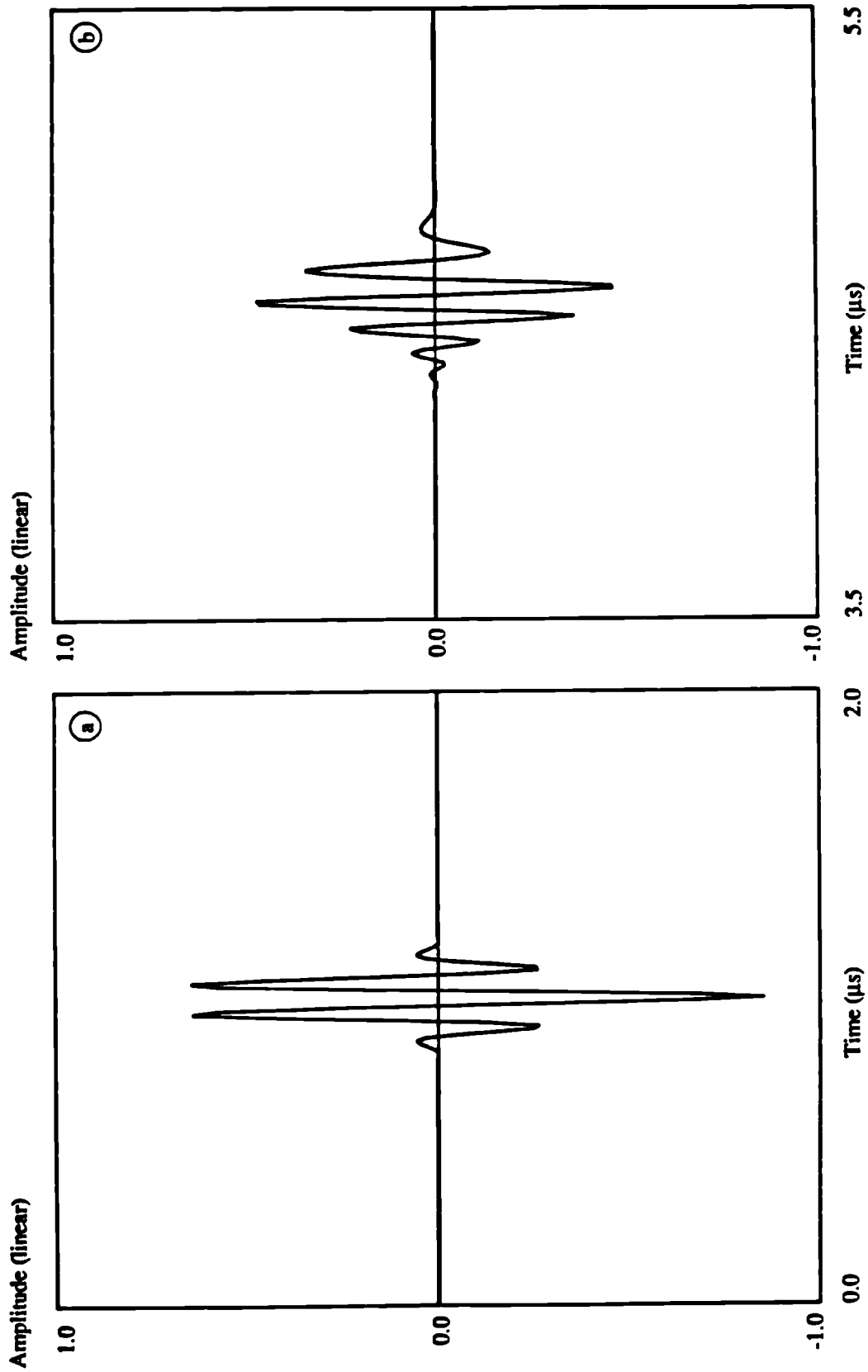
Fig. 3.15   Example of dispersion. The same longitudinal pulse received at positions 10 mm apart from each other. (a) at the point of application, (b) 10 mm away from the point of application. Phase velocity variation shown in fig. 3.14, attenuation 0.1 nepers per wavelength
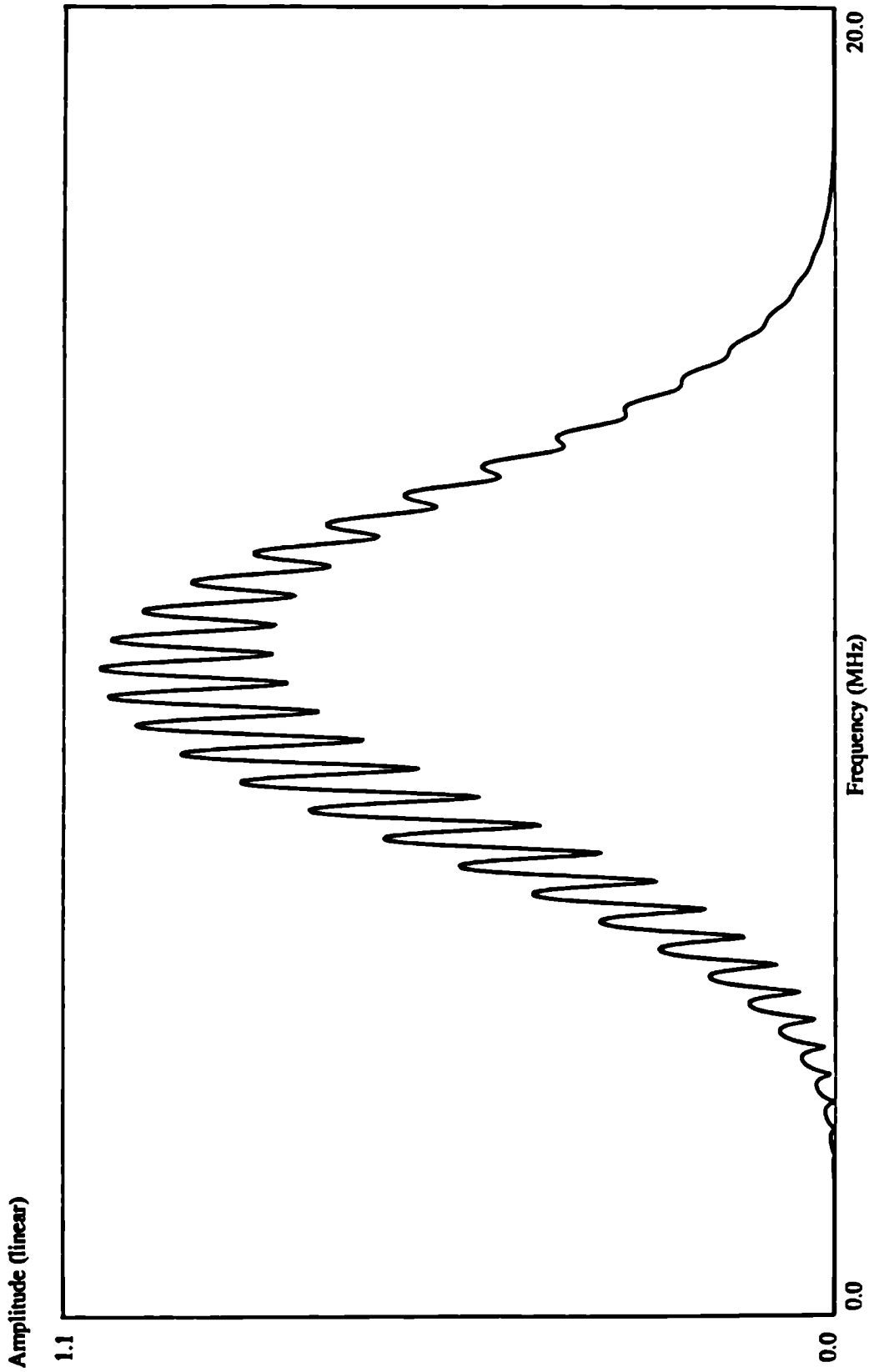
Fig. 3.16   Amplitude spectrum of the reflected field at normal incidence windowed by the frequency response of a typical 10 MHz transducer. 3.15 mm thick epoxy plate air-backed on one side and water-loaded on the other. Longitudinal attenuation 0.1 nepers per wavelength, variation of longitudinal velocity shown in fig. 3.14.
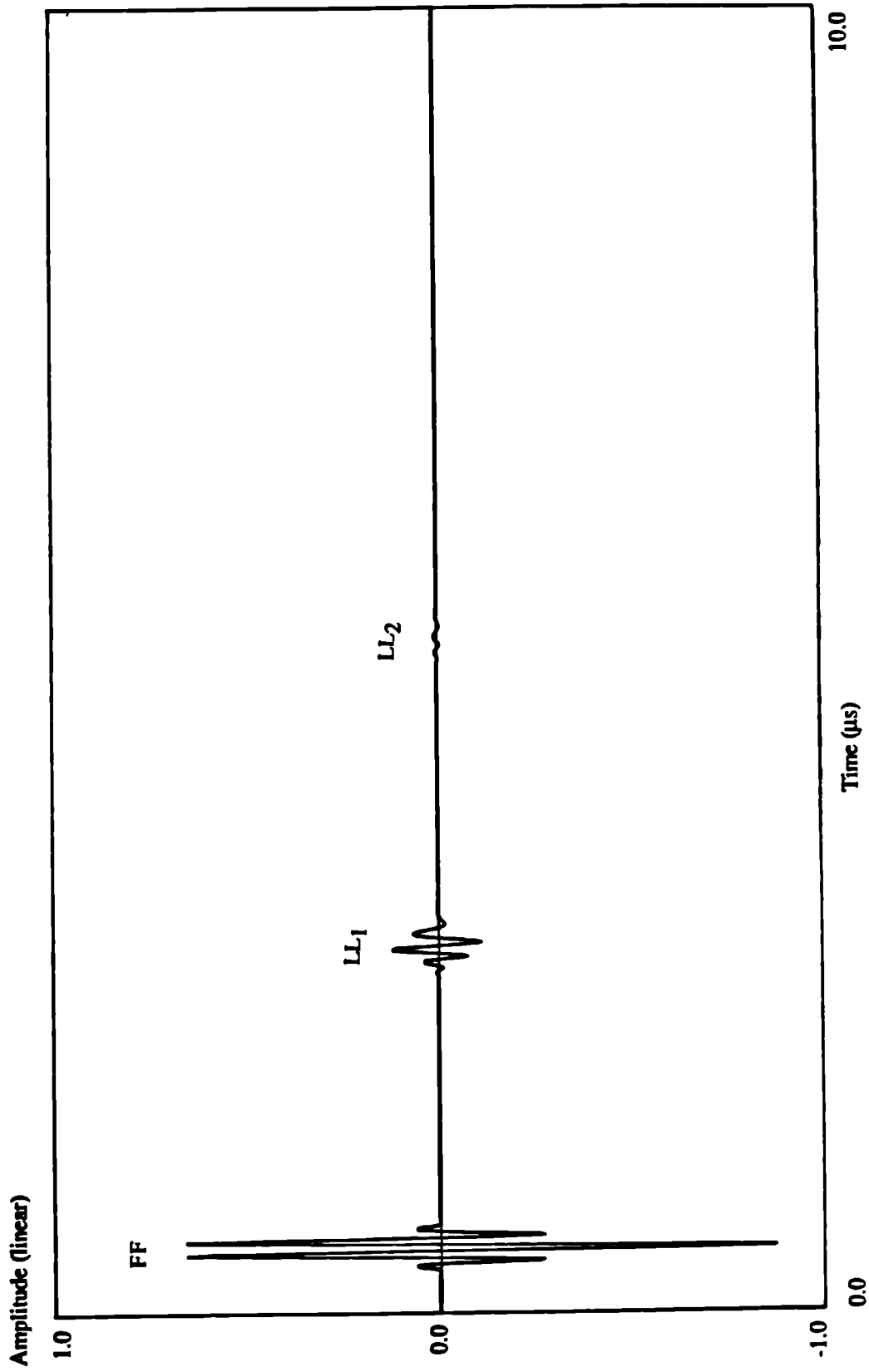
Fig. 3.17   Predicted time domain response of a 3.15 mm thick epoxy plate to a pulse excitation at normal incidence. Phase velocity is given in fig. 3.14, attenuation is 0.1 nepers per wavelength.
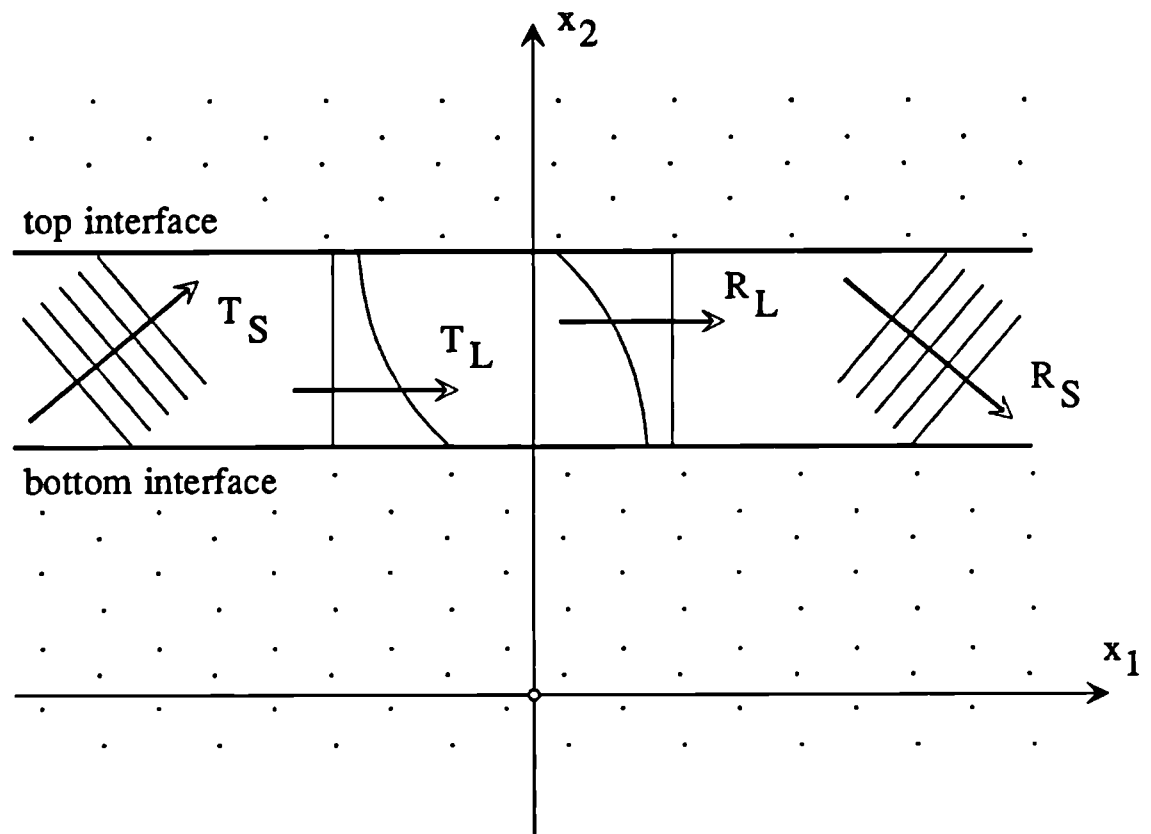
Fig. 3.18 Schematic diagram of transmitted and reflected waves within a layer in the case when longitudinal waves are inhomogeneous and shear waves are homogeneous.
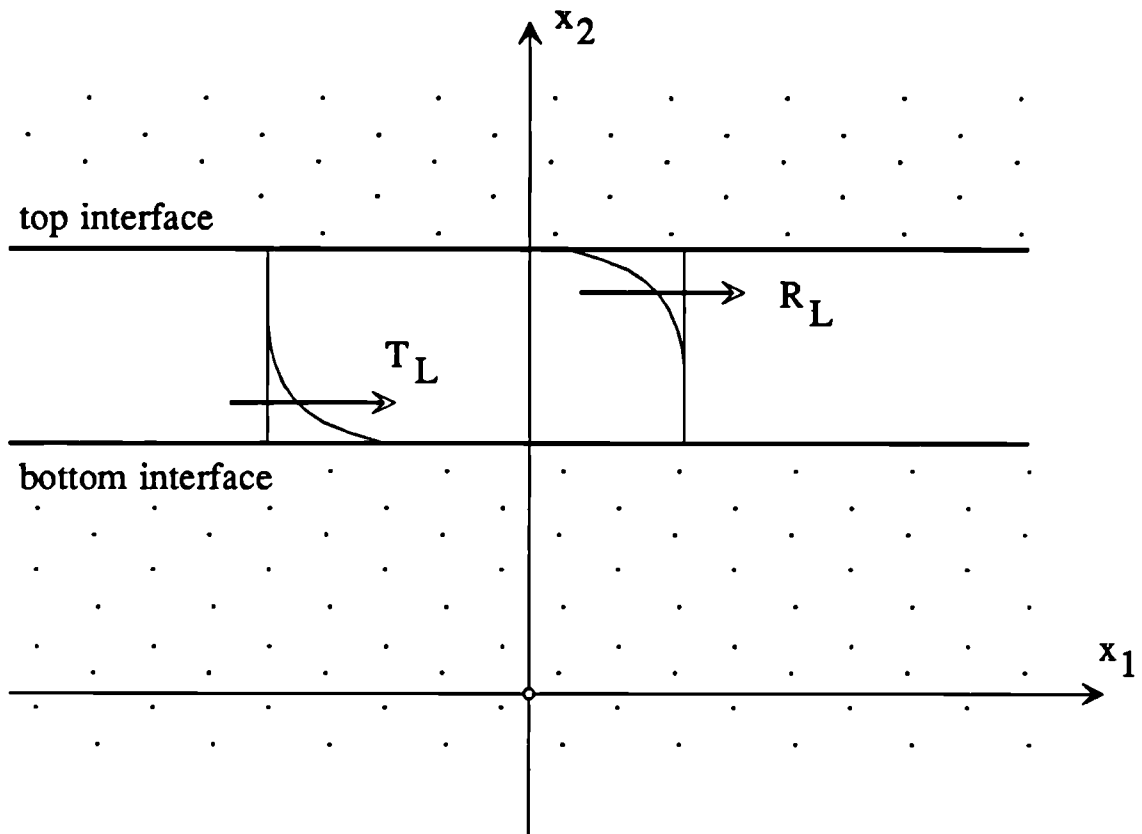
Fig. 3.19 Inhomogeneous waves in the case of higher frequencies of excitation. Large amplitudes on one side of the layer decaying to negligible values across the thickness of the layer.
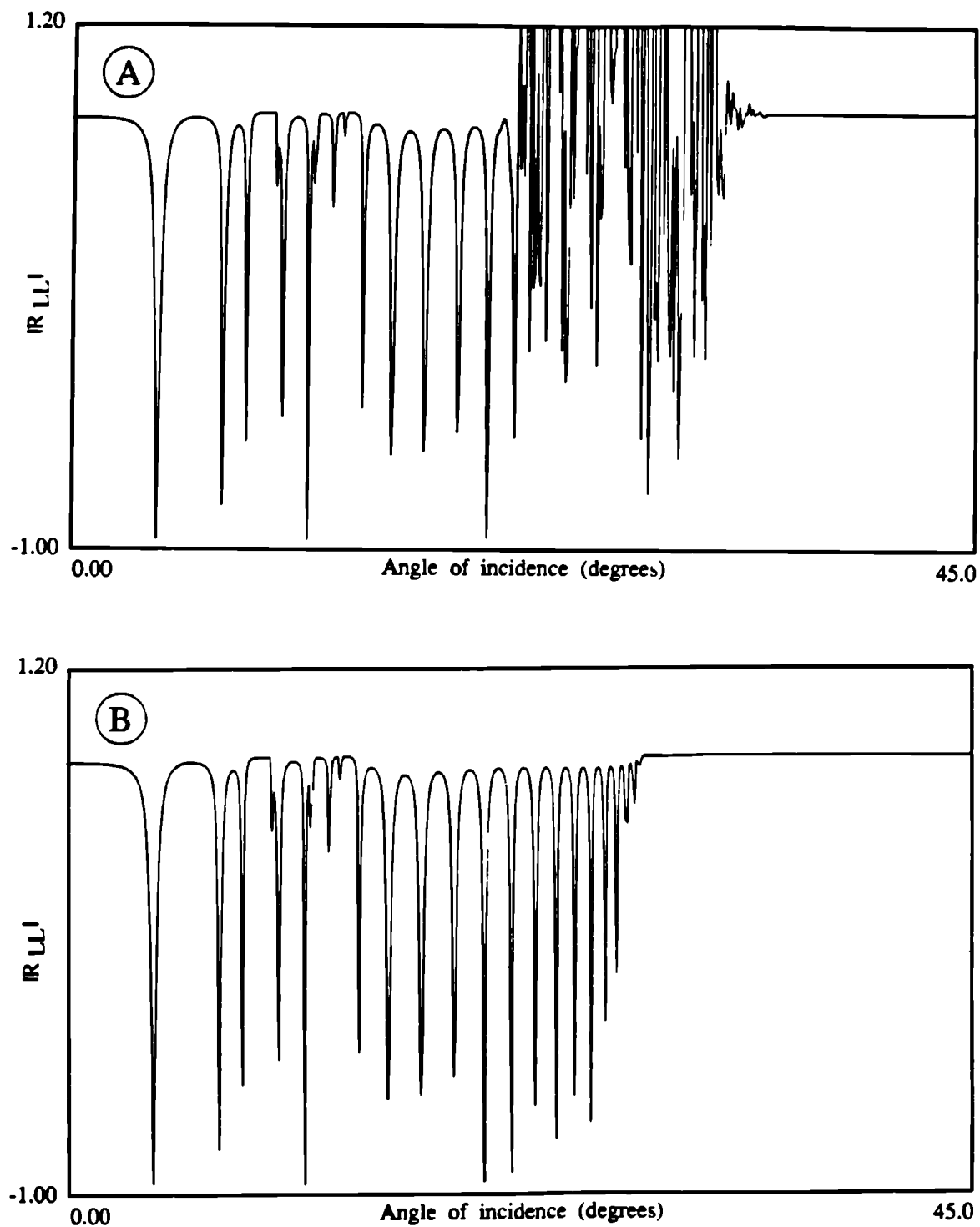
Fig. 3.20   Reflection coefficient from the 5 mm thick aluminium plate in water
at a frequency of 6 MHz. (A) Thomson-Haskell transfer matrices algorithm,
(B) global matrix technique.
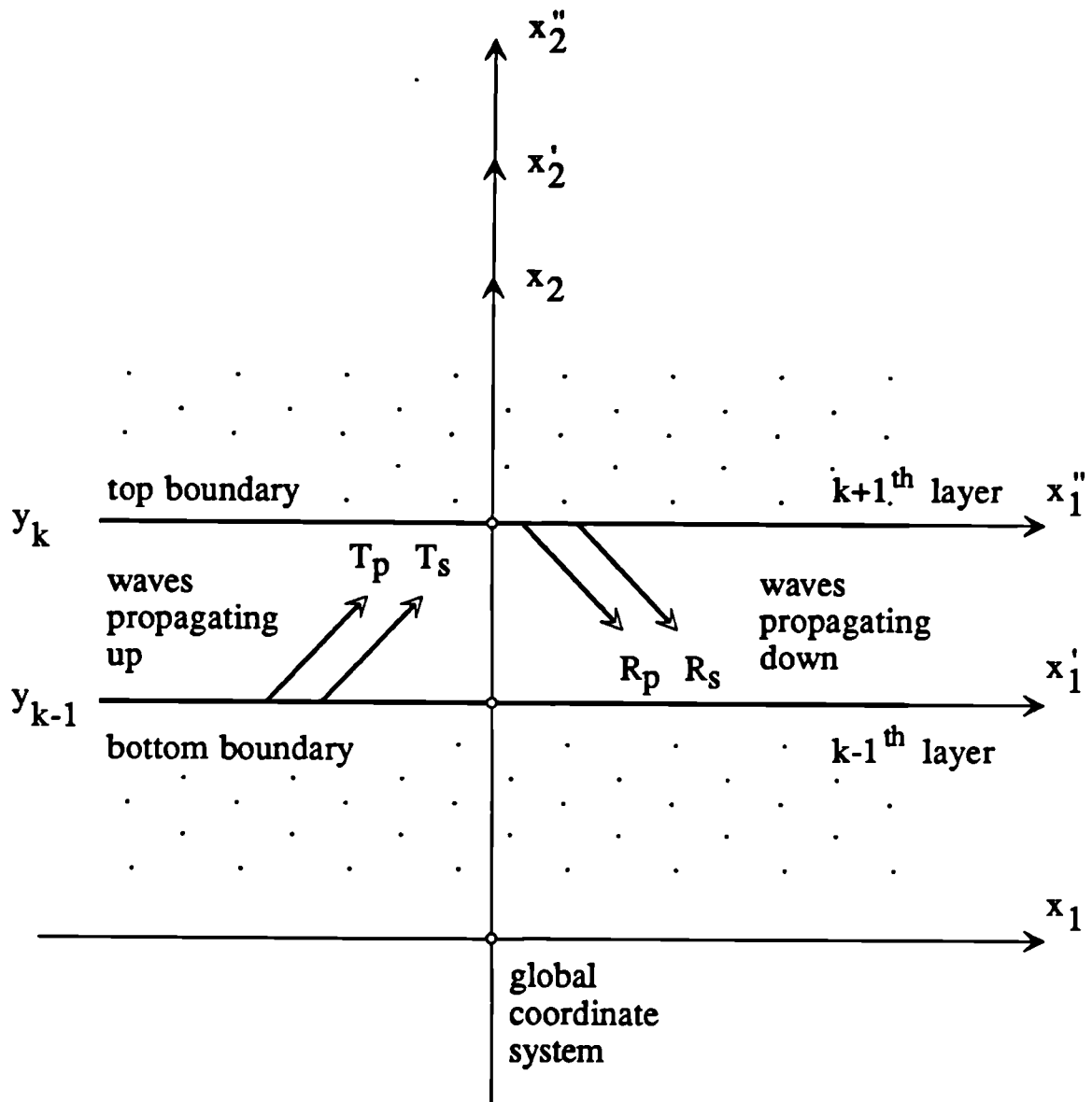
Fig. 3.21 Plane waves in the kth layer.
To improve numerical stability two local coordinate systems have been introduced with the origins at the bottom and the top of the layer.
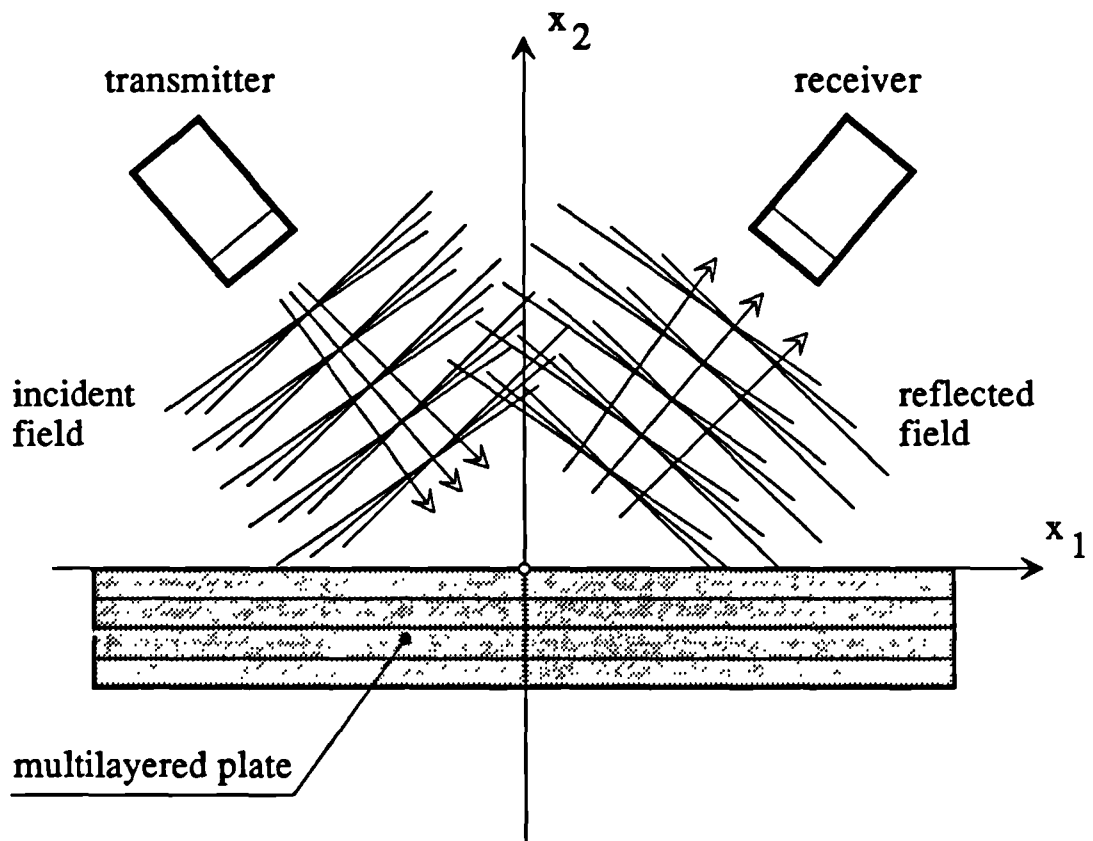
Fig. 3.22 Decomposition of the radiated field into plane wave components in order to solve the finite beam reflection problem.

CHAPTER 4

Theoretical predictions of the reflection coefficient from thin layers

4.1 Introduction

This chapter presents a systematic study of the reflection of ultrasonic waves from layers between semi-infinite half spaces. The intention of this chapter is to provide more insight into two important problems of ultrasonic nondestructive testing. The first one is the problem of the detectability of the presence of thin layers, especially embedded thin layers. Here we would like to know under what circumstances it is possible to detect the presence of a layer of given thickness and material properties. The second problem is the question of the ultrasonic evaluation of the properties of thin layers. In such cases we would like to know under what conditions it is possible to monitor differences in the thickness of a layer or its mechanical properties. In order to answer these questions, the multilayered viscoelastic plate theory developed in chapter 3 can be used. To gain better understanding of the physics involved, a normal incidence reflection theory is derived specifically for a single layer, and later in the chapter a thin layer approximation theory is derived as a simplification of the matrix formulation of chapter 3.

The notion of a viscoelastic layer has already been introduced and the exact form of the normal incidence reflection coefficient from an aluminium plate in water was given in Appendix A. In section 4.2, the general case of the normal incidence reflectivity from elastic layers is solved. Simple formulae are derived giving a considerable insight into the behaviour of the reflection coefficient at normal incidence.

Section 4.3 applies the multilayered plate theory developed in chapter 3, and the simple theory given in section 2.3, to the case of thin liquid layers between two solid half-spaces. This section is concerned with the detectability of the presence of liquid layers and the evaluation of their material properties using ultrasound.

Section 4.4 extends the investigations started in the previous section to the case of thin solid

layers. The problems of the detectability of the presence of the layers as well as evaluation of their material properties are addressed here.

A stress-displacement transfer matrix formulation of the mechanical behaviour of layers has been given in chapter 2. In section 4.5 the concept of a thin viscoelastic layer is introduced. This is achieved by expanding a stress-displacement transfer matrix in terms of the layer thickness. Under such an approximation the complicated stress-displacement transfer matrix considerably simplifies, offering us more insight into the physics of the thin layer reflectivity. In this section the comparison between the exact and the approximate formulation is given in order to show the limits of applicability of the simplified formulation.

Section 4.6 repeats the main conclusions of the chapter.

4.2 The reflection coefficient from solid and liquid layers at normal incidence

4.2.1 General

In chapter 3 we were concerned with the response of multilayered viscoelastic media. As an example, the normal incidence response from an aluminium plate was studied. In Appendix A the normal incidence longitudinal reflection coefficient from an aluminium plate in water was derived as a Fourier transform of the time domain response. In Appendix A and section 3.3 we learned (see fig. 7 of Appendix A and also fig. 3.4) that the normal incidence reflection coefficient curves feature equally spaced minima at frequencies which correspond to the resonant frequencies of the aluminium plate in vacuum, the depth of the minima depending on the ratio between the front face reflection from the plate and a series of the reflections from the back of the plate.

If the plate is to be between two dissimilar half-spaces, then obviously the balance between the front face and back face reflections change, affecting the depths of the minima. In this subsection we would like to answer what governs the shape of the normal incidence reflection coefficient curves from layers separating half-spaces of different mechanical properties. In order to do so we take the frequency domain approach introduced in chapter 2 and developed further in section 3.3. In this approach we will consider the steady state response of the layer to a harmonic normal incidence excitation. For the sake of the argument we will consider the longitudinal excitation bearing in mind that the same analysis applies to the normal incidence shear wave (if the system can support shear wave propagation).

Consider a system consisting of a layer separating two half-spaces (see fig. 4.1), being excited by a longitudinal wave in the direction perpendicular to the the layer. Using the notation introduced in chapter 2, the displacement field in the left half-space (medium number 1) can be expressed as the sum of two waves: an incident wave of amplitude T_1, and reflected one of amplitude R_1. In the layer (medium number 2) we have transmitted and reflected waves of amplitudes T_2 and R_2, respectively. In the right-hand side half-space, the displacement field will consist of only a single transmitted wave of amplitude T_3.

In general, a longitudinal plane wave propagating in a direction along the x coordinate can be expressed as,

$$u(x,t) = A\, e^{i\omega(x/\alpha - t)}, \tag{4.1}$$

where u is the displacement field in the x direction, A is the amplitude, ω is the frequency and α is, in general, a complex value characterising the velocity and damping of the wave. When α is real then the wave propagates without attenuation and $\alpha = c$, where c is the phase velocity of the wave. The normal stress in the x direction can be calculated from the standard stress-strain equation of the form,

$$\sigma = E\varepsilon, \quad \text{where} \quad \varepsilon = \frac{\partial u}{\partial x}, \tag{4.2}$$

and E is an elastic constant, satisfying the relationship,

$$E = \rho\alpha^2, \tag{4.3}$$

where ρ is the density of the medium. Substituting eqn (4.1) into (4.2), we have,

$$\frac{\partial u}{\partial x} = \frac{i\omega}{\alpha}\, u(x,t), \tag{4.4}$$

$$\sigma(x,t) = \frac{i\omega E}{\alpha}\, u(x,t). \tag{4.5}$$

Substituting eqn (4.3) into (4.5), we have,

$$\sigma(x,t) = i\omega z\, u(x,t), \tag{4.6}$$

where,

$$z = \rho\alpha, \tag{4.7}$$

is defined as an impedance of the medium, and relates the amplitude of the normal stress to the

velocity of the wave.

Using equations (4.1) and (4.6), we are now in position to describe the displacement and stress fields in the three media of fig. 4.1. Omitting the common time dependent term $e^{-i\omega t}$, for convenience, we can express the displacement and the stress fields in medium 1 as,

$$u_1(x) = T_1 e^{i\omega x/\alpha_1} + R_1 e^{-i\omega x/\alpha_1} , \qquad (4.8)$$

$$\sigma_1(x) = i\omega z_1 (T_1 e^{i\omega x/\alpha_1} - R_1 e^{-i\omega x/\alpha_1}) . \qquad (4.9)$$

Similarly, for the layer, we have,

$$u_2(x) = T_2 e^{i\omega x/\alpha_2} + R_2 e^{-i\omega x/\alpha_2} , \qquad (4.10)$$

$$\sigma_2(x) = i\omega z_2 (T_2 e^{i\omega x/\alpha_2} - R_2 e^{-i\omega x/\alpha_2}) . \qquad (4.11)$$

For the right-hand side half-space, we have,

$$u_3(x) = T_3 e^{i\omega x/\alpha_3} , \qquad (4.12)$$

$$\sigma_3(x) = i\omega z_3 T_3 e^{i\omega x/\alpha_3} . \qquad (4.13)$$

In order to solve the reflection coefficient problem it is necessary to 'connect' the stresses and displacements on both sides of the boundaries, so that the stress and displacement fields are continuous everywhere in space.

Using equations (4.10) and (4.11) we can calculate the stresses and displacements at both interfaces in terms of the amplitudes of the waves in the layer. At the left boundary of the layer, x = 0, and we have,

$$u(0) = T_2 + R_2 , \qquad (4.14)$$

$$\sigma(0) = i\omega z_2 (T_2 - R_2) , \qquad (4.15)$$

and at the right boundary, x = L, we have,

$$u(L) = T_2 g_p + R_2 g_p^{-1} , \qquad (4.16)$$

$$\sigma(L) = i\omega z_2 \left(T_2\, g_p - R_2\, g_p^{-1} \right). \tag{4.17}$$

In accordance with the notation introduced in chapter 2 (see eqn (2.77)), g_p accounts for the exponential term in equations (4.16) and (4.17),

$$g_p = e^{i\omega L/\alpha_2}. \tag{4.18}$$

For the purpose of the further derivations, let us assume that the layer is perfectly elastic, that is $\alpha_2 = c_2$, where c_2 is the phase velocity of the longitudinal wave in the layer. For such a case the argument in the exponential term of eqn (4.18) becomes real, and the magnitude of g_p is unity.

Using equations (4.12) and (4.13), the displacements and stresses at the right-hand side boundary of the layer can be expressed in terms of the transmitted wave in medium 3 as,

$$u(L) = T_3\, \gamma, \tag{4.19}$$

$$\sigma(L) = i\omega z_3\, T_3\, \gamma, \tag{4.20}$$

where,

$$\gamma = e^{i\omega L/\alpha_3}, \tag{4.21}$$

is the term arising from the offset of the coordinate system with respect to the right-hand side boundary by distance L. We could, for example, describe the stress-displacement field in medium 3 in its own local coordinate system having origin at $x = L$, and therefore removing γ from equations (4.19) and (4.20).

Having written equations describing the stresses and displacements for each of the three media present in the system, we are now in position to derive the reflection coefficient from the layer. This can be achieved by setting the incident wave amplitude, T_1, to unity, and equating the corresponding equations across the left-hand side boundary and the right-hand side boundary as we require the stress-displacement field to be continuous everywhere in space.

4.2.2   Reflection coefficient at the resonant frequency of the layer

Let us assume that the incident wave drives the system at the resonant frequency of the layer ($\omega = \omega_{res}$). Using eqn (16) of Appendix A we can express ω_{res} in terms of the layer thickness, L, and the phase velocity, c_2, of the wave within the layer,

$$\omega_{res} = \frac{\pi c_2}{L} m \ ,$$

(4.22)

where m is the resonance number. Now, using eqn (4.22) we can express the exponential term of eqn (4.18) as follows,

$$g_p = e^{i\omega_{res}L/c_2} = \begin{cases} 1 & \text{when m is even,} \\ -1 & \text{when m is odd} \end{cases}$$

(4.23)

Resonance mode number is odd

If the resonance number, m, is odd then, by eqn (4.23), $g_p = -1$, and equations (4.16) and (4.17) become,

$$u(L) = -(T_2 + R_2) \ ,$$

(4.24)

$$\sigma(L) = -i\omega z_2 (T_2 - R_2) \ .$$

(4.25)

Using equations (4.14) and (4.15) we can relate the stress and displacement fields on both sides of the layer as,

$$u(L) = -u(0) \ ,$$

(4.26)

$$\sigma(L) = -\sigma(0) \ .$$

(4.27)

Equations (4.26) and (4.27) reveal a very interesting feature of the stress-displacement field at the frequency $\omega = \omega_{res}$. When the frequency of the excitation is equal to that of an odd mode of the layer, then the relationship between stresses and displacements on both sides of the layer is independent of value of T_2 and R_2. This means that the relationship is independent of the mechanical properties of the media on both sides of the layer as well as independent of the impedance of the layer itself.

Using equations (4.26), (4.27), and (4.8), (4.9), (4.19), (4.20), we are now in position to link the stress and displacement fields on both sides of the layer and obtain the relationship between the incident, reflected and transmitted wave,

$$T_1 + R_1 = -T_3 \gamma \ ,$$

(4.28)

$$i\omega_{res} z_1 (T_1 - R_1) = -i\omega_{res} z_3 T_3 \gamma \ .$$

(4.29)

Dividing both sides of eqn (4.29) by $i\omega_{res}$, and substituting eqn (4.28) into (4.29) we have,

$$z_1 (T_1 - R_1) = z_3 (T_1 + R_1) . \tag{4.30}$$

In order to obtain reflection coefficient, we have to put $T_1 = 1$, and calculate R_1, which gives,

$$R_{res} = \frac{z_1 - z_3}{z_1 + z_3} . \tag{4.31}$$

As we can see from eqn (4.31), the value of reflection coefficient is independent of the impedance of the intermediate layer.

Resonance mode number is even

When the resonance number, m, is even then $g_p = 1$, and equations (4.16) and (4.17) become

$$u(L) = T_2 + R_2 , \tag{4.32}$$

$$\sigma(L) = i\omega z_2 (T_2 - R_2) . \tag{4.33}$$

Using equations (4.14) and (4.15) we have,

$$u(L) = u(0) , \tag{4.34}$$

$$\sigma(L) = \sigma(0) , \tag{4.35}$$

When the frequency of the excitation is equal to that of an even mode of the layer, then the relationship between stresses and displacements on both sides of the layer is independent of value of T_2 and R_2 and given by equations (4.34) and (4.35). Following the same steps as shown in equations (4.28), (4.29), and (4.30), we arrive at the same value of reflection coefficient as for the case of the odd-numbered mode frequency, given by eqn (4.31).

No layer between the half-spaces

If the layer between the half-spaces was removed, then we could link the stresses and displacements in medium 1 to those of medium 3 directly. This is exactly what is stated in equations (4.34) and (4.35). Therefore the value of reflection coefficient expressed in eqn (4.31) is also valid for the case of two semi-infinite media without the presence of the layer. Therefore, we can state that when the frequency equals the resonant frequency of the layer, the layer becomes entirely transparent to the acoustic waves, and the reflection coefficient is entirely defined by the impedances of the materials on both sides of the layer. This statement is only valid for a perfectly elastic layer, that is when $\alpha_2 = c_2$.

4.2.3 Reflection coefficient at the frequency halfway between two consecutive resonant frequencies of the layer

Another interesting case occurs when the frequency of excitation is halfway between two consecutive resonant frequencies of the layer. Let us investigate this case in more detail.

Using eqn (4.22) the frequency halfway between the mth and $m+1^{th}$ resonant frequency o the layer can be expressed as,

$$\omega_{half} = \frac{\pi c_2}{L} \left(m + \frac{1}{2} \right) .$$ (4.36)

When m is even then, using eqn (4.23), the exponential term of eqn (4.18) becomes,

$$g_p = i , \quad \text{and} \quad g_p^{-1} = -i .$$ (4.37)

Substituting eqn (4.37) into equations (4.16) and (4.17), we have,

$$u(L) = i (T_2 - R_2) ,$$ (4.38)

$$\sigma(L) = - \omega z_2 (T_2 + R_2) .$$ (4.39)

Using equations (4.14) and (4.15) we can relate the stress and displacement fields on both sides of the layer as,

$$u(L) = \frac{\sigma(0)}{\omega z_2} ,$$ (4.40)

$$\sigma(L) = - \omega z_2 u(0) .$$ (4.41)

Again, we have obtained the relationship between the stresses and displacements on both sides of the boundary as functions independent of the amplitudes of the waves within the layer. We can use this relationship to link the incident, reflected and transmitted waves to calculate the reflection coefficient at the frequencies $\omega = \omega_{half}$. Using equations (4.40), (4.41), and (4.8), (4.9), (4.19), (4.20), we therefore have,

$$T_3 \gamma = \frac{i z_1 (T_1 - R_1)}{z_2} ,$$ (4.42)

$$i z_3 T_3 \gamma = - z_2 (T_1 + R_1) .$$ (4.43)

Substituting eqn (4.42) into (4.43), we have,

Material properties of the aluminium oxide
were taken from Krauträmer and Krautkrämer
(1983).

Krautkrämer J. and Krautkrämer H (1983),
"Ultrasonic Testing of Materials",
Springer- Verlag, Berlin, Heidelberg, New York)

$$\frac{z_1}{z_2}(T_1 - R_1) = \frac{z_2}{z_3}(T_1 + R_1), \tag{4.44}$$

and after setting $T_1 = 1$, and simple algebra, we obtain the following expression for the reflection coefficient at the frequency $\omega = \omega_{half}$,

$$R_{half} = \frac{z_1 z_3 - z_2^2}{z_1 z_3 + z_2^2}. \tag{4.45}$$

It can be easily shown that eqn (4.45) holds also in the case when the index m in eqn (4.36) is odd, following the steps shown in equations (4.37)-(4.44).

Equation (4.45) gives us a very simple expression for the value of the reflection coefficient for the frequencies halfway between the resonant frequencies of the layer. It can be easily shown that eqn (4.45) holds for all frequencies halfway between the resonant frequencies of the layer.

4.2.4 Examples

Equations (4.22), (4.31), and (4.36), (4.45), can be very useful in predictions of the normal incidence reflectivity from layers separating two half-spaces because they are simple to use. Let us then apply these equations to some simple cases. We will calculate the normal incidence longitudinal reflection coefficient from a 100 μm thick aluminium oxide layer between half-spaces of various mechanical properties. The material properties used in the calculations are shown in table 4.1, and they are similar to those used in chapter 7, where the ultrasonic reflectivity from aluminium/epoxy joints are discussed in more detail (see tables 7.1 and 7.2).

material	density ρ (kg/m^3)	longitudinal velocity c_L (m/s)	longitudinal impedance z_L (kg/m^{2}s)
aluminium	2820	6330	17.85 E6
aluminium oxide (70 %porosity)	1170	10400	12.17 E6
epoxy resin	1170	2610	3.05 E6
water	1000	1490	1.49 E6

Table 4.1 Acoustic properties of materials used in calculations.

Using eqn (4.22) and the values in table 4.1 we can calculate the first resonant frequency for the 100 μm thick oxide layer, f_{res} = 52.0 MHz. Figure 4.2 shows the amplitudes of the normal incidence longitudinal reflection coefficients (R_{LL}) for two different systems. Curve 1 has been computed for a water/100 μm thick oxide/water system, while curve 2 has been calculated for a water/100 μm thick oxide/ epoxy system. As can be seen from the figure, at the resonant frequencies of the layer (0.0 MHz, 52.0 MHz, and 104.0 MHz) the R_{LL} coefficient reaches local minima, the value of which can be calculated from eqn (4.31). Halfway between the resonant frequencies of the layer (26.0 MHz, and 78.0 MHz) the curves attain shallow maxima. The amplitudes of R_{LL} can be computed at those frequencies using eqn (4.45). The first two rows of table 4.2 show the results of calculations using equations (4.31) and (4.45).

system	z_1 (kg/m^{2}s)	z_2 (kg/m^{2}s)	z_3 (kg/m^{2}s)	R_{res} (eqn 4.31)	R_{half} (eqn 4.45)
water/ oxide/ water	1.49 E6	12.17 E6	1.49 E6	0.0	- 0.970
water/ oxide/ epoxy	1.49 E6	12.17 E6	3.05 E6	- 0.344	- 0.940
aluminium/ oxide/ epoxy	17.85 E6	12.17 E6	3.05 E6	0.708	- 0.462
aluminium/ oxide/ water	17.85 E6	12.17 E6	1.49 E6	0.846	- 0.696

Table 4.2 Amplitudes of R_{LL} coefficient at f_{res} frequency and f_{half} frequency.

When the impedances of the two half-spaces are equal (ie $z_1 = z_3$) then, by eqn (4.31), the reflection coefficient at the resonance frequencies of the layer is null. This indeed is the case for the water/oxide/water system (see fig. 4.2). At 0.0 MHz, 52.0 MHz, and 104.0 MHz the R_{LL} coefficient decreases sharply to zero. For frequencies in between the resonant ones, the R_{LL} curve is close to unity. From table 4.2 it can be seen that the impedance of the layer is much higher than that of water ($z_1 = z_3$, $z_1 << z_2$), and using eqn (4.45) one can clearly see that the R_{half} will be dominated by the impedance of the layer, which results in the amplitude being close to unity. Exactly the same behaviour of the reflection coefficient can be observed in fig. 3.4, which was computed for the water/aluminium plate/water system.

Curve 2 of fig. 4.2 has been computed for a system consisting of water/100 μm thick oxide/epoxy. The resonant minima appear at exactly the same frequencies as for the curve 1, but are much shallower here than those of the curve 1, and they reach the value of 0.344, which

is the reflection coefficient of the water/epoxy system. The maximum values of the reflection coefficient can be found at frequencies equal to f_{half}, where the amplitude of R_{LL} is 0.940. From fig. 4.2 and table 4.2 it can clearly be seen that the amplitude variation of R_{LL} coefficient for the water/oxide/epoxy system is about half of that of the reflection coefficient of the water/oxide/water system.

Let us look at another example of the normal incidence reflectivity from the 100 μm thick oxide layer. Figure 4.3 shows R_{LL} coefficients for two different systems: curve 1 for an aluminium/ 100 μm thick oxide/water system, and curve 2 for an aluminium/100 μm thick oxide/epoxy system. The calculations for the R_{LL} coefficient at f_{res} and f_{half} for these two systems occupy the last two rows in table 4.2. From the table 4.2 it can be seen that the reflection coefficients do not always attain minima at the resonant frequencies of the layer.

The two examples presented in figures 4.2 and 4.3 show that the normal incidence reflectivity from layers varies substantially from one case to another and depends not only on the property of the layer itself but also on the impedances of the media on both sides of the layer. Let us therefore investigate the conditions governing the behaviour of the reflection coefficient curves.

Let us assume for the time being that the impedance of medium 1 is bigger than that of medium 3, that is, $z_3 < z_1$. From eqn (4.31) it can be seen that in such circumstances R_{res} is positive. This is, for example, the case when the aluminium/layer/epoxy system is considered (see table 4.2). The impedance of the intermediate layer z_2 can have, in general, any positive value. Let us identify different cases z_2 can satisfy.

Case 1 $z_3 < z_1 < z_2$, then $R_{res} < - R_{half}$

When the impedance of the layer in bigger than the impedances of both half-spaces, then , using eqn (4.31) and (4.45), one can show that $R_{res} < - R_{half}$, or in other words, the amplitude of the reflection coefficient reaches minima at the resonant frequencies of the layer (including zero frequency), and attains maxima at the frequencies exactly halfway between the resonant frequencies.

Case 2 $z_3 < z_1 = z_2$, then $R_{res} = - R_{half}$

When the impedance of the layer is equal to the larger impedance of the two half-spaces, then it is easy to show that $R_{res} = - R_{half}$. In such a case the amplitude of the reflection coefficient becomes a straight horizontal line.

Case 3 $z_3 < z_2 < z_1$, and $z_1 z_3 < z_2^2$, then $-R_{half} < R_{res}$

When the impedance of the layer is between the impedances of the half-spaces, then
$-R_{half} < R_{res}$, which means that the amplitude of the reflection coefficient reaches maxima at the resonant frequencies of the layer (including zero frequency), and attains minima at the frequencies exactly halfway between the resonant frequencies.

Case 4 $z_3 < z_2 < z_1$, and $z_1 z_3 = z_2^2$, then $R_{half} = 0$

When the impedance of the layer is between the impedances of the half-spaces, then there is a special case when $z_1 z_3 = z_2^2$. Looking at eqn (4.45) one can see that $R_{half} = 0$. In such a case the minima, which occur between the resonant frequencies of the layer, touch the zero line. The maximum values are found at the resonant frequencies (including zero frequency).

Case 5 $z_3 < z_2 < z_1$, and $z_2^2 < z_1 z_3$, then $R_{half} < R_{res}$

This is a similar case to that of No 3, but R_{half} changes its sign and becomes positive. Here the amplitude of the reflection coefficient has maxima at the resonant frequencies of the layer (including zero frequency), and reaches minima at the frequencies exactly halfway between the resonant frequencies.

Case 6 $z_2 = z_3 < z_1$, then $R_{res} = R_{half}$

This case is similar to that of No 2, but R_{half} is positive rather than negative. When the impedance of the layer is equal to the smaller impedance of the two half-spaces, then the reflection coefficient is frequency independent and equal to that of the two half-spaces without an intermediate layer.

Case 7 $z_2 < z_3 < z_1$, then $R_{half} < R_{res}$

When the impedance of the layer is smaller than the impedances of both half-spaces, then the amplitude of the reflection coefficient reaches minima at the resonant frequencies of the layer (including zero frequency), and attains maxima at the frequencies exactly halfway between the resonant frequencies. This case is similar to that of No 1, but here R_{half} is positive.

Let us illustrate all the cases above with a simple example. The system we will use for the parametric study is the aluminium/100 μm thick layer/epoxy resin system, the mechanical properties of the half-spaces being the same as those listed in table 4.1, therefore the longitudinal impedances of the half-spaces are, $z_1 = 3.05$ E6 kg/m^2s, and $z_3 = 17.85$ E6 kg/m^2s. The mechanical properties of the layer are based around those of the 70 % porous

aluminium oxide, whose properties are given in table 4.1. The longitudinal phase velocity of the layer is kept constant to maintain the resonant frequencies at the same position for all cases. In order to vary the impedance of the layer, we have chosen to alter its density to suit our purposes. Table 4.3 shows variation of the density of the layer, its longitudinal impedance and the resulting amplitude of the longitudinal reflection coefficient. The density of the layer was chosen so that the impedance of the layer falls into the seven cases discussed above, case numbers in the table corresponding to those above.

case number	ρ (kg/m^3)	c_L (kg/m^2s)	z_L (kg/m^2s)	R_{res} (eqn 4.31)	R_{half} (eqn 4.45)
1	200	10400	2.08 E6	0.708	0.853
2	293	10400	3.05 E6	0.708	0.708
3	480	10400	4.99 E6	0.708	0.373
4	709	10400	7.37 E6	0.708	0.00
5	1000	10400	10.40 E6	0.708	- 0.330
6	1716	10400	17.85 E6	0.708	- 0.708
7	3000	10400	31.20 E6	0.708	- 0.898

Table 4.3 Amplitudes of R_{LL} coefficient at f_{res} frequency and f_{half} frequency for different impedances of the layer between aluminium and epoxy half-spaces. Thickness of the layer is 100 μm.

Figures 4.4(a) and 4.4(b) show the reflection coefficient curves corresponding to the seven cases of table 4.3. It can clearly be seen from the figures that all the curves start at zero frequency with an amplitude of 0.708. This is the amplitude of the reflection coefficient at the frequencies corresponding to the resonant frequencies of the layer in vacuum, denoted as f_{res}. All the curves meet again at a frequency of 52.0 MHz, the first resonant frequency of the layer, then at 104.0 MHz, the second resonant frequency, and so on. The biggest difference in amplitude between the cases can be seen at the frequencies exactly between the resonant frequencies, denoted as f_{half}. From figures 4.4(a) and 4.4(b) it can clearly be seen that if the amplitudes of the reflection coefficient at frequencies f_{res} and f_{half} is known then the shape of the reflection coefficient curves can be quickly and conveniently predicted. The formulae to calculate these values are given in equations (4.22), (4.31), (4.36) and (4.45).

4.3 The reflection coefficient from thin liquid layers

This section is concerned with ultrasonic reflectivity from thin liquid layers between two solid half-spaces. This case is very important in our investigations because liquid can be considered as a limiting case of a very heavily deteriorated interface between epoxy and aluminium. In such cases it is usually assumed that the normal stiffness across the interface only changes slightly while the reduction in shear stiffness across the boundary is significant (see Rokhlin and Marom 1986, Rokhlin *et al.* 1990). This means that the deteriorated interface, which from the geometrical point of view can be modelled as a thin layer, changes its mechanical properties from those of a solid to those of a viscous liquid. Let us therefore study the reflection coefficient from the solid/thin liquid layer/solid system in more detail.

In our investigations we would like to answer two important questions. The first one is the problem of the detectability of a very thin layer between two solids. Here we will be concerned with the possibility of mere detection of a layer with given mechanical properties. The second question is the problem of the evaluation of a thin layer. Once the layer can be detected it is sometimes important to find its material properties and thickness.

4.3.1 Liquid layer between two glass half-spaces

As a first example let us consider a thin silicone fluid layer between two glass half-spaces (see fig. 4.5). Experimental investigations of the ultrasonic reflectivity from such a system is presented in chapter 5 of this thesis. Material properties of the glass and the silicone fluid are given in table 4.4.

material	density (kg/m3)	longitudinal velocity (m/s)	longitudinal attenuation (nepers)	shear velocity (m/s)	shear attenuation (nepers)
epoxy resin	1170	2610	0.0	1100	0.0
glass	2490	5808	0.0	3466	0.0
silicone fluid	985	1050	0.0	80.0	6.28
water	1000	1490	0.0	10.0	6.28

Table 4.4 Assumed properties of materials used in calculations.

Values of density and velocities shown in the table are typical for these two different materials.

Attenuation in glass and epoxy has been assumed to be negligible and the shear velocity and attenuation in the silicone fluid were calculated from the Navier-Stokes equation for a fluid of viscosity of 50 centistokes as shown in Appendix B It can be shown that in a liquid satisfying the Navier-Stokes equation, the shear waves attenuation is 2π nepers per wavelength for any frequency.

Figure 4.6 shows a parametric study of the longitudinal-longitudinal reflection coefficient (R_{LL}) from a thin silicone layer separating two semi-infinite glass half-spaces. The thickness of the silicone layer varies from 1.0 μm to 0.0 μm in 0.2 μm steps. As can be seen from the plot, the sensitivity of the R_{LL} reflection coefficient to the layer thickness is very good. For null thickness of the layer, the silicone interface ceases to exist. In such a case waves in the system propagate without any obstacles and the reflection coefficient is zero regardless of the frequency of the incident wave. When the layer is of a finite thickness then the amplitude of the R_{LL} reflection coefficient starts from a null value at zero frequency and monotonically increases with frequency up to 50 MHz. The thicker the layer the bigger the amplitude of the reflection coefficient. It is easy to resolve between thicknesses 0.1 μm apart.

As in all the plots presented in this chapter, the frequency-thickness scaling theorem can be applied here (see Appendix C). Using this theorem it is possible to generate all the curves for thicknesses of 0.8 μm and below from the curve for 1.0 μm by 'stretching' the frequency axis so that the frequency - layer thickness product remains the same. For example (see fig. 4.6) the reflection coefficient curve for the thickness of 0.6 μm can be generated from 1.0 μm curve by expanding the 0-30 MHz interval 10/6 times to obtain a 0-50 MHz range so that the point A will be mapped onto the point B.

Table 4.5 shows the sensitivity of the reflection coefficient to the silicone layer thickness. All the values in the table were obtained from the corresponding curves of fig. 4.6. As can be seen from the table, the sensitivity is excellent. In practice, it means that it is possible to detect the presence of extremely thin liquid layers and in many cases it is even possible to determine their thickness (if the material properties of the liquid are known).

thickness	1.0 μm	0.8 μm	0.6 μm	0.4 μm	0.2 μm	0.0 μm
R_{LL} at 25 MHz	0.720	0.639	0.529	0.384	0.204	0.0
change wrt 1.0 μm	0 %	11 %	27 %	47 %	72 %	100 %

Table 4.5 R_{LL} reflection coefficient sensitivity to the silicone layer thickness between two glass half-spaces at the frequency of 25 MHz.

Figures 4.7(a) and 4.7(b) show the theoretically predicted pulse response from a system comprising two 3.0 mm thick glass plates separated by silicone fluid layer of 0.5 μm thickness (fig. 4.7(a)) and zero thickness (fig. 4.7(b)). The pulse shape used as an input for the predictions is the same one we used for the time domain predictions of chapter 3 (see for example figures 3.6, 3.9 and 3.17), and corresponds to the pulse generated by a typical 10 MHz wideband transducer. In fig. 4.7(a) the reflection from the front face of the glass plate is marked as FF, while the reflection coming from the 0.5 μm thick silicone layer is marked as LL. The third pulse coming after FF and LL is the superposition of the pulse coming from the back face of the back glass sheet and reverberation within the front glass plate. Despite a very large wavelength-to-layer thickness ratio (more than 1000 here), the reflection from the silicone can be easily detected and analysed. The pulse shape of the reflection from the silicone layer (LL) is different from the front face reflection (FF). This is because the reflection coefficient from the layer is heavily frequency dependent (see fig. 4.6). When the thickness of the silicone layer is zero (see fig. 4.7(b)) then there is no LL reflection at all.

If a shear wave is used instead of the longitudinal wave then it is theoretically possible to detect presence of extremely thin layers (far too thin to exist in reality because of irregularities of the mating surfaces). Figure 4.8 shows the shear-shear reflection coefficient (R_{SS}) from a thin silicone layer separating two semi-infinite glass half-spaces. The thickness of the silicone layer varies from 1.0 μm to 5.0 nm. From the plot it can be seen that even a 5 nm thick silicone layer strongly reflects ultrasound for frequencies as low as 5 MHz. This extraordinary behaviour can be explained by looking at table 4.4. The shear velocity of the silicone is very low which means that the tangential stiffness of the liquid is also very low. Therefore, even for extremely thin layers the shear stiffness is too low to support any significant tangential stress at the glass/silicone boundary. In such circumstances, the interfacial conditions are close to the free boundary conditions for which the reflection coefficient is unity. The layer stiffness has to be dependent on the thickness of the layer; the thicker the layer the lower the tangential stiffness of the layer. From fig. 4.8 it can be seen that for larger values of the layer thickness (see for example the curve for 1.0 μm) the reflection coefficient is close to unity.

4.3.2   Liquid layer between glass and epoxy half-spaces

So far we have analysed the reflectivity from a thin liquid layer separating two half-spaces of the same material and we found that the detectability of such a layer is very good. Using a longitudinal wave at normal incidence it was possible to resolve layer thicknesses to within 0.1 μm. However, this is not the case when the thin layer separates two dissimilar materials. Even when there is no thin layer at all in such a system, the reflection coefficient can be still of

significant amplitude. The presence of the thin layer in such cases will modify the reflectivity at the interface only slightly. Let us use a simple example to illustrate the problem.

Normal incidence reflection coefficients

Figure 4.9 shows the normal incidence longitudinal-longitudinal (R_{LL}) reflection coefficient from a 1.0 μm thick silicone layer between two glass half-spaces and from a 1.0 μm thick silicone layer separating glass and epoxy half-spaces. The R_{LL} reflection coefficient was computed in the frequency range between 0 and 1.75 GHz, which is an order of magnitude higher than the practical testing range. The glass/silicone/glass R_{LL} curve for the practical testing frequency range was shown in fig. 4.6. Curve A of fig. 4.9 is actually a zoomed-out version of the 1.0 μm curve of fig. 4.6. As can be seen from fig. 4.9, the curve A starts from null at zero frequency and rapidly increases over the first 100 MHz to attain values close to unity at around 250 MHz. Then above 250 MHz the curve rapidly dives down to reach zero at around 500 MHz which is the first resonant frequency of the silicone layer. The curve then repeats itself over the next 500 MHz to reach the second resonance of the layer at around 1 GHz, and so on. Curve A is a typical reflection coefficient curve from a layer separating two identical materials. Indeed, exactly the same features can be seen looking at the R_{LL} curve of fig. 3.4, computed for an aluminium layer separating water half-spaces, or fig. 4.2 (curve 1), calculated for the water/aluminium oxide/water system.

However, if there are dissimilar materials on the opposite faces of the thin layer then, by eqn (4.31), the reflection coefficient curves no longer start sharply from zero at low frequencies. Curve B of fig. 4.9 shows the R_{LL} reflection coefficient for exactly the same layer as of the curve A but between glass and epoxy resin. Because the materials are dissimilar, the R_{LL} amplitude at zero frequency is 0.651, which is the reflection coefficient between glass and epoxy without any layer in-between. At low frequencies the B curve is still an increasing function of frequency but the increase is much slower that that of curve A. The resonant frequency minima are also much shallower than those of curve A. This results in a significant decrease in the sensitivity of the R_{LL} coefficient to the presence of thin layers. Figure 4.10 and table 4.6 show a parametric study of the R_{LL} reflectivity from thin silicone fluid layers of different thicknesses. As can be seen from the graph, the sensitivity of R_{LL} reflection coefficient to the layer thickness is rather low. Without the presence of the thin layer the R_{LL} coefficient is frequency independent and equal 0.651. When the silicone layer is present, then the longitudinal-longitudinal reflectivity across the glass/epoxy interface increases slightly, but only by a few percent.

Theoretical predictions of the reflection coefficient from thin layers

thickness	1.0 μm	0.8 μm	0.6 μm	0.4 μm	0.2 μm	0.0 μm
R_{LL} at 25 MHz	0.696	0.681	.669	0.659	0.653	0.651
change wrt 1.0 μm	0 %	2 %	4 %	5 %	6 %	6 %

Table 4.6 R_{LL} normal incidence reflection coefficient from silicone layers of different thicknesses between glass and epoxy resin. Frequency 25 MHz.

The curves of fig. 4.10 can be directly compared to the curves of fig. 4.6, and table 4.6 to table 4.5.

Using the theory developed in chapter 2 it is possible to generate the time domain pulse response of the glass plate/silicone layer/epoxy resin plate system in water. Figure 4.11(a) shows the theoretically predicted time domain response of a 3.0 mm thick glass plate/3.0 mm thick epoxy resin system in water being excited by a pulse from a typical 10 MHz transducer. FF is the front face reflection from the glass plate and LL_1 is the reflection coming from the glass/epoxy interface. The third pulse, LL_2, seen in the figure is the second reverberation of the longitudinal wave within the glass plate. It is the LL_1 reflection which will have to be monitored in order to detect presence of thin layers between glass and epoxy. Figure 4.11(b) shows what happens when a 0.5 μm thick silicone layer is present at the interface. The amplitude and shape of the LL_1 reflection of fig. 4.11(b) are practically the same as those of fig. 4.11(a). It is therefore practically impossible to detect the presence of the 0.5 μm thick liquid layer between the glass and epoxy resin using a 10 MHz transducer at normal incidence. Some noticeable change can be seen when the thickness of the silicone layer is increased. Figure 4.11(c) shows the time domain response of the system with a 5.0 μm thick layer, that is 10 times thicker than that of fig. 4.11(b). Here it can be seen that LL_1 reflection is 20 % bigger than those of fig. 4.11(a) and 4.11(b).

The frequency domain and the time domain study presented here show clearly that if thin liquid layers are entrapped between two different materials then it is not always possible to detect their presence using the normal incidence longitudinal-longitudinal reflection coefficient method. This was not the case when analysing normal incidence R_{LL} reflectivity from a thin layer having the same material on both sides (glass/silicone/glass system).

Let us now investigate the use of the shear-shear (R_{SS}) normal incidence reflection coefficient for the case of dissimilar materials across the interface. Figure 4.12 shows a parametric study of the glass/silicone layer/epoxy resin system with silicone layers of different thickness. When there is no silicone layer present then the R_{SS} reflection coefficient is frequency independent

and assumes a constant value of 0.740. When the silicone layer is present then at zero frequency the layer is not 'visible' to the shear wave, and R_{SS} is 0.740. This can be shown in a more rigourous manner as follows. When the frequency is zero then the frequency - layer thickness product is zero. Exactly the same value of frequency - layer thickness product can be obtained when the layer thickness is zero, that is, when there is no layer present. Because the frequency - thickness is invariant in the wave equation (see Appendix C), then at zero frequency, the reflection coefficient has to be the same as for the layer of zero thickness. Frequency - thickness invariance also means that for a layer of zero thickness, R_{SS} has to be constant with frequency.

At zero frequency (see fig. 4.12) the Rss coefficient is 0.740 for all layer thicknesses and is equal to the glass/epoxy resin R_{SS} reflection coefficient. Then, for higher frequencies, the presence of the fluid layer becomes visible. Because of the very heavy damping of shear waves in the fluid, the thin layer effectively decouples the glass from the epoxy at higher frequencies. In such cases, the R_{SS} coefficient is solely a function of the interfacial conditions on the incident side of the fluid layer, that is, R_{SS} increases monotonically to reach the value of the glass/silicone fluid reflection coefficient, which is close to unity.

It can be seen from fig. 4.12 that the normal incidence R_{SS} coefficient is much more sensitive than the normal incidence R_{LL} coefficient (see fig. 4.10), and can therefore be used to detect the presence of thin fluid layers. The higher the frequency used, the better the sensitivity of the method. However, because of inconsistent coupling between shear wave probes and plates, quantiative measurements of the normal incidence R_{SS} reflection coefficients are very cumbersome in practice. Therefore, the normal incidence R_{SS} method for determination of the fluid thickness can only be used in a very carefully conducted experiment, provided that the shear wave velocity and damping in the fluid is known.

Oblique incidence reflection coefficients

From the investigations conducted so far it clearly appears that there is no straightforward means of detection and quantitative measurement of the properties of thin liquid layers between two dissimilar materials. It is therefore necessary to investigate the sensitivity of the reflection coefficient techniques at different angles of incidence.

Since there are two different types of bulk waves in solids then, in general, there are four different types of reflection coefficients to compute:

R_{LL} - longitudinal wave incident and longitudinal wave reflected,

R_{LS} - longitudinal wave incident and shear wave reflected,

R_{SL} - shear wave incident and longitudinal wave reflected,

R_{SS} - shear wave incident and shear wave reflected.

These four reflection coefficients are functions of frequency and angle of incidence of the incident wave (longitudinal for R_{LL} and R_{LS}, and shear for R_{SL} and R_{SS}).

Figures 4.13 - 4.16 show a parametric study of the set of all four reflection coefficients at a glass/epoxy resin interface with silicone fluid of different thicknesses present. In fig. 4.13 the amplitude of the R_{LL} coefficient is shown. The frequency of the incident longitudinal wave is kept constant here at 10 MHz, and the angle of incidence varies from 0 to 90 degrees. At normal incidence (0 degrees) there is virtually no difference between all five cases computed. This is in agreement with the previous findings presented in fig. 4.10. However, fig. 4.13 shows that the sensitivity of the R_{LL} coefficient increases significantly with the angle of incidence, and at the angle of 52.0 degrees it is rather easy to determine the presence of the silicone layer, even when it is very thin. Indeed, when the liquid layer is not present at the interface, the R_{LL} coefficient is zero at around 52 degrees and the presence of even a very thin layer 'pushes' the amplitude of R_{LL} upwards making it possible to detect. Similar features can be seen in fig. 4.14, where the parametric study of R_{SS} reflection coefficient was carried out. Here the best angle of incidence is at around 28.4 degrees. The R_{SS} coefficient is zero for zero thickness of the silicone layer, and relatively large even for a thickness of 0.05 μm. At normal angle of incidence, the R_{SS} coefficient also shows very good sensitivity to the thickness of the silicone layer. This is not the case with the longitudinal-longitudinal reflection coefficient (see fig. 4.13).

In fig. 4.15 parametric study of R_{LS} reflectivity is presented. The most sensitive angular region is between 40 and 60 degrees. The difference between R_{LS} reflectivity with and without the silicone layer is of the order of 10 percent.

Figure 4.16 shows the shear-longitudinal (R_{SL}) reflection coefficients for the same silicone layer thicknesses as in figures 4.13 - 4.15. Here, all the curves are close to each other everywhere in the angular domain which means that the R_{SL} sensitivity to the presence of the liquid layer is very small.

Figures 4.13 - 4.16 show clearly that for certain angles and certain types of reflection coefficient we may expect a significant improvement in sensitivity over the normal incidence technique. It is therefore of practical interest to be able to generate oblique incidence waves at particular angles within a specimen and to be able to receive them for further signal processing.

Figure 4.17 shows schematically how oblique incidence longitudinal waves can be generated

within a glass/silicone layer/epoxy plate in water. The angle of incidence of the longitudinal wave in water is adjusted to be 11.7 degrees, so that the transmitted longitudinal wave in glass hits the silicone layer at 52.0 degrees. This is the angle of incidence where the biggest sensitivity of R_{LL} reflection coefficient is expected. (see fig. 4.13). In fig. 4.17, FF is the reflection from the front face of the glass plate. The amplitude of this reflection is a function of the material properties of glass and water and does not tell us anything about the glass/epoxy interface. The further three reflections: SS, LS+SL, and LL, come from the glass/epoxy interface and are influenced by the presence of the silicone layer. If the thickness of the glass plate is known then it is possible to calculate times of arrival of these reflections, since the angles of refraction in glass can be obtained from Snell's law. Let us assume that the thickness of the glass plate is 3.0 mm. Table 4.7 shows angles of refraction and times of arrivals of the SS, LS+SL, and LL reflections for the case when the longitudinal wave is incident from water at 11.7 degrees. Despite the longer distance travelled within the plate, the LL reflection arrives first, because the longitudinal wave velocity is much greater than that of the shear wave. The LS and SL reflections arrive exactly at the same time because each of them travel one half of the way as the longitudinal wave and the other half as the shear wave. The SS reflection comes last because the shear wave is considerably slower than the longitudinal wave.

Type of reflection	Angle of incidence at glass/epoxy (degrees)	Time of arrival wrt FF (μs)
LL	longitudinal: 52.0	0.64
LS+SL	longitudinal: 52.0 shear: 28.0	1.08
SS	shear: 28.0	1.53

Table 4.7   Angles of refraction in glass and times of arrival for different reflections coming from glass/epoxy interface for the longitudinal wave incident at 11.7 degrees in water. Thickness of glass plate is 3.0 mm. See also fig. 4.17.

Figure 4.18(a) shows the time domain response of a 3.0 mm thick glass plate/3.0 mm thick epoxy resin system in water to an infinite plane wave pulse excitation. The shape and duration of the pulse is typical for a wideband 10 MHz transducer. The angle of incidence from water is 11.7 degrees. FF is the front face reflection from the glass plate, and $(LS+SL)_1$ is the first combined longitudinal-shear and shear-longitudinal reflection from the glass/epoxy interface, and arrives 1.08 μs after the FF reflection. The subscript here denotes the reflection number of a given wave type in the plate. The second reverberation of the LS+SL type arrives 2.16 μs after FF and is denoted as $(LS+SL)_2$. The first reflection of the SS type arrives 1.53 μs after FF, and therefore appears between $(LS+SL)_1$ and $(LS+SL)_2$. The LL_1 reflection, with delay

time of 0.64 μs, should be found between FF and $(LS+SL)_1$. However, LL_1 is not present in fig. 4.18(a) because the R_{LL} reflection coefficient is zero in this case.

When a 0.5 μm thick silicone layer is present then, according to the R_{LL} reflection coefficient predictions of fig. 4.13, we should expect an LL_1 reflection to be present. This is indeed the case. Figure 4.18(b) shows the time domain pulse response of the 3.0 mm thick glass/0.5 μm thick silicone layer/3.0 mm thick epoxy resin system in water. The LL_1 reflection is clearly visible here, and its time of arrival is in agreement with the calculations shown in table 4.7.

Figures 4.18(a) and 4.18(b) have been calculated for exactly the same system as those of figures 4.11(a) and 4.11(b). Comparison of the plots clearly shows that oblique incidence can significantly improve the sensitivity of the reflection coefficient method for detection of thin liquid layers.

4.4 The reflection coefficient from thin solid layers

One of the most significant differences between solids and liquids is that solids can sustain large shear stresses while liquids cannot. The only mechanism through which liquids can support shear stresses is viscosity. The higher the viscosity of the liquid, the larger the shear stresses which can be produced for the same displacements and frequency. In ideal liquids, therefore, shear stresses cannot exist. Another important feature of real (viscous) fluids is that the same mechanism which supports the shear wave propagation is also responsible for the attenuation of the shear waves. It is easy to show that in a liquid satisfying the Navier-Stokes equation, the shear wave attenuation is 2π nepers per wavelength, and is frequency independent and the same for all liquids. Therefore, even thin layers of liquids have very low shear stiffness and heavy attenuation of shear stresses.

Solid materials, however, can support shear stresses in a similar manner as they support longitudinal stresses, that is, by reacting elastically to deformations imposed on them. Therefore, viscosity is not the main mechanism for supporting shear wave propagation here. The Poisson's ratio determines the shear stiffness of materials. Viscosity is responsible for attenuation of shear waves and affects their velocity only by a small amount.

Let us calculate reflection coefficients at an aluminium/epoxy interface in an adhesive joint. At first sight, such a case should not pose any theoretical complications as it involves only two semi-infinite half-spaces. In real adhesive joints, however, aluminium surfaces are electro-chemically treated prior to bonding in order to form thin oxide layers. The epoxy resin is

therefore in contact with an oxide layer rather than aluminium. Therefore, in order to model the aluminium/epoxy interface, a thin oxide layer has to be introduced between relatively thick aluminium and epoxy layers. These can be considered in our model as semi-infinite half-spaces.

Normal incidence reflection coefficients

Let us first calculate the normal incidence longitudinal reflection coefficient from a thin oxide layer between aluminium and epoxy. In table 4.8 the acoustic properties of the different materials used for calculations are shown.

material	density (kg/m^3)	longitudinal velocity (m/s)	longitudinal attenuation (nepers)	shear velocity (m/s)	shear attenuation (nepers)
aluminium	2820	6330	0.0	3120	0.0
aluminium oxide	3896	10400	0.0	6490	0.0
epoxy resin	1170	2610	0.0	1100	0.0

Table 4.8 Acoustic properties of materials used in reflection coefficients calculations.

Taking the values of velocities and densities from table 4.8, we obtain the longitudinal impedances of aluminium and epoxy, z_{Al} = 17.85 E6 kg/m^{2}s, and z_{epoxy} = 3.05 E6 kg/m^{2}s. Properties of the aluminium oxide layer, listed in table 4.8, are correct for the material without any porosity (Wang and Rokhlin 1990). In reality, however, oxide has a porous structure and therefore its mass will drop accordingly. Let us assume that the longitudinal velocities in oxides are independent of porosity. Some justification of this is given in section 7.2.2 of this thesis, where the problem of the theoretical modelling of oxides layers is discussed in more detail. Table 4.9 shows how the density and longitudinal impedance of the oxide layer changes with porosity, and fig. 4.19 shows the normal incidence longitudinal reflection coefficients for 50 μm thick oxide layers with different percentages of porosity.

As can be seen from fig. 4.19, there is a significant variation of R_{LL} reflectivity due to different densities of the oxide. According to eqn (4.31), all the curves, however, have the same value of 0.708 at frequencies of 0.0 MHz, and at 104.0 MHz, which is the first resonant frequency of the layer.

Theoretical predictions of the reflection coefficient from thin layers

porosity of aluminium oxide (%)	density ρ (kg/m^3)	longitudinal velocity c_L (m/s)	longitudinal impedance z_L (kg/m^{2}s)	resonant frequency f_{res} (MHz)	R_{LL} amplitude at f_{half}
30	2730	10400	28.39 E6	104.0	0.873
40	2340	10400	24.34 E6	104.0	0.831
50	1950	10400	20.28 E6	104.0	0.766
56	1716	10400	17.85 E6	104.0	0.708
60	1560	10400	16.22 E6	104.0	0.657
70	1170	10400	12.17 E6	104.0	0.462

Table 4.9   Change in reflection coefficient for the aluminium/50 μm thick oxide/epoxy system for different porosity of the oxide. R_{LL} curves shown in fig. 4.19.

At a frequency of 52.0 MHz the difference in the reflectivity is the biggest, and eqn (4.45) can be used to calculate the RLL coefficient here. When the oxide porosity is between 30 % and 50 % then the impedance of the oxide is bigger than those of the aluminium and epoxy half-spaces, that is, $z_{epoxy} < z_{Al} < z_{oxide}$. From eqn (4.45) it can be seen that the larger the oxide impedance here, the more pronounced is the maximum at the frequency of 52.0 MHz. When the porosity of the oxide is 56 %, then $z_{epoxy} < z_{Al} = z_{oxide}$, and the reflection coefficient becomes a straight horizontal line. For porosities of the oxide of 60 % and 70 %, the oxide impedance decreases further and satisfies the conditions $z_{epoxy} < z_{oxide} < z_{Al}$, and $z_{epoxy} z_{Al} < z_{oxide}^2$. In such a case the amplitude at 52.0 MHz becomes a minimum, and the smaller the value of the oxide impedance, the deeper the minimum.

Figure 4.20 shows the normal incidence R_{LL} coefficients for different oxide layer thicknesses. Here, the frequency - thickness scaling theorem is demonstrated again (see Appendix C). The first resonance frequency of the 50 μm thick layer is at 104.0 MHz, while for the 100 μm thick oxide the first natural frequency is 52.0 MHz. For the 75 μm thick layer the frequency of the first resonance is 69.3 MHz which lies between the two previous cases. The porosity of the oxide was chosen to be 70 %, which places the impedance of the layer between those of epoxy and aluminium. Therefore the curves bend downwards for low frequencies. As the impedance of the oxide was kept the same for all three curves, then, according to eqn (4.45), all of them reach the same minimum amplitude at the half the first resonant frequency.

Figure 4.21 shows the third parametric study of the aluminium/oxide/epoxy system. This time we have chosen to vary the longitudinal velocities of the oxide layers, keeping their density and thickness constant, so that the impedance of the layer is between those of epoxy resin and aluminium. In accordance with the findings discussed previously and shown in figures 4.19 and 4.20, we should expect two major effects. Firstly for the higher velocities the resonances move towards higher frequencies to satisfy eqn (4.22), and secondly for higher velocities the impedance of the oxide layer increases and approaches that of the aluminium. Therefore, by eqn (4.45), the minima of the R_{LL} curves should become shallower when velocity is increased. Table 4.10 shows the variation of the longitudinal impedance, the first resonant frequency of the layer, and the minimum value of the R_{LL} coefficient at half the resonant frequency of the oxide.

longitudinal velocity c_L (m/s)	density ρ (kg/m^3)	first resonant frequency f_{res}(MHz)	longitudinal impedance z_L(kg/m^{3}s)	R_{LL} amplitude at f_{half}
8000	1170	80.0	6.84 E6	0.233
10400	1170	104.0	12.17 E6	0.462
12000	1170	120.0	14.04 E6	0.567
13863	1170	138.6	16.22 E6	0.657

Table 4.10   Change in reflection coefficient from the aluminium/50 μm thick oxide/epoxy system for different longitudinal velocities of the oxide. R_{LL} curves shown in fig. 4.21.

With the porosity of the aluminium oxide between 60 % and 70 %, the typical aluminium/oxide/epoxy system satisfies conditions $z_{epoxy} < z_{oxide} < z_{Al}$, $z_{epoxy} z_{Al} < z_{oxide}^2$. Using equations (4.22), (4.31) and (4.54), we can state that

- when the density of the oxide increases then the amplitude of the minimum increases (see fig. 4.19);

- when the thickness of the oxide increases then the frequency of the minimum decreases (see fig. 4.20);

- when the velocity of the oxide increases then the frequency of the minimum increases, and the amplitude of the minimum increases (see fig. 4.21).

Figure 4.22 shows schematically possible movement of the minimum point due to changes in the oxide properties. From fig. 4.22 it can be seen that if the thickness, density or longitudinal

velocity of the oxide layer changes, then it is possible to use the normal incidence R_{LL} coefficient to monitor the changes.

At this stage, it is important to find out how many independent properties of the layer can be measured using normal incidence longitudinal reflection coefficient. In general there are four independent mechanical properties of the layer to be measured: thickness, density, longitudinal velocity and shear velocity. Examining fig. 4.22 we can see that there are two independent features the normal incidence curves possess, namely the frequency and the amplitude of the reflection coefficient at half of the resonant frequency of the layer (see equations (4.36) and (4.45)). (The R_{LL} amplitude at zero frequency is solely governed by the properties of the half-spaces and is independent of the layer properties (see eqn 4.31)). These two features are dependent on three layer properties: density, thickness, and longitudinal velocity. This means that if the thickness of the layer is known then it is possible to extract the density and longitudinal velocity of the layer from one normal incidence longitudinal reflection coefficient measurement. However, if the shear velocity of the layer is to be monitored, then the normal incidence R_{LL} coefficient is not capable of providing any information about it.

Note that the curve shown in fig. 4.22 was generated for a 50 μm thick oxide layer. A typical thickness of the oxide in aluminium/epoxy joints is about 3.5 μm, that is fifteen times thinner. In such circumstances we can expect a significant deterioration in the sensitivity of the reflection coefficient method to changes in the properties of the layer. To illustrate this point, fig. 4.23 shows the normal incidence longitudinal reflection coefficient from a 5.0 μm thick oxide layer in between the aluminium and epoxy resin half-spaces. The properties of the aluminium, the epoxy and of the oxide are given in table 4.11 and are very similar to those shown in table 4.9 which were used to compute the curves of fig. 4.21. Because in fig. 4.23 the layer is 10 times thinner than that of fig. 4.21, the R_{LL} reflection coefficient shows very little sensitivity to a large variation in the longitudinal velocity of the oxide. Indeed, comparing the curves corresponding to the oxide 1 and the oxide 4 in fig. 4.23 it can be seen that at a frequency of 100 MHz, a 30 % change in velocity (from 10400 m/s to 7280 m/s) results in only a 3 % change in R_{LL} coefficient (from 0.696 to 0.674).

If, for some reason, the shear velocity of the layer is to be monitored then the normal incidence R_{LL} coefficient cannot be used for such a purpose. It is useful, therefore to investigate the normal incidence shear wave reflectivity (R_{SS}). Figure 4.24 shows the amplitude of the R_{SS} coefficient from the 5.0 μm thick oxide layer with different shear velocities. For comparison with the longitudinal reflection coefficient, the mechanical properties of the aluminium and the epoxy are the same as those of fig. 4.23, and the oxide shear velocity is altered in the same proportions as the longitudinal velocities in fig. 4.23, as shown in table 4.11.

material	density (kg/m3)	longitudinal velocity (m/s)	shear velocity (m/s)	reduction in velocities wrt oxide 1
aluminium	2820	6330	3120	N/A
epoxy resin	1170	2610	1100	N/A
oxide 1 (70 % porosity)	1170	10400	6500	0 %
oxide 2	1170	9360	5850	10 %
oxide 3	1170	8320	5200	20 %
oxide 4	1170	7280	4550	30 %
oxide 5	1170	5200	3250	50 %

Table 4.11 Mechanical properties of the aluminium/5.0 μm thick oxide/epoxy system used for valuation of the sensitivity of the normal and oblique incidence reflection coefficients.

The R_{SS} curves of fig. 4.24 show some improvement of sensitivity over the corresponding curves of fig. 4.23. For example, comparing curves corresponding to the oxide 1 and the oxide 4, it can be seen that at a frequency of 100 MHz, a 30 % reduction in the shear velocity (from 6500 m/s to 4550 m/s) results in an 8 % change in R_{SS} coefficient (from 0.732 to 0.674). The R_{SS} coefficient therefore shows twice the sensitivity of the R_{LL} coefficient.

Oblique incidence reflection coefficients

Figures 4.23 and 4.24 show clearly that the normal incidence R_{SS} and R_{LL} coefficients are not sensitive enough even to large variations in the material properties of a 5 μm thick oxide in adhesive joints over the range of frequencies up to 100 MHz. It is therefore crucial to investigate whether the oblique incidence reflection coefficients have better sensitivity than the normal incidence techniques.

The system chosen for the parametric studies is the same as that used to compute the normal incidence curves of figures 4.23 and 4.24, and comprises a 5.0 μm thick oxide between the aluminium and epoxy resin half-spaces. The density of the oxide layer is kept constant, but its velocities vary. The initial values of the longitudinal and shear velocities are those of 70 %

porous oxide, then the velocities are reduced in the same proportions with respect to their initial values by 10 %, 20 % and so on. The material properties of the aluminium, epoxy, the 70 % porous oxide, and the modified oxides are given in table 4.11. Figure 4.25 shows variations of the four reflection coefficients, R_{LL}, R_{SS}, R_{LS}, and R_{SL}, to the changes in the oxide layer velocities at a frequency of 50 MHz.

Figure 4.25(a) shows the longitudinal-longitudinal (R_{LL}) reflection coefficient from the oxide layers at a frequency of 50 MHz. It can be seen here that at the normal incidence (0 degrees), the curves corresponding to oxides 1-4 cannot be separated. However, at angles of incidence in the range between 55.0 and 85.0 degrees, the sensitivity increases substantially, and good separation of all the four curves can be seen. Table 4.12 compares the sensitivity of the R_{LL} coefficient at normal incidence (0.0 degrees) and at 65.0 degrees.

angle of incidence	$\|R_{LL}\|$ of curve 1 (% change wrt oxide 1)	$\|R_{LL}\|$ of oxide 2 (% change wrt oxide 1)	$\|R_{LL}\|$ of oxide 3 (% change wrt oxide 1)	$\|R_{LL}\|$ of oxide 4 (% change wrt oxide 1)
0.0 deg	0.705 (0.0 %)	0.704 (- 0.1 %)	0.702 (- 0.4 %)	0.700 (- 0.7 %)
65.0 deg	0.473 (0.0 %)	0.422 (- 10.8 %)	0.381 (- 19.5 %)	0.356 (- 24.7 %)

Table 4.12 Sensitivity of R_{LL} coefficient to the change in the oxide velocities. Frequency 50 MHz.

From table 4.12 it can be seen that a 30 % decrease in velocities ($\|R_{LL}\|$ curve of oxide 4) reduces the amplitude of R_{LL} by as much as 24.7 % at an angle of 65.0 degrees, and by as little as 0.7 % at normal incidence (0.0 degrees) with respect to the R_{LL} reflection coefficient from oxide 1.

Figure 4.25(b) shows the shear-shear (R_{SS}) reflection coefficient from the oxide layers at the frequency of 50 MHz. As with the R_{LL} coefficient, using oblique incidence can increase the sensitivity of the measurements quite substantially. At normal incidence (0.0 degrees) all four curves are very close to each other while, for example, at 32.4 degrees, good separation between the curves can be seen. Table 4.13 compares the sensitivity of R_{SS} coefficient at normal incidence (0.0 degrees) and at 32.4 degrees. For example, a 30 % decrease in velocities ($\|R_{SS}\|$ curve of oxide 4) reduces the amplitude of R_{SS} by 19.5 % at an angle of 32.4 degrees, and by 0.7 % at normal incidence (0.0 degrees) with respect to the R_{SS} reflection coefficient from oxide 1.

Theoretical predictions of the reflection coefficient from thin layers

angle of incidence	$|R_{SS}|$ of oxide 1 (% change wrt oxide 1)	$|R_{SS}|$ of oxide 2 (% change wrt oxide 1)	$|R_{SS}|$ of oxide 3 (% change wrt oxide 1)	$|R_{SS}|$ of oxide 4 (% change wrt oxide 1)
0.0 deg	0.741 (0.0 %)	0.739 (- 0.3 %)	0.734 (- 0.9 %)	0.728 (- 1.8 %)
32.4 deg	0.657 (0.0 %)	0.623 (- 5.2 %)	0.581 (- 11.6 %)	0.529 (- 19.5 %)

Table 4.13 Sensitivity of R_{SS} coefficient to the change in the oxide velocities. Frequency 50 MHz.

Figure 4.25(c) shows the longitudinal-shear (R_{SL}) reflection coefficient from the oxide layers at a frequency of 50 MHz. Here, the best sensitivity can be observed at angles around 65.0 degrees. Table 4.14 shows the sensitivity of the R_{SL} coefficient at an angle of 65.0 degrees.

angle of incidence	$|R_{SL}|$ of oxide 1 (% change wrt oxide 1)	$|R_{SL}|$ of oxide 2 (% change wrt oxide 1)	$|R_{SL}|$ of oxide 3 (% change wrt oxide 1)	$|R_{SL}|$ of oxide 4 (% change wrt oxide 1)
65.0 deg	0.544 (0.0 %)	0.569 (4.6 %)	0.586 (7.7 %)	0.594 (9.2 %)

Table 4.14 Sensitivity of R_{SL} coefficient to the change in the oxide velocities.Frequency 50 MHz.

Figure 4.25(d) shows the shear-longitudinal (R_{SL}) reflection coefficient from the oxide layers at a frequency of 50 MHz. The practically usable range is between 0.0 degrees and the longitudinal critical angle, which is 29.5 degrees here. Above the longitudinal critical angle, the reflected longitudinal wave is inhomogeneous and cannot propagate away from the oxide interface. Some sensitivity can be found at angles just a few degrees below the longitudinal critical angle (see fig. 4.25(d)). Table 4.15 shows the sensitivity of the R_{SL} coefficient at an angle of 28.0 degrees.

angle of incidence	$|R_{SL}|$ of oxide 1 (% change wrt oxide 1)	$|R_{SL}|$ of oxide 2 (% change wrt oxide 1)	$|R_{SL}|$ of oxide 3 (% change wrt oxide 1)	$|R_{SL}|$ of oxide 4 (% change wrt oxide 1)
28.0 deg	0.610 (0.0 %)	0.653 (7.0 %)	0.683 (12.0 %)	0.700 (14.8 %)

Table 4.15 Sensitivity of R_{SL} coefficient to the change in the oxide velocities.Frequency 50 MHz.

From fig. 4.25 and tables 4.12-4.15 it can clearly be seen that the oblique incidence technique can substantially increase the sensitivity of the reflection coefficient method to variations in material properties of thin layers.

The last example to be given in this section is the frequency domain shear-shear reflection coefficient at an angle of 32.4 degrees. This angle of incidence was determined from fig. 4.25(b) as the angle increased sensitivity. Figure 4.26 shows the frequency domain R_{SS} reflectivity at an angle of 32.4 degrees. The sensitivity of the R_{SS} coefficient here is good and increases with frequency. Figure 4.26 can be directly compared to figures 4.23 and 4.24, because they were obtained using the same material properties for the aluminium, the epoxy and the oxide layers, given in table 4.11. The comparison shows that the 32.4 degree R_{SS} coefficient of fig. 4.26 is much more sensitive to changes in the oxide layer than the normal incidence R_{LL} coefficient of fig. 4.23, and the normal incidence R_{SS} coefficient of fig. 4.24.

4.5 Thin layer approximation.

Derivation

The theory for calculating the ultrasonic reflectivity from a multilayered viscoelastic plate is given in chapter 3. This theory is exact and valid for layered systems of any thicknesses. There are some simple cases, however, where an approximate theory can be obtained as a simplification of the exact theory. Simplification means that for a specific case, only the most important parts of a general theory are used. Simplified theory is no longer general, but it can give us better physical insight into the phenomena. The exact theory can then be used to find the limits of applicability of the approximation. The derivation of the matrix formulation of the thin layer approximation has been done together with my co-worker Mike Lowe.

The starting point of our derivations is eqn (3.7) of chapter 3 of this thesis, relating the stress-displacement vector one side of the layer to the stress-displacement on the other side,

$$\{V_k(d_k)\} = \mathscr{L}_k \{V_k(0)\}, \tag{4.46}$$

where the transfer matrix is given by eqn (3.8) as,

$$\mathscr{L}_k = \mathscr{M}_k(d_k) \; \mathscr{M}_k^{-1}(0). \tag{4.47}$$

The transfer matrix $\mathscr{L}_k$ is expressed here as a product of two 4 × 4 complex matrices given by eqn. (3.1). Let us assume that the origin of the coordinate system lies on the bottom boundary of the layer (see fig. 4.27). Therefore, at the bottom of the layer $x_2 = 0$, and at the top of the layer $x_2 = d_k$, where d_k is the thickness of the layer Equation (4.47) can be re-written as,

$$\mathscr{L} = \mathscr{M}(d) \; \mathscr{M}^{-1}(0), \tag{4.48}$$

where the subscript, k, was omitted here for clarity. It is possible to calculate the transfer matrix $\mathscr{L}$ in closed form. Its terms are given below:

$$L_{11} = \frac{C}{2}(g_p + g_p^{-1}) + \beta^2 s^2 (g_s + g_s^{-1}),$$

$$L_{12} = \frac{\alpha s C}{2A}(g_p - g_p^{-1}) + B\beta s(-g_s + g_s^{-1}),$$

$$L_{13} = i\omega\rho C\beta^2 s (g_p + g_p^{-1} - g_s - g_s^{-1}),$$

$$L_{14} = \frac{i\omega\rho C^2 \alpha}{2A}(g_p - g_p^{-1}) + 2i\omega\rho B\beta^3 s^2 (g_s - g_s^{-1}),$$

$$L_{21} = \frac{Ab^2 s}{\alpha}(g_p - g_p^{-1}) + \frac{C\beta s}{2B}(-g_s + g_s^{-1}),$$

$$L_{22} = \beta^2 s^2 (g_p + g_p^{-1}) + \frac{C}{2}(g_s + g_s^{-1}),$$

$$L_{23} = \frac{2Ai\omega\rho s^2 \beta^4}{\alpha}(g_p - g_p^{-1}) + \frac{i\omega\rho C^2 \beta}{2B}(g_s - g_s^{-1}),$$

$$L_{24} = L_{13},$$

$$L_{31} = \frac{s}{2i\omega\rho}(g_p + g_p^{-1} - g_s - g_s^{-1}),$$

$$L_{32} = \frac{\alpha s^2}{2Ai\omega\rho}(g_p - g_p^{-1}) + \frac{B}{2\beta i\omega\rho}(g_s - g_s^{-1}),$$

$$L_{33} = L_{22},$$

$$L_{34} = L_{12},$$

$$L_{41} = \frac{A}{2\alpha i\omega\rho}(g_p - g_p^{-1}) + \frac{\beta s^2}{2Bi\omega\rho}(g_s - g_s^{-1}),$$

$$L_{42} = L_{31},$$

$$L_{43} = L_{21},$$

$$L_{44} = L_{11},\qquad\qquad\qquad\qquad\qquad\qquad\qquad\qquad (4.49)$$

where the terms A, B, C, g_p, and g_s, are given by eqn (3.2), putting $x_2 = d$,

$$A = (1-\alpha^2 s^2)^{1/2}, \quad B = (1-\beta^2 s^2)^{1/2}, \quad C = 1-2\beta^2 s^2,$$

$$g_p = e^{i\omega A\alpha^{-1}d}, \quad g_s = e^{i\omega B\beta^{-1}d}. \tag{4.50}$$

When thickness of the layer, d, becomes small then,

$$g_p \approx 1 + i\omega A\alpha^{-1}d,$$

$$g_s \approx 1 + i\omega B\beta^{-1}d, \tag{4.51}$$

which gives,

$$g_p + g_p^{-1} \approx 2,$$

$$g_p - g_p^{-1} \approx 2i\omega A\alpha^{-1}d,$$

$$g_s + g_s^{-1} \approx 2,$$

$$g_s - g_s^{-1} \approx 2i\omega B\beta^{-1}d. \tag{4.52}$$

The approximation here takes into account only the constant and linear terms of the Taylor expansion with respect to d, around d = 0. Equations (4.51) states therefore the assumption on which the whole thin layer approximation will be built. Substituting eqn (4.52) into eqn (4.49) gives the expression for the transfer matrix $\mathscr{L}$ as,

$$\mathscr{L} = \begin{bmatrix} 1 & -i\omega s d & 0 & -\omega^2 \rho x_2 \\ i\omega s(2\beta^2\alpha^{-2}-1)d & 1 & -\omega^2\rho[1-4s^2\beta^2(1-\beta^2\alpha^{-2})]d & 0 \\ 0 & \dfrac{1}{\rho\beta^2}d & 1 & -i\omega s d \\ \dfrac{1}{\rho\alpha^2}d & 0 & i\omega s(2\beta^2\alpha^{-2}-1)d & 1 \end{bmatrix}. \tag{4.53}$$

Equation (4.53) is the thin layer approximation of the stress-displacement transfer matrix of eqn. (4.49) and is dependent on three parameters: the frequency of excitation ω, thickness of the layer d, and a variable s, defined in eqn (2.60), characterising the angle of incidence of the exciting wave.

When the incident wave propagates in the direction perpendicular to the layer then the direction cosine of eqn (2.60) $N_1 = 0$, and therefore s = 0. The stress-displacement transfer matrix $\mathscr{L}$ of

eqn (4.53) then simplifies to,

$$
\mathscr{L} = \begin{bmatrix}
1 & 0 & 0 & -\omega^2 \rho d \\
0 & 1 & -\omega^2 \rho d & 0 \\
0 & \dfrac{1}{\rho \beta^2} d & 1 & 0 \\
\dfrac{1}{\rho \alpha^2} d & 0 & 0 & 1
\end{bmatrix} .
$$
(4.54)

The form of the matrix $\mathscr{L}$ in eqn (4.54) is simple and its terms have a straightforward physical interpretation, as described below. Using eqn (2.17) we have,

$$
\rho \alpha^2 = \lambda + 2\mu - i(\lambda' + 2\mu') ,
$$
(4.55)

and therefore,

$$
\frac{1}{\rho \alpha^2} x_2 = \frac{1}{k_N} ,
$$
(4.56)

where k_N is the dynamic stiffness per unit area of the layer in the direction perpendicular to the plane of the layer (normal stiffness). Using eqn (2.18) we have,

$$
\rho \beta^2 = \mu - i\mu' ,
$$
(4.57)

$$
\frac{1}{\rho \beta^2} x_2 = \frac{1}{k_T} ,
$$
(4.58)

where k_T is the dynamic stiffness per unit area of the layer in the direction parallel to the plane of the layer (tangential stiffness). Since ρ is the density of the layer and x_2 is the layer thickness then,

$$
\rho x_2 = m ,
$$
(4.59)

where m is the mass of the layer per unit area. Combining equations (4.54), (4.56), (4.58), and (4.59) we have,

$$
\begin{bmatrix}
1 & 0 & 0 & -\omega^2 m \\
0 & 1 & -\omega^2 m & 0 \\
0 & \dfrac{1}{k_T} & 1 & 0 \\
\dfrac{1}{k_N} & 0 & 0 & 1
\end{bmatrix}
\begin{Bmatrix}
\sigma_{22} \\
\sigma_{21} \\
u_1 \\
u_2
\end{Bmatrix}_{bottom}
=
\begin{Bmatrix}
\sigma_{22} \\
\sigma_{21} \\
u_1 \\
u_2
\end{Bmatrix}_{top} .
$$
(4.60)

Here we can see that even for a simple normal incidence case the stress components are not equal on each side of the layer. This is not the case when simple 'spring' boundary conditions, given by eqn (2.111), are used instead of the thin layer approximation. There we assumed that stresses are equal on both side of the boundary, ie the layer has a negligible mass.

Comparison of the spring model with the exact theory

There are three different models of the behaviour of thin layers available and discussed in this thesis. The first one is an exact model, developed in chapters 2 and 3, and used in sections 4.1-4.4 of this chapter. In the exact model the layer is considered as a volume of continuum material where the mechanical waves propagate in the same manner as in an infinite medium. The response of the layer is defined by the boundary conditions at both sides of the layer, and is obtained in terms of the amplitudes of the bulk waves present in the layer.

The second model presented in this thesis is an 'engineering' discrete model of the layer behaviour. Here it is assumed that when the frequency of excitation is low, the only important feature of a thin layer is its stiffness (see section 1.4.1 for more details). Therefore, for low frequencies, the layer can replaced by a spring. Such a model, if accurate enough, can give us good insight into the physics of thin layers at low frequencies of excitation. Let us call this model the spring model.

The third model is the thin layer approximation derived directly from the continuous model. In such a model, it is firstly assumed that the layer conforms to the equations of continuum mechanics, and the response of the layer is described in terms of the plane wave amplitudes propagating in the layer. Then the thickness of the layer is assumed to be small and the limiting case of the stress-displacement relationship on both sides of the layer is derived. The derivations show that the general case of the thin layer approximation is far from being simple. The simplest case is when the incident wave strikes the layer at normal incidence. Here, the thin layer can be modelled it terms of its stiffness and mass. In other words, the derivations show that the thin layer responding to normal incidence excitation can be modelled as a discrete mass-spring system rather than a spring only system.

Let us therefore compare the two approximate models to the exact one. The first example is a 0.1 mm thick epoxy layer between two aluminium half-spaces. Material properties of the aluminium and the epoxy are given in table 4.1. Figure 4.28 shows the normal incidence longitudinal reflection coefficient from the layer. The three different curves on the plot show the predictions of the three different models. As can be seen from the figure, in the low frequency

range, the spring model and the mass+spring model approximate the exact solution rather well. The mass+spring model underestimates the exact theory, while the spring model overestimates it.

In fig. 4.29 the normal incidence longitudinal reflection coefficient from an 0.1 mm thick epoxy layer in water is calculated (see table 4.1 for the material properties). Here it can be seen that the mass+spring model approximates the exact theory well, while the spring model is not capable of providing reasonable results even for very low frequencies.

Figure 4.30 shows the normal incidence longitudinal reflection coefficient from a 50.0 μm thick oxide, embedded between aluminium and epoxy half-spaces. Material properties of the aluminium, the oxide and the epoxy are given in table 4.1. The figure shows that the spring approximation generates a reflection coefficient which is an increasing function of frequency, which is the opposite to what the exact theory gives. The mass+spring model, however, approximates the exact theory in the low frequency region rather well.

Figure 4.31 shows the normal incidence reflection coefficient predictions from an oxide wafer in water. As before, material properties of the oxide and water are given in table 4.1. It can clearly be seen from the fig. 4.31 that the spring model fails to model the response of the layer even approximately, while the mass+spring model can be used to accurately predict the behaviour of the layer in the low frequency range.

Limits of applicability of the spring model

Looking at figures 4.28 - 4.31, one can see that the mass+spring model can be successfully used as a low frequency approximation of a thin continuous layer. This is not the case, however, with the spring model which sometimes fails to work well. Let us therefore determine the conditions in which the spring model can be used as a thin layer approximation. In order to do so the normal incidence reflection coefficient using the mass+spring approximation will be derived and compared with the reflection coefficient using the spring model.

Consider a layer of thickness L in between two half spaces as shown in fig. 4.32. Let us denote the half-space, extending downwards from the bottom of the layer as medium number 1, the layer as medium number 2, and the top half-space as medium number 3. Each of the three media are given their own densities and wave velocities, ρ_i and c_i, i = 1,2,3. Let us furthermore assume that the layer (medium 2) has been approximated by a mass+spring boundary. Using eqn (4.60), which was derived for the mass+spring model, the normal stresses and displacements at the top of the layer can be described in terms of the stresses and

displacements at the bottom of the layer as,

$$u(L) = u(0) + \frac{1}{k_2} \sigma(0) \, , \tag{4.61}$$

$$\sigma(L) = \sigma(0) - \omega^2 m_2 u(0) \, , \tag{4.62}$$

where, by equations (4.56), the stiffness of the layer is given by,

$$k_2 = \frac{\rho_2 c_2^2}{L} \, , \tag{4.63}$$

and, by equations (4.59), the mass of the layer is given by,

$$m_2 = \rho_2 L \, . \tag{4.64}$$

Setting $x = 0$ in equations (4.8) and (4.9), the displacements and normal stresses at the bottom of the layer can be expressed as,

$$u(0) = T_1 + R_1 \, , \tag{4.65}$$

$$\sigma(0) = i\omega z_1 (T_1 - R_1) \, , \tag{4.66}$$

where ω is the frequency of excitation, T_1 and R_1 are the wave amplitudes in the bottom half-space, and z_1 is the acoustic impedance of medium 1, $z_1 = \rho_1 c_1$. Similarly, using equations (4.19) and (4.20), the displacements and normal stresses at the top of the layer can be expressed as,

$$u(L) = T_3 \, , \tag{4.67}$$

$$\sigma(L) = i\omega z_3 T_3 \, , \tag{4.68}$$

where T_3 is the amplitude of the transmitted wave in the top half-space, and z_3 is the acoustic impedance of medium 1, $z_3 = \rho_3 c_3$. Putting equations (4.65), (4.66), and (4.67) into eqn (4.61), we have,

$$T_3 = T_1 + R_1 + \frac{1}{k_2} i\omega z_1 (T_1 - R_1) \, . \tag{4.69}$$

Putting equations (4.66), (4.67), and (4.68) into eqn (4.62), we have,

$$i\omega z_3 T_3 = i\omega z_1 (T_1 - R_1) - \omega^2 m_2 (T_1 + R_1) \, . \tag{4.70}$$

In order to solve the reflection coefficient problem, it is necessary to set the amplitude of the incident wave, T_1, to unity and solve for the amplitude of the reflected wave, R_1. Putting $T_1 = 1$, and eliminating T_3 from equations (4.69) and (4.70) the following expression can be finally derived,

$$R_1 = \frac{z_1 - z_3 - \frac{i\omega}{k_2}(z_1 z_3 - z_2^2)}{z_1 + z_3 - \frac{i\omega}{k_2}(z_1 z_3 + z_2^2)} \ . \tag{4.71}$$

Equation (4.71) describes the normal incidence reflection coefficient from the mass+spring boundary in terms of its acoustic impedance and stiffness as well as acoustic impedances of the neighbouring half-spaces. In order to obtain an expression for the reflection coefficient from the spring only boundary, it is necessary to set the mass of the layer to zero. Setting, $m_2 = 0$, means that the density of the layer, $\rho_2 = 0$, by eqn (4.64), and therefore its impedance, $z_2 = 0$. The reflection coefficient from the spring boundary can then be obtained by setting $z_2 = 0$ in eqn (4.71),

$$R_1 = \frac{z_1 - z_3 - \frac{i\omega}{k_2} z_1 z_3}{z_1 + z_3 - \frac{i\omega}{k_2} z_1 z_3} \ . \tag{4.72}$$

The normal incidence reflection coefficient from a spring boundary was derived by Tattersal (1973), and shown in eqn (1.3) of this thesis. Equation (1.3) can be obtained from eqn (4.72) by taking the frequency, ω, to be negative, thus conforming to Tattersal's notation convention.

Having derived the expressions for reflection coefficients from mass+spring and spring boundaries, it is now possible to find the conditions in which the spring model gives poor approximations. Comparing equations (4.71) and (4.72) it can clearly be seen that the spring model will be a satisfactory approximation of the mass+spring model only when the square of the layer's impedance is much smaller then the product of the impedances of the neighbouring half-spaces, that is,

$$z_2^2 \ll z_1 z_3 \ . \tag{4.73}$$

It has been shown in this chapter (see equations (4.51) - (4.60)) that the mass+spring model approximates the behaviour of thin layers satisfactorily only at low frequencies, when the conditions stated in eqn (4.51) are met. Therefore, the spring model can be applied successfully

only when both requirements, stated in equations (4.51) and (4.73) are concurrently satisfied.

Let us then analyse figures 4.28 - 4.31 again applying the criterion stated in eqn (4.73). Table 4.16 shows the impedances of the materials used in the reflection coefficients calculations of figures 4.28 - 4.31 as well as the left hand side and the right hand side terms used in criterion (4.74). The values of impedances were taken from table 4.1.

Figure	system analysed	z_1	z_2	z_3	z_2^2	$z_1 z_3$
Fig. 4.28	aluminium/ epoxy/ aluminium	17.85 E6	3.05 E6	17.85 E6	9.3 E12	319.0 E12
Fig. 4.29	water/ epoxy/ water	1.49 E6	3.05 E6	1.49 E6	9.3 E12	2.2 E12
Fig. 4.30	aluminium/ oxide/ epoxy	17.85 E6	12.17 E6	3.05 E6	161.3 E12	54.4 E12
Fig. 4.31	water/ oxide/ water	1.49 E6	12.17 E6	1.49 E6	161.3 E12	2.2 E12

Table 4.16 Application of criterion given in (4.73) to the results shown in fig. 4.28 - 4.31.

Looking at table 4.16 it can now clearly be seen that the system of fig. 4.28, aluminium/epoxy/aluminium, is the only one which satisfies criterion (4.73). The other systems fail to do so to a greater or lesser extend indicating that the application of the spring model approximation will be erroneous there, even at very low frequencies. This is particularly the case for the system of fig. 4.31 where z_2^2 is much higher than $z_1 z_3$, which is the opposite to what criterion (4.73) demands. Inspection of figures 4.28 - 4.31 confirms the above findings.

4.6   Conclusions

It has been shown in this chapter that the reflection coefficient method can be used to detect the presence of thin liquid and solid layers. The liquid layers are rather easy to detect using normal incidence techniques with either longitudinal or shear waves. If it is impossible to detect the presence of the liquid layer using the conventional normal incidence longitudinal technique, then the shear wave normal incidence method is capable of providing the answer. The shear stiffness of liquid layers is extremely low, therefore the normal incidence shear wave reflectivity from these layers is close to unity. However, because the normal incidence shear wave method suffers from unreliable coupling, it might be desirable to avoid this problem by

using the oblique incidence technique.

When there are solid layers to be detected, then the reflection coefficient methods may not be sufficiently sensitive, particularly when the impedance of the solid layer is similar to one of the neighbouring half-spaces. As the solid layer is stiff in the shear direction, the normal incidence shear wave reflection coefficient is not as advantageous from the sensitivity point of view as it was with liquids. However, it has been shown that the oblique incidence method can be much more sensitive to variations in the properties of solid layers than either the normal incidence longitudinal or shear wave techniques.

It has been also shown in this chapter that, in general, the 'engineering' spring model approximation of a thin layer is not accurate enough to be used even at very low frequencies. The mass plus spring model should be used instead. However, in some circumstances it is valid to apply the spring model as an approximation of a thin layer.
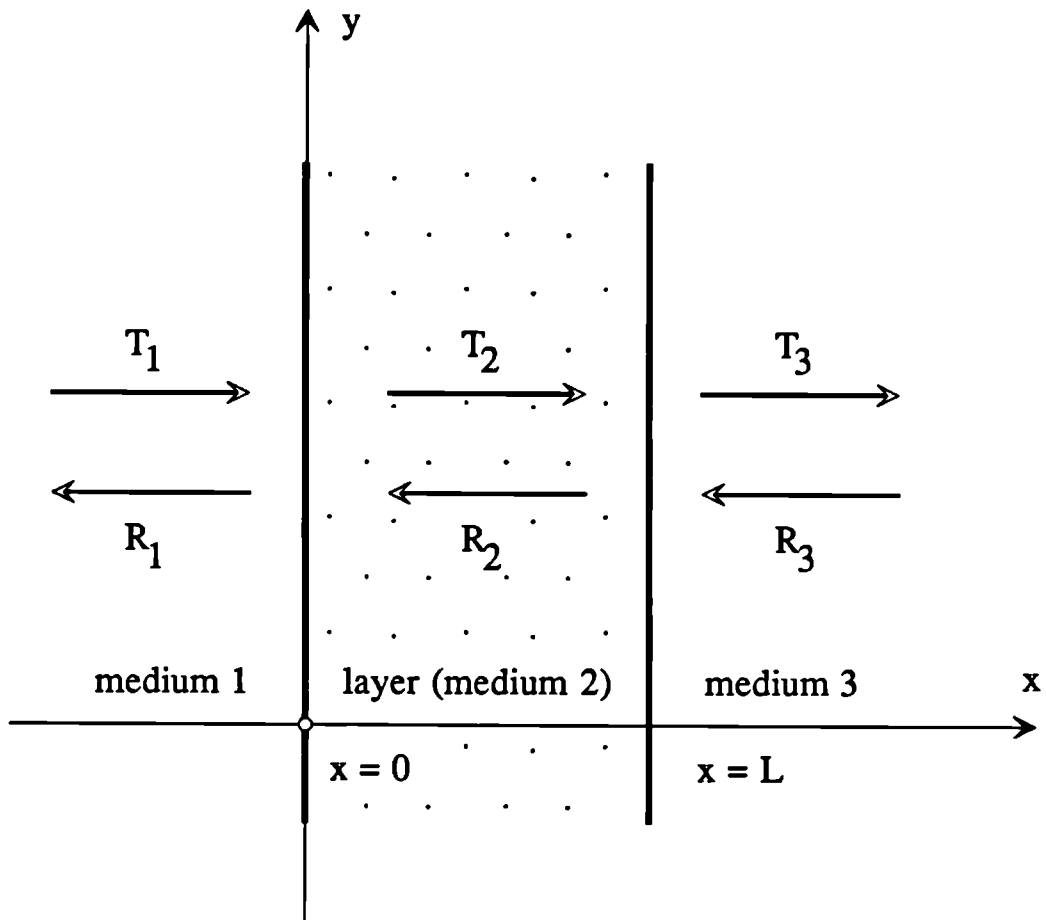
Fig 4.1   System used for the calculation of the normal
incidence reflection coefficient from the layer.
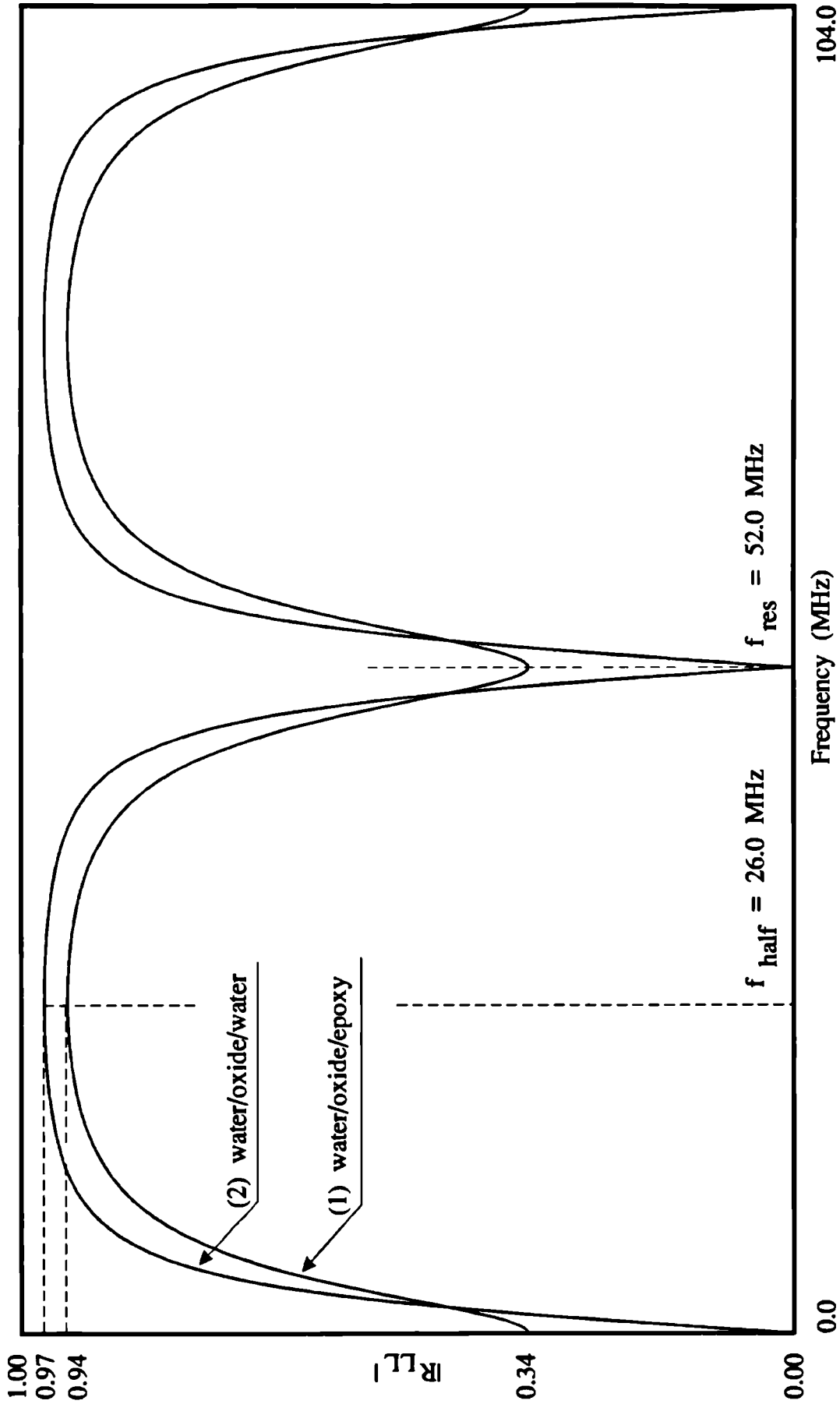
Fig 4.2 Amplitudes of the normal incidence longitudinal reflection coefficients from the water/100 μm thick oxide/water system and the water/100 μm thick oxide/epoxy system. Material properties are given in table 4.1.
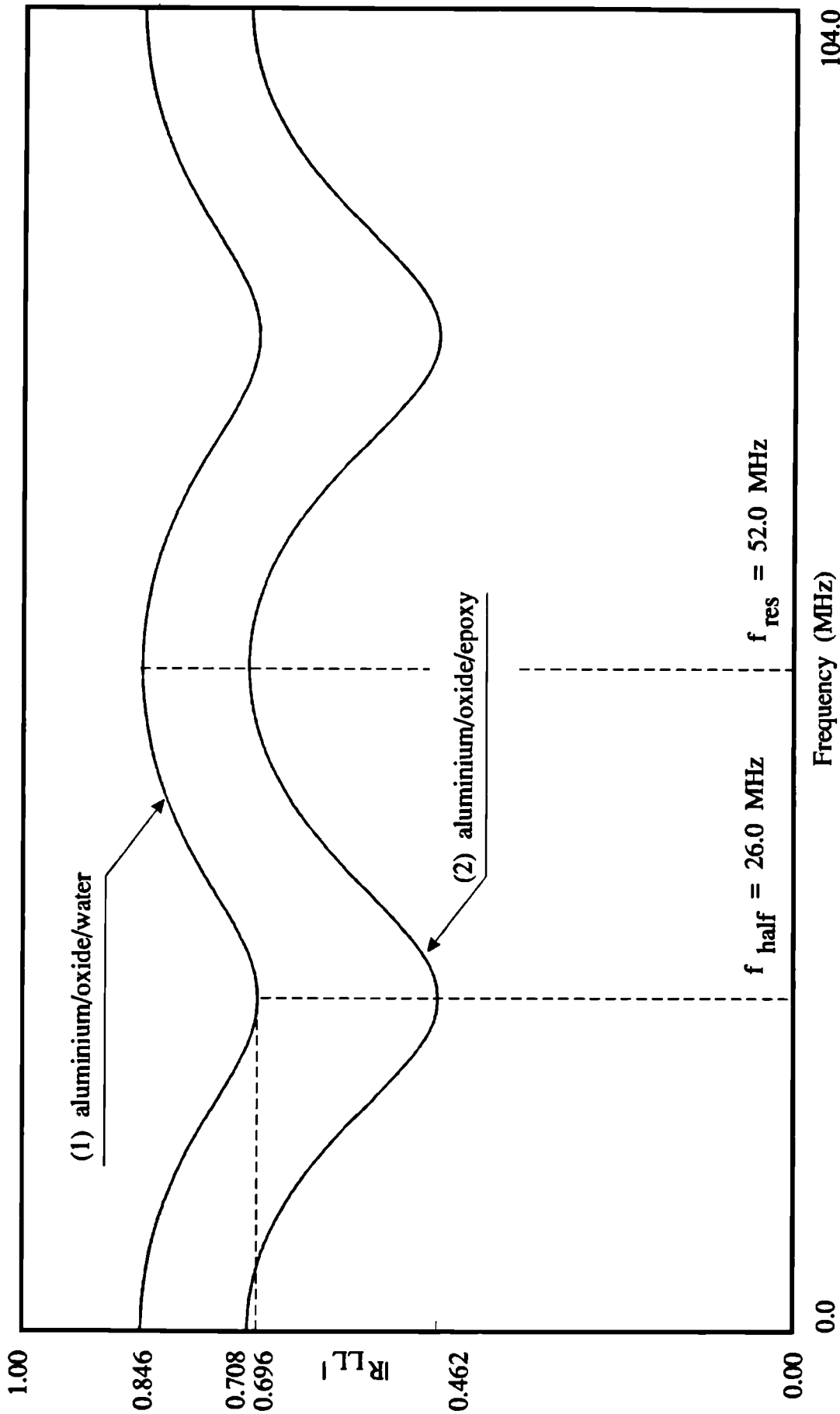
Fig 4.3 Amplitudes of the normal incidence longitudinal reflection coefficients from the aluminium/100 μm thick oxide/water system and the aluminium/100 μm thick oxide/epoxy system. Material properties are given in table 4.1.
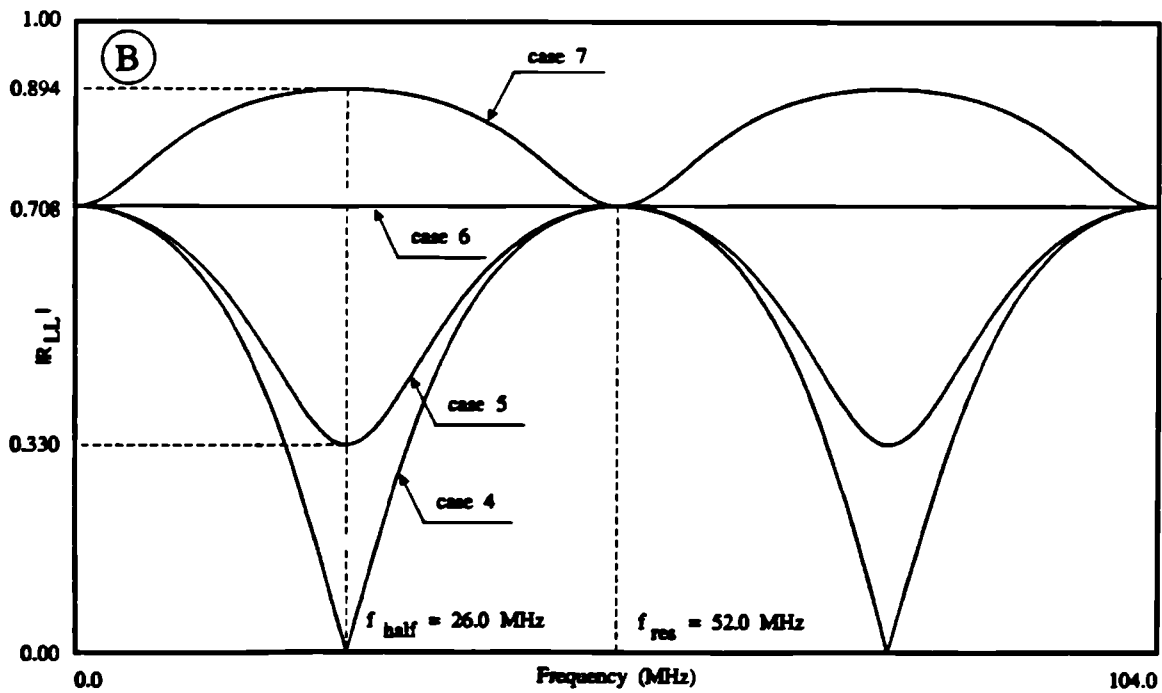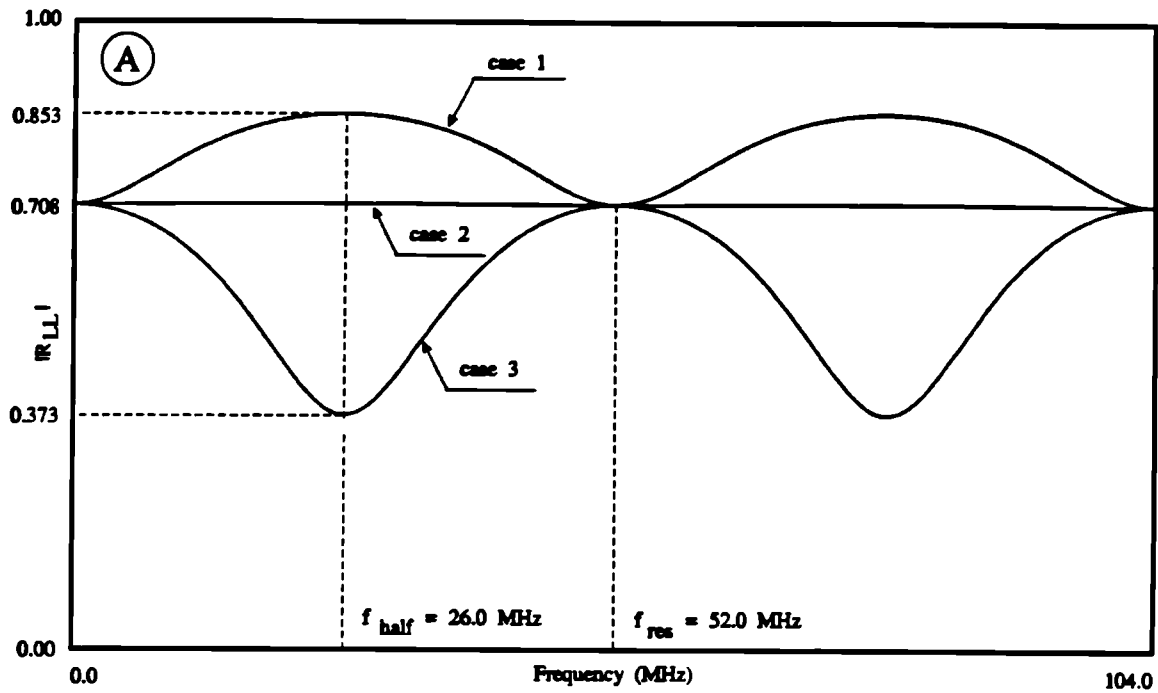
Fig. 4.4   Normal incidence reflection coefficient from the aluminium/ 100 μm thick
layer/epoxy system. Properties of aluminium and epoxy are given in table 4.1, and
properties of the layer are given on table 4.3. (a) Curves corresponding to cases 1-3
in table 4.3, (b) Curves corresponding to cases 4-7 in table 4.3.
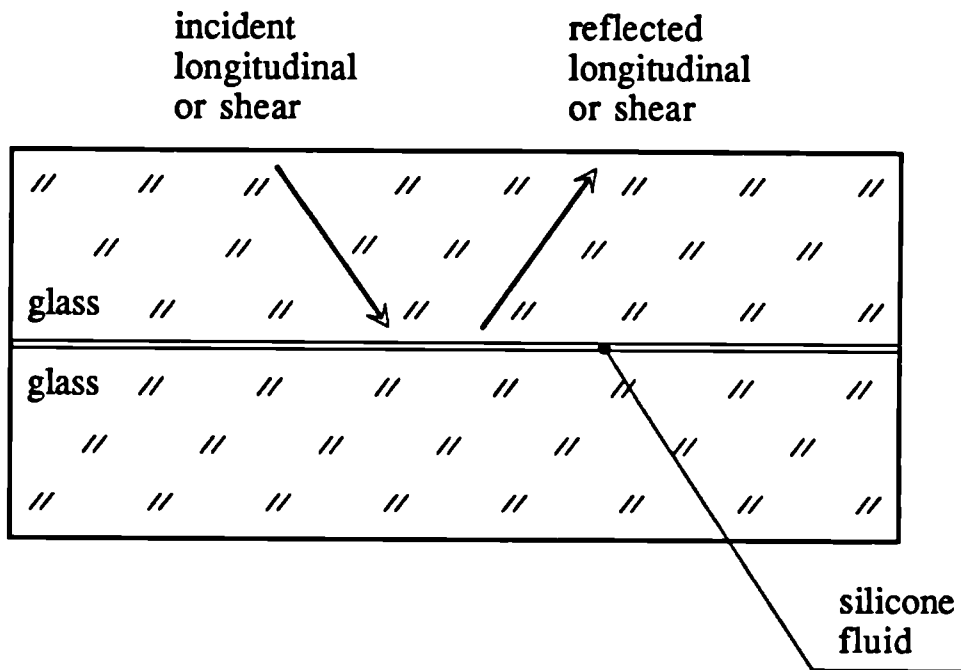
Fig 4.5 Thin silicone fluid layer separating glass half-spaces. Material properties used in reflection coefficient calculations are given in table 4.4.
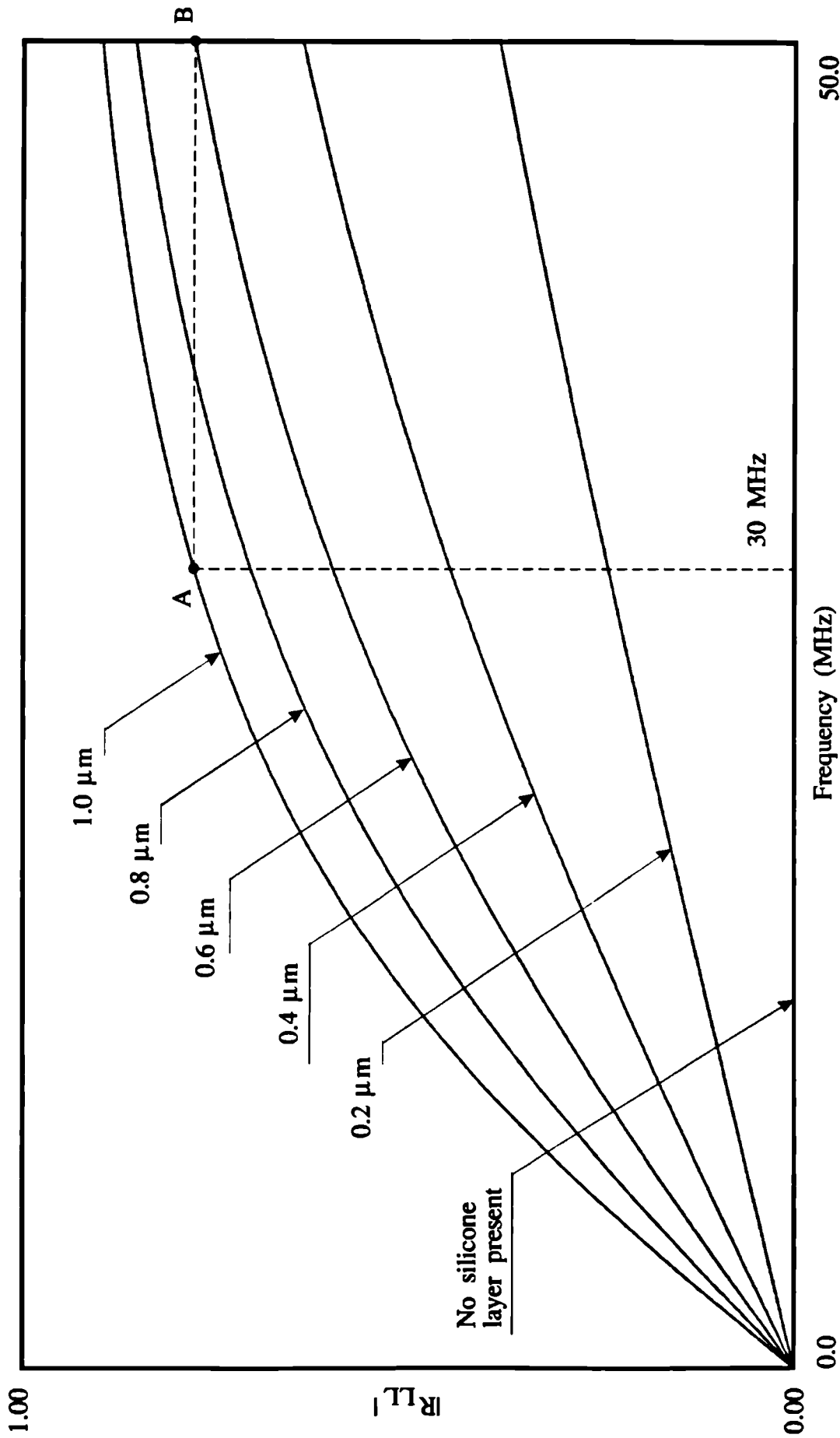
Fig 4.6 Amplitudes of the normal incidence longitudinal reflection coefficients from the silicone layers of different thicknesses in glass. Properties of glass and silicone liquid are given in table 4.4.
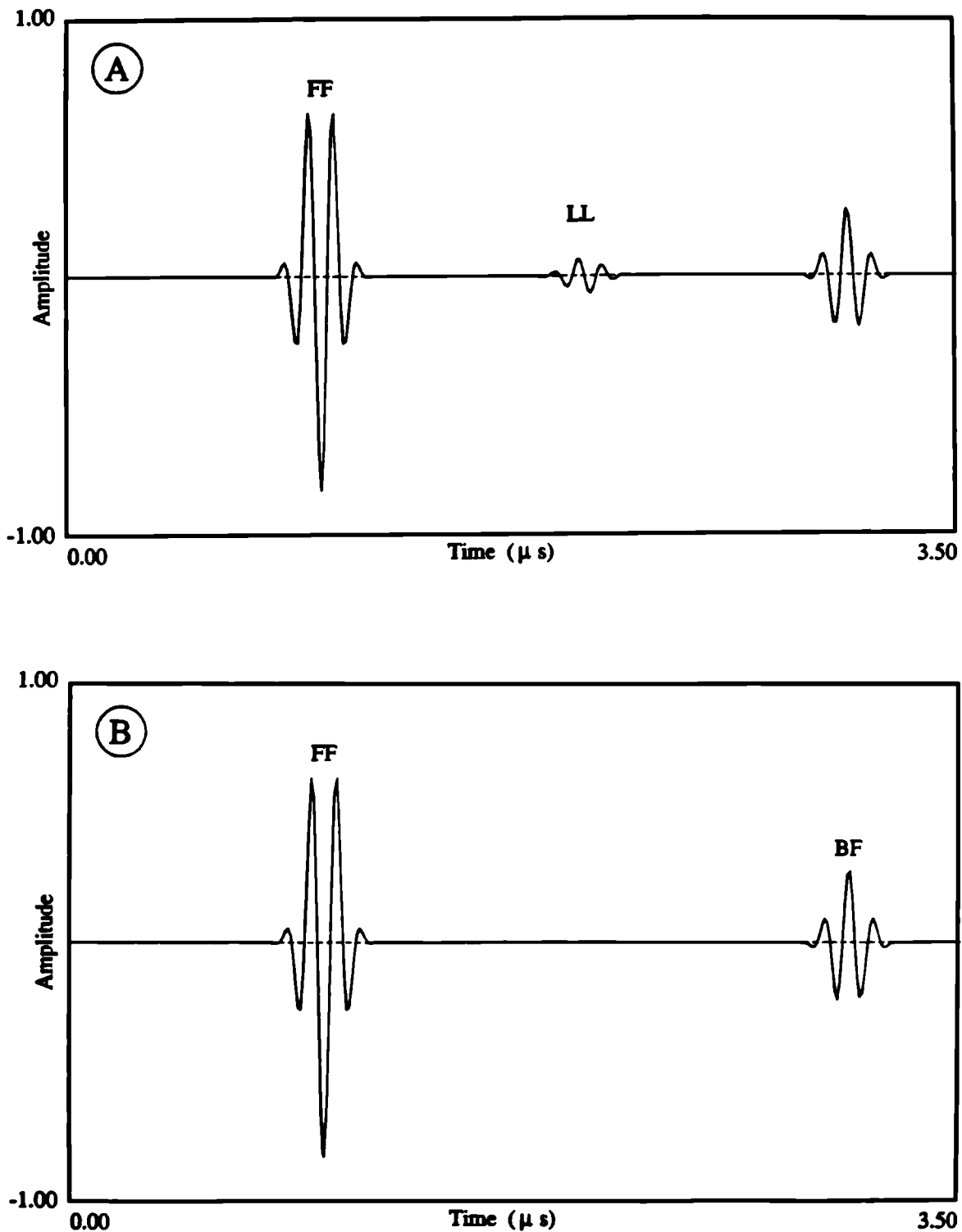
Fig. 4.7   Normal incidence longitudinal excitation response of the system comprising two 3.0
mm thick glass plates with and without 0.5 μm thick silicone fluid in between. FF
is the front face reflection, LL is the longitudinal reflection coming from the silicone
layer, while BF is the reflection coming from the back of the glass/silicone/glass
system. (a) Silicone layer present, (b) No silicone layer present.
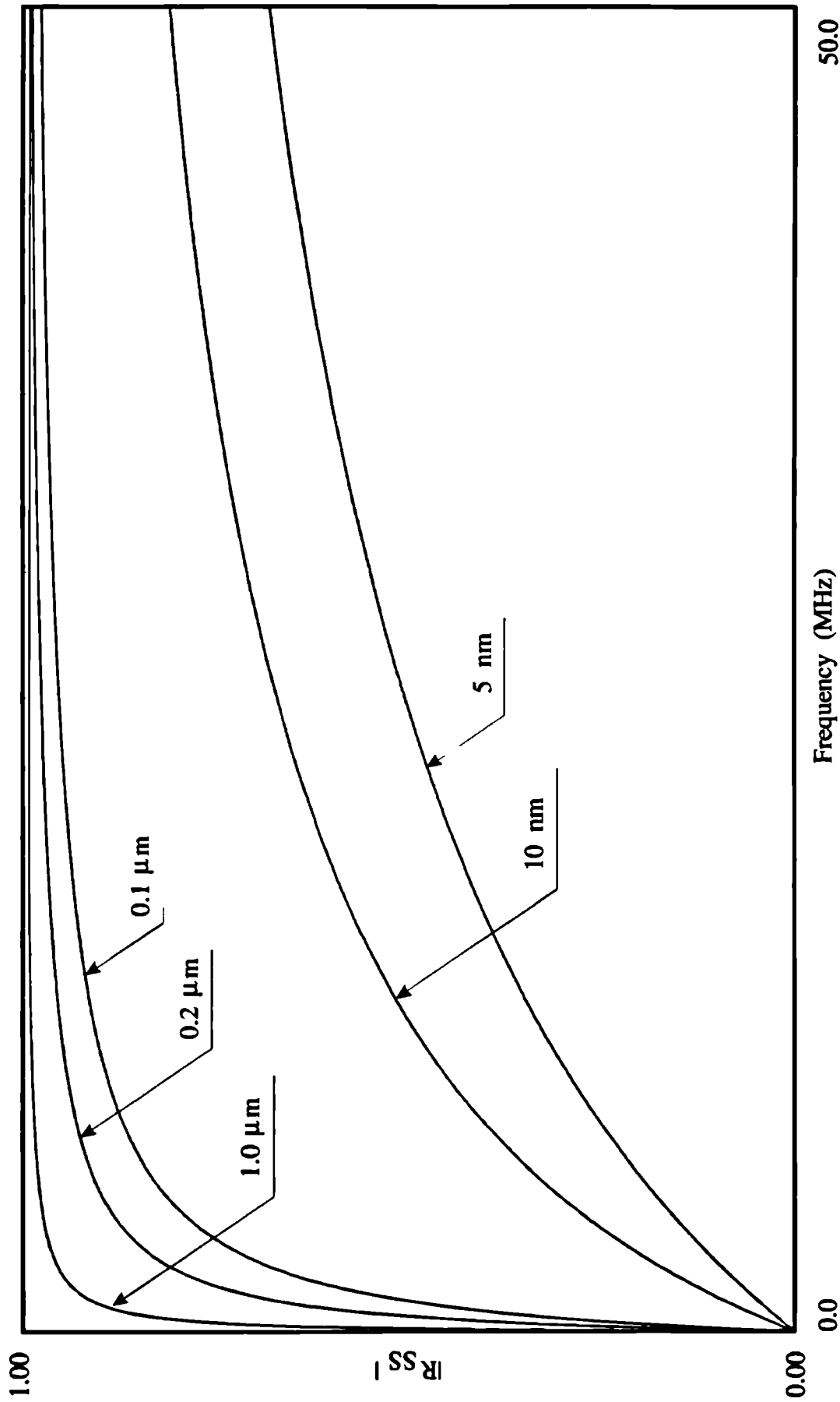
Fig. 4.8 Amplitudes of the normal incidence shear reflection coefficients from the silicone layers of different thicknesses in glass. Properties of glass and silicone liquid are given in table 4.4. Theoretical calculations.
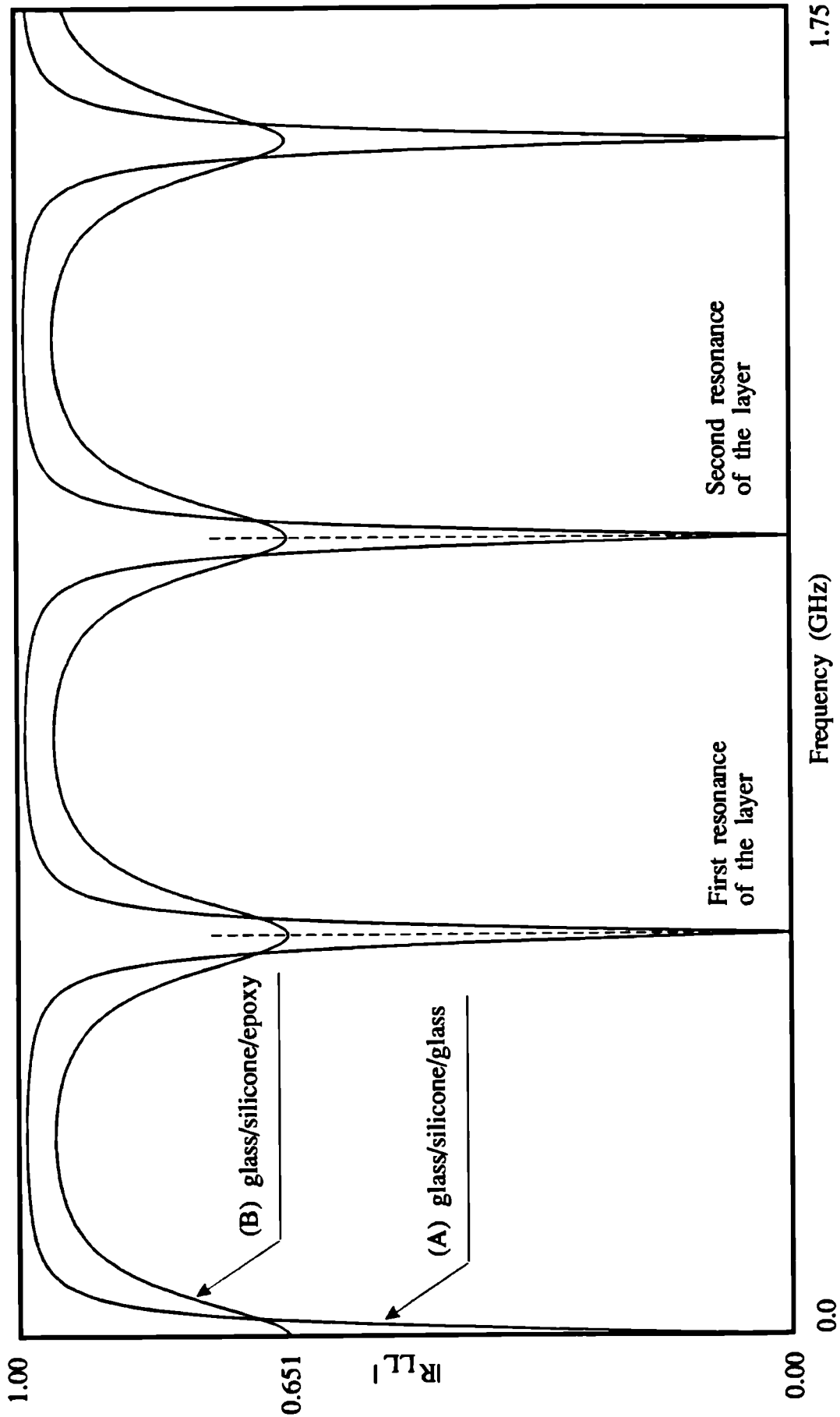
Fig. 4.9   Amplitudes of the normal incidence longitudinal reflection coefficients from the
1.0 μm thick silicone layers between two half-spaces. (A) glass/silicone/glass,
(B) glass/silicone/epoxy. Material properties are given in table 4.4.
Theoretical calculations.
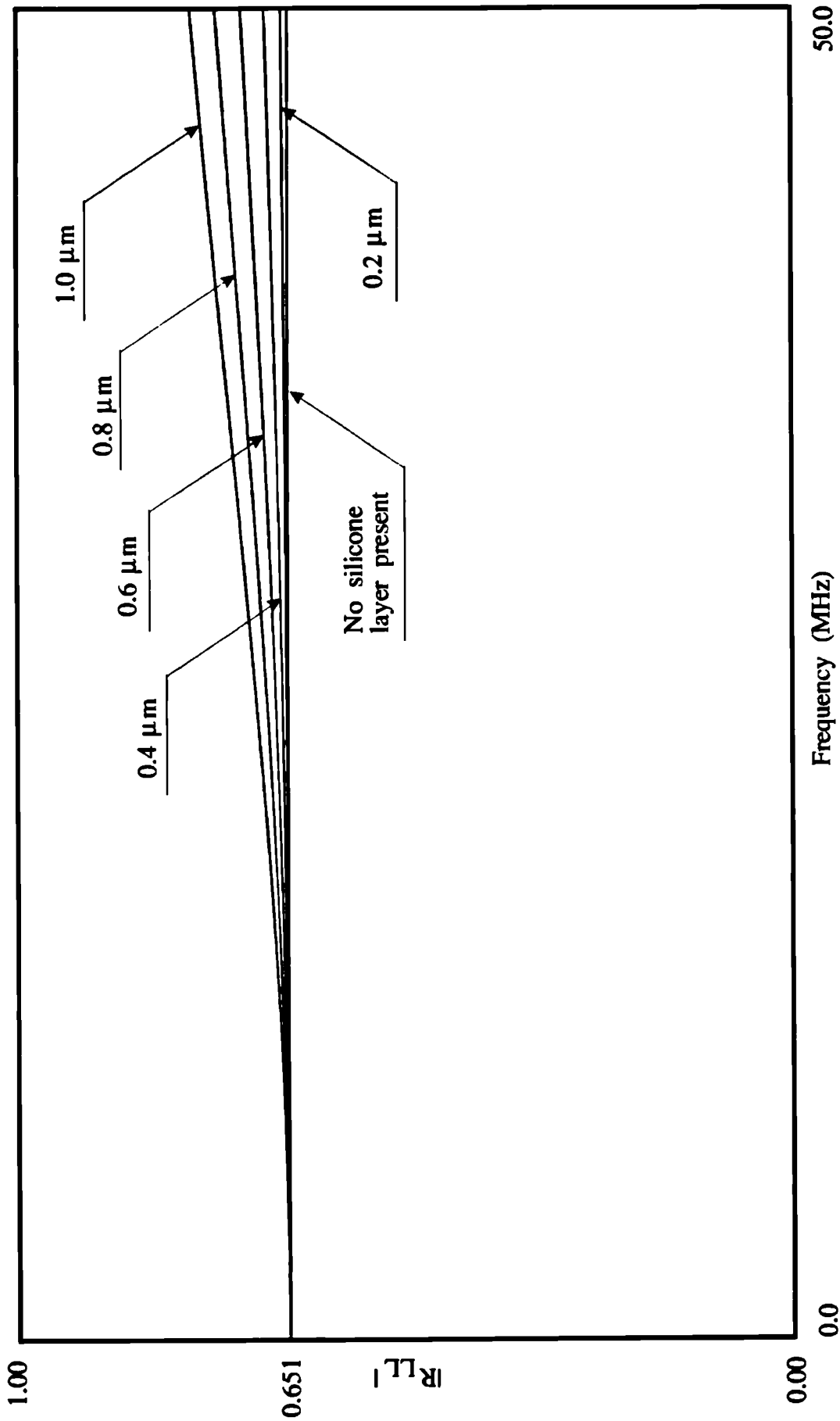
Fig. 4.10 Amplitudes of the normal incidence longitudinal reflection coefficients from the silicone layers between glass and epoxy half-spaces. Properties of glass, silicone liquid and epoxy resin are given in table 4.4. *Theoretical calculations.*
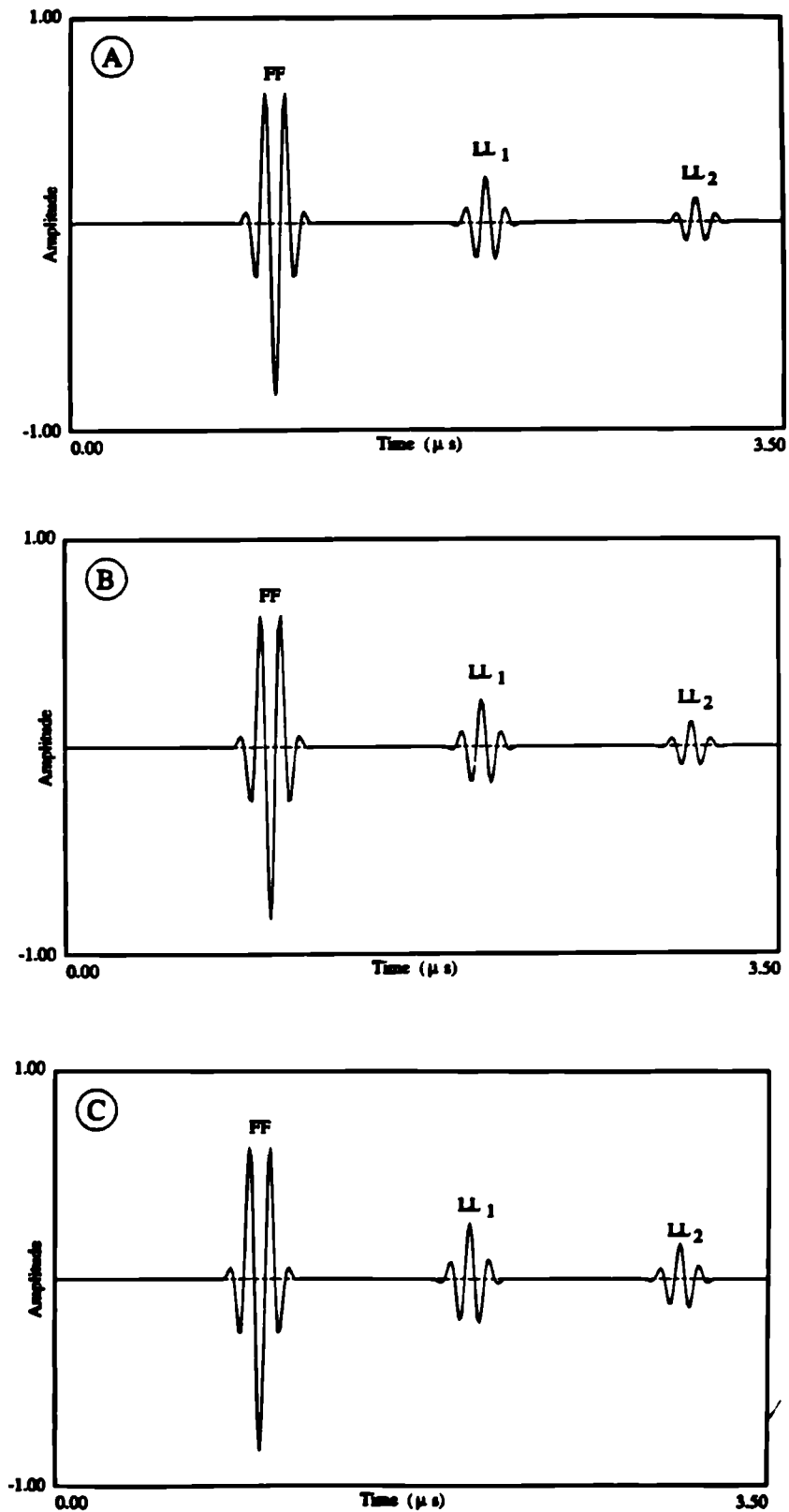
Fig. 4.11 Normal incidence longitudinal excitation response of the system comprising a 3.0 mm thick glass plate and a 3.0 mm thick epoxy resin with and without a silicone fluid in between. (a) No silicone layer present, (b) 0.5 μm thick silicone layer present, (c) 5.0 μm thick silicone layer present. FF is the front face reflection, LL_1 and LL_2 are the longitudinal reflections reflected from the silicone layer,

Theoretical calculations.
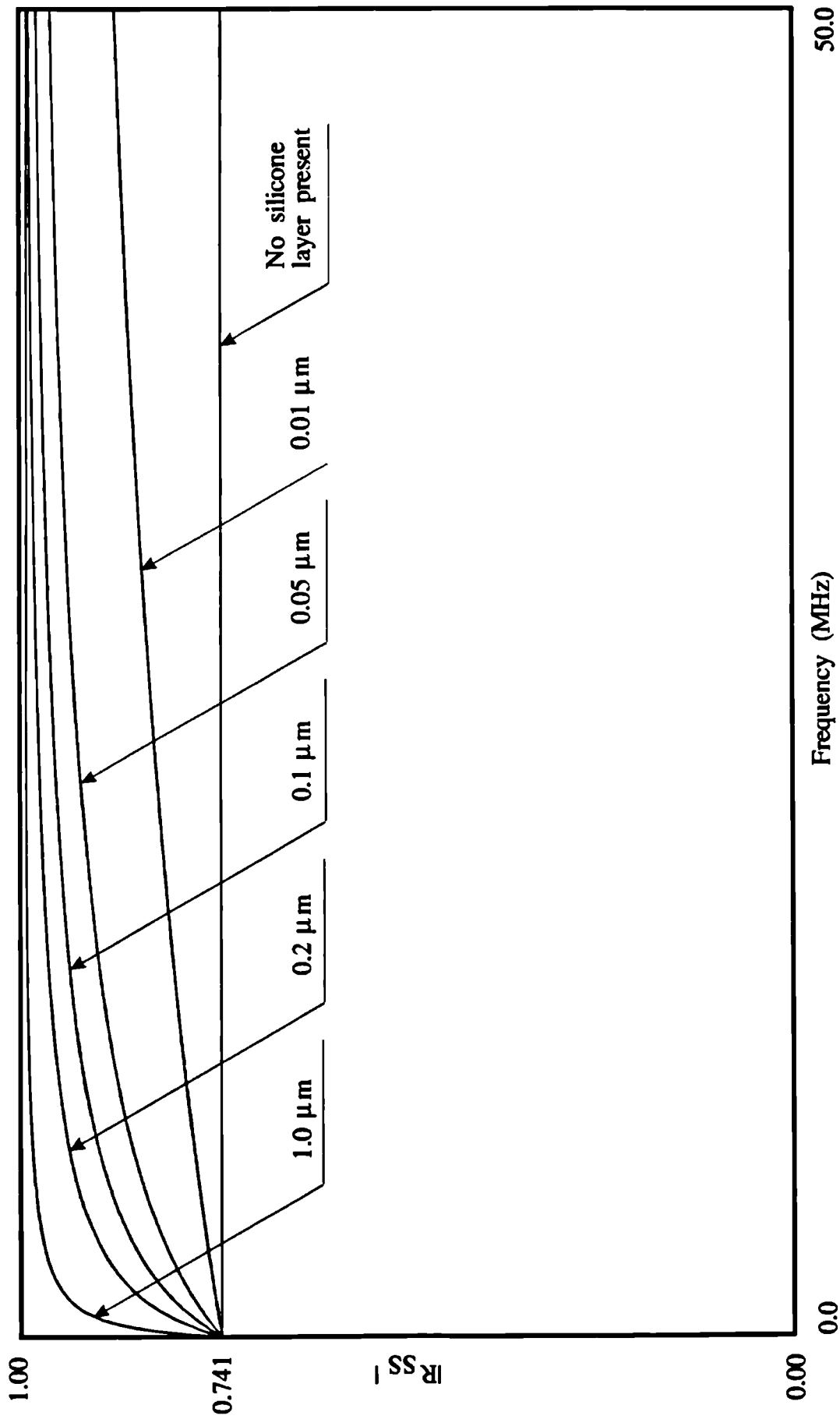
Fig. 4.12 Amplitudes of the normal incidence shear reflection coefficients from the silicone layers of different thicknesses separating glass and epoxy resin half-spaces. Properties of glass, silicone fluid and epoxy resin are given in table 4.4. *Theoretical calculations.*
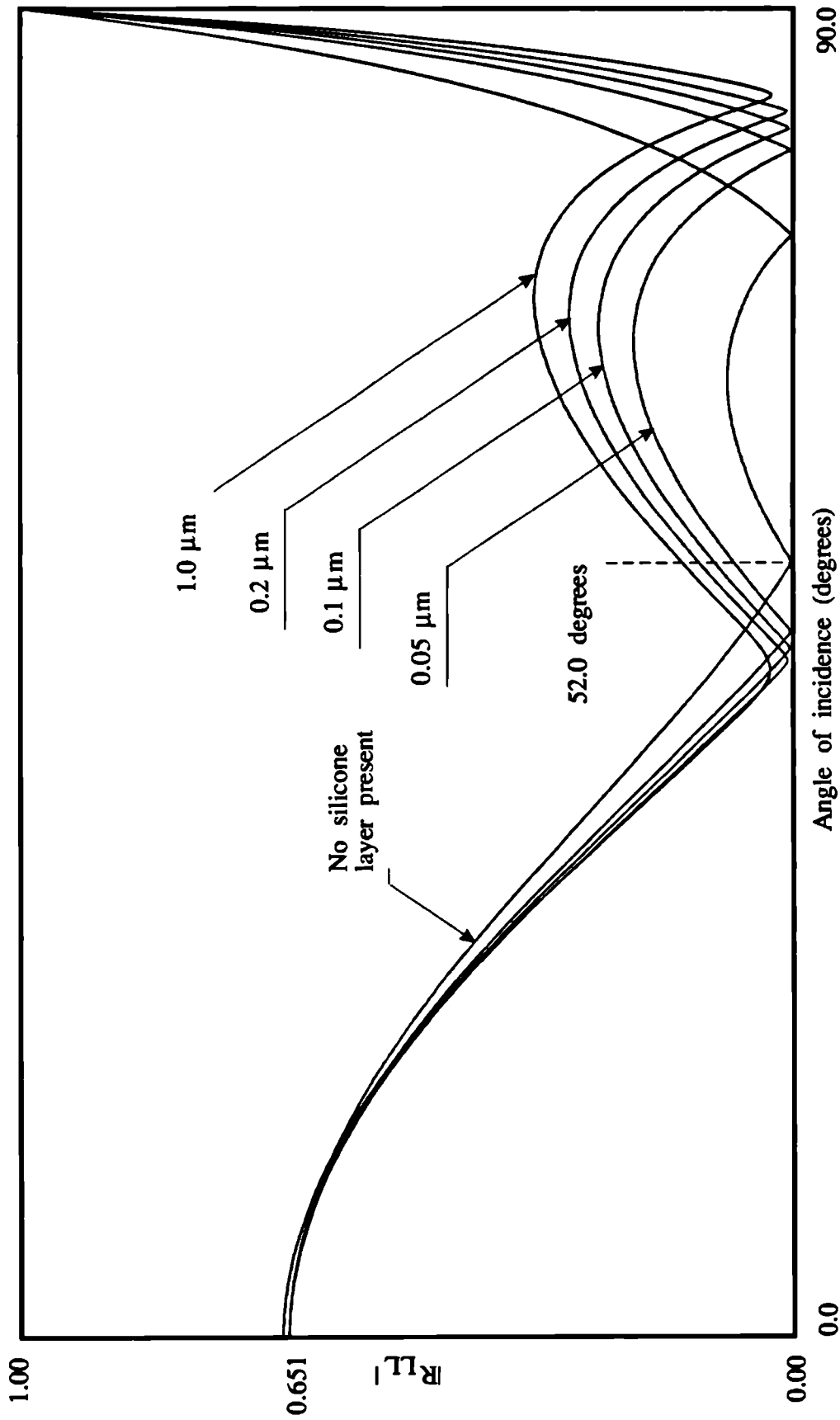
Fig. 4.13 Amplitudes of the longitudinal-longitudinal reflection coefficients from the silicone layers of different thicknesses between glass and epoxy. Frequency 10 MHz. Material properties are given in table 4.4. *Theoretical calculations.*
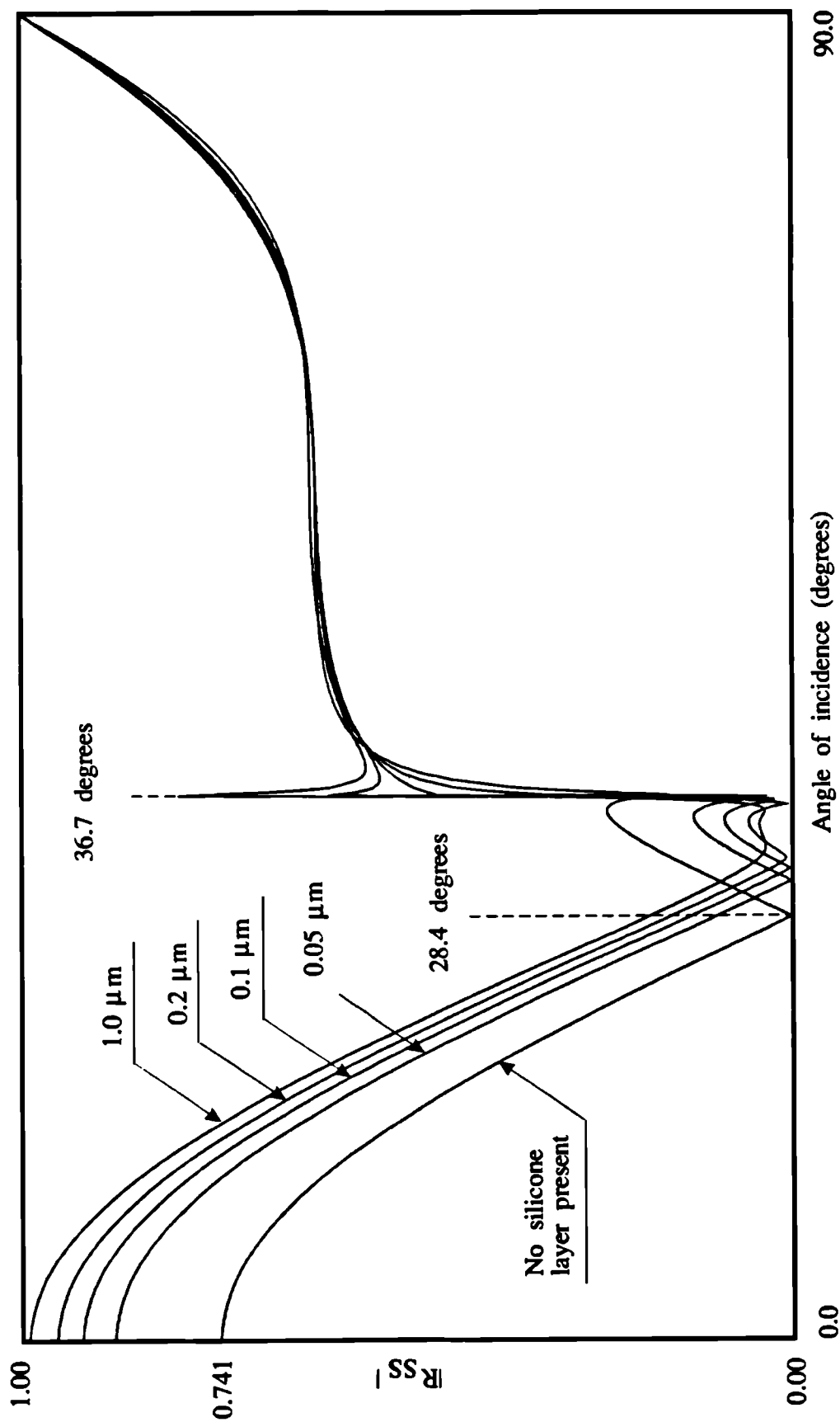
Fig. 4.14 Amplitudes of the shear-shear reflection coefficients from the silicone layers of different thicknesses between glass and epoxy. Frequency 10 MHz. Material properties are given in table 4.4. *Theoretical calculations.*
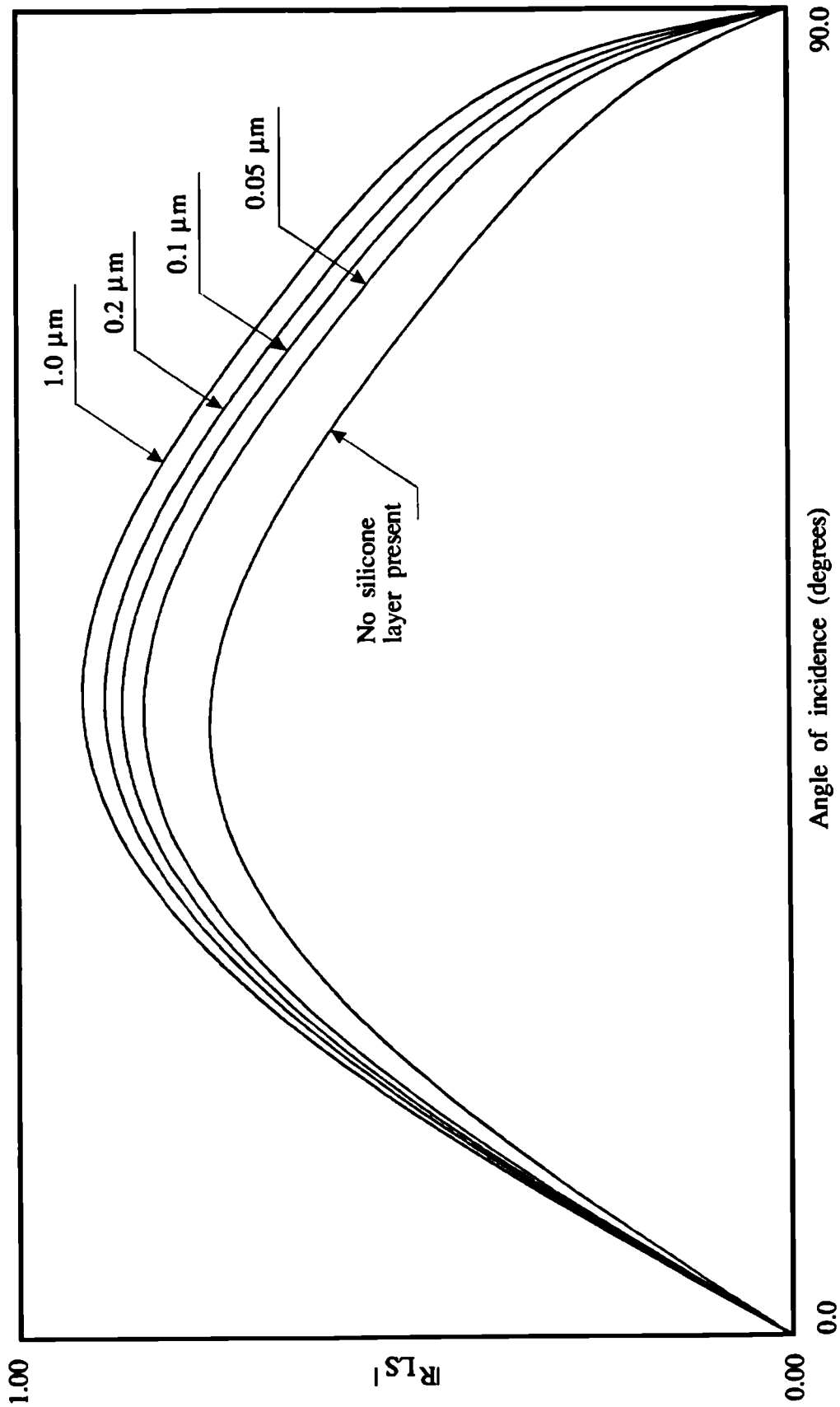
Fig. 4.15 Amplitudes of the longitudinal-shear reflection coefficients from the silicone layers of different thicknesses between glass and epoxy. Frequency 10 MHz. Material properties are given in table 4.4. *Theoretical calculations.*
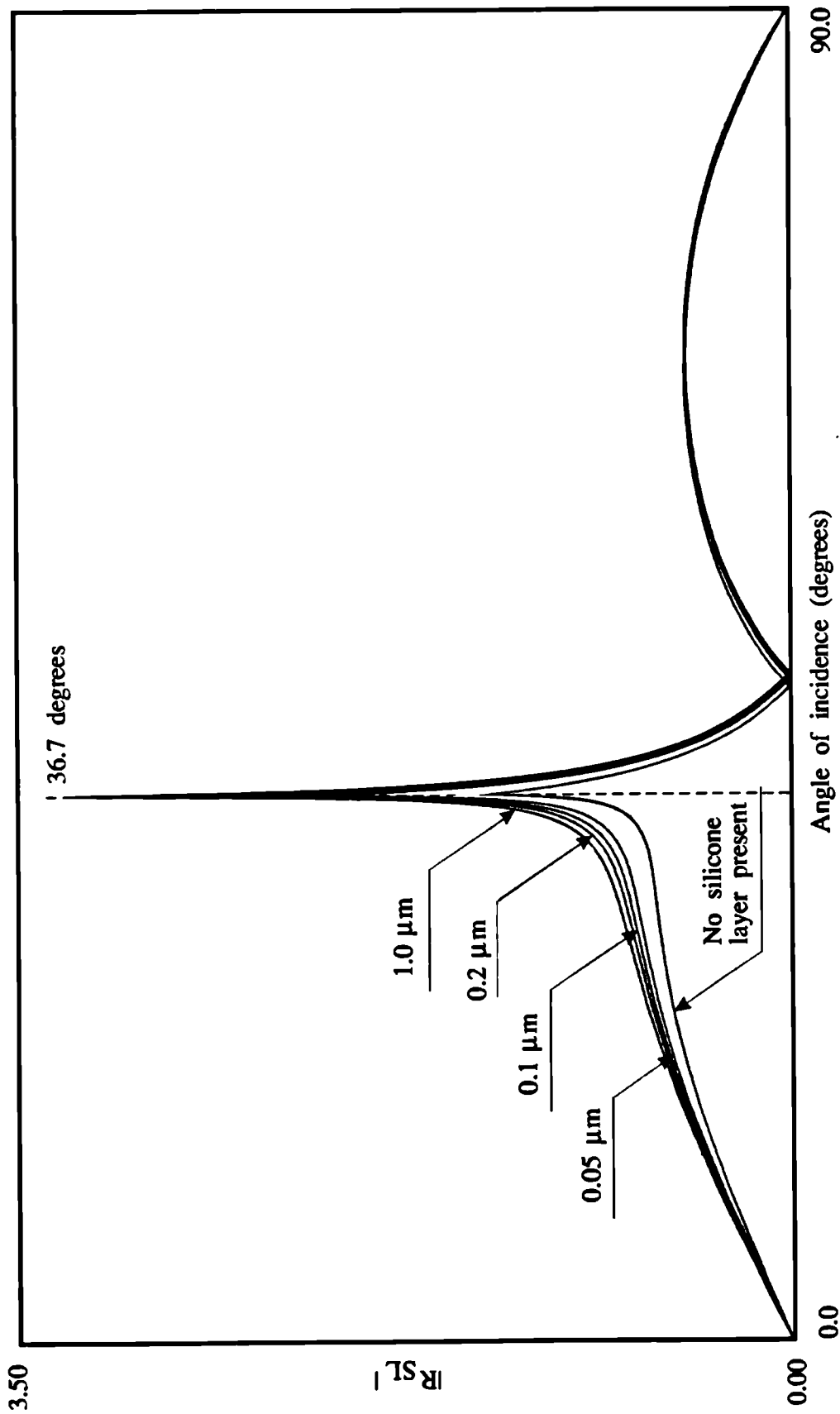
Fig. 4.16 Amplitudes of the shear-longitudinal reflection coefficients from the silicone layers of different thicknesses between glass and epoxy. Frequency 10 MHz. Material properties are given in table 4.4. *Theoretical calculations.*
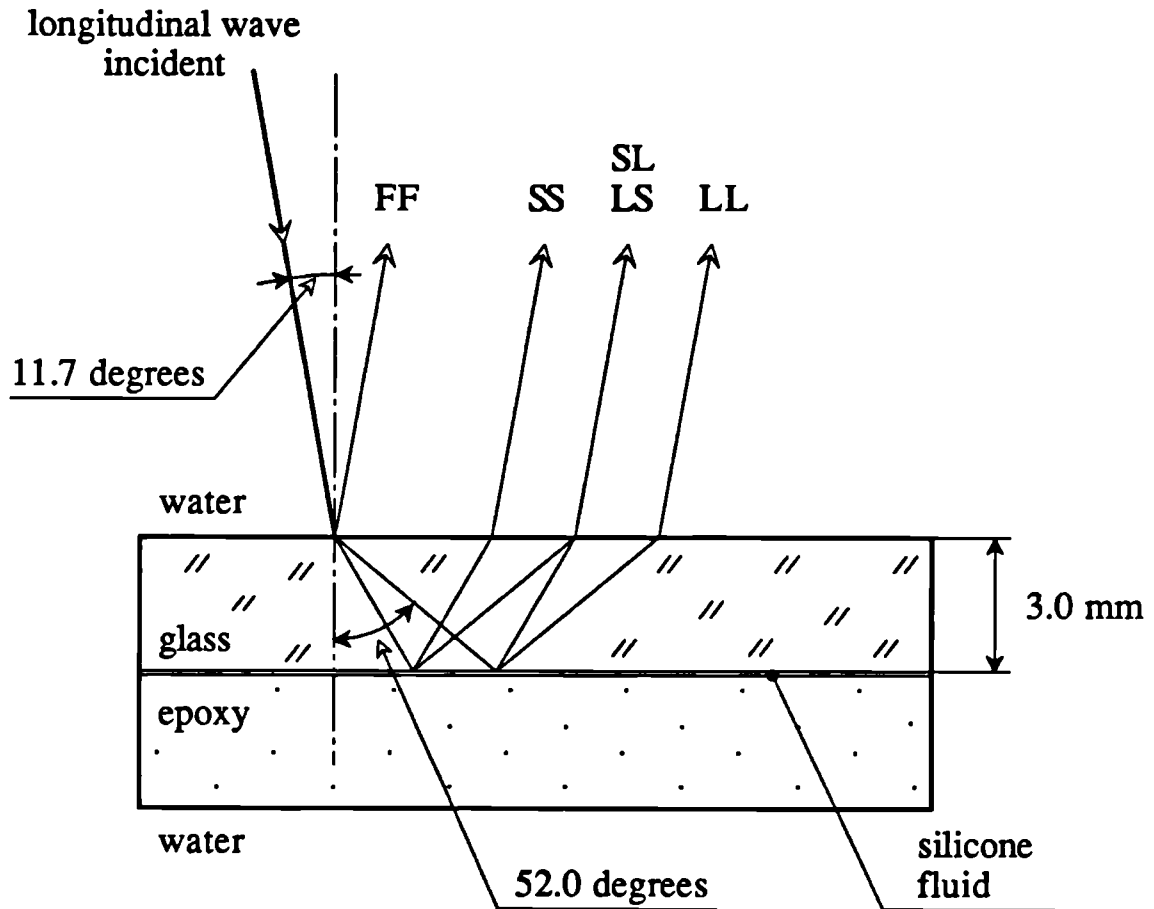
Fig 4.17 Generation of the oblique incidence longitudinal wave in glass.
Angle of incidence in water is adjusted to 11.7 degrees
in order to generate the longitudinal wave in glass incident
at 52.0 degrees at the glass/silicone interface.

FF is the front face reflection,
SS is the shear-shear reflection from the silicone layer,
LS is the longitudinal-shear reflection from the silicone layer,
SL is the shear-longitudinal reflection from the silicone layer,
LL is the longitudinal-longitudinal reflection from the layer.
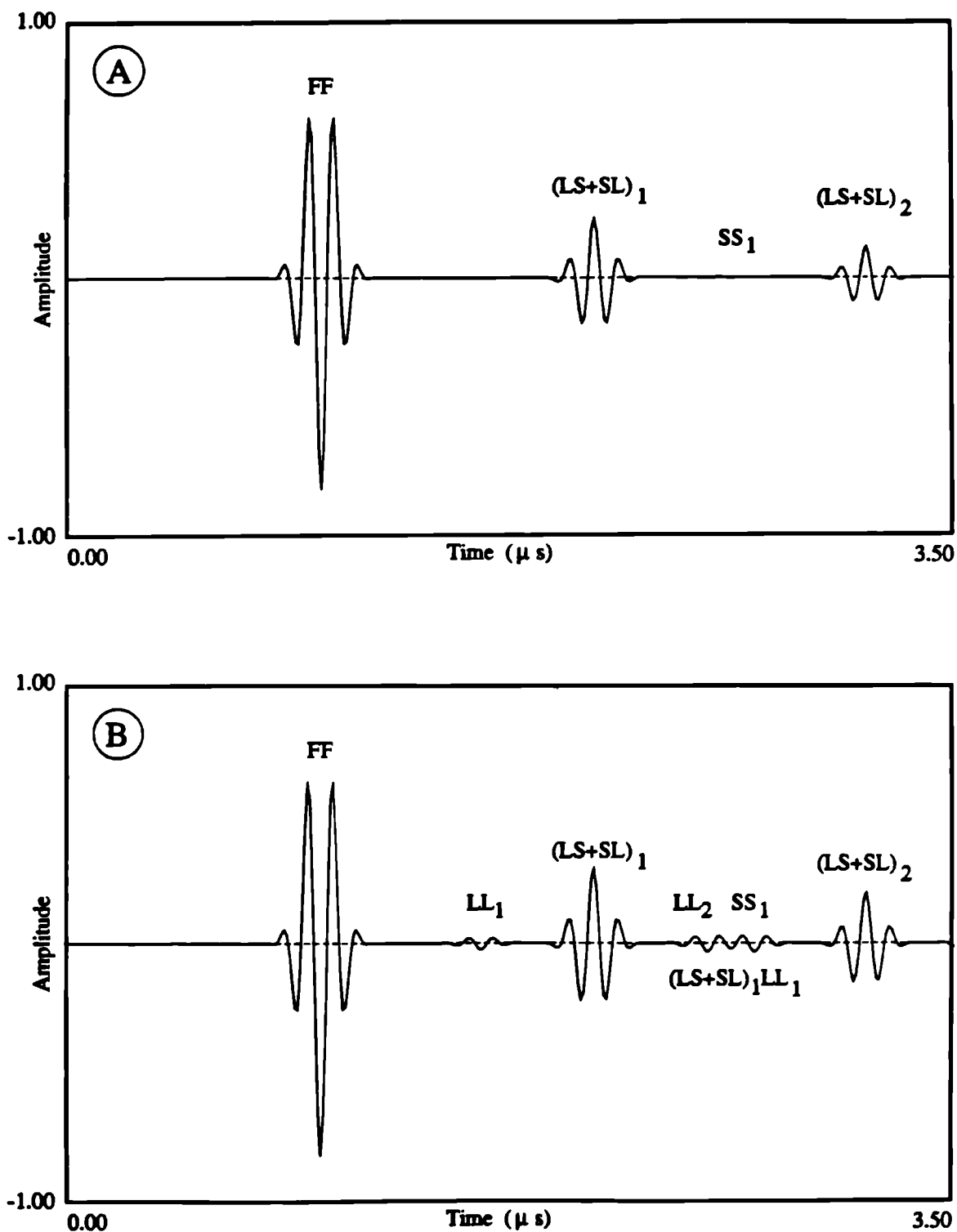
Fig. 4.18 Oblique incidence response of the system comprising a 3.0 mm thick glass plate and
a 3.0 mm thick epoxy resin with and without a silicone fluid in between.
Longitudinal wave excitation at 11.7 degrees in water. (a) No silicone layer present,
(b) 0.5 μm thick silicone layer present. FF is the front face reflection, LS+SL is the
combined LS and SL reflection, LL is the longitudinal-longitudinal reflection, and
SS is the shear-shear reflection from the glass/epoxy interface.
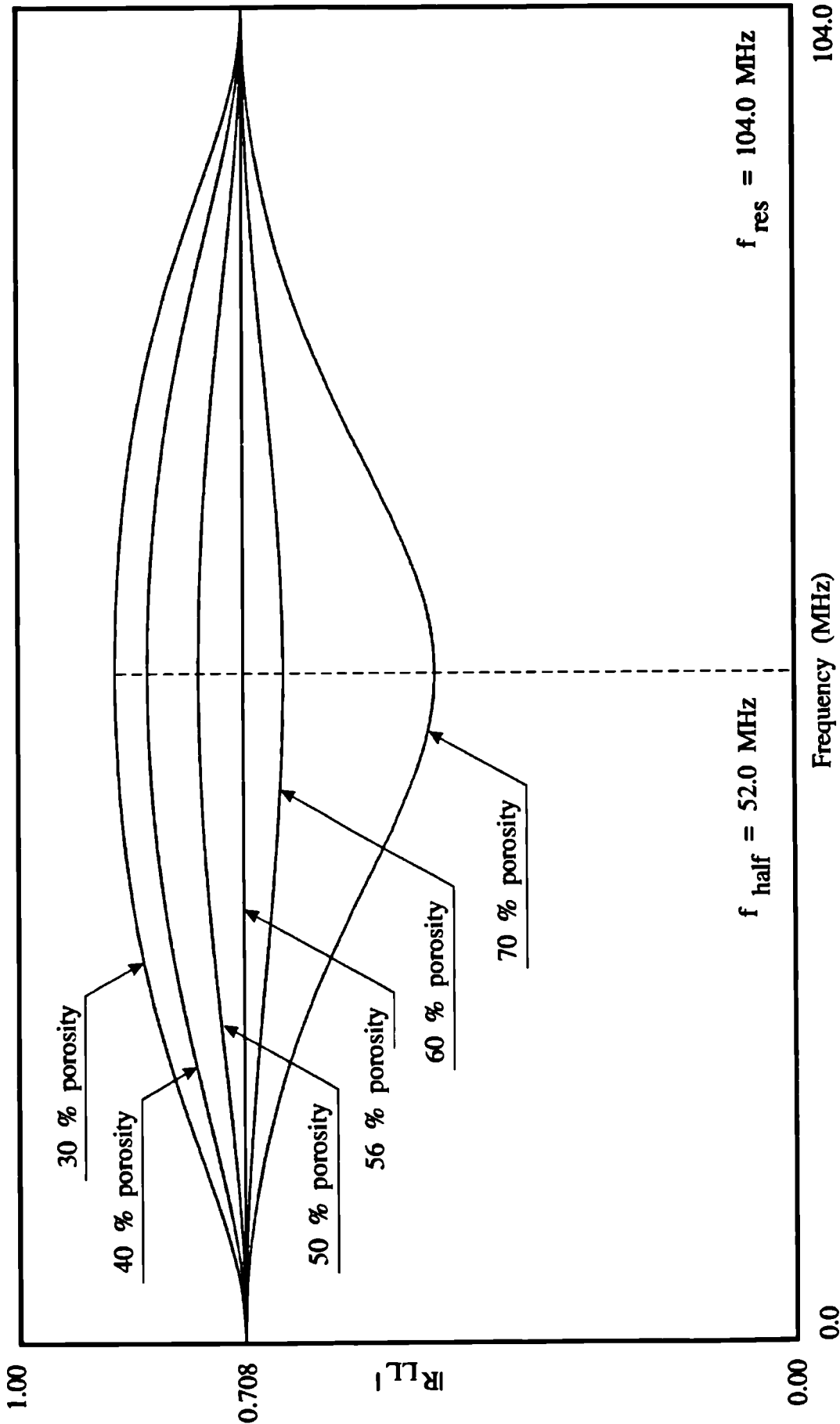
Fig. 4.19 Amplitudes of the normal incidence longitudinal reflection coefficients from the 50 μm thick oxide layers between the aluminium and epoxy half-spaces. Material properties are given in tables 4.8 and 4.9.
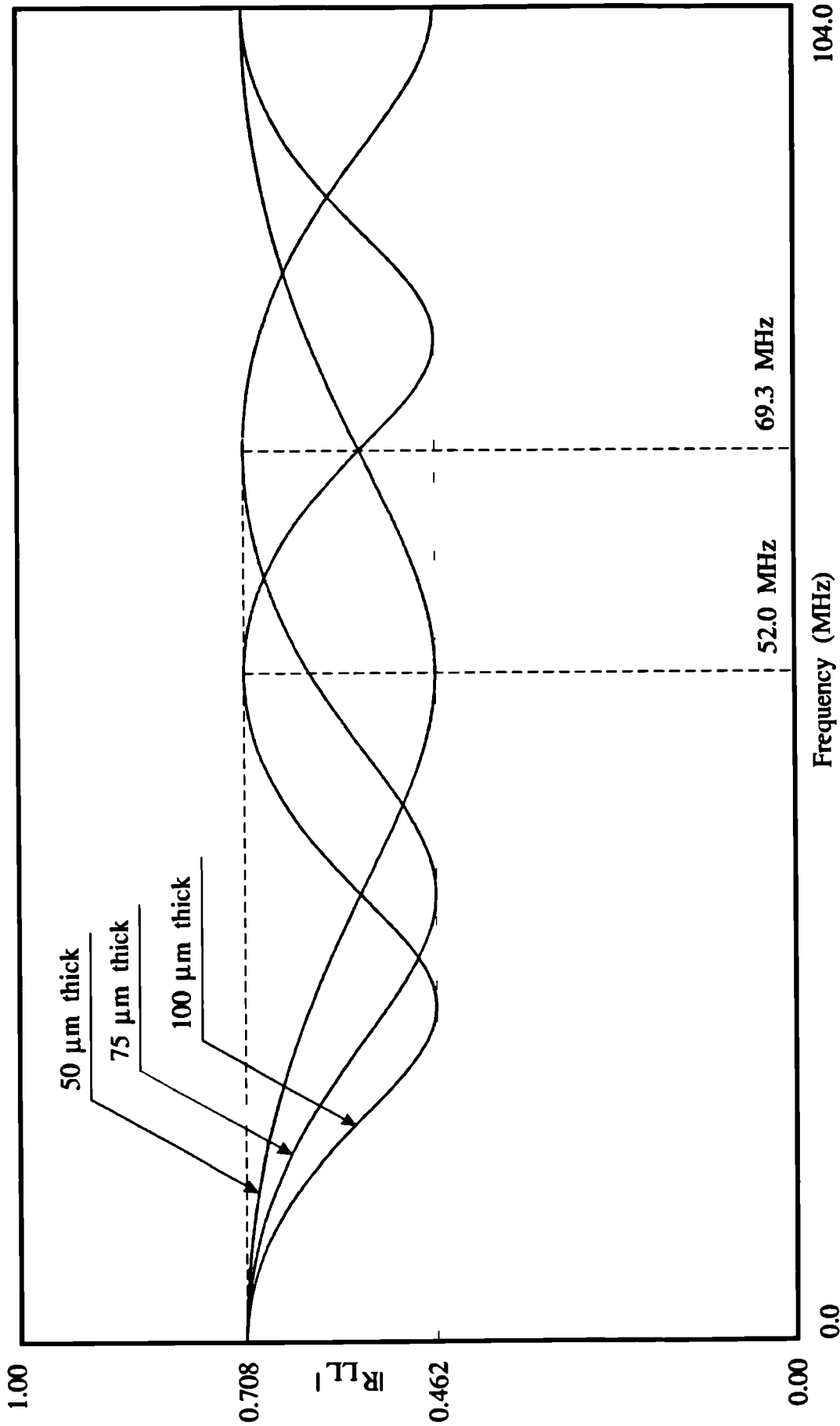
Fig. 4.20 Amplitudes of the normal incidence longitudinal reflection coefficients from the 70 % porous oxide layers between the aluminium and epoxy half-spaces. Different thicknesses of the layers. Material properties are given in tables 4.8 and 4.9.
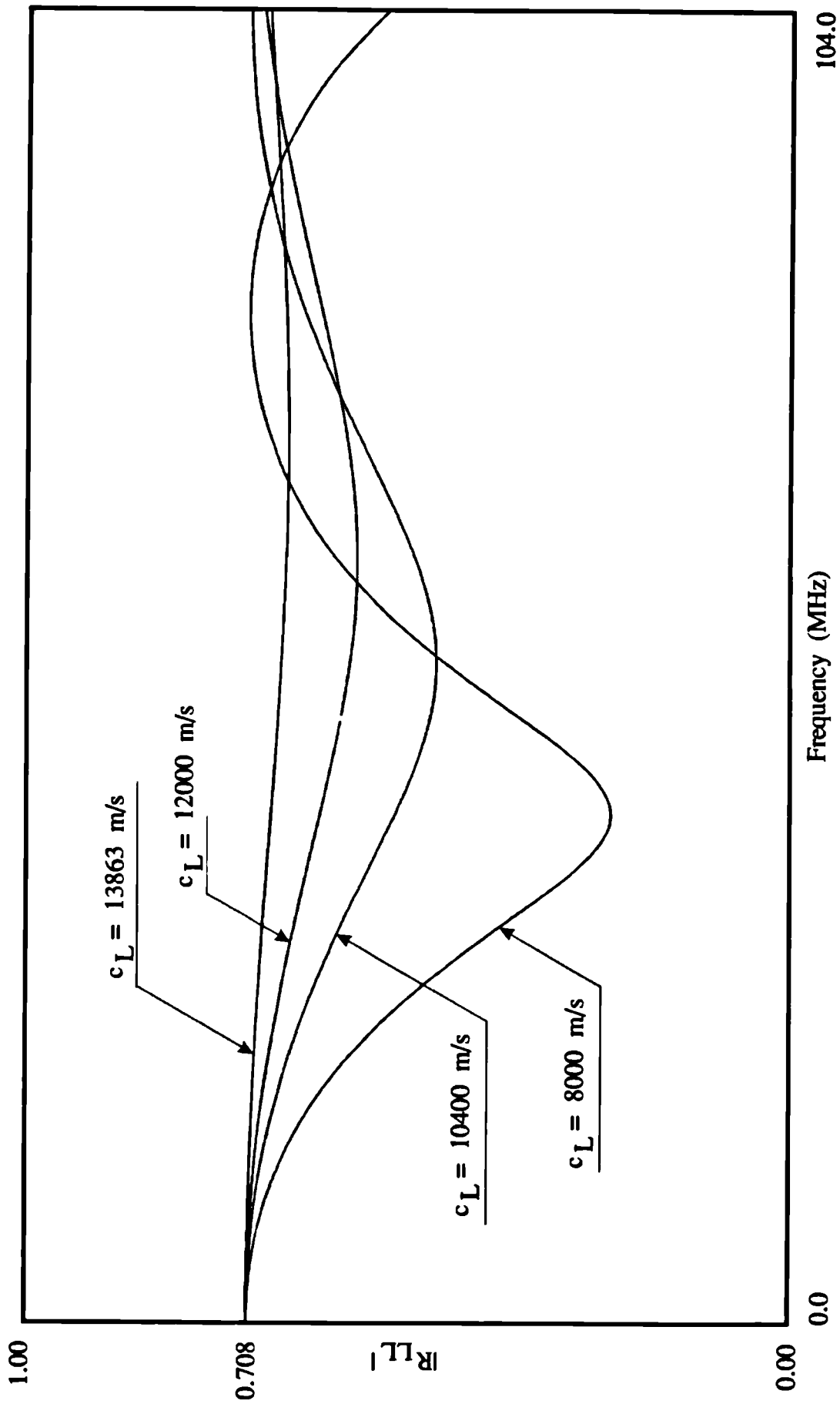
Fig. 4.21 Amplitudes of the normal incidence longitudinal reflection coefficients from the 50 μm thick, 70 % porous oxide layers between aluminium and epoxy. Different longitudinal velocities. Material properties of the half-spaces given in table 4.8.
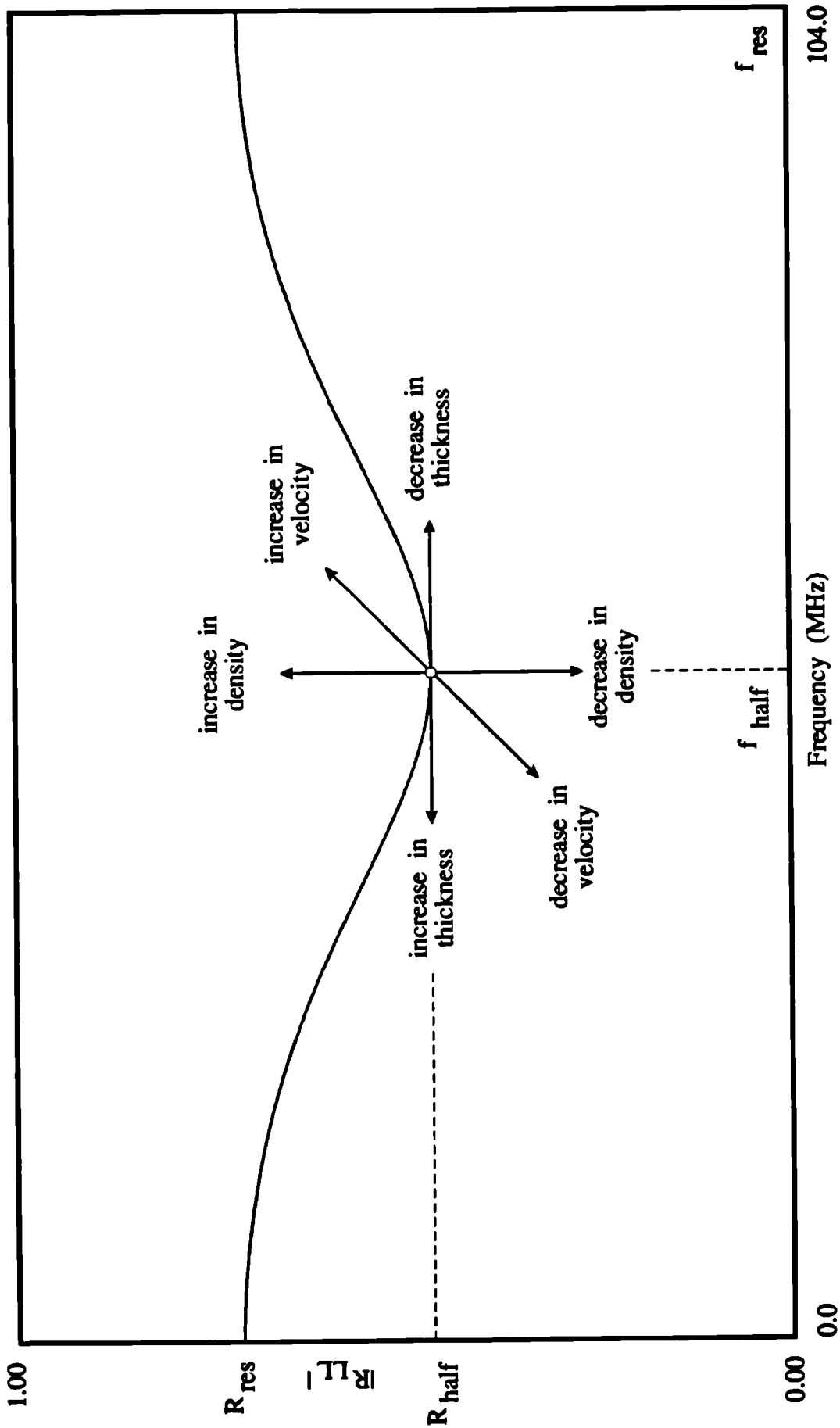
Fig. 4.22 Possible movement of the minimum of the normal incidence longitudinal reflection coefficient for the typical aluminium/oxide/epoxy joint due to the change in the oxide thickness, density and longitudinal velocity.
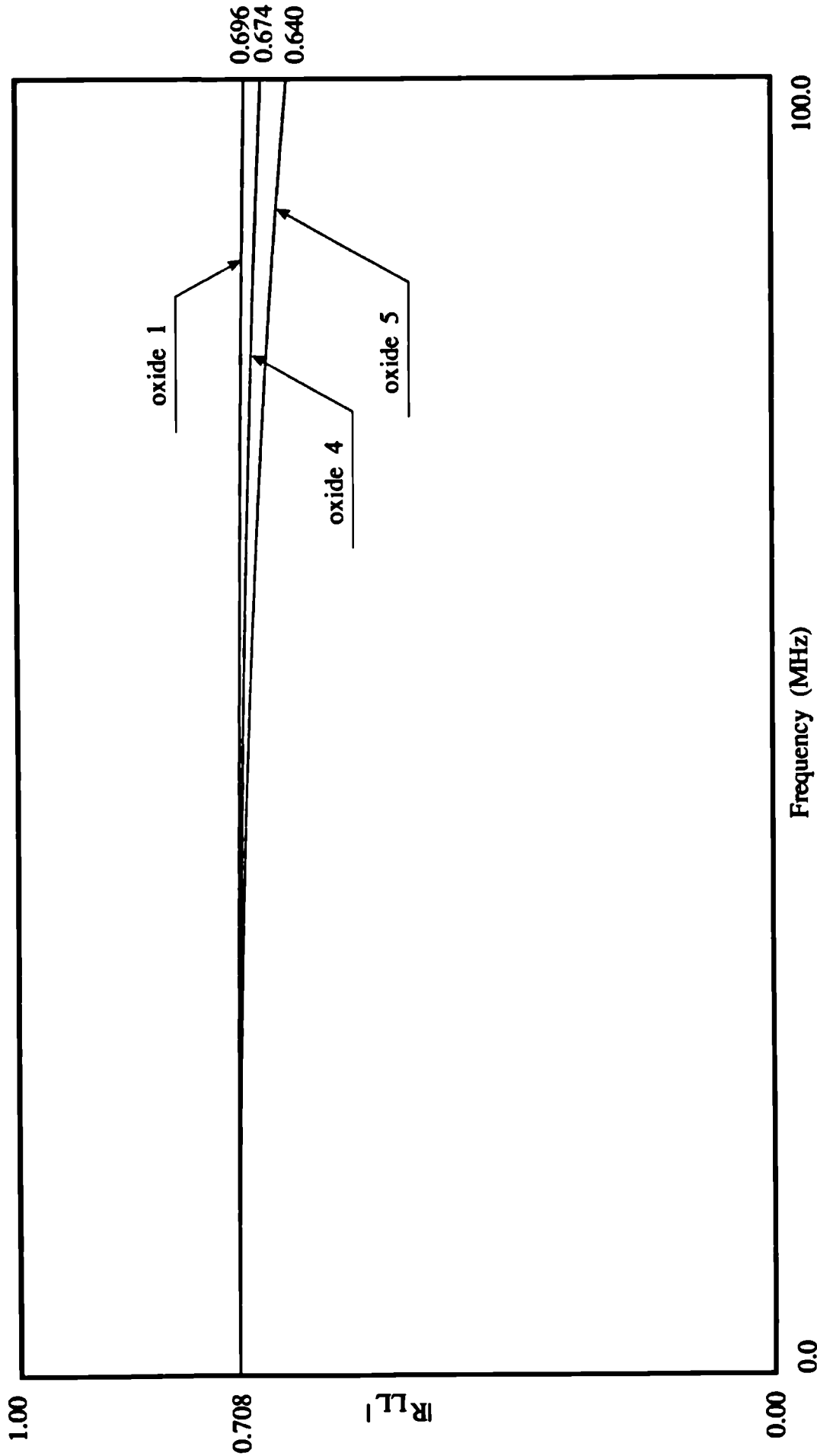
Fig. 4.23 Amplitudes of the normal incidence longitudinal reflection coefficients from the 5 μm thick oxide layers between aluminium and epoxy half-spaces. Longitudinal velocity of oxide varies. Material properties are given in table 4.11.
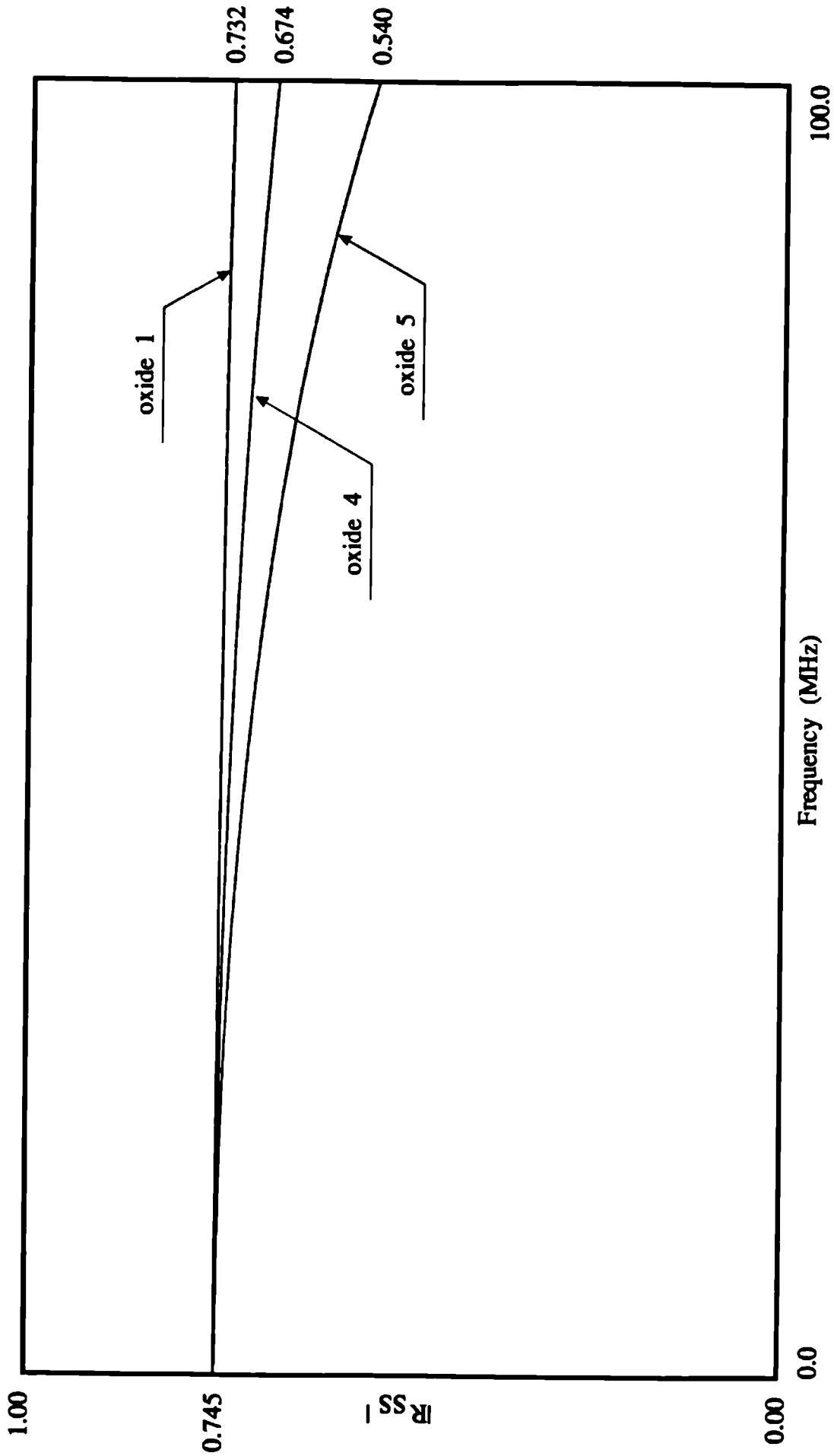
Fig. 4.24 Amplitudes of the normal incidence shear reflection coefficients from the 5 μm thick oxide layers between aluminium and epoxy half-spaces. Shear velocity of oxide varies. Material properties are given in table 4.11.
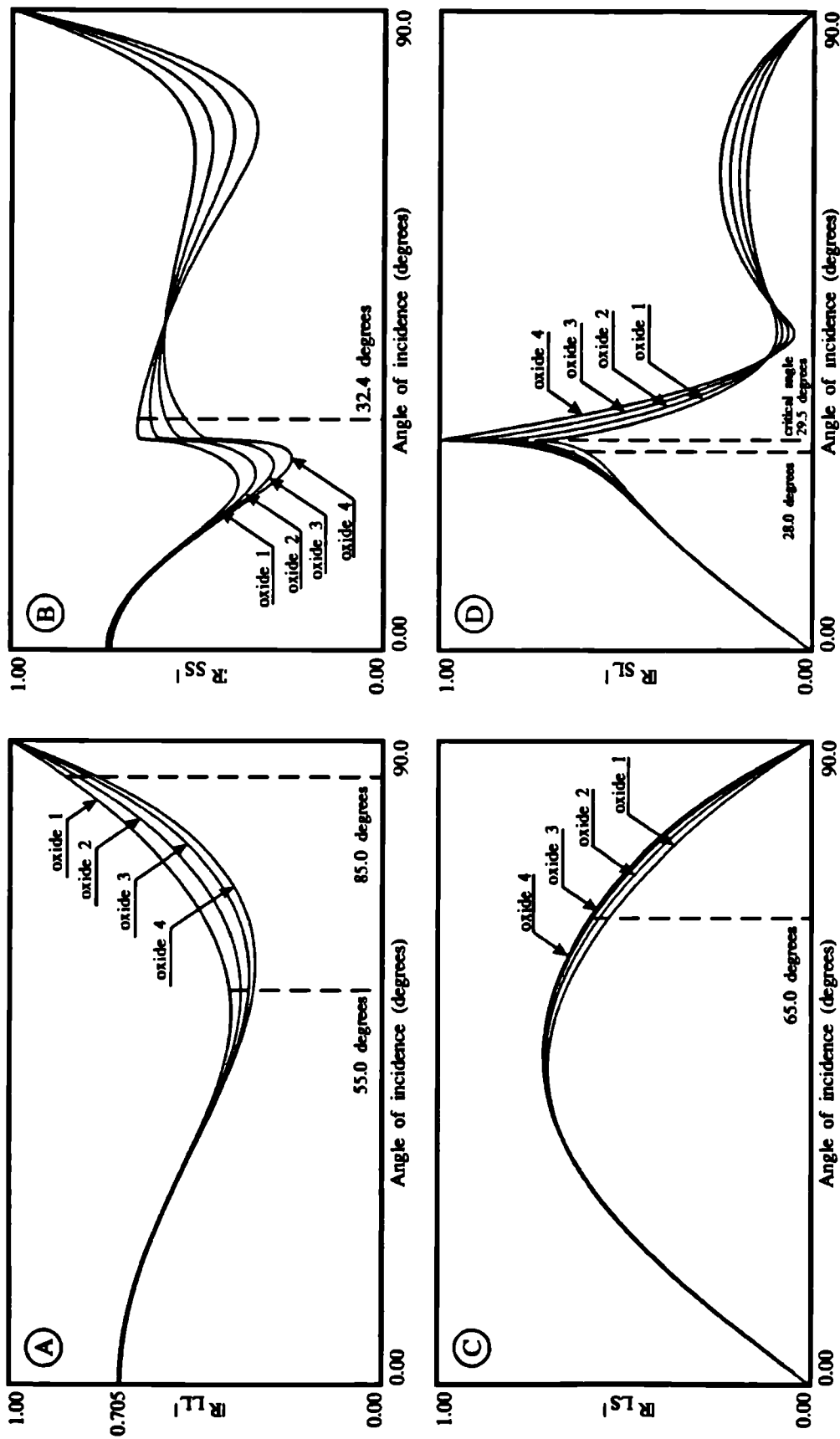
Fig. 4.25 Amplitudes of the reflection coefficients from 5.0 μm thick oxide layers between aluminium and epoxy half-spaces. Frequency 50 MHz. Material properties are given in table 4.11. (A) longitudina-longitududinal, (B) shear-shear, (C) longitudinal-shear, (D) shear-longitudinal.
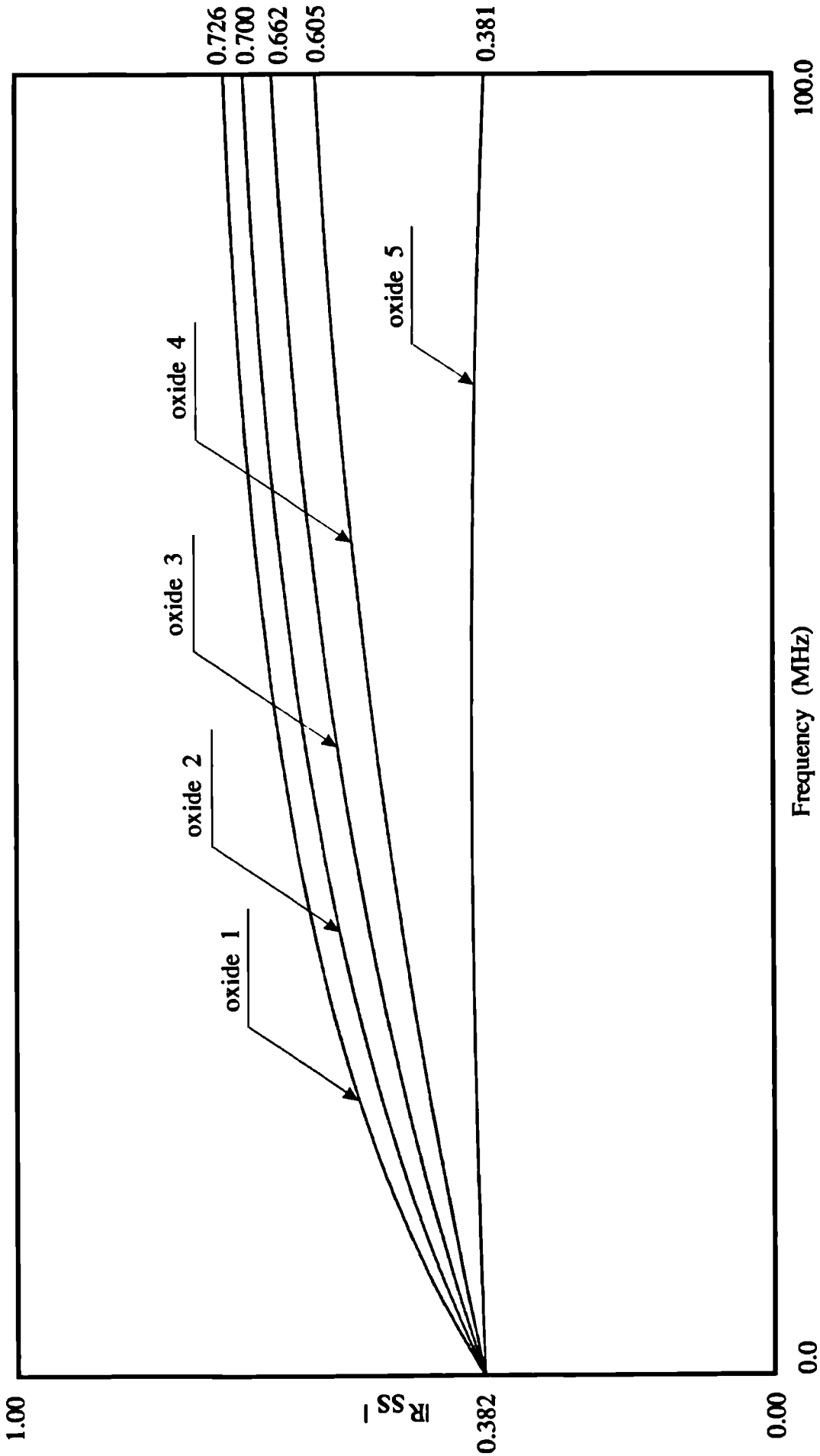
Fig. 4.26 Amplitudes of the shear-shear reflection coefficients from 5.0 um thick oxide layers between aluminium and epoxy half-spaces. Angle of incidence 32.4 degrees. Material properties are given in table 4.11.
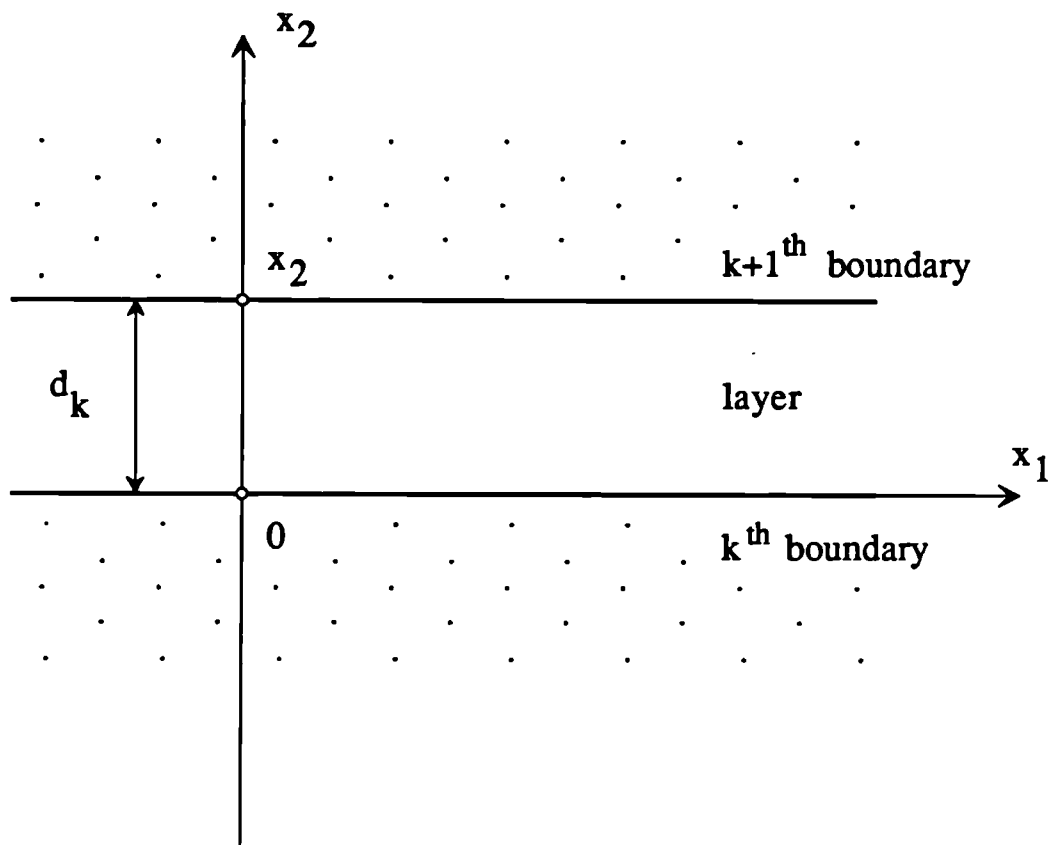
Fig. 4.27   Derivations of thin layer approximation.
Coordinate system position with respect to the layer.
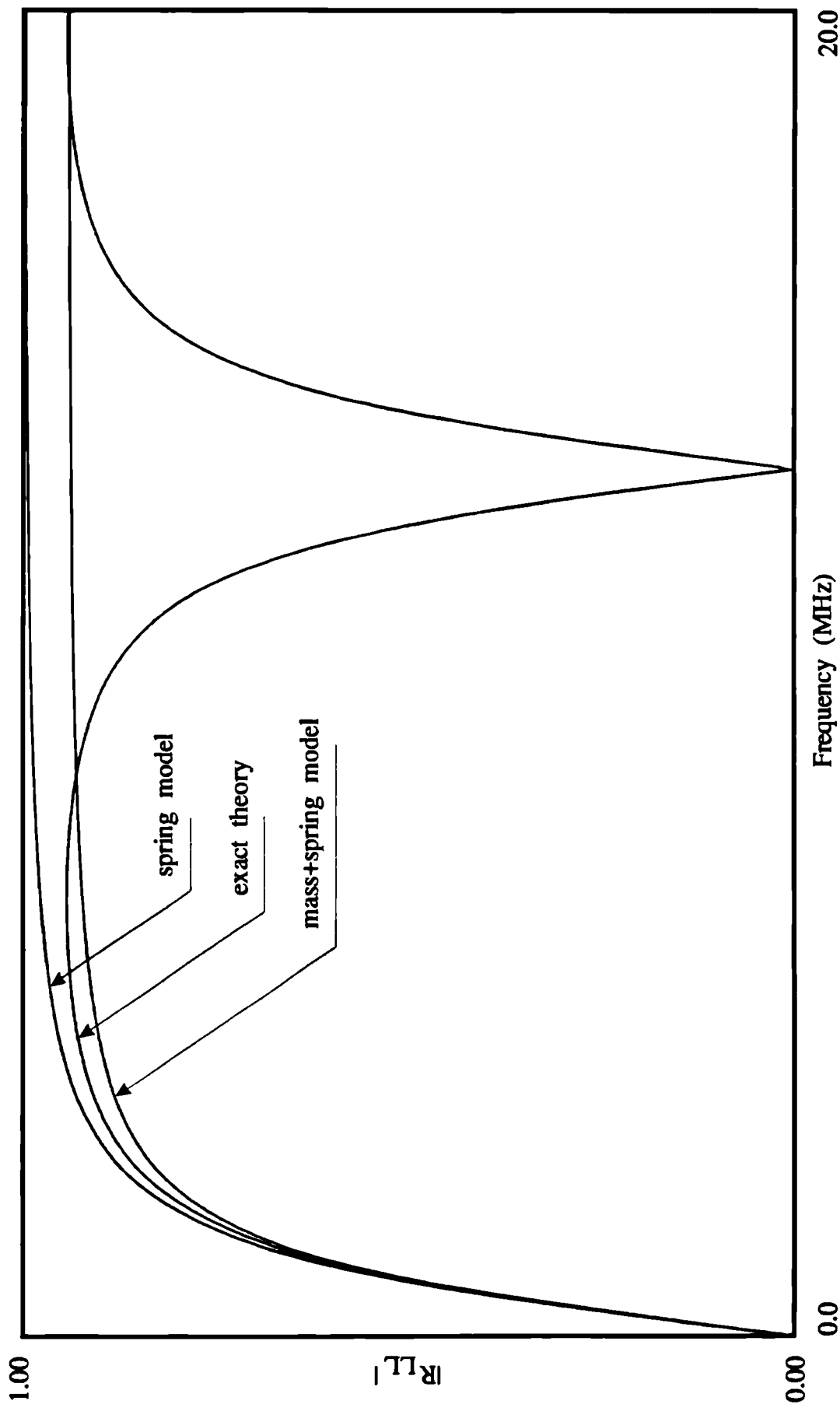
Fig. 4.28 Amplitudes of the normal incidence longitudinal-longitudinal reflection coefficients from 0.1 mm thick epoxy layer between aluminium half-spaces. Comparison between the exact solution and the approximate theories.
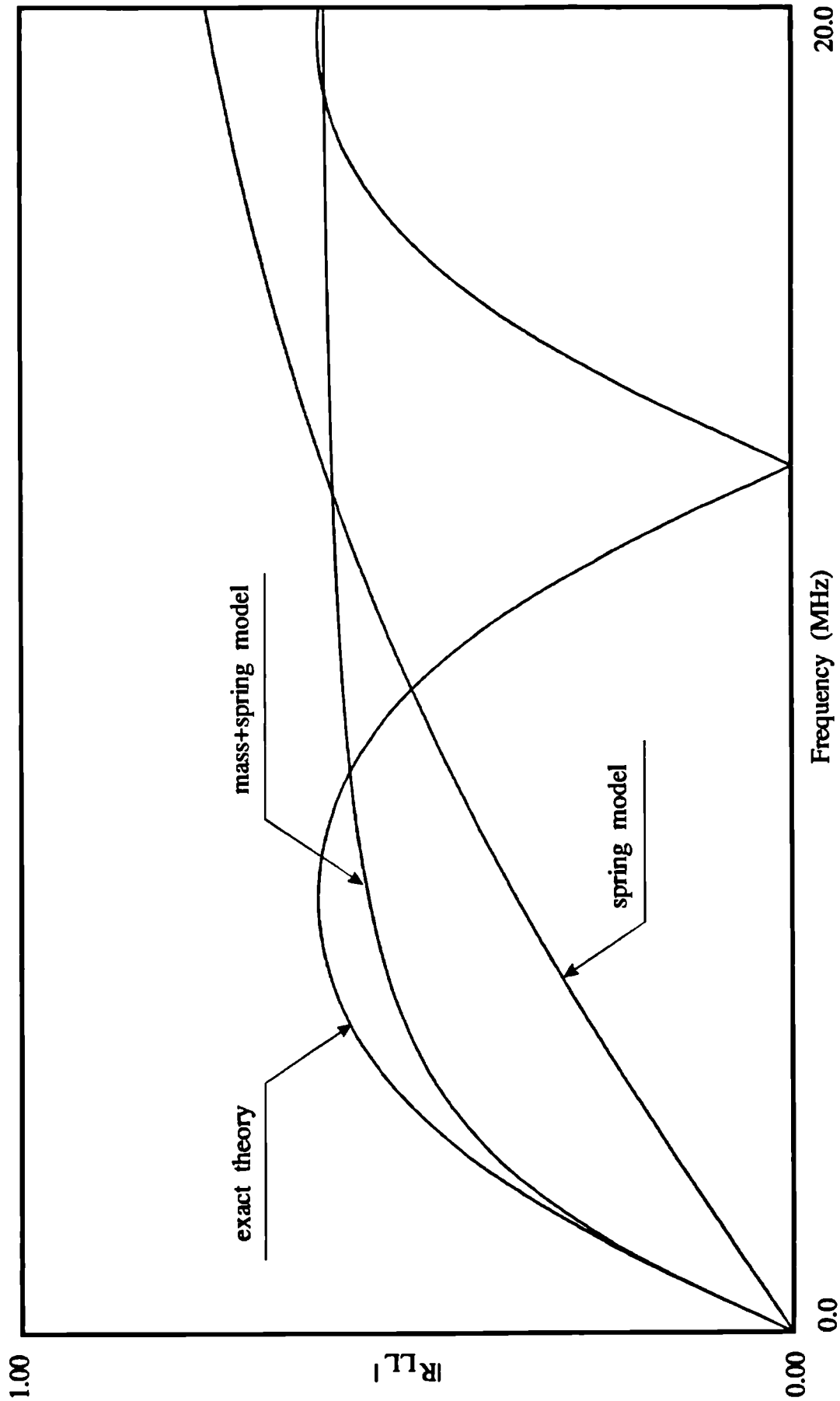
Fig. 4.29 Amplitudes of the normal incidence longitudinal-longitudinal reflection coefficients from 0.1 mm thick epoxy layer in water. Comparison between the exact solution and the approximate theories.
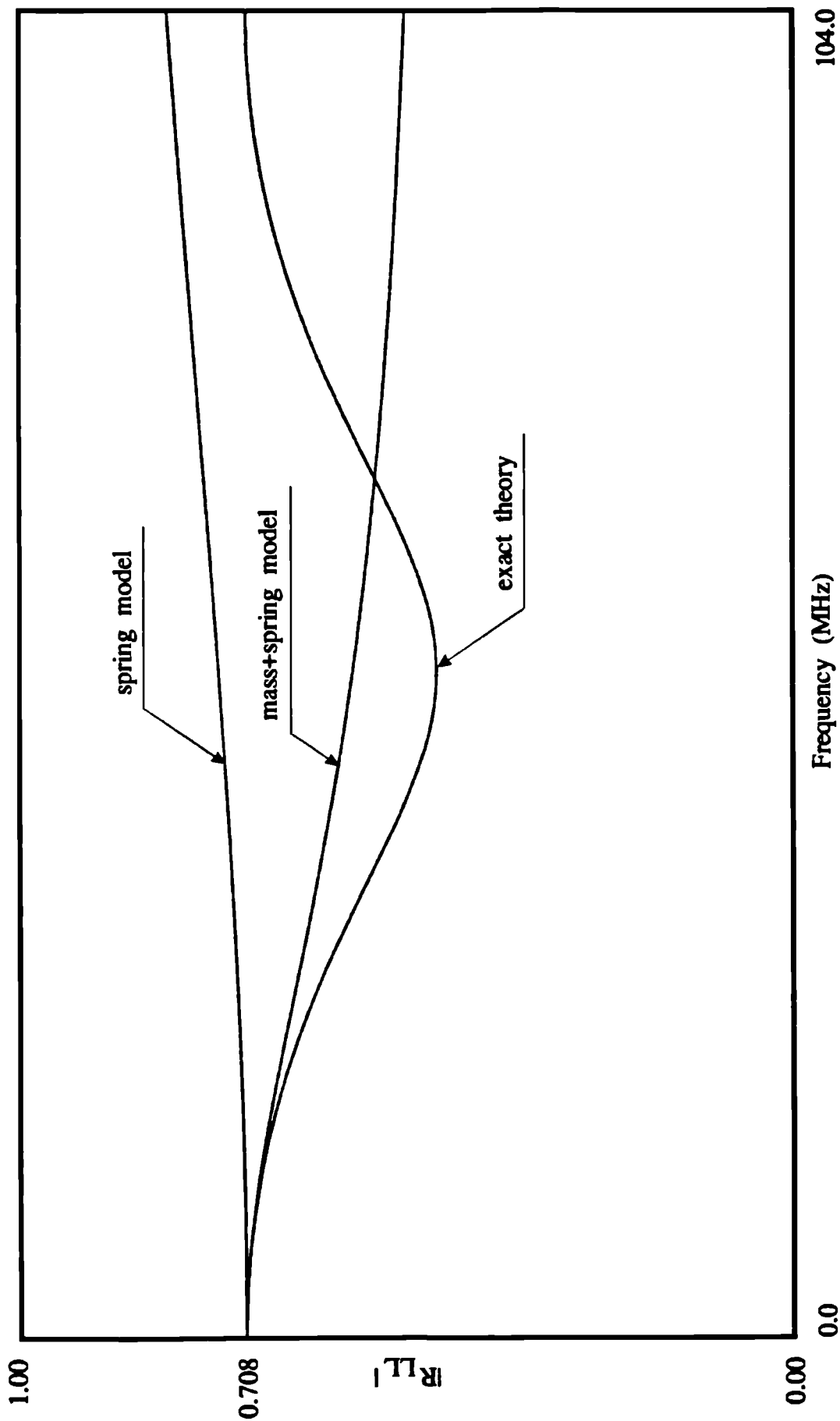
Fig. 4.30 Amplitudes of the normal incidence longitudinal-longitudinal reflection coefficients from the 50 μm thick oxide layer between the aluminium and epoxy half-spaces. Comparison between the exact solution and the approximate theories.
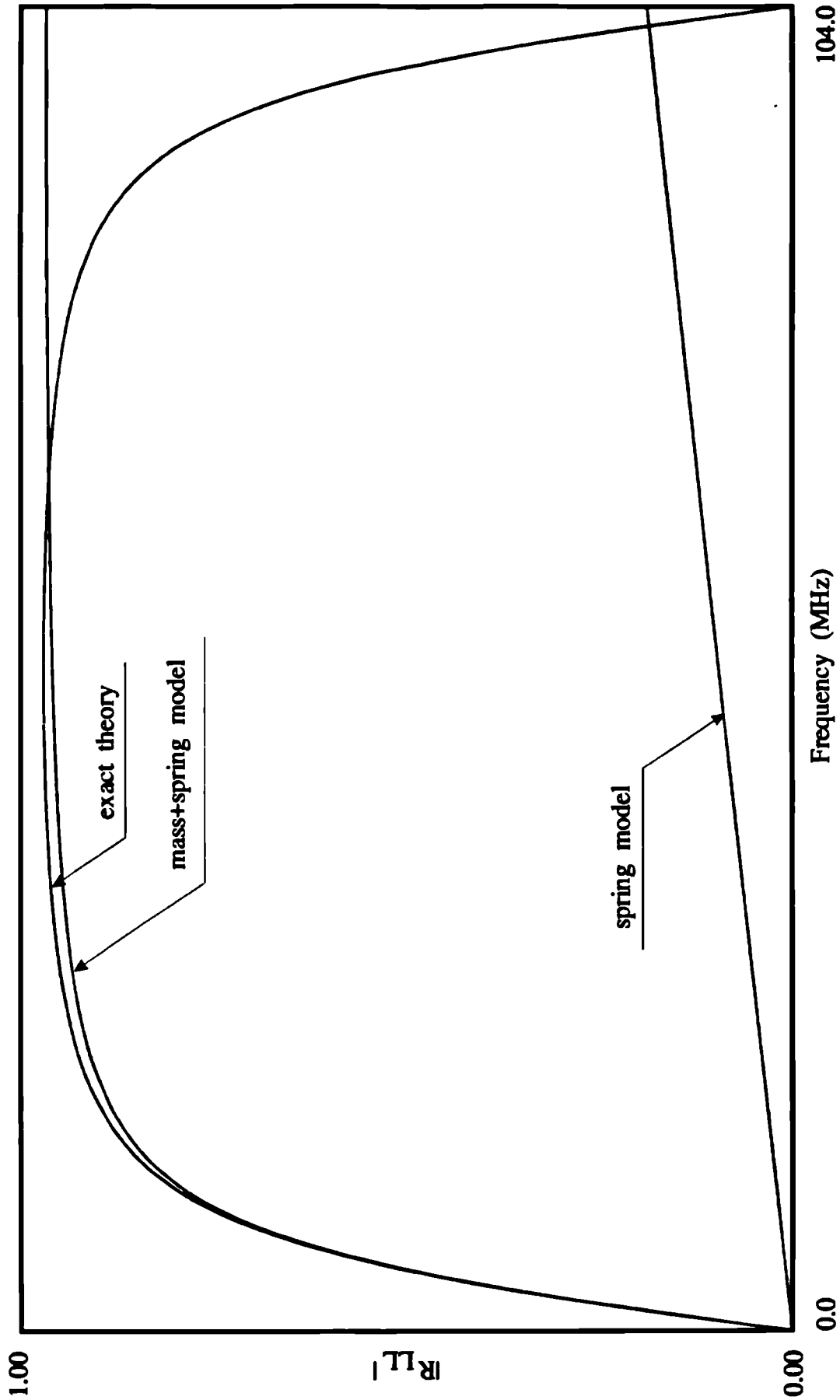
Fig. 4.31 Amplitudes of the normal incidence longitudinal-longitudinal reflection coefficients from the 50 μm thick oxide layer in water. Comparison between the exact solution and the approximate theories.
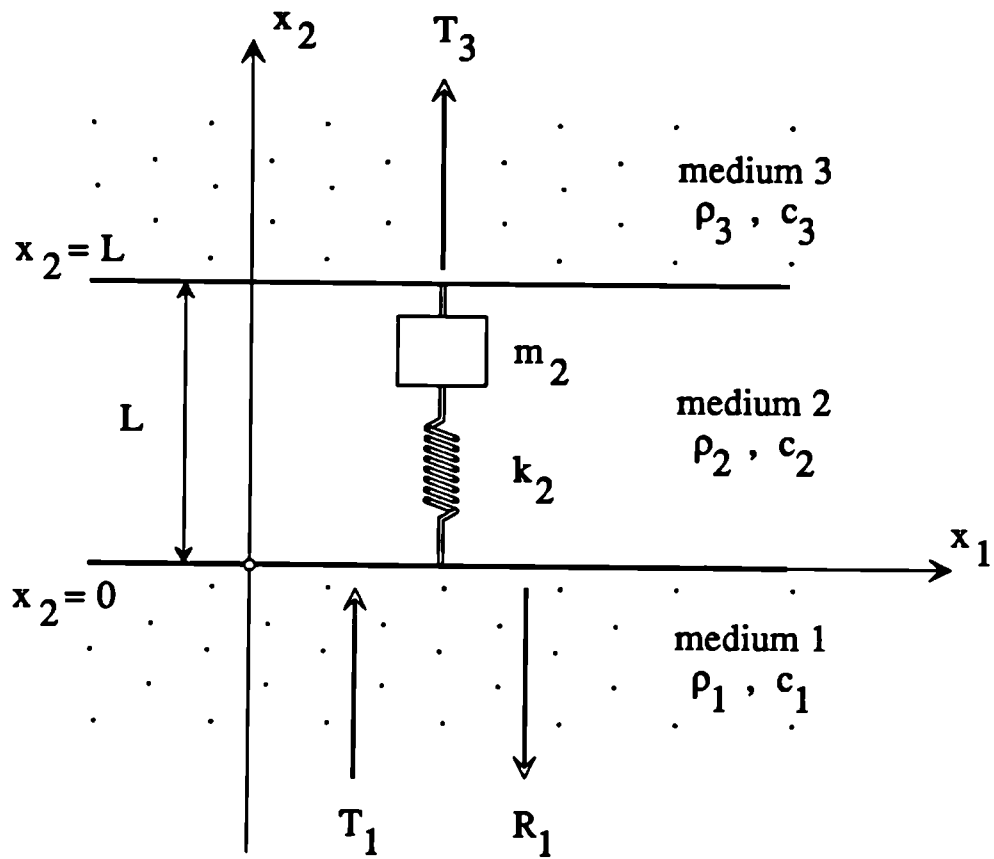
Fig. 4.32 Mass+spring approximation of a thin layer.

CHAPTER 5

Validation of the theory.
Accuracy of the reflection coefficient measurements

5.1 Introduction

Chapter 5 is concerned with the practical aspects of ultrasonic reflection coefficient measurements from multilayered viscoelastic plates at normal and oblique incidence. Here a detailed description of the measurements is given, the validation of the theory developed so far is carried out, and an error assessment of the experiments is worked out.

In chapters 2, 3, and 4 various theories were developed in order to model the response from multilayered viscoelastic plates to real ultrasonic transducer excitation. The most complicated one has been given in section 3.4 where the steady state harmonic field generated by a finite-sized transducer is represented as a Fourier integral of the plane waves of the same frequency, but different angles of propagation. Similarly, the plate response to such an excitation is obtained in the form of the Fourier integral of the reflected plane wave components. Despite its generality, however, this theory suffers major drawbacks in practical use. First of all, in order to model responses of multilayered systems to impulse excitation, the input pulse has to be firstly Fourier-transformed to the frequency domain, and then, for each harmonic steady-state process, further decomposition of the finite beam has to be carried out (a single Fourier integral for the two-dimensional case, a the double Fourier integral for the three-dimensional model). After solving the plane-wave reflection coefficient problems for each of the wave components, the inverse Fourier integrals, first in the spatial domain and then the frequency domain, have to be calculated. As one can clearly see, this poses a very substantial demand on the power of the computer used. For this reason, only the two-dimensional models were used for the purpose of the theory validation. The second drawback is that the more general theory is complicated and cumbersome to use, and therefore a better physical insight into the ultrasonic reflection problem might be obtained using less sophisticated, and perhaps less general, but simpler models. These simplified models can be less accurate than the exact one, but they are very handy to use, and therefore more appealing in practice. However, an awareness of their limitations have to be born in mind, as limits of applicabilty are inherent parts of the simplified theories.

Chapter 5   176

Validation of the theory. Accuracy of the reflection coefficient measurements

The infinite plane wave reflection coefficient model is one of the simplified theories used in this chapter. Here, the transmitter and receiver are treated as infinite planes, or in other words, the sizes of the transducers are considered as second order factors and are therefore disregarded.

When a reliable measurement procedure is established and the theoretical models derived, the most important question is the degree of agreement between the two. First of all we would like to know how good the most sophisticated theory is in comparison with the measurements and, if discrepancies are encountered, where the differences come from. Then, the simplified theory can be validated against the measurements and the more accurate theory. The intention of this chapter is to give a quantitative answer to these problems.

In section 5.2 the methodology of the reflection coefficient measurements at oblique incidence is given in detail. Descriptions of the measurement rigs, the transducer arrangements, as well as the electronic equipment and data processing procedures are given.

In section 5.3 one of the experimental procedures described in section 5.2 is used to measure the reflection coefficient at a water/aluminium interface, which serves here as an example of an easily accessible interface. The theoretical predictions using the infinite plane wave model and the finite transducer theory are compared with the measurements.

In section 5.4 measurements of the reflection coefficients from an aluminium/water interface are performed. This is the first example of the embedded interface problem, where the measurement procedure has to take into account different angles of refraction of different waves, and the pulse reverberations within the plate. The measurements are compared here with the finite transducer and the infinite plane wave models.

In section 5.5 the system comprising a very thin silicone fluid layer between two glass plates is analysed both experimentally and theoretically. Comparisons between the theoretical predictions and the measurements at some chosen angles of incidence are presented to establish the validity of the theoretical models, as well as the accuracy of the experiments.

Section 5.6 summarises the main points of the chapter.

5.2 Methodology of the reflection coefficient measurements

In section 2.3, the reflection coefficient was defined as the ratio of the amplitudes of the reflected harmonic plane waves to the amplitudes of the incident harmonic plane waves. Thus

the reflection coefficient measurement procedure can be performed in two stages. Firstly, in order to measure the incident wave, a reference signal can be captured in a face-to-face transducer arrangement as shown schematically in fig. 5.1(a). Subsequently, the probes can be arranged as shown schematically in fig. 5.1(b), so that the transmitter and receiver are inclined at a given angle θ with respect to the perpendicular to the interface. Division of the spectrum of the reflected signal by the spectrum of the reference signal then yields a reflection coefficient spectrum for a given angle of incidence θ and a given frequency range.

5.2.1 Description of the measurement rig

In order to be able to measure oblique incidence reflection coefficients a mechanism for the probe arrangement was designed and manufactured. Let us illustrate the concept behind the design of the mechanism. Figure 5.2 shows two ultrasonic transducers, transmitter and receiver, attached to two arms, the right arm and the left arm, which are in turn attached to a bearing which is the common axis of rotation for the two arms. Both transducers are positioned so that they point towards the axis of rotation of the arms. It can clearly be seen from the drawing that both transducers point towards the axis of rotation of the arms regardless of the angle, θ, they make with the line perpendicular to the specimen. If the top face of the specimen lies in the plane of the axis of rotation of the arms, then the transmitter and the receiver are directed towards the same point on the face of the specimen regardless of the angle θ. This in turn means that the reflection coefficients from free surfaces can be measured at different angles of incidence by simple adjustments of the angle θ, and without any repositioning of the specimen. The specimen, however, has to be carefully positioned before the first measurement is taken, as its top surface must lie in the plane of the axis of rotation of the arms and be perpendicular to the vertical plane which bisects the angle between the arms. Therefore, the measurement rig has to be capable of fine adjustments of the the specimen's vertical position, (translation along the y direction), pitch (θ_z rotation), as well as roll (θ_x rotation).

Figure 5.3 shows the drawing of the reflection coefficient meter (RCM). The whole rig can be divided into three separate mechanisms, the first being the arm and the transducer holder mechanism, the second the lead screw and follower mechanism, and the third one the specimen positioning table mechanism.

As described above, the arm and the transducer holder mechanism is responsible for the accurate and reliable positioning of the ultrasonic probes. The axis of rotation of the two arms is near the base of the RCM, where a large diameter bearing can be seen. This bearing is the most important element of the RCM design, as it is required that the two transducers stay in plane regardless of the angle of inclination of the arms.

Chapter 5   178

Validation of the theory. Accuracy of the reflection coefficient measurements

The lead screw and follower mechanism is responsible for the rotation of the arms so that the angle of incidence of the transducers can be adjusted. The main requirement here is that the positional links are of the same length and the follower path is a straight line passing through the axis of the main bearing.

The specimen positioning mechanism is responsible for the adjustment of the position of a specimen before the reflection coefficients are taken. As described previously, the mechanism can rotate a specimen about two perpendicular axes (pitch and roll), and can change its elevation.

5.2.2 Electronic equipment used

The electronic equipment used for the reflection coefficient measurements can be divided into three main parts, the first being responsible for the dynamic excitation and reception of the response from the specimen under test, the second one is the data acquisition unit, while the third performs signal processing of the incoming data (see fig. 5.4).

The system used for the dynamic excitation and reception of the response from the tested specimen comprises the pulser-receiver and a pair of ultrasonic transducers. The pulser generates short duration electrical spikes, hundreds of volts high, which are converted into acoustic pulses by the transmitting ultrasonic transducer. The receiving ultrasonic probe converts the acoustic pulses coming from the system under test into electrical pulses which, in turn, are amplified to obtain signals whose amplitudes are of the order of one volt.

A digital oscilloscope has been used as the data acquisition unit. It converts the data coming from the pulser-receiver system into digital format, which can be stored in a file or processed.

A desktop IBM PC compatible microcomputer has been used for the signal processing. The microcomputer also controls the digital oscilloscope and other peripheral devices like plotters and printers.

5.2.3 Description of data processing sequence

The reflection coefficient is defined as the ratio of the amplitude of the reflected wave to the amplitude of the incident wave. In experimental work, the reflection coefficient is obtained in two stages. Firstly the transmitter and receiver are carefully arranged face-to-face, as shown in fig. 5.1(a), and a pulse transmitted between them is captured. This pulse can be regarded as the

reference signal with respect to which reflected signals can be assessed. After the specimen has been mounted on the table, carefully aligned, and the angle of the probes adjusted (see fig. 5.1(b)), the reflected pulse is captured and a Fast Fourier Transformation is performed on it. The division of the spectrum of the reflected pulse by the spectrum of the reference pulse yields the reflection coefficient curve in the frequency domain. Figure 5.5 shows schematically the data processing sequence described above. Examples of the reference signal and the reflected pulse signal are given in section 5.3, where the ultrasonic reflectivity from a water/aluminium interface is measured.

5.3 The reflection coefficient from the water/aluminium interface

The water/aluminium interface reflection coefficient is the first of several systems used in this thesis for comparison between the various theoretical models and the measurements. The choice to run the first comparison on the water/aluminium system is rather natural. Indeed, the measurements of reflections from exposed surfaces are relatively straightforward; they are much less complicated than measurements from the embedded interfaces. From the theoretical point of view, the water/aluminium system involves modelling the reflection coefficient between two semi-infinite half-spaces, which is one of the simplest cases to compute.

5.3.1 Theoretical predictions using the infinite plane wave model and totally elastic media

In order to find out what we should expect to get from the measurements in terms of amplitude variation at different angles of incidence, let us first investigate the water/aluminium interface reflectivity theoretically. Figure 5.6 shows the calculated reflection coefficient curve as a function of angle of incidence for a water/aluminium interface when assuming a single infinite plane wave on the boundary. The water is modelled here as an inviscid liquid, and the aluminium as a totally elastic solid. From fig. 5.6 it can be seen that there are three important angular ranges featuring different states of the reflected and transmitted fields.

The first angular zone is between zero and about 13 degrees. Here the transmitted field (the field in aluminium) consists of simple plane longitudinal and shear waves where the wavenumbers are real vectors. In other words both longitudinal and shear waves propagate from the interface carrying energy away from the boundary.

The next angular zone is the incidence range between approximately 14 and 28 degrees. In this range, by Snell's law, the wavenumber of the longitudinal wave in the aluminium is complex,

Chapter 5   180

Validation of the theory. Accuracy of the reflection coefficient measurements

while the wavenumber of the shear plane wave in the aluminium remains real. This means that the longitudinal wave becomes inhomogeneous and does not propagate from the interface, but moves in the direction parallel to the boundary. As in the angular range 0 - 13 degrees, the shear wave is homogeneous and capable of taking some energy away from the boundary.

The third angular range lies between 29 and 90 degrees, where both longitudinal and shear waves are inhomogeneous. Here both kinds of waves propagate in the direction parallel to the interface making it impossible to take the energy away from the boundary. Therefore this angular range is called the range of total internal reflection as the energy input from the incident wave is returned back to the fluid making the reflection coefficient equal to unity.

5.3.2 Measurements

A 25 mm thick aluminium block was used to measure the reflection coefficient from a single interface (see fig. 5.7). The data processing procedure used for this experiment is simple and involves division of the pulse reflected from the interface by the reference pulse captured in the face-to-face arrangement of the probes at the beginning of the measurement session or immediately after it.

Figure 5.8(a) shows the time history of the reference pulse obtained during the measurements, which were carried out using a pair of the 10 MHz Rolls-Royce Mateval wideband transducers. The characteristics of spectrum of the reference signal, shown in fig. 5.8(b), are typical for current good quality ultrasonic probes. The centre frequency is around 9.5 MHz, while the useful bandwidth for accurate measurements lies between about 7 MHz and 14 MHz.

Figure 5.9(a) shows the time history of the pulse reflected from the water/aluminium interface when the transmitter and receiver were inclined at an angle of 20 degrees with respect to the normal to the interface (see fig. 5.7).

The division of the reflected pulse spectrum of fig. 5.9(b) by the reference spectrum of fig. 5.8(b) yields the reflection coefficient for the angle of incidence of 20 degrees. Figure 5.10 shows the result of the division. Here it can be seen that in the useful frequency range (between 4 MHz and 14 MHz), the measurement is less noisy than anywhere else, and therefore, it makes sense to take the measurements only in this frequency band. It is now possible to divide this frequency range into ten 1 MHz wide intervals, and plot the average values of the reflection coefficient for each of the intervals. For the angle of 20 degrees the values of the reflection coefficient are almost the same indicating that at this angle of incidence the reflection phenomenon is frequency independent.

Chapter 5   181

Validation of the theory. Accuracy of the reflection coefficient measurements

Applying the procedure described above, it is possible to obtain the reflection coefficient curves for different angles of incidence and different frequency bands. Figure 5.11 shows the results of measurements performed for angles of incidence in the range between 9.5 and 40.0 degrees. At the angle of incidence of 9.5 degrees the transmitter and receiver were touching each other. It was therefore impossible to measure the reflection coefficient below 9.5 degrees. The *solid* curve is the average value of the reflection coefficient in the frequency band between 4.5 and 5.5 MHz, while the *dotted* curve . has been obtained for the frequency band between 7.5 and 8.5 MHz.

5.3.3 Comparison between the infinite plane wave theory and the measurements

Comparing the theoretically calculated curve (see fig. 5.6) with the measured one (see fig. 5.11) it can be seen that agreement is good everywhere except for the angular range in the vicinity of the longitudinal critical angle and the angular range between about 28 and 33 degrees, where the Rayleigh mode is excited. It was therefore necessary to improve the theoretical model to account for this phenomenon, since the confidence in the measurement was high.

5.3.4 Refinement of the infinite plane wave model to include viscoelastic effects in the aluminium

Figure 5.12 shows the reflection coefficient curve for the aluminium/water interface assuming no attenuation in water, small attenuation in aluminium (longitudinal attenuation 0.002 nepers per wavelength, shear attenuation 0.0002 nepers per wavelength, frequency 7 MHz) and a single infinite plane wave input. Comparison between fig. 5.12 and fig. 5.6 clearly shows that the inclusion of small attenuation in the solid affects the reflection coefficient amplitude around the Rayleigh angle, but only by a small amount. Therefore, the damping in the aluminium was increased in order to reach agreement between the plane wave theory and the experiments. In order to do so, the influence of longitudinal and shear wave attenuation on the reflection coefficient was studied.

Figure 5.13 shows the variation of the reflection coefficient due to different shear attenuation in aluminium. Here the longitudinal attenuation was removed from the model, and the shear attenuation set at 0.0001, 0.001, 0.01, and 0.05 nepers per wavelength. The frequency of the incident wave is 7 MHz. From fig. 5.13 it can be seen that the shear attenuation does not affect the reflection coefficient amplitude around the longitudinal critical angle, but strongly influences

the depth of the dip at the Rayleigh angle.

Fig. 5.14 shows the angular variation of the reflection coefficient due to the different longitudinal attenuation in the aluminium. This time, the shear attenuation was removed from the system, while the longitudinal attenuation was set at 0.001, 0.01, 0.1, and 0.2 nepers per wavelength. The frequency of the incident wave is 7 MHz. The figure shows that the longitudinal attenuation affects the reflection coefficient both in the vicinity of the longitudinal critical angle and around the Rayleigh angle.

The influence of the material damping on the reflection coefficients in the vicinity of the critical angle has been reported in a number of papers (see for example Becker and Richardson 1970, 1972)

To achieve agreement between the measurement and the theory, firstly the longitudinal attenuation was set so that the amplitude of the reflection coefficient around the longitudinal critical angle (13.45 degrees) was reduced from 1.0 for the non-attenuating system (see fig. 5.6) to about 0.93 (see fig. 5.11), as the longitudinal attenuation is solely responsible for that change (see fig. 5.13). Subsequently, the shear attenuation was chosen to obtain the required dip in the vicinity of the Rayleigh angle. The attenuation coefficients were found to be 0.1 and 0.02 nepers at 7 MHz for the longitudinal and shear waves respectively.

Figure 5.15 shows the result of "tuning" the longitudinal and shear attenuation coefficients in the viscoelastic model, so as to obtain good agreement with the experimental results in fig. 5.11. Good agreement between the two curves can be seen. However, the coefficients obtained in this way are far too high for aluminium and hence the depth of the dip at the Rayleigh angle and the reduction of amplitude at the longitudinal critical angle must be due to some other physical phenomenon. The results shown above indicate that the infinite plane wave theory cannot fully explain the observed behaviour and it will be shown in the next section that it needs to be refined to include the finite dimensions of the transmitter and receiver.

5.3.5   Theoretical calculations using the finite transducer model predictions

Figure 5.16 shows the variation of the reflection coefficient at a frequency of 7 MHz, as a function of angle of incidence for a pair of finite transducers obtained using the model discussed in chapter 3. The longitudinal and shear wave attenuation in aluminium was 0.002 and 0.0002 nepers per wavelength. The theoretically obtained curve agrees well with the experimental results shown in fig. 5.11.

Chapter 5   183

Validation of the theory. Accuracy of the reflection coefficient measurements

Comparing the reflection coefficient curve obtained from the infinite plane wave theory (see fig. 5.12), and the same curve obtained using the finite transducer model (see fig. 5.16), a marked reduction of the amplitude around the longitudinal critical angle and a considerable increase of the dip magnitude at the Rayleigh angle can be seen.

It can be shown that the decrease in the received signal is caused by the nonspecular reflection of the bounded beam. Here, the receiving transducer 'misses' part of the reflected field and therefore does not capture the whole reflected signal. This phenomenon has been reported in a number of papers, see for example the experimental work done by Neubauer (1973), Breazeale et al. (1974, 1977), and the theoretical work done by Bertoni and Tamir (1973).

To illustrate this phenomenon the spatial variation of the reflected field along the aluminium/water interface was calculated for an incident beam 10 mm wide, and Gaussian variation of the field amplitude across the beam. Figure 5.17 shows the displacement component normal to the face of the receiver for the arrangement of the probes shown schematically in fig. 2.14. The horizontal axes in fig. 5.17 correspond to the x_1'' axis of the receiver coordinates in fig. 2.14, but their directions are opposite to that shown in fig. 5.17. The vertical axes in fig. 5.17 are the amplitudes of the displacement field in the direction of x_2'' axis of the receiver coordinates in fig. 2.14.

The frequency of the incident field and the damping coefficients within the aluminium are the same as used for the calculations presented in figures 5.16 and 5.12.

Figure 5.17(a) shows the profile of the reflected field at normal incidence and the reference field which was obtained setting the reflection coefficient equal to unity. The reflected field has the same distribution of displacements as the reference signal and it is effectively the incident field multiplied by the infinite plane wave reflection coefficient for normal incidence which is about 0.84 (see fig. 5.6). From fig. 5.17(a) it can be seen that at normal incidence the reflection is specular.

Figure 5.17(b) shows the reflected field at the longitudinal critical angle. Here it can be seen that the shape of the reflected beam is somewhat changed. Indeed, some non-specular reflection takes place, caused most probably by the presence of the inhomogeneous longitudinal wave. At the longitudinal critical angle the longitudinal wave becomes inhomogeneous, being capable of transmitting energy in the direction parallel to the interface. The presence of water at the boundary causes the inhomogeneous wave to 'leak' the energy back to the water causing the visible deformation of the reflected field by superimposing the leaky type of radiation which decays exponentially along the interface. If the receiver is positioned to capture the specular

(geometric) reflection only, then clearly, some reduction in the signal amplitude will take place.

Figure 5.17(c) shows the reflected field at an angle of incidence of 16.5 degrees, which is about 3 degrees higher than the longitudinal critical angle. From this figure it can be seen that the reflection is specular. The longitudinal wave is inhomogeneous here, and therefore transmits some energy along the interface. The energy transmission of an inhomogeneous wave is closely related to the magnitude and the extent of the displacement field due to that wave. The bigger the amplitude and the extent of the field, the better the energy transmission. The displacement field due to the inhomogeneous wave vanishes exponentially in the direction perpendicular to the interface in the aluminium. The bigger the incidence angle above the critical angle the more rapid the amplitude decay within the aluminium and therefore the energy transmission in the direction parallel to the interface is smaller.

Figure 5.17(d) shows the reflected field at an angle of incidence of 25.0 degrees. It can be seen that the reflection is specular here. The reflected field can be obtained by multiplication of the reference reflection (see fig. 5.17(a)) by the reflection coefficient calculated for the infinite plane wave excitation.

Figures 5.17 (e), (f) and (g) show the reflected field around the Rayleigh angle. From these figures it can be seen that in the vicinity of this angle non-specular reflection takes place. Figure 5.17(f) shows the field at the Rayleigh angle (30.45 degrees). Here, the reflected field consists of the specular (geometrical) reflection part and the leaky Rayleigh wave part, which increases quickly within the specular reflection range and then decays exponentially along the interface in a leaky wave manner. These two components are out of phase with respect to each other and therefore some cancellation of the signal within the specular reflection range takes place. The maximum intensity of the reflected signal shifts to the right and a significant part of the overall signal is therefore not received by a transducer if it is placed to receive specular reflections. Moreover, as the specular reflection component is out of phase with the leaky Rayleigh wave component, the integral of the displacement field over the receiver's face may cancel to zero for a given width and frequency of the incident beam.

Figure 5.17(h) shows the reflected field at an angle of incidence of 35.0 degrees. The reflection is specular here and the amplitude of the field is almost equal to the amplitude of the reference field giving a reflection coefficient value almost equal to unity.

Figures 5.18 (a) - (d) show the reflected field at the Rayleigh angle for beamwidths varying between 5 mm and 40 mm for the frequency of excitation of 5 MHz. The figures show that the position of the peak with respect to the central line does not appear to be a function of the beam

Chapter 5   185

Validation of the theory. Accuracy of the reflection coefficient measurements

width.

Figure 5.19 shows the reflected field at the Rayleigh angle for different frequencies of the incident field. The beam was 10 mm wide and had a Gaussian variation of displacement across its width. Figures 5.19 (a), (b), (c), (d), (e), (f), (g), (h) show the field at 2 MHz, 4 MHz, 6 MHz, 8 MHz, 10 MHz, 15 MHz, 25 MHz, and 50 MHz respectively. From these figures it can be seen that the beam displacement is larger for lower frequencies and therefore the finite beam reflection coefficient will be strongly frequency dependent here. For higher frequencies, the shift is less pronounced causing the reflection coefficient to increase with frequency. This argument does not take into account the variation of the damping coefficients within the aluminium which are also frequency dependent. Therefore the reflection coefficient will be affected by two independent factors. Firstly, the frequency variation of the longitudinal and shear damping coefficients can cause changes in the reflection coefficient at the longitudinal critical angle and the Rayleigh angle as has been shown in figures 5.13 and 5.14. Secondly, the non-specular reflection phenomenon strongly affects the measured reflection coefficient around these angles. The non-specular reflection effect is dependent on the incidence beamwidth and its frequency as has been shown in figures 5.18 and 5.19.

It can be also seen from fig. 5.19 that the Rayleigh wave leaks energy more rapidly at higher frequencies.

The numerical results shown in figures 5.17, 5.18 and 5.19 are in close agreement with the theoretical and numerical work done by Ngoc and Mayer (1979, 1980), Nayfeh and Chimenti (1984).

The theoretical and experimental investigations conducted in this section lead us to conclude that the infinite plane wave theory can be successfully used to predict reflection coefficients from single interfaces as long as the angle of incidence is not in the vicinity of the Rayleigh angle. At the Rayleigh angle the leaky surface wave is generated, which is capable of carrying energy along the interface. The energy, carried away from the area isonified by the transmitter, is subsequently re-radiated ('leaked') back to the fluid as the Rayleigh wave propagates. Therefore, the presence of the leaky surface wave alters the composition of the reflected beam and shifts the reflected beam so that a non-specular reflection phenomenon takes place (see fig. 5.17(f)). Here the use of the finite beam model is essential to predict the behaviour of the system quantitatively. A small beam shift and the effect of energy 'leaking' can be also seen the longitudinal critical angle (see fig. 5.17(b)). Therefore, also at the longitudinal critical angle the finite transducer model should be used for quantitative predictions of the reflection coefficient.

5.4 The reflection coefficient from an aluminium/water interface

In this section measurements and theoretical investigations of the ultrasonic reflection coefficient from the aluminium/water interface are discussed. As the interface used for the study here is the same as that of section 5.3, the work presented here can be considered as a continuation of the previous section. Indeed, from the theoretical point of view, the aluminium/water reflection coefficient again involves two semi-infinite half-spaces, one of them aluminium and the other water. The calculations of reflection coefficient have to be conducted here in terms of the incident and reflected waves in the aluminium half-space rather than the water half-space as was in case of the water/aluminium system analysed in section 5.3.

5.4.1 Measurement technique and theoretical predictions.

The experimental work with the aluminium/water system poses some complications which were not encountered in section 5.3. Because the incident waves have to hit the boundary from the side occupied by the solid, the transmitter has to be positioned on the side of the solid half-space rather than the liquid half-space. It is therefore necessary to use an aluminium plate of finite thickness, and to rely on the refracted waves within the aluminium plate to deliver the ultrasonic pulse to the interface.

Figure 5.20 shows schematically the idea adopted here to carry out the measurements. The pulse generated by the transmitter, incident on the top surface of the aluminium plate at the chosen angle of incidence θ, generates the refracted wave within the solid at the angle of incidence θ_1, related to θ by Snell's law. The refracted wave hits the aluminium/water at the angle θ_1 and is reflected back towards the top surface of the plate. Subsequently, the pulse transmitted from the plate back to the water is received by the receiver.

The amplitude of the signal at the receiver is defined by the amplitude of the wave generated by the transmitter, the transmission coefficient across the water/aluminium interface at the angle of incidence θ, the reflection coefficient from the aluminium/water interface at the angle of incidence θ_1, and finally, the transmission coefficient across the aluminium/water boundary at the angle of incidence θ. It can clearly be seen here that, in order to quantitatively measure the reflection coefficient from the bottom boundary, the transmission coefficients across the top boundary have to be known beforehand.

Another very important problem here is the arrangement of the transmitter and receiver with respect to each other. From fig. 5.20, it can be seen that the receiver has to be positioned at

exactly the right position in space to capture the reflection coming from within the plate, and this position is determined by the thickness of the plate and angles at which the waves propagate in the water and in the aluminium. Note that the refracted wave and the reflected wave can be either longitudinal or shear, as the solid medium supports these two types of bulk waves. Let us discuss this problem in more detail.

Figure 5.21 shows a more detailed picture of the measurement concept described in fig. 5.20. The transmitter generates a longitudinal pulse in water which, at the top surface of the plate, generates the reflected pulse denoted by the abbreviation FF, and two refracted waves, one of them being the longitudinal wave, and the other one shear. These two waves propagate in the direction towards the bottom of the the plate. At the aluminium/water interface, the incident longitudinal wave mode-converts into reflected longitudinal and shear waves. Each of the incident shear and longitudinal waves mode-convert into longitudinal and shear waves propagating in the upward direction towards the receiver. Therefore, there are four different pulses coming from the back of the plate: the shear-shear (SS) reflection, the shear-longitudinal (SL) reflection, the longitudinal-shear (LS) reflection, and the longitudinal-longitudinal (LL) reflection, the amplitude of each of them depending on the corresponding reflection coefficient for the aluminium/water interface. All the four reflected pulses propagate towards the top surface of the aluminium plate, where all of them are partially mode-converted to longitudinal pulses in water. Because the longitudinal wave in solids is about twice as fast as the shear wave, the different reflections coming from the back of the plate arrive at different times at the face of the receiver. The angles of refraction for the longitudinal and shear waves are also different, which means that the two types of waves do not follow the same path within the plate. This means that the reflections coming from the bottom interface emerge from the plate at different points. Note that the LS and SL reflection arrive at exactly the same time at the receiver, and also appear at exactly the same position in space. The two different pulses therefore merge to form a single pulse, which will be denoted as LS+SL reflection.

From the comments above one can deduce that in order to successfully receive the reflection of our choice from the back of the plate, the position of the receiver has to be carefully adjusted with respect to the transmitter. Indeed, fig. 5.21 shows the receiver positioned to capture the LS+SL reflection. If, for example, the FF reflection was to be captured then the receiver would have to be moved to the position marked with the dashed line.

A 4.85 mm thick aluminium plate was chosen for the experiments. The plate density as well as the longitudinal and shear velocity were measured prior to the experiments using the technique described in Appendix A. The longitudinal and shear attenuation in aluminium were assumed. The shear velocity and attenuation in water were calculated using Navier-Stokes equations as

shown in Appendix B. The longitudinal attenuation in water was assumed. Table 5.1 shows the acoustic properties of the plate and water taken for theoretical predictions.

material	density (kg/m^3)	longitudinal velocity (m/s)	longitudinal attenuation (nepers)	shear velocity (m/s)	shear attenuation (nepers)
aluminium	2820	6330	0.01	3120	0.02
water	1000	1495	0.001	10	6.28

Table 5.1 Acoustic properties of materials used for theoretical predictions

It was decided that the comparisons would be conducted at two angles of incidence: 10 degrees and 20 degrees. Using the material properties of table 5.1, it is possible to calculate the angles of refraction within the aluminium plate, as well as the time of arrival of the LL, LS+SL, and SS pulses with respect to the front face reflection, FF. Table 5.2 shows the results of such calculations, and fig. 5.22 shows the time domain simulation of the response from the plate being excited at the angle of 10 degrees in water using the infinite plane wave theory.

Type of reflection	Angle of incidence at aluminium/water (degrees)	Time of arrival wrt FF (µs)
LL_1	longitudinal: 47.3	1.04
$(LS+SL)_1$	longitudinal: 47.3 shear: 21.2	1.97
LL_2	longitudinal: 47.3	2.08
SS_1	shear: 21.2	2.90
$((LS+SL)_1 LL)_1$	longitudinal: 47.3 shear: 21.2	3.01
LL_3	longitudinal: 47.3	3.12

Table 5.2   Angles of refraction and times of arrival of different reflections coming from the back of the 4.85 mm thick aluminium plate. Angle of incidence in water 10.0 degrees.

From table 5.2 and fig. 5.22 it can be seen that the LL_1 pulse comes first after the FF pulse, with a delay of 1.04 µs. The $(LS+SL)_1$ pulse comes next but only a fraction of a microsecond before the second reverberation of the LL reflection. Indeed, the delay of the $(LS+SL)_1$ pulse with respect to FF is 1.97 µs, and the delay of the LL_2 pulse is twice the delay of the LL_1

Chapter 5 189

Validation of the theory. Accuracy of the reflection coefficient measurements

pulse, that is, $1.04 \times 2 = 2.08$ μs. Therefore, the LL_2 pulse arrives only 0.11 μs behind $(LS+SL)_1$ pulse, and the two pulses are superimposed if standard 10 MHz probes are used for the experiments. A similar situation happens with the first shear-shear reflection. From table 5.2 it can be seen that two other pulses have a very similar time of arrival to that of SS_1. The LL_3 pulse arrives only 0.22 μs behind SS_1, and the $((LS+SL)_1 LL)_1$, which is the LS+SL reflection in the first traverse followed by the LL reflection in the second traverse, arrives 0.11 μs behind SS_1. If 10 MHz probes are used for the experiments, then the pulses generated by the transducers are about 0.20 μs long, which means that the SS_1, $((LS+SL)_1 LL)_1$, and LL_2, superimpose. Indeed, fig. 5.22 shows that this is the case.

5.4.2 Experiments

The experimental set up used here is described in detail in section 5.2 of this chapter. A pair of 10 MHz Rolls-Royce Mateval probes were used here as the transmitter and receiver. The measurements were carried out for two different angles of incidence, 10 and 20 degrees, the transducers being arranged to receive the FF, LL_1, $(LS+SL)_1$, and SS_1 reflections in turn.

Angle of incidence of 10 degrees

Figure 5.23 shows the response of the 4.85 mm thick aluminium plate to pulse excitation at an angle of incidence of 10 degrees in water. The transducers were arranged to receive FF reflection, as shown schematically with the dashed line in fig. 5.21. Comparing fig. 5.23 with 5.22 it clearly can be seen that the two plots do not look similar at all. The front face reflection (FF), on which the probes were focussed, looks very similar on both plots. However, the reflections which follow FF are much smaller in fig. 5.23 than in fig. 5.22. These differences can be explained looking at fig. 5.21, where the spatial positions occupied by different reflection are schematically shown. Here it can be seen that, if the receiver is positioned to capture the FF reflection, then the probe 'misses' the zones isonified by LL_1, $(LS+SL)_1$, and SS_1 reflections, which appear further to the right in fig. 5.21. The biggest reduction in amplitude is experienced by LL_1 as it is farthest away from the receiver. All the other reflections coming after SS_1 practically miss the receiver entirely and therefore do not appear in fig. 5.23.

From figures 5.21, 5.22, and 5.23 it can be seen that the infinite plane wave model is not capable of predicting the oblique incidence responses from the aluminium plate even approximately. It is therefore important to investigate whether the finite transducer model can bring us closer to the reality. Figure 5.24 shows the theoretically calculated response from the 4.85 mm thick aluminium plate in water to pulse excitation at the angle of 10 degrees in the

liquid. The finite transducer model was used here to calculate the time history. The dimensions of the transducers as well as their combined frequency response was measured prior to the calculations and used as the input to the model together with the acoustic properties of the plate and water, given in table 5.1. The transmitter and receiver were positioned in the model in exactly the same fashion as during the measurement, that is to receive the FF reflection primarily. Comparing figures 5.23 and 5.24 it can clearly be seen that the finite transducer model can accurately predict the response of the plate to finite transducer excitation. This is not the case when the infinite model is used (see fig. 5.22).

When the receiver is moved to receive primarily the SS_1 reflection (see fig. 5.25(a)) then the front face reflection becomes smaller as it is partially 'missed'. At the same time LL_1, and $(LS+SL)_1$ reflections become larger because the receiver is closer to the areas isonified by them. The shear-shear reflection is still very small in comparison with the others because the mode conversion from the longitudinal wave in water to the shear wave in the aluminium and then back from the shear in the aluminium to the longitudinal in the liquid is very weak. Therefore, despite the best conditions for the reception of the SS_1 reflection, its apparent amplitude is strongly affected by the other pulses coming from the back of the plate at a similar time to the SS_1 pulse (see table 5.2). Figure 5.25(b) shows the finite transducer predictions for the case showed in fig. 5.25(a). Excellent agreement between the measurements and predictions can be seen.

Figure 5.26 shows what happens when the transducers are focussed on $(LS+SL)_1$ reflection. The arrangement of the probes or this particular case is schematically shown in fig. 5.21. In fig. 5.26(b) the measured response of the plate is shown. Here, further reduction of the FF reflection can be seen (note the different vertical scale to those of the previous figures), while the $(LS+SL)_1$ reflection amplitude substantially increased. Figure 5.26(b) shows the results of the theoretical predictions for this arrangement of the transducers, again demonstrating excellent agreement between the finite transducer theory and the experiment.

The last case left for the comparison is the situation when the transducers are positioned to receive the longitudinal-longitudinal reflection from the aluminium/water interface. Figure 5.27(a) shows the measurement performed for this case. From the figure it can be seen that the FF reflection has been reduced to a very small amplitude, and its signature is drastically distorted. This is because the receiver is further away from the area isonified by the FF pulse, and the transducer 'catches' only some parts of the beam. In fig. 5.27(b) the same case has been reproduced theoretically using the finite transducer theory. Excellent agreement in terms of the time of arrival for each of the reflections as well as their relative amplitudes can be appreciated. However, the FF pulse shape in fig. 5.27(b) is somewhat different than that

Chapter 5   191

Validation of the theory. Accuracy of the reflection coefficient measurements

obtained in the experiment, shown in fig. 5.27(a). This kind of discrepancy can be expected here since the receiving transducer is positioned at the fringe of the area isonified by the FF beam. In such circumstances small differences in the displacement pattern at the face of transmitter can produce visible changes in the signature of the signal captured by the receiver. In the theoretical predictions shown here a Gaussian displacement pattern at the face of the transmitter was assumed (see figures 2.7(a), 2.8(a) and 2.9(a)), and no attempt was made to alter the displacement pattern function to match that of the real transducer.

Angle of incidence of 20 degrees

The comparisons between the measurements and theory is now continued for the excitation being at an angle of incidence of 20 degrees in water. Table 5.3 shows the times of arrival of reflections coming from the back of the aluminium plate. Because the angle of the incident wave is above the longitudinal critical angle, the longitudinal wave is inhomogeneous here, and LL reflections do not exist in practice. The (LS+SL) reflections do not exist either because they, like the LL pulses, rely on the longitudinal wave to propagate towards or away from the aluminium/water interface. The only wave left to propagate in the aluminium is the shear wave, and the only reflection from the aluminium/water interface which can be received and measured here is the SS pulse.

Type of reflection	Angle of incidence at aluminium/water (degrees)	Time of arrival wrt FF (μs)
LL	wave inhomogeneous	N/A
SS_1	shear: 45.5	2.18
SS_2	shear: 45.5	4.36

Table 5.3   Angles of refraction and times of arrival of different reflections coming from the back of the 4.85 mm thick aluminium plate. Angle of incidence in water 20.0 degrees.

Figure 5.28 shows the time domain prediction of the response of the 4.85 mm thick aluminium plate in water to a pulse excitation, incident from the water half-space at the angle of 20.0 degrees. The infinite plane wave theory was used to generate the curve of fig. 5.28. As discussed above, the only type of wave able to propagate here is the shear wave. Figure 5.28 shows the SS reflections coming from the back of the plate. All of them are equally spaced in time, the delay between them being 2.18 μs.

To compare the results of the infinite plane wave theory with the experiment, fig. 5.29(a)

Chapter 5   192

Validation of the theory. Accuracy of the reflection coefficient measurements

shows the measured response from the aluminium plate at 20 degrees. The receiver was positioned in the middle of the area isonified by the front face reflection and misses a significant part of the area isonified by the SS_1 beam. The higher order SS reflections emerge from within the plate further away from the receiver and therefore they are not present in fig. 5.29(a) at all. Figure 5.29(b) shows the finite transducer predictions for the case presented in fig. 5.29(a). Comparing fig. 5.28 with 5.29(a), and 5.29(b) it can be seen that the infinite plane wave model is not capable of predicting the aluminium plate response to a realistic excitation, while the finite transducer model gives a very accurate account of what should be expected in practice.

The last figure presented in this section is the comparison between the finite transducer model with the experiment when the receiver is positioned to capture the SS_1 reflection. Figure 5.30(a) shows the result of the experiment for this case. The amplitude of the front face reflection is much smaller here than that of fig. 5.29 because the receiver misses a significant part of the FF beam. However, the apparent amplitude of SS_1 reflection increased here substantially. It is interesting to note that in fig. 5.30(b) the receiver captures a little of the SS_2 reflection, which is not the case in fig. 5.29, when the receiver was positioned to measure FF primarily. Comparing the experimental results of fig. 5.30(a) with the theoretical predictions using the finite transducer model shown in fig. 5.30(b), again, excellent agreement between both plots can be seen.

5.5 The reflection coefficient from a thin silicone layer in glass

In this section a theoretical and experimental investigation of the ultrasonic reflectivity from a thin silicone layer in glass is described. The case of the thin liquid layer between two solid plates is the next logical step towards quantitative reflection measurements from the interfaces in the adhesive joints. Indeed, the glass plate/thin silicone layer/glass plate system is as complicated theoretically and experimentally as the aluminium plate/thin oxide layer/epoxy layer system in adhesive joints. For the purposes of the comparison of the theory with the measurements, however, the glass/silicone/glass system is very convenient. The mechanical properties of the glass plates and the silicone fluid can be accurately measured before making the glass plate/thin silicone layer/glass plate system ready for the experiments. The measured material properties can then be used for the theoretical predictions of the system response to normal and oblique incidence excitation.

5.5.1 Specimen

Figure 5.31 shows schematically the specimen used for the measurements. It comprises two

5.85 mm thick glass plates and a very thin silicone liquid layer between them. The glass plates were polished in order to achieve a high degree of flatness before a very small quantity of the silicone liquid was let between them. The acoustic properties of the glass plates and the silicone liquid are given in table 5.4. The density of glass and its longitudinal and shear velocity were measured using the technique presented in Appendix A. The density, the longitudinal velocity and the kinematic viscosity of the silicone fluid were taken form the manufacturer's specification sheet. The shear wave velocity and shear wave attenuation in the silicone liquid and water were calculated from the Navier-Stokes equation, assuming that the kinematic viscosities of water and of the silicone liquid are 1.0 cSt, and 50.0 cSt, respectively. The details of the derivations can be found in Appendix B. The longitudinal attenuation in the silicone fluid and in water were assumed.

material	density (kg/m^3)	longitudinal velocity (m/s)	longitudinal attenuation (nepers)	shear velocity (m/s)	shear attenuation (nepers)
glass	2490	5808	0.0	3466	0.0
DOW CORNING 510 silicone fluid	985	1050	0.0	79	6.28
water	1000	1495	0.0	10	6.28

Table 5.4 Acoustic properties of the materials used in theoretical predictions.

Before the measurements were started, the acoustic properties and dimensions of all the components of the system were known apart from the thickness of the silicone layer. Therefore the idea of the experiment conducted here was first to find the thickness of the silicone layer using the longitudinal normal incidence reflection coefficient, and then to use the measured thickness of the layer for predictions of the oblique incidence responses of the system and to compare them with measurements at few chosen angles.

5.5.2   Measurement of the silicone layer thickness

As has been described in detail in chapter 4, the glass/thin silicone layer/glass system creates no serious problem as far as the quantitative evaluation of the thickness of the layer is concerned. Indeed, looking at table 5.4, it can be seen that the longitudinal impedance of the layer (a density-velocity product) is very different from the longitudinal impedance of the glass. This makes the longitudinal reflection coefficient from the thin silicone layer to be a strongly increasing function of frequency. The second very important factor which makes the detection of the silicone layer possible is that the layer separates two half-spaces of exactly the same

material, and in such circumstances the normal incidence reflection coefficient is very sensitive to the layer properties. A more detailed discussion of this was given in chapter 4.

The glass/silicone liquid/glass system, shown schematically in fig. 5.31, was submerged in water, and the system response to normal incidence longitudinal excitation was measured. The pulse-echo method was used here, which involves the use of a single transducer positioned at normal incidence to the plate and working as the transmitter and receiver. A 10 MHz wideband Rolls-Royce Mateval probe of the diameter of 10 mm was used for the experiments. The distance between the transducer and the tested plate was 45 mm. Figure 5.32 shows the result of the measurement. There are two reflections present in fig. 5.32, the front face reflection (FF) from the water/glass interface, and the longitudinal-longitudinal reflection (LL_1) coming from the silicone layer. The amplitude of the FF reflection depends solely on the properties of the the the glass and water and is independent of the properties of the embedded silicone layer interface. It is therefore convenient to use FF as the reference pulse for the evaluation of the reflectivity from the silicone layer. This involves the division of the Fourier transform of the LL_1 reflection by the Fourier transform of the FF pulse.

Curve 1 of fig. 5.33 shows the result of the spectral division of LL_1 by FF of fig. 5.32, while curves 2, 3, and 4 of fig. 5.33 show the results of theoretical calculations of the longitudinal reflection coefficient from silicone layers of different thicknesses normalised to the front face (water/glass) reflection coefficient. The low frequency behaviour of the measured reflection coefficient: the hump at around 1 MHz and the shallow minimum at about 2 MHz, was ignored on basis of poor signal-to-noise ratio and a significant beam spread effect at these frequencies. Since at normal incidence the non-specular reflection phenomenon does not take place, the infinite plane wave theory was used for quantitative predictions of the reflection coefficient from the silicone layer. The acoustic properties of the silicone layer and the glass plates were taken from table 5.4. Curve number 2 of fig. 5.33 was calculated for a 0.15 μm thick silicone layer, while curve numbers 3 and 4 correspond to layer thicknesses of 0.17 μm and 0.20 μm.

Since the infinite plane wave theory was used here for quantitative comparisons with the experimental data, it is necessary to estimate the error of the theoretical predictions due to the beam spread effect. Using the technique presented by Papadakis (1972) it is possible to estimate this error, assuming that the transmitter is a circular piston source. Table 5.5 shows the calculated diffraction loss for FF and LL_1 reflections at different frequencies. Tabulated integral functions describing diffraction effects in the ultrasonic field of a circular piston source, given by Benson and Kiyohara (1974), was used here. Table 5.5 shows that the error is larger for lower frequencies, and is about 9 % at the frequency of 5 MHz.

Frequency (MHz)	Diffraction correction factor for FF	Diffraction correction factor for LL_1	Diffraction correction factor for LL_1/FF	Estimated error for LL_1/FF
2	0.739	0.636	0.86	- 14 %
5	0.807	0.736	0.91	- 9 %
10	0.848	0.813	0.96	- 4 %

Table 5.5   Estimated error of the division LL_1/FF due to the diffraction loss of the FF and LL1 reflections when the infinite plane wave theory is used for comparisons with the experimental data.

From fig. 5.33 it can be seen that, using the longitudinal normal incidence technique, it is possible to determine the thickness of the silicone layer in glass to within a fraction of a micron. A silicone layer thickness of 0.17 μm was taken for further comparisons with the experiments at the oblique incidence.

5.5.3 Comparisons with theory at the oblique incidence

The oblique incidence reflection coefficient measurements were taken at angles of incidence of 10 degrees and 20 degrees in water. The measurements were conducted according to the general descriptions of the technique given in section 5.2 of this chapter. This involves the spectral division of the appropriate reflection coming from the embedded glass/silicone/glass interface by the reference reflection obtained when the probes were arranged face-to-face (see fig. 5.1). Subsequently, the measurements were compared with the infinite wave theory predictions using the mechanical properties of the system given in table 5.4, and assuming that the silicone fluid layer is 0.17 μm thick. The infinite plane wave theory was used here because at the angle of incidence of 10 and 20 degrees a non-specular reflection at the water/glass interface does not take place.

Angle of incidence of 10 degrees

At the angle of incidence of 10 degrees, there are three different reflection coefficients to be measured, namely LL_1, $(LS+SL)_1$, and SS_1. Figure 5.21 shows schematically the technique used to extract the appropriate reflection from an embedded interface. For a more detailed description of the method refer to section 5.4 of this chapter. Table 5.6 shows the angles of refraction in the glass as well as the times of arrival of the different reflections coming from the silicone layer.

Type of reflection	Angle of incidence at glass/silicone layer (degrees)	Time of arrival wrt FF (μs)
LL$_1$	longitudinal: 42.4	1.49
(LS+SL)$_1$	longitudinal: 42.4 shear: 23.7	2.30
LL$_2$	longitudinal: 42.4	2.98
SS$_1$	shear: 23.7	3.09
((LS+SL)$_1$ LL)$_1$	longitudinal: 42.4 shear: 23.7	3.79
LL$_3$	longitudinal: 42.4	4.47

Table 5.6 Angles of refraction and times of arrival of different reflections coming from the embedded silicone layer between 5.85 mm thick glass plates. Angle of incidence in water 10.0 degrees.

The transducers used for the oblique incidence experiments were the wideband 10 MHz Rolls-Royce Mateval probes giving ultrasonic pulses about 0.2 μs long. From table 5.6 it can be seen that, if the pulse duration is around 0.2 μs, very good separation between the LL$_1$, (LS+SL)$_1$, and LL$_2$ can be achieved. However, the SS$_1$ pulse is in the vicinity of LL$_2$, which may affect the accuracy of the SS reflectivity measurements, as it is impossible to separate these two reflections from each other.

Curve number 1 of fig. 5.34 shows the experimentally obtained division of the LL$_1$ reflection by the reference pulse obtained from the face-to-face arrangement of the probes. Curve 2 of fig. 5.34 shows the theoretically calculated reflectivity (using the infinite plane wave model) at exactly the same conditions as during the experiments, assuming the layer thickness of 0.17 μm, measured in the normal incidence experiment, and using the acoustic properties given in table 5.4. Excellent agreement between the two curves can be seen.

Figure 5.35 shows the division of the (LS+SL)$_1$ pulse by the reference signal obtained when the probes were arranged face-to-face. Curve 1 was obtained experimentally, while curve 2 is the result of theoretical calculations making use of table 5.4 and setting the layer thickness to 0.17 μm. Excellent agreement between the theory and experiment can be seen.

Figure 5.36 is the comparison between the theory and the measurement for the case of the shear-shear reflection coming from the glass/silicone/glass interface. The comparison between the measurement (curve 1) and the theoretical results (curve 2) is good. However, the

predictions are not as accurate here as is the case in figures 5.34, and 5.35. The most likely cause of this is the presence of the LL_2 reflection in the vicinity of the SS_1 pulse (see table 5.6). The SS_1 reflection cannot be cleanly separated in time from the LL_2 reflection and therefore, after time domain windowing, some of the LL_2 reflection still pollutes the SS_1 signal, affecting the final results.

Angle of incidence of 20 degrees

At the angle of incidence of 20 degrees, the longitudinal wave is inhomogeneous and cannot propagate in the glass plate. Therefore, there is only one type of reflection here, the SS_1 pulse and its multiples, which can be received from the embedded silicone layer and compared with the theoretical model. Table 5.7 shows the angle of refraction and the time of arrival of the shear-shear reflection pulse from the silicone layer.

Type of reflection	Angle of incidence at glass/silicone layer (degrees)	Time of arrival wrt FF (µs)
LL	wave inhomogeneous	N/A
SS_1	shear: 52.5	2.06
SS_2	shear: 52.5	4.12

Table 5.7   Angles of refraction and times of arrival of different reflections coming from the silicone layer between two 5.85 mm thick glass plates. Angle of incidence in water 20.0 degrees.

Figure 5.37 shows the division of the SS_1 pulse by the reference signal obtained when the probes were face-to-face. The angle of the incident wave is 20 degrees from water. Curve number 1 shows the results of the experiment. The oscillations visible in the low frequency range, which are most probably due to a beam spreading effect and a poor signal-to-noise ratio, were ignored. Curve numbers 2, 3, and 4 are the theoretical predictions for silicone layer thicknesses of 0.15 µm, 0.17 µm, and 0.20 µm, respectively. The infinite plane wave theory was used to compute these curves. From fig. 5.37 it can be seen that the sensitivity of the reflection coefficient to the layer thickness is high. Indeed, it is possible to determine the silicone layer thickness to within a small fraction of a micrometer. Again, the theoretical curve corresponding to the layer thickness of 0.17 µm comes very close to the experimental curve, demonstrating excellent agreement between the theory and the measurements.

5.6 Conclusions

This chapter demonstrated excellent agreement between the measured and predicted reflection coefficients from a series of model systems.

The accuracy of the measurements depends very much on whether the interface is easily accessible or not. Measurements of the reflection coefficient from an easily accessible surface can be carried out with an accuracy better than 2 percent of the reference pulse, usually obtained at the beginning of the measurement session when the probes are positioned face-to-face.

If it is required to obtain the values of the reflection coefficients from embedded interfaces then the problem of the measurement accuracy is more complex than in the previous case. In principle, the same accuracy during the experiments should be expected. However, the problem of small misalignments of the probes with respect to the measured plate can affect the amplitudes of the received pulses from within the plate much more than those reflected from the front face.

Another very important problem regarding the embedded interfaces is that in order to quantitatively measure the reflection coefficient somewhere within the layered structure, full knowledge of the part of the system between the embedded interface and the receiver has to be assumed. For example, in order to determine the thickness of the silicone layer in section 5.5 of this chapter, the material properties of the top glass plate had to be known. The information about the thickness and the wave velocities in the glass plate also determined the arrangement of the probes during the oblique incidence tests. The embedded interface reflectivity measurement is therefore a classical example of a situation where the quality of the first set measurements (material properties of the system components) influences the quality of the next set of experiments (reflection coefficients). The overall error of the measurements therefore may vary, but for a single parallel plate separating the interface from the water half-space the measurement error is not bigger than 5 percent.

The finite transducer theory used in the investigations of this chapter has been shown to be capable of predicting the amplitudes of each of the echoes received from multilayered systems. The error between the experiments and the finite transducer theory predictions is smaller than 10 percent. The finite transducer theory was also able to explain the Rayleigh angle dip phenomenon which could not be satisfactorily accounted for using an infinite plane wave model.

It has been shown in this chapter that the infinite plane wave theory can be successfully used to

predict reflection coefficients from single interfaces measured by finite transducers when two conditions are satisfied. The first one is that the non-specular reflection phenomenon does not take place during the measurement, and the second requirement is that the receiving transducer has to be placed in the middle of the area isonified by the reflected beam which is to be measured. The measurements of reflection coefficient at the water/aluminium interface presented at the beginning of this chapter showed that only at two angles of incidence, namely the longitudinal critical angle and the Rayleigh angle, was it necessary to use the finite transducer model to achieve excellent agreement with the experiments. The measurements of the reflection coefficients form the silicone liquid layer between two glass plates, presented at the end of this chapter, have clearly shown that, when testing at the angles of incidence away from the critical angles, the infinite plane wave theory can be used with confidence provided that the receiver is placed at the appropriate spatial position to capture the reflection of interest.

Because of its very modest computing power requirements, the infinite plane wave model is an excellent tool for fast calculations of the sensitivity of the reflection coefficients to various changes in the system under investigations. The infinite plane wave theory is also very useful in the calculations of the time of arrival of various pulses coming from embedded interfaces, which is extremely helpful information during the experiments.

transmitter

receiver
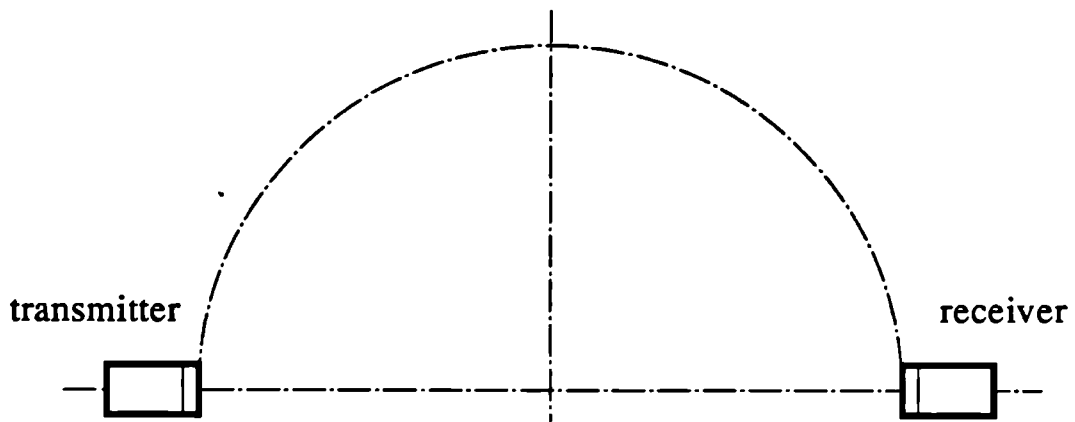
Fig. 5.1(a)The reference measurement.

transmitter

receiver

θ θ

water

solid
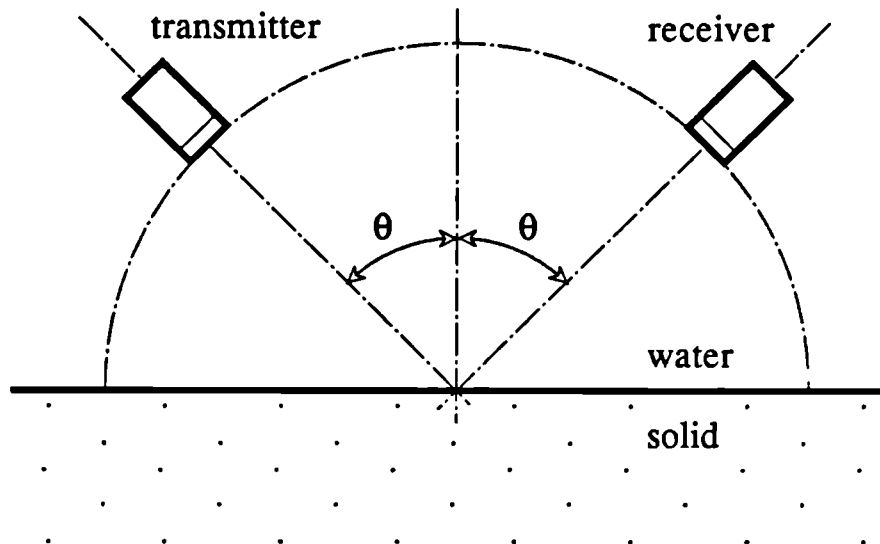
Fig. 5.1(b) Reflection measurement.
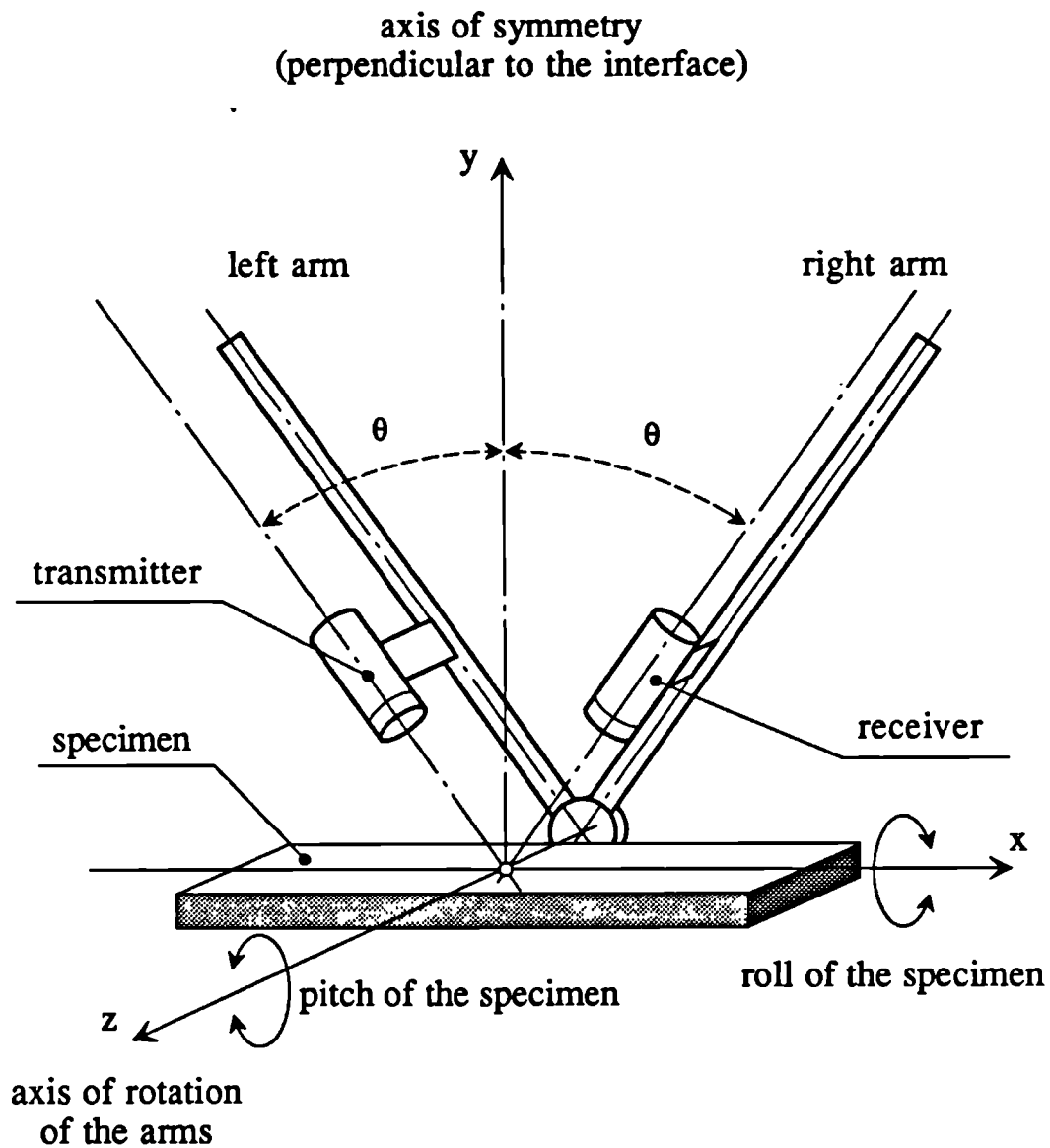
Fig 5.2 Concept behind the design of the reflection coefficient
        meter (RCM)

Chapter 5   202

Validation of the theory. Accuracy of the reflection coefficient measurements
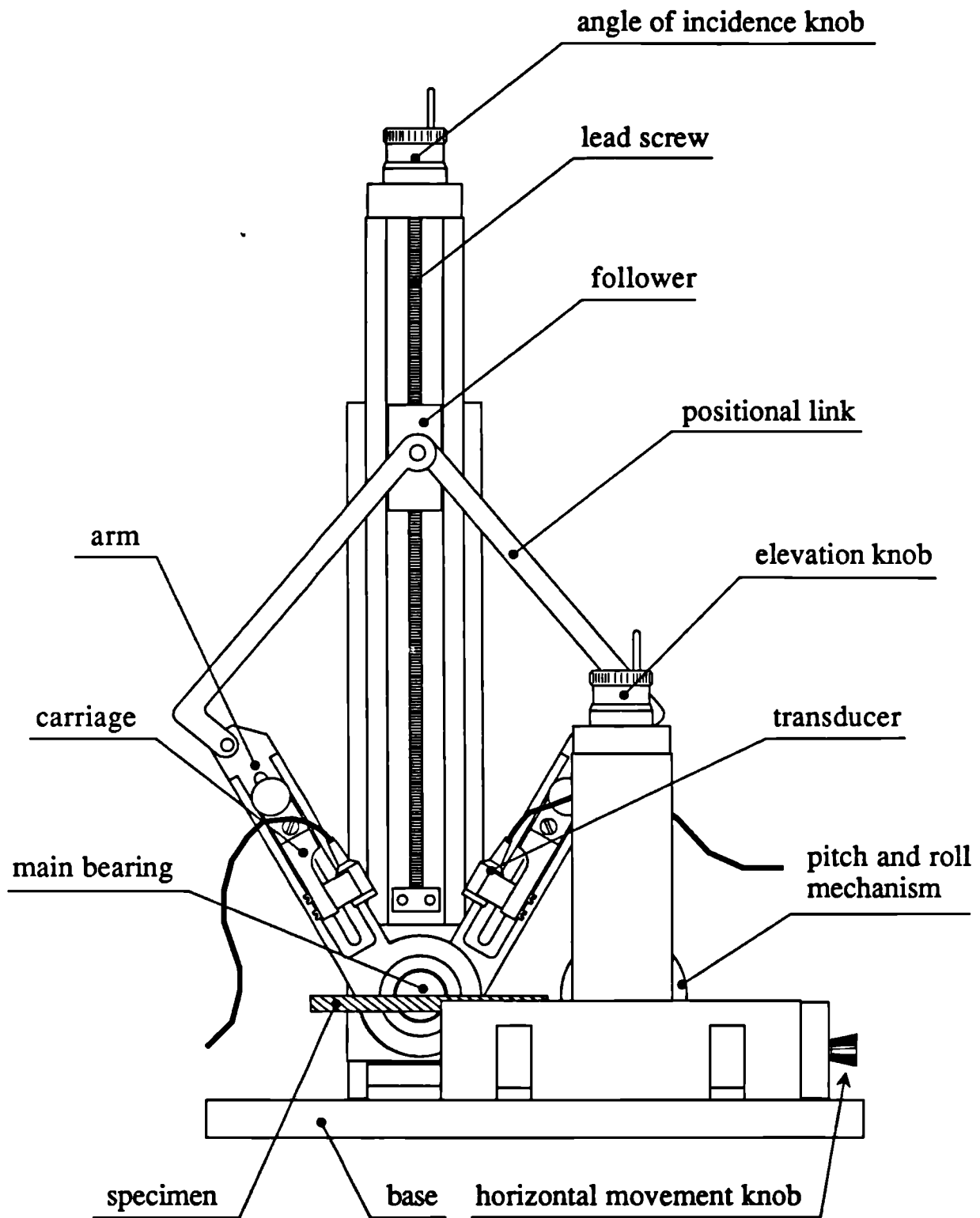
Fig 5.3 The reflection coefficient meter designed and manufactured
         for the purposes of the project

Chapter 5

Validation of the theory. Accuracy of the reflection coefficient measurements

203

GPIB

pulser/receiver
Panametrics
5052PRX75

microcomputer
DELL 310

digital oscilloscope
LeCroy 9400

transmitter

receiver

water

specimen
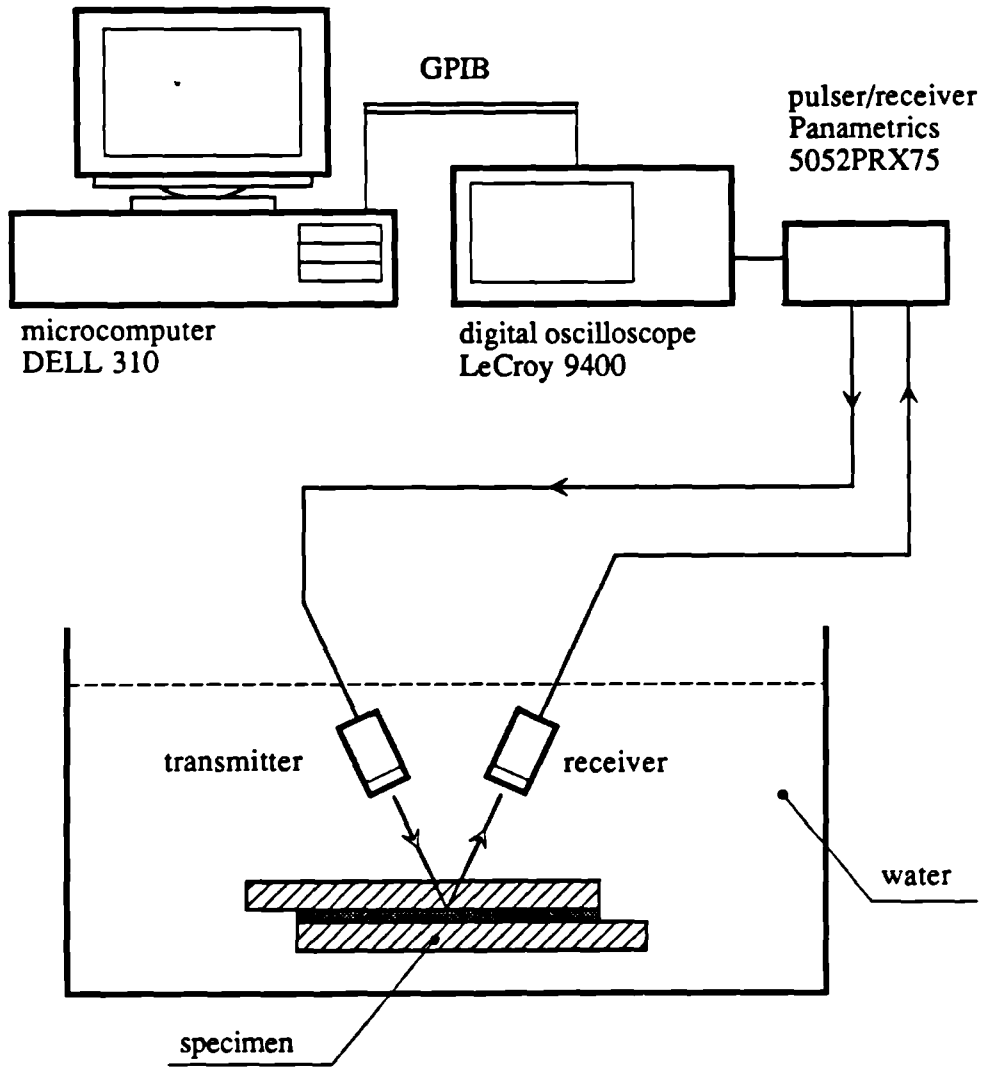
Fig 5.4   Electronic equipment used for experiments.

```
┌─────────────────────────┐
│  Position the transducers │
│        face-to-face       │
└─────────────────────────┘
            │
┌─────────────────────────┐
│       Capture the        │
│      reference pulse     │
└─────────────────────────┘
            │
┌─────────────────────────┐
│     Perform FFT on the   │
│      reference pulse     │
└─────────────────────────┘
            │
┌─────────────────────────┐
│   Mount the specimen and │
│    align it with respect to │
│       the transducers    │
└─────────────────────────┘
            │
┌─────────────────────────────┐
│ Adjust the angle of incidence and │
│  position the receiver to capture │
│    the reflection of interest     │
└─────────────────────────────┘
            │
┌─────────────────────────┐
│       Capture the        │
│      reflected pulse     │
└─────────────────────────┘
            │
┌─────────────────────────┐
│     Perform FFT on the   │
│      reflected pulse     │
└─────────────────────────┘
            │
┌──────────────────────────────────┐
│ Divide the spectrum of the reflected pulse by │
│   the spectrum of the reference pulse         │
└──────────────────────────────────┘
            │
            ▼
┌─────────────────────────┐
│  Reflection coefficient in │
│    the frequency domain   │
└─────────────────────────┘
```

Fig 5.5 Data processing sequence used for the measurement of
the reflection coefficient
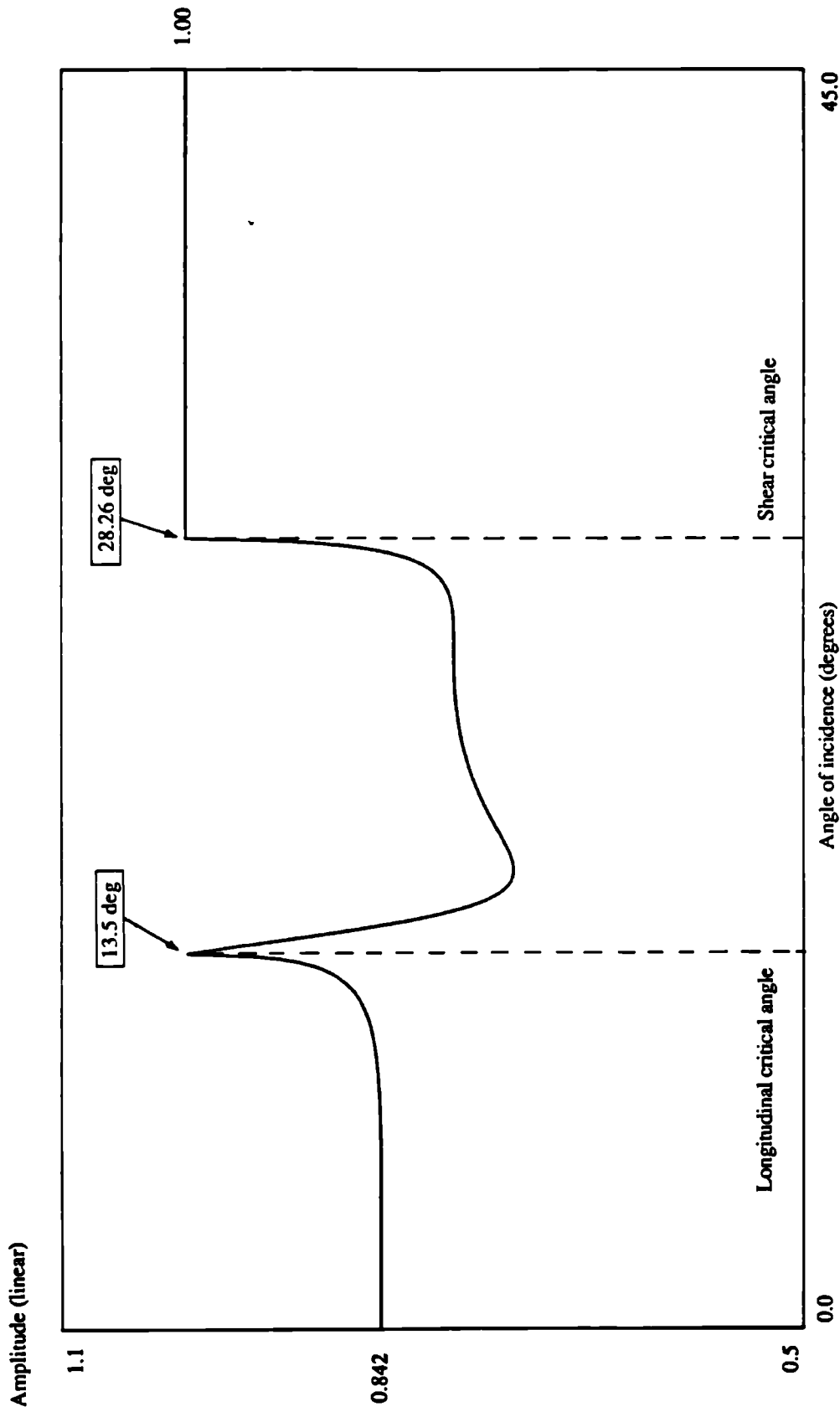
Fig. 5.6   Theoretically calculated reflection coefficient from aluminium/water interface using a totally elastic model and an infinite plane wave theory. The critical longitudinal and shear angles are shown.

Chapter 5

Validation of the theory. Accuracy of the reflection coefficient measurements

206
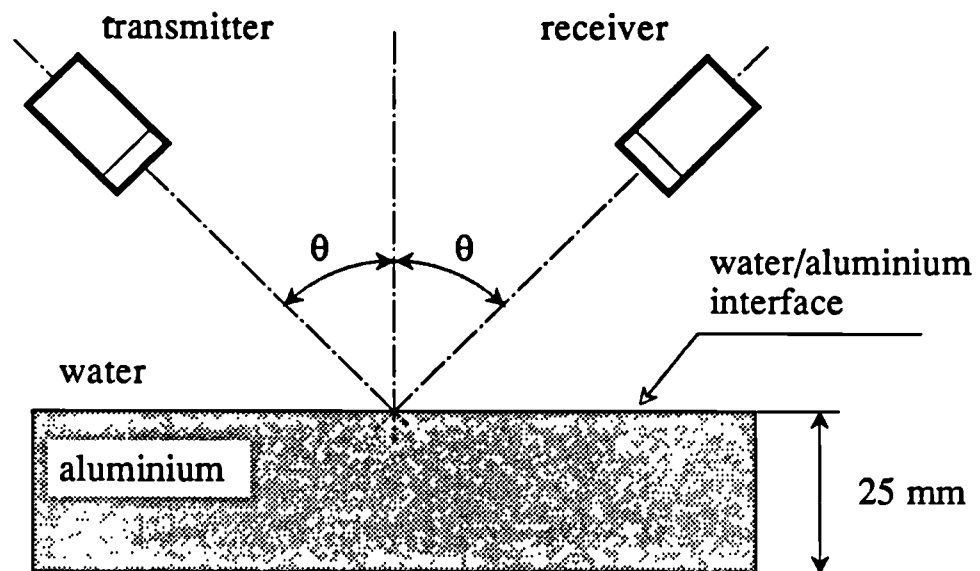
Fig 5.7 Schematic diagram of the system used for the measurements of the water/aluminium reflection coefficient.

Chapter 5

Validation of the theory. Accuracy of the reflection coefficient measurements

207
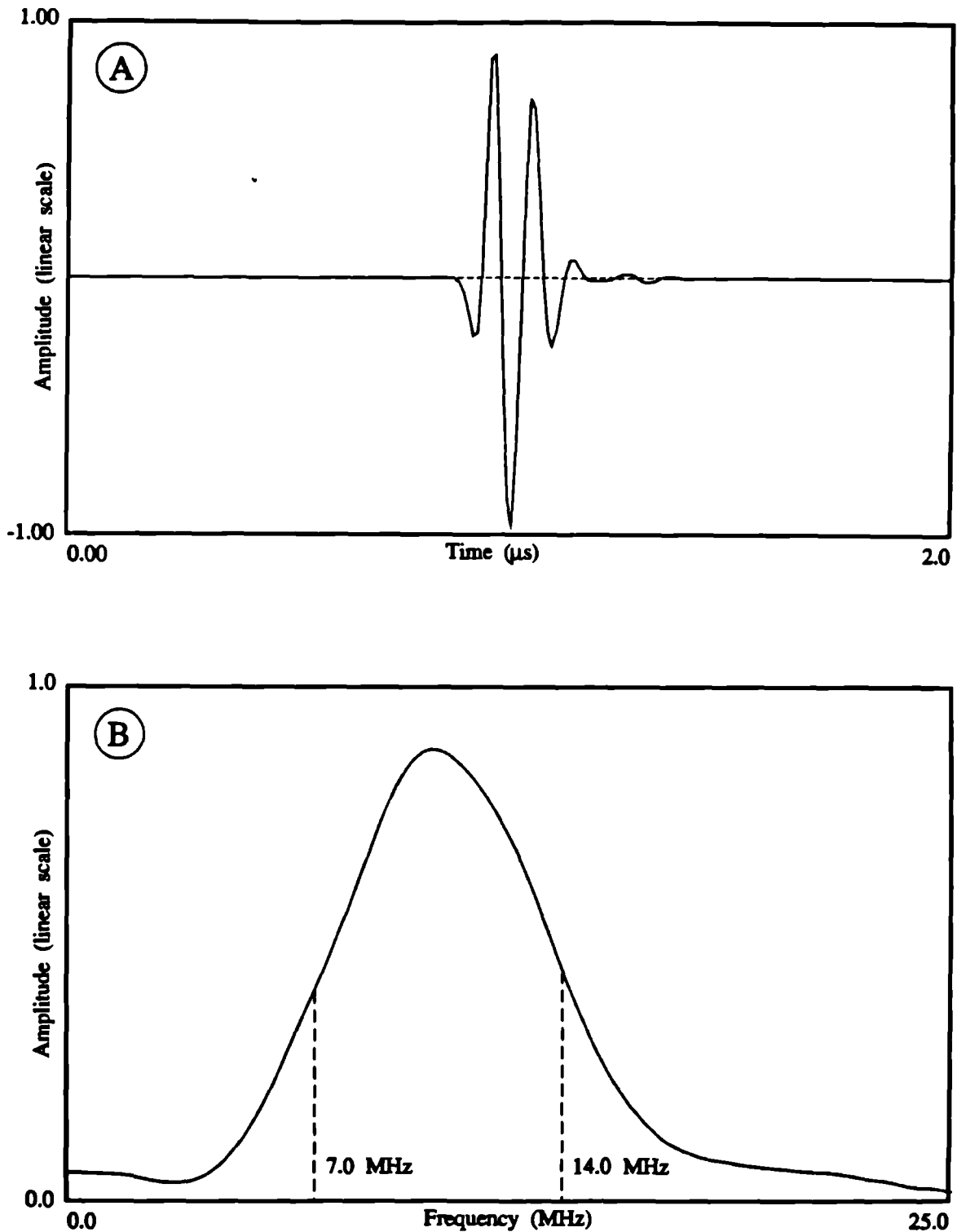
Fig. 5.8   The time domain and the frequency domain representations of the reference
pulse obtained when the transducers were positioned face-to-face. A pair of 10
MHz wideband Rolls-Royce Mateval transducers were used for the experiments.
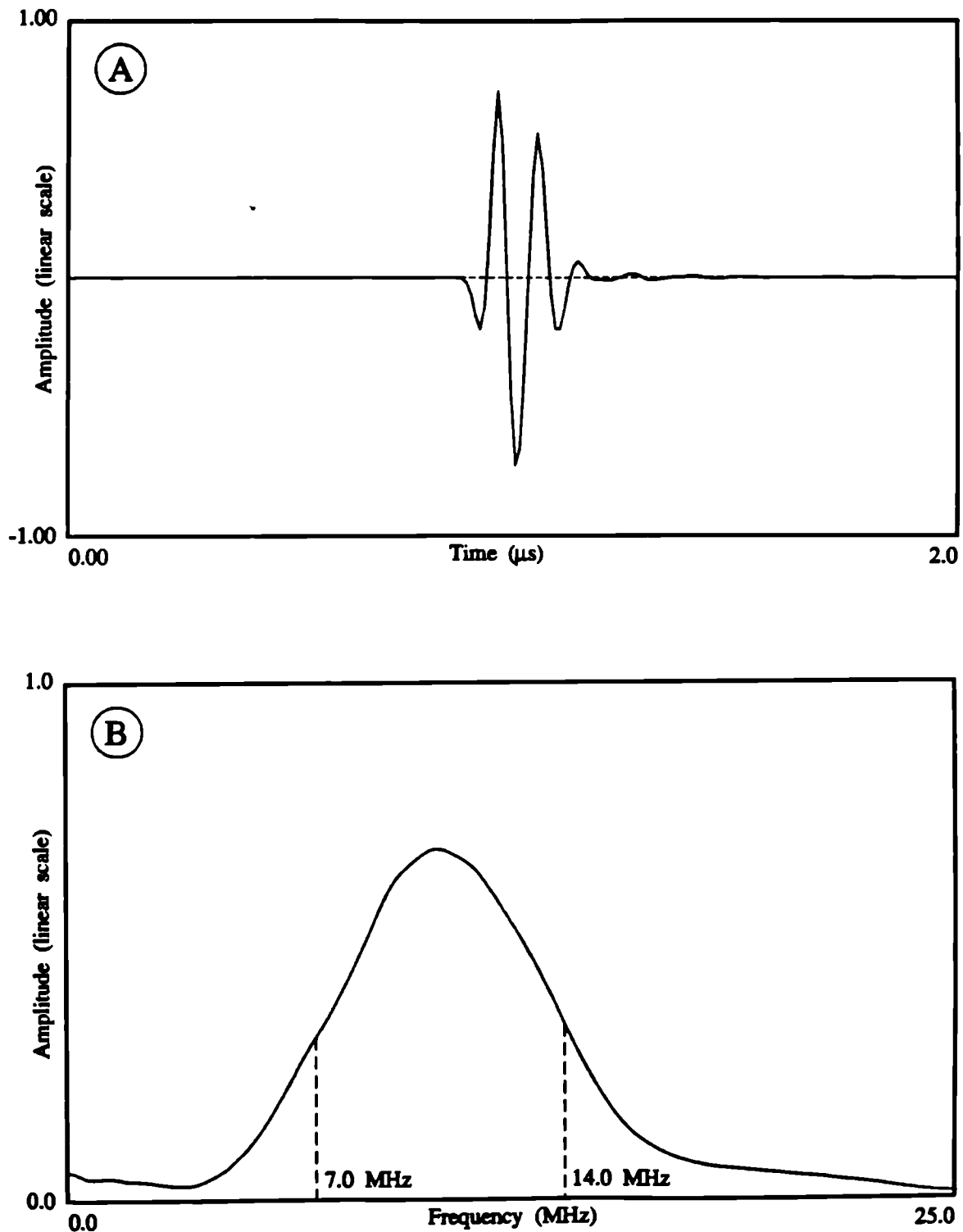
Fig. 5.9   The time domain and the frequency domain representations of the reflected
pulse from the front face of the 20 mm thick aluminium block. Angle of
incidence was 20 degrees.A pair of 10 MHz wideband Rolls-Royce Mateval
transducers were used for the experiments.
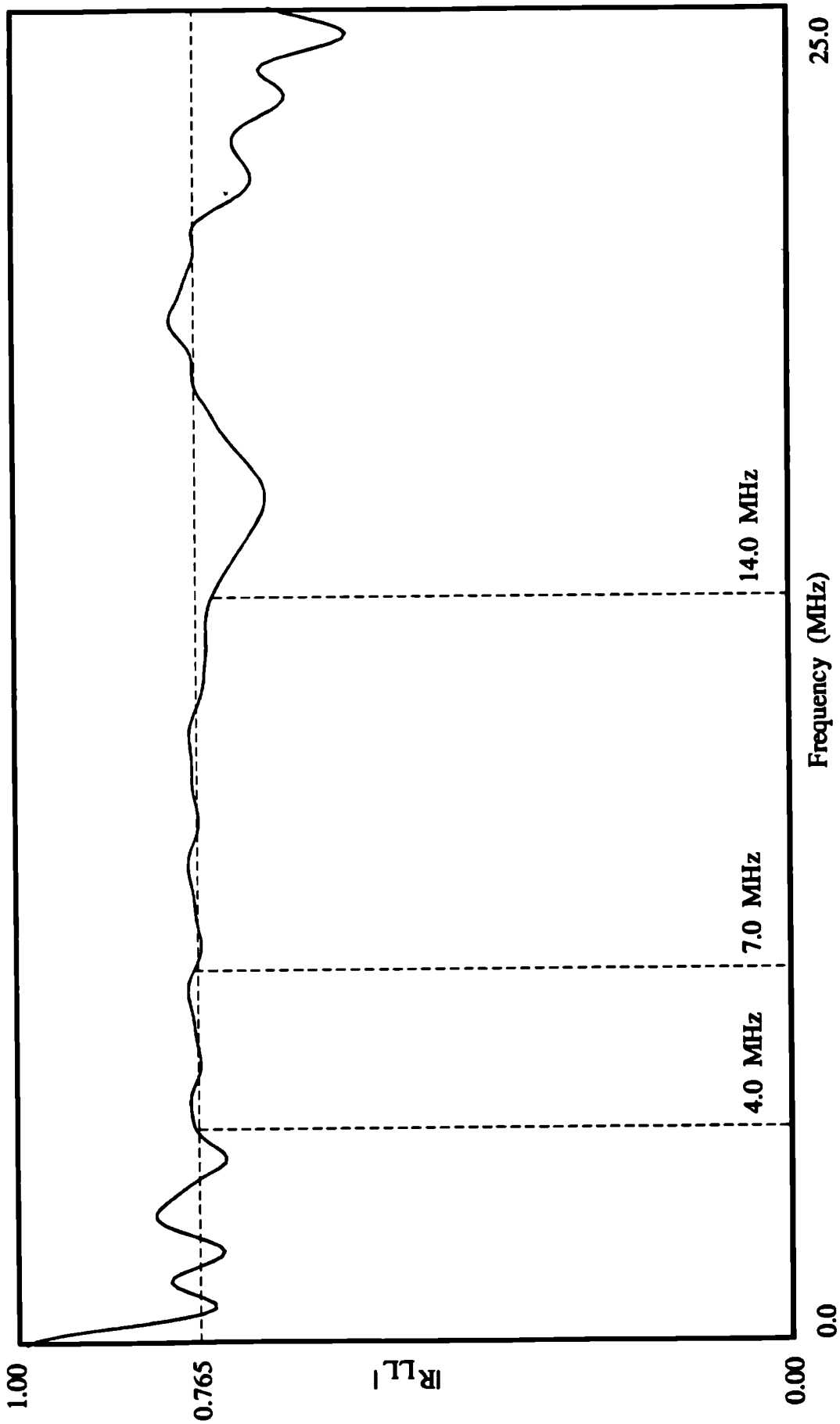
Fig. 5.10 Division of the reflected pulse spectrum by the reference spectrum. The reflection coefficient in the frequency range between 4.0 MHz and 14.0 MHz is obtained.

Chapter 5

Validation of the theory. Accuracy of the reflection coefficient measurements

210
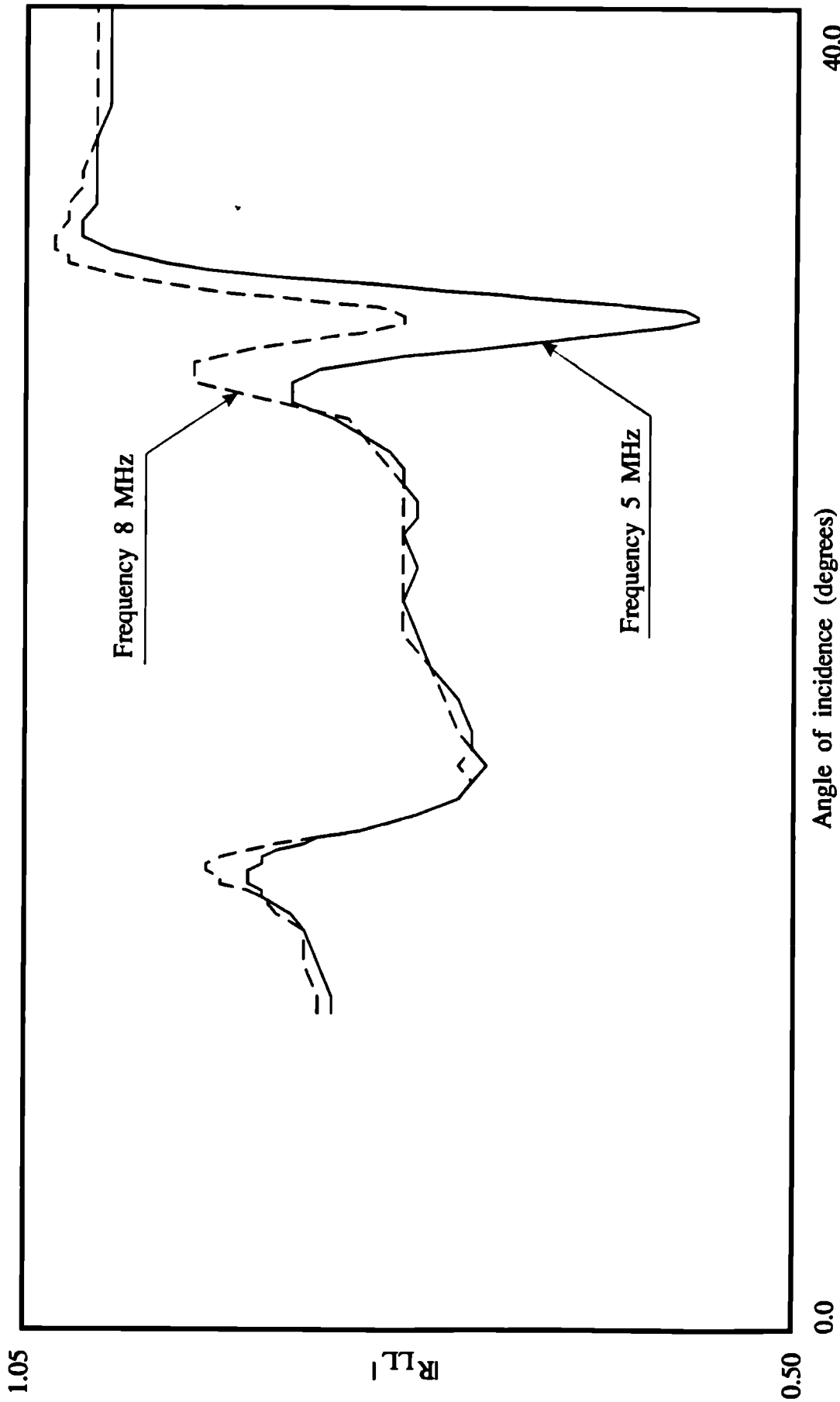
Fig. 5.11 Reflection coefficient measured from the surface of 20 mm thick aluminium block in water. A pair of 10 mm unfocussed transducer were used. Two curves show the reflection coefficient measured at two different frequencies, 8 MHz and 5 MHz.
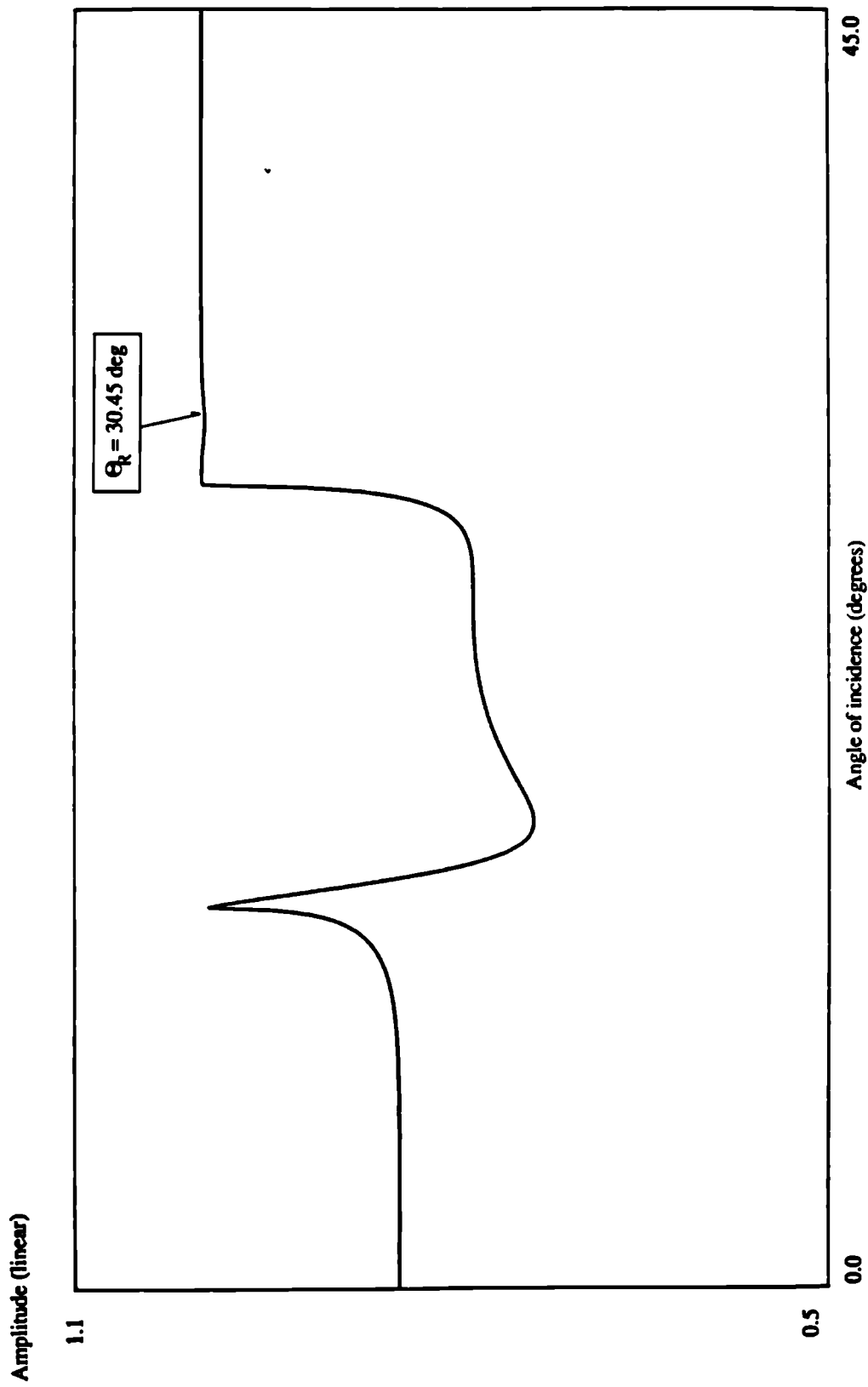
Fig. 5.12   Theoretically calculated reflection coefficient from aluminium/water interface using an infinite plane wave theory. Attenuation assumed a_L=0.002, a_S=0.0002 nepers per wavelength. Frequency 7 MHz. Small dip at the Rayleigh angle is visible.

Chapter 5

Validation of the theory. Accuracy of the reflection coefficient measurements

212
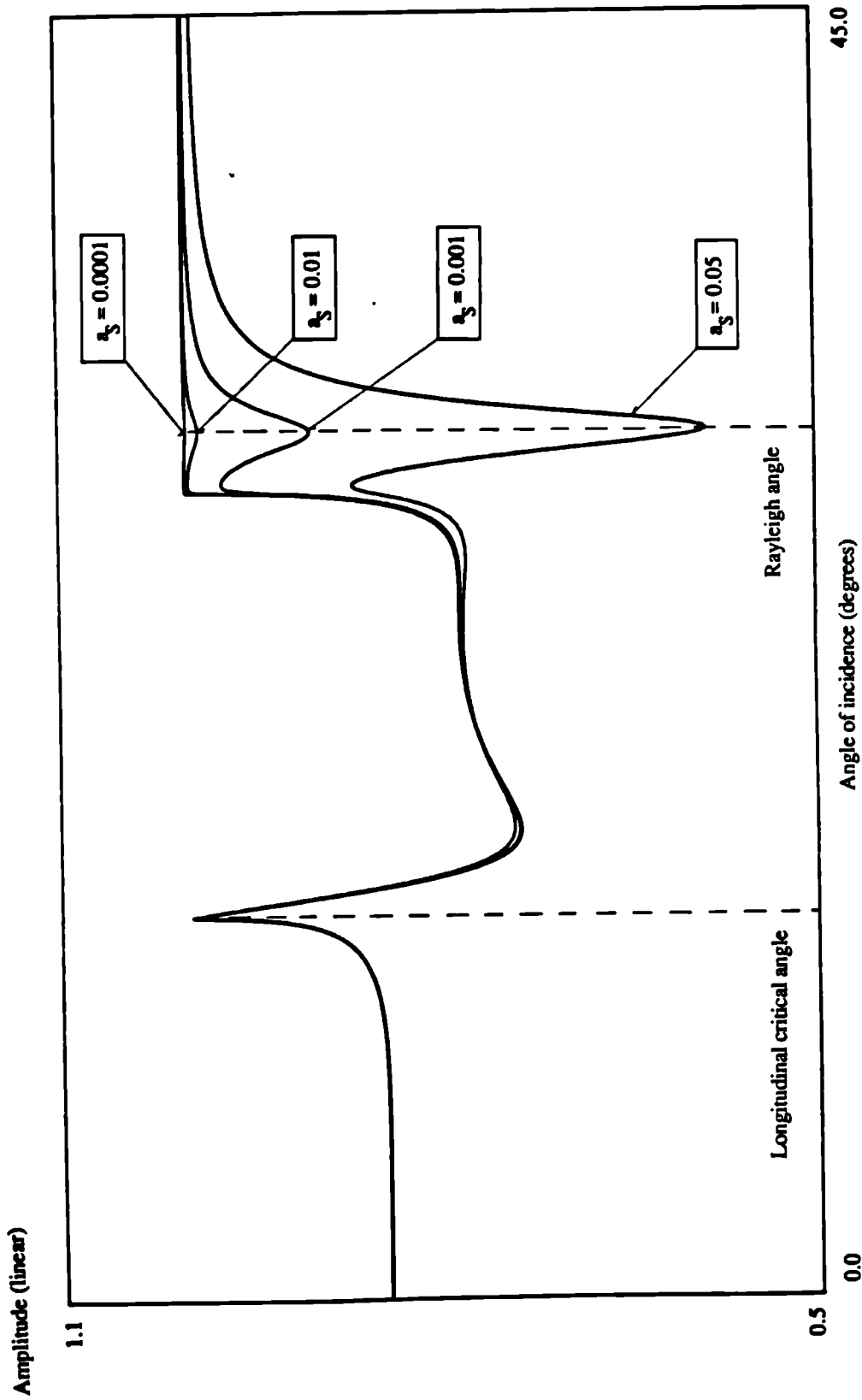
Fig. 5.13   Theoretically calculated reflection coefficient from aluminium/water interface using an infinite plane wave theory. Longitudinal attenuation in aluminium is zero, shear attenuation varies . a_S=0.0001, 0.001, 0.01, 0.05 nepers per wavelength. Frequency 7 MHz.
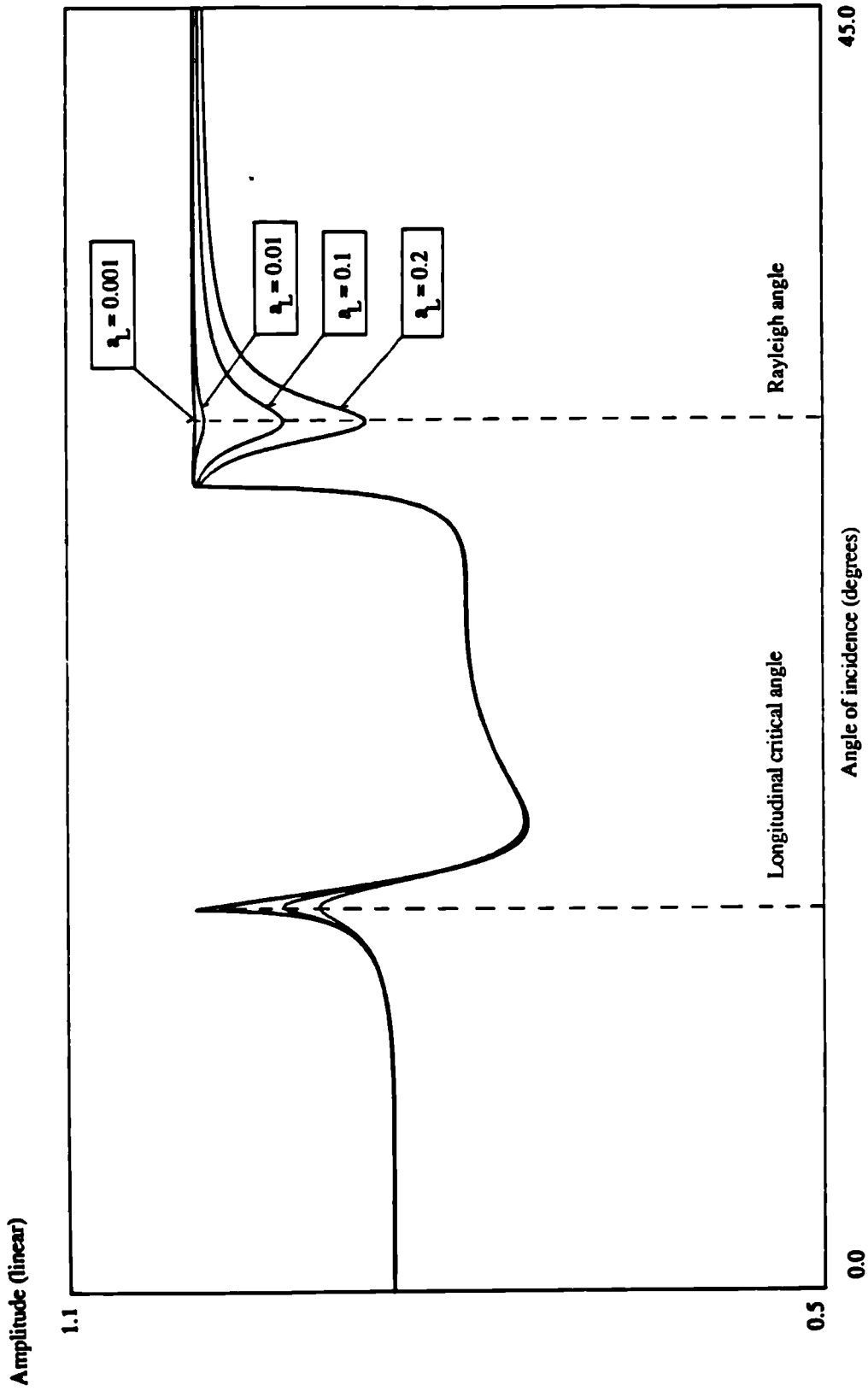
Fig. 5.14   Theoretically calculated reflection coefficient from aluminium/water interface using an infinite plane wave theory. Shear attenuation in aluminium is zero, longitudinal attenuation varies. a_L=0.001, 0.01, 0.1, 0.2 nepers per wavelength. Frequency 7 MHz.

Chapter 5

214

Validation of the theory. Accuracy of the reflection coefficient measurements
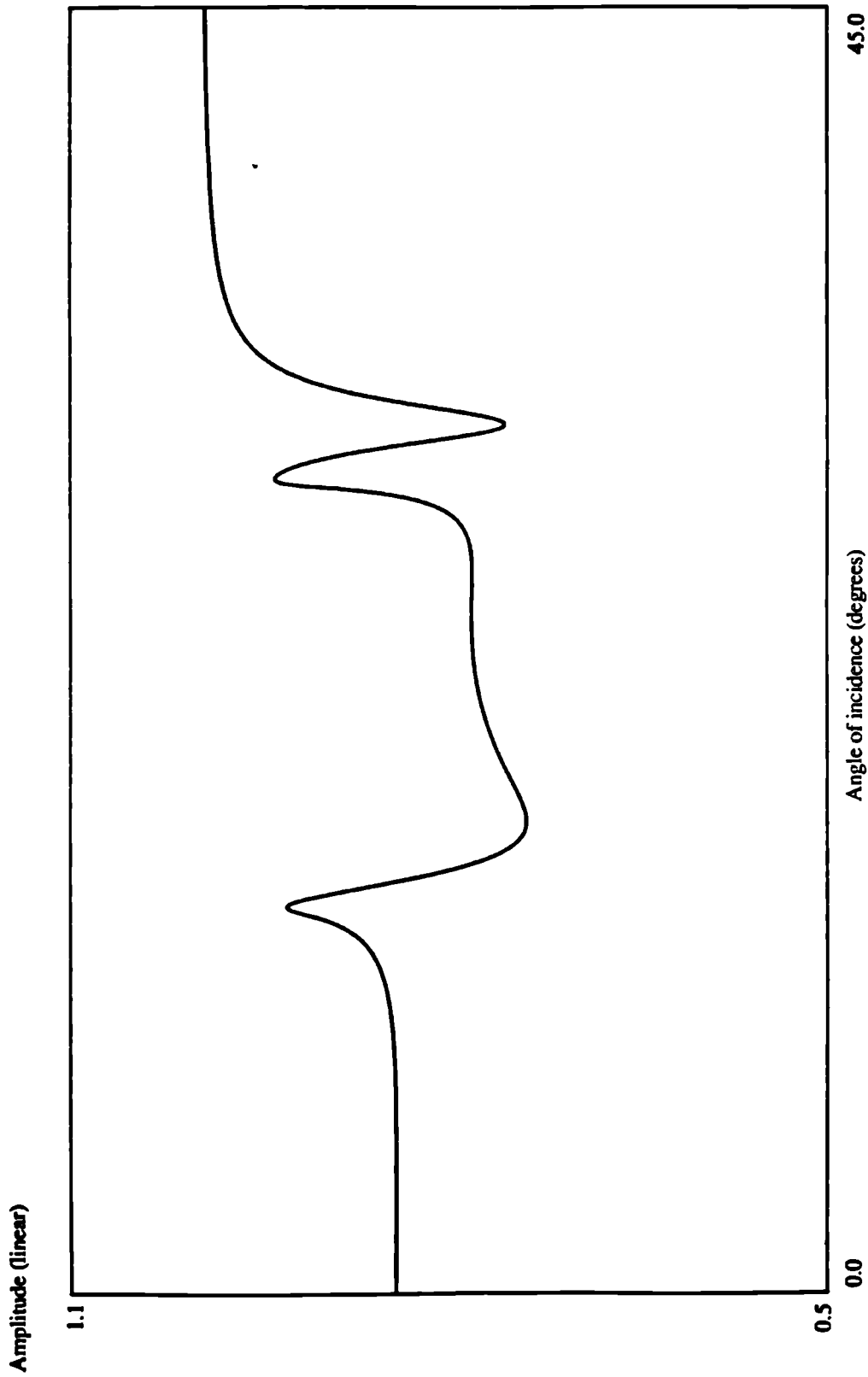
Fig. 5.15   Theoretically calculated reflection coefficient from aluminium/water interface using an infinite plane wave theory and viscoelastic model. Shear attenuation a_S=0.02, longitudinal attenuation a_L=0.1 nepers per wavelength. Frequency 7 MHz.

Chapter 5

Validation of the theory. Accuracy of the reflection coefficient measurements

215

Amplitude (linear)

1.1

0.5

Angle of incidence (degrees)

$\theta_R = 30.45$ deg

0.0

45.0
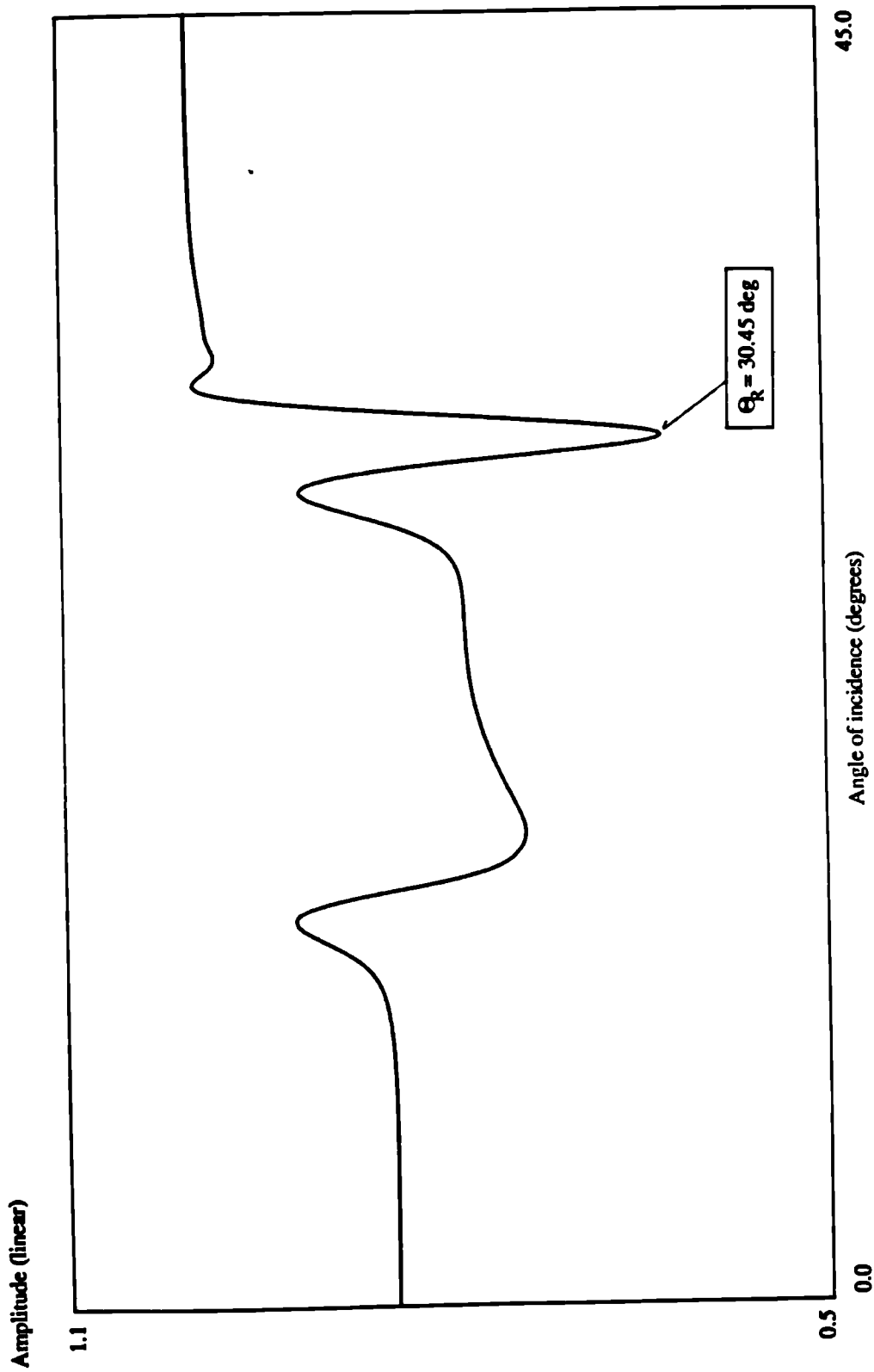
Fig. 5.16 Theoretically calculated reflection coefficient from aluminium/water interface using finite transducer theory and assuming small damping, the same as in fig. 5.12. Transmitter and receiver 10 mm wide, distance 100 mm, frequency 7 MHz.
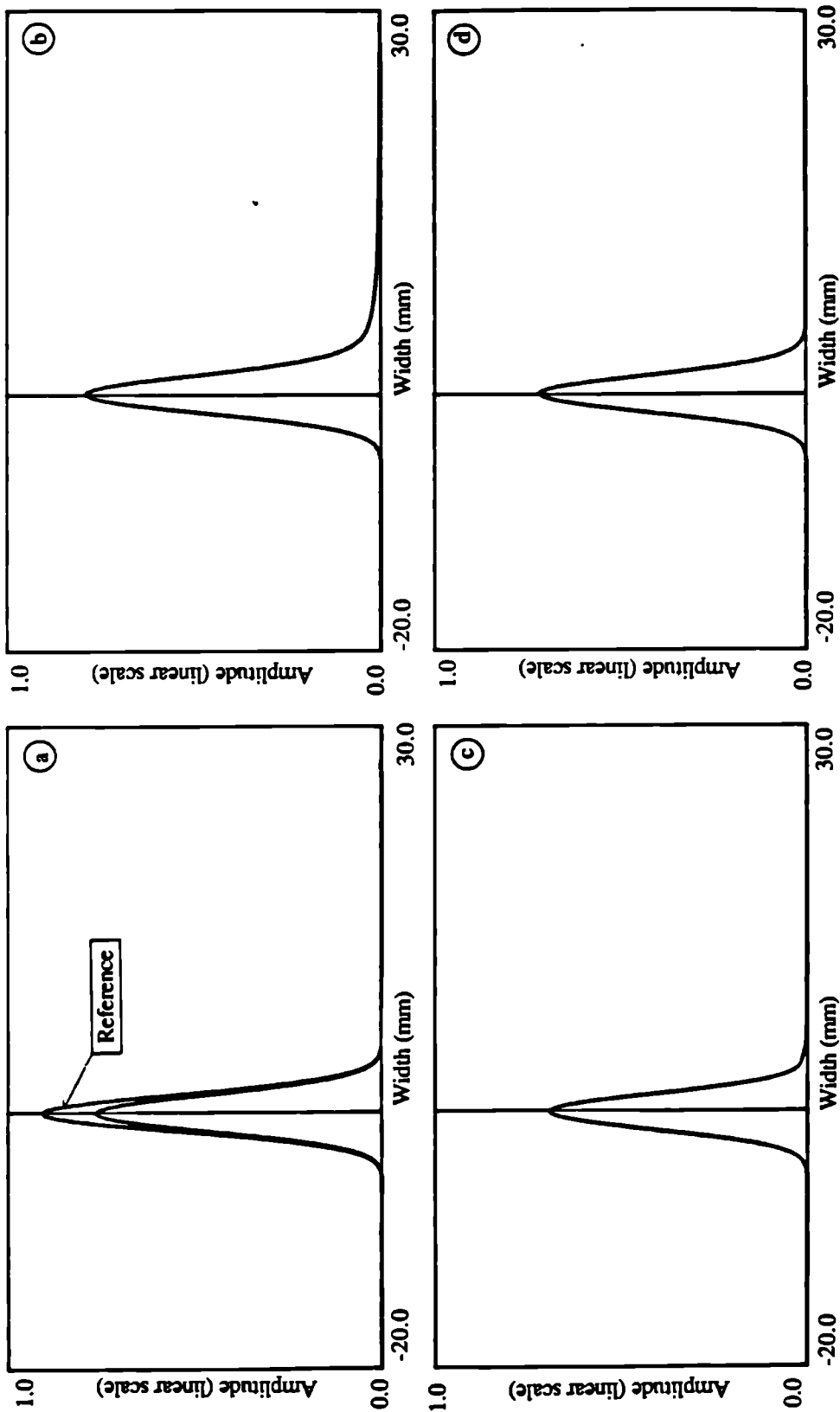
Validation of the theory. Accuracy of the reflection coefficient measurements

Fig. 5.17   Finite beam reflection from aluminium/water interface. Damping in the system as in fig.
5.16. Transmitter 10 mm wide, Gaussian displacement pattern, frequency 7 MHz.
Different angles of incidence.
(a) Normal incidence, and the reference signal, (b) longitudinal critical angle (13.45
degrees) incidence, (c) 16.5 degrees incidence, (d) 25.0 degrees incidence.
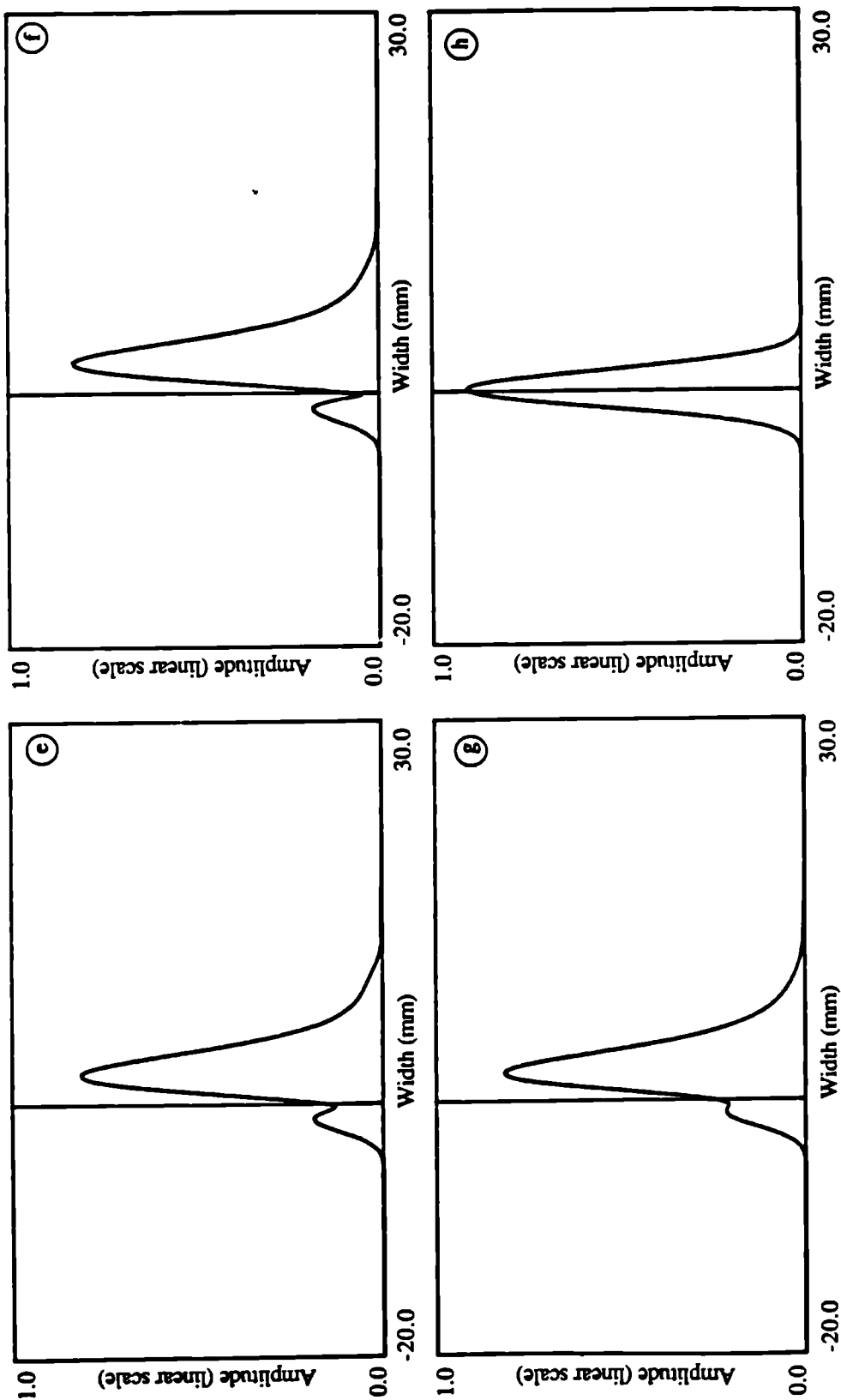
Chapter 5
Validation of the theory. Accuracy of the reflection coefficient measurements

217

Fig. 5.17 Finite beam reflection from aluminium/water interface. Damping in the system as in fig. 5.16. Transmitter 10 mm wide, Gaussian displacement pattern, frequency 7 MHz. Different angles of incidence.
(e) Θ_R-0.5 degrees incidence, (f) (Rayleigh angle (Θ_R=30.45 degrees) incidence, (g) Θ_R+0.5 degrees incidence, (h) Θ_R+5.0 degrees incidence.

Chapter 5

Validation of the theory. Accuracy of the reflection coefficient measurements

218
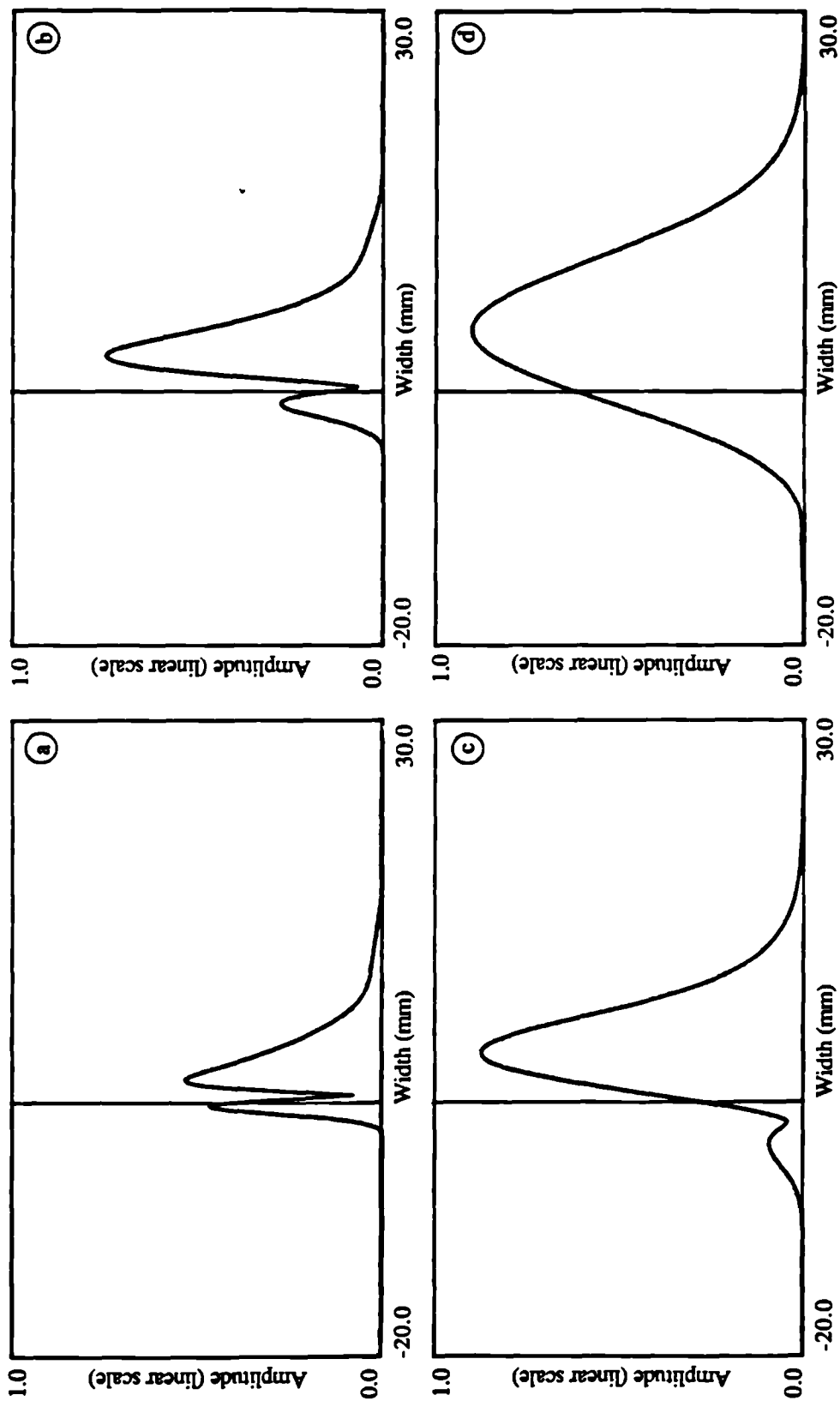
Fig. 5.18   Finite beam reflection from aluminium/water interface. Damping in the system as in fig. 5.16. Transmitter 10 mm wide, Gaussian displacement pattern, frequency 7 MHz. Rayleigh angle incidence. Different widths of the transmitter. (a) 5 mm wide, (b) 10 mm wide, (c) 20 mm wide, (d) 40 mm wide.
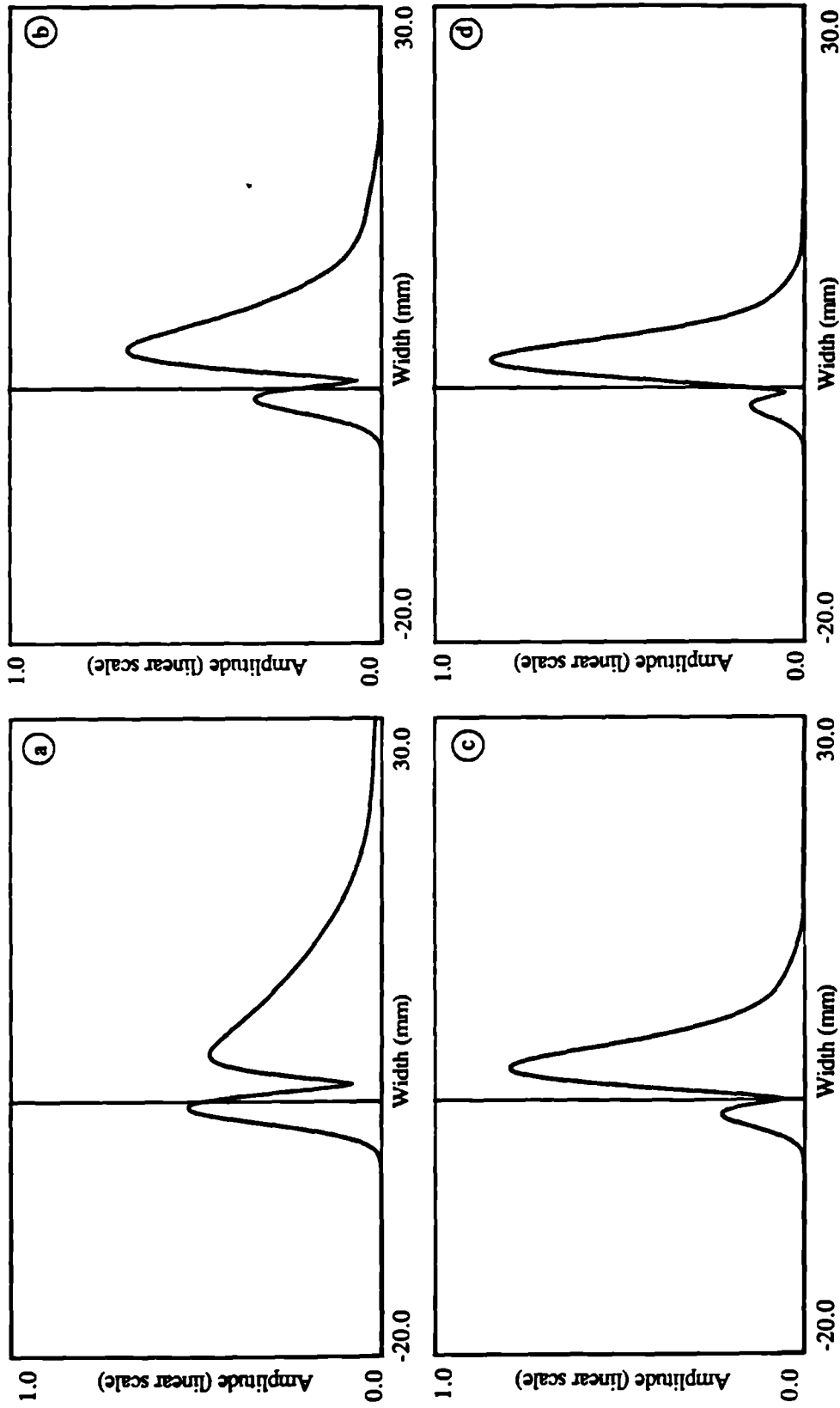
Fig. 5.19   Finite beam reflection from aluminium/water interface. Damping in the system as in fig. 5.16. Transmitter 10 mm wide, Gaussian displacement pattern. Rayleigh angle incidence. Transmitter 10 mm wide. Different frequencies of excitation. (a) 2 MHz, (b) 4 MHz, (c) 6 MHz, (d) 8 MHz.
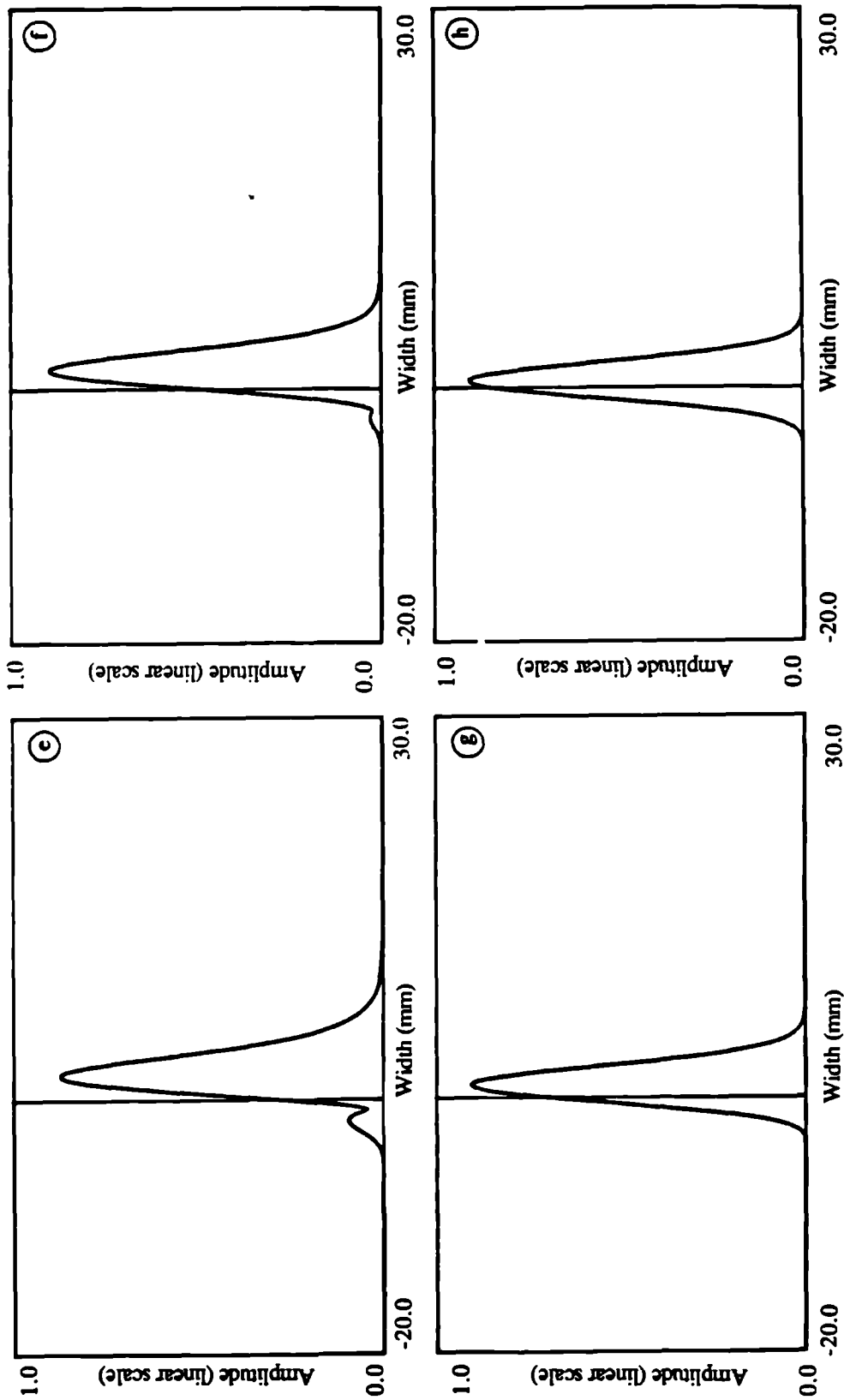
Chapter 5

Validation of the theory. Accuracy of the reflection coefficient measurements

220

Fig. 5.19   Finite beam reflection from aluminium/water interface. Damping in the system as in fig. 5.16. Transmitter 10 mm wide, Gaussian displacement pattern. Rayleigh angle incidence. Transmitter 10 mm wide. Different frequencies of excitation. (e) 10 MHz, (f) 15 MHz, (g) 25 MHz, (h) 50 MHz.

Chapter 5

Validation of the theory. Accuracy of the reflection coefficient measurements

221
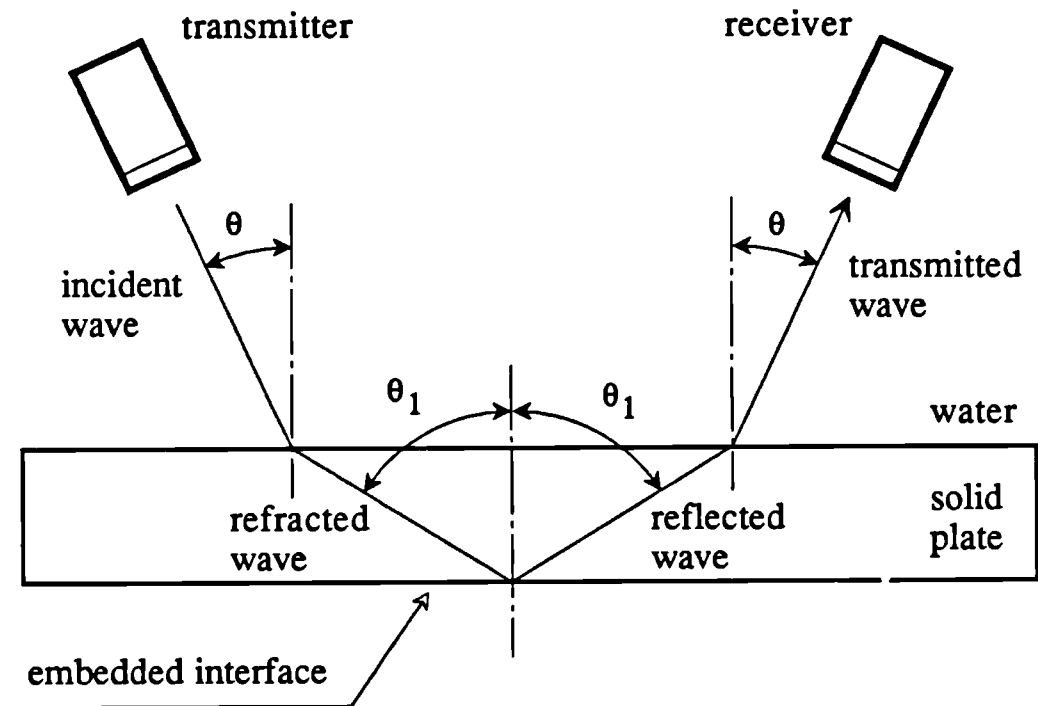
Fig 5.20 The concept of the measurements of the reflection coefficient from the embedded interfaces.

Chapter 5

Validation of the theory. Accuracy of the reflection coefficient measurements

222
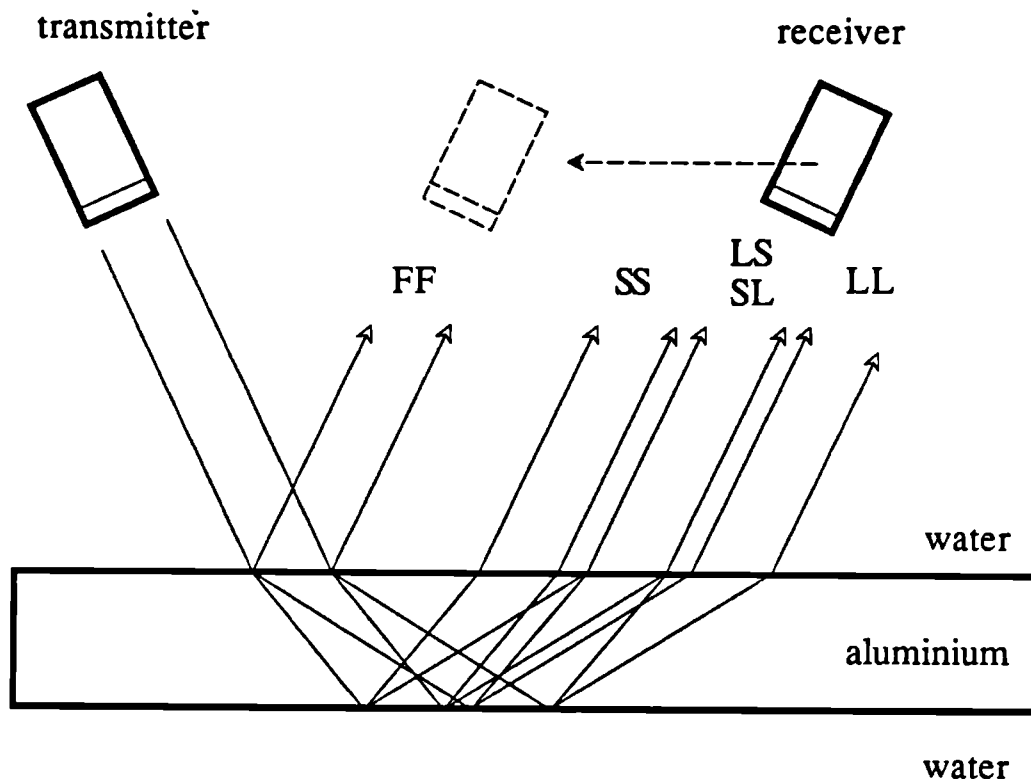
Fig 5.21 Measurements of reflections from an aluminium plate in water
at the oblique incidence.

Chapter 5

Validation of the theory. Accuracy of the reflection coefficient measurements

223
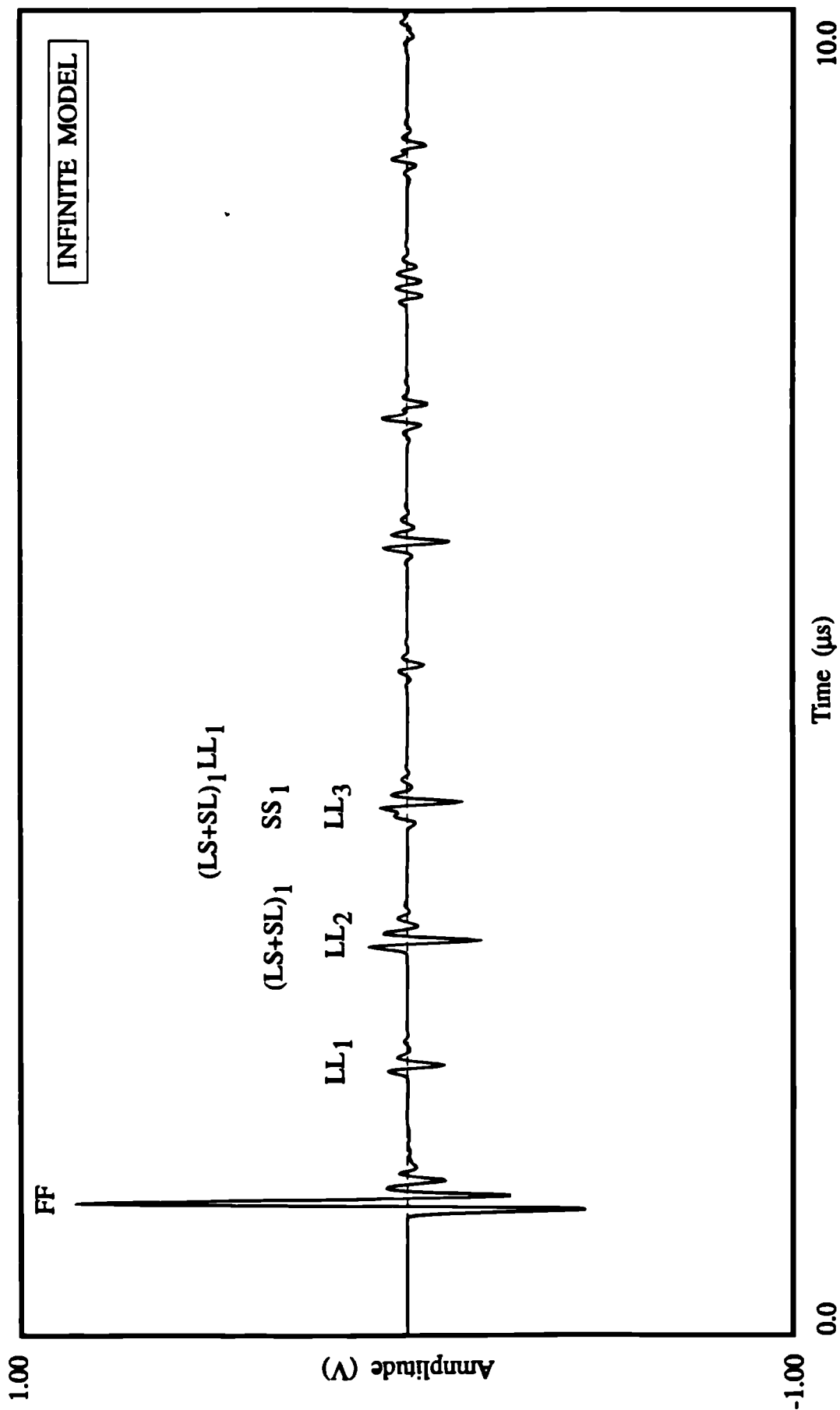
Fig. 5.22   Response of the 4.85 mm thick aluminium plate in water to a pulse excitation incident at 10 degrees from water. Infinite plane wave model.

Chapter 5

224

Validation of the theory. Accuracy of the reflection coefficient measurements
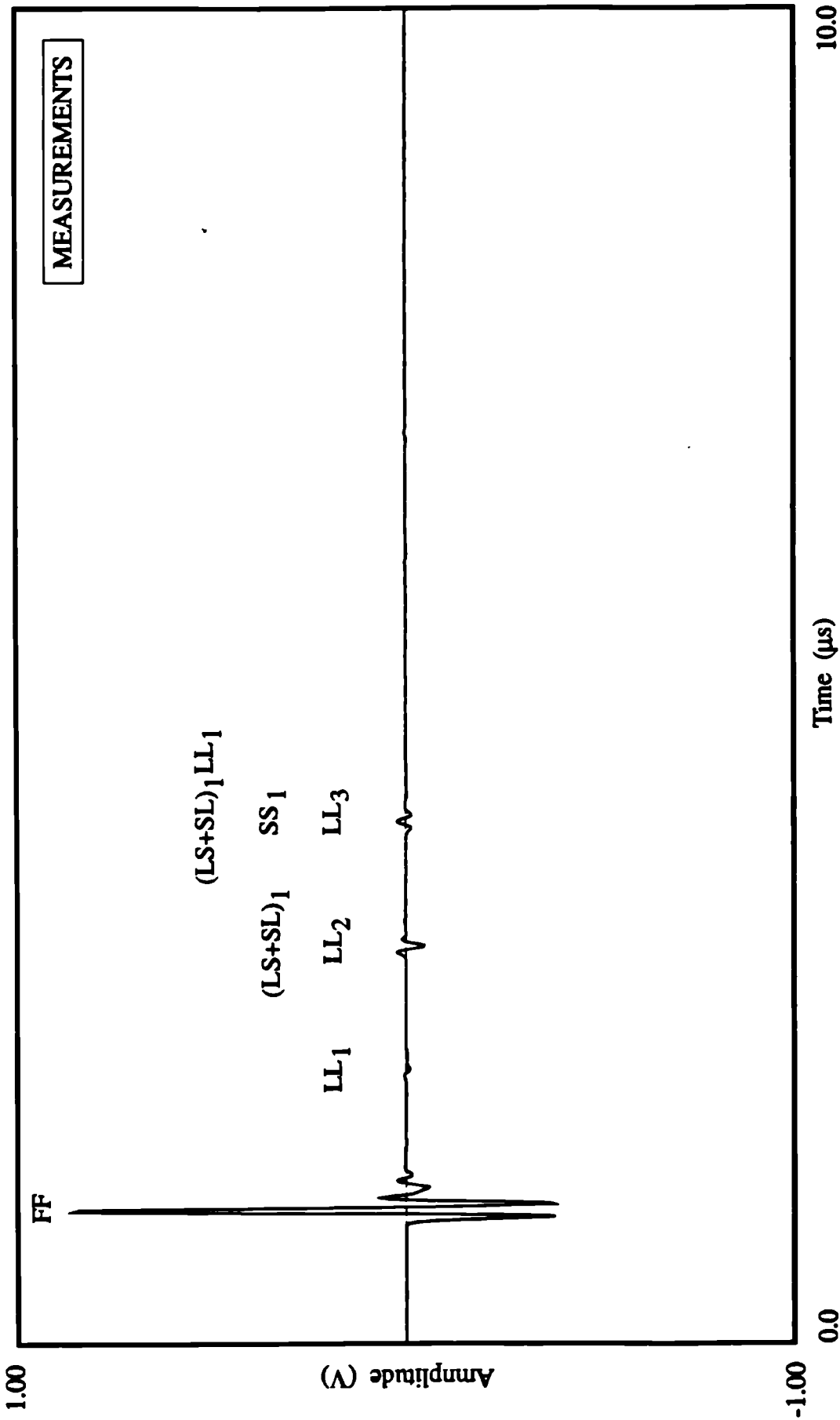
Fig. 5.23 Measured response of the 4.85 mm thick aluminium plate in water to a pulse excitation from the 10 MHz wideband transducer. Angle of incidence is 10 degrees. Transducers focussed to receive the FF reflection.

Chapter 5

225

Validation of the theory. Accuracy of the reflection coefficient measurements

FINITE TRANSDUCER MODEL

FF

LL_1

$(LS+SL)_1$ LL_2

$(LS+SL)_1$ SS_1

$(LS+SL)_1 LL_1$

LL_3

Amplitude (V)

1.00

-1.00

Time (μs)

0.0

10.0
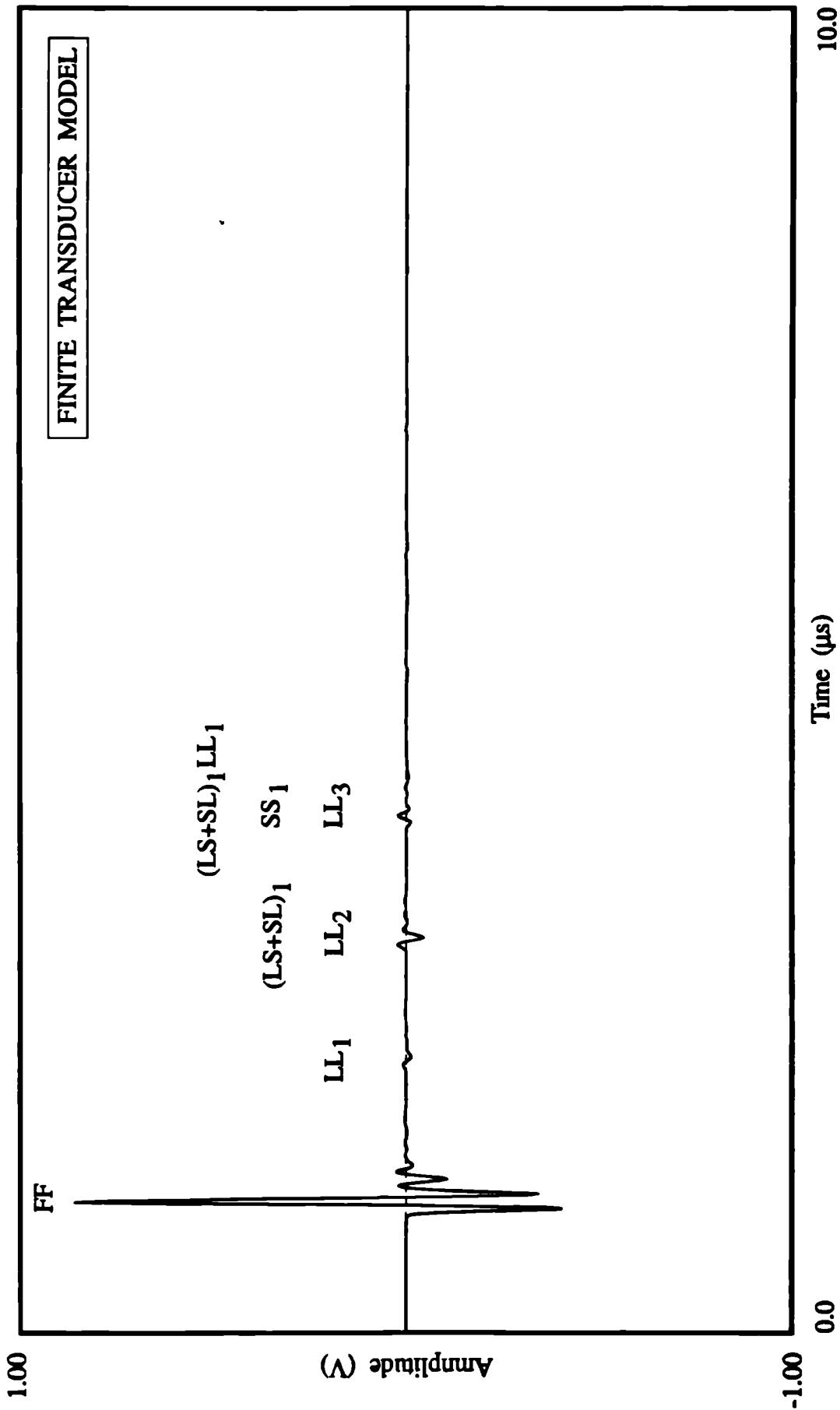
Fig. 5.24 Theoretically calculated response from the 4.85 mm thick aluminium plate in water. Angle of incidence is 10 degrees. Diameters of the probes are 10 mm. Transducers focussed to receive the FF reflection.
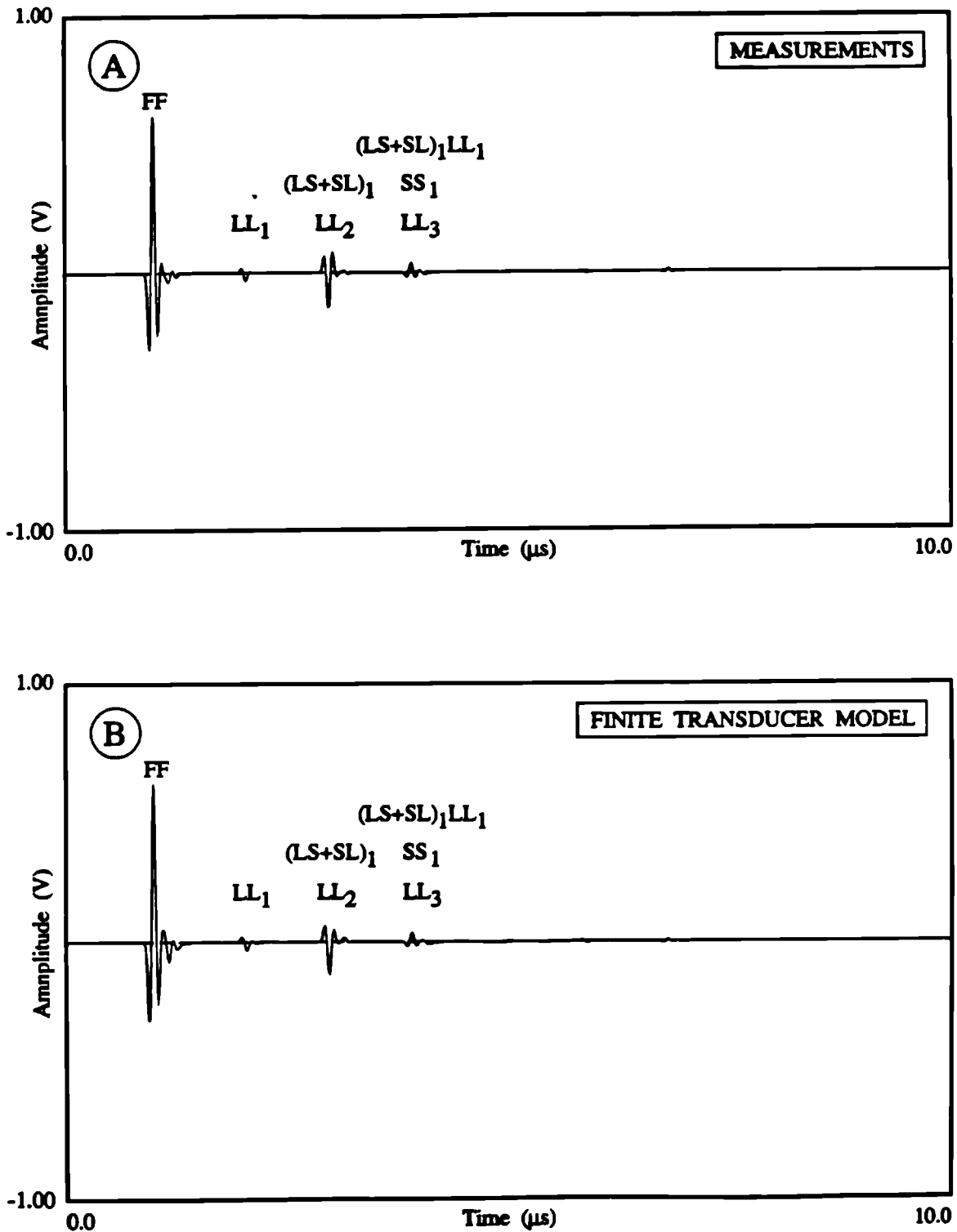
Fig. 5.25   Response from the 4.85 mm thick aluminium plate in water. Angle of incidence
is 10 degrees. The receiver is positioned to capture SS_1 reflection. Comparison
between the measurements (a), and theory (b).
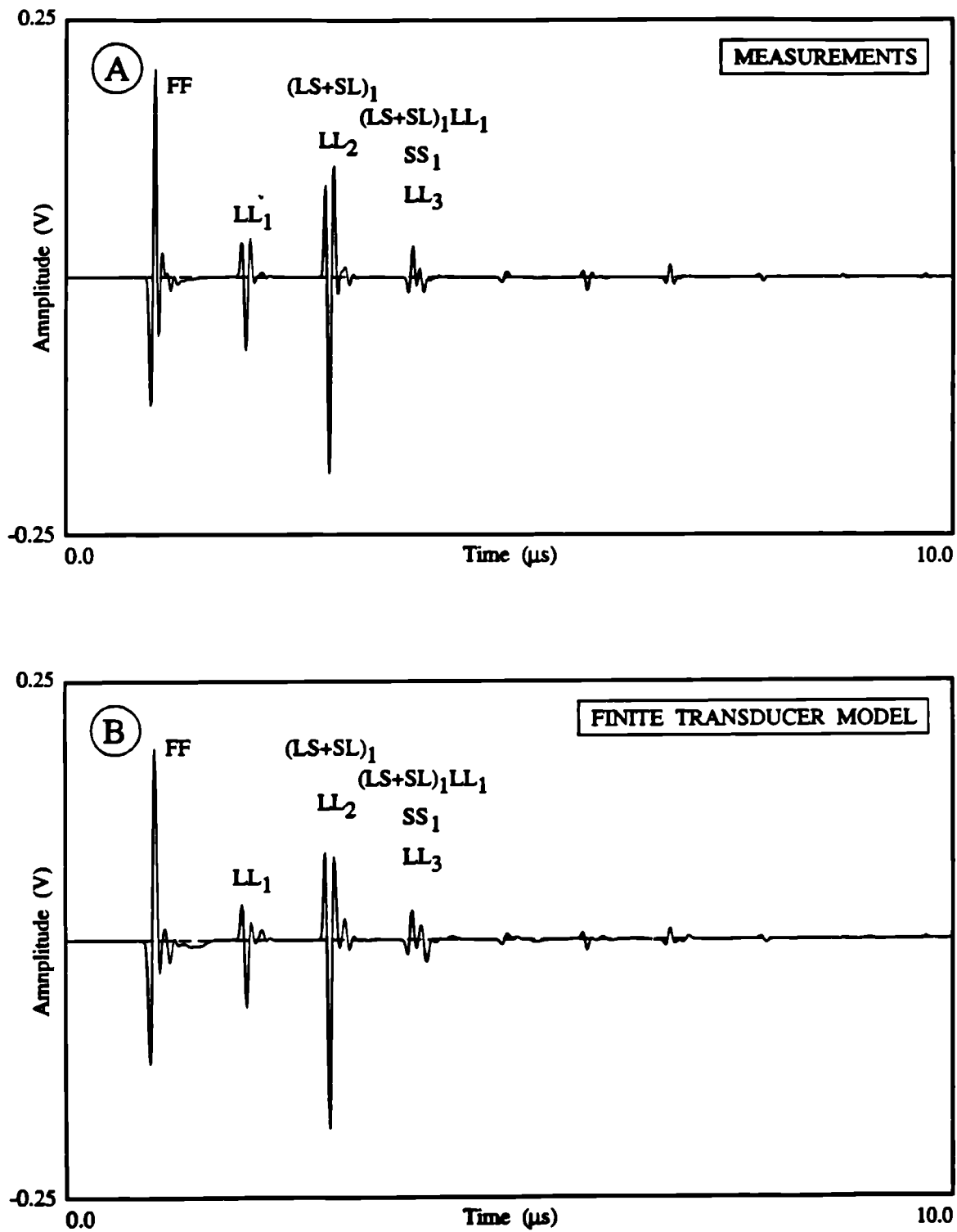
Fig. 5.26   Response from the 4.85 mm thick aluminium plate in water. Angle of incidence
is 10 degrees. The receiver is positioned to capture $(LS+SL)_1$ reflection.
Comparison between the measurements (a), and theory (b).

Chapter 5
Validation of the theory. Accuracy of the reflection coefficient measurements

228
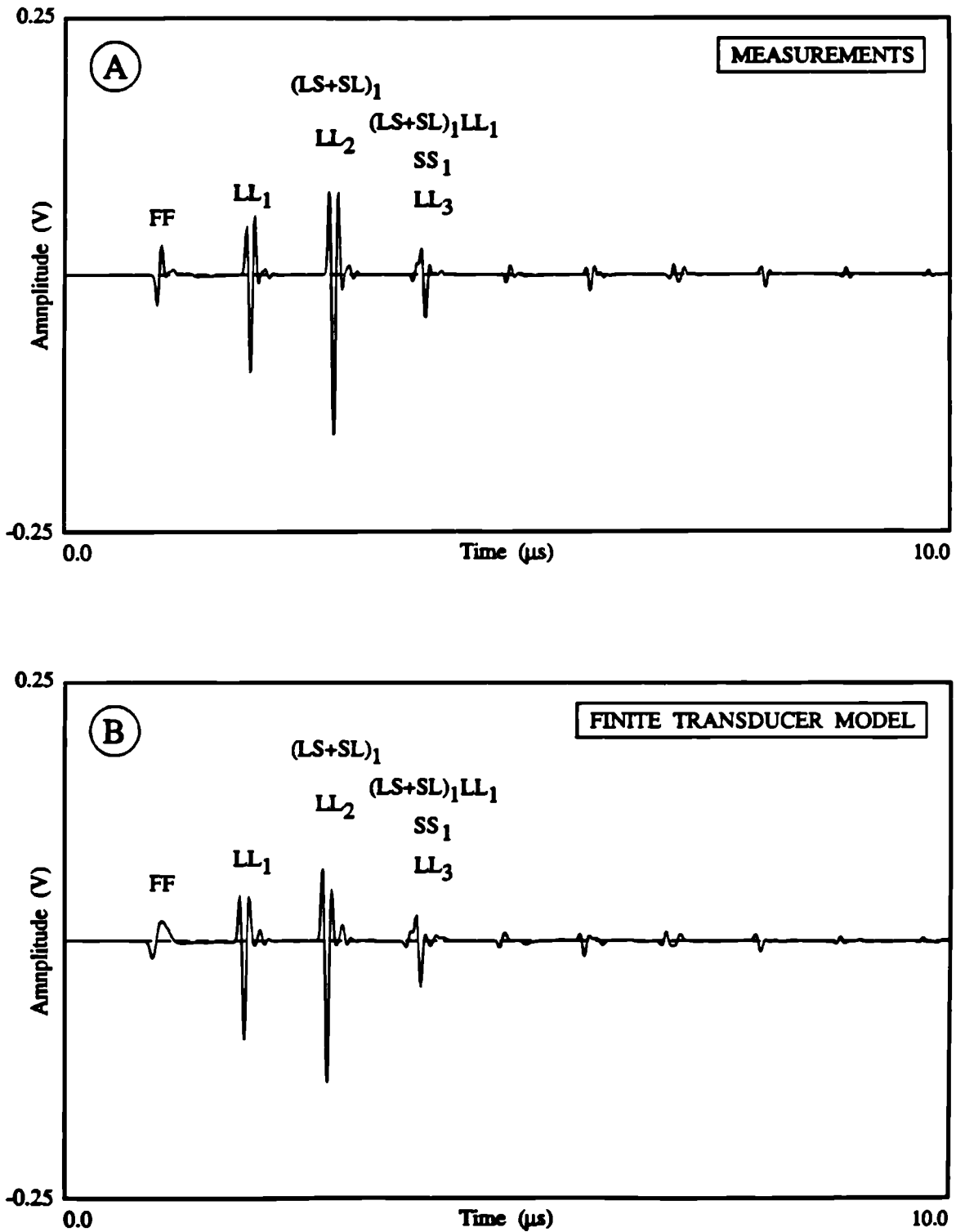
Fig. 5.27 Response from the 4.85 mm thick aluminium plate in water. Angle of incidence is 10 degrees. The receiver is positioned to capture LL_1 reflection. Comparison between the measurements (a), and theory (b).
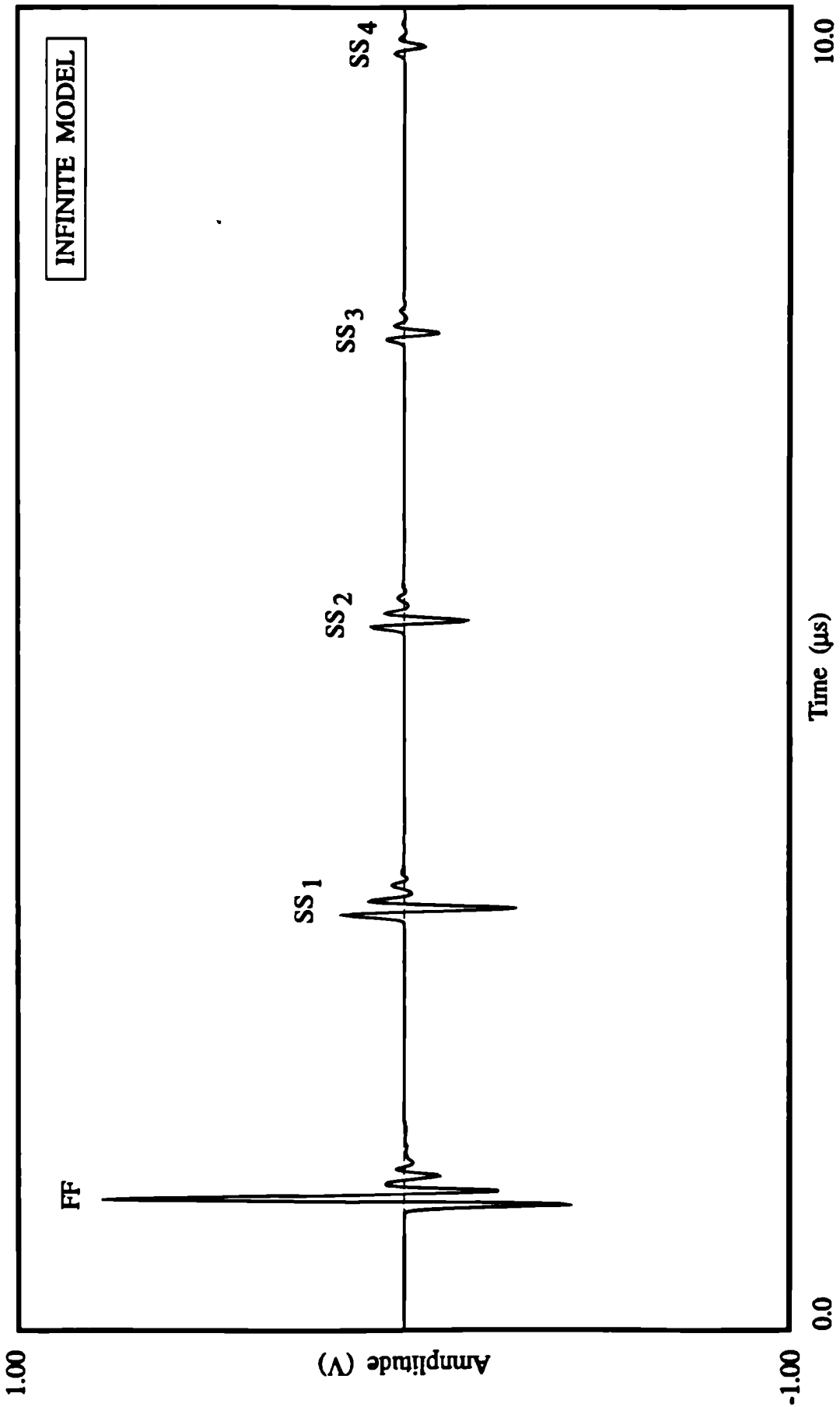
Fig. 5.28 Response of the 4.85 mm thick aluminium plate in water to a pulse excitation incident at 20 degrees from water. Infinite plane wave model.
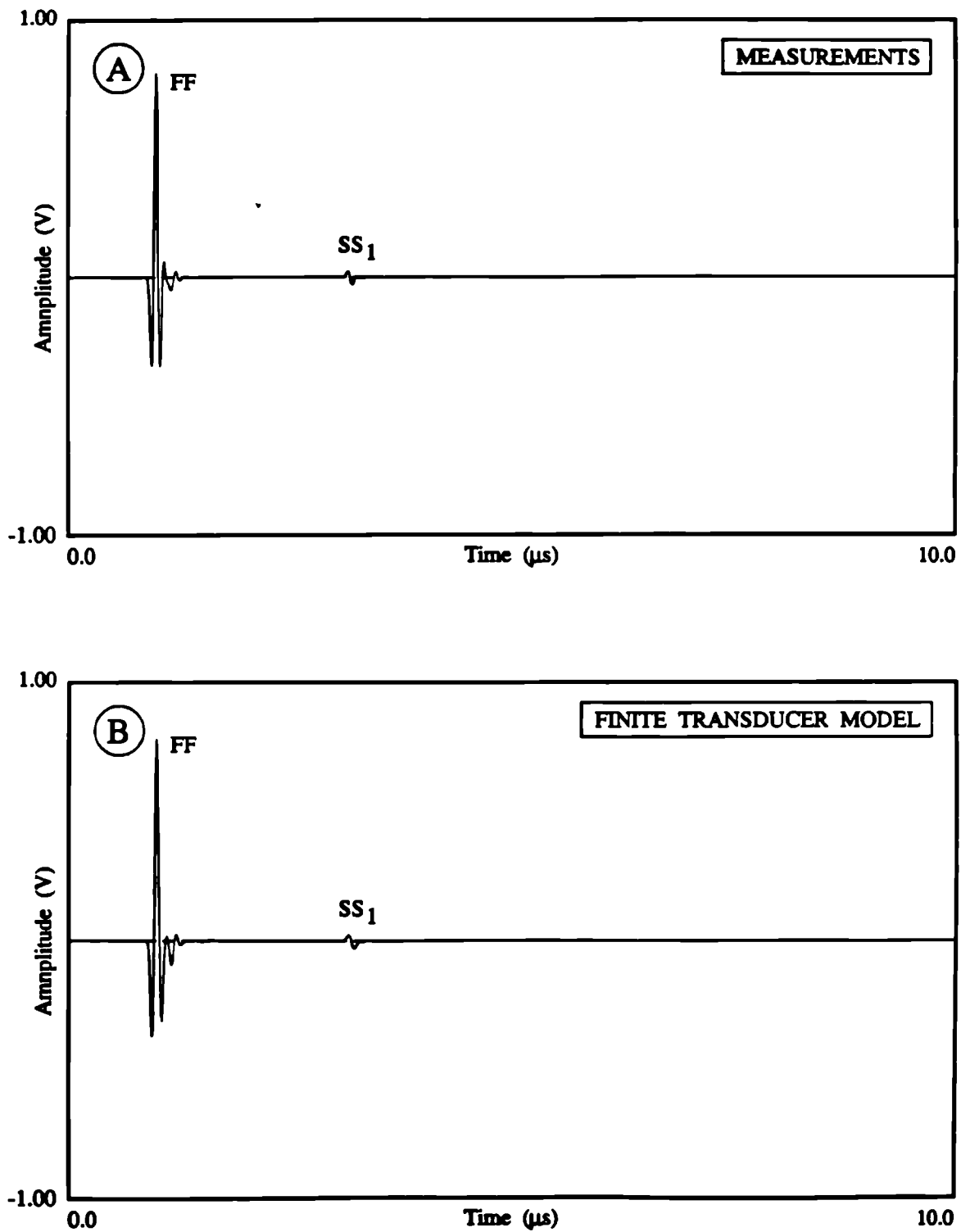
Fig. 5.29   Response from the 4.85 mm thick aluminium plate in water. Angle of incidence
             is 20 degrees. The receiver is positioned to capture FF reflection. Comparison
             between the measurements (a), and theory (b).
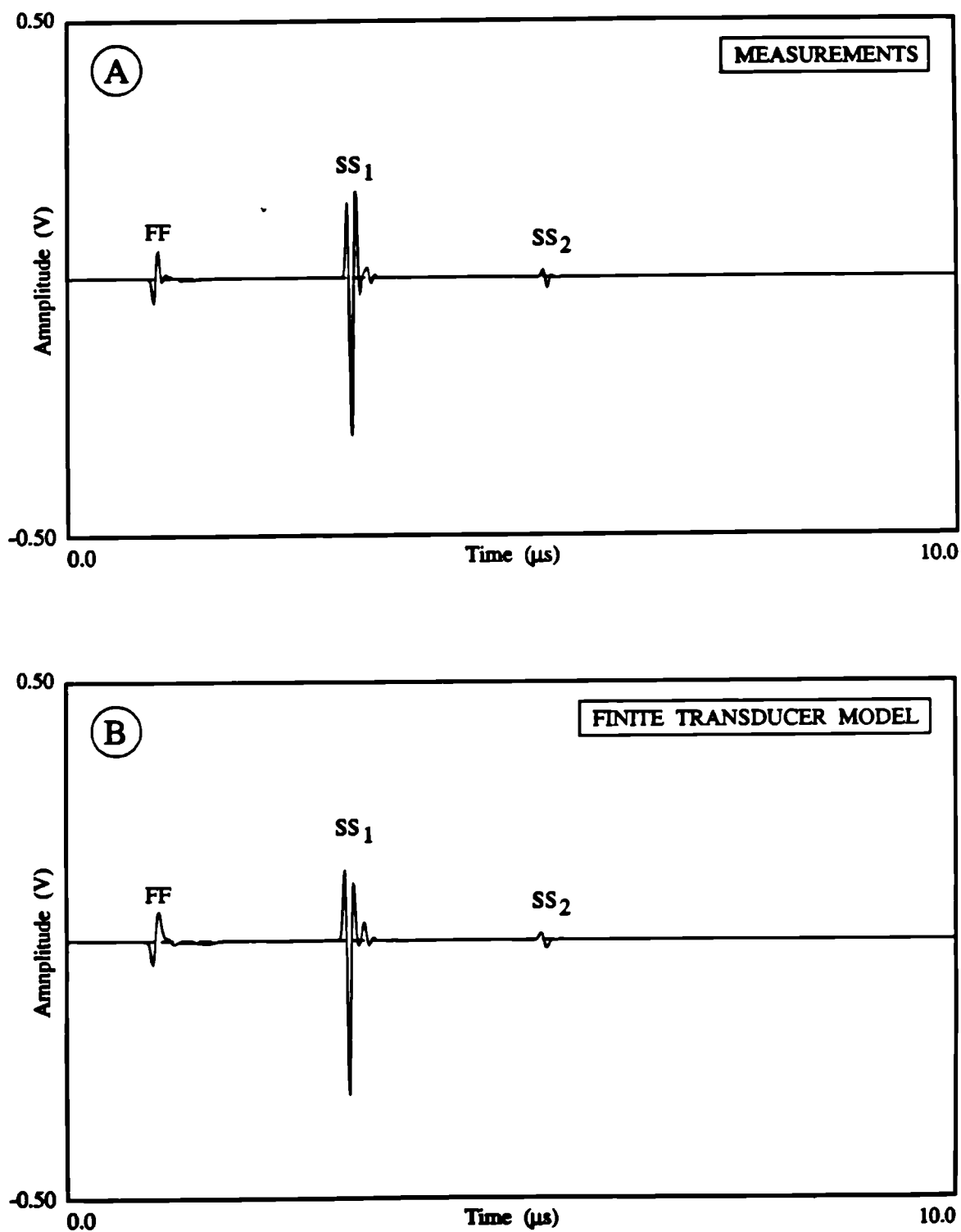
Fig. 5.30   Response from the 4.85 mm thick aluminium plate in water. Angle of incidence is 20 degrees. The receiver is positioned to capture SS_1 reflection. Comparison between the measurements (a), and theory (b).

5.85 mm thick
glass plates

silicone liquid layer
(exaggerated thickness)
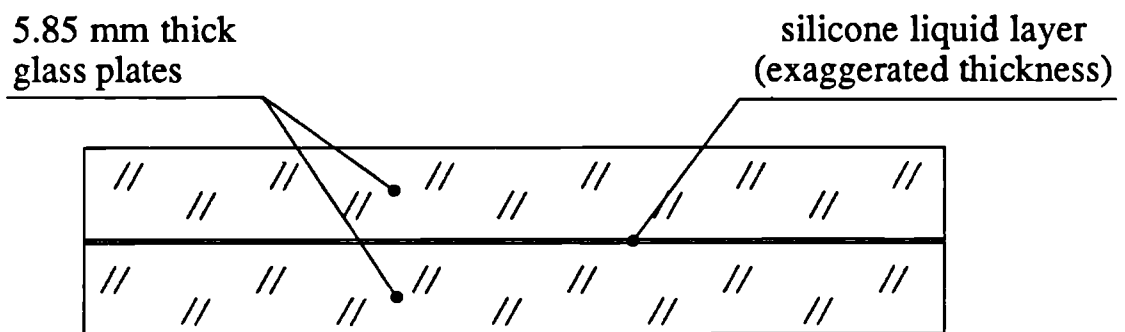
Fig 5.31 Schematic diagram of the glass/silicone/glass system
used for the experiments.

Chapter 5

233

Validation of the theory. Accuracy of the reflection coefficient measurements
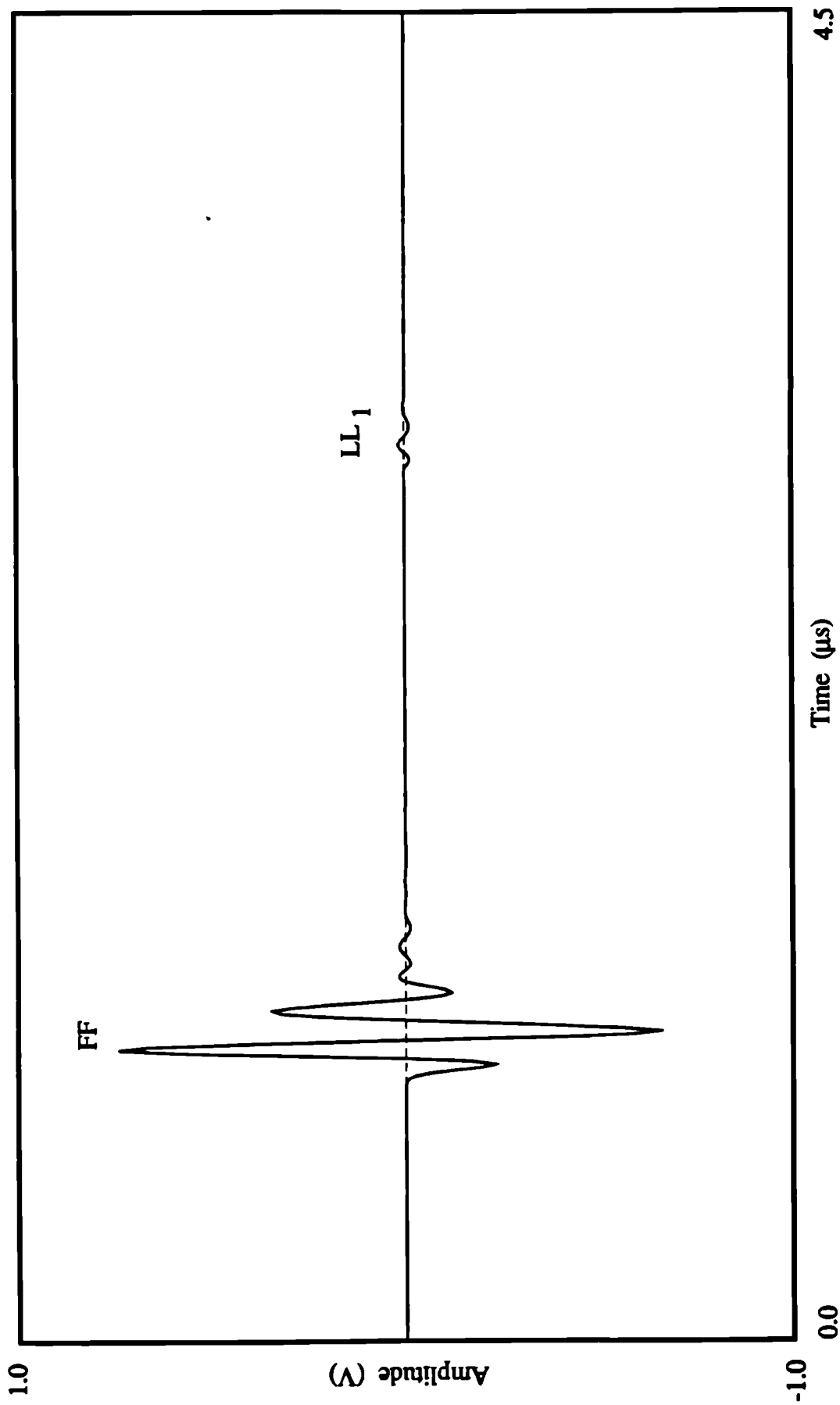
Fig. 5.32 Time domain response from the glass/silicone layer/glass system in water to the normal incidence longitudinal excitation from the 10 MHz wideband transducer.

Chapter 5

234

Validation of the theory. Accuracy of the reflection coefficient measurements
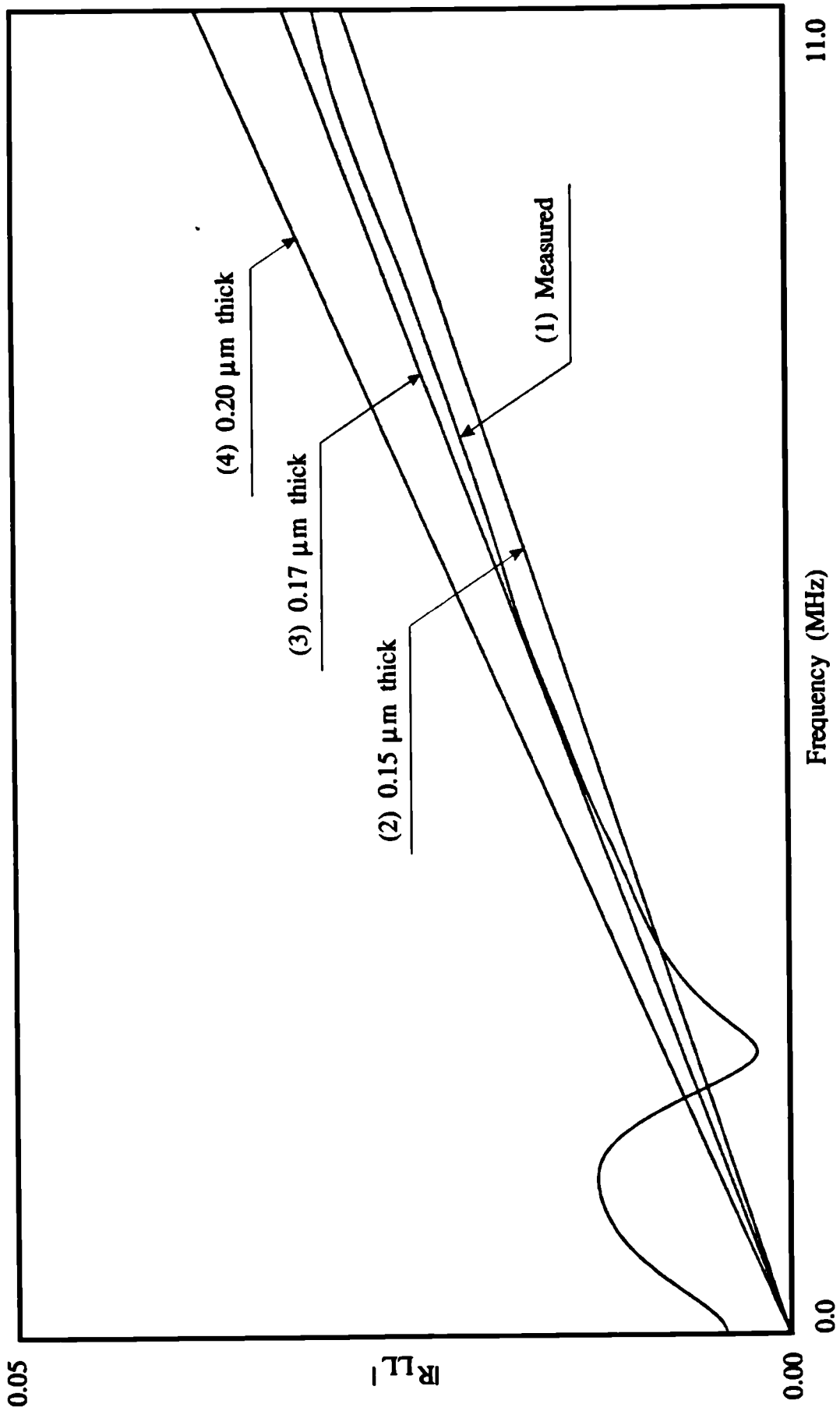
Fig. 5.33   Normal incidence longitudinal reflection coefficient from the silicone layer in glass. Comparison between the measurements and theoretically computed curves. Properties of glass and silicone liquid are given in table 5.4.

Chapter 5   235

Validation of the theory. Accuracy of the reflection coefficient measurements
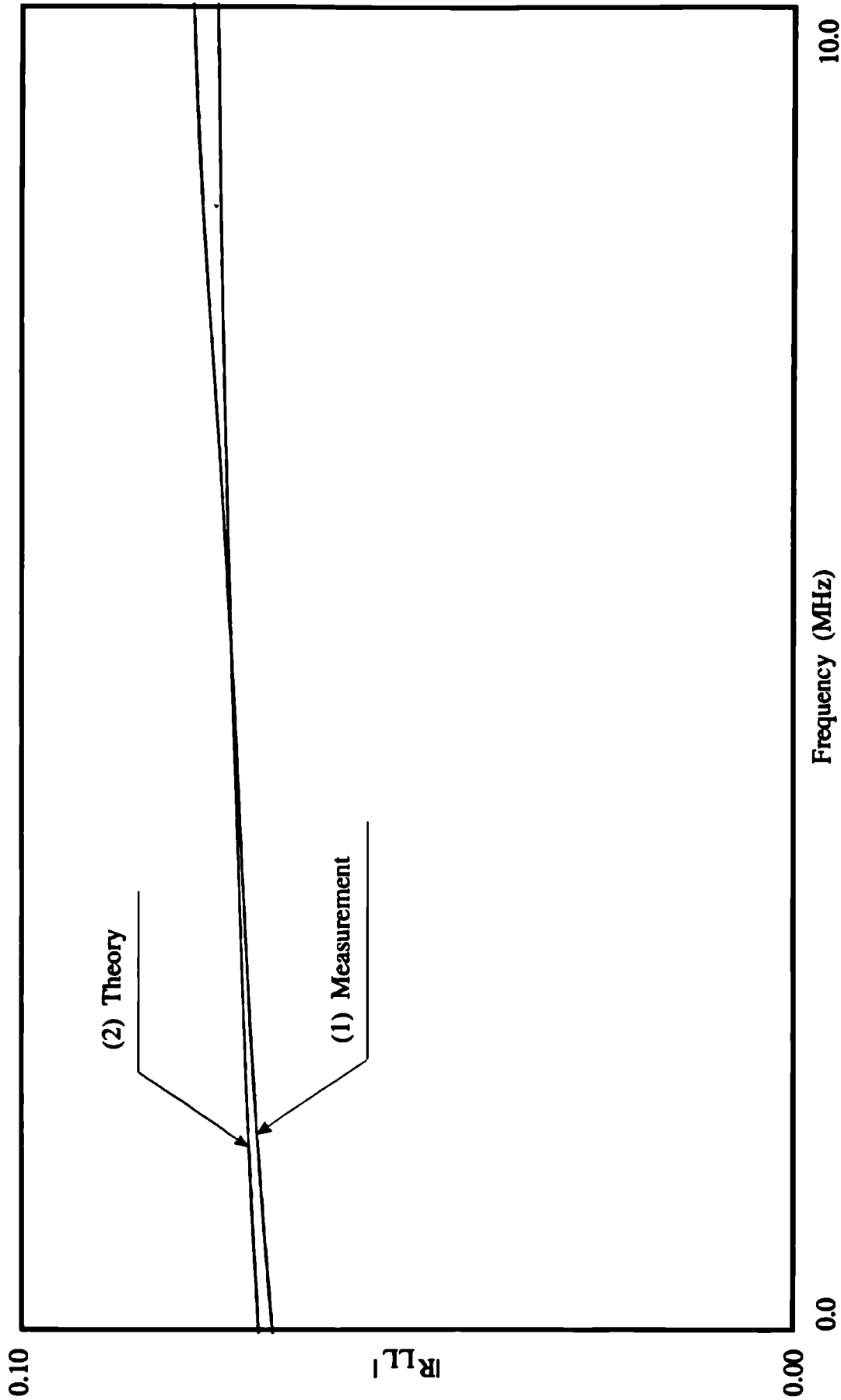
Fig. 5.34 Logitudinal-longitudinal reflectivity from the silicone layer in glass. Angle of incidence is 10 degrees from water. Comparison between theory and measurements.

Chapter 5 236

Validation of the theory. Accuracy of the reflection coefficient measurements
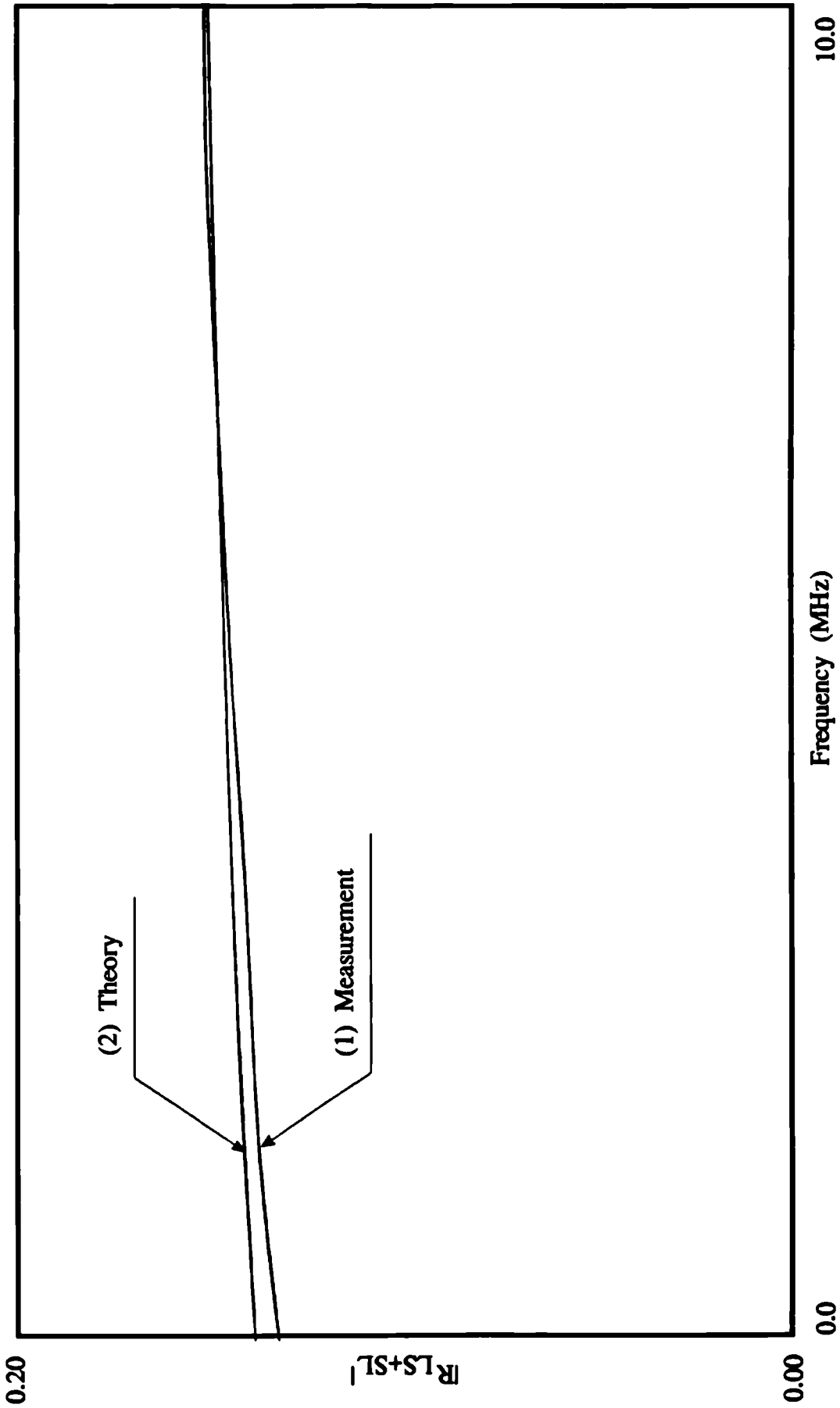
Fig. 5.35 Longitudinal-shear and shear-longitudinal combined reflectivity from the silicone layer in glass. Angle of incidence is 10 degrees from water. Comparison between theory and measurements.

Chapter 5   237

Validation of the theory. Accuracy of the reflection coefficient measurements
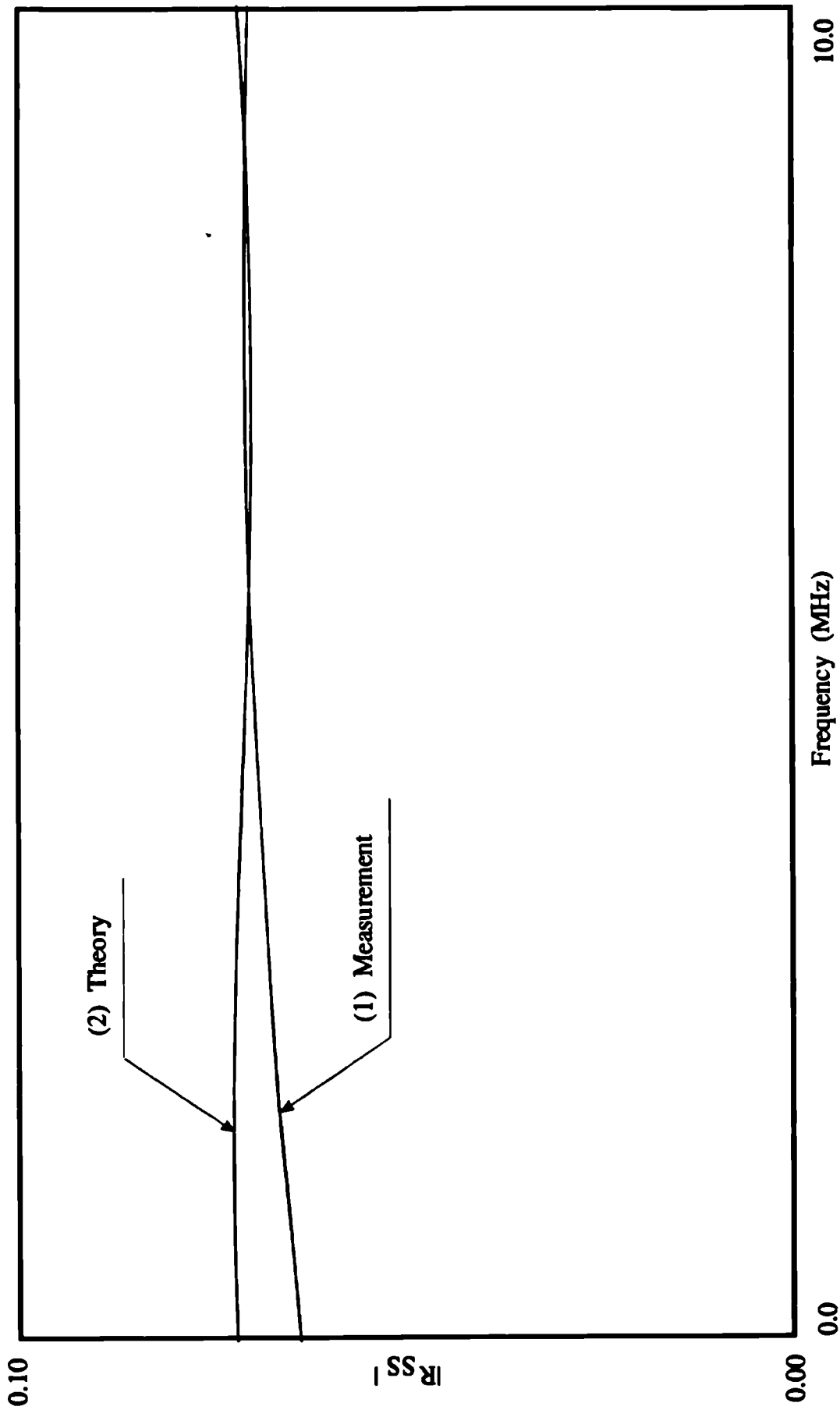
Fig. 5.36 Shear-shear reflectivity from the silicone layer in glass. Angle of incidence is 10 degrees from water. Comparison between theory and measurements.

Chapter 5

238

Validation of the theory. Accuracy of the reflection coefficient measurements
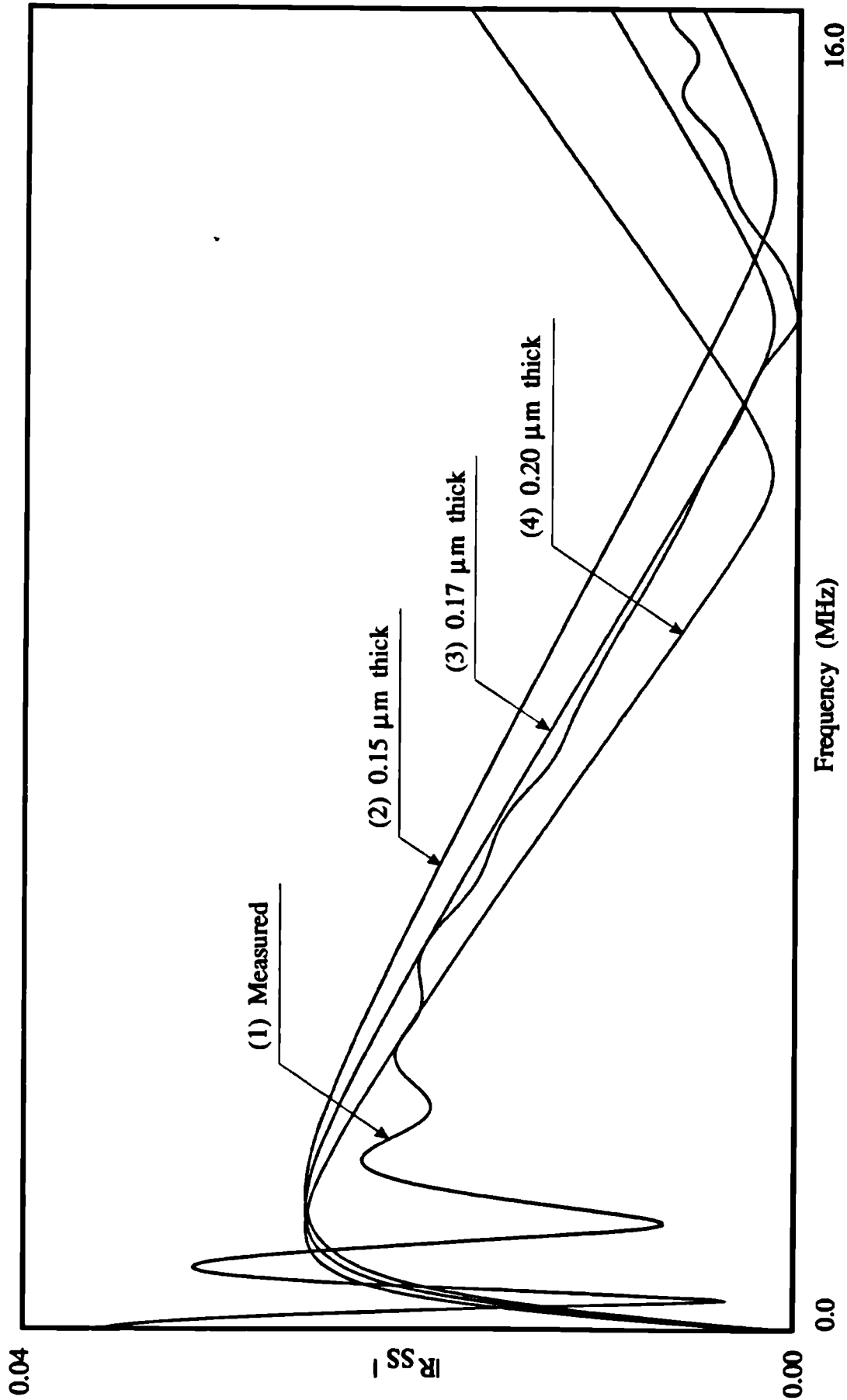
Fig. 5.37 The shear-shear reflectivity from the silicone layer in glass. Comparison between the measurements and the infinite plane wave theory. Angle of incidence from water is 20 degrees. Properties of glass and silicone liquid are given in table 5.4.

CHAPTER 6

Monitoring of interfacial conditions at a glass/epoxy interface using the reflection coefficient technique

6.1 Introduction

In the previous chapters of this thesis we were concerned with the development and validation of theoretical and experimental techniques for the monitoring of the interfacial condition in adhesive joints. The intention of this chapter is to apply all this knowledge to practically monitor changes in material properties across adherend/adhesive interfaces. The initial study described in this chapter uses the glass/epoxy system as it is very convenient to make and rather simple to model theoretically. Two types of specimens are considered here, those with strong and weak adhesion on the glass/epoxy interface. The specimens with strong adhesion properties were manufactured by applying liquid epoxy resin onto acetone cleaned glass plates. In the case of joints with reduced interfacial strength, the adherends were painted with Frekote 44 mould release agent prior to application of epoxy resin. This the simplest defective interface to produce and the idea is similar to that of Pilarski et al. (1987).

In section 6.2 experimental work to monitor changes in the normal incidence reflection coefficient from a glass/epoxy interface while the epoxy is curing, changing its properties from those of the viscous fluid towards a solid material, is described. The epoxy is applied to glass plates with and without a very thin layer of mould release agent applied prior to bonding.

In section 6.3 an experimental and the theoretical evaluation of the glass/epoxy interface at oblique incidence is described. Here, using the infinite plane wave theory, the angles of incidence to achieve the best sensitivity of the reflection coefficient to the interfacial conditions between the glass and the epoxy are determined. The reflection coefficient measurement at two theoretically determined angles is carried out to demonstrate that it is possible to measure small changes across the glass/epoxy boundary.

Section 6.4 summarises the main findings of this chapter.

6.2 Changes in the reflection coefficient across the glass/epoxy resin interface during cure

There are two important problems in the NDT of adhesive joints which we would like to address in this section. The first of them is whether it is possible to determine the state of cure of the epoxy resin using the reflection coefficient method, and to what accuracy the measurements have to be conducted in order to successfully use this technique in practice. The second question is whether it is possible to detect a weak bond created by the presence of the very thin layer of mould release agent between the adherend and the adhesive.

Two sets of measurements were conducted to answer these two questions. The first of them was to monitor the normal incidence shear and longitudinal reflectivity from the boundary between a clean glass surface and the epoxy resin during the process of curing. The second set of experiments was conducted using exactly the same setup as the first one, but the glass adherend was treated with the mould release agent, Frekote 44, prior to bonding.

6.2.1 Measurements

The monitoring of the shear and longitudinal reflection coefficient at the glass epoxy interface was performed using the experimental setup shown schematically in fig. 6.1. The longitudinal probe, 10 MHz wideband unfocussed Rolls-Royce Mateval transducer, was placed on the top of the glass buffer plate and coupled to the structure with the low viscosity machine oil. The shear probe, 10 MHz wideband Ultran transducer, was pressed into the glass buffer alongside the longitudinal probe and coupled to the structure by honey. Since the ultrasonic transducers were coupled to the structure by thin layers of viscoelastic liquids, lack of cosistency in the coupling could be expected. It was therefore required to create a thin reference interface in the glass buffer. The glass buffer (see fig. 6.1) consisted of two glass sheets, 4.85 mm thick and 2.0 mm thick, bonded together by a very thin layer of epoxy. In this way the reference interface, a glass/thin epoxy layer/glass, was created with respect to which the longitudinal and shear reflectivity from the monitored glass/epoxy interface could be accurately measured.

Figure 6.2 shows the time domain responses measured by the longitudinal wave probe at different stages of the experiment. Figure 6.2(a) shows the longitudinal wave response of the specimen before the epoxy resin was applied. The first reflection shown in the picture is the reference pulse coming from the reference interface in the glass buffer, while the second reflection comes from the glass/air interface. Figure 6.2(b) shows the response of the system just after the liquid epoxy resin (Ciba Geigy Araldite MY 750 resin and HY 931 hardener) had

made contact with the glass buffer. For such a case the normal incidence longitudinal reflectivity should drop because the impedance of the epoxy resin is much higher that that of air. From the figure it can clearly be seen that the first pulse (reference pulse) did not change its amplitude, while the second one is visibly smaller than that of fig. 6.2(a), confirming our expectations. Figure 6.2(c) shows the response of the specimen 4.5 hours after the application of the epoxy. Here the reflection from the glass/epoxy interface is even smaller than that of fig. 6.2(b) indicating that the impedance of the epoxy increases during the curing process. Figure 6.2(d) shows the response of the system 17.5 hours after the epoxy resin was applied, and corresponds to the case of solid epoxy.

The time domain signal shown in fig. 6.2(a) can be used for the calibration purposes as it is known that the normal incidence reflection coefficient at the glass/air boundary is practically unity. Therefore, in order to quantitatively determine the reflection coefficients at the glass/epoxy boundary at the different stages of the experiment, the following simple procedure can be adopted. Using the time domain response of fig. 6.2(a) the glass/air reflection can be divided by the reference pulse in the frequency domain giving the reference transfer function. Then all the other signals obtained during the experiment can be normalised by the reference transfer function giving the required glass/epoxy reflection coefficient in the frequency domain.

Figure 6.3 shows the results of the normalisation calculations described above. From the figure it can clearly be seen that the normal incidence longitudinal reflection coefficient from the glass/epoxy interface is frequency independent throughout the entire time of the experiment.

Figure 6.4 shows the normal incidence shear time domain response from the tested specimen at different stages of the experiment. In fig. 6.4(a) the time history of the response from the system is shown before the epoxy resin was poured in. As in the case of longitudinal wave excitation, the first pulse coming back from the tested specimen is the echo from the reference interface in the glass buffer (see fig. 6.1). The second echo visible on fig. 6.4(a) is the reflection from the glass/air boundary. Figure 6.4(b) shows what happens when the liquid epoxy makes contact with the glass buffer. Here it can be seen that amplitude of the reflection from the glass/epoxy is somewhat smaller than that of the glass/air case of fig. 6.4(a) indicating that the reflection coefficient is smaller than unity here. This phenomenon is in accordance with our expectations. Indeed, liquid epoxy resin has high viscosity and therefore supports shear wave propagation (see Appendix B). This means that the shear impedance of the liquid epoxy resin is not zero and the shear reflection coefficient should be less than unity for such cases. Figure 6.4(c) shows the response from the system 4.5 hours after the epoxy had been poured in. The reflection from the glass/epoxy boundary is significantly lower than that of figures 6.4(a) and (b), indicating that the epoxy considerably increased its shear impedance over that time. Figure 6.4(d) shows the result

of the measurement performed 17.5 hours from the beginning of the experiment. Comparing this measurement to that of fig. 6.4(c) it can be seen that there is no significant change in the response from the specimen, indicating that the major changes in the state of the epoxy took place within the first 4.5 hours of the experiment.

As in the case of the longitudinal excitation, using the signal of fig. 6.4(a) for the calibration purposes, it is possible to quantitatively determine the shear reflectivity from the glass/epoxy boundary. Figure 6.5 shows the experimentally obtained normal incidence shear reflection coefficient for this case. Looking at the R_{SS} curves of fig. 6.5 it can be seen that the shear reflection coefficient measurements are slightly frequency dependent and the frequency dependence is more pronounced for the measurements taken in the later stage of the experiment. This oscillation of the R_{SS} curves is most probably due to unreliable coupling between the shear transducer and the glass plate which could have changed during the 20 hours long experiment.

The same set of experiments was conducted for the specimen treated with a mould release agent prior to bonding. Figure 6.1 shows schematically the setup used for the measurements. The monitored interface in this case was painted twice with Frekote 44 liquid which, after setting, forms a very thin layer of mould release.

As the thickness of the Frekote layer is very small, the normal incidence shear and longitudinal reflection coefficient from the glass/Frekote 44/air is practically unity. For both types of bulk waves, longitudinal and shear, the calibration of the reflections coming from the reference interface (see fig. 6.1) was conducted by capturing of the reference signal from the glass/Frekote 44/air interface before the epoxy resin was poured. Then, during the experiment, the reflection coefficient results were obtained quantitatively in exactly the same manner as described at the beginning of this subsection. The results of the measurements are shown in figures 6.6 and 6.7.

Fig 6.6 shows the normal incidence longitudinal reflection coefficient from the glass/Frekote 44/air interface as epoxy cures.

The normal incidence shear reflection coefficient measurements for the case of the glass/Frekote 44/epoxy interface is shown in fig. 6.7. As in the case of the longitudinal reflection coefficient, the results are normalised here with respect to the glass/Frekote 44/air shear reflection coefficient, which was assumed to be unity. From fig. 6.7 it can clearly be seen that the shear reflectivity drops as the epoxy cures which indicates that the shear impedance of the epoxy increases as it changes state from liquid to solid.

6.2.2 Comparison of results with and without mould release

The results of four experiments described above were plotted in fig. 6.8 for convenient comparisons.

In fig. 6.8(a) the curve marked 'clean interface' shows the average values of the normal incidence longitudinal reflection coefficient taken from the curves of fig. 6.3. The figure shows that the amplitude of the normal incidence longitudinal reflection coefficient changes from about 0.77 for the liquid state of epoxy to about 0.66 when the epoxy resin is solid. This demonstrates that it is possible to monitor changes in the cure state of the epoxy by longitudinal reflection coefficient measurements provided that the absolute error of the measurements is of order of a few percent.

Figure 6.8(b) the curve marked 'clean interface' shows the average values of the normal incidence shear reflection coefficient in the frequency range of between 6 and 12 MHz as the epoxy resin cures, taken from the curves of fig. 6.5. The figure shows that the amplitude of the normal incidence longitudinal reflection coefficient changes from about 0.93 for the liquid state of epoxy to about 0.71 when the epoxy resin is solid. This demonstrates that it is possible to monitor changes in the cure state of the epoxy by longitudinal reflection coefficient measurements provided that the absolute error of the measurements is of order of a few percent. From figures 6.3 and 6.5 it can be also seen that the sensitivity of the shear normal incidence reflectivity is higher than that of the longitudinal reflectivity. Indeed, the variation of the longitudinal reflection coefficient during the experiment is about 15 %, while the variation of the shear reflectivity is about 24 %.

In fig. 6.8(a) the curve marked '2 coats of Frekote 44' shows the average values of the normal incidence longitudinal reflection coefficient taken from the curves of fig. 6.6. The figure shows that the amplitude of the normal incidence longitudinal reflection coefficient changes from about 0.77 for the liquid state of epoxy to about 0.66 when the epoxy resin is solid. Comparing figures 6.3 and 6.6 as well as two curves of fig. 6.8(a) showing the average values of R_{LL} coefficients, it can be seen that the curing speed of the epoxy in the previous experiment was higher than here. Indeed, the 6 h 30 min curve of fig. 6.3 almost touches the bottom level of the reflection coefficient range, indicating that 6.5 hours after the application of the epoxy, the curing process was coming to an end, while the 7 h 30 min curve of fig. 6.6 is still far from the bottom line. The higher curing speed of the epoxy in the previous experiment is the result of a higher ambient temperature in the laboratory at the time when the measurements were conducted, as the higher the ambient temperature, the faster the epoxy cures. However, after the curing process is over, the longitudinal reflection coefficient for both cases is very similar, 0.657 for

the glass/epoxy interface, and 0.662 for the glass/Frekote 44/epoxy system indicating that, in both experiments, the epoxy attained very similar mechanical properties.

Figure 6.8(b) the curve marked '2 coats of Frekote 44' shows the variation of the shear reflection coefficient with time. The average values in the frequency range of 6 - 12 MHz, taken from the curves of fig. 6.7, are presented here. The figure shows that the amplitude of the normal incidence shear reflection coefficient changes from about 0.95 for the liquid state of epoxy to about 0.80 when the epoxy resin is solid.

Looking at fig 6.8(b) it can clearly be seen that the normal incidence shear reflection coefficient from the glass/Frekote 44/epoxy system (curve marked '2 coats of Frekote 44') is significantly higher than that from the glass/epoxy interface without the mould release (curve marked 'clean interface'), even after the epoxy has been cured. Indeed, from the figure it can be seen that by the end of the experiment, when the epoxy was solid, the amplitude of R_{SS} coefficient from the glass/epoxy interface attains the asymptotic value of 0.71. The asymptotic amplitude of the R_{SS} coefficient from the glass/Frekote 44/epoxy system is 0.80, which is about 12 % higher that that of glass/epoxy interface without the mould release.

From figure 6.8(a) and (b) it can clearly be seen that the normal incidence longitudinal wave reflection coefficient technique was incapable of the detection of the presence of the mould release agent at the glass/epoxy interface, while using the shear wave probe it was possible to do so. This results of the experiments indicate that the shear stiffness of the glass/epoxy interface treated with the mould release prior to bonding was lower than that of the untreated interface. However, the exact mechanism of the reduction in shear stiffness across the glass/epoxy interface with the mould release in between is unclear. It might be due to a very low shear stiffness of the mould release agent layer itself, or perhaps a partial kissing bond (see page 10) formed between the mould release and the epoxy resin.

As shown above, the normal incidence shear reflection coefficient can be used to detect presence of Frekote 44 mould release agent between glass and epoxy. However, the shear wave method suffers a major drawback when it comes to the quantitative reflection coefficient measurements because of the unreliable coupling between the transducer and the examined specimen. Differences in shear wave reflectivity of the order of ten percent can only be measured reliably when the position of the shear transducer is left unchanged for the entire duration of the experiment, as was the case here. This requirement severely restricts the application of the normal incidence shear wave technique in an industrial environment.

6.3 Determination of the presence of the mould release agent between glass and epoxy half-spaces using the oblique incidence technique. Problem of detectability.

It was shown in section 6.3 that it is possible to determine the presence of the mould release agent, Frekote 44, at the glass/epoxy interface using the normal incidence shear wave technique. This subsection extends the scope of the investigations to oblique angles of incidence. Here the objective is to find theoretically the angles of incidence for which the reflection coefficient is most sensitive to the interfacial conditions at the glass/epoxy boundary. Then, the experimental determination of the reflection coefficients from the glass/epoxy interface and the glass/Frekote 44/epoxy system will be conducted at these chosen angles to verify the capability of the technique.

Figure 6.9 shows schematically the specimens manufactured for the measurements. The specimens consist of a 4.0 mm thick layer of epoxy resin poured onto a flat sheet of 5.85 mm thick float glass and allowed to cure. The surfaces of the glass plates were either cleaned with acetone prior to bonding or painted three times with Frekote 44 liquid to form a very thin layer of the mould release on the glass surface before the epoxy resin was applied.

6.3.1 Sensitivity study using the infinite plane wave theory

For the theoretical investigations such an interface can be modelled as two semi-infinite half-spaces with or without a thin solid interlayer between them. Table 6.1 shows the acoustic properties of the glass and the epoxy resin as well as the properties of the interlayers used for the sensitivity studies. The interlayers were assumed to be 10 μm thick, and their acoustic properties are based on the properties of the epoxy resin. Since the normal incidence measurements, (see section 6.2.2) indicated that the interface has reduced stiffness in shear direction, the shear velocities of the interlayers were reduced from 1100 m/s for the interlayer 1, to 1000 m/s for the interlayer 2, and 800 m/s for the interlayer 3, keeping the longitudinal velocities equal that of the epoxy resin.

Figure 6.10 shows the angular variation of the longitudinal-longitudinal (R_{LL}) reflection coefficient from the glass/epoxy interface with and without the 10 μm thick interlayer in between. The frequency of the longitudinal incident wave was 10 MHz. Since the longitudinal properties of the interlayers were kept the same as those of the epoxy resin, the R_{LL} coefficient does not show any sensitivity at normal incidence. The best sensitivity of the R_{LL} coefficient can be seen at the angles of incidence of around 54.2 and 72.4 degrees. Indeed, when there is no interlayer present at the glass/epoxy boundary, the R_{LL} coefficient is null for these two angles of

material	density (kg/m³)	longitudinal velocity (m/s)	longitudinal attenuation (nepers)	shear velocity (m/s)	shear attenuation (nepers)
glass	2454	5815	0.00	3455	0.00
epoxy	1170	2625	0.00	1177	0.00
interlayer 1	1170	2625	0.00	1100	0.00
interlayer 2	1170	2625	0.00	1000	0.00
interlayer 3	1170	2625	0.00	800	0.00
water	1000	1495	0.00	10	6.28

Table 6.1 Acoustic properties of materials used for the oblique incidence reflection coefficient calculations.

incidence. Any small change in the properties of the thin interlayer influence the R_{LL} coefficient at these angles significantly. Table 6.2 shows the amplitudes of the R_{LL} coefficient at the angles of 54.2 and 72.4 degrees for the four cases of fig. 6.10. As can be seen from table 6.2 the R_{LL} coefficient is highly sensitive to the interfacial conditions at the angles of incidence of 54.2 and 72.2 degrees. Indeed, when there is no interlayer present, the R_{LL} reflection coefficient is null and even a small variation in the interfacial properties (see interlayer 1 curve) raises the amplitude of the reflection coefficient from the zero level. Therefore, the sensitivity of the R_{LL} coefficient technique at these two angles of incidence is limited primarily by the signal-to-noise ratio of the equipment used for the experiments.

material	R_{LL} coefficient at 54.2 degrees	R_{LL} coefficient at 72.4 degrees
No interlayer present	0.000	0.000
interlayer 1	0.011	0.018
interlayer 2	0.028	0.045
interlayer 3	0.071	0.117

Table 6.2 The amplitude of the R_{LL} coefficient from the glass/epoxy interface with and without the 10 μm thick interlayers present in between.

Figure 6.11 shows the angular variation of the shear-shear reflection coefficient (R_{SS}) from the boundary between the glass and the epoxy half-spaces separated by 10 μm thick interlayers of different shear stiffnesses. The frequency of the incident shear wave is 10 MHz. The curve numbers in fig. 6.11 correspond to the interlayer numbers in table 6.1. It can be seen from the figure that the best sensitivity of the R_{SS} coefficient is at normal incidence and at around 28.4 degrees, where the reflection coefficient curve for the glass/epoxy boundary without an interlayer touches the zero line. At such an angle of incidence very small changes in the reflection coefficient curve can be detected because they are large in proportion to the reference curve which attains a null value here. Table 6.3 shows the amplitudes of the R_{SS} coefficient at normal incidence (0.0 degrees) and at an angle of 28.4 degrees. The absolute changes in the amplitude of the R_{SS} coefficient is similar at both angles of incidence. However, in terms of the relative changes in amplitude, the shear-shear reflection coefficient at 28.4 degrees is much more sensitive to the interfacial changes than at normal incidence. In practice, the sensitivity of the technique at 28.4 degrees depends on the signal-to-noise ratio of the equipment used.

material	R_{SS} coefficient at 0.0 degrees	R_{SS} coefficient at 28.4 degrees
No interlayer present	0.721	0.000
interlayer 1	0.730	0.011
interlayer 2	0.749	0.026
interlayer 3	0.814	0.071

Table 6.3   The amplitude of the R_{SS} coefficient from the glass/epoxy interface with and without the 10 μm thick interlayers present in between.

Figure 6.12 shows the longitudinal-shear reflection coefficients (R_{LS}) from the glass/epoxy boundaries with and without 10 μm thick interlayer. The frequency of the longitudinal incident wave is 10 MHz, and the material properties of the glass, the epoxy and the interlayers are given in table 6.1. From the figure it can be seen that the sensitivity of the R_{LS} reflection coefficient is rather poor.

Figure 6.13 shows the shear-longitudinal reflection coefficient curves (R_{SL}) calculated for the systems comprising the glass and the epoxy half-spaces separated by 10 μm thick interlayers, whose mechanical properties are given in table 6.1. From the plot it can be seen that the sensitivity of the R_{SL} coefficient to small changes at the interface is rather poor.

6.3.2 Measurements of the oblique incidence reflectivity from the glass/epoxy system with and without a Frekote 44 layer

It has been shown in subsection 6.3.1 that, using certain angles of incidence and types of reflections, it is possible to ultrasonically monitor very small changes across the glass/epoxy interface. In the theoretical investigations, the shear stiffness of the glass/epoxy interface with the mould release layer in between was reduced with respect to the shear stiffness of the interface without the mould release present, while the longitudinal stiffness was kept the same. These assumptions are in qualitative agreement with the normal incidence longitudinal and shear reflection coefficient measurements, presented in section 6.2.2.

Two types of glass/epoxy specimens were manufactured for the experiments (see fig. 6.9), the first one being a simple glass/epoxy joint, and the other one containing a thin Frekote 44 mould release layer applied on the glass surface prior to the application of the epoxy. The measurements of the ultrasonic reflectivity from the glass/epoxy interface were conducted at four different angles of incidence using the reflection coefficients R_{LL}, R_{SS}, and $(R_{LS}+R_{SL})$ at the angles of incidence corresponding to the best sensitivity of each of the reflection coefficients. Figure 6.14 shows schematically the oblique incidence technique adopted for the measurements. Here the longitudinal wave, generated by the transmitter, a 10 MHz wideband Rolls-Royce Mateval transducer, refracts at the water/glass boundary generating oblique incidence shear and longitudinal pulses in the glass. The reflected pulses from the glass/epoxy interface mode convert back into longitudinal waves in water to be captured by the receiver, also a 10 MHz wideband Rolls-Royce Mateval transducer. For a more detailed description of the experimental setup, the measurement technique, and the data processing sequence used in the experiment, refer to section 5.2.

Figure 6.15 shows the measured longitudinal-shear and shear-longitudinal (LS+SL) reflection coefficient from the glass/epoxy interfaces with and without the Frekote 44 mould release at two different angles of incidence. The measurements involved spectral division of the pulse of interest (in this case LS+LS pulse) by the reference pulse captured in face-to-face arrangement of the probes. The reflection coefficient measurement technique from embedded interfaces was described in detail in section 5.4.

In fig. 6.15(a) the angle of incidence was set to 11.8 degrees in water which, in glass, corresponds to an angle of incidence of 52.7 degrees for the longitudinal wave and 28.2 degrees for the shear wave. From fig. 6.15(a) it can be seen that the LS+SL reflection coefficient is practically the same for the glass/epoxy interface with the Frekote 44 layer and without it. This result is in accordance with our expectations. Indeed, the (LS+SL) reflection at the angle of

incidence of 11.8 degrees is the summation of two different reflection coefficients, the R_{LS} coefficient at 52.7 degrees (see fig. 6.12), and R_{SL} coefficient at 28.2 degrees (see fig. 6.13). It can be seen from figures 6.12 and 6.13 that the sensitivity of both reflection coefficients at their corresponding angles of incidence is rather poor which means that the (LS+SL) reflectivity is not sensitive enough to be used successfully for the detection of the presence of the Frekote 44 layer across the glass/epoxy interface.

Figure 6.15(b) shows another example of the (LS+SL) reflectivity measurement, this time at an angle of incidence of 13.9 degrees from water which corresponds to angles of incidence of 69.1 degrees for the longitudinal wave, and 33.7 degrees for the shear wave in the glass. As the (LS+SL) reflectivity at 13.9 degrees is the summation of the R_{LS} coefficient at 69.1 degrees (see fig. 6.12), and R_{SL} coefficient at 33.7 degrees (see fig. 6.13), then the sensitivity of the measurement to the presence of the mould release should be practically the same as for the angle of incidence of 11.8 degrees. Again, no significant change between the reflection coefficient over the glass/epoxy interface with and without the Frekote 44 layer can be seen.

A more interesting result can be obtained when, at the angle of incidence from water of 11.8 degrees, instead of measuring the (LS+SL)$_1$ reflection, the SS$_1$ pulse is taken for the analysis. Using Snell's law it can be shown that the shear wave refracts in the glass at the angle of 28.2 degrees which, looking at fig. 6.11, is the angle at which the shear-shear reflection coefficient becomes most sensitive to the interfacial properties across the glass/epoxy boundary. Figure 6.16(a) shows the time domain response of the glass/epoxy plate to a 10 MHz wideband pulse excitation at the angle of incidence of 11.8 degrees from water. The transmitter and receiver were arranged so that they captured the SS$_1$ reflection primarily. Table 6.4 lists the angles of refraction and the times of arrival of different pulses reflected from the glass/epoxy interface.

Note that the vertical scales of figures 16(a) and (b) were chosen primarily to show the amplitudes of the SS$_1$ pulses coming from the glass/epoxy interfaces. Some other pulses of much bigger amplitudes than those of SS$_1$ type are clipped by the boundaries of the drawings.

Looking at table 6.4 and fig. 6.16(a) it can be seen that the first pulse arriving from the glass/epoxy boundary is the LL$_1$ reflection, arriving 1.22 μs behind the front face reflection (FF). The (LS+SL)$_1$ pulse arrives together with the LL$_2$ reflection but is not really affected by it. This is because the receiver effectively misses the area isonified by LL$_2$, as the pulse emerges from within the glass plate far away from the receiver. The next reflection received by the probe is the SS$_1$ reflection which is slightly superimposed on the ((LS+SL)$_1$LL)$_1$ pulse arriving 0.34 μs later. As with the LL$_2$ pulse, the ((LS+SL)$_1$LL)$_1$ reflection is almost entirely missed by the receiver and therefore appears very small on fig. 6.16(a). The last significant pulse visible on

Type of reflection	Angle of incidence at glass/epoxy (degrees)	Time of arrival wrt FF (μs)
LL_1	longitudinal: 52.7	1.22
$(LS+SL)_1$	longitudinal: 52.7 shear: 28.2	2.10
LL_2	longitudinal: 52.7	2.44
SS_1	shear: 28.2	2.98
$((LS+SL)_1 LL)_1$	longitudinal: 52.7 shear: 28.2	3.32
LL_3	longitudinal: 52.7	3.66
$(LS+SL)_2$	longitudinal: 52.7 shear: 28.2	4.20

Table 6.4   Angles of refraction and times of arrival of different reflections coming from the back of the 5.85 mm thick glass plate. Angle of incidence in water 11.8 degrees.

fig. 6.16(a) is the $(LS+SL)_2$ reflection, arriving 0.88 μs behind the $((LS+SL)_1 LL)_1$. From fig. 6.16(a) it can be seen that the amplitude of the SS_1 reflection is very small here. This observation is in accordance with the theoretical predictions of fig. 6.11, which show that the R_{SS} coefficient is very close to zero at the angles of incidence around 28.4 degrees.

Figure 6.16(b) shows the time domain response from the glass/epoxy plate with the mould release applied prior to bonding. The excitation and the transducer configuration was exactly the same here as in the case of fig. 6.16(a). As one can see, the FF, LL_1, $(LS+SL)_1$ and $(LS+SL)_2$ pulses have almost identical signatures in figures 6.16(a) and (b), which indicates that the reflection coefficients R_{LL} and R_{LS} at 52.7 degrees as well as R_{SL} at 28.2 degrees are not sensitive to the presence of the Frekote 44 layer. However, looking at fig. 6.16(b), it can clearly be seen that the SS_1 reflection from the glass/epoxy interface treated with the mould release prior to bonding is about three times larger than that obtained from the glass/epoxy boundary without the Frekote 44 layer present and showed in fig. 6.16(a). This finding clearly indicates that the 28.2 degree shear-shear reflection coefficient technique is capable of detection of the mould release layer between glass and epoxy.

Another very interesting result can obtained at an angle of incidence of 12.0 degrees from water. Table 6.5 shows the angles of refractions and times of arrivals of different pulses coming from the glass/epoxy boundary and fig. 6.17(a) shows the time domain response of the glass/epoxy plate to a 10 MHz wideband pulse excitation. The receiver was positioned so that it primarily

received the LL_1 pulse.

Type of reflection	Angle of incidence at glass/epoxy (degrees)	Time of arrival wrt FF (μs)
LL_1	longitudinal: 54.0	1.18
$(LS+SL)_1$	longitudinal: 54.0 shear: 28.7	2.08
LL_2	longitudinal: 54.0	2.36
SS_1	shear: 28.7	2.97
$((LS+SL)_1 LL)_1$	longitudinal: 54.0 shear: 28.7	3.26
LL_3	longitudinal: 54.0	3.54
$(LS+SL)_2$	longitudinal: 54.0 shear: 28.7	4.16

Table 6.5   Angles of refraction and times of arrival of different reflections coming from the back of the 5.85 mm thick glass plate. Angle of incidence in water 12.0 degrees.

As the angle of refraction for the longitudinal wave is 54.0 degrees, in order to fully receive the LL_1 pulse, the receiver had to be positioned far away from the area isonified by front face reflection (see fig. 6.14), which resulted in a severe deterioration of the FF signal, as can be seen in fig. 6.17(a). The LL_1 reflection, which comes first after the front face pulse, is the one we are interested in. Its amplitude in fig. 6.17(a) is very small as theoretically predicted on fig. 6.10, where at around 54.2 degrees the glass/epoxy R_{LL} coefficient touches the zero line. Figure 6.17(b) shows the response of the glass/Frekote 44/epoxy plate to the exactly the same excitation and for the same probe arrangement as in fig. 6.16(a). Here it can be seen that the longitudinal-longitudinal reflectivity is double that for the case of the glass/epoxy boundary without the Frekote layer.

6.4   Conclusions

It has been shown in this chapter that it is possible to monitor small interfacial changes across the glass/epoxy boundary using the ultrasonic reflection coefficient method.

Normal incidence longitudinal reflection coefficient measurements are not capable of the detection of the presence of a thin mould release layer between glass and epoxy. The normal

incidence shear reflection coefficient, measured over the glass/epoxy interface treated with Frekote 44 prior to bonding, increases its amplitude by about 10 percent with respect to the untreated glass/epoxy interface at a frequency of around 10 MHz. This finding provides us with a means of detection of the presence of the mould release agent at the glass/epoxy boundary at least in a laboratory environment.

Theoretical and experimental investigations using the oblique incidence technique showed that there are certain angles of incidence where the reflection coefficient becomes very sensitive to small interfacial changes at the glass/epoxy boundary. The angles of increased sensitivity were identified as those at which the reflection coefficients from good interfaces assume a null value. The measurements carried out to monitor the longitudinal-longitudinal and shear-shear reflectivity at the appropriate angles confirmed the theoretical predictions and showed that the oblique incidence technique can be used to detect the presence of the Frekote 44 layer.
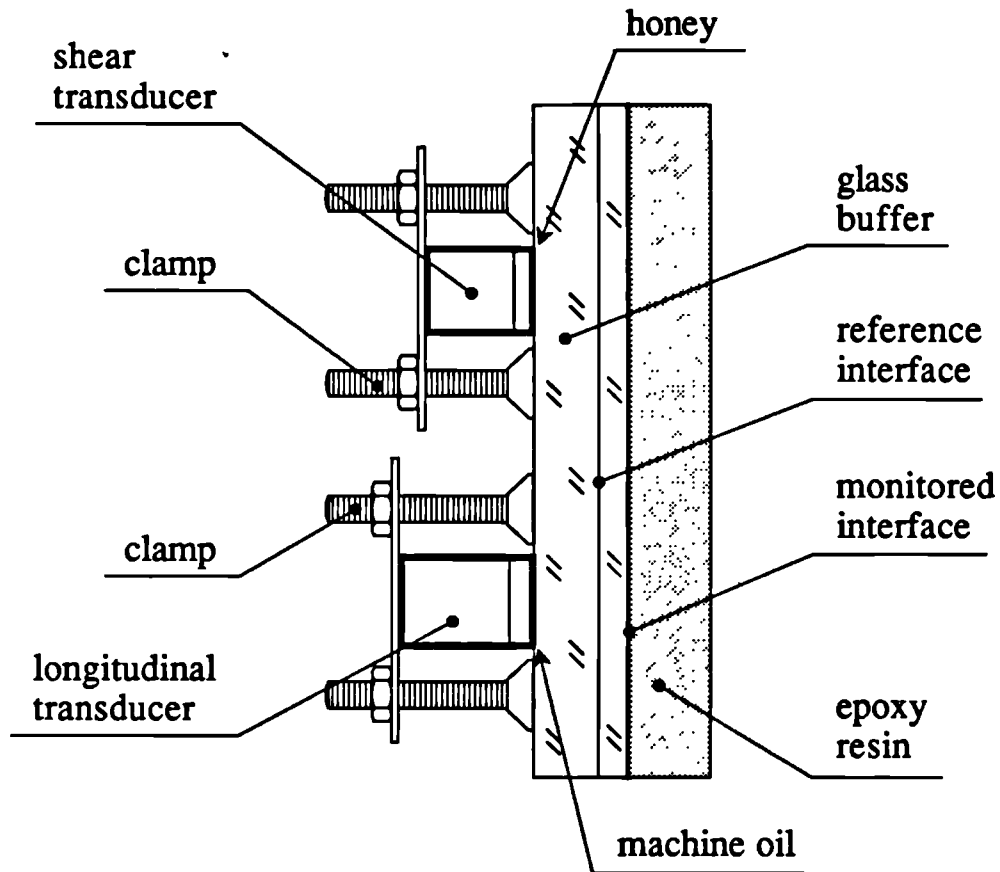
Fig 6.1   Experimental setup for the normal incidence longitudinal and shear reflection coefficient measurements from the glass/epoxy interface.
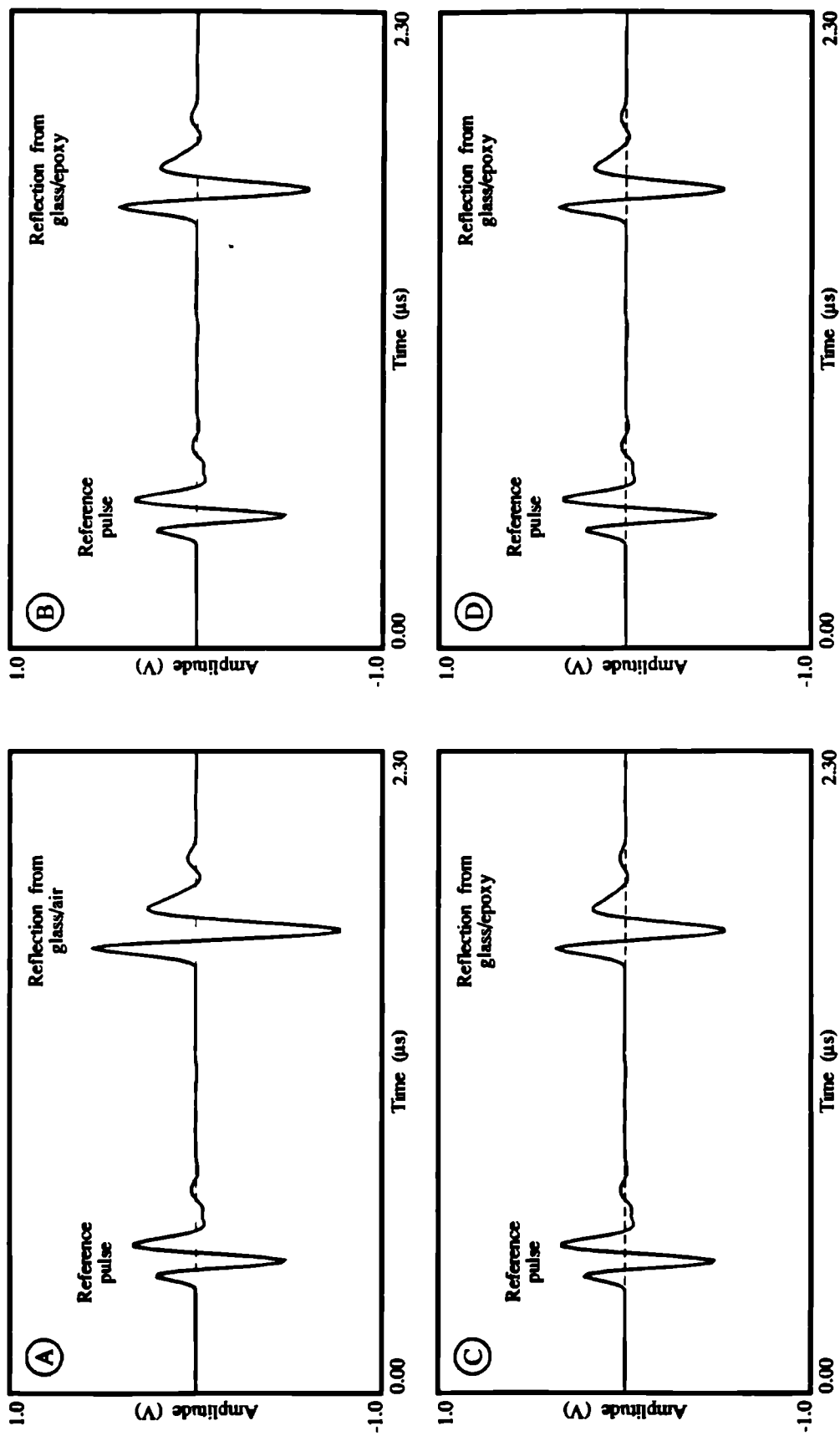
Fig. 6.2   Normal incidence longitudinal response of the system of fig. 6.1 at different stages of the experiment. (A) before the application of epoxy, (B) just after the epoxy was poured in, (C) after 4.5 hours of curing, (D) after 19.5 hours of curing.
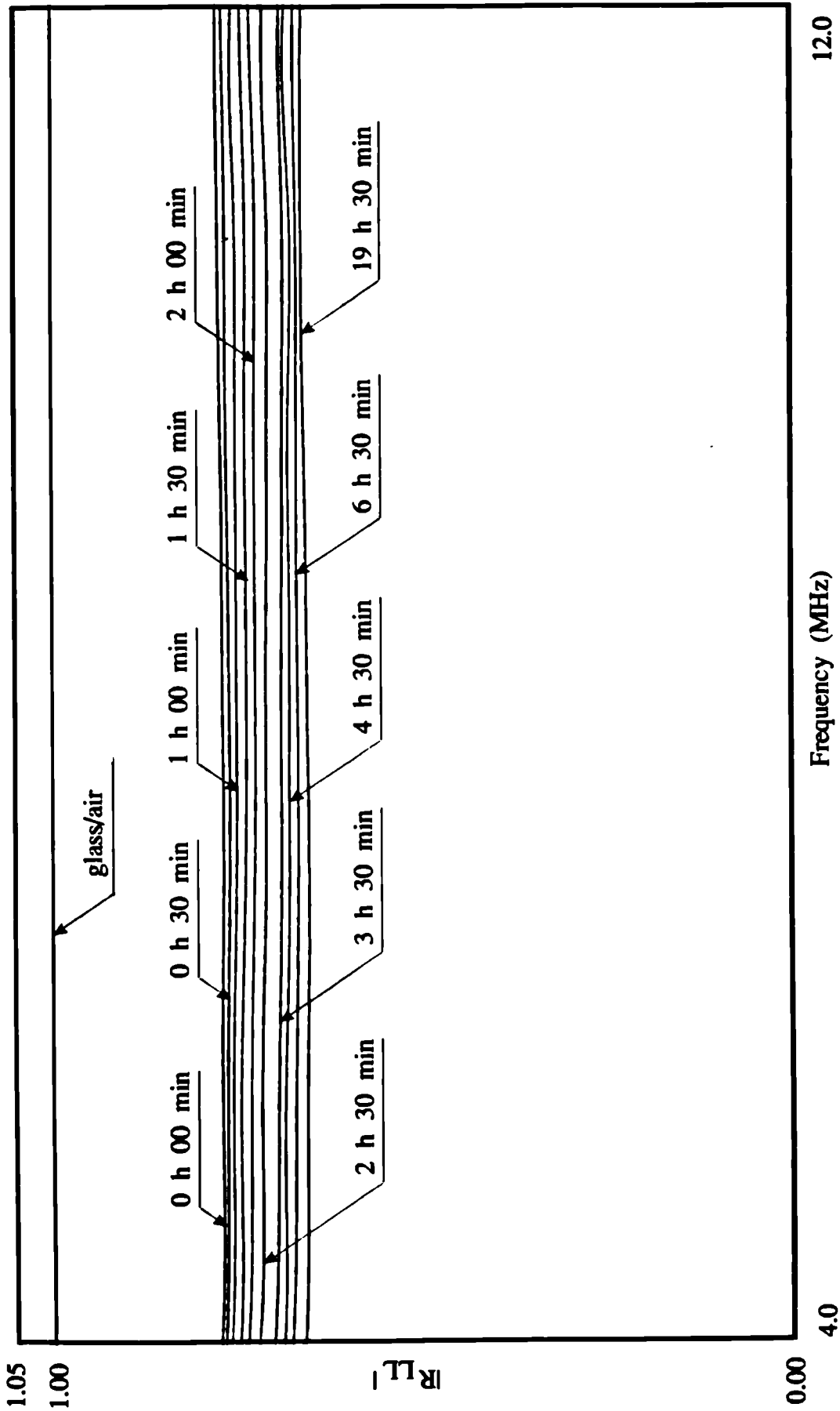
Fig. 6.3   Normal incidence longitudinal reflection coefficient from the glass/epoxy interface as the epoxy cures. Curve lables correspond to the curing time of the epoxy. Results normalised with respect to the glass/air reflection coefficient.
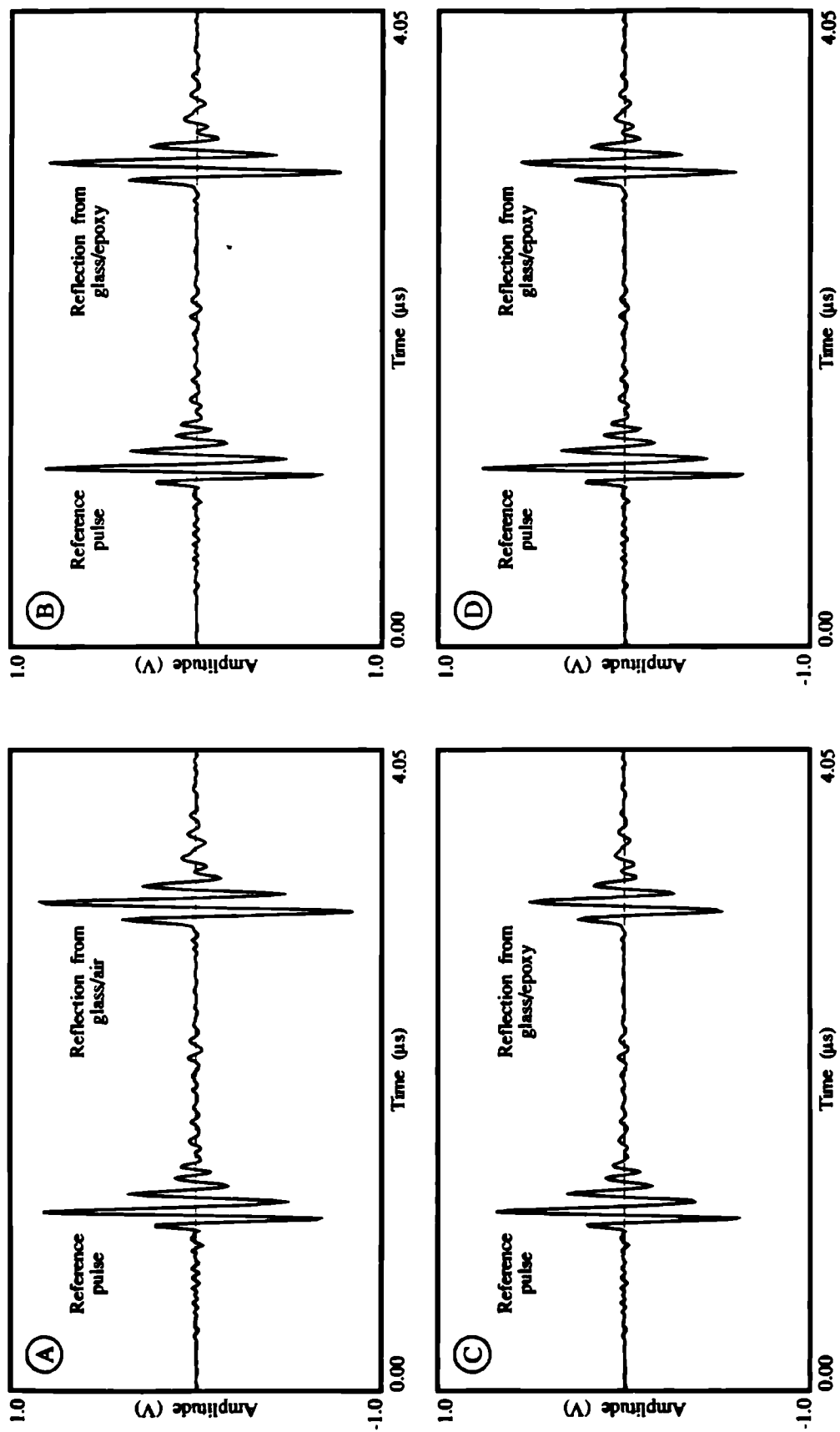
Fig. 6.4   Normal incidence shear wave response of the system of fig. 6.1 at different stages of the experiment. (A) before the application of epoxy, (B) just after the epoxy was poured in, (C) after 4.5 hours of curing, (D) after 19.5 hours of curing.
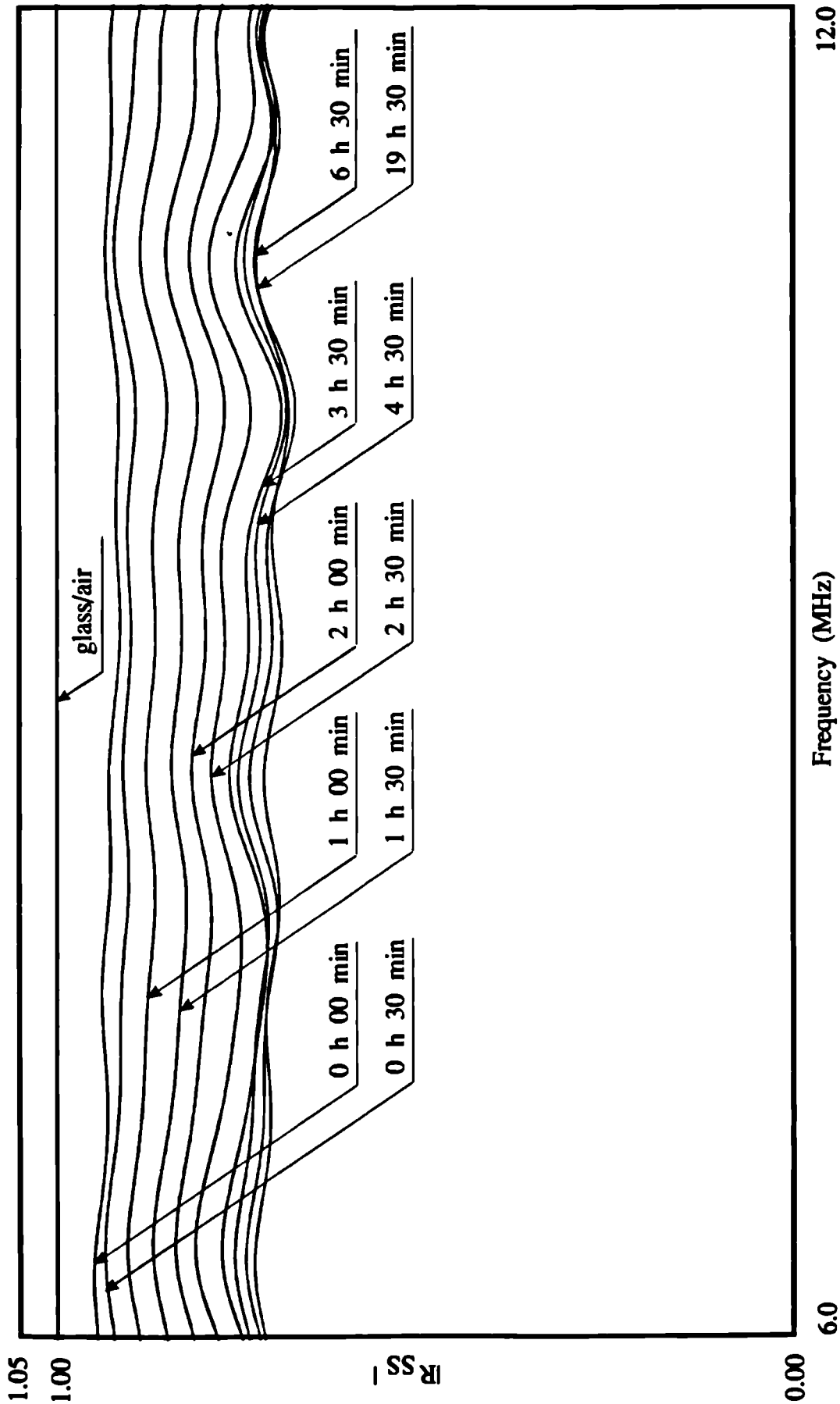
Fig. 6.5   Normal incidence shear reflection coefficient from the glass/epoxy interface as the epoxy cures. Curve lables correspond to the curing time of the epoxy. Results normalised with respect to the glass/air reflection coefficient.
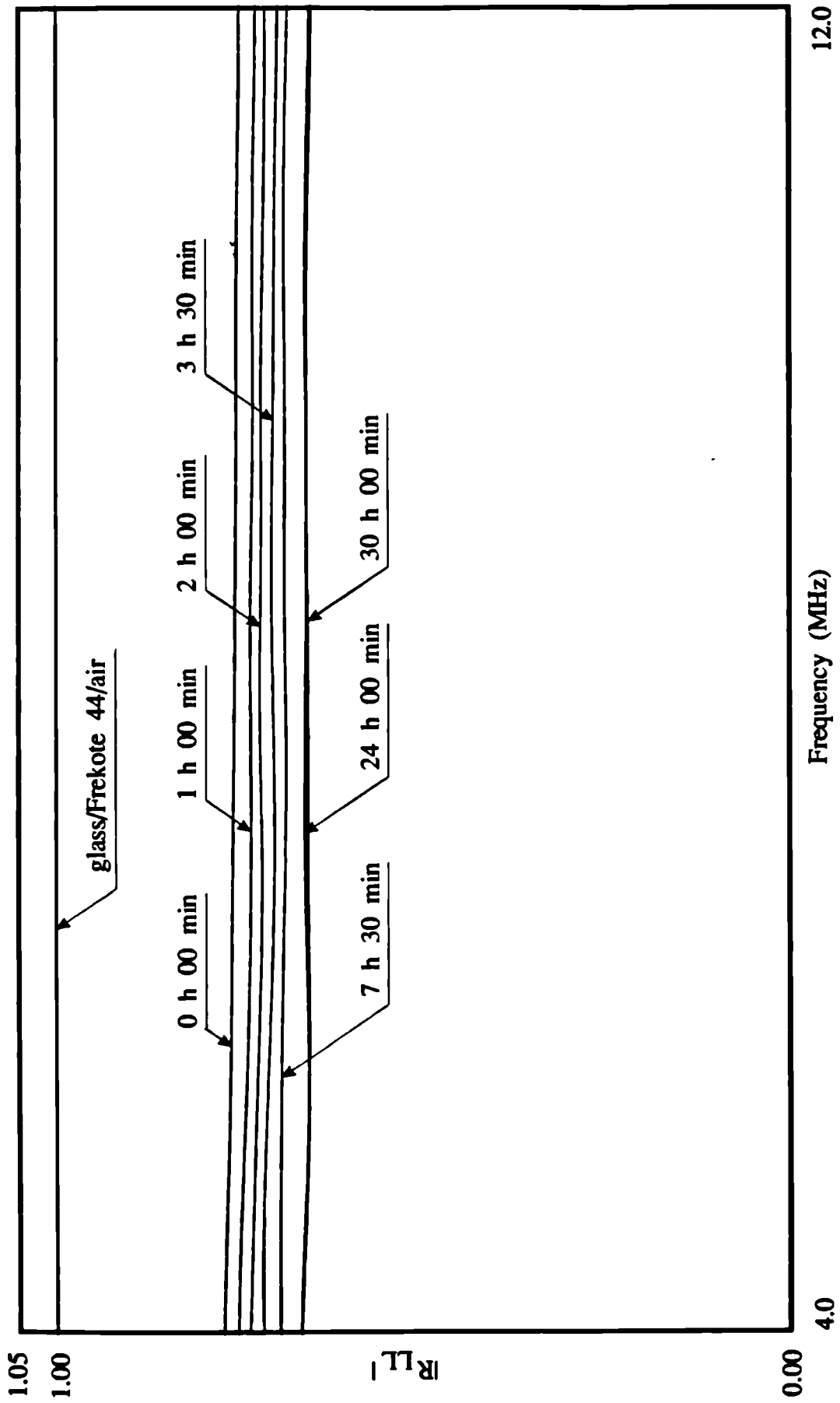
Fig. 6.6   Normal incidence longitudinal reflection coefficient from the glass/Frekote 44/epoxy interface as the epoxy cures. Results normalised with respect to the glass/Frekote 44/air reflection coefficient.
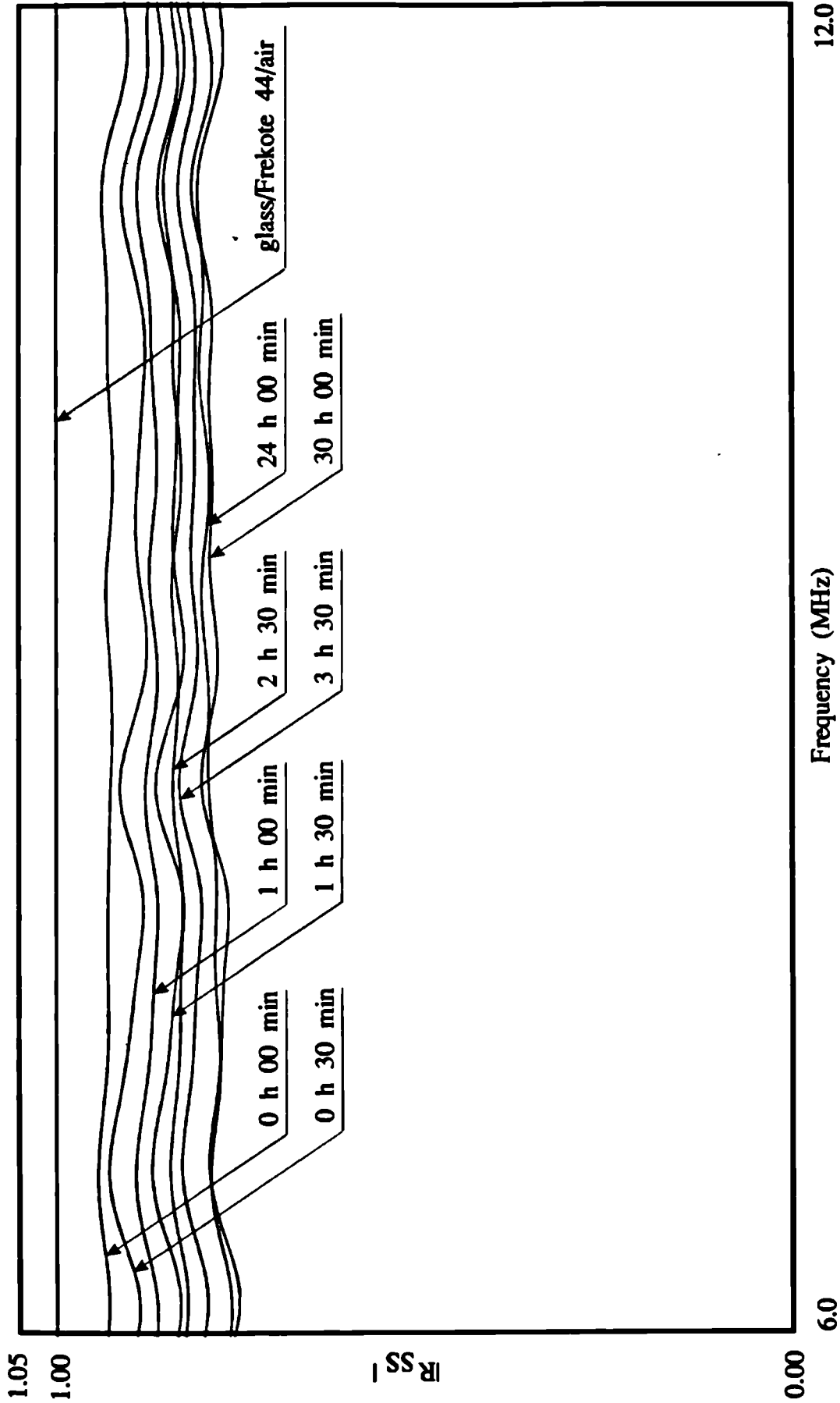
Fig. 6.7   Normal incidence shear reflection coefficient from the glass/Frekote44/epoxy interface as the epoxy cures. Curve lables correspond to the curing time of the epoxy. Results normalised with respect to the glass/Frekote44/air reflection coefficient.
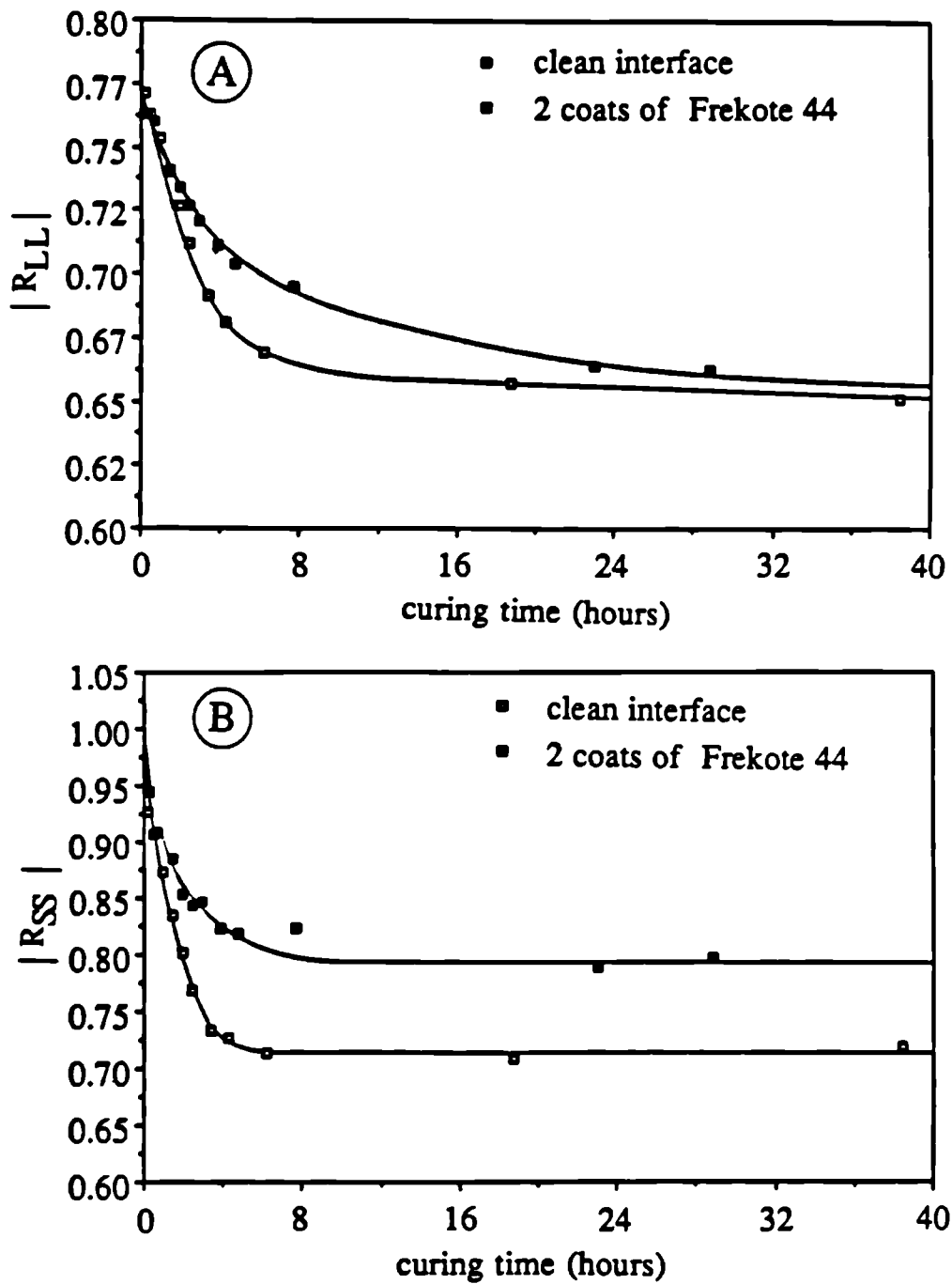
Fig 6.8   Variation of the average reflection coefficient amplitudes
           in the frequency range 4 - 12 MHz from the glass/epoxy
           interfaces with and without the mould release being applied
           to the glass prior to the application of the adhesive.
           (A) normal incidence longitudinal reflection coefficient,
           (B) normal incidence shear reflection coefficient.

transmitter   receiver

5.85 mm thick
glass plate

water

monitored
interface
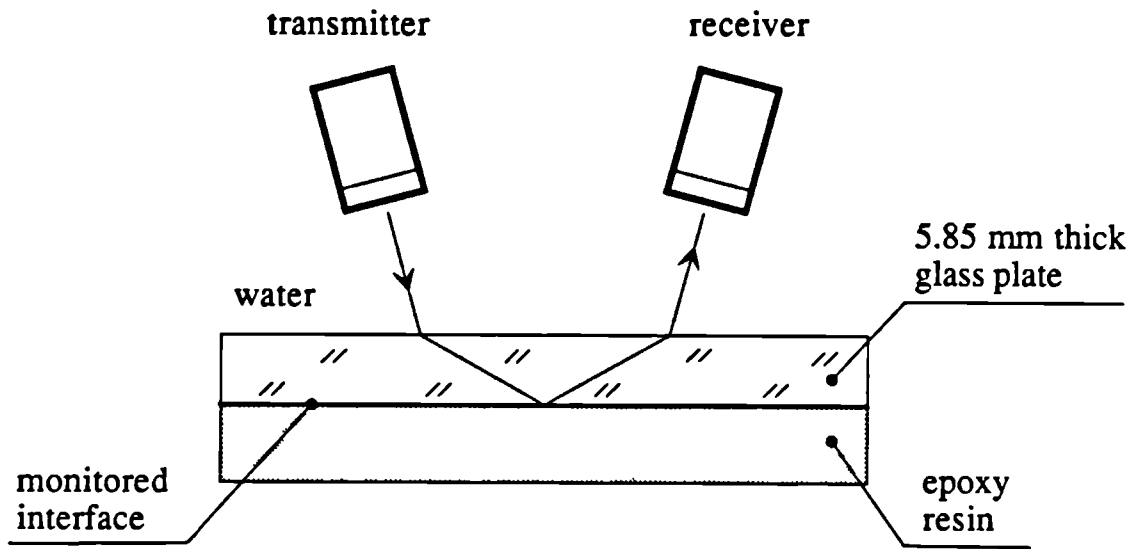
epoxy
resin

Fig 6.9   The glass/epoxy specimen manufactured for the oblique incidence
           experiments. Two types of the specimens were manufactured, with
           and without a thin layer of the Frekote 44 mould release applied
           on the glass surface prior to bonding.
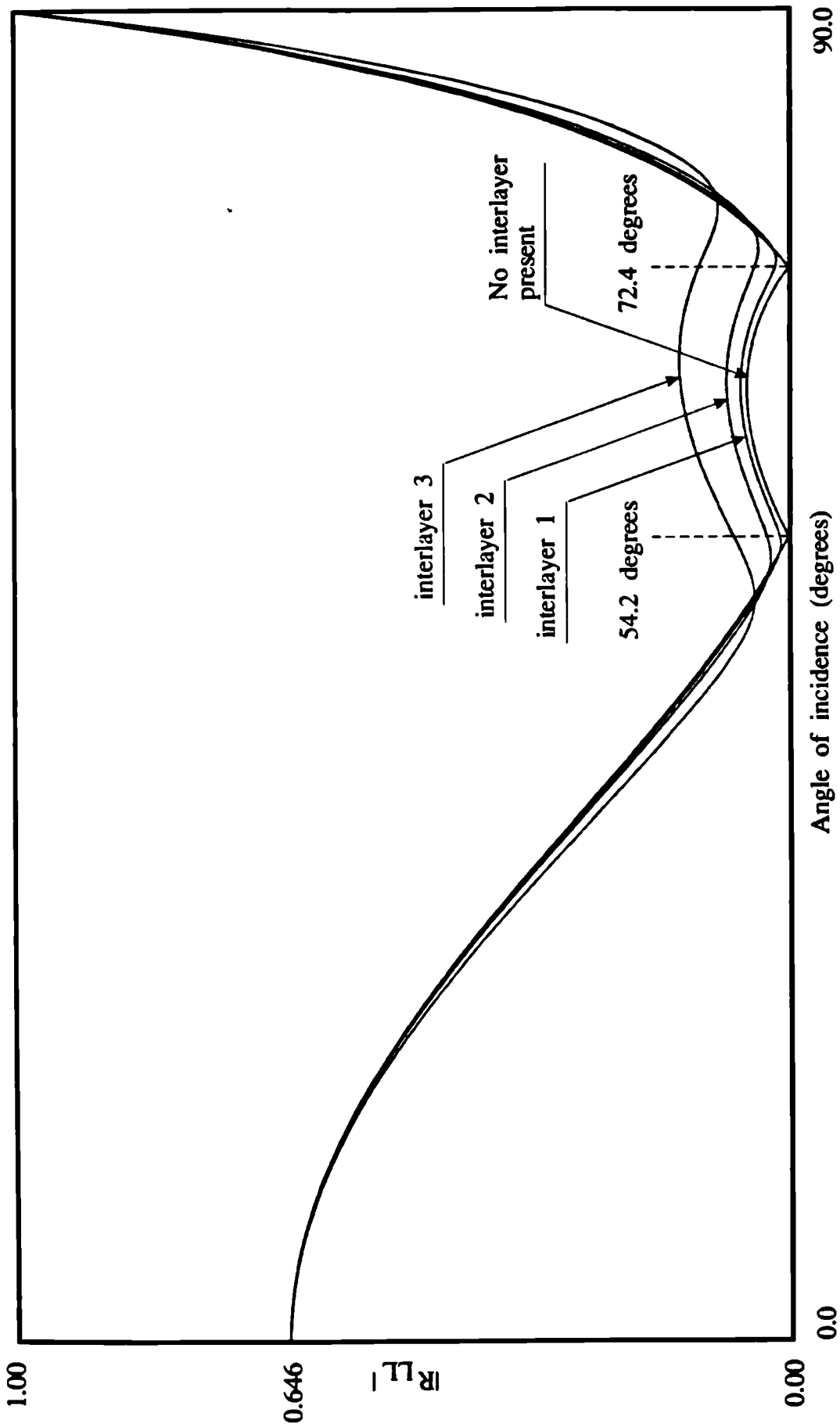
Fig. 6.10 Amplitudes of the longitudinal-longitudinal reflection coefficients from the glass/epoxy interfaces with 10 um thick interlayer of reduced shear stiffness. Frequency 10 MHz. Material properties are given in table 6.1.
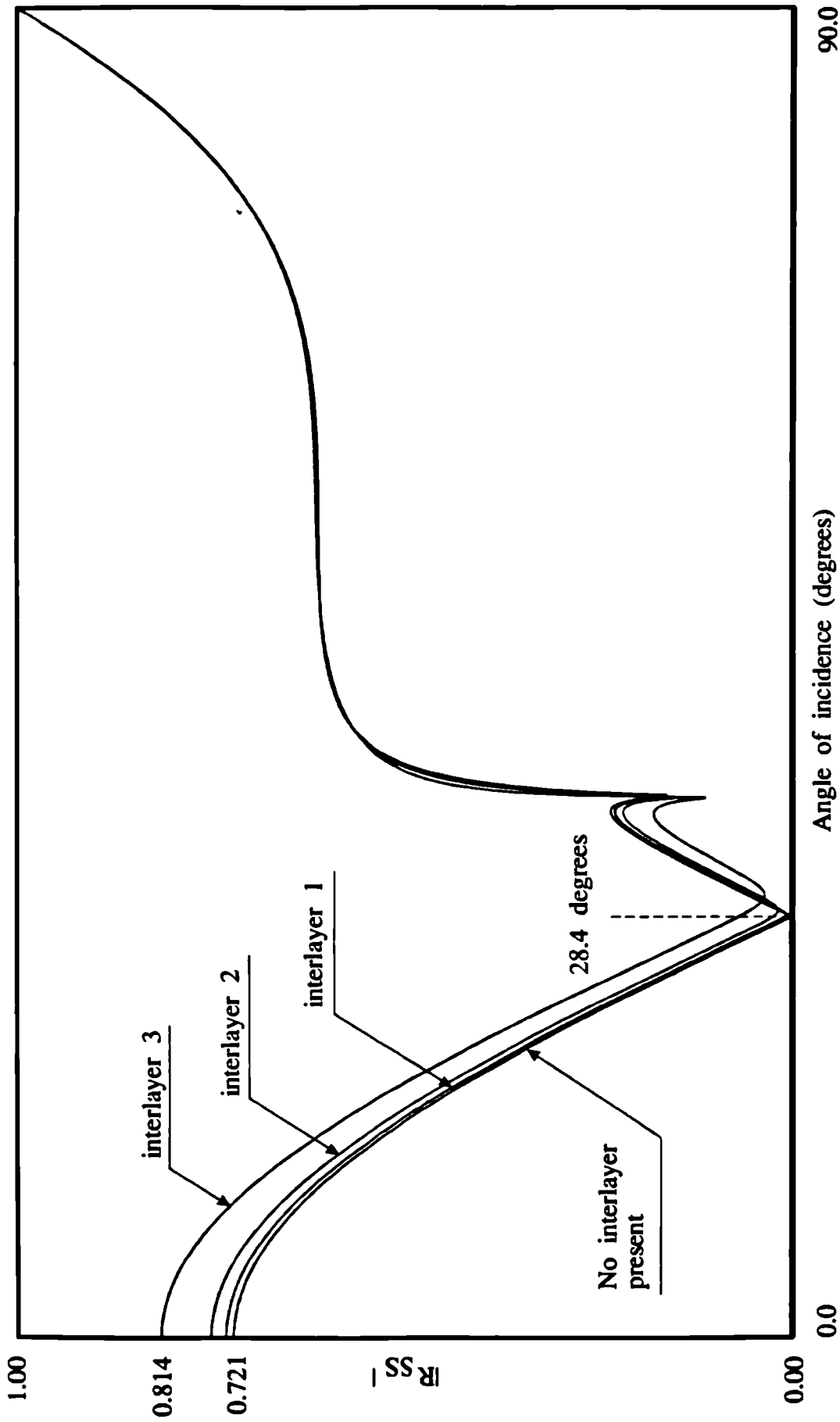
Fig. 6.11 Amplitudes of the shear-shear reflection coefficients from the glass/epoxy interfaces with 10 um thick interlayer of reduced shear stiffness. Frequency 10 MHz. Material properties are given in table 6.1.
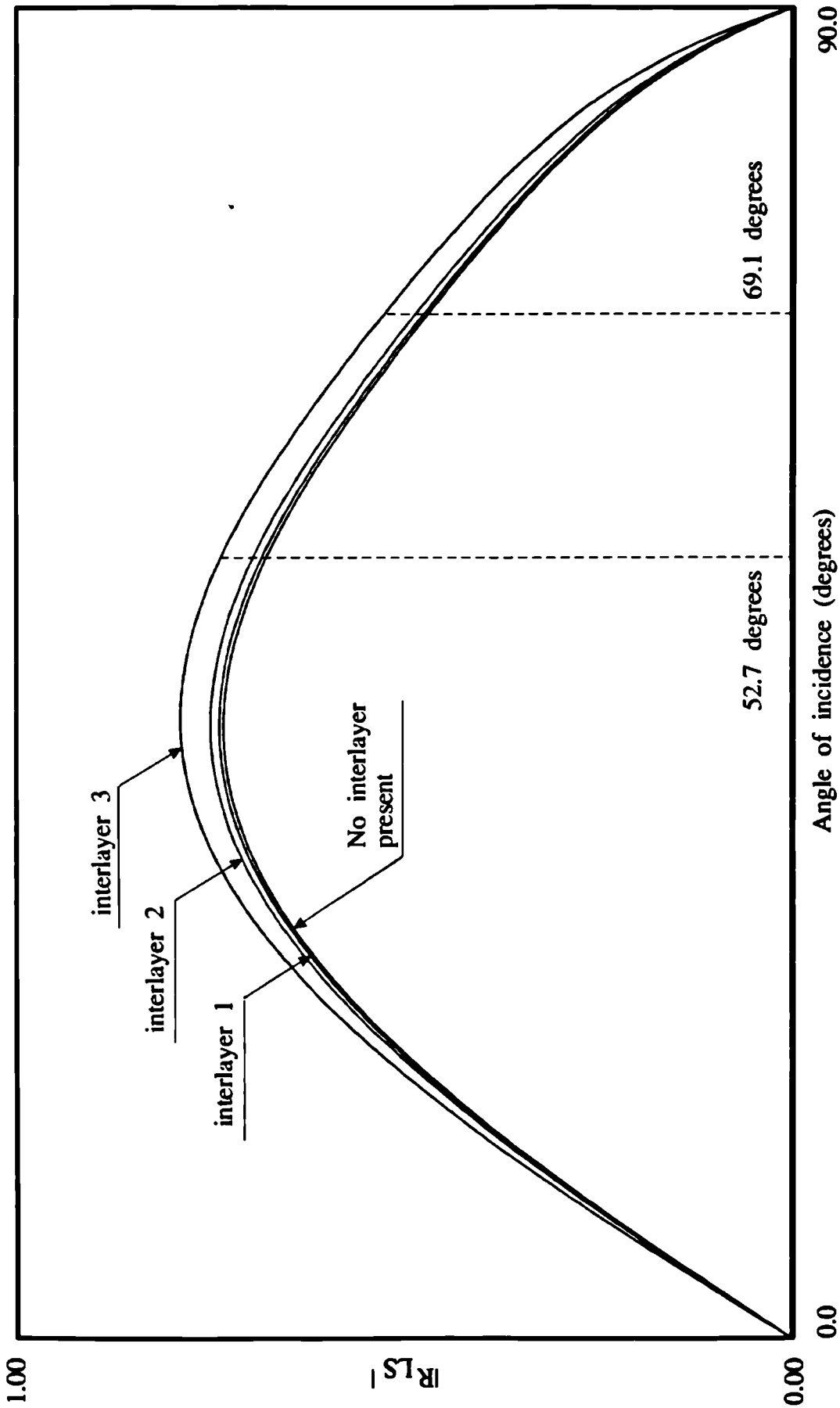
Fig. 6.12 Amplitudes of the longitudinal-shear reflection coefficients from the glass/epoxy interfaces with 10 um thick interlayer of reduced shear stiffness. Frequency 10 MHz. Material properties are given in table 6.1.
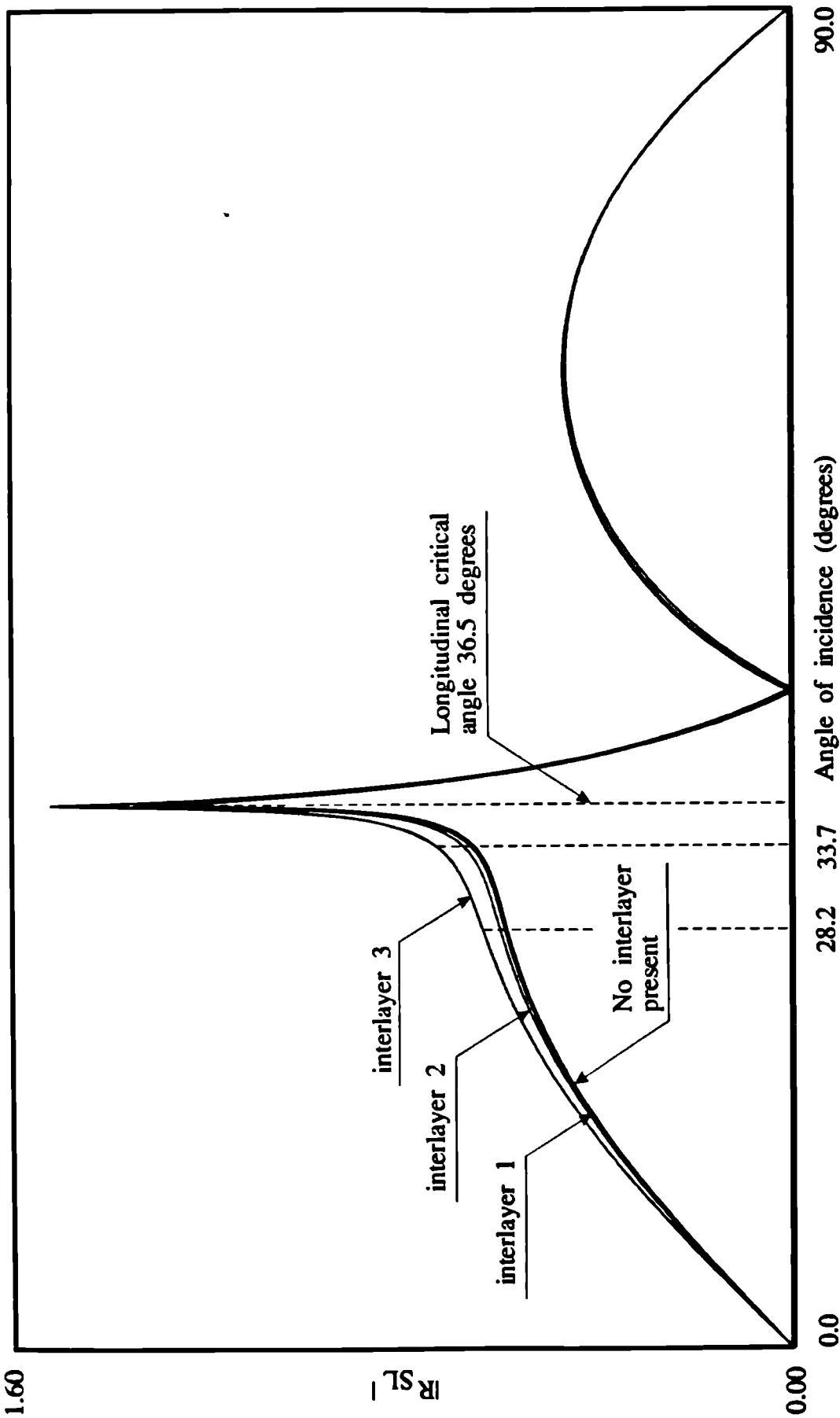
Fig. 6.13 Amplitudes of the shear-longitudinal reflection coefficients from the glass/epoxy interfaces with 10 um thick interlayer of reduced shear stiffness. Frequency 10 MHz. Material properties are given in table 6.1.
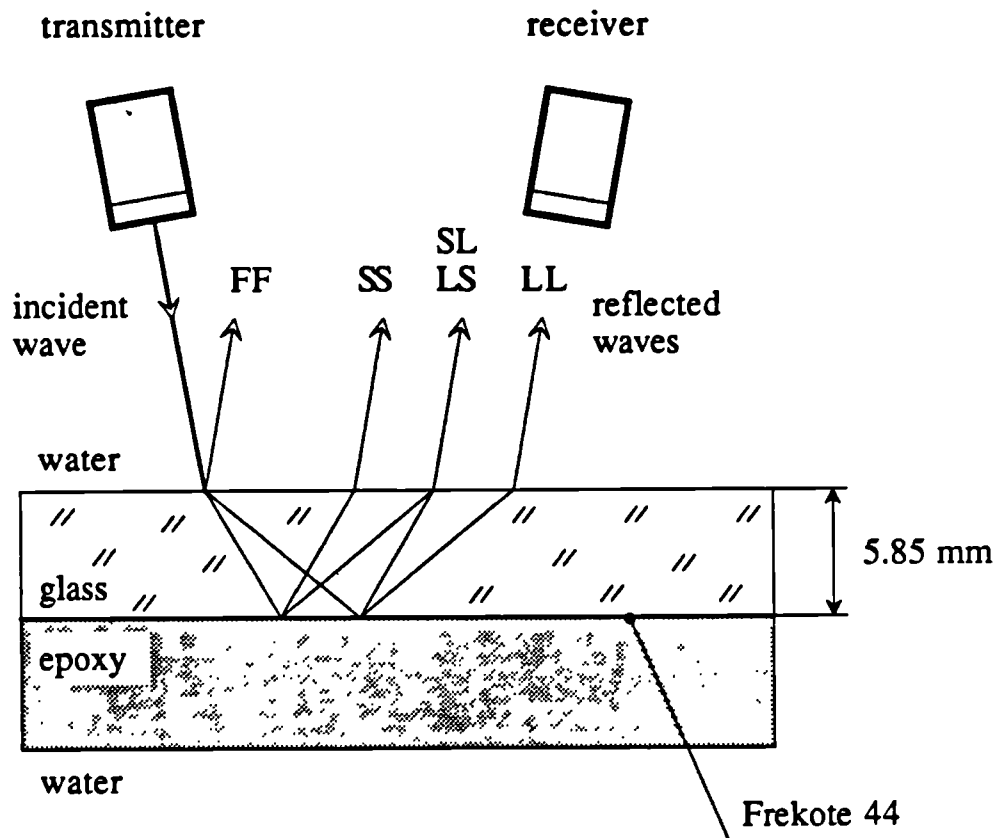
Fig 6.14 Method of generation of the oblique incidence longitudinal
          and shear waves in glass.

FF is the front face reflection,
SS is the shear-shear reflection from the silicone layer,
LS is the longitudinal-shear reflection from the silicone layer,
SL is the shear-longitudinal reflection from the silicone layer,
LL is the longitudinal-longitudinal reflection from the layer.
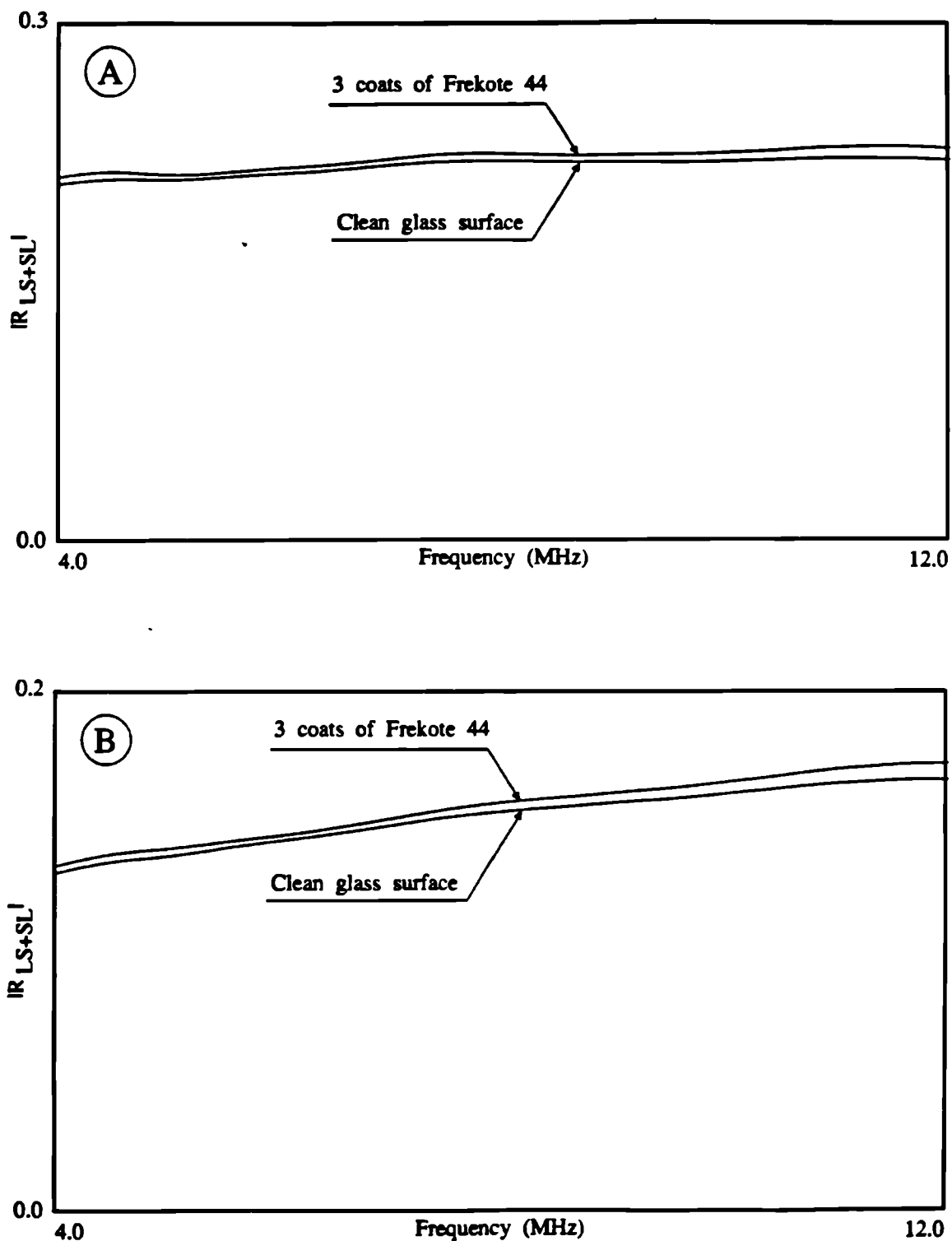
Fig. 6.15   Measured longitudinal-shear and shear-longitudinal combined (LS+SL) reflectivity from glass/epoxy interfaces with and without a mould release layer. (a) angle of incidence 11.8 degrees from water, (b) angle of incidence 13.9 degrees from water. Results normalised with respect to face-to-face signal.
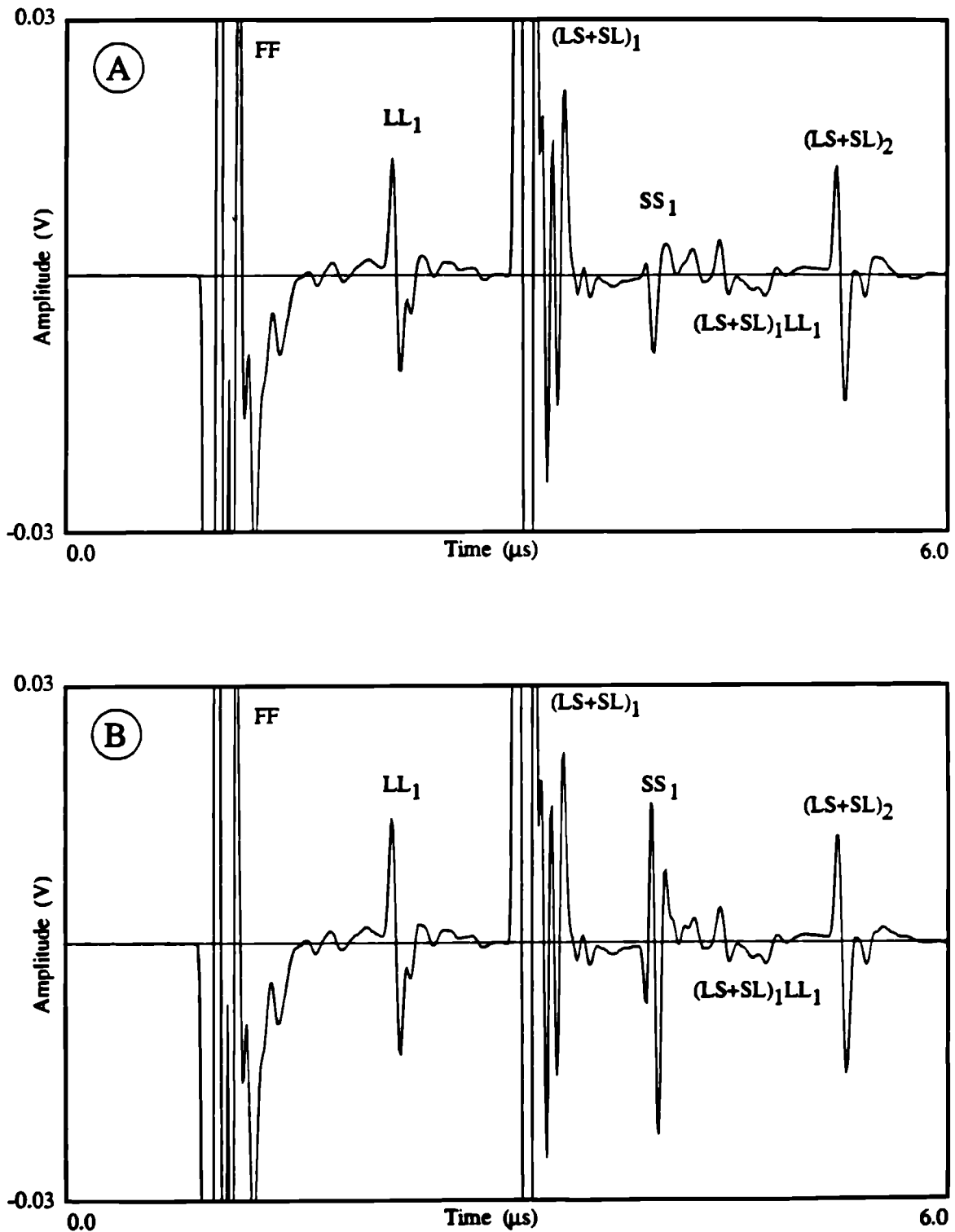
Fig. 6.16   Measured time domain response from glass/epoxy interface to a 10 MHz pulse excitation at the angle of incidence 11.8 degrees from water, which corresponds to 28.2 degrees for shear wave and 52.7 degrees for longitudinal wave in glass. (a) clean glass surface prior to bonding, (b) glass surface coated with the Frekote 44 mould release agent prior to bonding.
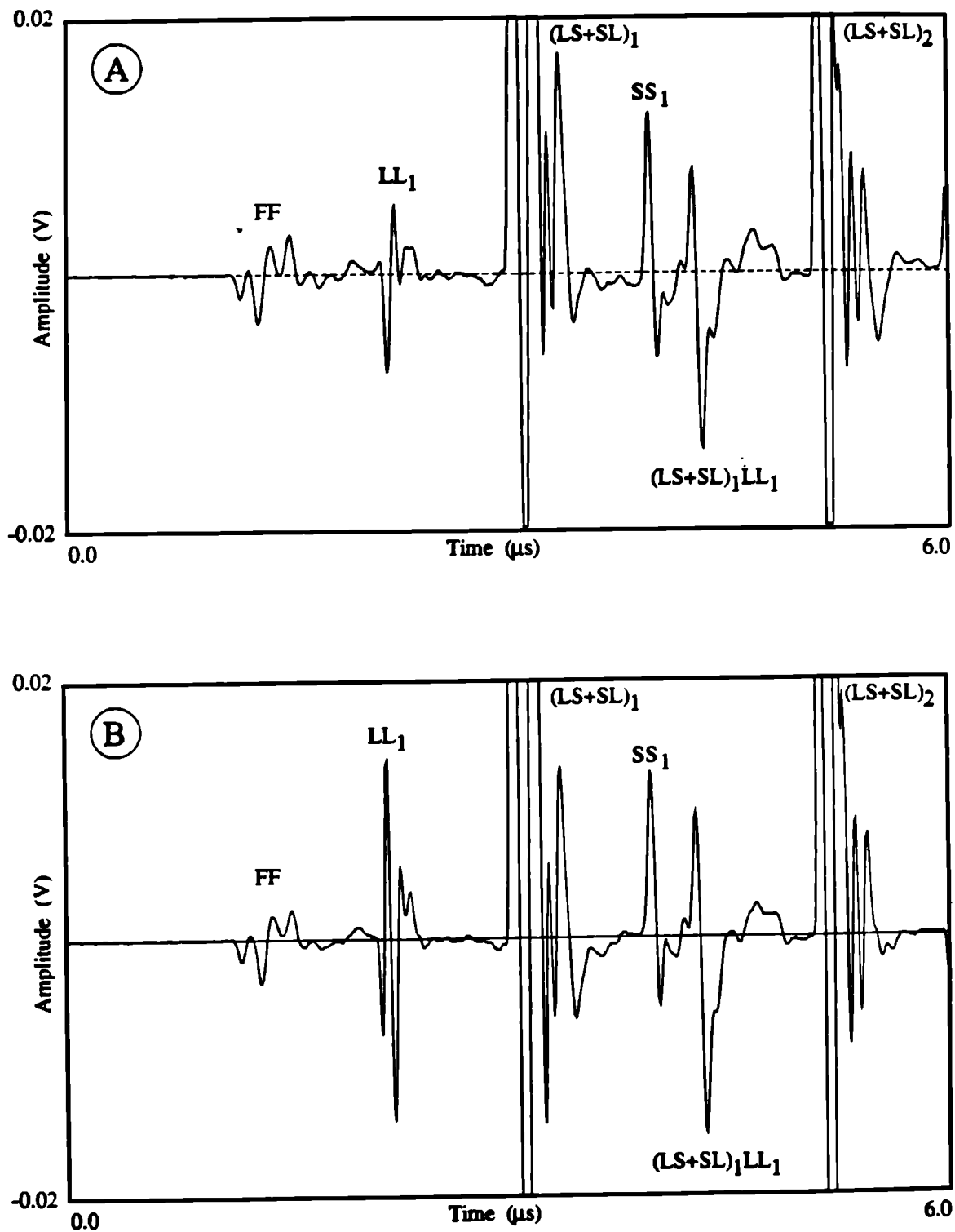
Fig. 6.17   Measured time domain response from glass/epoxy interface to a 10 MHz pulse
excitation at the angle of incidence 12.0 degrees from water, which corresponds
to 28.7 degrees for shear wave and 52.7 degrees for longitudinal wave in glass.
(a) clean glass surface prior to bonding, (b) glass surface coated with the Frekote
44 mould release agent prior to bonding.

CHAPTER 7

Sensitivity of the reflection coefficient method for the determination of the interfacial properties in adhesive joints

7.1 Introduction

In this chapter an analysis of the problem of the determination of the interfacial properties in adhesive joints using the reflection coefficient technique is attempted. More specifically, the chapter addresses the question whether it is possible to detect the presence of a thin oxide layer between aluminium and epoxy half-spaces and whether the method is capable of detection of the degradation of the interface due to surface contamination before bonding or environmental attack of the adhesive joint during service.

In section 7.2 the infinite plane wave theory is used to determine the angles of incidence, the frequency of excitation as well as the type of reflection coefficient which give the best sensitivity of the oblique incidence method to the interfacial conditions across the aluminium/epoxy boundary. The interface is modelled here as an isotropic elastic layer having its own thickness, density and longitudinal and shear wave velocities. Theoretical predictions are then compared with experiments conducted on aluminium/epoxy joints with SAA and CAA oxides to determine the degree of agreement between theory and practice.

Section 7.3 summarises the most important points of the chapter.

7.2 Choice of frequency and angles of incidence for the detection of interfacial properties in adhesive joints

A typical aluminium-aluminium joint used in the aerospace industry consists of two aluminium sheets bonded together by epoxy resin. Before the epoxy resin is applied to form the adhesive joint, the aluminium plates undergo surface treatment procedures in order to increase the joint's resilience to environmental attack (Kinloch 1983). In order to model the mechanical properties of an aluminium/epoxy interface layer successfully, it is necessary to know its composition and morphology.

7.2.1 Description of the aluminium/epoxy joint used in aerospace industry

There are four different surface preparation procedures which are commonly applied to the aluminium surface prior to bonding (Allen 1989), namely the Forest Products Laboratory (FPL) etch, Phosphoric Acid Anodising (PAA), Chromic Acid Anodising (CAA), and Sulphuric Acid Anodising (SAA). The first two treatments, FPL etch and PAA, are used in the USA industry, while the third one, CAA, is used in the European and British aerospace industries. The Sulphuric Acid Anodising (SAA) is not commonly used in aerospace applications, but it has been used in this thesis for comparison purposes in experimental work. Let us briefly describe each of these surface treatment procedures; a fuller description can be found in Davies (1989).

Forest Products Laboratory (FPL) etch pretreatment

This is the simplest surface pretreatment of all three, and starts with solvent and alkaline degreasing (see fig. 7.1). After the grease contamination has been removed from the surface, the aluminium plate is etched for 10 minutes in a water solution of sulphuric acid and sodium dichromate for 10 minutes at a temperature of 70° C. In this process, the aluminium plate is stripped of its thin protective layer comprising a mixture of the oxide and other random chemicals present when the plate was manufactured. The subsequent rinsing of the aluminium plate in running tap water builds the layer again, but this time it consists of almost pure aluminium oxide. The oxide layer produced using the FPL etch process is about 0.07 μm thick. Fig 7.2 shows a schematic diagram of the FPL etch oxide structure (Davies 1989).

Phosphoric Acid Anodising (PAA)

In the PAA procedure, after the solvent and alkaline degreasing and FPL etching process (see fig. 7.1), the aluminium plate is anodised in a 10 % solution of orthophosphoric acid at a temperature of 22° C for 20 minutes at 10 Volts, while the oxide layer is formed at the aluminium surface. The oxide layer obtained after this process is about 0.6 μm thick (Davies 1989). Fig 7.3 shows a schematic diagram of the PAA oxide structure.

Chromic Acid Anodising (CAA)

The CAA process initially follows the same path as the previous two, namely the solvent and the alkaline degreasing (see fig. 7.1). Then, following alkaline etching and chromic acid etching, the plate is anodised in a 10 % solution of chromic acid at temperature of 40° C for 40 minutes, while the aluminium oxide is built on the surface of the plate. The voltage is changed several times

during the process of anodising being raised in two steps from zero to 40 V in the first 10 minutes, then maintained at the 40 V level for 20 minutes and gradually raised up to 50 V over the next 5 minutes and then maintained unchanged for the last 5 minutes of the anodising. The thickness of the oxide layer obtained in the CAA process is about 3.5 μm (Davies 1989). Fig 7.4 shows a schematic diagram of the CAA oxide structure.

Sulphuric Acid Anodising (SAA)

The SAA surface treatment initially follows the same process as the FPL etch. After the FPL etching and rinsing in running tap water the aluminium surface is anodised in 10 % sulphuric acid solution at a temperature of -5° C for 12 minutes maintaining the electric current density at 4 A/dm^2 (Davies 1989). The oxide layer obtained during the anodising is about 12 μm thick. Figure 7.5 shows a schematic diagram of the SAA oxide structure. It is interesting to note here that it is possible to obtain different thicknesses of SAA oxide by anodising aluminium samples for different lengths of time. If, for example, the sample is kept in the bath for 50 minutes then the oxide is about 50 μm thick.

7.2.2   Theoretical model of the aluminium/epoxy joint

As can be seen from subsection 7.2.1, the aluminium adhesive joint does not simply consist of the aluminium material directly bonded to the epoxy resin. Since even 'as received' aluminium plate has a thin oxide layer, a 'barrier' layer is always present regardless of whether the surface is anodised or not. In other words, the epoxy resin is bonded to the interlayer formed on the aluminium surface rather than to the aluminium itself. The surface treatments presented in subsection 7.2.1 make this interlayer thicker and more uniform. It is therefore important to account for the presence of the oxide layer in our theoretical model.

Figure 7.6(a) shows schematically the aluminium/epoxy interface with the oxide layer in between formed using CAA process. From fig. 7.4 it clearly can be seen that the structure of the CAA oxide is very complicated. However, because the layer is very thin, the theoretical model of the aluminium/epoxy interface used for the reflection coefficient predictions assumes a simplified model consisting of aluminium and the epoxy half-spaces separated by a 3.5 μm thick isotropic layer with mechanical properties similar to those of the oxide structure. The acoustic properties of the interlayer were calculated using the properties of solid aluminium oxide and the assumed porosity of the anodised oxide as follows.

Let us denote the density, longitudinal and shear velocities of the solid oxide as ρ, c_L and c_S, respectively. The moduli of the material in the longitudinal and shear directions will be denoted as

E and G, respectively. The density, longitudinal and shear velocities of the anodised oxide are denoted as ρ^*, c_L^* and c_S^*, respectively. The porosity of the anodised oxide will be denoted as ζ here. The moduli of the porous oxide material in the longitudinal and shear direction are denoted as E^* and G^*, respectively. Using the symbols introduced above the density, the moduli in the longitudinal and shear directions of the porous oxide can be calculated as,

$$\rho^* = (1-\zeta)\,\rho\,, \tag{7.1}$$

$$E^* = (1-\zeta)\,E\,, \tag{7.2}$$

$$G^* = (1-\zeta)\,G\,. \tag{7.3}$$

Equations (7.2) and (7.3) state that the longitudinal and shear moduli of the oxide layer changes linearly with porosity. No account has been taken here of the stress distribution around the pores which can alter the moduli values to some extend.

In an isotropic material like the solid aluminium oxide, the longitudinal and shear velocities are related to the longitudinal and shear moduli and the density by the following equations,

$$E = \rho\, c_L^2\,, \tag{7.4}$$

$$G = \rho\, c_S^2\,. \tag{7.5}$$

In the theoretical investigations, it is assumed that the interlayer between aluminium and epoxy is isotropic, and therefore satisfying similar relationships between the moduli of elasticity and the wave velocities as the bulk oxide.

$$c_L^* = \left(\frac{E^*}{\rho^*}\right)^{1/2} \tag{7.6}$$

$$c_S^* = \left(\frac{G^*}{\rho^*}\right)^{1/2} \tag{7.7}$$

Substituting equations (7.1) - (7.5) into equations (7.6) and (7.7), we have,

$$c_L^* = c_L\,, \tag{7.8}$$

$$c_S^* = c_S\,. \tag{7.9}$$

Equations (7.1), (7.8), and (7.9) were used to calculate the equivalent acoustic properties of the porous oxide layer. The equations show that in the theoretical model the longitudinal and shear

velocities of the oxide layers are independent of the oxide porosity. The only property which changes its value is the density of the interlayer as given by eqn (7.1). However, due to the very complicated morphology of oxide layers (see figures 7.2, 7.3, 7.4 and 7.5), equivalent acoustic properties calculated from equations (7.1), (7.8), and (7.9) should be considered as approximate. Indeed, the layer has been modelled here as an isotropic material which means that its acoustic properties, like phase velocities of the longitudinal and shear waves, are not dependent on the direction of wave propagation, which is not the case in reality. However, because the thickness of oxide layers are usually very thin in comparison with the wavelength of the ultrasound used in experiments, and the isotropic layer model is relatively simple and readily available, the decision was made to use it here as an approximation.

Table 7.1 shows the assumed acoustic properties of the solid aluminium oxide and the acoustic properties of the interlayer representing porous oxides obtained using equations (7.1), (7.8), and (7.9).

material	density ρ (kg/m^3)	longitudinal velocity c_L (m/s)	shear velocity c_S (m/s)
aluminium oxide	3900	10200	6500
10 % porous oxide	3510	10200	6500
20 % porous oxide	3120	10200	6500
30 % porous oxide	2730	10200	6500
40 % porous oxide	2340	10200	6500
50 % porous oxide	1950	10200	6500
60 % porous oxide	1560	10200	6500
70 % porous oxide	1170	10200	6500

Table 7.1 Acoustic properties of porous aluminium oxides calculated from equations (7.1), (7.8) and (7.9).

The acoustic properties of the aluminium and epoxy half-spaces used for the reflection coefficient calculations are given in table 7.2.

material	density ρ (kg/m^3)	longitudinal velocity c_L (m/s)	shear velocity c_S (m/s)
aluminium	2820	6330	3120
epoxy	1170	2610	1100

Table 7.2 Acoustic properties of aluminium and epoxy resin used for the reflection coefficient calculations.

7.2.3 Normal incidence longitudinal reflection coefficient from aluminium/ epoxy joints

Figure 7.7 shows a parametric study of the normal incidence longitudinal reflection coefficient at the aluminium/oxide/epoxy interface calculated using the properties given in tables 7.1 and 7.2. The oxide layer was assumed to be 50 μm thick, which is one order of magnitude thicker than that obtained using the CAA treatment employed in the British and European aerospace industries. From fig. 7.7 it can be seen that if the porosity of the oxide is small (10 % - 20 %) then the longitudinal normal incidence reflection coefficient from the oxide layer is greater than the reflection coefficient from the aluminium/epoxy interface without the oxide layer present, and the curve is bending in the upward direction for low frequencies. For oxide porosity between 50 % and 60 % the longitudinal normal incidence curve is very close to that of the reflection coefficient from the aluminium/epoxy without any oxide layer at all, making the presence of the oxide layer impossible to detect regardless of the oxide thickness or the frequency range used. When the porosity of the oxide is big (60 % - 70 %) then the reflection coefficient curve is bending downwards for low frequencies. It has been discovered empirically (Sullivan and Wood 1970, Arrowsmith et al 1985, Xu et al 1985, Arrowsmith and Moth 1986) that the porosity of anodised oxides depend on the electrolyte type, its concentration and temperature. More extensive theoretical analysis of the normal reflection coefficient from thin oxide layers is given in chapter 4 of this thesis.

The experimental investigation of the normal incidence longitudinal reflectivity was carried out using single-interface aluminium-epoxy joints with a 50 μm thick SAA oxide layer anodised on the aluminium surface prior to bonding (see fig. 7.8). Three types of samples were prepared, 'healthy' SAA oxide joints, 'hydrated' SAA oxide joints and the reference joints. The 'hydrated' type of oxide layer was obtained by keeping the anodised aluminium plates for 48 hours in a water bath at 55° C, while the 'healthy' samples were kept in dry air for this period of time. The

reference samples were manufactured by cleaning the aluminium surfaces with acetone. Then all the samples, the 'hydrated' and the 'healthy' SAA samples as well as the reference ones, were bonded at the same time and using the same adhesive system (Ciba-Geigy Araldite AY 103 with Hardener HY 951).

The procedure of the reflection coefficient measurement involving the time domain gating and spectral division by a reference signal has been described in detail in chapter 5 of this thesis. Figure 7.9 shows the normal incidence reflection coefficient from the healthy and hydrated 50 μm thick SAA oxide normalised with respect to the reflection coefficient from the sample without the oxide layer present (the reference sample). From the figure it can clearly be seen that it is relatively easy to detect presence of 50 μm thick oxide layer between aluminium and epoxy. The reflection coefficient from the healthy oxide bends downwards indicating that the porosity of the layer is greater than 60 %. The reflection coefficient from the hydrated 50 μm thick oxide layer moved in the upward direction with respect to the healthy oxide indicating that the longitudinal impedance of the layer is higher than that of the healthy layer. More detailed discussion about the behaviour of the normal incidence reflection coefficient from the interlayer as a function of its impedance is presented in section 4.4 of this thesis.

Figure 7.10 shows the theoretically calculated normal incidence longitudinal reflection coefficient from a 50 μm thick 67 % porous oxide layer and table 7.3 shows the material properties of the oxides taken for the reflection coefficient calculations. The acoustic properties for the hydrated 67 % porous layer were calculated assuming that after 48 hours in water bath the pores in the oxide were filled with water, and applying similar reasoning to that given by equations (7.1) - (7.9).

material	density ρ (kg/m^3)	longitudinal velocity c_L (m/s)	shear velocity c_S (m/s)
67 % porous healthy oxide	1287	10200	6500
67 % porous hydrated oxide	1957	8510	5400

Table 7.3   Acoustic properties of healthy and hydrated aluminium oxides assumed in calculations shown in fig. 7.10.

Comparison between figures 7.9 and 7.10 indicates that at normal incidence the theoretical model is capable of quantitative predictions of the reflection coefficient from the oxides. This will need to be verified by measuring the levels of porosity, probably by sectioning the samples and using optical microscopy. Further tests with different levels of porosity will also be required.

The experimental and theoretical results shown in figures 7.7, 7.9 and 7.10 considered an oxide layer of the thickness of 50 μm, which is one order of magnitude higher than the CAA anodised oxide whose typical thickness is about 3.5 μm. Figure 7.11 shows the normal incidence longitudinal reflection coefficients calculated for 70 % porous oxide layers of different thicknesses. From the figure one can see that while the presence 50 μm thick oxide is rather easy to detect, the 20 μm thick oxide of the same properties is very unlikely to be detected in practice using frequencies up to 50 MHz. If it is assumed that in the frequency range up to 50 MHz the presence of the 30 μm thick oxide is detectable then the presence of a 3.5 μm thick oxide of the same properties will require frequencies up to 500 MHz to secure successful detection of the presence of the oxide. This requirement cannot practically be met in ultrasonic nondestructive testing which uses frequencies up to 100 MHz. It is therefore concluded here that at normal incidence the detection of the presence of 3.5 μm thick CAA oxide layer, let alone its hydration, is impossible.

In order to illustrate this, the normal incidence longitudinal wave reflection coefficient was measured from aluminium/epoxy boundaries with 15 μm thick SAA oxide, 3.5 μm thick CAA oxide and 0.07 μm thick FPL etch oxide layers created on the surface of the aluminium plates prior to the application of epoxy resin. The thickness of the SAA oxide was checked with an electromagnetic gauge, while the thicknesses of the CAA and the FPL etch oxides were taken from the surface pretreatment specifications (see fig. 7.1). The specimens manufactured for the experiments were the single-interface type (see fig. 7.8) and the signal processing sequence was exactly the same as that used to obtain results of fig. 7.9, and involved the time domain gating of pulses reflected from interfaces of interest and spectral division of the data by the reference signal. Figure 7.12 shows the normal incidence longitudinal reflection coefficient from the aluminium/ epoxy interfaces with 15 μm thick 'healthy' SAA oxide and 3.5 μm thick 'healthy' oxide layers normalised with respect to the normal incidence longitudinal reflection coefficient from the specimen with the 0.07 μm thick FPL etch oxide layer. The results presented in the figure show that the reflection coefficients from the three interfaces cannot be distinguished from each other. This is in agreement with the theoretical predictions shown in fig. 7.11.

7.2.4 Oblique incidence reflection coefficients from aluminium/epoxy joints

Figure 7.13 shows the theoretically calculated longitudinal-longitudinal (R_{LL}), shear-shear (R_{SS}), longitudinal-shear (R_{LS}) and shear longitudinal (R_{SL}) reflection coefficients from an aluminium-epoxy interface with and without oxide layer as a function of the angle of incidence in the aluminium half-space. Curves number 1 in fig. 7.13 correspond to the case of a 3.5 μm

thick 60 % porous oxide excited at the frequency of 30 MHz. Curves number 2 correspond to the same case as those bearing number 1 but being excited at a frequency of 10 MHz. Curves number 3 correspond to the case of an aluminium/epoxy boundary without the oxide layer present, the reflection coefficients being frequency independent in this case.

There are three important observations which can be drawn from fig. 7.13. The first one is that the sensitivity of the reflection coefficient method is frequency dependent. Indeed, it can clearly be seen that the reflection coefficient method is more sensitive at the frequency of 30 MHz (curves number 1) in comparison with the results obtained at the frequency of 10 MHz (curves number 2). However, since none of the curves shown in fig. 7.13 touches the zero line, the sensitivity of the reflection coefficient method will be significantly lower for the aluminium/epoxy interface than for the glass/epoxy interface studied in chapter 6. Indeed, it was shown in chapter 6 that at the angles of incidence where the reflection coefficients form the glass/epoxy interface are zero (see figures 6.10 and 6.11 and compare them with figures 7.13(a) and (c)), the sensitivity of the reflection coefficient method substantially increases. The third observation is that the biggest sensitivity of the reflection coefficient method is when the shear-shear reflection coefficient (R_{SS}) at an angle of incidence of around 32.0 degrees in aluminium is used (see fig. 7.13(c)). Table 7.4 shows the amplitude of the shear-shear reflection coefficient (R_{SS}) obtained from the curves of fig. 7.13(c).

curve number	description of the interface	frequency of excitation	R_{SS} amplitude at 32.0 deg	change wrt curve No 3
1	3.5 μm thick 60 % oxide from table 7.1	30 MHz	0.574	52 %
2	3.5 μm thick 60 % oxide from table 7.1	10 MHz	0.458	21 %
3	No oxide present	frequency independent	0.374	0 %

Table 7.4 The amplitude of the R_{SS} coefficient at 32.0 degrees taken from fig. 7.13(c)

There is also a very important practical consideration in favour of the use of the shear wave at this angle. When the shear wave is incident on the boundary, reflected longitudinal and shear wave will be generated. However, when the incident shear wave angle is greater than 29.5 degrees, the longitudinal wave is inhomogeneous so only the shear wave is seen. Indeed, taking the longitudinal and shear phase velocity values for aluminium from table 7.2 the maximum shear wave angle for which the longitudinal wave is homogeneous can be calculated as $\sin^{-1}(c_S/c_L) =$ $\sin^{-1}(3120/6330) = 29.5$ degrees. Above this angle the longitudinal wave becomes

inhomogeneous. This means that the only propagating pulses in the aluminium are the shear wave pulses which greatly simplifies the process of capturing them and data processing. Let us investigate the sensitivity of the R_{SS} reflectivity at the angle of 32.0 degrees in aluminium.

As we mentioned before, during the process of CAA anodising, an approximately 3.5 μm thick aluminium oxide layer is produced on the surface of the adherend. Due to the nature of the anodising process, it is sensible to assume that the thickness of the oxide may vary ± 0.5 μm over the tested sample. This means that, in practice, the lower and the upper bounds for the oxide layer thickness are 3.0 μm and 4.0 μm, respectively. Therefore, to be useful in practice, the reflection coefficient variations due to the fluctuations in the layer thickness have to be well separated from the changes in the reflectivity caused by the absence of the interlayer or by changes of its properties.

Figure 7.14 shows a parametric study of the shear-shear reflection coefficient at an angle of incidence of 32.0 degrees in the frequency domain. The horizontal line corresponds to the case when the oxide layer does no exist at the interface, or in other words, when its thickness is null. The remaining three curves on this figure correspond to oxide layer thicknesses of 3.0 μm, 3.5 μm, and 4.0 μm with 60 % porosity. The area of the fluctuation of the reflection coefficient due to the variation of the oxide thickness is contained between the lines corresponding to the 3.0 μm and 4.0 μm thick oxides, and is shaded.

It is easy now to find the frequencies at which the detection of the presence of the oxide layer is possible. For example if we require a 20 percent difference in the reflectivity between the interface with and without the oxide, then the   frequency for which the shaded zone is above the 0.37 × 1.2 = 0.45 level can be found from the fig. 7.14 as 10.6 MHz.

The theoretical investigations shown in figures 7.13 and 7.14 were carried out assuming the oxide porosity of 60 %. It is most likely that 3.5 μm thick CAA oxide will have porosity between 10 % and 20 %. Figure 7.15 shows a parametric study of the shear-shear reflection coefficient from aluminium/3.5 μm thick oxide/epoxy interfaces at an angle of incidence of 32.0 degrees in aluminium for different porosities of the oxide layer. It can clearly be seen from the figure that the smaller the porosity of the oxide the better the chances of the detection of the oxide layer. Looking at figures 7.15 and 7.14 we can therefore conclude that the detection of the presence of 3.5 μm thick oxide layer between the aluminium and epoxy half-spaces should pose no problems if the shear-shear reflection coefficient at the angle of 32.0 degrees is used.

Experimental investigations were carried out to validate the theoretical predictions of figures 7.14

and 7.15 on the three types of aluminium-epoxy joints, which were used for the normal incidence longitudinal reflection coefficient measurements of fig. 7.12. The first type of specimens were aluminium/0.07 μm thick FPL etch oxide/epoxy joints, the second type were aluminium/3.5 μm thick CAA oxide/epoxy joints, while the third type of specimens were aluminium/15 μm thick SAA oxide/epoxy joints. Figure 7.16 shows the shear-shear reflection coefficients from the CAA oxide and SAA oxide layers at an angle of 32.0 degrees normalised with respect to the reflection coefficient from the FPL etched oxide interface. Since the FPL oxide thickness is 0.07 μm, the reflection coefficient from the aluminium/FPL etch oxide/epoxy is practically the same as the aluminium/epoxy coefficient without the oxide layer present.

Comparing the experimental results presented in figures 7.12 and 7.16, a significant improvement of sensitivity of the oblique incidence technique over the normal incidence method can be seen. Indeed, it was impossible to detect the presence of the 15 μm thick SAA oxide using the normal incidence longitudinal wave technique operating in the frequency range up to 50 MHz (see fig. 7.12), while the shear-shear reflection coefficient at 32.0 degrees readily revealed the presence of the oxide layer in the frequency range up to 15 MHz (see fig. 7.16). Also the reflection coefficient from 3.5 μm thick CAA oxide appears to be slightly higher than that from 0.07 μm thick FPL etch oxide and the difference between them increases with frequency. This is qualitatively in agreement with the theoretical predictions shown in fig. 7.13.

However, according to the theoretical predictions shown in fig. 7.15 we should expect significant differences in amplitude (at least 30 %) between the CAA and FPL curves of fig. 7.16. This is not the case here. The shear-shear reflection coefficients from the 3.5 μm thick CAA oxide and 0.07 μm thick FPL etch oxide look practically the same in the frequency range between 5 MHz and 15 MHz. This indicates that the theoretical model used for the oblique incidence reflection coefficient calculations is incapable of accurate quantitative predictions of the behaviour of the real aluminium/ oxide/epoxy systems. The problem here lies in the oversimplification of the mechanical behaviour of the oxide which was modelled as an isotropic layer rather than an anisotropic honeycomb-like structure (see figures 7.4 and 7.6).

The curves of fig. 7.15 were obtained assuming that the longitudinal and shear velocities in the oxide layer are as high as 10200 m/s and 6500 m/s and that they are independent of the direction of propagation in the oxide (isotropic model). This assumption also means that the moduli of elasticity of the layer are direction independent. The schematic diagrams of the PAA oxide (fig 7.3), CAA oxide (fig 7.4) and SAA oxide (fig 7.5) show that all three types of anodised oxides have a vertical cellular structure suggesting that the oxides have the highest stiffness in the vertical direction and the lowest stiffness in the horizontal direction. It is therefore very possible that,

when testing at oblique incidence, the equivalent wave velocities are significantly lower than calculated in table 7.1.

Figure 7.17 shows the theoretically calculated shear-shear reflection coefficient at an angle of incidence of 32.0 degrees in aluminium from 60 % porous oxide layers in between aluminium and epoxy half-spaces, when the longitudinal and shear velocities have been reduced to 60 % of the values of table 7.1. Table 7.5 shows the acoustic properties used for the calculations.

material	density ρ (kg/m^3)	longitudinal velocity c_L (m/s)	shear velocity c_S (m/s)
oxide	1560	6210	3900

Table 7.5   Acoustic properties of aluminium oxide used for the reflection coefficient calculations shown in fig. 7.17.

The theoretically obtained curves of fig. 7.17 are much closer to the experimentally determined reflection coefficients presented in fig. 7.16 than those of fig. 7.14. However, the acoustic properties of the oxide material shown in table 7.5 were deliberately chosen so that figures 7.16 and 7.17 are in a reasonably good agreement. The example shown in fig. 7.17 has been solely devised to show the need for the development of an anisotropic model of the aluminium oxide interface, in which the directionality of the material properties of the layer can be taken into account.

7.3 Conclusions

It has been shown in this chapter that the normal incidence reflection coefficient technique operating up to a frequency of 100 MHz is capable of the detection of the presence of an oxide layer in adhesive joints provided that the oxide layer is at least 30 μm thick and its effective porosity is not between 50 % and 60 %. Detection of the 3.5 μm thick CAA oxide is not possible using this technique because the oxide is one order of magnitude thinner than the minimum detectable thickness.

A theoretical analysis of the oblique incidence reflection coefficient from the aluminium/oxide/epoxy systems shows that at certain angles of incidence and for certain types of reflection coefficients the sensitivity of the method is much greater than at normal incidence. In order to show this in practice, the normal incidence longitudinal reflection coefficient and the 32.0

degrees incidence shear-shear reflection coefficient from 15 μm thick SAA oxide layer at an aluminium/epoxy boundary was experimentally determined. A significant improvement of the oblique incidence method over the conventional normal incidence technique could be seen and the measurements were in qualitative agreement with theory.

The theoretical study of the oblique incidence reflection coefficient from the aluminium/epoxy interface shows that the sensitivity of the technique to the interfacial changes is not as good as in the case of the glass/epoxy system, analysed in chapter 6. This is because there are certain angles of incidence where the oblique angle reflection coefficients from the glass/epoxy interface attain null values. At these particular angles, the reflection coefficient method substantially increases its sensitivity. The oblique incidence reflection coefficients from the aluminium/epoxy interface, however, do not attain any zero value within the entire permissible range of angles of incidence.

The theoretical predictions indicated that, if the shear-shear reflection coefficient at an angle of incidence 32.0 degrees is used, then it should be possible to detect the presence of a 3.5 μm thick CAA oxide layer in the adhesive joint using a frequency as low as 10 MHz. However, the experiments carried out to monitor the shear-shear reflectivity from CAA oxides in adhesive joints at an angle of incidence of 32.0 degrees in the frequency range from 5 to 15 MHz showed only very small sensitivity to the presence of 3.5 μm thick CAA oxide layers. It has therefore been concluded that the isotropic model of the oxide layer is too simplistic to quantitatively predict the mechanical response of the layer when excited by an oblique incident wave.

In order to quantitatively predict the oblique incidence reflection coefficient from complicated systems like oxides it will be necessary to take into account their strongly anisotropic properties. The mechanical properties of oxide layers depend on porosity, morphology and composition of the layers and these are affected by the type of anodising process used as well as the concentration and temperature of the electrolyte used. It is therefore expected that there will be significant dependence of the mechanical properties on the thickness of the oxide layers. Further work is therefore needed to incorporate an anisotropic layer model into the existing theory, to find appropriate material constants and to validate the model on aluminium/ oxide/epoxy systems.

The preliminary experimental study performed here indicates that it will be very difficult to see the presence of a 3.5 μm thick CAA oxide layer in the adhesive joint, let alone the detection of degraded properties of the layer due to, for example, hydration. However, this conclusion may change if, for example, the anisotropic model suggests other test angles or types of reflection coefficient.

Aluminium bonding
USA specification

Aluminium bonding
European specification

| solvent degrease | | solvent degrease |

| dry: warm air, 30 min | | dry: warm air, 30 min |

| alkaline degrease | | alkaline degrease |

| rinse: 1. tap water, 5 min
2. deionised water, 3 min | | rinse: 1. tap water, 5 min
2. deionised water, 3 min |

| FPL etch (BAC 5514) * | FPL etch (BAC 5514) * | | alkaline etch |

| rinse (as above) | rinse (as above) | | rinse (as above) |

| dry (as above) | PAA (BAC 5555) ** | | chromic acid etch process |

| apply primer | rinse (as above) | | CAA (DEF. STAN. 03-24/1) *** |

| | dry (as above) | | rinse (as above) |

| | apply primer | | dry (as above) |

| | | | apply primer |

Fig. 7.1 General comparison between European and American surface pretreatments
(after Davies 1989).

  * Chromic acid etch to BAC 5514, Boeing Aircraft Specification 5514.
 ** Phosphoric acid anodising to BAC 5555, Boeing Aircraft Specification 5555.
*** Chromic acid anodising to UK Defence Standard 03-24/1.

oxide   130 nm

aluminium   70 nm
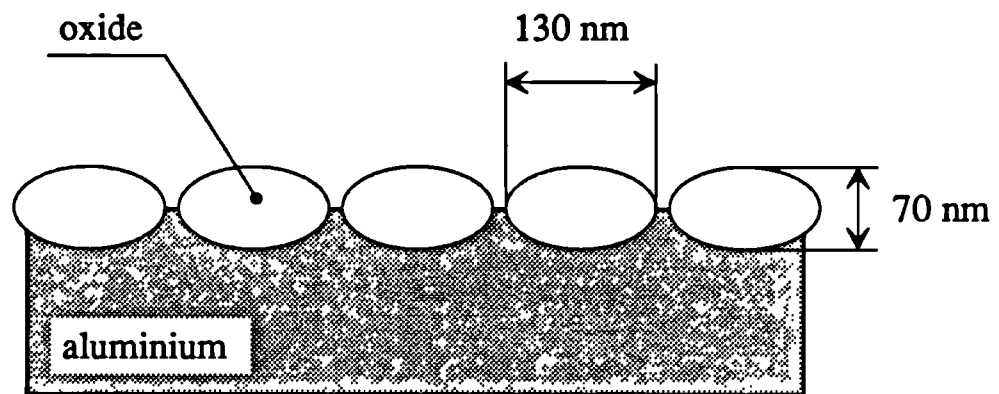
Fig 7.2 Schematic of FPL oxide (after Davies 1989).
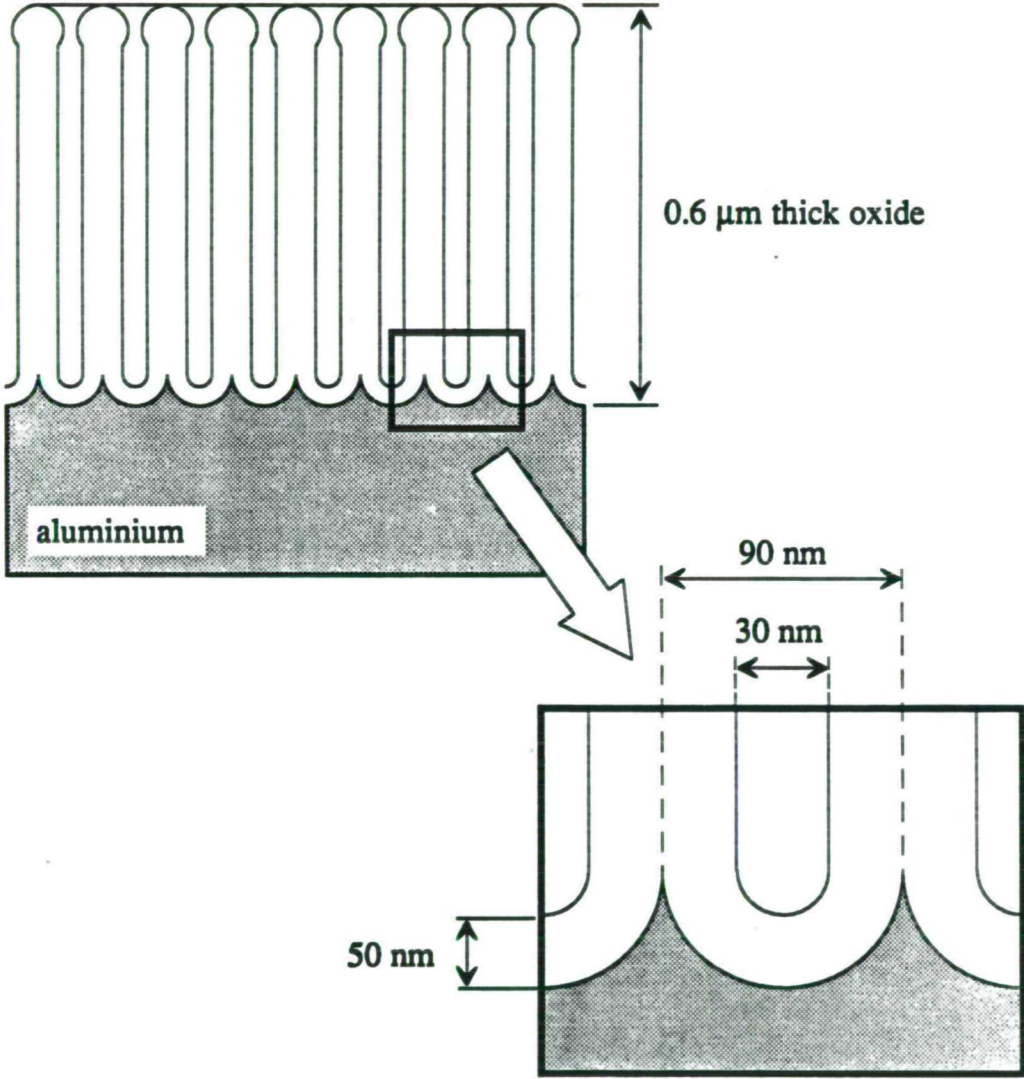
Fig 7.3 Schematic of PAA oxide (after Davies 1989).
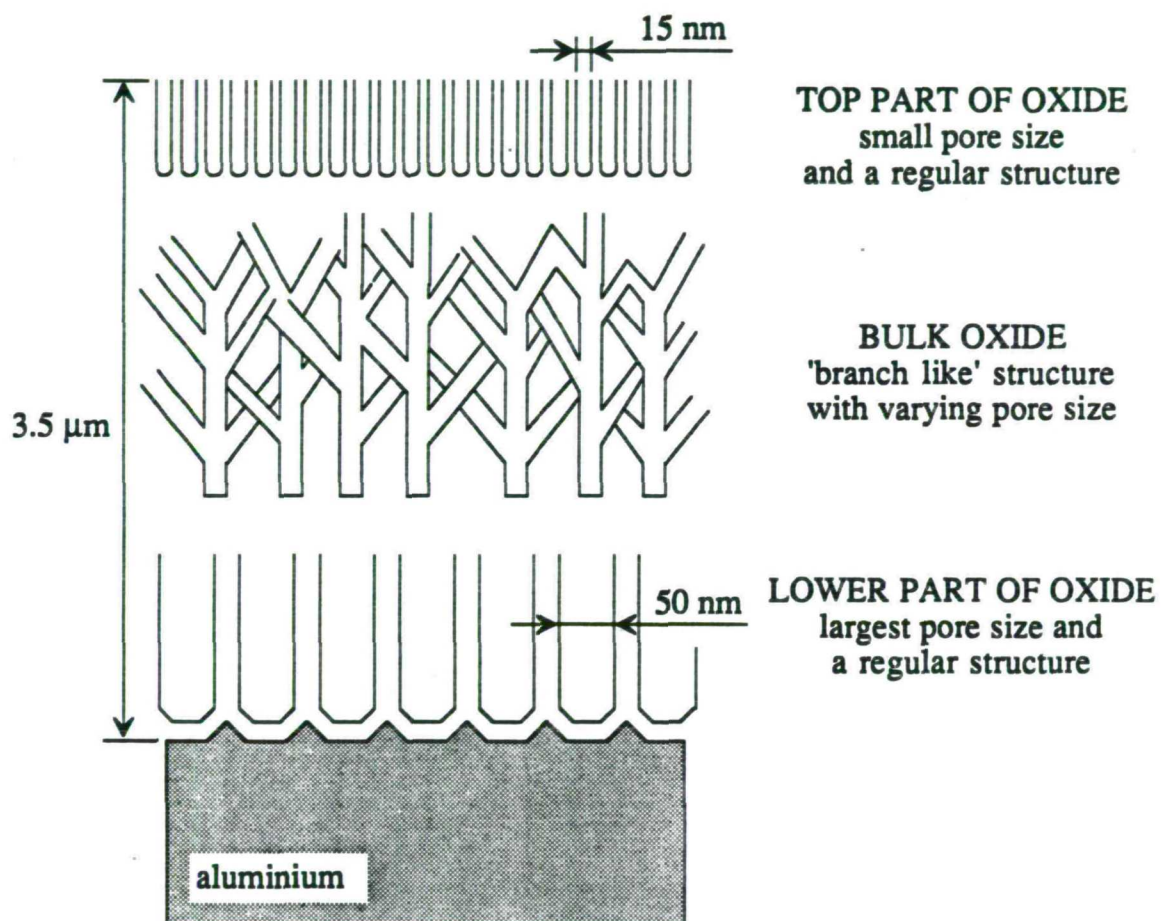
Fig 7.4 Schematic of CAA oxide (after Davies 1989)
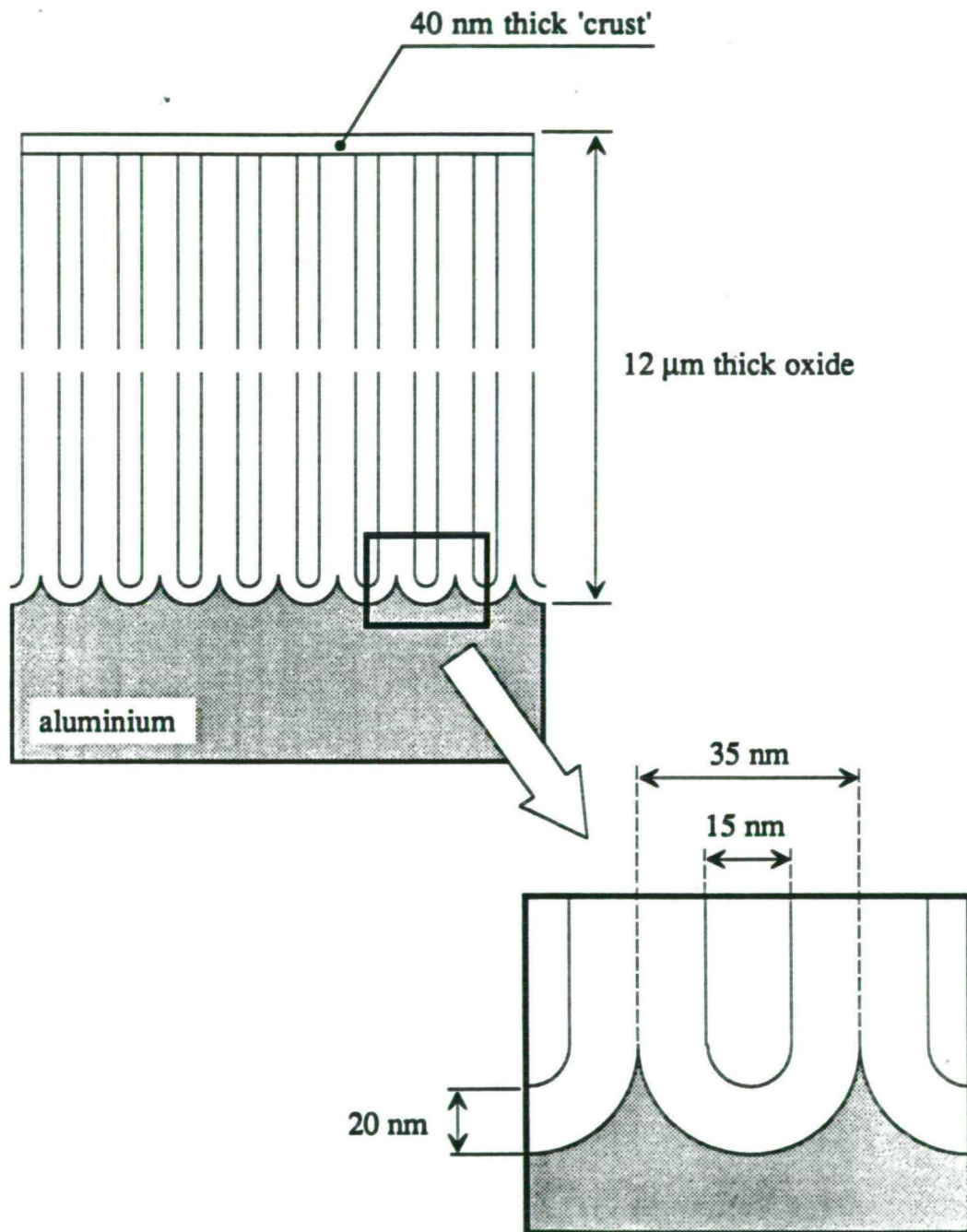
Fig 7.5 Schematic of SAA oxide (after Davies 1989).
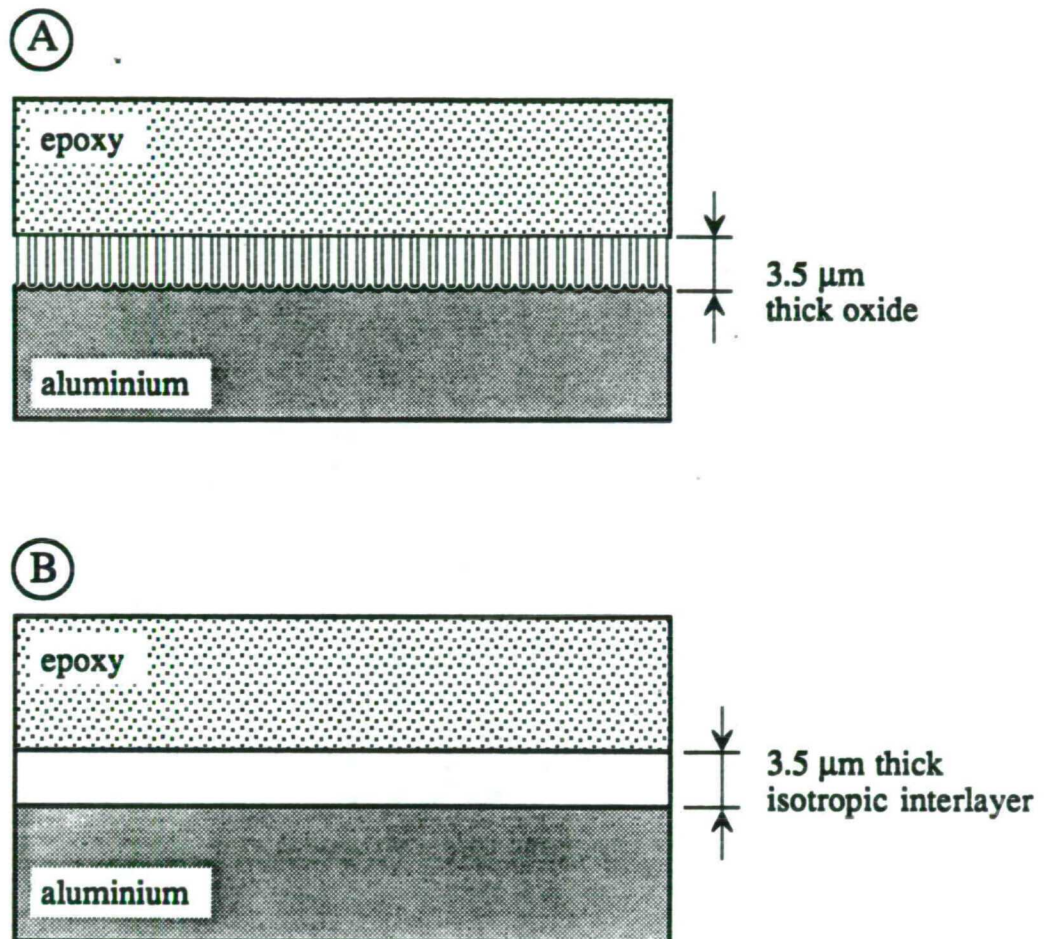
Fig 7.6 Theoretical model used for the reflection coefficient calculations.
(a) Structure of the aluminium/epoxy interface,
(b) Theoretical model of the interface incorporating an isotropic
interlayer between the aluminium and epoxy half-spaces
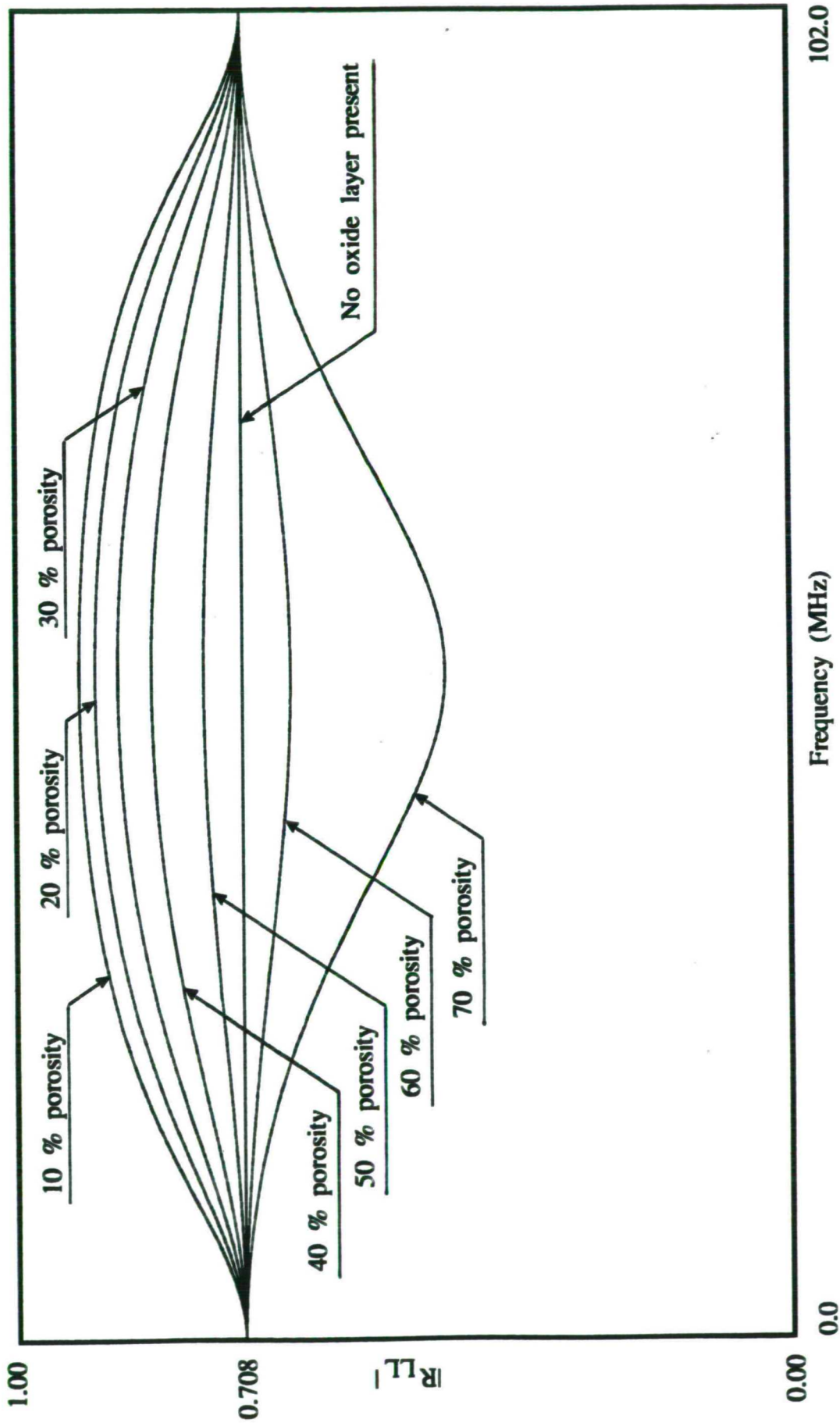
Fig. 7.7   Predicted normal incidence longitudinal reflection coefficients from 50 μm thick oxide layers of different porosities between aluminium and epoxy half-spaces. Material properties are given in tables 7.1 and 7.2.

transmitter/receiver

water

aluminium   4.5 mm

epoxy   7 mm

water

aluminium/epoxy
interface
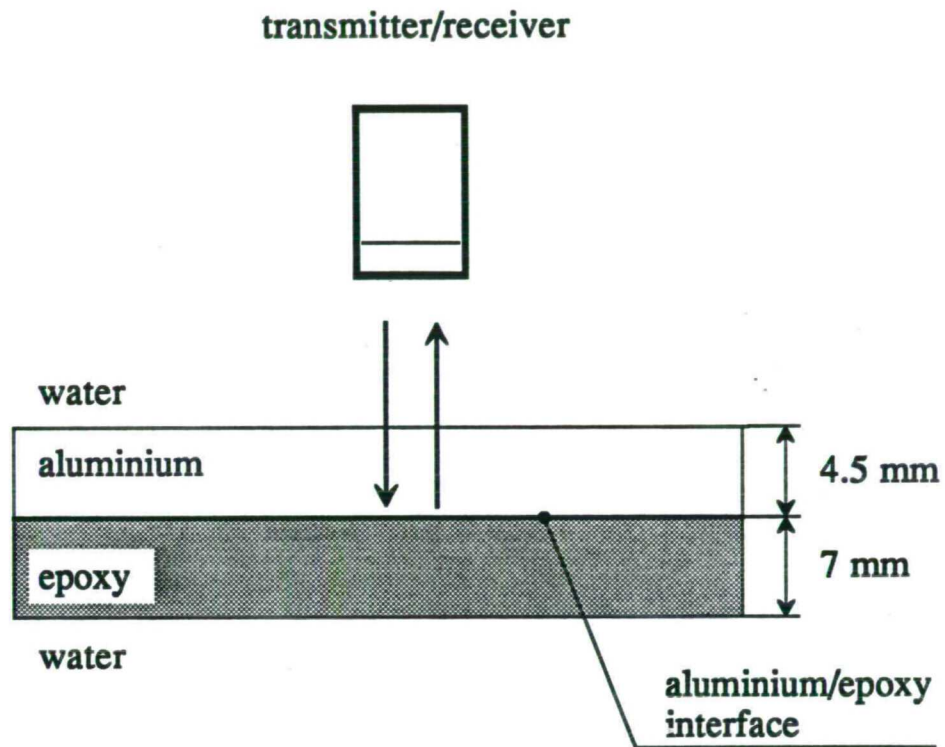
Fig 7.8 Normal incidence longitudinal wave reflection coefficient
         measurements from the aluminium/epoxy boundary.
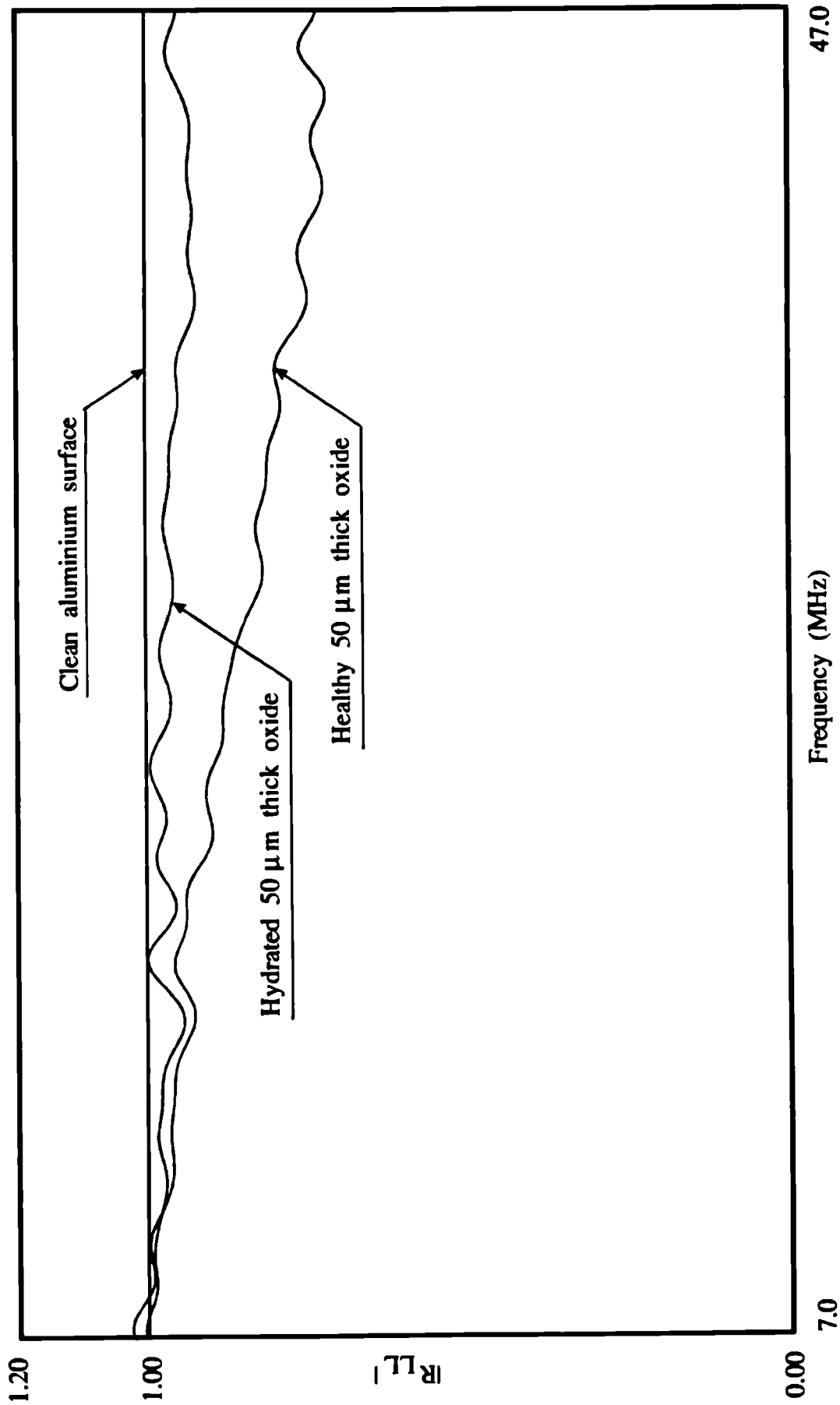
Fig. 7.9   Measured normal incidence longitudinal reflection coefficient from the aluminium/
oxide/epoxy interface normalised wrt the aluminium/epoxy reflection coefficient.
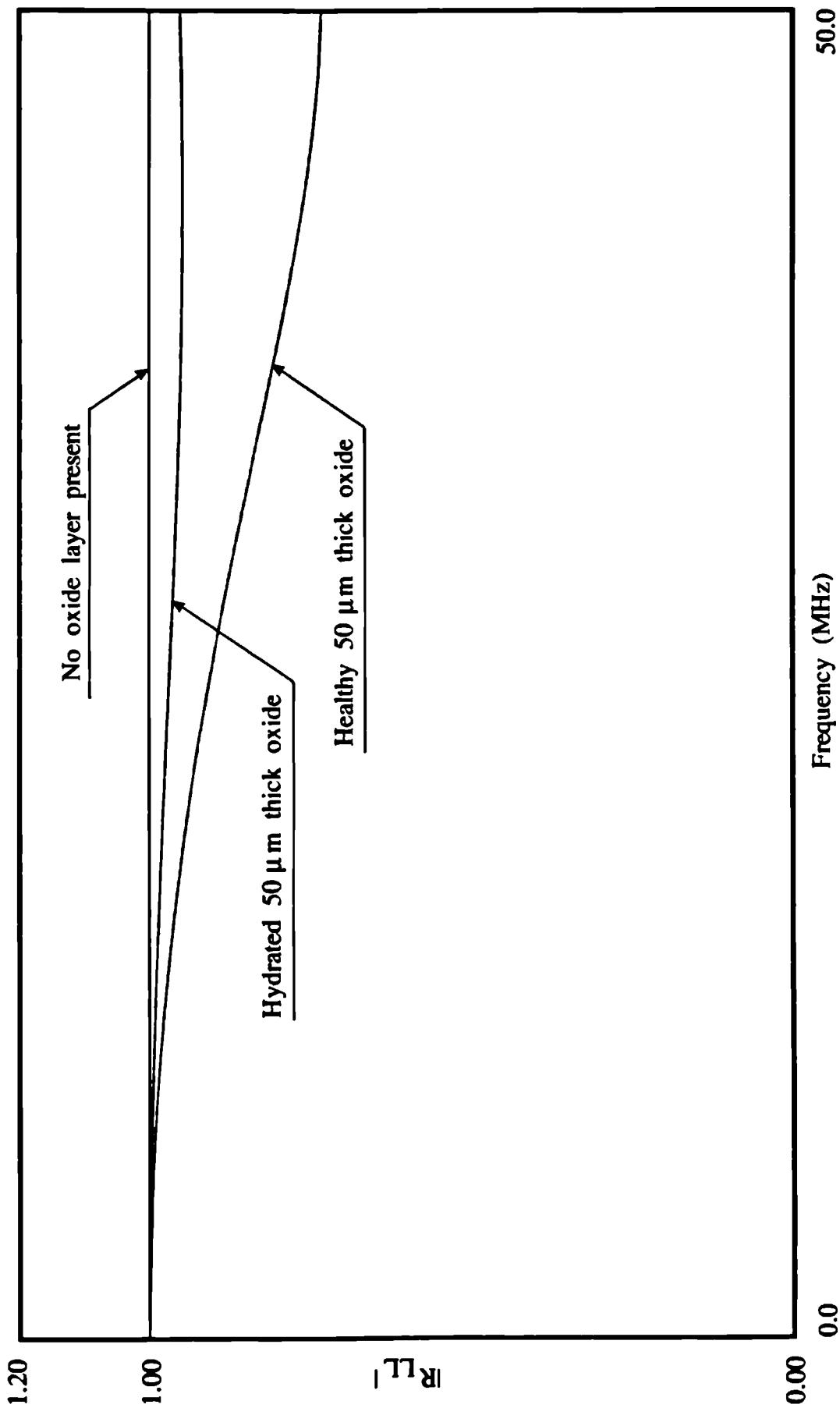
Fig. 7.10   Predicted normal incidence longitudinal reflection coefficient from the aluminium/epoxy interface with 67 % porous, 50 μm thick aluminium oxide layer. Curves normalised wrt the case when there is no oxide layer present.
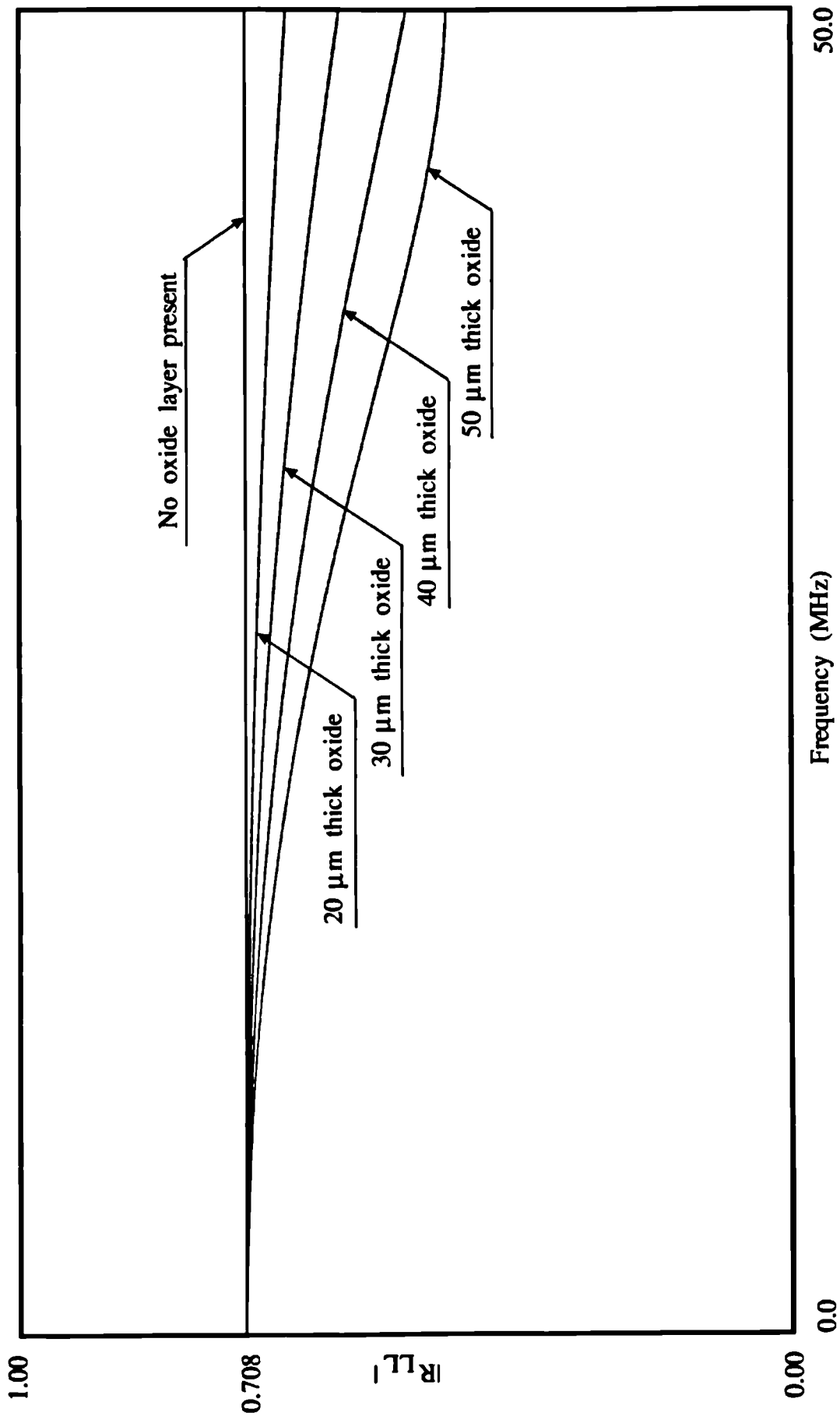
Fig. 7.11 Predicted normal incidence longitudinal reflection coefficients from the aluminium/epoxy interface with 70 % porous aluminium oxide layers of different thicknesses present.
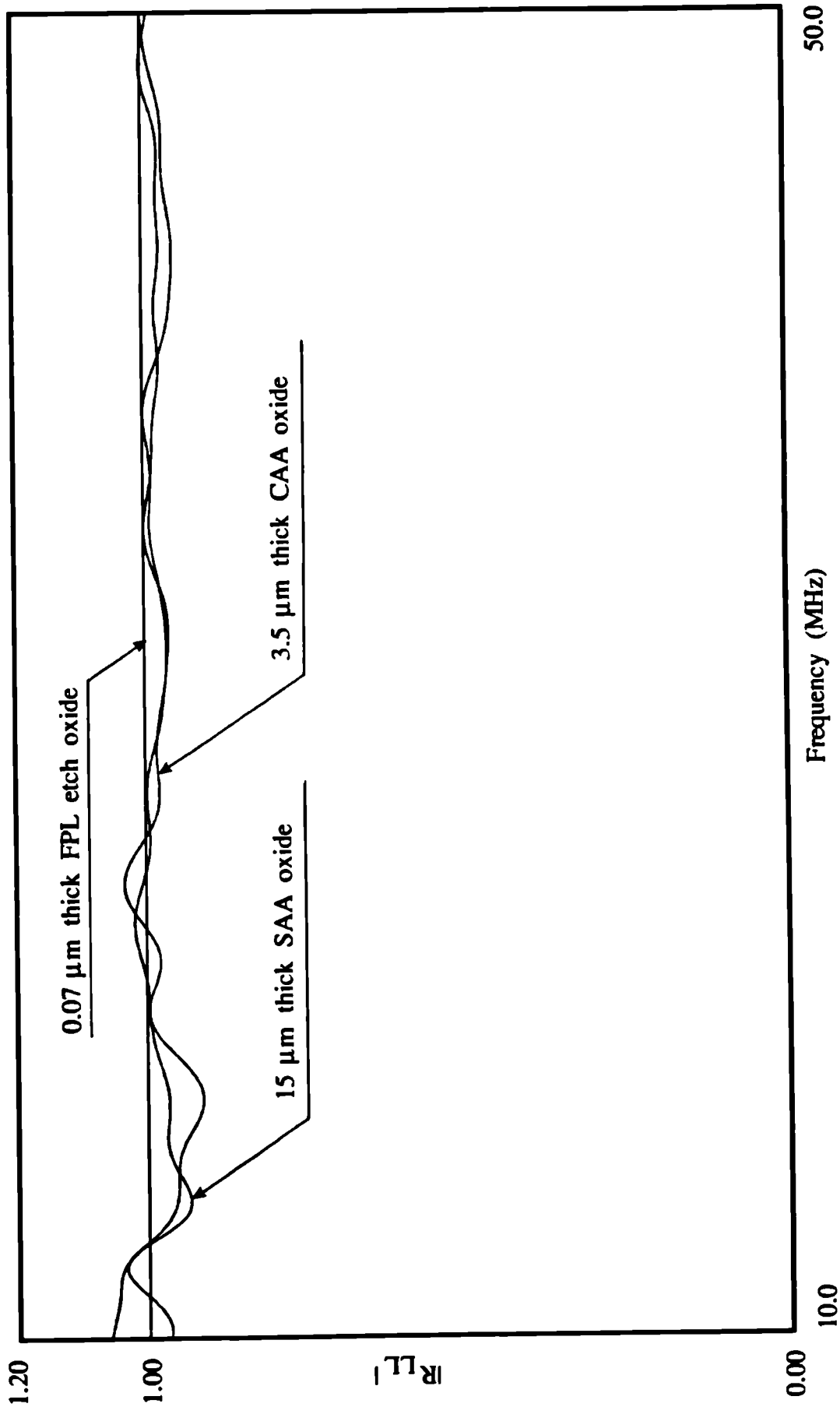
Fig. 7.12   Measured normal incidence longitudinal reflection coefficient from the aluminium/ oxide/epoxy interfaces. Curves normalised wrt the reflection coefficient from the aluminium/epoxy interface with 0.07 μm thick FPL etched oxide.
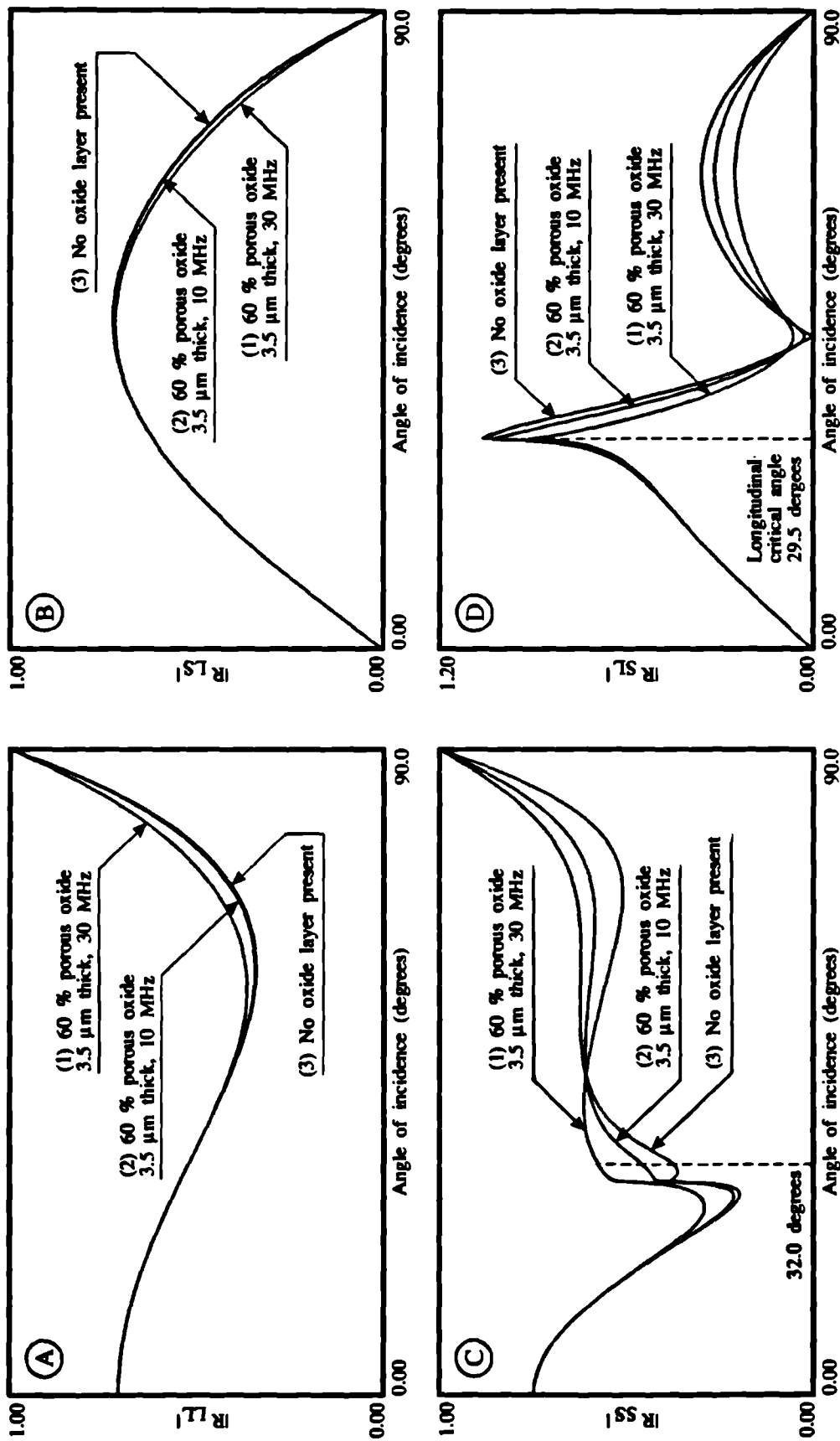
Fig. 7.13 Reflection coefficients from the aluminium/epoxy interfaces with and without the 3.5 μm thick CAA oxide layer. (1) frequency of excitation 30 MHz, (2) frequency of excitation 10 MHz, (3) No oxide layer present.
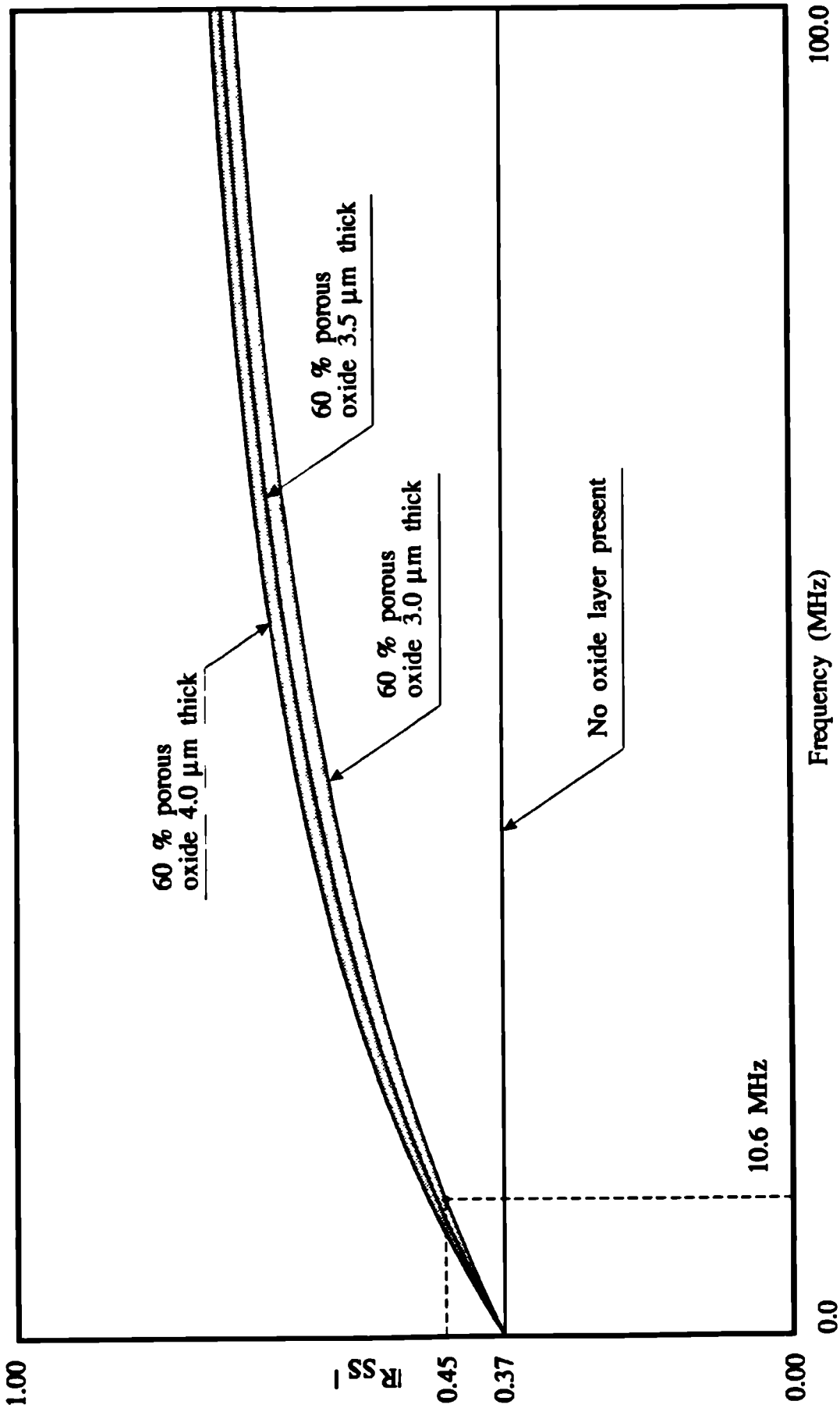
Fig. 7.14 Shear-shear reflection coefficients from the aluminium/oxide/epoxy interfaces at the angle of incidence of 32.0 degrees. Different thicknesses of the oxide layer. Material properties are given in tables 7.1 and 7.2.
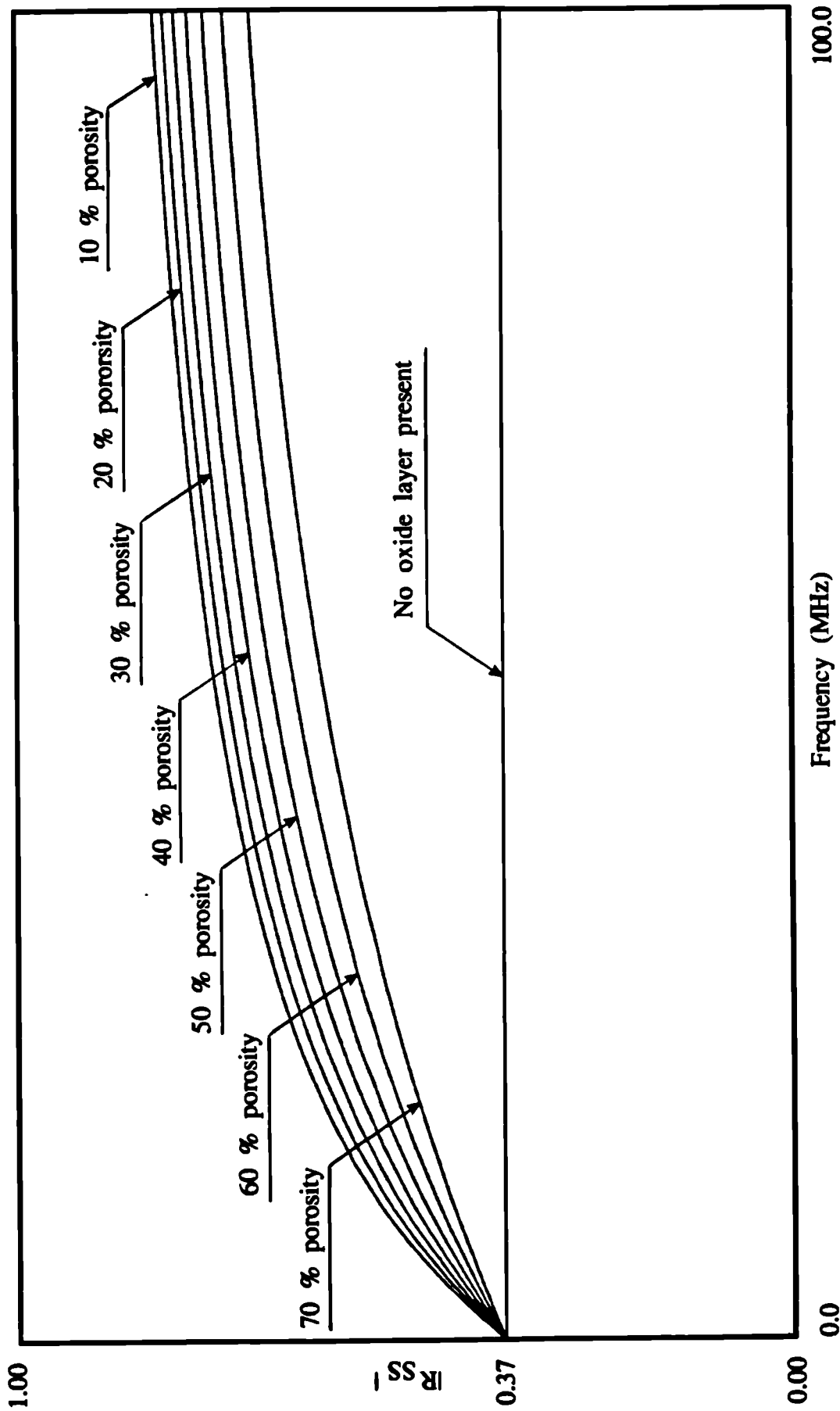
Fig. 7.15   Theoretically calculated shear-shear reflection coefficients at the aluminium/3.5 µm thick oxide/epoxy interfaces. Angle of incidence is 32.0 degrees. Different porosities of the oxide layers. Material properties are given in tables 7.1 and 7.2.
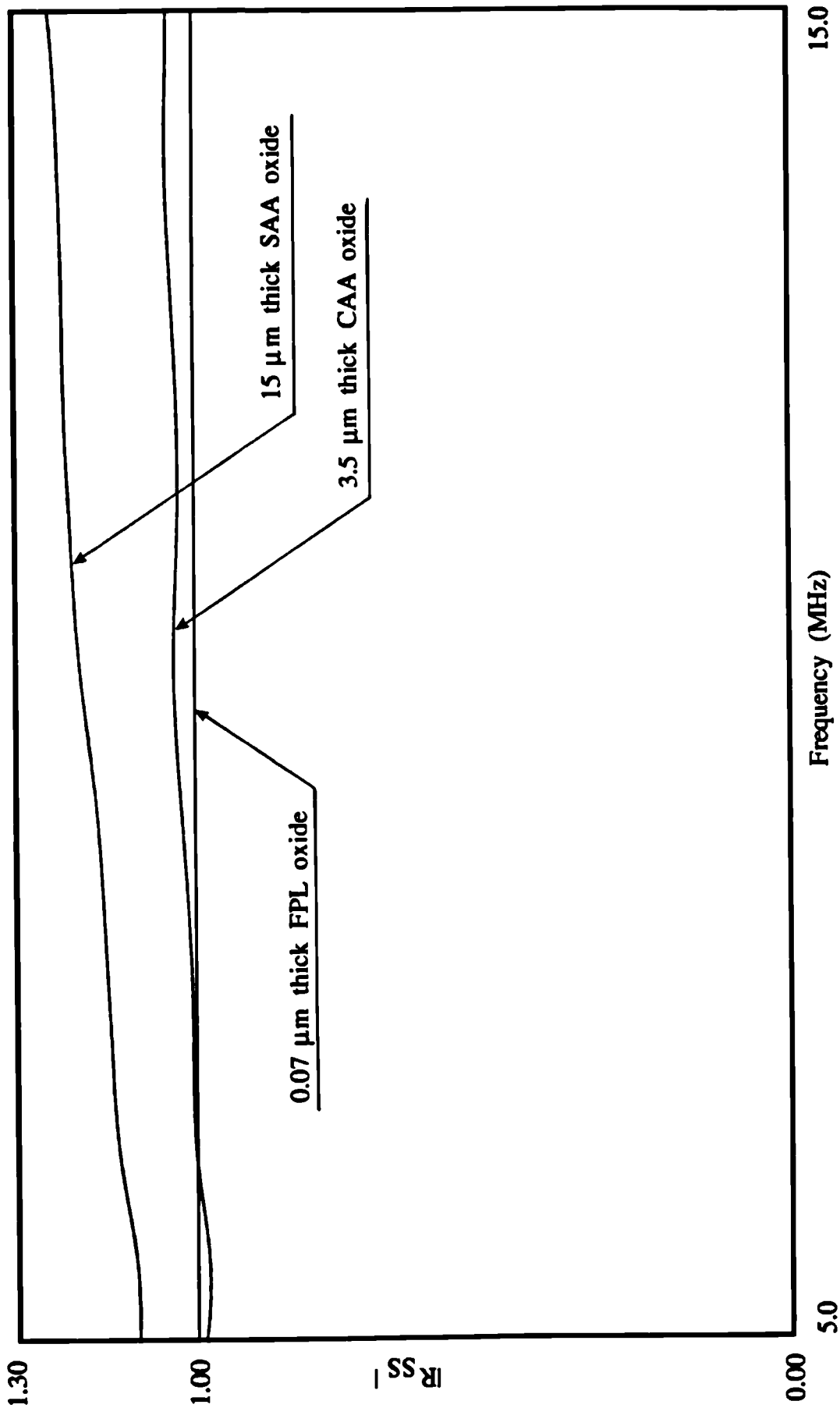
Fig. 7.16 Experimentally determined shear-shear reflection coefficients from 15 μm thick SAA oxide and 3.5 μm thick oxide layers separating aluminium and epoxy resin. Angle of incidence is 32.0 degrees from aluminium. Curves normalised wrt reflection from 0.07 um thick FPL etch oxide layer.
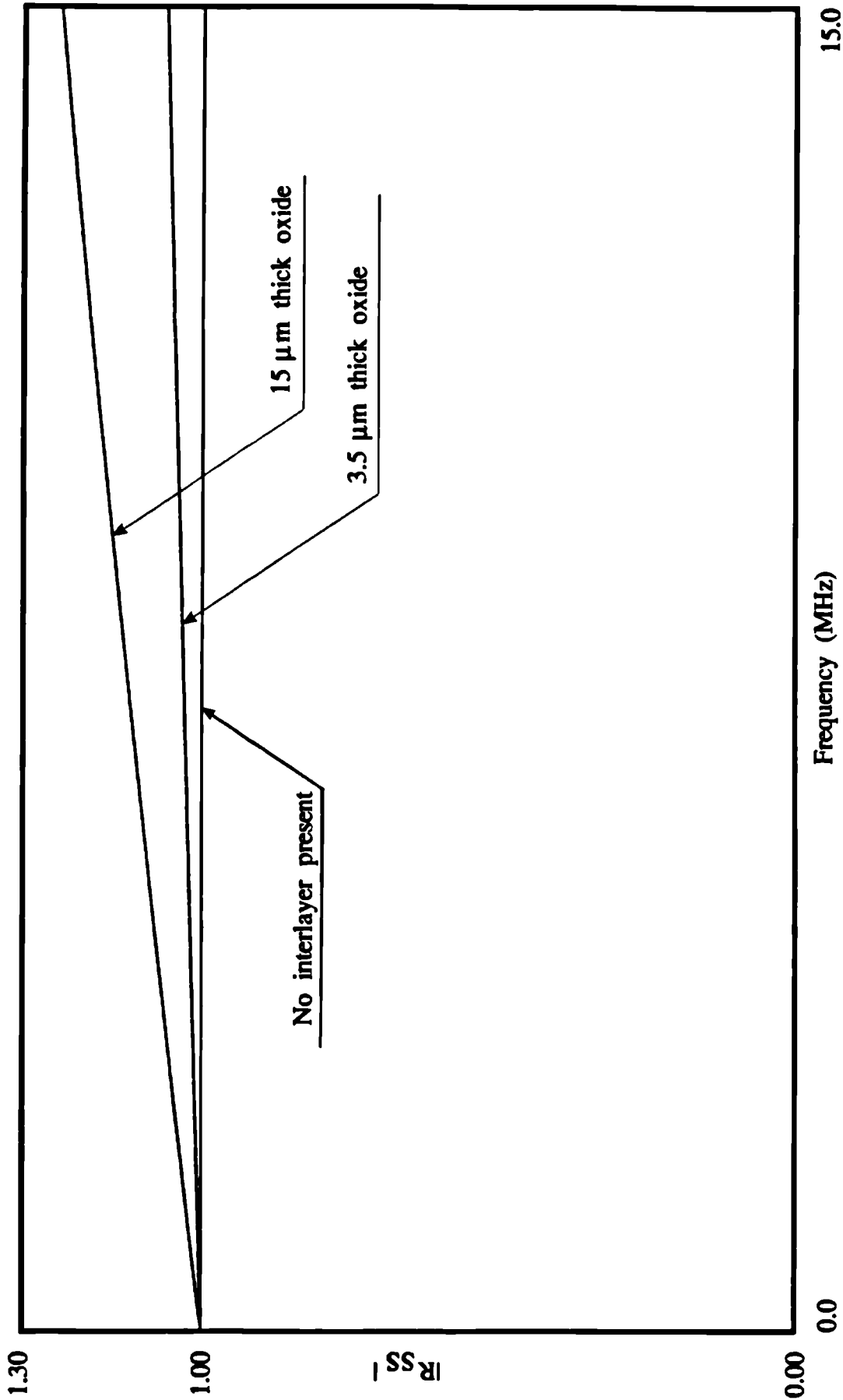
Fig. 7.17 Theoretically calculated shear-shear reflection coefficients from 15 μm thick and
3.5 μm thick oxide layers between aluminium and epoxy. Angle of incidence is
32.0 degrees. Curves normalised wrt reflection coefficient from aluminium/epoxy
interface without an interlayer present. Material properties given in tables 7.1 and 7.5.

CHAPTER 8

Conclusions and suggestions for further work

8.1 General

The application of adhesive joints in industry has been limited by the lack of reliable nondestructive testing procedures for assessing the integrity of joints.

Substantial research effort has been put towards the development of such testing techniques, and methods have been devised to test for disbonds and porosity. The problem of poor cohesion has been addressed recently by many authors and some progress has been noted in this field. Dewen (1992) showed that it is possible to determine the longitudinal bulk wave velocity in a bond line to within 6 % of its nominal value and the bond line thickness to within a micron.

There is no currently available technique for testing the interfacial properties between the adhesive and adherend. The problem here lies in the thickness of the interfacial layer which is usually smaller than 5 microns. This excludes all standard ultrasonic testing techniques.

It was suggested by Pilarski and Rose (1988) that oblique incidence methods might be employed in order to improve the sensitivity of the reflection coefficient technique. The technique uses two ultrasonic transducers inclined at an angle with respect to the tested joint and operating in a pitch-catch mode. This thesis has reported the investigations carried out to assess the viability of this idea for the nondestructive testing of adhesive joints, and in particular, for characterisation of the adherend/adhesive interface.

The oblique incidence technique has been shown to be far more complicated, both from the theoretical and experimental point of view, than the standard normal incidence method. When a specimen is excited at normal incidence, the theory required to explain the observed phenomena is essentially a one-dimensional model involving propagation of a single wave type (shear or longitudinal). However, at an oblique angle of incidence the complication of the model increases substantially. The theory of the response of the structure is now two-dimensional, involving concurrent shear and longitudinal bulk wave propagation, and embracing problems of

surface wave, interface wave, and plate wave excitation and propagation. The theory of wave propagation, transmission and reflection from multilayered viscoelastic plates has been developed and implemented in a package of computer programs for the prediction of the response of multilayered viscoelastic plates to finite transducer excitation.

Also, from the experimental point of view, the oblique incidence method requires substantially more sophisticated experimental procedures than the standard normal incidence technique. It was therefore necessary to design and build a very accurate mechanism (Reflection Coefficient Meter) to carry out the tests.

The conclusions reported below can be divided into those associated with the development of theory and those arising from experimental work.

8.2 Theoretical model for predictions of reflection coefficients from adhesive joints

Numerical instability of Thomson-Haskell formulation

An adhesive joint has been modelled in this project as a multilayered viscoelastic plate and initially the Thomson-Haskell wave coupling algorithm was used for computation of the reflection coefficients from the plates. However, it has been shown in this thesis that in cases when inhomogeneous waves are generated in plates and the frequency of excitation is high, then the wave coupling algorithm becomes unstable. It has been shown in this thesis that the global matrix technique avoids the instability problem, and therefore has been adopted for the purposes of this project.

Infinite model versus finite model

When the reflection coefficients are to be measured from a single interface then the infinite model can be used successfully provided that the angle of incidence is away from the critical angles and the receiver is located in the middle of the area isonified by the reflected beam. However, at angles of incidence close to the critical angles of the interface, the finite transducer theory should be used in order to obtain quantitative agreement with experiments.

Initial tests performed on a single interface water/aluminium system revealed that the infinite plane wave model cannot fully describe the Rayleigh angle phenomenon at which the surface wave in the aluminium was excited. It was therefore required to develop the theoretical model

further to include the finite transducer excitation of the multilayered plate and the finite transducer reception of the ultrasonic field reflected from the tested structure.

When measuring the response from multilayered systems, for example a plate, due to multiple reflections within the plate, the energy is carried along the plate and the receiver misses a significant part of the reflected signal. In such circumstances it is necessary to use the finite transducer model to obtain quantitative agreement between theory and measurements. This has been demonstrated in chapter 5 of this thesis where the measured response from an aluminium plate in water was compared with theoretical predictions using the infinite plane wave theory and the finite transducer theory.

However, if it is required to measure the reflection coefficient from embedded interfaces then the infinite theory can be successfully applied provided that the beam generated by the transmitter does not excite any surface or interface waves on its path from the transmitter down to the monitored interface and back, from the measured interface to the receiver. In other words, the infinite theory is a sufficient approximation of the finite beam theory when there is only a specular reflection and transmission of the beam in the measured system. The second requirement is that the receiver has to be placed in the centre of the area isonified by the reflection of interest coming from the embedded interface. This has been demonstrated using a glass/silicone fluid/glass system where a simple plane wave theory was used to quantitatively predict the reflection coefficient from an embedded interface. The measured reflection coefficient amplitudes have been found to be within 5 % of the predicted values. If non-specular reflection or transmission takes place during the experiment, then the finite beam theory is required to quantitatively predict the measured response.

Modelling of the interfacial layers in aluminium/epoxy joints

In aerospace applications aluminium adherends undergo well defined surface treatment procedures prior to bonding in order to form porous oxide layers on those surfaces. Epoxy resin, therefore, bonds to the porous aluminium oxide rather than to the aluminium adherend itself. In this way the oxide layer becomes an interface layer between the aluminium and epoxy. This interface layer has very complicated morphology, usually a cellular, irregular structure with 'columnar-like' topography and the thickness of the layer is of the order of 1 micron or less depending on the specific surface preparation procedure.

Because of its small thickness, the interface layer in theoretical investigations is frequently approximated by a spring model. It has been shown in this thesis that the spring model can only be used in specific circumstances and, in general, it is prone to produce erroneous results. A

better thin layer approximation, the mass+spring model, has been proposed in this thesis. This has been shown to approximate the behaviour of thin layers at low frequencies very satisfactorily.

It has also been shown in this thesis that the spring model or even the mass+spring model becomes a poor approximation when the layer is excited at oblique incidence. Therefore, a thin isotropic layer has been used in this project to model the behaviour of the interface layer between the adherend and the adhesive.

8.3 Monitoring of the interfacial properties between adherend and adhesive using the reflection coefficient technique

Degree of agreement between the theory and measurement

It has been shown in this thesis that it is possible to achieve agreement between the measurement of the oblique incidence reflection coefficient from embedded interfaces and theoretical predictions to within 5 %. This has been demonstrated in chapter 5 where the normal incidence and the oblique incidence reflection coefficients from a thin silicone layer between two glass substrates were measured and compared with the infinite plane wave theory.

Monitoring of interfacial properties in glass/epoxy joints

It has been demonstrated in this thesis that it is possible to detect the presence of a thin layer of mould release (Frekote 44) between glass and epoxy using the normal incidence shear reflection coefficient technique, while it was impossible to detect the Frekote layer using the normal incidence longitudinal reflection coefficient method.

It has also been demonstrated here that the oblique incidence method can be very sensitive to the interfacial properties at the glass/epoxy boundary. It has been shown both theoretically and experimentally that the sensitivity of the method is greatly enhanced at the angles of incidence where the reflection coefficients from a good interface are zero.

Monitoring of interfacial properties in aluminium/epoxy joints

It has been shown that the normal incidence longitudinal reflection coefficient operating in the frequency range up to 100 MHz cannot be used successfully to detect the presence of oxide layers whose thicknesses are of the order of 1 micron in aluminium/epoxy joints. In order to

secure positive detection of such thin oxide layers, the frequency of excitation would have to be as high as 1 GHz. This requirement cannot be satisfied in practical NDT applications.

Theoretical investigations have shown that the oblique incidence reflection coefficients from the aluminium/ epoxy interfaces have no zeroes over the entire possible range of angles of incidence. This finding makes the technique devised to monitor the glass/epoxy interface inapplicable to the case of the aluminium/epoxy interface. Therefore the sensitivity of the reflection coefficient method to interfacial changes across the aluminium/epoxy boundary is expected to be significantly lower than in the case of the glass/epoxy system.

The experimental and theoretical investigations showed that the theoretical predictions of the oblique incidence reflection coefficients from aluminium/oxide layer/epoxy interfaces are not in good quantitative agreement with the measurements. The most probable reason for this discrepancy is the oversimplification of the mechanical behaviour of the oxide layer. The model which has been used for the predictions assumed that the oxide layer can be approximated to a thin isotropic layer. However, the results obtained suggest that an anisotropic model should be used in order to achieve quantitative agreement between theory and experiments.

8.4 Detectability of presence of oxide layers in aluminium/epoxy joints using reflection coefficient technique

Theoretical and experimental work has been carried out to find the optimal arrangement of the probes, frequency range and type of reflection in order to achieve maximum sensitivity to changes in the adherend/adhesive interfaces. It has been found that the oblique incidence techniques can offer a substantial increase in sensitivity to interfacial properties over the current standard inspection techniques, but the results obtained indicate that the improvement is unlikely to be sufficient for the technique to be used as a new reliable nondestructive procedure. There is a small chance that the development of an anisotropic layer model may indicate a test configuration where improved sensitivity may be obtained.

8.5 Suggestions for future work

It has been shown in this thesis that the isotropic model of the oxide layer is too simplistic to be used for quantitative comparisons with experiments at oblique angles of incidence. Further refinement of the theory is therefore recommended, which will extend the existing isotropic model of the layer to incorporate the anisotropic properties of the oxide.

The theoretical and experimental results presented in this thesis suggest that the detectability of oxide layers between the aluminium and epoxy is very dependent on the level of porosity in the oxide layer, and if the porosity is between 50 % and 60 % then the detection of the oxide at normal incidence is impossible regardless of the thickness of the layer. It is therefore suggested that further work can be carried out to quantitatively relate the reflection coefficient to the oxide porosity, the level of porosity being obtained independently by optical measurements on sections takes through the interface.

References

Abo-Zena, A. (1979), Dispersion function computations for unlimited frequency values, *Geophys. J. R. astr. Soc.*, Vol. 58, pp 91-105

Achenbach, J. D. and Kitahara, M. (1986), Reflection and transmission of an obliquely incident wave by an array of spherical cavities, *J. Acoust. Soc. Am.*, Vol. 80, No 4, pp 1209-1214

Adams, R. D. and Wake, C. W. (1984), *Structural Adhesive Joints in Engineering*, (Elsevier Applied Science Publishers, London and New York)

Adams, R. D. and Cawley, P. (1989), The Sensitivity of the Coin-Tap method of Non-Destructive Testing, *Materials Evaluation*, Vol. 47

Alers, G. A. (1976), Adhesive Interfaces and Failure Related Phenomena - Overview, *Proceedings of The ARPA/AFML Review of Quantitative NDE*, (Air Force Materials Laboratory, Technical Report AFML-TR-75-212)

Alers, G. A. and Thompson, R. B. (1976), Application of Trapped Modes in Layered Media to the Testing of Adhesive Bonds, *Ultrasonics Symposium Proceedings*, IEEE Cat. #76 CH1120-5SU, pp 138-142

Allen, K. W. (ed) (1989), *Adhesion*, (Applied Science Publishers, London and New York)

Angel, Y. C. and Achenbach, J. D. (1985), Reflection and transmission of elastic waves by a periodic array of cracks, *J. Appl. Mech.*, Vol. 53

Arakawa, T. A. (1983), A study on the transmission and reflection of an ultrasonic beam at machined surfaces pressed against each other, *Mat. Eval.*, Vol. 41

Arrowsmith, D. J. and Moth, D. A. (1986), Chromic acid anodizing of aluminium, *Trans. Inst. Metal Finishing*, Vol. 64, part 3, pp 91-93

Arrowsmith, D. J., Clifford, A. W. and Moth, D. A. (1985), Phosphoric acid anodizing of aluminium, *Trans. Inst. Metal Finishing*, Vol. 63, part 2, pp 41-46

Bar-Cohen, Y. (1986), NDE of fiber-reinforced composite materials - a review, *Mat. Eval.*, Vol. 44, pp 446-454

Becker, F. L. and Richardson, R. L. (1970), Ultrasonic Critical Angle Reflectivity, *Research Techniques in NDT*, (Academic Press, London & New York)

Benson, C. G. and Kiyohara O. (1972), Tabulation of some integral functions describing diffraction effects in the ultrasonic field of a circular piston source, *J. Acoust. Soc. Am.*, Vol. 55, No. 1, pp 184-185

Bertoni, H. L. and Tamir, T. (1973), Unified Theory of Rayleigh-Angle Phenomena for Acoustic Beams at Liquid-Solid Interfaces, *Appl. Phys.*, Vol. 2

Bracewell, R. (1965), *The Fourier Transform and Its Applications*, (McGraw-Hill)

Breazeale, M. A. and Adler L. (1974), Reflection of a Gaussian ultrasonic beam from a liquid-solid interface, *J. Accoust. Soc. Am.*, Vol. 56, No 3, pp 866-872

Breazeale, M. A., Adler L. and Scott, G. W. (1977), Interaction of ultrasonic waves incident at the Rayleigh angle onto a liquid-solid interface, *J. Appl. Phys.*, Vol. 48, No 2

Brekhovskikh, L. M. (1980), *Waves in Layered Media*, (Academic Press, New York)

Cawley, P. (1987), The Sensitivity of the Mechanical Impedance Method of Non-Destructive Testing, *NDT International*, Vol. 20, pp 209-215

Cawley, P. (1990), Low Frequency NDT Techniques for the Detection of Disbonds and Delaminations, *British Journal of NDT*, Vol. 32, No 9, pp 454-461

Cawley, P. (1992), The Non-Destructive Testing of Adhesive Bonds, *NASA Monograph on Flight-Vehicle Materials, Structures and Dynamics Technologies - Assessment and Future Directions*, (in press)

Cawley, P. and Adams, R. D. (1988), The Mechanics of the Coin-Tap Method of Non-Destructive Testing, *J. Sound and Vibration,* Vol. 122

Cawley, P. and Hodson, M. J. (1988), The Non-Destructive Testing of Adhesive Joints Using Ultrasonic Spectroscopy, *Review of Progress in Quantitative Nondestructive Evaluation,* Vol. 8, pp 1377-1384

Dale, J. and Rose, J. L. (1990), An ultrasonic frequency dependent interface layer model for bond evaluation, submitted to *Int. Journal of Adhesives and Adhesion*

Davies, R. J. (1989), The Durability of an Adhesively Bonded Aluminium Alloy, Ph.D. Thesis, Mech. Eng. Dept., Imperial College, London

Deschamps, M. (1990), Réflexion-réfraction de l'onde plane hétérogène: répatrition de l'énergie, *J. Acoustique,* Vol. 3, pp 251-261

Dewen, P. N. (1992), The Nondestructive Evaluation of the Cohesive Properties of Adhesively Bonded Joints, Ph.D. Thesis, Mech. Eng. Dept., Imperial College, London

Dunkin, J. W. (1965), Computation of Modal Solutions in Layered Elastic Media at High Frequencies, *Bull. Am. Seismological Soc.,* Vol. 55, No 2

Fahy, F. (1985), *Sound and Structural Vibration Radiation, Transmission and Response,* (Academic Press, London)

Fiorito, R., Madigosky W. and Überall, H. (1985), Theory of ultrasonic resonances in a viscoelastic layer, *J. Acoust. Soc. Am.,* Vol. 77, pp 489-498

K. F. Graff. (1975), *Wave motion in elastic solids,* (Clarendon Press, Oxford)

Guy, P. (1992), Contribution à l'étude de la propagation des ondes de Lamb dans les plaques et les milieux plans stratifiés, Ph.D. Thesis, Universite Paris, Paris

Guyott C. C. H. and Cawley, P. (1988), The measurement of through thickness plate vibration using a pulsed ultrasonic transducer, *J. Acoust. Soc. Am.,* Vol. 83

Guyott C. C. H., Cawley, P. and Adams, R. D. (1986), The Non-Dectructive Testing of Adhesively Bonded Structure: A Review, *Journal of Adhesion*, Vol. 20, No 2, pp 129-159

Guyott C. C. H., Cawley, P. and Adams, R. D. (1987), Use of the Fokker Bond Tester on joints with varying adhesive thickness, *Proc. I. Mech. E.*, Vol. 201, Part B, pp 41-49

Haines, N. F. (1980), The Theory of Sound Transmission and Reflection at Contacting Surfaces, (Central Electricity Generating Board, RD/B/N4744)

Haskell, N. A. (1953), The dispersion of surface waves on multilayered media, *Bull. Am. Seismological Soc.*, Vol. 43, pp 17-34

Hung, Y. Y. (1989), Shearography: a novel and practical approach for nondestructive evaluation, *J. Nondestructive Evaluation.*, Vol. 8

Jeffrey, K., Pollock, E., Hayward, D., Affrossmann, S. and Pethrick, R. A. (1988), Nondestructive analysis of adhesive joint structures - dielectric measurements, *Proc. Adhesives, Sealants and Encapsulants (ASE 88)*, Brighton, UK, ISBN: 1 870208 110

Kinloch, A. J. (ed) (1983), *Durability of structural adhesives*, (Applied Science Publishers, London and New York)

Kinloch, A. J. (1987), *Adhesion and Adhesives*, (Chapman and Hall, London and New York)

Knopoff, L. (1964), A matrix method for elastic wave problems, *Bull. Am. Seismological Soc.*, Vol. 54, pp 431-438

Krolikowski, J., Szczepek, J. and Witczak, Z. (1989), Ultrasonic investigation of contact between solids under high hydrostatic pressure, *Ultrasonics*, Vol. 27

Kühn, G. J. and Lutsch, A. (1961), Elastic Wave Mode Conversion at a Solid-Solid Boundary with Transverse Slip, *J. Acoust. Soc. Am.*, Vol. 33, No. 7, pp 949-952

Leomy, F. de Billy, M. and Quentin, G. (1989), Dispersive ultrasonic waves in adhesive bonds, *Review of Progress in Quantitative Nondestructive Evaluation*, Vol. 8, pp 1409-1416

Light, G. M. and Kwun, H. (1989), Nondestructive Evaluation of Adhesive Bond Quality, State-of-the-Art Review, (Nondestructive Testing Information Analysis Center, NTIAC-89-1)

Lokberg, O. J. and Malmo, J. T. (1988), Detection of defects in composite materials by TV holography, *NDT Iternational*, Vol. 21, pp 223-228

Love, A. E. H. (1944), *A Treatise on the Mathematical Theory of Elasticity*, (Dover, New York)

Malvern, L. E. (1969), *Introduction to the Mechanics of a Continuous Medium*, (Prentice-Hall, Englewood Cliffs, New York)

Matiss, I. and Shtrauss, V. D. (1988), Multi-parameter dielectric relaxation spectrometry for quality control of composites, *NDT Iternational*, Vol. 21, pp 266-276

Morse, P. M. and Ingard, K. U. (1968), *Theoretical Acoustics*, (McCraw-Hill, New York)

Murty, G. S. and Kumar, V. (1991), Elastic Wave Propagation with Kinematic Discontinuity Along a Non-Ideal Interface Between Two Isotropic Elastic Half-Spaces, *J. Nondestructive Evaluation*, Vol. 10, No 2

Nagy, P. B. (1990), Ultrasonic Detection of Kissing Bonds at Adhesive Interfaces, submitted to *Int. Journal of Adhesives and Adhesion*

Nagy, P. B. and Adler, L. (1989 (a)), Adhesive joint characterisation by leaky guided interface waves, *Review of Progress in Quantitative Nondestructive Evaluation*, Vol. 8, pp 1417-1424

Nagy, P. B. and Adler, L. (1989 (b)), Nondestructive evaluation of adhesve joints by guided waves, *J. Appl. Phys.*, Vol. 66, No. 10, pp 4658-4663

Nagy, P. B. and Adler, L. (1991), Interface characterization by true guided modes, *Review of Progress in Quantitative Nondestructive Evaluation*, Vol. 10, pp 1295-1302

Nagy, P. B., Rypien, D. V. and Adler, L. (1990), Dispersive Properties of Leaky Interface Waves in Adhesive Layers, *Review of Progress in Quantitative Nondestructive Evaluation*, Vol. 9, pp 1247-1254

Nayfeh, A. H. and Chimenti D. E. (1984), Reflection of finite acoustic beams from loaded and stiffened half-spaces, *J. Accoust. Soc. Am.*, Vol. 75, No 5, pp 1360-1368

Neubauer, W. G. (1973), Ultrasonic reflection of a bounded beam at Rayleigh and critical angles for a plane liquid-solid interface, *J. Appl. Phys.*, Vol. 44, No 1

Ngoc, Tran D. K. and Mayer W. G. (1979), Ultrasonic nonspecular reflectivity near longitudinal critical angle, *J. Appl. Phys.*, Vol. 50, No 12

Ngoc, Tran D. K. and Mayer W. G. (1980), Numerical integration method for reflected beam profiles near Rayleigh angle, *J. Accoust. Soc. Am.*, Vol. 67, No 4

Papadakis, E. P. (1972), Ultrasonic Diffraction Loss and Phase Change for Broad-Band Pulses, *J. Acoust. Soc. Am.*, Vol. 52, No. 3, pp 847-849

Pilarski, A. (1983), The coefficient of reflection of ultrasonic waves from an adhesive bond interface, *Archives of Acoustic*, Vol. 8, No. 1, pp 41-54

Pilarski, A. (1985), Ultrasonic Evaluation of the Adhesion Degree in Layered Joints, *Mat. Eval.*, Vol. 43, pp 765-770

Pilarski, A. and Rose, J. L. (1988), Ultrasonic oblique incidence for improved sensitivity in interface weakness determination, *NDT International*, Vol. 21, No 4, pp 241-246

Pilarski, A., Rose, J. L. and Balasubramaniam, K. (1990), The angular and frequency characteristics of reflectivity from a solid layer embedded between two solids with imperfect boundary conditions, *J. Acoust. Soc. Am.*, Vol. 87, No. 2, pp 532-542

Pilarski, A., Rose, J. L. and Dale, J. (1987), An ultrasonic oblique incidence technique for adhesive bond quality evaluation, 4th European NDT Conference, London

Randall, R. B. (1987), *Frequency analysis*, (Brüel & Kjœr, Denmark)

Reynolds, W N. (1988), Inspection of laminates and adhesive bonds by pulse-video thermography, *NDT International,* Vol. 21, pp 229-232

Reynolds, W N. (1984), Video-compatible thermography, *Brit. J. NDT,* Vol. 26

Rokhlin, S. I. (1982), Adhesive joint characteristics by ultrasonic surface and interface waves, *Organic Coating and Applied Polymer Science Proceedings,* Vol. 47, American Chemical Society, Kansas City, pp 488-492

Rokhlin, S. I., Hefets, M. and Rosen, M. (1981), An ultrasonic interface-wave method for predicting the strength of adhesive bonds, *J. Appl. Phys.,* Vol. 52, No 4, pp 2847-2851

Rokhlin, S. I. and Marom, D. (1986), Study of adhesive bonds using low-frequency obliquely incident ultrasonic waves, *J. Acoust. Soc. Am.,* Vol. 80, No. 2, pp 585-590

Rokhlin, S. I., Wang, W. and Wang, Y. J. (1990), Ultrasonic evaluation of interphasial properties in adhesive joints, *Review of Progress in Quantitative Nondestructive Evaluation,* Vol. 9, pp 1231-1238

Rose, J. L., Dale, J. and Ngoc, T. D. K. (1990 (a))), Ultrasonic oblique incidence experiments for interface weakness, *British J. NDT,* Vol. 32, No 9

Rose, J. L., Dale, J., Ngoc, T. D. K. and Balasubramaniam, K. (1990 (b)), Evaluation of various interfacial models for ultrasonic inspection of weak bonds, *Review of Progress in Quantitative Nondestructive Evaluation,* Vol. 9, pp 1309-1316

Sachse, W. and Pao, Y.- H. (1978), On the determination of phase and group velocities of dispersive waves in solids, *J. Appl. Phys.,* Vol. 49, No 8, pp 4320-4327

Schliekelmann, R. J. (1975), Non-destructive testing of bonded joints, recent developments in testing systems, *Non-destructive Testing,* Vol. 8

Schoenberg, M. (1980), Elasic wave behaviour across linear slip interfaces, *J. Acoust. Soc. Am.,* Vol. 68, No. 5, pp 1516-1521

Sotiropoulos, D. A. and Achenbach, J. D. (1988), Ultrasonic Reflection by a Planar Distribution of Cracks, *J. Nondestructive Evaluation*, Vol. 7, Nos 3/4, pp 123-129

Stone, D. E. W. (1986), Non-destructive Methods of Characterising the Strength of Adhesive-Bonded Joints - A Review, (Royal Aircraft Establishment, Technical Report 86058)

Stone, D. E. W. and Clarke, B. (1987), Non-destructive evaluation of composite structures - an overview, Proc ICCM VI/ECCM II, F. L. Matthews, N. C. R. Buskell, J. M. Hodgkinson and J. Morton (eds), (Elsevier Applied Science)

Sullivan, J. P. O. and Wood, G. C. (1970), The morphology and mechanism of formation of porous anodic films on aluminium, *Proc. Roy. Soc. of London*, Series A, Vol. 317

Tattersall, D. E. W. (1973), The ultrasonic pulse-echo as applied to adhesion testing, *J. Phys. D: Appl. Phys.*, Vol. 6, pp 819-832

Thompson, B. and Thompson, B. (1988), Past Experience in the Development of Tests for Adhesive Bond Strength, *Transcripts of presentations at Workshop on NDE of Adhesive Bond Strength*, 13-14 April 1988, Orlando, organised by NTIAC, San Antonio, Texas

Thomson, W. T. (1950), Transmision of Elastic Waves through a Stratified Solid Medium, *J. Appl. Phys.*, Vol. 21, pp 89-93

Timoshenko, S. P. and Goodier, J. N. (1970), *Theory of Elasticity*, (McGraw-Hill Kogakusha Ltd, Tokyo)

Wang, T. T., Ryan, F. W. and Schonhorn, H. J. (1971), *J. Appl. Polymer Sci.*, Vol. 16, p 1901

Wang, W. and Rokhlin, S. I. (1990), Ultrasonic characterisation of a thin layer of anodised porous aluminium oxide, *Review of Progress in Quantitative Nondestructive Evaluation*, Vol. 9, pp 1629-1636

Xu, Y., Thompson, G. E. and Wood, G. C. (1985), Mechanism of anodic film growth on aluminium, *Trans. Inst. Metal Finishing*, Vol. 63, part 3 and 4, pp 98-103

Appendix A

Amplitude spectrum method for the measurement of phase velocity

This paper was based on work carried out by T. P. Pialucha, the contribution of Dr P. Cawley being that normally associated with the supervision of PhD students. Dr C. C. H. Guyott was involved in early work on the topic. The presentation in the paper was developed entirely by T. P. Pialucha.

Amplitude spectrum method for the measurement of phase velocity

T. Pialucha, C.C.H. Guyott and P. Cawley

Department of Mechanical Engineering, Imperial College, London SW7 2BX, UK

An amplitude spectrum technique for the measurement of the phase velocities of waves in media, which can be dispersive and attenuating is presented. In this method the variation of phase velocity with frequency is calculated from the longitudinal resonant frequencies, the corresponding mode numbers and the distance between the boundaries of the tested material. The amplitude spectrum method has been found to be superior to the existing phase spectrum technique when testing thin specimens, where the different reflections from the two boundaries cannot be separated in the time domain. Comparison between the phase spectrum technique and the amplitude spectrum method has been carried out on a 3.2 mm thick aluminium plate (non-dispersive medium) and a 3.15 mm thick epoxy resin (dispersive medium), excellent agreement being shown between the two methods.

Keywords: material property measurements; ultrasonic dynamic measurements; phase velocity; ultrasonic resonances

Ultrasonic velocity measurements are widely used in non-destructive testing to check elastic constants and to monitor residual stress[1-6]. It is frequently necessary to obtain very accurate velocity values, particularly for stress measurements, since the influence of stress on velocity is relatively small. Measurements can be made in either the time or frequency domains. In the time domain approach, the transit time between two parallel faces of a specimen is determined by the velocity of sound in the tested material and the distance between its boundaries. The major limitation of this technique is the difficulty of resolving the consecutive echoes from the plate when the thickness of the sample is small, and therefore deconvolution theory has recently been applied to enhance the resolution[7]. The time domain technique, however, is unable to cope with dispersive media, where the pulse changes its shape as it propagates, which is the case when some non-metals are to be tested. To cater for these applications, frequency domain techniques have been employed[8].

The first frequency domain methods used to measure phase velocities employed continuous monochromatic waves or narrow band pulses[9]. Subsequently, the application of the Fourier transform of wide band pulses in the experimental determination of phase and group velocities has been discussed[9]. Here the phase spectra of the pulses were used to evaluate the variation of phase and group velocities in the material. Sachse and Pao[9] compared the results obtained using this method with those from the existing narrow band 'π-point' phase comparison technique, where the half-wavelength of a harmonic wave is determined by varying the distance between the transmitting and receiving probe and determining the shift required to change the phase of the receiving signal by π (Reference 9). The experimental results of the two methods showed very good agreement.

However, if it is necessary to measure the phase velocity in a thin layer of, for example, adhesive, it may not be possible to separate the consecutive reflections from its boundaries, making it impossible to use the phase spectrum approach. In this Paper an amplitude spectrum[10-13] method is proposed to evaluate the variation of the phase velocity in dispersive, attenuating media. To compare the amplitude spectrum approach with the existing theories, the phase spectrum method is reviewed and phase velocities are obtained experimentally using both the amplitude and phase spectrum techniques.

Theory

Background

If it is assumed that a harmonic wave propagating in an unbounded medium in a positive direction can be expressed as[8]

$$u(x, t) = A \exp[i(\omega t - kx - \phi)]\exp[-\alpha x] \qquad (1)$$

where A is an arbitrary amplitude, ω is the angular frequency of the wave, k denotes the wave number ($k = \omega/c$, where c is the phase velocity of the harmonic wave and in general can be frequency dependent), ϕ is the phase, and x denotes the decay constant as the wave propagates through the medium. It can be shown that any permissible waveform propagating in a positive direction can be expressed as a linear combination of all harmonic waves of Equation (1)[8], that is

$$u(x, t) = 1/(2\pi) \int_{-\infty}^{+\infty} \left\{ \int_{-\infty}^{+\infty} A(\omega, t) \exp[-i\phi] \, d\phi \right\}$$

$$\times \exp[i(\omega t - kx)] \exp[-\alpha x] \, d\omega \qquad (2)$$

For $x = 0$ the equation above reduces to

$$u(0, t) = 1/(2\pi) \int_{-\infty}^{+\infty} \left\{ \int_{-\infty}^{+\infty} A(\omega, t) \exp[-i\phi] d\phi \right\}$$

$$\times \exp[i\omega t] d\omega \qquad (3)$$

Applying forward and inverse Fourier transforms, the time history $u(0, t)$ at $x = 0$ can be expressed as

$$u(0, t) = 1/(2\pi) \int_{-\infty}^{+\infty} \left\{ \int_{-\infty}^{+\infty} u(0, t) \exp[-i\omega t] dt \right\}$$

$$\times \exp[i\omega t] d\omega \qquad (4)$$

Comparing Equation (3) with Equation (4) it can be seen that the inner integral of Equation (3) must be equal to the Fourier transform of the waveform at $x = 0$, i.e.

$$\int_{-\infty}^{+\infty} A(\omega, t) \exp[-i\phi] d\phi = \int_{-\infty}^{+\infty} u(0, t) \exp[-i\omega t] dt$$

$$= F(u(0, t)) \qquad (5)$$

where F denotes the Fourier transform operator. Therefore Equation (2) takes the form

$$u(x, t) = 1/(2\pi) \int_{-\infty}^{+\infty} F(u(0, t)) \exp[i(\omega t - kx)]$$

$$\times \exp[-\alpha x] d\omega \qquad (6)$$

which can be re-written as

$$u(x, t) = 1/(2\pi) \int_{-\infty}^{+\infty} \left\{ F(u(0, t)) \exp[-ikx] \exp[-\alpha x] \right\}$$

$$\times \exp[i\omega t] d\omega \qquad (7)$$

Using the same argument as in Equation (4), the expression in curly brackets is the Fourier transform of $u(x, t)$ so finally

$$F(u(x, t)) = F(u(0, t)) \exp[-ikx] \exp[-\alpha x] \qquad (8)$$

An expression of this form was obtained by Sachse and Pao in reference 9.

The phase spectrum approach

Sachse and Pao[9] presented a method of obtaining the phase velocity of a wave from two separate measurements. For the first measurement, two transducers operating in through transmission mode were placed in intimate face-to-face contact to obtain a reference phase spectrum. For the second measurement, one transducer was positioned on each face of the test specimen to find the phase spectrum of the pulse propagating through the material. The phase velocity was then calculated from the difference between these two phase spectra.

A minor modification of this technique is to use a single transducer, working in pulse-echo mode at normal incidence, to excite a specimen immersed in water. In this case, the phase spectrum of the reflection the front face can be taken as a reference, and may be used with the first reflection from the back face to calculate the phase velocity. The time history of the signal reflected from a
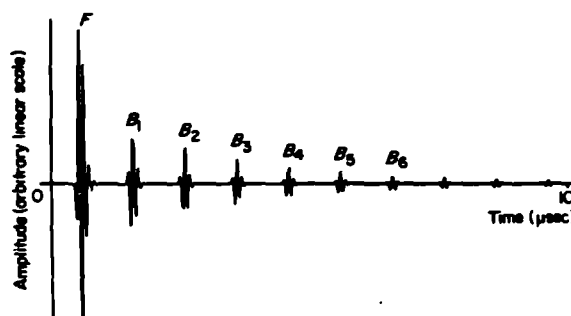
Figure 1 Response of 3.2 mm thick aluminium plate to pulse at normal incidence. F is the front face reflection and B, are successive reflections from the back face

plate of thickness L consists of the reflection from the front face of the plate followed by a family of consecutive reflections from the back of the specimen (see Figure 1). The time-lag between two consecutive reflections is determined by twice the thickness of the plate as the wave has to traverse the specimen twice to be received back by the probe. The front face reflection is out of phase with the reflections from the back of the specimen because the impedance of the tested material is higher than the impedance of water.

Consider the face reflection and the first reflection from the back of the specimen. If the first reflection from the back of the plate is denoted as $u(0, t)$, then the front face reflection can be expressed as

$$U(t) = -qu(-2L, t); \qquad q > 0 \qquad (9)$$

where q is a real constant and the minus sign accounts for the change of phase of the front face reflection with respect to the reflections from the back of the plate. From Equation (8) the Fourier transform of the front face reflection is given by

$$F(U(t)) = F(-qu(-2L, t)) = -qF(u(0, t))$$

$$\times \exp[ik2L] \exp[\alpha 2L] \qquad (10)$$

where $\alpha 2L$ represents the apparent damping of the system 'seen' from the point of view of the receiving probe. The apparent damping is not only dependent on the attenuation of the wave within the plate, but also on the impedance of the tested material compared with that of the media on both sides of the specimen. In many cases (e.g. aluminium or glass plates immersed in water) the attenuation of the wave within the test piece is negligible compared with the loss due to transmission into the medium behind the plate, and since the transmission coefficient is frequency independent it is reasonable to assume that the apparent damping coefficient, α, is constant with frequency. If $Q = q \exp[\alpha 2L]$

$$F(U(t)) = -QF(u(0, t)) \exp[ik2L] \qquad Q > 0 \qquad (11)$$

Therefore

$$F(u(0, t)) = |F(u(0, t))| \exp[i\phi] \qquad (12)$$

where $|F(u(0, t))|$ is the amplitude spectrum of the first back face reflection, and ϕ is the corresponding phase spectrum. From Equation (11) the Fourier transform of the front face reflection can be expressed as

$$F(U(t)) = -QF(u(0, t)) \exp[ik2L]$$

$$= |QF(u(0, t))| \exp[i\phi_0] \qquad (13)$$

where $|QF(u(0, t))|$ is the amplitude spectrum of the front face reflection, and $\phi_0 = \phi + 2kL + \pi$ is the corresponding phase spectrum. The constant π in the expression for ϕ_0 appears because the front face reflection is out of phase with the back face reflection. To remove this constant, the front face reflection can be multiplied in the time domain by -1 and the Fourier transform $F(-U(t))$ rather than $F(U(t))$ can be calculated in Equation (13). The difference in the phase spectra of these two reflections is then $\Delta\phi = \phi_0 - \phi = 2kL = 2L\omega/c$, so finally the phase velocity can be calculated from[9]

$$c = 2L\omega/\Delta\phi \qquad (14)$$

Amplitude spectrum approach

An alternative technique using the amplitude spectrum has been developed, which overcomes the requirement for the separation of successive pulses in the time domain. The analytical derivation of the equation from which the phase velocity can be evaluated is presented below in two stages. First, the spectrum of the front face reflection and the first back face reflection alone is discussed. Then the whole time history received from the tested specimen (the front face reflection and the family of the back face reflections) is analysed, and the equation for the determination of the phase velocity is derived.

Front face and the first back face reflection only. The time history consisting of the front face and the first back reflection from the tested plate can be expressed as $U(t) + u(0, t)$. Therefore, from Equations (12) and (13), the Fourier transform of the sum of the two reflections can be written as

$$F\{u(0, t) + U(t)\} = |F(u(0, t))|\{\exp[i\phi]$$
$$- Q \exp[i(\phi + k2L)]\}$$
$$= |F(u(0, t))|(1 - Q \exp[ik2L])$$
$$\times \exp[i\phi] \qquad (15)$$

From Equation (15) it can be seen that the amplitude spectrum is $|F(u(0, t))|(1 - Q \exp[ik2L])$, so if $|F(u(0, t))|$ is a slowly varying function of frequency then, since Q is a positive constant, the minima of the amplitude spectrum will occur when $\exp[ik2L] = 1$, that is when

$$2L\omega/c = 2\pi m; \qquad m = 0, 1 \ldots \qquad (16)$$

If the frequency of a minimum is measured and the index, m, of the minimum is known, it is possible to determine the phase velocity from

$$c = 2L\omega/2\pi m = 2Lf \, m \qquad (17)$$

where $f = \omega/2\pi$. Equation (17) can also be derived directly from Equation (14) by setting $\Delta\phi = 2\pi m$. Comparing the two approaches, it is immediately seen that the phase spectrum method gives an estimate of the phase velocity as a continuous function of frequency, while the amplitude method gives values of phase velocity only at discrete frequencies. Therefore, if good separation of the reflections can be achieved, the phase spectrum approach gives more points on the graph (a continuous function). However, when successive reflections captured by the transducer are superimposed (which can occur when the thickness of the plate is small, or when different families of waves with different velocities are excited, for example when longitudinal and shear waves are present), the amplitude spectrum technique can still extract the

phase velocities. However, in this instance it will not be possible to analyse the front face and the first back face reflection alone since the first back face reflection will not be separated from the subsequent reflections. Therefore it is necessary to consider the complete time history of the received signal.

Front face and all back face reflections. The time history $R(t)$ of the signal received by the transducer can be expressed as the sum of the reflection from the front face and the series of the reflections from the back of the test plate

$$R(t) = U(t) + \sum_{n=0}^{\infty} u(2Ln, t) \qquad (18)$$

Let us concentrate on the second term of Equation (18). From Equation (8) the Fourier transform of the family of reflections from the back of the specimen can be expressed as

$$F\left\{\sum_{n=0}^{\infty} u(2Ln, t)\right\} = \sum_{n=0}^{\infty} F\{u(2Ln, t)\}$$
$$= \sum_{n=0}^{\infty} \{F(u(0, t)) \exp[-ik2Ln]$$
$$\times \exp[\alpha 2Ln]\} \qquad (19)$$

so

$$F\left\{\sum_{n=0}^{\infty} u(2Ln, t)\right\} = F(u(0, t)) \sum_{n=0}^{\infty} \{\exp[-ik2Ln]$$
$$\times \exp[-\alpha 2Ln]\} \qquad (20)$$

Setting $z = \exp[-2L(ik + \alpha)]$, the summation in Equation (20) can be expressed as a geometric series

$$\sum_{n=0}^{\infty} \{\exp[-ik2Ln] \exp[-\alpha 2Ln]\} = \sum_{n=0}^{\infty} z^n \qquad (21)$$

and assuming that $\alpha > 0$ so that $|z| < 1$, which is the requirement for convergence of the geometric series

$$\sum_{n=0}^{\infty} z^n = \lim_{N \to \infty} (1 - z^N)/(1 - z) = (1 - z)^{-1} \qquad (22)$$

The assumption that α is positive means that each consecutive reflection from the back of the specimen is smaller than the previous one, which is the case in reality. From Equations (20) and (22) and putting $k = \omega \, c$

$$F\left\{\sum_{n=0}^{\infty} u(2Ln, t)\right\} = F(u(0, t))$$
$$\times \{1 - \exp[-2L(i\omega \, c + \alpha)]\}^{-1} \qquad (23)$$

From Equation (23) it can be seen that the spectrum of the family of reflections from the back of the test sample is equal to the spectrum of the first reflection multiplied by $\{1 - \exp[-2L(i\omega/c + \alpha)]\}^{-1}$. The term $F(u(0, t))$ characterizes the properties of the pulser-receiver and the probe, while the information about the plate is contained in the term $\{1 - \exp[-2L(i\omega/c + \alpha)]\}^{-1}$.

If it is assumed that the apparent attenuation, α, is independent of frequency, the locus of the points described by the expression $1 - \exp[-2L(i\omega \, c + \alpha)]$ in the complex plane forms a circle with its centre at $Re = 1$, $Im = 0$ and radius, $r = \exp[-2L\alpha]$. Therefore the term $\{1 - \exp[-2L(i\omega \, c + \alpha)]\}^{-1}$ in Equation (23) is the
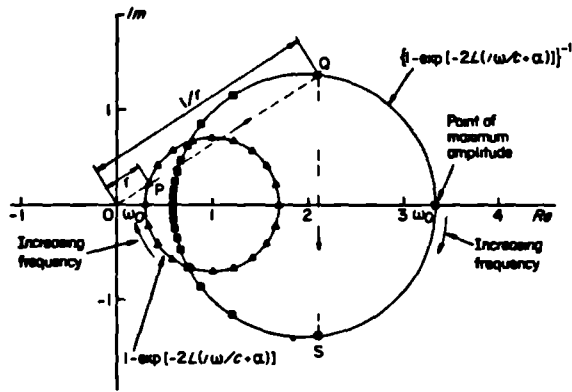
Figure 2 Circle described by expression $1 - \exp[-2L(i\omega/c + \alpha)]$ and its inverse mapping $2L\alpha = 0.7$, $L = 3.2$ mm, $\alpha = 109.4$ m^{-1}, $2\pi k < 2L\omega/c < 2\pi(k + 1)$, $k = 0, 1, \ldots$

inverse mapping of this circle. Since $\alpha > 0$ and $r < 1$, the locus of the circle will never include the origin of the complex plane. Hence the inverse mapping will always transform the circle into another circle. The smaller circle in Figure 2 is the locus of the points described by the term $1 - \exp[-2L(i\omega c + \alpha)]$. The triangles mark the positions of points equally spaced in frequency, with frequency increasing in the clockwise direction. The larger circle is the inverse mapping of the smaller one and is described by the term $\{1 - \exp[-2L(i\omega \alpha)]\}^{-1}$, which characterizes the sum of all the reflections from the back face. Note that points whose frequencies satisfy the equation $2L\omega c - 2\pi k = $ const, $k = 0, 1, \ldots$ appear at the same point on the circle.

In the complex plane, the inverse mapping may be regarded as a change in the magnitude of the position vector of the point from r to $1/r$ followed by reflection about the real axis. Thus, in Figure 2, P is mapped to Q and finally to S. The dotted lines show the geometric construction performed to obtain the inverse mapping so that the points marked by the triangles are mapped into the points marked by the squares. As can be seen from the graph, the loci of the points described by the term $\{1 - \exp[-2L(i\omega c + \alpha)]\}^{-1}$ orbit the circle non-uniformly, the rate of change of phase increasing near points of maximum amplitude. If it is assumed that $|F(u(0, t))|$ is a slowly-varying function of frequency, then the maxima in the amplitude spectrum

$$\left| F\left\{ \sum_{n=0}^{\alpha} u(2Ln, t) \right\} \right|$$

will be defined by the term $\{1 - \exp[-2L(i\omega c + \alpha)]\}^{-1}$ alone.

Hence the peaks in the amplitude spectrum of the Fourier transform of the family of reflections from the back of the plate occur when the circle in Figure 2, describing all the reflections from the back face, crosses the real axis. Therefore the condition for the occurrence of the maxima can be expressed as,

$$\exp[-2Li\omega \ c] = 1 \tag{24}$$

which is equivalent to Equation (16). From Equations (11) and (23) the spectrum of the whole time history captured by the probe including the reflection from the front face can be expressed as

$$F\left\{ \sum_{n=0}^{\alpha} u(2Ln, t) + U(t) \right\} = F(u(0, t))$$

$$\{1 - \exp[-2L(i\omega \ c + \alpha)]\}^{-1} - Q \exp[i2L\omega \ c] \tag{25}$$

The term $Q \exp[i2L\omega \ c]$, characterizing the reflection from the front face in Equation (25), can be visualized in the complex plane as a circle with its centre at the origin and radius Q as seen in Figure 3. The term $\{1 - \exp[-2L(i\omega/c + \alpha)]\}^{-1}$, which was already discussed and plotted in Figure 2, is also shown for convenience in Figure 3. The Fourier transform of the whole time history, calculated from Equation (25), which is the sum of the Fourier transforms of the back face reflections and the front face reflection, forms a kidney-shaped curve in the complex plane (see Figure 3). The points equally spaced in frequency, marked by squares, show that for the majority of the frequency range, the amplitude (which is represented by the radius from the origin of the complex plane) is roughly constant, with rapidly decreasing magnitude near the minimum. Note that the frequencies of these minima correspond to those of the maxima of the spectrum of the reflections from the back face, and therefore satisfy the conditions of Equation (16).

For the condition stated in Equation (16) ($\omega = \pi mc \ L$) the absolute value of the expression in the curly brackets in Equation (25) goes to a minimum value given by

$$\{(1 - \exp[-2L(i\omega \ c + \alpha)])^{-1} - Q \exp[i2L\omega \ c]\}|_{\omega = \pi mc \ L}$$

$$= \{(1 - \exp[-2L\alpha])^{-1} - Q\} \tag{26}$$

From the above equation it can be seen that the depths of the minima depend on the apparent attenuation α of the wave as well as on the relationship, Q, between the amplitudes of the reflections from the front and back faces of the specimen. The value of Q depends on the impedances of the medium between the transducer and the specimen, the tested material and the medium at the back of the plate.

Figure 4 shows the Bode plots of the three terms discussed above, namely $Q \exp[i2L\omega \ c]$ (characterizing the front face reflection), $\{1 - \exp[-2L(i\omega \ c + \alpha)]\}^{-1}$

Figure 3 Nyquist plot of the term $\{1 - \exp[-2L(i\omega \ c + \alpha)]\}^{-1}$ from Equation (23) characterizing the spectrum of all the reflections from the back face and the term $\{1 - \exp[-2L(i\omega/c + \alpha)]\}^{-1} - Q \exp[i2L\omega/c]$ from Equation (25) characterizing the spectrum of the whole time history received from the plate at normal incidence. $2L\alpha = 0.7$, $L = 3.2$ mm, $\alpha = 109.4$ m^{-1}, $Q = 3.4$, $c = 6348$ ms^{-1}, $2\pi k < 2L\omega/c < 2\pi(k + 1)$ $k = 0, 1, \ldots, \omega$, denote equally spaced in frequency

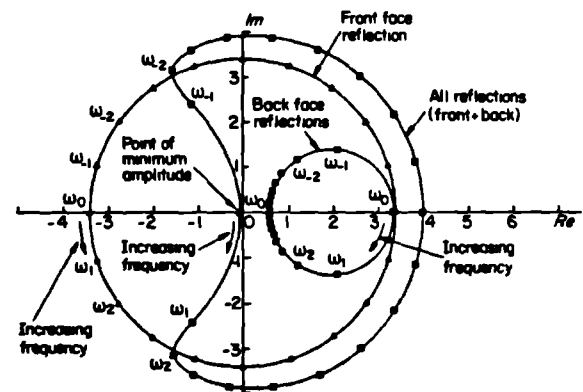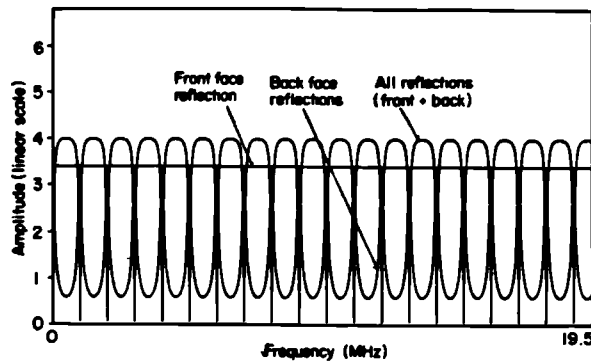Figure 4 The amplitude variation of the term $\{1 - \exp[-2L(i\omega/c+\alpha)]\}^{-1}$ from Equation (23) characterizing the spectrum of all the reflections from the back face and the term $\{1 - \exp[-2L(i\omega/c+\alpha)]\}^{-1} - Q\exp[i2L\omega/c]$ from Equation (25) characterizing the spectrum of the whole time history received from the plate at normal incidence. $2L\alpha = 0.7$, $L = 3.2$ mm, $\alpha = 109.4$ m^{-1}, $Q = 3.4$, $c = 6348$ ms^{-1}

Figure 5 Setup to perform the measurements

(characterizing the sum of all the reflections from the back face), and their sum (characterizing the whole response from the plate). In *Figure 4* the amplitude of the Fourier transform of the front face reflection becomes a straight horizontal line of amplitude Q. The spectrum of all the reflections from the back face shown in *Figure 4* produces a family of maxima, whose sharpness depends on the apparent attenuation of the system, and whose spacing depends on the phase velocity, c, of the wave within the tested medium and the distance, L, between its boundaries. The amplitude spectrum of the whole time history from the tested plate (see *Figure 4*) produces a family of minima, which occur at the same frequencies as the maxima of the Fourier transform of the reflections from the back of the plate. Therefore, when the Fourier transform of the time history including the front face reflection is known, the phase velocity can be calculated from Equation (17), the frequencies being those where the amplitude spectrum is a minimum.

Experiments

Equipment

To compare the amplitude spectrum method with the phase spectrum technique, three experiments were carried out. As an example of a non-dispersive medium, a 3.2 mm thick aluminium plate was taken. Then, to investigate the variation of phase velocity with frequency in a dispersive material, a 3.15 mm thick sample of epoxy resin (Ciba-Geigy MY750) modified by ATBN rubber was examined. In the third test, to show the application of the amplitude spectrum method to data in which the front and back face reflections could not be separated, a 0.40 mm thick steel shim was used.

The setup used for the test was similar to that described in reference 14 and is shown schematically in *Figure 5*. The ultrasonic transducer (10 MHz Rolls Royce MatEval, unfocussed) was excited by a Panametrics 5052 PRX75 pulser-receiver. The time history received by the same transducer was amplified in the pulser-receiver unit and digitized at a 50 MHz sampling rate using the LeCroy 9400 oscilloscope. The signal captured by the oscilloscope was averaged 50 to 100 times to improve the signal-to-

noise ratio. To perform an FFT of the captured waveform, the time data was passed via a Hewlett Packard 9816 microcomputer to a B&K 2033 High Resolution Spectrum Analyser. The time record consisted of between 1000 and 2500 points at a 50 MHz sampling rate from the oscilloscope, which were padded with zeros to form a 10240-point data record. The complex spectrum from the spectrum analyser was then transferred back to the microcomputer to carry out the necessary calculations.
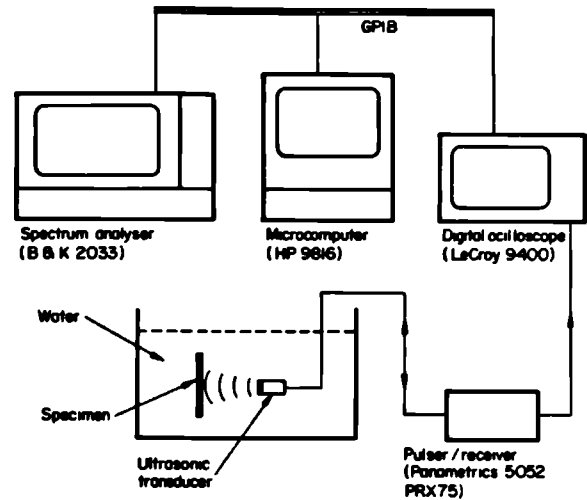
Aluminium plate

To test the new method on a non-dispersive material, a 3.2 mm thick aluminium plate was examined. *Figure 1* shows the time history of the captured signal. The time-lag between the consecutive reflections is determined by the distance between the front face and the back face of the test plate and the velocity of sound in the material. *Figure 6* shows the amplitude spectra of the front face reflection and the train of the back face reflections from *Figure 1*. The variation in the amplitude spectrum of the front face reflection (corresponding to Equation (11)) characterizes the property of the pulser-receiver and the probe and the impedances of water and aluminium. The

Figure 6 Spectra of the front face reflection and the family of the reflections from the back face from the 3.2 mm thick aluminium plate The mode numbers of the longitudinal modes are indicated on the spectrum of the back face reflection The time domain response is shown in *Figure 1*

plot reaches its maximum value at a frequency of ≈ 10 MHz, which is in agreement with the specification of the probe used for the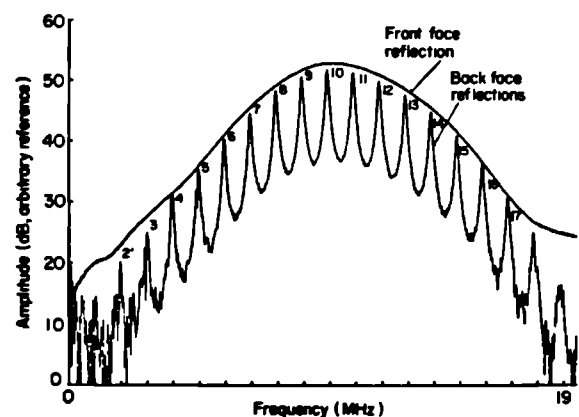 experiment. The amplitude spectrum of the reflections (corresponding to Equation (23)) follows the same trend as the front face reflection, with the superposition of a series of maxima (corresponding to the term $\{1 - \exp[-2L(i\omega/c + \alpha)]\}^{-1}$ in Equation (23)). The double peaks seen in *Figure 6* at frequencies of about 3, 5 and 7 MHz are caused by the presence of shear modes in the plate due to the generation of edge waves by the probe. This phenomenon is discussed in detail elsewhere[14]. *Figure 7* shows the amplitude spectrum of the whole time-response from *Figure 1*. The minima in *Figure 7* occur at the same frequencies as the maxima of the amplitude spectrum of the reflections from the back face shown in *Figure 6*.

Equation (23) shows that the ratio of the amplitude spectrum of the reflections from the back face of the specimen to that of the front face reflection is given by

$$F\left\{ \sum_{n=0}^{\infty} u(2Ln, t) \right\} / F(U(t))$$

$$= \{1 - \exp[-2L(i\omega/c + \alpha)]\}^{-1} Q^{-1} \qquad (27)$$

and Equation (25) shows that the ratio of the amplitude spectrum of all reflections to that of the front face reflection is given by

$$F\left\{ \sum_{n=0}^{\infty} u(2Ln, t) + U(t) \right\} / F(U(t))$$

$$= (\{1 - \exp[-2L(i\omega/c + \alpha)]\}^{-1}$$

$$- Q \exp[i2L\omega/c])Q^{-1} \qquad (28)$$

Figure 8 shows the experimentally determined ratios of the spectra from the data of *Figures 6* and *7*, while *Figure 4* shows the theoretically computed plots of the terms $\{1 - \exp[-2L(i\omega\ c + \alpha)]\}^{-1}$ and $\{1 - \exp[-2L(i\omega c + \alpha)]\}^{-1} - Q \exp[i2L\omega\ c]$ using values of L, c and α appropriate to a 3.2 mm thick aluminium plate immersed in water. There is a good agreement between the form of the two diagrams; the noise seen at high and low frequencies in *Figure 8* is due to the low signal levels produced by the transducer in these regions (see *Figure 6*).

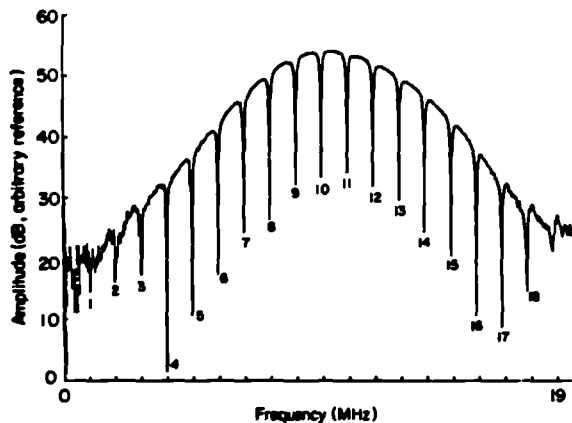The points on *Figure 9* show the phase velocities calculated from Equation (17) for each of the minima in

Figure 7 Spectrum of the whole time history (front face and the all back face reflections) shown in *Figure 1* Mode indices of the longitudinal modes are shown
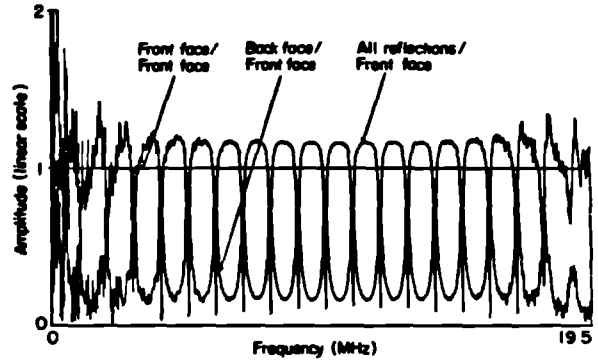

Figure 8 Division of the spectrum of the reflections from the back face by the spectrum of the front face reflection, corresponding to Equation (27), and division of the spectrum of the whole time history by the spectrum of the front face reflection, corresponding to Equation (28)
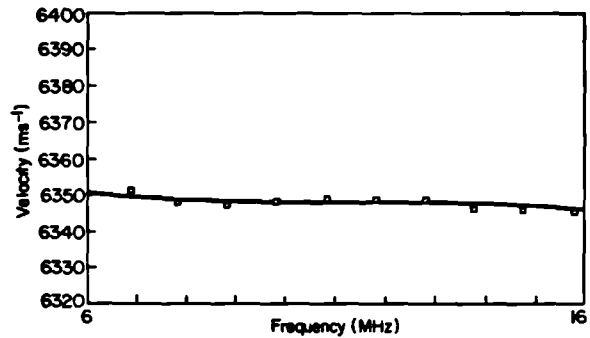
Figure 9 Measured phase velocity in 3.2 mm thick aluminium plate Comparison between the phase spectrum (solid line) and amplitude spectrum (discrete points) technique

Figure 7 and so indicate the relationship between phase velocity and frequency. As expected, since aluminium is non-dispersive, there is very little variation of phase velocity with frequency. The phase velocity was then calculated using the phase spectrum technique. This was achieved by gating out the front face and first back reflections in turn and computing their spectra. The phase spectrum of each reflection is then given by

$$\phi(\omega) = \arctan(Im(\omega)\ Re(\omega)) - 2\pi m \qquad (29)$$

where $Im(\omega)$ and $Re(\omega)$ are the imaginary and real parts of the spectrum and m is an integer, which increases with frequency to give a continuous phase spectrum. This presents no problem if reliable data are obtained at low frequencies since m can be taken as zero at zero frequency and can be indexed at each successive discontinuity in $\arctan(Im(\omega)\ Re(\omega))$ as the frequency is increased. However, if noise is present in the lower frequency range, as is usually the case (see *Figure 6*), this procedure is unreliable and the appropriate value of m at the start of the usable frequency range of the probe must be estimated by considering the frequency spacing of the discontinuities in the region of high signal-to-noise ratio. This procedure is satisfactory provided that the variation of phase velocity with frequency is modest. Another way of obtaining an appropriate value of m is to use the amplitude spectrum approach to find phase velocity values at discrete points and then to use the phase spectrum technique to determine more data points in the frequency range where the signal-to-noise ratio is satisfactory.

The solid curve in *Figure 9* shows the phase velocities calculated using the phase spectrum technique. There is excellent agreement between the two methods, the maximum difference between them being under 0.1%. From Equation (17) it can be seen that the error in the velocity calculation is dependent upon the errors in the measurements of the plate thickness and the resonant frequencies. The determination of the resonant frequencies depends on the frequency resolution, Δf, of the spectrum. In the experiment, $\Delta f = 4.88$ kHz giving a velocity error due to frequency resolution of $\pm 15.4/m$ (ms^{-1}), where m is the mode number. The plate thickness was measured with an uncertainty, $\Delta L \approx 0.005$ mm leading to a velocity uncertainty of ± 5 m s^{-1}, so the overall uncertainty was $\pm (15.4/m + 5)$ ms^{-1}.

3.15 mm thick resin plate

A similar procedure was applied to measure the phase velocity in a 3.15 mm thick epoxy resin plate (Ciba-Geigy MY750 modified by 15% ATBN rubber, HYCAR 1300 × 16 manufactured by BF Goodrich Chemical UK). *Figure 10* shows the time history of the response from the plate. In this test, to enhance the strength of the signal reflected from the back face, the plate was air-backed. This was achieved by bonding a thin walled cylindrical cap to the reverse side of the specimen at the test position. Transmission losses into the water when the specimen was immersed were then greatly reduced. *Figure 11* shows the amplitude spectra of the front face reflection and of the family of the back face reflections. Here it can be seen
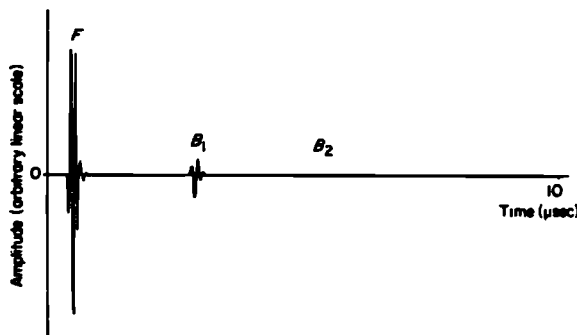
Figure 10 Response of 3.15 mm thick epoxy resin sample to pulse at normal incidence. *F* is the front face reflection and *B₁* are successive reflections from the back face
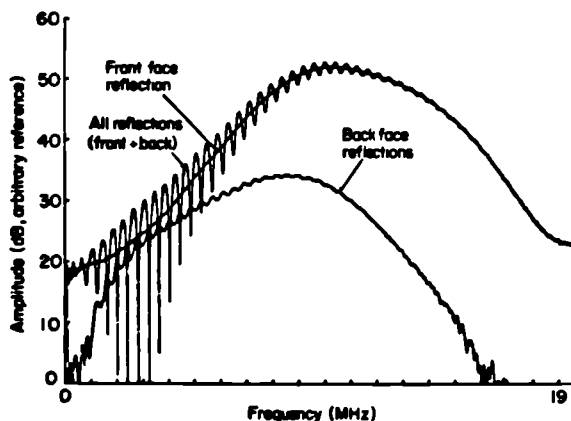
Figure 11 Spectra of the front face reflection, the family of reflections from the back face and the whole time response of 3.15 mm thick epoxy resin plate. Time response is shown in *Figure 10*

that the apparent attenuation of the wave is no longer constant and increases with frequency. Indeed, in the low frequency region (1.5 to 5.5 MHz), the two amplitude spectra are of roughly the same amplitude, while as the frequency goes higher, the two plots diverge substantially. This is in contrast with the experiment with the aluminium plate, where the amplitude spectrum of the reflections from the back face followed the same trend as the amplitude spectrum of the front face reflection (see *Figure 6*), producing the series of minima of similar depths (see *Figure 7*) throughout the whole working frequency range of the transducer used.

When the Fourier transform of the whole time response of the resin plate is performed (see *Figure 11*), the deepest minima occur in the range between ≈ 1.5 and 5.5 MHz, that is when the amplitude spectrum of the family of the back face reflections is nearly equal to the amplitude spectrum of the front face reflection, and in this frequency range the phase velocity can be calculated from Equation (17) with little error. At higher frequencies the accurate determination of the frequencies of the minima is more difficult. To obtain sharper minima in the higher frequency region, it is possible to divide the amplitude of the front face reflection or to multiply the back face reflections by a real constant (in the time domain) to reduce the differences between the Fourier transforms of the front face reflection and the family of reflections from the back face.

Figure 12 shows the FFT of the edited signals. Here it can be seen that it is possible to highlight the different ranges of the spectrum by means of simple multiplications or divisions of the different reflections from the test plate in the time domain. Multiplication of the back face reflections is equivalent to the division of the front face reflection by the same constant. For example, multiplication of the back face reflections by 24 or division of the front face reflection by 24 would have a similar effect to multiplication of the back face reflection by 6 and division of the front face reflection by 4 (which can be more convenient when, for example, the waveform in the computer is represented in integer form). The validity of this approach is demonstrated in the Appendix. In practice, the multiplication or division is achieved by a multiplication of the reflection of interest by a window function[15].

Figure 13 shows the variation of the phase velocity calculated from Equation (17) together with the

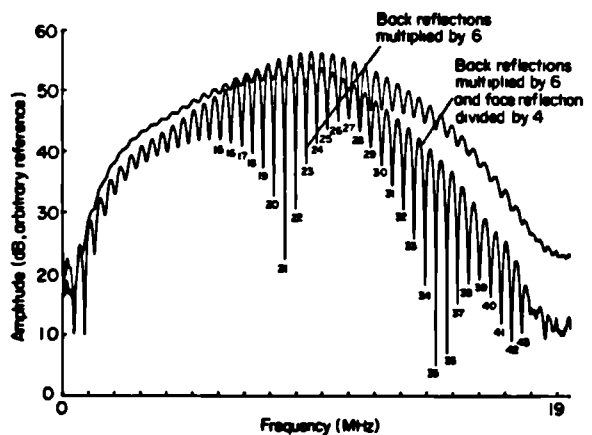**Figure 12** Spectra of the edited time history from *Figure 10* Mode numbers of longitudinal modes are shown
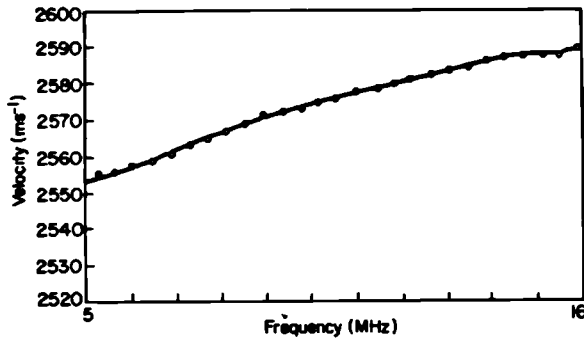
Figure 13 Measured phase velocity in 3.15 mm thick epoxy resin plate. Comparison between. —, phase spectrum, ○, amplitude spectrum method

Figure 14 Response of 0 40 mm thick steel shim to pulse at normal incidence

corresponding plot obtained using the phase spectrum technique. Again, there is excellent agreement between the two methods. The variation of the phase velocity with frequency in *Figure 13* indicates that the epoxy resin is weakly dispersive. In the experiment, the frequency resolution of the spectrum, $\Delta f = 4.88$ kHz and the plate thickness measurement uncertainty, $\Delta L = 0.005$ mm, giving an overall velocity uncertainty of $\pm(15.4/m + 2)$ ms^{-1}, where m is the mode number.

Steel shim

To test the amplitude spectrum method for the case when the different reflections are superimposed, a 0.40 mm thick steel shim was used. *Figure 14* shows the response of the shim when excited by the 10 MHz transducer used in the earlier tests. From the plot it can be seen that it is impossible to distinguish between the reflections, while in the frequency domain (see *Figure 15*) the minima give the opportunity to extract the required phase velocity if the thickness of the plate is known. *Table 1* shows the results obtained from *Figure 15* using Equation (17).

The Table shows that it is still possible to obtain the variation of the phase velocity with frequency though the points are widely spaced in frequency.

Conclusions

It has been shown that the phase velocity of a given wave can be accurately measured using the amplitude spectrum technique. One of the biggest advantages of this method over the phase spectrum method[9], is that measurements can be obtained even when successive reflections from the boundaries of the plate cannot be separated in the time domain. The method will therefore be particularly useful when a thin layer of, for example adhesive, must be tested. Excellent agreement between the amplitude spectrum and phase spectrum methods was obtained on both non-dispersive and dispersive materials when the specimens were sufficiently thick for the different echoes to be separated. In cases when the different reflections from the test specimen can be separated, the phase spectrum technique is advantageous because many more data points are computed. This facilitates the calculation of group velocity since this effectively requires differentiation of the phase velocity with respect to frequency[9]. However, it has been shown that the implementation of the phase spectrum technique is difficult when the signal-to-noise ratio is poor in the low frequency region. It is therefore suggested that a combination of the two methods may
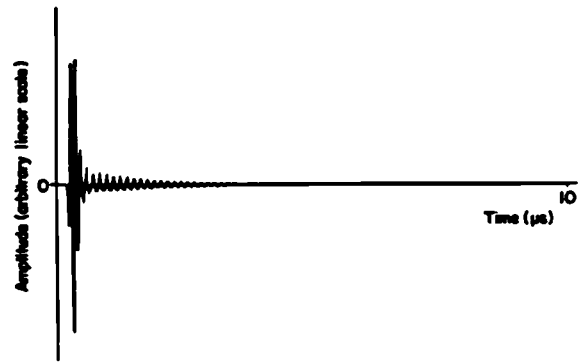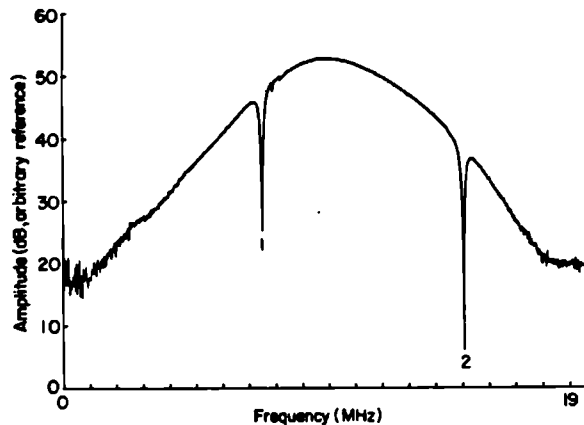
Figure 15 Spectrum of the time history shown in *Figure 14* The mode numbers of the longitudinal modes are shown

Table 1 Phase velocity calculated from *Figure 15*

Index of minimum	Frequency (MHz)	Phase velocity (ms^{-1})
1	7.510	6008
2	15 068	6027

give satisfactory results. Firstly the amplitude spectrum technique can be used to determine values of the phase velocity at discrete points, then the phase spectrum method can be applied to obtain more data points in the region of frequencies where the signal-to-noise ratio is adequate to obtain a continuous phase spectrum without ambiguity.

References

1 Vary, P. Ultrasonic Measurement of Material Properties. In: *Research Techniques in Nondestructive Testing* Vol 4 (1980) Academic Press. London. UK

2 Shreiber, E., Anderson, O.L. and Soga, N. *Elastic Constants and Their Measurements* McGraw-Hill, New York (1973)

3 Klinman, R. and Stephenson, E.T. Ultrasonic Prediction of Grain Size and Mechanical Properties in Plain Carbon Steel *Materials Evaluation* (1981) **39** 1116–1120

4 Papadakis, E.P. Ultrasonic Velocity and Attenuation Measurements Methods with Scientific and Industrial Applications. *Physical Accoustic Principles and Methods* Academic Press, New York, USA (1976) Vol. 12, 277–374

5 Crecraft, D.I. Ultrasonic measurement of stress *Ultrasonic Testing* John Wiley & Sons (1982) 437–458

6 Thompson, R.B., Smith, J.F. and Lee, S.S. Microstructure-

independent acoustoelastic measurement of stress *Appl. Phys. Lett.* (1984) **44** 296–298

7   Hayward, G. and Lewis, J.E. A Theoretical Approach for Inverse Filter Design in Ultrasonic Applications *IEEE Trans* in press

8   Brekhovskikh, L.M. *Waves in Layered Media* Academic Press, New York (1980)

9   Sachse, W. and Pao, Y.-H. On determination of phase and group velocities of dispersive waves in solids *J. Appl. Phys.* (1978) **49** 4320–4327

10   Bell, J.C. and Haines, N.F. Measuring corrosion layers on inaccessible surfaces *Ultrasonics* (1974) **12** 237

11   Haines, N.F., Bell, J.C. and McIntyre, P.J. The application of broadband ultrasonic spectroscopy to the study of layered media *J. Acoust. Soc. Am* (1978) **64** 1645–1651

12   Cheriff, M., Izhicki, J.L., Maze, G. and Ripoche, J. The influence of Resonances in Plane Multilayer Structures Immersed in Water *Acustica* (1987) **64** 180–187

13   Guyott, C.C.H. and Cawley, P. The ultrasonic vibration characteristics of adhesive joints *J. Acoust. Soc. Am.* (1988) **83** 632–640

14   Guyott, C.C.H. and Cawley, P. The measurement of through thickness plate vibration using a pulsed ultrasonic transducer *J. Acoust. Soc. Am.* (1988) **83** 623–631

15   Randall, R.B. *Application of B&K Equipment to Frequency Analysis* Bruel & Kjaer (1977)

16   Bracewell, R. *The Fourier Transform and Its Applications* McGraw-Hill (1965)

Appendix

Position of minima in amplitude spectrum when the apparent damping is frequency dependent

Consider the Fourier transform of the family of the back face reflections. From Equation (20) we have

$$F\left\{\sum_{n=0}^{\infty} u(2Ln, t)\right\} = F(u(0, t)) \sum_{n=0}^{\infty} \{\exp[-ik2Ln] \times \exp[-\alpha 2Ln]\} \quad (20)$$

where both k and α are now frequency dependent functions. Variation of k with frequency effectively means that the points forming the smaller circle shown in *Figure 2* will not be equally spaced, but the radius of the circle will remain the same. Therefore the shape of the inverse mapping of this circle, shown in the same figure, will be also unchanged. When α is frequency dependent, the circle shown in *Figure 2* will be distorted to a spiral, which will be of decreasing radius if α increases with frequency. It is necessary to check whether the minumum condition stated in Equation (16) still holds for this case. To simplify the calculations, the spectra of the front and the back reflections will be expanded as a first order polynomial (the first two terms of the Taylor series) in the vicinity of the frequency for which the condition stated in Equation (16) is satisfied. Next the difference between the expansions will be evaluated to determine the position of the minimum.

Let us first calculate the values of the Fourier transforms of the front and back reflections at the points satisfying condition in Equation (16), that is $\exp[ik2L] = 1$. Putting $F(u(0, t)) \approx 1$, as this term is of no importance here, from Equations (11) and (23), the front and back reflections can be written as

$$F(U(t))_{\omega - \pi\pi c \, L} = -Q \quad (30)$$

$$F\left\{\sum_{n=0}^{\infty} u(2Ln, t)\right\}_{\omega - \pi\pi c \, L} = \{1 - \exp[-2L\alpha]\}^{-1} \quad (31)$$

where $m = 0, 1, \ldots$ and

$$Q = q \exp[-2L\alpha] \qquad q > 0 \quad (32)$$

Now let us calculate the frequency derivative of $F\left\{\sum_{n=0}^{\infty} u(2Ln, t)\right\}$. Putting $F(u(0, t)) \approx 1$ and setting

$$B(\omega) = \sum_{n=0}^{\infty} \{\exp[-ik2Ln] \exp[-\alpha 2Ln]\}$$

$$\begin{aligned} dB/d\omega = -\sum_{n=0}^{\infty} \{ &\exp[-ik2Ln] \exp[-\alpha 2Ln] \\ &\times 2Ln(i \, dk/d\omega + d\alpha/d\omega)\} \end{aligned} \quad (33)$$

Now setting $b = \exp[-ik2L] \exp[-\alpha 2L]$, the equation above can be expressed as

$$dB/d\omega = -2L(i \, dk/d\omega + d\alpha/d\omega) \sum_{n=0}^{\infty} (nb^n) \quad (34)$$

The polynomial $\sum_{n=0}^{\infty} (nb^n)$ is the z transform[16]

$$F(z) = \sum_{n=0}^{\infty} (f(n)z^{-n}) = z^{-1}/(1 - z^{-1})^2 \quad (35)$$

where $z = b^{-1}$ and $f(n) = n$. Therefore

$$\sum_{n=0}^{\infty} (nb^n) = b/(1 - b)^2 \quad (36)$$

Equation (34) can now be expressed as

$$\begin{aligned} dB/d\omega = -2L(i \, dk/d\omega + d\alpha/d\omega) \exp[-ik2L] \\ \times \exp[-\alpha 2L]/(1 - \exp[-ik2L] \\ \times \exp[-\alpha 2L])^2 \end{aligned} \quad (37)$$

For the condition stated in Equation (16), $\exp[-ik2L] = 1$, and Equation (37) becomes

$$\begin{aligned} dB/d\omega = -2L(i \, dk/d\omega + d\alpha \, d\omega) \exp[-\alpha 2L] \\ /(1 - \exp[-\alpha 2L])^2 \end{aligned} \quad (38)$$

The frequency derivative of the Fourier transform of the front face reflection can be evaluated from Equation (10). Putting $F(u(0, t)) \equiv 1$, as before

$$\begin{aligned} d\{F(U(t))\} \, d\omega = d(-q \exp[\alpha 2L] \exp[ik2L]) \, d\omega \\ = -q \exp[\alpha 2L] \exp[ik2L] \\ \times 2L(i \, dk/d\omega + d\alpha \, d\omega) \end{aligned} \quad (39)$$

For the condition stated in Equation (16), $\exp[ik2L] = 1$, and the equation above becomes

$$\begin{aligned} d\{F(U(t))\} \, d\omega_{\omega - \pi\pi c \, L} = -q \exp[\alpha 2L]2L(i \, dk \, d\omega \\ + d\alpha \, d\omega) \end{aligned} \quad (40)$$

Figure A1 shows the Nyquist plot of the Taylor expansions of the front and the back reflections. This is effectively an expanded version of *Figure 3* in the vicinity of the point where the front face reflection and the family of the back face reflections cross the real axis for the case when the apparent damping of the system, α, increases with frequency ω. The notation used in *Figure A1* is as follows

$$V_{Br} = -2LP \, d\alpha \, d\omega; \quad V_{Bt} = -2LP \, dk \, d\omega;$$

$$V_{Fr} = -2LQ \, d\alpha \, d\omega; \quad V_{Ft} = -2LQ \, dk \, d\omega \quad (41)$$

where V_{Br} and V_{Bt} are the radial and tangential components of the back face spectrum derivative; V_{Fr}, V_{Ft}, are the radial and tangential components of the front face spectrum derivative; $P = \exp[-\alpha 2L] (1 - \exp[-\alpha 2L])^2$; $Q = q \exp[-2L\alpha]$; and $D = Q - (1 - \exp[-\alpha 2L])^{-1}$.
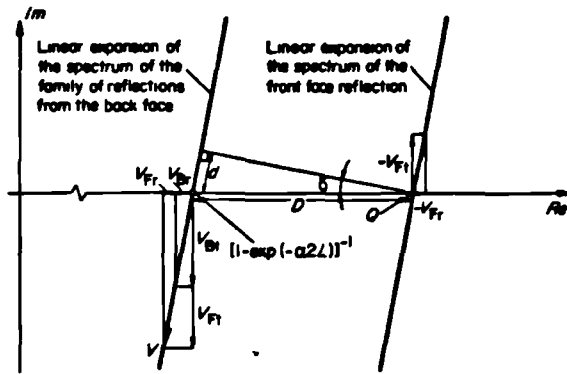
Figure A1 Linear expansions of the reflections from the front face and the family of reflections from the back face

From *Figure A1*

$$\tan \delta = \frac{V_{Br} + V_{Fr}}{V_{Bi} + V_{Fi}} = \frac{d\alpha}{dk}\frac{d\omega}{d\omega} \tag{42}$$

$$d \approx D \tan \delta = [Q - (1 - \exp[-\alpha 2L])^{-1}] \tan \delta \tag{43}$$

$$V = [(V_{Br} + V_{Fr})^2 + (V_{Bi} + V_{Fi})^2]^{1/2} \tag{44}$$

$$d = -V \Delta \omega \tag{45}$$

where $\Delta \omega$ denotes the frequency error between the points where the minimum of the difference between the linear expansions occurs and the points where the condition in Equation (16) is satisfied. After simple conversions, it may be shown that

$$\Delta \omega = \frac{d\alpha}{dk}\frac{d\omega}{d\omega}\frac{[(1 - \exp[-\alpha 2L])^{-1} - Q]}{2L(P + Q)[(d\alpha\ d\omega)^2 + (dk/d\omega)^2]^{1/2}} \tag{46}$$

If it is assumed that $d\alpha/d\omega > 0$, then the sign of the error function, $\Delta \omega$, is defined by the sign of the term in the square brackets in the numerator, that is by the sign of the difference between the amplitude spectra of the front face reflection and that of the family of the back reflections. Therefore, when the amplitude spectrum of the back face reflections is greater than the amplitude spectrum of the front face reflection, the shift $\Delta \omega > 0$ occurs, which means that the velocity will be overestimated if Equation (17) is used. In the case when $(1 - \exp[-\alpha 2L])^{-1}$ is less than Q, the shift $\Delta \omega < 0$ occurs, which means that the velocity will be underestimated if Equation (17) is used. If the amplitudes of both spectra are equal, then the numerator of Equation (46) equals zero, and $\Delta \omega = 0$. From our previous calculations (see Equation (26)) it is known that this is the requirement for the deepest minima. Therefore the deeper the minima the better the estimation of the phase velocity from Equation (17). If the attenuation α is independent of frequency, that is when $d\alpha/d\omega = 0$, then Equation (46) reduces to $\Delta \omega = 0$.

Multiplication or division of the amplitude of the front face reflection in the time domain is equivalent to a change of the constant q in Equation (32), which depends on the impedances of the tested material and the media on both sides of the specimen. Therefore, multiplication or division of the front face reflection or of the family of the back face reflections in the time domain is similar to a change of the relationship between the impedances of the elements of the system under test. It is therefore valid to adjust the relative sizes of the different reflections by multiplication or division to obtain sharper minima in the amplitude spectrum, and so to improve the accuracy of the determination of the frequencies, and also to reduce the error term $\Delta \omega$.

Appendix B

Phase velocity and attenuation of the shear wave in viscous fluids

The phase velocity and the attenuation of the shear wave in a viscous fluid can be readily obtained by substituting the plane wave equation into the constitutive equation.

In a viscous fluid the one-dimensional constitutive equation for shear stresses can be written as (see for example Malvern 1969),

$$\tau = \eta \frac{\partial}{\partial x} \left(\frac{\partial u}{\partial t} \right) , \tag{B.1}$$

where τ is the shear stress component in the y direction in the plane perpendicular to the x axis, η is the dynamic viscosity of the liquid, u is the displacement in the y direction, and $\frac{\partial}{\partial x} \left(\frac{\partial u}{\partial t} \right)$ is the gradient of the velocity in the y direction along the x axis (see fig. B.1).

Consider a shear harmonic plane wave propagating along the x axis as shown in fig. B.1. The displacement field for the shear wave is,

$$u(x,t) = e^{i\omega(x\beta^{-1} - t)} , \tag{B.2}$$

where ω is the frequency of the harmonic process, and β characterises the phase velocity and damping of the wave. For the harmonic wave described by eqn (B.2), the operator of eqn (B.1) becomes,

$$\frac{\partial}{\partial t} = -i\omega , \tag{B.3}$$

and eqn (B.1) becomes,

$$\tau = -i\omega\eta \frac{\partial u}{\partial x} . \tag{B.4}$$

Equation (B.4) can be also written as,

$$\tau = E \epsilon , \tag{B.5}$$

where,

$$\varepsilon = \frac{\partial u}{\partial x},$$ (B.6)

is the shear strain component in the plane perpendicular to the x axis and acting in the direction of y axis, while E is the shear stiffness of the liquid and is given by,

$$E = -i\omega\eta.$$ (B.7)

Equation (B.5) is the shear stress - shear strain relationship for the viscous fluids, from which the expression for the value of β can be obtained as follows.

The equation of motion for the transverse displacements and shear stresses can be easily obtained by writing the equilibrium equation for the infinitesimal cube and considering the plane stress assumption,

$$\frac{\partial \tau}{\partial x} = \rho \frac{\partial^2 u}{\partial t^2},$$ (B.8)

which states that the transverse acceleration of the liquid volume is caused by the difference in the shear stresses acting on this volume. Now, using the stress-strain equation (B.5), as well as the definition of the shear strain given by eqn (B.6), the equation of motion can be expressed in terms of the displacement field as,

$$E\frac{\partial \varepsilon}{\partial x} = \rho \frac{\partial^2 u}{\partial t^2},$$ (B.9)

and also,

$$\frac{E}{\rho} \frac{\partial u}{\partial x} = \frac{\partial^2 u}{\partial t^2},$$ (B.10)

which, after the substitution of the displacement field u, given by eqn (B.2), provides us with the following equation,

$$\beta^2 = \frac{E}{\rho} = -i\omega\nu,$$ (B.11)

where ν is defined as the kinematic viscosity of the fluid, and is defined as,

$$\nu = \frac{\eta}{\rho},$$ (B.12)

where η is the dynamic viscosity of the fluid. The result of eqn (B.11) can be also obtained directly from eqn (2.18) of chapter 2,

$$\beta^2 = \frac{\mu - i\mu'}{\rho} , \tag{B.13}$$

by setting $\mu' = \omega\eta$, and $\mu = 0$, which is the case for all viscous fluids. From eqn (B.11) the following expression for β can be derived,

$$\beta = \zeta - i\zeta , \tag{B.14}$$

where,

$$\zeta = \frac{1}{2}\omega\nu . \tag{B.15}$$

After the substitution of the eqn (B.14) into eqn (B.2) we have,

$$u(x,t) = e^{i\omega(\frac{x}{2\zeta} - t)} \; e^{-\frac{\omega}{2\zeta} x} , \tag{B.16}$$

The first term of eqn (B.16) is responsible for the propagation of the shear wave, while the second one characterises the attenuation of the wave. From eqn (B.16) it can be seen that the phase velocity of the shear wave is given by,

$$c = 2\zeta = (2\omega\nu)^{1/2} = (4\pi f\nu)^{1/2} , \tag{B.17}$$

where f is the frequency of the shear wave. Equation (B.17) states that the liquid satisfying the Navier-Stokes equation supports the shear plane waves whose phase velocities are an increasing function of the kinematic viscosity of the liquid and the frequencies of the waves in the liquid. The attenuation of the shear wave in nepers per wavelength can be obtained from the second term of eqn (B.16) by setting $x = \lambda$, where λ is the shear wavelength given by,

$$\lambda = \frac{c}{f} . \tag{B.18}$$

Setting $x = 1$ in the argument of the second term of eqn (B.16) and using eqn (B.18) and (B.17), we have,

$$\frac{\omega}{2\zeta}\lambda = 2\pi . \tag{B.19}$$

Equation (B.19) states that all viscous fluids which satisfy the Navier-Stokes equation attenuate shear waves by the constant amount per wavelength. Substituting equations (B.17) and (B.19) into (B.16)the shear wave can be now described as,

$$u(x,t) = e^{i\omega(\frac{x}{c} - t)} \; e^{-2\pi \frac{x}{\lambda}}, \tag{B.20}$$

where the expressions for the wavelength λ and the phase velocity c are given by eqn (B.18) and (B.17).

Example 1

Let us calculate the phase velocity and attenuation of the 10 MHz shear wave in water at the temperature of 20 degrees Celsius.

The kinematic viscosity of water at 20° C is 1 cSt, therefore,

$$\nu = 1 \, cSt = 10^{-6} \, m^2/s \,. \tag{B.21}$$

Using eqn (B.16), for the frequency of 10 MHz the phase velocity can be calculated as,

$$c = (4\pi f \nu)^{1/2} = (4\pi \times 10 \times 10^{6} \times 10^{-6})^{1/2} = 11 \; (m/s). \tag{B.22}$$

By eqn (B.19), the attenuation of the shear wave in nepers per wavelength is equal 2π.

Example 2

The second example is the calculation of the phase velocity and the attenuation of the 10 MHz shear wave in the silicone fluid whose kinematic viscosity is 50 cSt.

Using eqn (B.16), and putting f = 10 E6, and ν = 50.0 E-6, the phase velocity can be calculated as,

$$c = (4\pi f \nu)^{1/2} = (4\pi \times 10 \times 10^{6} \times 50 \times 10^{-6})^{1/2} = 79 \; (m/s). \tag{B.23}$$

By eqn (B.19), the attenuation of the shear wave in nepers per wavelength is equal 2π for all viscous liquids.
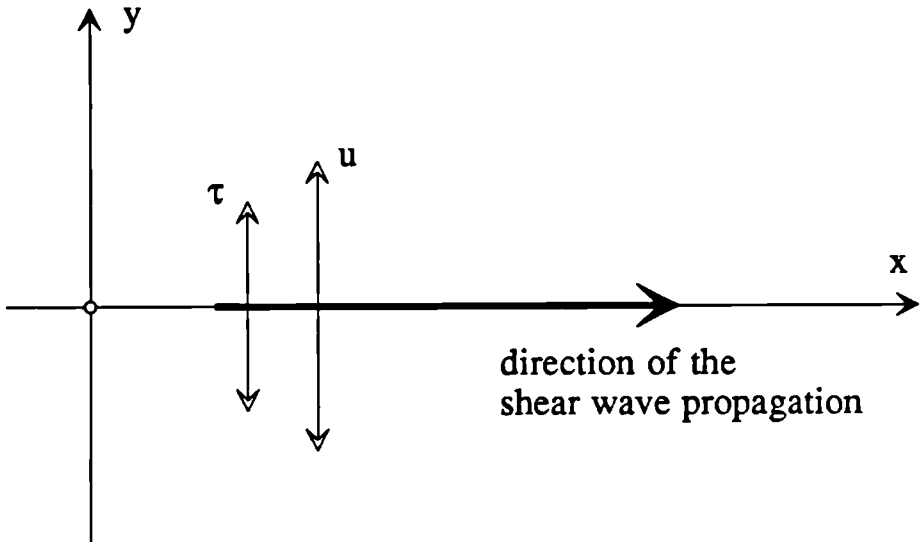
Fig. B1 The stress and displacement fields of the shear wave.

Appendix C

Frequency-thickness product invariance of the wave equation

In problems of reflections from thin layers it is often convenient to consider the variations of parameters with frequency-thickness product rather than frequency and thickness independently. The validity of this approach for all dynamic problems may readily be demonstrated by considering the wave equation, given by eqn (2.4),

$$\mu\nabla^2\bar{u} + (\lambda+\mu)\nabla(\nabla\bullet\bar{u}) + \frac{\mu'}{\omega}\nabla^2\frac{\partial}{\partial t}\bar{u} + \frac{\lambda'+\mu'}{\omega}\nabla(\nabla\bullet\frac{\partial}{\partial t}\bar{u}) = \rho\frac{\partial^2}{\partial t^2}\bar{u} \qquad (C.1)$$

For a harmonic process of frequency ω the time derivative operators become,

$$\frac{\partial}{\partial t} = i\omega, \quad \text{and} \quad \frac{\partial^2}{\partial t^2} = -\omega^2. \qquad (C.2)$$

After substitution of eqn (C.2) into eqn (C.1) we have,

$$\frac{\mu+i\mu'}{\rho}\nabla^2\bar{u} + \frac{(\lambda+\mu)+i(\lambda'+\mu')}{\rho}\nabla(\nabla\bullet\bar{u}) = -\omega^2\bar{u}. \qquad (C.3)$$

Using eqn (2.17) and (2.18), the equation above becomes,

$$\beta^2\nabla^2\bar{u} + \alpha^2\nabla(\nabla\bullet\bar{u}) = -\omega^2\bar{u}. \qquad (C.4)$$

Equation (C.4) can be used as a general equation of motion for any continuous mechanical medium. The mechanical property of the medium is characterised by two functions α and β which, in general, are continuous functions in space and can be frequency dependent.

Let us consider two mechanical systems, one being a scaled-down version of the other (see fig C.1). Each of these systems has its own coordinate system, again, one being a scaled-down version of the other. If we denote the first coordinate system as (x_1, x_2, x_3), and the second system as (y_1, y_2, y_3) then the relationship between these two coordinate systems is,

$$\bar{y} = s\bar{x}, \qquad (C.5)$$

where s is the scaling factor. For example if we measured the distance in inches using the $\bar{x}$ coordinate system, and in millimetres using the $\bar{y}$ coordinate system, then s = 25.4 .

If we furthermore assume that both mechanical systems are built from the same material then α and β are the same in both systems. From equations (2.17), (2.18) it can be seen that,

$$\alpha \text{ and } \beta \quad \text{have units of} \quad \frac{\text{distance}}{\text{time}} \ . \tag{C.6}$$

Units of time are the same in both coordinate systems. Units of distance are different and related by eqn (C.5). Therefore, if we denote variables in the first coordinate system by subscript x, and in the second system by subscript y then, for the same medium in both systems, the relationship is

$$\alpha_y = s\,\alpha_x \ , \text{ and } \quad \beta_y = s\,\beta_x \ . \tag{C.7}$$

Equation (C.7) is always valid when $\omega_x = \omega_y$. If $\omega_x \neq \omega_y$ then we will have to assume that α and β are frequency independent.

Now, we are in position to write equations of motion for the two mechanical systems, each equation being written in its own coordinates.

$$\beta_x^2 \nabla^2 \bar{u} + \alpha_x^2 \nabla(\nabla \bullet \bar{u}) = -\omega_x^2 \bar{u} \ , \tag{C.8}$$

$$\beta_y^2 \nabla^2 \bar{u} + \alpha_y^2 \nabla(\nabla \bullet \bar{u}) = -\omega_y^2 \bar{u} \ , \tag{C.9}$$

Using eqn (C.7) (bearing in mind the assumption about the frequency independence of α and β), eqn (C.9) becomes,

$$\beta_x^2 \nabla^2 \bar{u} + \alpha_x^2 \nabla(\nabla \bullet \bar{u}) = -\omega_y^2 \, s^{-2} \bar{u}. \tag{C.10}$$

In order to yield the same amplitude fields, equations (C.10) and (C.8) have to be the same, which means that the right-hand sides of the equations have to be equal,

$$\omega_y^2 \, s^{-2} = \omega_x^2, \tag{C.11}$$

which means that,

$$\omega_y = s\,\omega_x. \tag{C.12}$$

Equation (C.12) states that in order to maintain the same displacement field in a scaled-down model of a given mechanical system, we have to drive it with a frequency scaled-up by the same scaling factor. For example, if we had a solution of eqn (C.4) for a 10 mm thick plate at a frequency of 1 MHz, then we can immediately obtain the displacement field for a 1 mm thick plate at a frequency of 10 MHz as a scaled-down model version of the first solution, with the scaling factor $s = 10$. The reflection coefficient computed for the 10 mm thick plate at a frequency of 1 MHz is exactly the same as the reflection coefficient for a 1 mm thick plate of the same material at a frequency of 10 MHz (provided that the phase velocity and attenuation per wavelength for longitudinal and shear waves in both systems are frequency independent).

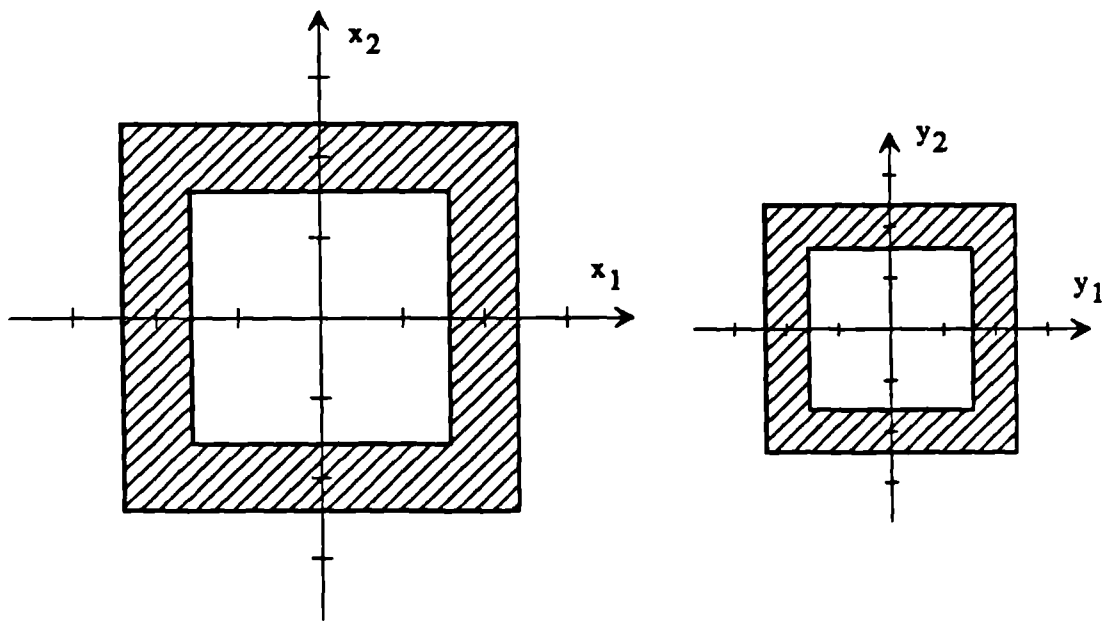Frequency-thickness product invariance of the wave equation

Fig. C1 Two mechanical systems, one being the scaled-down version of the other